

REPORT DOCUMENTATION PAGE				Form Approved OMB No. 0704-0188	
<p>Public reporting burden for this collection of information is estimated to average 1 hour per response, including the time for reviewing instructions, searching existing data sources, gathering and maintaining the data needed, and completing and reviewing the collection of information. Send comments regarding this burden estimate or any other aspect of this collection of information, including suggestions for reducing the burden, to Department of Defense, Washington Headquarters Services, Directorate for Information Operations and Reports (0704-0188), 1215 Jefferson Davis Highway, Suite 1204, Arlington, VA 22202-4302. Respondents should be aware that notwithstanding any other provision of law, no person shall be subject to any penalty for failing to comply with a collection of information if it does not display a currently valid OMB control number.</p> <p>PLEASE DO NOT RETURN YOUR FORM TO THE ABOVE ADDRESS.</p>					
1. REPORT DATE (DD-MM-YYYY) 09-05-2007		2. REPORT TYPE Conference Proceedings		3. DATES COVERED (From - To) 12 March 2007 - 15 March 2007	
4. TITLE AND SUBTITLE Advances on Propulsion Technology for High-Speed Aircraft <i>Volume II</i>				5a. CONTRACT NUMBER FA8655-07-1-5052	
				5b. GRANT NUMBER	
				5c. PROGRAM ELEMENT NUMBER	
6. AUTHOR(S) Conference Committee				5d. PROJECT NUMBER	
				5d. TASK NUMBER	
				5e. WORK UNIT NUMBER	
7. PERFORMING ORGANIZATION NAME(S) AND ADDRESS(ES) von Karman Institute Chaussee de Waterloo 72 Sint Genesius Rode B-1640 Belgium				8. PERFORMING ORGANIZATION REPORT NUMBER N/A	
9. SPONSORING/MONITORING AGENCY NAME(S) AND ADDRESS(ES) EOARD PSC 821 BOX 14 FPO AE 09421-0014				10. SPONSOR/MONITOR'S ACRONYM(S)	
				11. SPONSOR/MONITOR'S REPORT NUMBER(S) CSP 07-5052	
12. DISTRIBUTION/AVAILABILITY STATEMENT Approved for public release; distribution is unlimited. (approval given by local Public Affairs Office)					
13. SUPPLEMENTARY NOTES Volume II					
14. ABSTRACT The Final Proceedings for Advances on Propulsion Technology for High-Speed Aircraft, 12 March 2007 - 15 March 2007 The demand for supersonic vehicles is believed to boost in the incoming years. This VKI/RTO lecture series will review the current state of the art of high speed propulsion for both airplanes and space launchers. Hypersonic air-breathing vehicles technology benefits and challenges will be discussed, with particular attention to the recent hypersonic activities in the USA. Then recommendations for future technology development will be presented. A series of specific talks will address advanced engine technology cycles, pulsed detonation engines and turbine based cycles. A couple of lectures dedicated to rocket engines will discuss turbomachinery issues and recent developments on materials and the combustion chamber. Afterwards, ramjets, scram jets and dual mode operation will be examined. Dedicated sessions will present the experience acquired in recent years in developing advanced demonstrators in the USA, Russia, Australia and the European Union. In the light of existing environmental concerns, the program will be completed with specific sessions on noise generation from high-speed jets and chemical pollution. The requirements to implement a complete hydrogen technology will be analyzed based on the experience gained in the Cryoplane project. The Directors of this VKI/RTO Lecture Series are Prof. G. Paniagua of the von Karman Institute and Prof. J. Steelant of the European Space Agency ESTEC.					
15. SUBJECT TERMS EOARD, Propulsion, Combustion, Hypersonics					
16. SECURITY CLASSIFICATION OF:			17. LIMITATION OF ABSTRACT UL	18. NUMBER OF PAGES	19a. NAME OF RESPONSIBLE PERSON SURYA SURAMPUDI
a. REPORT UNCLAS	b. ABSTRACT UNCLAS	c. THIS PAGE UNCLAS			19b. TELEPHONE NUMBER (Include area code) +44 (0)20 7514 4299

von Karman Institute for Fluid Dynamics
Chaussée de Waterloo, 72
B - 1640 Rhode Saint Genèse - Belgium

RTO-AVT-VKI Lecture Series 2007

**ADVANCES ON PROPULSION TECHNOLOGY
FOR HIGH-SPEED AIRCRAFT**

Volume II

March 12-15, 2007

Edited by: G. Paniagua & J. Steelant
von Karman Institute for Fluid Dynamics, Belgium & ESTEC, France

**Distribution A:
Approved for public release;
distribution is unlimited.**

AQ F08-02-00544

20071113017

RTO-AVT-VKI LS 2007

©2007 by the von Karman Institute

*The contents of this book are the property of the von Karman Institute for Fluid Dynamics.
No part of this book may be reproduced or distributed in any form of by any means, or stored in a
database or retrieval system, without the prior written permission of the von Karman Institute.*

von Karman Institute for Fluid Dynamics

RTO-AVT-VKI Lecture Series 2007

**ADVANCES ON PROPULSION TECHNOLOGY
FOR HIGH-SPEED AIRCRAFT**

March 12-15, 2007

CONTINUOUS DETONATION WAVE ENGINE

F. Falempin
MBDA, France

CONTINUOUS DETONATION WAVE ENGINE

F. Falempin
MBDA France

Detonation wave engines, thanks to their more efficient thermodynamic properties, are expected to exhibit a higher level of performance than more conventional propulsion systems that rely on constant-pressure combustion processes. Nevertheless, it still has to be proved that this advantage is not superseded by the difficulties which could be encountered to practically define a real engine and to implement it in an operational flying system. In that respect, continuous detonation wave principle appears less challenging than the pulsed detonation process and should lead to the development of more efficient propulsion systems, even if such radical adaptation of the overall engine concept and of the vehicle architecture would be necessary. During past years, MBDA performed some theoretical and experimental works, mainly in cooperation with the Lavrentyev Institute of Hydrodynamics in Novosibirsk. These studies aimed at obtaining a preliminary demonstration of the feasibility of a Continuous Detonation Wave Engine for air-breathing and rocket application. Compared to a Pulsed Detonation Engine, this design allows an easier operation in reduced-pressure environment and an increase in engine mass flow rate and thrust-to-weight ratio. Those studies were focused on global performance and understanding of the unsteady, three dimensional flow behind the detonation wave. On the basis of these results, a preliminary design of an operational Continuous Detonation Wave Rocket Engine usable for the upper stage of a space launcher has been performed taking into account all engine/airframe integration issues in order to optimize the benefit of detonation wave engine. Then, specific experimental works have been undertaken to address some key issues like noise generated by a Continuous Detonation Wave Engine operating at several kHz, heat fluxes (intensity, areas) and cooling strategies, composite materials (Carbon / Silicon Carbide) compatibility, engine thrust vectoring capability. Those results were used to validate 1-D and 2-D unsteady computations. Beyond these first steps, a full scale demonstrator has been designed and should be tested within the next years.

Nomenclature

CC	=	Combustion Chamber
CDWE	=	Continuous Detonation Wave Engine
CD	=	Continuous Detonation
PDE	=	Pulse Detonation Engine
TDW	=	Transverse Detonation Wave
h	=	height of the fresh mixture layer before detonation
h^*	=	minimum height of the fresh mixture to support a detonation
L	=	combustion chamber length
l	=	distance between two consecutive detonation waves
θ	=	exit angle of the flow
d_1	=	combustion chamber inside diameter
d_2	=	center-body diameter
δ	=	combustion chamber width
S_{inj}	=	injection area

Introduction

Due to its thermodynamic cycle, a detonation wave engine has theoretically a higher performance than a classical propulsion concept using the combustion process. Nevertheless, it still has to be proven that this advantage is not compensated by the difficulties which could be encountered to practically define a real engine and to implement it in an operational flying system.

Ya. Zel'dovich¹ was the first investigator who considered the theoretical problem of a detonation mode for the combustion of fuel. He showed that detonation regime of combustion at the same initial state is more useful than the deflagration because of the lower entropy of reaction products in the case of detonation. He also stated that a practical attempt to use detonation processes was very difficult and that decisive factors like simplicity of implementation and reduction of losses in a continuously operating machine were in favor of constant-pressure combustion devices.

This comment was very sensible in 1940, but now, after more than 65 years of research and improvements, constant-pressure combustion devices have reached a point where any performance increase will be limited and costly, so some efforts should be devoted to the study of other devices that could deliver increased performances or reduce the complexity, weight or cost.

J.A. Nicholls, E.K. Dabora and R.A. Gealler realized the combustion of fuel in stationary compression shock waves originating near the exit of supersonic jet to the atmosphere².

During the last ten decade, the renewal of the interest for Pulsed Detonation Engine (PDE) led to the performance of a lot of dedicated R&T programs and a first flight test program performed by AFRL³.

In that context, MBDA France performed some theoretical and experimental works on Pulsed Detonation Engine (PDE), mainly in cooperation with LCD laboratory at ENSMA Poitiers. These studies aimed at obtaining a preliminary demonstration of the feasibility of the PDE in both rocket and air breathing modes and at verifying the interest of such a PDE for operational application. Further studies are still in progress with CIAM and Semenov Institute in Moscow.

On this basis, several engine concepts have been studied and evaluated at preliminary design level, for both space launcher and missile application. Today, the effort is focused on the

development of a small caliber air breathing engine able to power a UAV with very demanding requirements in terms of thrust range.

B.V. Voitsekhovskii proposed an alternative method of realization of continuous detonation. He used the analogy with the process of running wave occurring in the case of spin-detonation propagation in a round tube^{4 5}. In both cases the burning of the mixture is achieved in a transversal detonation wave (TDW) moving normally from the main direction of the combustion products. During ordinary spin detonation, transversal detonation wave propagates along the forward shock front in a spiraling trajectory relatively to the tube and burns a shock-compressed mixture. The concept of the Continuous Detonation Wave Engine (CDWE) has been extensively studied during the last decades at the Lavrentyev Institute of Hydrodynamics (LIH).

The use of such a CDWE can be considered to reduce the environmental conditions generated by PDE while reducing the importance of initiation issue and simplifying some integration aspects. As it was done for PDE, MBDA France is leading a specific R&T program, including basic studies led with the Lavrentiev Institute of Novosibirsk, to assess some key points for the feasibility of an operational Continuous Detonation Wave Rocket Engine (CDWRE) for space launcher.

But, continuous detonation wave can have also other application for turbojets and for ramjets. In order to address all these possible applications, a ground demonstrator has been designed and should be developed and tested within the next years within the framework of the National Research & Technology Center (CNRT) "Propulsion for Future" located in Orleans/Bourges region.

CDWE overview and generalities

The main difference between a deflagration and a detonation is linked to the mechanism of the flame propagation. In a deflagration, the flame propagation is a function of the heat transfer from the reactive zone to the fresh mixture (generally conduction). The detonation is a shock induced flame, resulting in the coupling of a reaction zone and a shock wave. The shock wave compresses and heats the fresh mixture, bringing it above its self-ignition point. On the other side, the energy released by the flame contributes to the propagation of the shock wave.

The main feature of a CDWE is an annular combustion chamber closed on one side (and where the fuel injection takes place) and opened at the other end. Inside this chamber, one or more detonation waves propagate normally to the direction of injection (Figure 1).

In fact a CDWE is very close to an infinite number of small PDE globally running at very high frequency (typically several kHz) and dephased and so the mean pressure inside the chamber is higher than for a typical PDE. If for a PDE the injection pressure could be as low as the ambient pressure, in the case of a CDWE the injection pressure should be higher and this kind of engine is better suited for rocket operation than for air-breathing operation if no air pre-compression is provided.

The flow inside this chamber is very heterogeneous, with a 2D expansion fan behind the leading shock (Figure 2). The transverse detonation wave (BC and B'C') propagates in a small layer of fresh mixture (AB') near the injection wall. The necessary condition for the propagation of a detonation wave is the continuous renewal of the layer of combustible mixture ahead the TDW. The height of this layer h must be not less than the critical value h^* for detonation. In the case of a LH_2/LO_2 engine, the dispersion of liquid oxygen droplets and the quick mixing of the components should be fast enough to decrease the value of h^* and to enable the realisation of CD in small chambers.

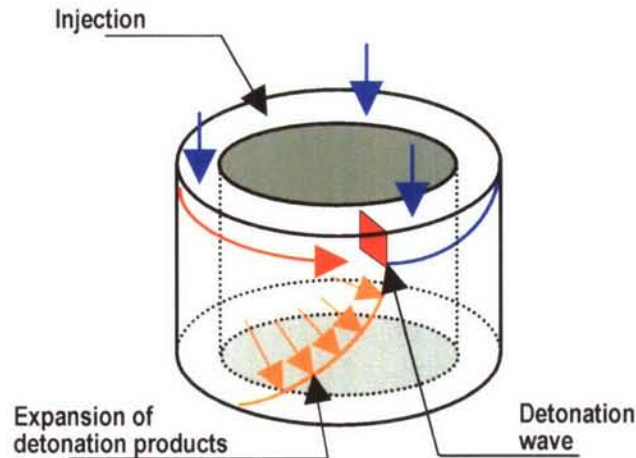


Figure 1.- Simplified diagram of a CDWE combustion chamber.

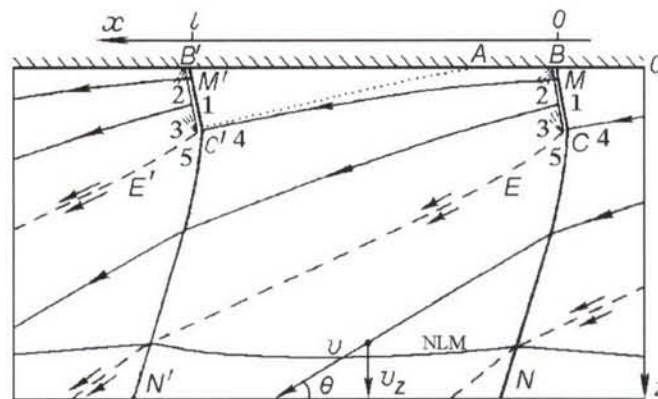


Figure 2. Structure of the flow inside the combustion chamber.

The detonation velocity observed in the reference laboratory is generally less than the Chapman – Jouguet detonation velocity. Several explanations could be given to this phenomenon:

- due to the very small time between two detonation waves, the mixing is less than ideal and the detonation characteristics could be changed,
- the fresh gases could partially mix with the detonation products and do not react,
- due to the expansion fan behind a detonation wave and the speed of the flow, the fresh mixture gain some speed in the X direction, so the detonation propagates in counter-flowing fresh mixture.

With this singular flow structure, this kind of engine possesses some unique characteristics:

- during the expansion, the flow velocity on the X axis changes direction from $-X$ (just after the detonation wave) to $+X$ (Figure 2),
- the flow velocity on the Z axis exhibits a transition from subsonic to supersonic inside the constant section duct, through a neutral line of Mach (NLM),
- there is no need for a geometric throat at the end of the combustion chamber,
- the flow exit the combustion chamber at the velocity v with an angle θ .

The pressure ratio across the detonation front is typically 10, a value lower than the Chapman – Jouguet detonation wave pressure ratio characteristic (18 for hydrogen – oxygen mixture, and higher than 30 for a hydrocarbon – oxygen mixture).

The first application for CDWE is the rocket mode (CDWRE) for which continuous detonation process can lead to a compact and very efficient system enabling lower feeding pressure and thrust vectoring with very attracting integration capability for axi-symmetrical vehicles. But, the CDWE could also be applied to simplified Ramjet Engine with short ram-combustor and possible operating from Mach 0+ without integral booster or to Turbojet with improved performances or simplified compression system (lower compression ratio required).

Basic experiments

Using the mock-up design principle described by Figure 3, some basic experiments have been first performed with the Lavrentiev Institute:

- experiments performed in CC with inner diameter of 50 mm, 100 mm and 280 mm,
- homogeneous (gas / gas) and heterogeneous (liquid / gas) mixture studied,
- detonation regime obtained in 100 mm diameter CC with GH2/LOx,
- detonation regime obtained in 330 mm diameter CC with kerosene/air,
- high thrust density achieved in small CC (275 daN for a 50 mm inner diameter kerosene/GO2 engine).

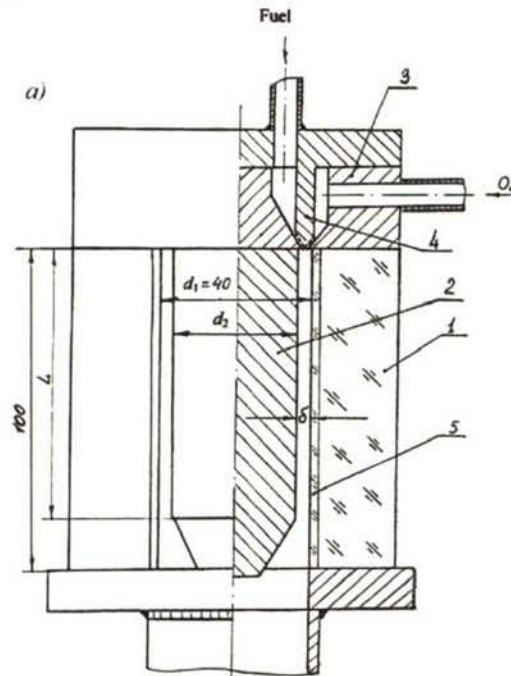


Figure 3. Mock-up design principle

From these experiments, some key points can be derived for the general sizing of a CDWE combustion chamber:

- The height of the fresh mixture layer h is a function of the detonation cell size.
- The frequency of the engine is given by the ratio D/l , where D is the detonation velocity and l the distance between two consecutives detonation waves, typically several kHz.
- The length of the combustion chamber L should be longer than 80% of l (to ensure transition from subsonic to supersonic inside the CC). If not the detonation could be unstable.

Performance model

Based on its extensive knowledge, the Lavrentyev Institute of Hydrodynamics developed an analytical model of such engine performance.

The main hypotheses are:

- the wall heat losses are negligible,
- the detonation is a self-sustaining CJ wave,
- the region in front of the wave is called "1", and the region behind the wave is called "2",
- the pressure P_2 is the maximum pressure inside the CC,
- the flow outside region 2 is supersonic everywhere relative to the TDW, except in the front wave (not analyzed) and maybe in the small domain 5 behind the oblique shock wave CN near the point C.

This model will not be detailed here and only the main parameters needed for the sizing of the engine are reported. They are:

- h , the height of the TDW,
- k , the flow mass fraction going thru MC'
- $h_1 = (1 - k)h$, the "effective" height of the TDW,
- $\alpha = \frac{p_x}{p_z}$, the ratio of the mean pressure acting along MC',
- $\eta = \frac{h_1}{l}$, the aspect ratio of the TDW,
- θ_1 , the inclination of the streamlines.

Calculations have been done for H_2-O_2 stoichiometric mixture (Table 1) for η and θ_1 values directly found from experiments.

Table 1. specific impulse of stoichiometric H_2-O_2 mixture in a CDWE (without nozzle).

α	$\frac{\rho}{\rho_2}$	$\frac{p}{p_2}$	$\frac{D}{\sqrt{2}I_T}$	θ , deg.	M_z	i , (km/s)	I , (sec)
1	0.0834	0.0520	0.530	44.43	1.974	3.108	316.8
$\frac{3}{4}$	0.0875	0.0551	0.552	42.15	1.872	3.048	310.7
$\frac{1}{2}$	0.0923	0.0587	0.573	39.82	1.765	2.985	304.3

On the basis of experimental results, α is considered equal to 0.75.

System Study and engine sizing

The comparison between an advanced LRE and a CDWRE has been done^{6 7}, taking the same maximum pressure inside the combustion chamber of both engine (and not the same injection pressure).

It was found that the needed combustion chamber length for stabilizing the detonation process could be very short, shorter than 200 mm and even close to 100 mm with H_2-O_2 mixture. Such a short combustion chamber length will be helpful to reduce the wetted area of the engine because an annular chamber exhibits an inherently greater wetted area than a classical combustion chamber of the same length.

With the capability to use a reduced length combustion chamber (and a smaller wetted area), the CDWRE will have a slightly better design flexibility than a conventional LRE, with the possibility to minimize the engine heat losses.

From a performance point of view, for a given maximum pressure inside the combustion chamber, the detonation cycle gives 15 %-20 % higher temperature and a lower burned gas molecular mass so the exhaust velocity is higher than with a LRE.

This difference between the CDWRE and the LRE decreases as the operating pressure inside the engine and the nozzle expansion ratio increases, but the CDWRE system presents the advantage that the considered performances are obtained with largely lower feeding pressure (here 2.2 MPa instead 7.0 MPa) (Table 2).

Moreover, the integration of a CDWRE can be very attractive when considering an aerospike configuration as it is shown by Figure 4.

Table 2. Specific impulse and thrust of a CDWE and a LRE (*) operating at the same maximum pressure, with different nozzle expansion ratio.

d_n , (m)	S_n/S_1	p_n/p	v_n/v_z	I , sec	I^* , sec	J , (kN)	J^* , (kN)	$\Delta J/J^*$
0.4	1.333	0.6337	1.10	326	296	107.97	98.01	0.101
1.1	10.08	0.0399	1.486	396	383	131.10	126.73	0.034
2.15	38.5	0.0073	1.623	424	415	140.06	137.05	0.022

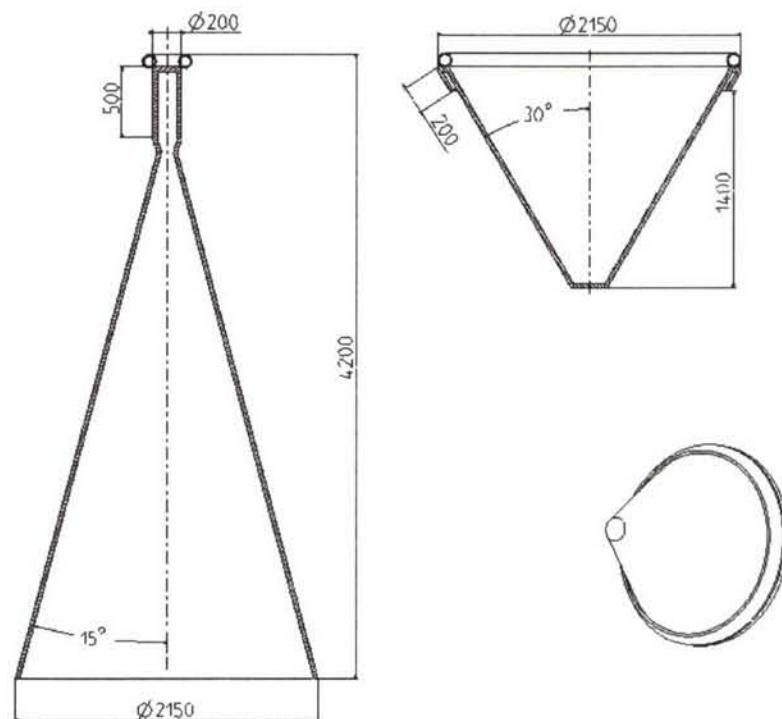


Figure 4. Comparison between equivalent classical LRE and CDWRE

Experimental evaluation of key technology points

In order to better assess the feasibility of such a system, specific experiments have been performed to address some key points like thrust vectoring, heat fluxes and material compatibility, operation in low pressure environment.

Thrust vectoring investigations

One of the peculiarities of a CDWE is that the number of detonation waves inside the chamber is not constant and is a function of the combustible mixture, the combustion chamber geometry and also the mass flow rate. For a given mixture in a given chamber, changing the mass flow rate (and the injection pressure) will change the number of detonation waves inside the chamber.

This effect could be explained with the assumption that behind a TDW (and between two consecutive TWD), there is a complex series of shock waves. If we increase the mass flow rate, the height of the fresh mixture behind two consecutive detonations is sufficient to support a new detonation wave ($h > h^*$) and a shock induced combustion (a detonation) could occur and a new TDW appears. If we decrease the mass flow rate inside the combustion chamber, the height of the fresh mixture between two consecutive TDW decreases and could be not sufficient to support a shock-induced combustion and the TWD degenerates into a simpler shock wave.

This self-adaptation of the detonation to the fresh mixture local mass flow made it possible to gain thrust vectoring with the local increase of the mass flow.

Some experiments were done in a 100 mm internal diameter combustion chamber. The injection wall consists of 190 holes for the injection of fuel and oxidizer. In one series of experiments the equivalence ratio was changed in one half of the engine compared to the other half. In another series, injectors' diameter was increased in order to double the local mass flow rate in one half of the engine. Eight pressure probes (P1 to P8) were located along the circumference of the outer wall of the annular chamber.

In all experiments it was possible to obtain an increase of the thrust on one side of the engine. The most promising experiments show that a 30 % increase of the thrust-wall overpressure was possible if we double the mass flow rate. This increase is lower than expected but the small diameter of the test engine limited the heterogeneity of the flow inside the combustion chamber. With a larger engine, a 100% increase of the thrust on one side (compared to the other side) should be possible (Figure 5).

We found also that there was a small shift of the maximum and minimum pressure values. Those extreme value seems to be located between P7 and P8 (for the maximum) and between P3 and P4 (for the minimum) instead of directly near P1 and P5.

Compared to a LRE (with a gimbaled nozzle), this thrust vectoring capability is interesting because there is no change in the thrust direction and the response time is limited only by the response time of the injectors, which could be very fast, enabling the positive control of the vehicle attitude at high frequency without using much power. The complete pressure field and flow velocity should still be investigated to check the effect of the flow deflection and flow expansion in the nozzle.

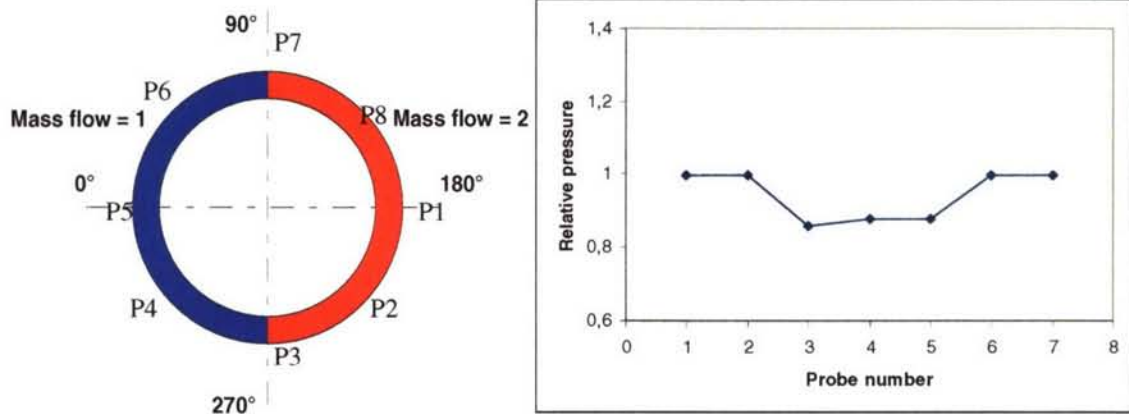


Figure 5. Example of thrust wall relative pressure from probes P1 to P7 (P1 is the reference value)

Heat fluxes and cooling system

Due to the transverse velocity of the flow behind the detonation wave (several hundreds of meter per second), the highest heat load inside the CC occurs near the thrust wall and decreases along the axial axis.

Wall temperatures in heat-sink combustion chambers were recorded with hydrogen-oxygen and kerosene-oxygen mixtures (Figure 6).

The cooling system design could be critical because for metallic structures the mean heat fluxes near the thrust wall were measured between 12 MW.m^{-2} and 15 MW.m^{-2} with local values even higher.

This heat flux repartition is also very different from the one obtained in a LRE where the maximum heat fluxes occurs near the combustion chamber geometric throat⁸. This point could be beneficial for the engine design because the vaporization of the injected oxygen will be faster and the mixing between hydrogen and oxygen will be better.

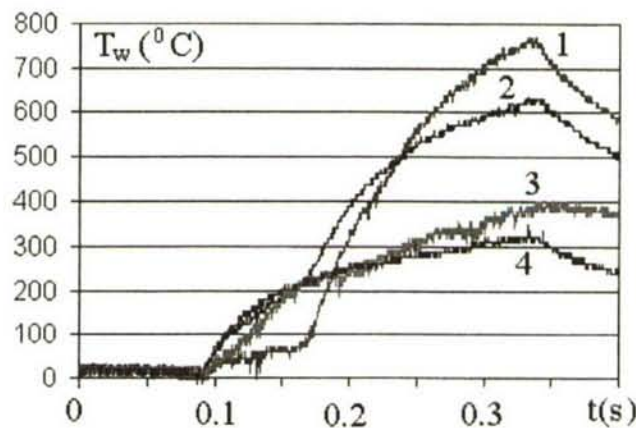


Figure 6. Typical wall temperature along the combustion chamber with $\text{H}_2 + \text{O}_2$ mixture (1-8 mm from thrust wall ; 2-20 mm ; 3-50 mm ; 4-90 mm).

The high heat fluxes anticipated in a CDWRE lead to the issue of active cooling, a very difficult task with metallic structures with a wall temperature limited to the vicinity of 1000 K.

Composite materials could achieve higher wall temperature (up to 1800 K) even in oxidative conditions.

After a careful review of existing products, some C/SiC composite materials were selected.

Then, two composite parts, constituting the inner wall of the annular detonation chamber, have been designed and manufactured to be tested in the LIH 100 mm CDWE combustion chamber. Recently, these two parts successfully sustained a series of short duration (0.5 s) tests without apparent damage to the material surface (Figure 7). Detailed analysis of these parts is still in progress and new test series with harder conditions could be performed in near term.



Figure 7. Composite parts before (left) and after the first test (right).

Operation in space environment

Ignition of an engine in very low pressure environment could be a real problem, even for a conventional rocket engine.

For CDWRE operation, the lack of geometric throat adds to the potential difficulty of a sufficient filling of the chamber with no counter pressure.

This issue was investigated using LIH 100 mm ID detonation chamber connected to a 0.5 m³ vacuum tank with an initial pressure of 0.06 10⁵ Pa.

The first step was to investigate the effect of the injection conditions (specific mass flow and equivalence ratio), and after that to decrease the ignition energy until it was impossible to achieve an initiation of the detonation.

Blasting copper wires were used for initiating the detonation inside the combustion chamber and ignition energy could be changed with the change of the applied voltage and the wire diameter.

Gaseous hydrogen and oxygen at ambient pressure were selected for those experiments and injection pressure between 1.6 10⁵ and 25 10⁵ Pa (for hydrogen), and 5 10⁵ Pa and 11 10⁵ Pa (for oxygen) allowed the investigation of ignition within a wide range of low specific mass flow (between 21 kg.s⁻¹.m⁻² and 57 kg.s⁻¹.m⁻²).

This mass flow rate is ten times lower than mass flow used in previous experiments but was mandatory given the relatively small volume of the vacuum tank.

From the pressure signal and the direct visualization of the flow with high-speed camera (Figure 8), it was possible to determine the minimum injection conditions for the positive ignition of the TDW system inside the combustion chamber as a function of the mixture equivalence ratio.

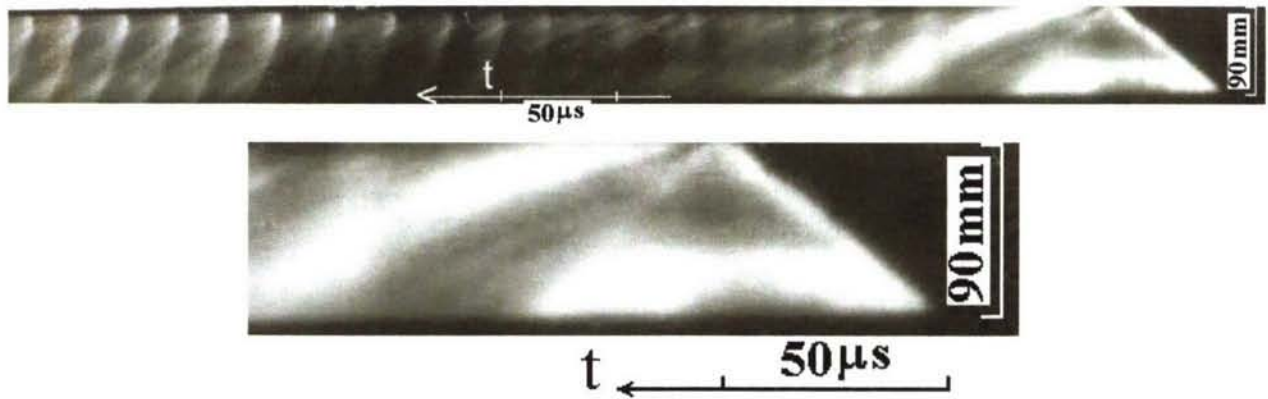


Figure 8 - Fragment of the photographic record with rotating detonation initiation.

In the case of a positive TDW initiation, the static pressure inside the combustor increases to a much higher level (between $0.8 \cdot 10^5$ Pa and $1.25 \cdot 10^5$ Pa) than when no detonation occurs (due to the lack of a geometric throat at the exit of the combustion chamber).

It was found that increasing the specific mass flow rate increases both lean and rich ignition limits of the engine and that it was possible to start a TDW at very low combustion chamber pressure in a wide range of equivalence ratio (0.5 – 1.7), with a very low amount of energy (less than 1 J) (Figure 9).

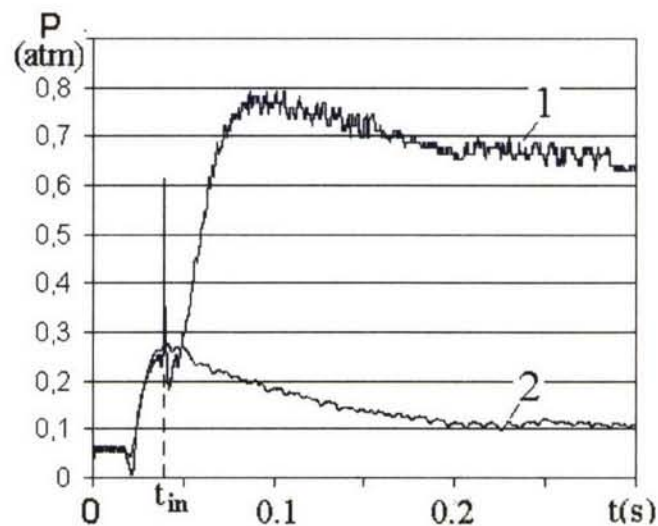


Figure 9 - Static pressure history with detonation initiation (1) and without detonation initiation (2).

Numerical simulations

Some preliminary simulations were performed using FLUCEPA code and a 9 step kinetic model for H_2 and O_2 combustion and considering a single detonation wave with forced ignition.

It was found that this code was sufficiently robust to deal with the large pressure and velocity gradients found in a detonation front without the need to use mesh adaptation (Figure 10).

This robustness is a critical point because in the case of cylindrical detonation propagation, the pressure and velocity slopes before and after the shock wave are infinite, so in this case the detonation wave is a true double discontinuity, a real difference between CDWE and PDE internal flow simulations.

The steadiness of the Transverse Detonation Wave propagation is also very sensitive to the injection conditions while the existence of consecutive detonation waves radically changes the flow structure.

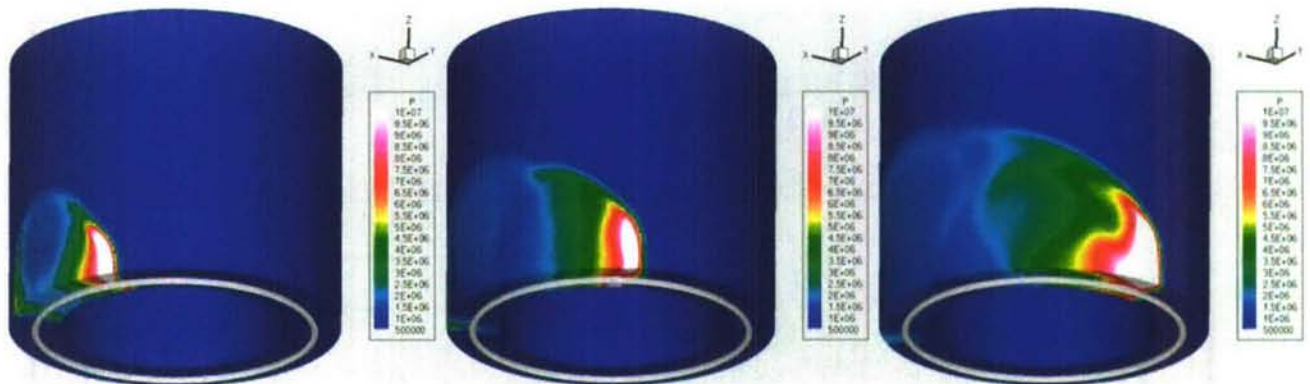


Figure 10 - Detonation propagation in an annular chamber 10 ms, 20 ms and 30 ms after ignition (H_2+O_2 stoichiometric mixture in a 100 mm diameter chamber).

In order to better represent the actual flow field, further works have been performed by the French ICARE Research Lab. 2D Euler simulation has been used with a H_2/O_2 chemistry model using 6 species and 7 reactions. On the basis of experimental results, the width of the computation grid is determined as the distance between two consecutive detonation waves. Then a periodical condition is imposed: conditions on the right end of the grid being imposed to the left end. Figure 11 gives the circumferential U and axial V speed components. One can note that the exhausting flow is mainly oriented to the chamber axis with limited remaining U speed compared to the large V speed.

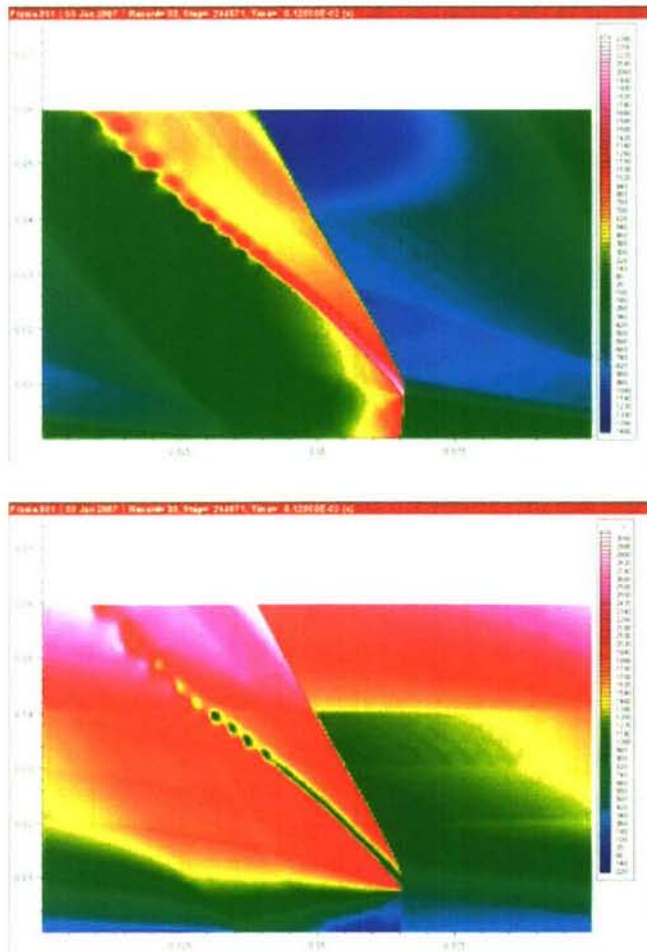


Figure 11. Circumferential U and axial V speed components

Computation results exhibit a neutral line of Mach number at approximately 40% of the distance between two consecutive detonation waves (Figure 12).

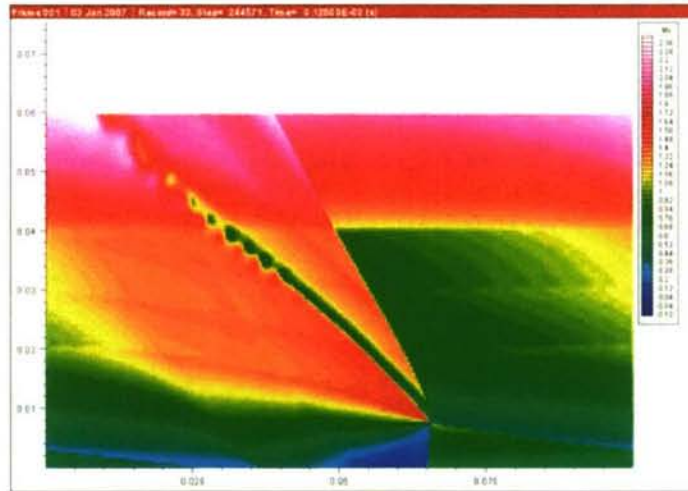


Figure 12. Axial Mach number field

Demonstration engine

Based on previous studies and the growing potential of such concept, a demonstration engine has been designed. This actual-size engine (Figure 13) is to be manufactured and tested in existing test facility. The combustion chamber is 350 mm (external inner diameter) and 280 mm (internal inner diameter) and will be able to operate with $\text{GH}_2 / \text{GO}_2$ or $\text{GH}_2 / \text{LO}_2$ with the change of supply lines and injection wall. This engine mock-up is modular and actively cooled.

The injection pressure will be limited (between 1 MPa and 1.5 MPa) and resulting mean pressure inside the combustion chamber with the envisioned mass flow rate (between 12 kg.s^{-1} and 15 kg.s^{-1} , depending on the equivalence ratio) is expected near 0.5 MPa, a value sufficient to deliver several thousands daN of thrust.

The injection wall is divided in 8 sectors in order to be able to change the local mass flow rate and investigate the thrust vectoring effect with a diverging nozzle or with a center core nozzle (aerospike). Moreover, the engine will be equipped with a complete weighing system providing thrust vector components and corresponding moments.

Thanks to its modularity, the engine will be used, in a first step, as a non-flying workhorse which will allow addressing all the key points such as:

- effect of injection configuration and conditions (2-phases mixing),
- stable operation domain and key parameters influencing it,
- effects of high speed tangential flow (skin friction and heat fluxes),
- thermal and mechanical strength of the combustion wall (fuel-cooled structure, high frequency mechanical shocks),
- effect of non-symmetric injection on thrust vectoring when including a full nozzle,
- generated environment (vibration and acoustics),
- ...

In a second step, the modularity will allow to progressively replace all the engine components by flight-worthy ones in order to finally obtain a flight-worthy demonstrator which will be tested to really assess the achievable performance when taking into account all the technology issues.

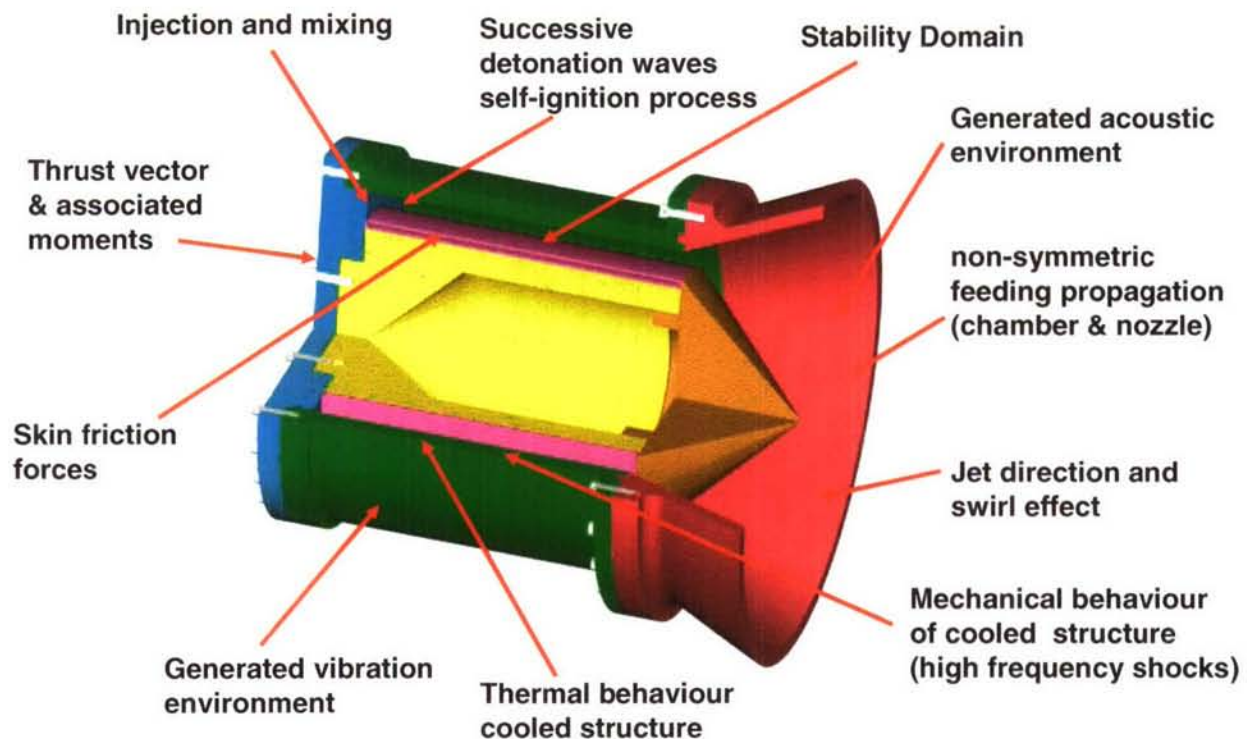


Figure 13 - cutout of the demonstration engine

Conclusion

Since a few years, MBDA France leads R&T works in cooperation with the Lavrentyev Institute of Hydrodynamics on the Continuous Detonation Wave Engine.

The mixtures used in the different experiments were mainly $\text{GH}_2 - \text{LO}_2$ or $\text{LHC} - \text{GO}_2$. The goals of those experiments were to address some key technology points in order to be able to evaluate the global interest of an engine using TDW for the combustion process.

It was found that such engine could deliver impressive thrust in a very small package (275 daN for a 50 mm (internal diameter) and 100 mm long, kerosene – oxygen engine) and that could be increased with the use of a diverging nozzle.

Due to the geometry of the combustion chamber, a plug or aerospike nozzle seems to be the best design, the thrust vectoring capability of this engine (with the local change of the mass flow rate) being a way to solve the problem of attitude control.

The heat fluxes are very high but located mostly near the injection wall. This point will help the gasification of the liquid component injected inside the combustion chamber. The transverse flow velocity could also help the mixing of the fresh products, but also the mixing of the fresh mixture with the detonation products.

Some preliminary tests have been performed to evaluate the capability of C/SiC composite materials to sustain the very severe mechanical environment generated by the rotating detonation waves.

Beyond these first steps, a full scale demonstrator has been designed and should be tested within the next years.

References

- ¹ Ya.B. Zel'dovich, "The question about energetic use of detonation combustion" in *Zh. Tech. Fiz.*, 1940, vol.10, iss.17, pp. 1453-1461, also available in *JPPOEL* vol.22, issue.3, pp. 588-592.
- ² J.A. Nicholls, E.K. Dabora, R.A. Gealler, "Studies in Connection with stabilized Gaseous Detonations waves" in the *11th Symposium (International) on Combustion and Detonation*, London, 1959, pp. 766-772.
- ³ F. Schauer, "Pulsed Detonation Engine" in *LS Zh. Tech. Fiz.*, 1940, vol.10, iss.17, pp. 1453-1461, also available in *JPPOEL* vol.22, issue.3, pp. 588-592.
- ⁴ B.V. Voitsekhovskii, V.V. Mitrofanov, and M.E. Topchiyan, "Structure of a detonation front in gases". *Siberian Branch of the USSR Academy Sci., Novosibirsk*, 1963.
- ⁵ B.V. Voitsekhovskii, "Stationary spin detonation", in *Sov. J. of Applied Mechanics and Technical Physics*. 1960. No 3. pp. 157-164.
- ⁶ E. Daniau, F. Falempin, F.A. Bykovskii, S Zhdan, "Pulsed and Rotating Detonation Propulsion System : First Step Toward Operational Engines", *AIAA 2005-3233*.
- ⁷ F. Falempin, E. Daniau, F.A. Bykovskii, S Zhdan, "Detonation Waves Propulsion Systems : First Step Toward Operational Engines", *ISABE 2005-1302*.
- ⁸ Knob, O., Fröhlich, A., Wennerberg, D., and Haslinger, W., "Advanced Cooling Circuit Layout for the VINCI Expander Cycle Thrust Chamber", *AIAA 2002-4005*.

von Karman Institute for Fluid Dynamics

RTO-AVT-VKI Lecture Series 2007

**ADVANCES ON PROPULSION TECHNOLOGY
FOR HIGH-SPEED AIRCRAFT**

March 12-15, 2007

SCRAMJETS

M. Smart
The University of Queensland, Australia

Scramjets

Michael Smart

Centre for Hypersonics,

The University of Queensland,

Brisbane, Australia. 4072

Nomenclature

A	area (m^2)	T	temperature (K)
C_f	skin friction coefficient	T_t	total temperature (K)
C_D	drag coefficient	V	velocity (m/s)
C_L	lift coefficient	w_{cap}	capture width of scramjet (m)
c_p	specific heat (J/kgK)	x	axial distance (m)
D	drag (N), hydraulic diameter (m)	α	angle-of-attack (degrees)
f	specific uninstalled thrust (m/s)	ϕ	equivalence ratio
f_{st}	stoichiometric ratio	ϑ	constant in mixing curve
F	stream thrust (N)	γ	ratio of specific heats
F_{add}	additive drag (N)	η	efficiency
F_{un}	uninstalled thrust (N)	ζ	flight path angle (degrees)
g	gravitational acceleration (m/s^2)	ρ	density (kg/m^3)
h	altitude (km), enthalpy (J/kg)		
h_{pr}	heat of combustion (J/kg of fuel)		
H_t	total enthalpy (0K basis) (J/kg)		
Isp	specific impulse (s)		
L	lift (N)		
m	mass (kg)		
m_c	mass capture ratio		
\dot{m}	mass flow rate (kg/s)		
M	Mach number		
p	pressure (Pa)		
q	dynamic pressure (Pa)		
Q	heat (J)		
R	gas constant (J/kgK)		

Subscript

c	combustor entrance
out	outflow
f	fuel
i	initial
in	inflow
m	mixing
n,N	nozzle
o	initial
p	payload
s	structural

1. Introduction

The desire for hypersonic flight within the atmosphere has motivated multiple generations of aerodynamicists, scientists and engineers. In the late 1950's and early 1960's it became clear that while rocket propulsion had the potential for access-to-space and the ability to reach many parts of the globe on ballistic trajectories, only an airbreathing propulsion system could facilitate practical hypersonic flight. Antonio Ferri aptly described the important differences between rockets and airbreathing engines (Ferri 1964) as:

1. The potential specific impulse of airbreathing propulsion is much larger than any chemical rocket, due to the fact it carries only fuel and not oxidiser.
2. Structural weight of an airbreathing engine is larger for the same thrust than a rocket, because it must process air (oxygen and nitrogen) and have an intake, whereas the rocket has an oxidiser tank and pressurization system.
3. The thrust of an airbreathing engine is a function of flight Mach number and altitude. Large thrust per unit frontal area can only be obtained in the dense atmosphere, while rockets can operate at high thrust per unit frontal area in a vacuum.

4. The necessity for flight in the atmosphere introduces severe structural problems for the airbreathing engine associated with aerodynamic heating and vehicle drag. However, the vehicle has a greater potential for manoeuvring than a rocket traveling in a vacuum, through the use of aerodynamic lift.

It was recognised at the time that a hypersonic airbreathing propulsion system could fulfill many roles that a rocket could not, including hypersonic cruise and recoverable space launchers. Figure 1 shows a futuristic hypersonic airbreathing vehicle concept from that time period.



Figure 1 - 1960's hypersonic airplane

The airbreathing engine cycle best suited to hypersonic flight is the supersonic combustion ramjet, or the scramjet. This type of engine can be properly viewed as an extension of the very successful ramjet engine cycle, which uses shock wave compression in the inlet in lieu of the compressor in a gas-turbine engine. In a ramjet, air entering the combustor is first decelerated to subsonic speeds, where fuel is injected and burnt, and finally expanded through a second throat to a thrust nozzle. As flight speeds increase above Mach 5, reducing the air to subsonic conditions produces two problems; (1) significantly increased shock losses in the inlet, particularly at the terminal normal shock, and (2) significantly increased flow temperatures in the combustor. The second of these problems not only creates material/structural issues in the combustor, but leads to chemical dissociation in the nozzle expansion and a consequent energy loss from the engine cycle.

The idea of adding heat to a supersonic stream was first investigated in the late 1940's, but only attracted serious attention in the late 1950's with the investigation by Weber and McKay (1958) at the NASA Lewis Research Centre. This work compared the estimated performance of the ramjets and scramjet engine cycles at increasing Mach number using hydrogen fuel, and calculated that the scramjet cycle was superior above Mach 7. Results of a further study of the efficiency of airbreathing engines (Anderson et. al. 2001) are shown in Fig. 2. Once again the switch over between ramjet and scramjet cycles was calculated to occur at Mach 6-7, however it was also pointed out in the same reference that the high combustor static pressure of a ramjet operating above Mach 5 may be a more important reason for choosing a scramjet cycle than fuel efficiency. As is also shown in Fig.2, as speeds increase the specific impulse of scramjets reduces, and was calculated to reach the performance level of a rocket somewhere above Mach 16.

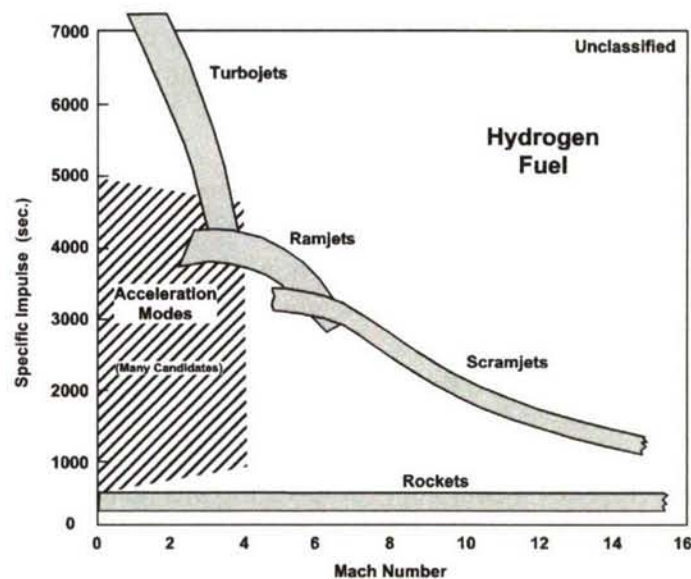


Figure 2 - Specific impulse levels for different propulsion systems

Early researchers quickly grasped the difficulties of designing scramjet engines, including:

1. Mixing and ignition of fuel and air in the short residence times of a supersonic combustor.
2. The high heat loads and friction losses that occur at hypersonic speeds.
3. The control of thermal choking.
4. Non-equilibrium nozzle flows and the loss of energy from the cycle due to incomplete combustion.

Current day scramjet designers grapple with these same issues, although we now have 40 years of experience to guide us. Two further critical issues for practical hypersonic propulsion using scramjets are:

5. No thrust production below a flight Mach number ranging from 3.5-5, depending on the particular engine design. A booster or low-speed propulsion system is therefore required to raise the vehicle to the scramjet take-over Mach number.
6. Operating over a large Mach number range with a “realistic” engine structure requires some finesse and many compromises for adequate performance at the upper and lower limits of the desired speed range.

The reason for (5) is straight forward; an engine that relies on shock compression in the inlet requires supersonic inflow, and further, if supersonic flow needs to be maintained in the combustor, this raises the lower limit for thrust production even higher.

The reasons for (6) becomes abundantly clear as soon as scramjet performance calculations are attempted at different flight Mach numbers. At lower speeds where the stoichiometric heat of combustion is relatively large compared to the kinetic energy of the airflow, combustion fuel can produce large pressure rises in constant area combustors and possible choking or disruption to the flow through the engine, known as an unstart. Divergent combustors and/or step increases in combustor area are needed to burn a respectable proportion of the air captured by the engine in this instance. At higher speeds, however, where the kinetic energy of the airflow is significantly higher, combustor divergence can lead to chemical kinetics issues and incomplete combustion. Inlet contraction ratio requirements also change significantly with Mach number. Creating an engine that can operate over a large Mach number range is one of the key technological challenges in current times.

In this article an historical perspective on important scramjet development programmes in the United States is first presented, followed by a description of recent scramjet flight programmes. The stream thrust based cycle analysis methods used to calculate scramjet performance are then

presented, followed by a description of the component analysis used to determine the performance of a scramjet. The article closes with a discussion of scramjet application to a system for acceleration to low earth orbit.

2.0 Historical perspective on past scramjet development programmes in the United States

The history of scramjet programmes throughout the world, up to the year 2000, is well described in an article by Curran (2001). Following is a short history of some past scramjet development programmes in the United States.

2.1 Scramjet Development in the United States

The 1960's saw an increased interest in scramjet propulsion, which in the United States was concentrated in two groups; one at NASA Langley Research Center, and the other supported by the US Navy at the Applied Physics Laboratory, Johns Hopkins University (APL). A significant amount of scramjet research was also conducted in industry through support from the US Air Force. These groups followed quite different technological paths leading up to the mid-1980's, when the National Aerospace Plane (NASP) Program brought most of the US scramjet community together.

Considerable experimental research on inlets and combustor components had been conducted at NASA Langley prior to 1964. This work demonstrated the validity of supersonic combustion, and indicated the potential of an integrated scramjet with hydrogen as both fuel and coolant. The Hypersonic Research Engine (HRE) Project was formulated to put this into practice, with the objectives of (a) demonstrating high internal thrust performance for a scramjet engine over a Mach number range of 4-8, and (b) development of hydrogen cooled engine structures technology (Andrews & Mackley 1994). Figure 3 shows a photograph of the HRE, which was an axisymmetric pod type configuration with a translating spike and an annular combustor. This program continued till 1974 with both a boiler plate, water-cooled model used for scramjet testing, and a flight weight, hydrogen-cooled model for structural testing.

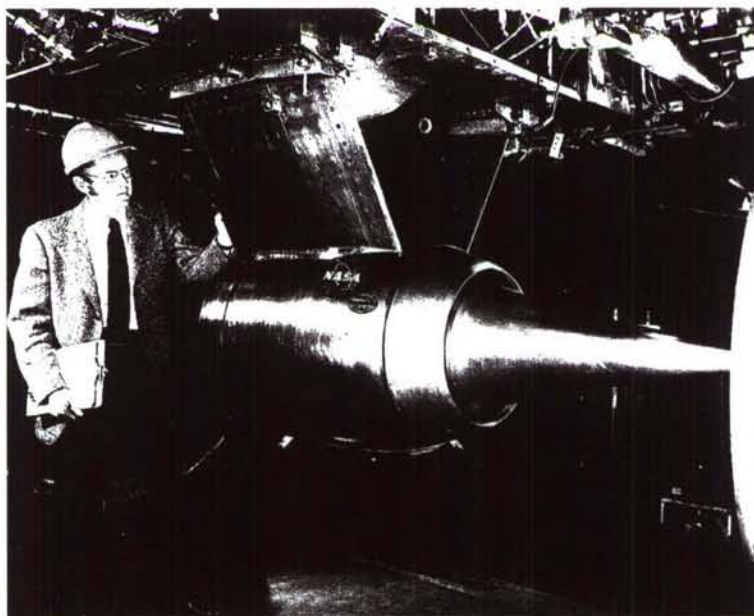


Figure 3 - HRE engine model in wind tunnel

A total of 52 scramjet tests were completed with the water cooled engine at equivalent flight Mach numbers of 5, 6 and 7 with a range staged injector options (Andrews & Mackley 1994). Figure 4 shows a plot of the calculated combustion efficiency based on the pressure measurements

in the combustor at Mach 6, together with a schematic showing the different fuel injection options. A tremendous amount of knowledge about fuel ignition and combustion was gained from this testing, including a demonstration of a smooth transition from a supersonic to a subsonic combustion mode of operation. Figure 5 shows a plot internal thrust coefficient vs Mach number for the HRE at $\phi = 1$, which met the performance goals of the project. Unfortunately, the pod type configuration of the HRE also had significant external drag, and during the program it was realized that scramjet engines must be integrated with the vehicle in order to have good installed thrust.

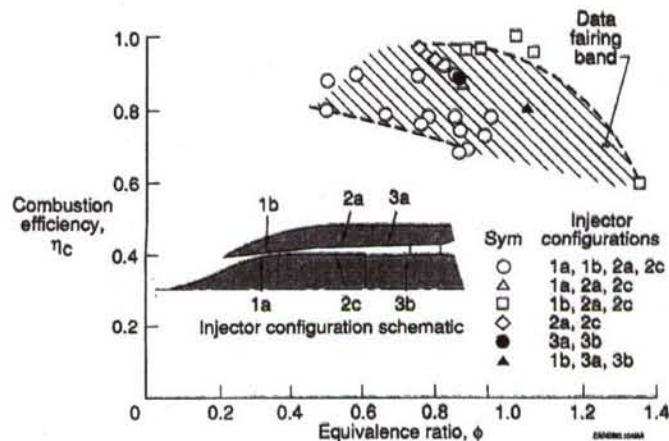


Figure 4 - HRE combustion efficiency data at Mach 6

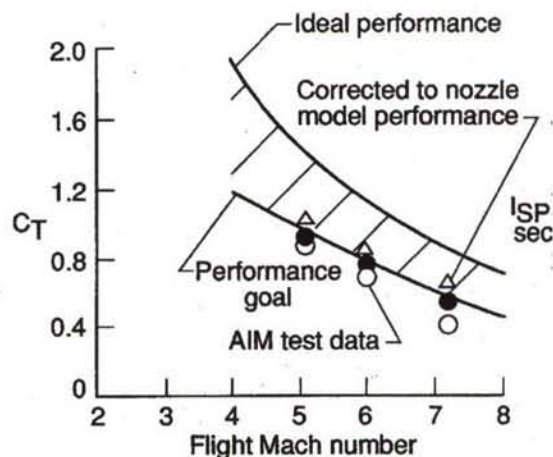


Figure 5 - HRE internal thrust performance

NASA Langley responded to the need for airframe integration with the 3-D swept side-wall compression scramjet. This fixed geometry configuration, a schematic of which is shown in Fig. 6, had low external drag, a rectangular cross-section, was modular in design, and fit snugly inside the bow shock of a vehicle flying at hypersonic speed (Trexler & Souders 1975). Being a fixed geometry scramjet, these engines were designed to operate over a large Mach number range with self-starting inlets. Particular areas of research related to the development of these engines were, (1) control of the swept shock interactions in the inlet, (2) reduction of flow distortion at the inlet throat, (3) introduction of fuel injection struts to reduce engine length and weight, and (4) integration with the vehicle fore and aft bodies. Many hundreds of component and integrated scramjet tests were conducted in support of this engine concept at Langley's hypersonic facilities through the 1970's and 80's.

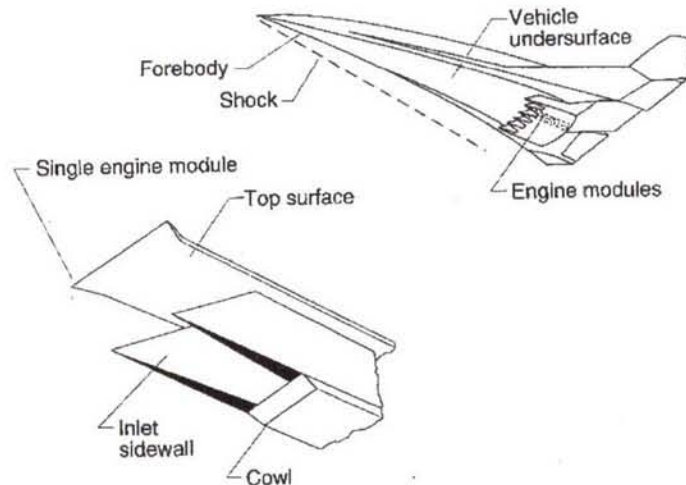


Figure 6 - Langley swept side-wall compression scramjet

Scramjet research at APL was concentrated on the hypersonic missile application rather than a large scale vehicle, hence it followed quite a different path to NASA. In the early 1960's the US Navy was interested in a Mach 6-8 follow-on to its ramjet powered missiles. The APL research was therefore concentrated on liquid hydrocarbon fuelled engines. Research was conducted to better understand the physical and chemical processes governing supersonic combustion, and a technology database on inlets, fuel injectors, combustors, nozzles and fully integrated engines was developed during the 1960's and 70's (Waltrup 1990). Figure 7 shows one integrated scramjet missile concept to be developed at APL during this period, known as the Supersonic Combustion Ramjet Missile (SCRAM), which was designed for maximum cruise at Mach 8 (Billig 1995). In 1978, emphasis was placed on development of the Dual Combustor Ramjet (DCR), which used conventional liquid hydrocarbon fuels and had a maximum Mach number of 6. A schematic of the engine concept is shown in Fig. 8, showing a missile with a spike nose, both supersonic and subsonic inlets, fuel injection into the flow processed by the subsonic inlet, and a supersonic combustor leading to a thrust nozzle (Waltrup 1990). Development of this concept continues today as part of the DARPA HyFly Program.

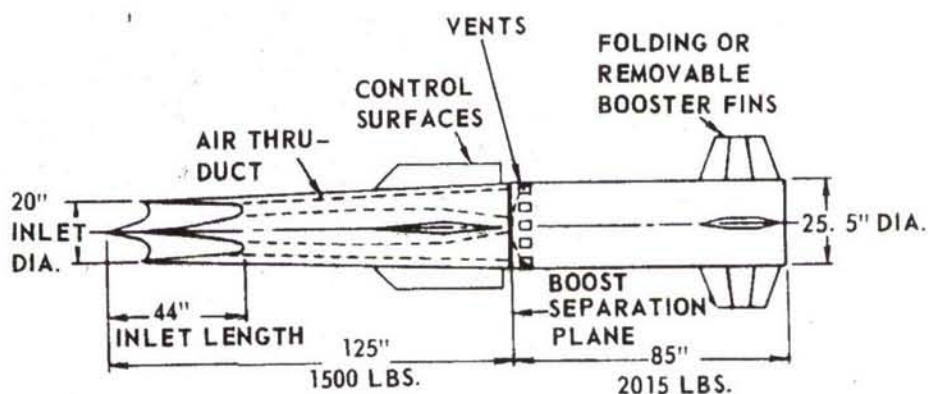


Figure 7 - APL Supersonic Combustion Ramjet Missile

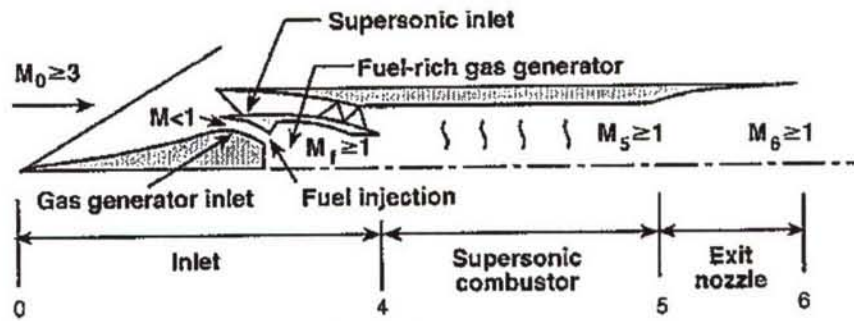


Figure 8 - Schematic of the APL DCR engine concept

A significant amount of scramjet configuration development and testing was supported by the US Air Force during the 1960's. This involved numerous industry contractors, including General Electric, Marquardt, United Technologies Research Laboratories, and General Applied Science Laboratories (GASL). One product of this support, shown in Fig. 9, was developed by GASL and called the low-speed fixed geometry scramjet. It was designed to operate from Mach 3-12 with fixed geometry, and used fuel scheduling and thermal compression effects in place of variable geometry. It was tested at Mach 7.4 at the GASL hypersonic facilities in 1968.

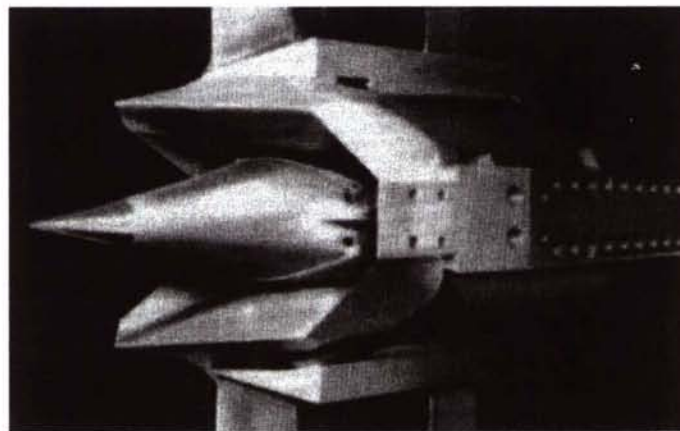


Figure 9 - GASL Mach 3-12 scramjet

The one project that combined most (if not all) US knowledge of hypersonic airbreathing propulsion, was the National Aerospace Plane (NASP) Program. This aggressive effort was initiated in 1985 by the Defense Advanced Research Projects Agency (DARPA) with the goal of developing a single-stage-to-orbit (SSTO) airplane called the X-30 (Barthelemy 1989). This vehicle was envisioned to take-off horizontally under gas-turbine power, accelerate to low earth orbit insertion velocity (Mach 25) through the use of hydrogen-fuelled scramjets and rockets, and then return to earth for horizontal landing. It really was a "space-plane" which would have brought aircraft-like operational flexibility to space. The seminal study at the beginning of the project was by Tony Du Pont, a schematic of which is shown in Fig.10. The Du Pont vehicle weighed 50,000 lb at take-off, used hydrogen fuel and a combined cycle air-breathing engine.

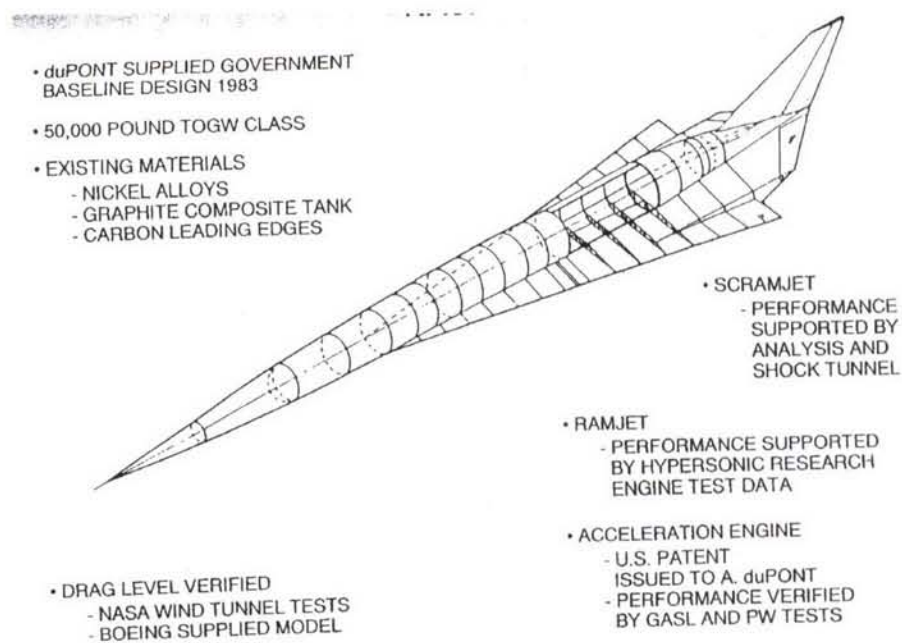


Figure 10 - Original space plane concept for NASP

Over its 10-year span the NASP Program involved NASA, the US Air Force, APL and a large contingent of industry players (Schweikart 1998). Many scramjet configurations were designed and tested in various facilities (Andrews 2001), and the understanding of air-breathing hypersonic propulsion was considerably deepened. Some examples of hardware tested during the NASP program are shown in Figs.11 and 12. The 3-D sidewall compression inlet model in Fig. 11 was based on a Rocketdyne (Rockwell) engine concept with heritage to earlier NASA Langley engines of similar configuration. The two-dimensional engine model in Fig.12 was known as the Concept Demonstration Engine (CDE), and was tested towards the end of the NASP program at simulated Mach 6.8 flight conditions in the 8-Foot High Temperature Tunnel at NASA Langley (Volland & Rock 1995).



Figure 11 - 3-D Sidewall compression inlet model

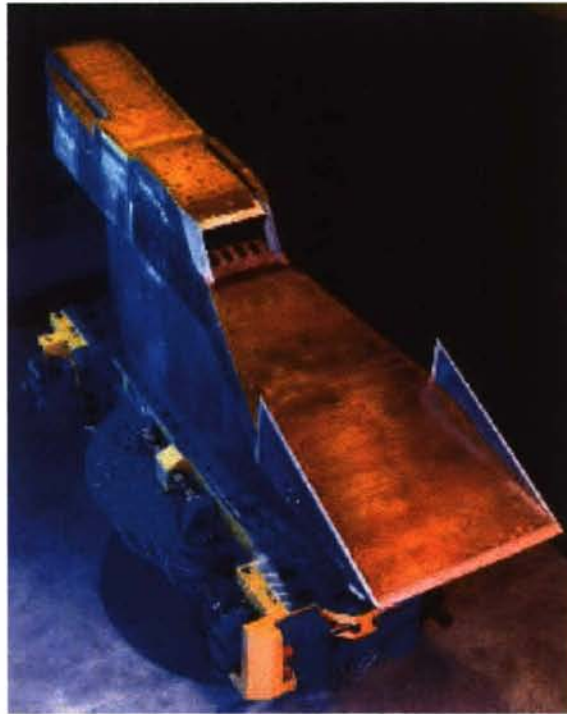


Figure 12 - 2-D engine model tested at Mach 6.8

An artists impression of a possible NASP configuration is shown in Fig. 13. While not producing its goal of a working X-30 aircraft, the NASP Program spurred the development of many technologies related to hypersonics, including computation fluid dynamics, high temperature materials and light-weight aerospace structures. It was also the genesis for the Hyper-X flight Program. Most current concepts for air-breathing access-to-space have moved away from SSTD systems, and make use of the significant advantages of multiple stage vehicles.



Figure 13 - Proposed NASP configuration

3.0 Scramjet Flight Programmes

The flight corridor for hypersonic airbreathing vehicles, either for cruise or ascent to low-earth-orbit, is constrained at upper altitude by the need to operate the airbreathing engine, and at lower altitude by structural limits of the vehicle. Figure 14 gives an indication of these limits, and includes a suggested ascent trajectory for an airbreathing SSTO vehicle (Hunt & Rausch 1998) with the applicable range of different propulsion cycles indicated. The goal of all scramjet flight testing is to fly scramjets at some point, or over some range, within this flight corridor. Three scramjet flight programmes will be reviewed here; (1) a joint CIAM/NASA flight test conducted in 1998, (2) the HyShot 2 flight conducted by The University of Queensland in 2002, and (3) NASA's Hyper-X which flew twice in 2004.

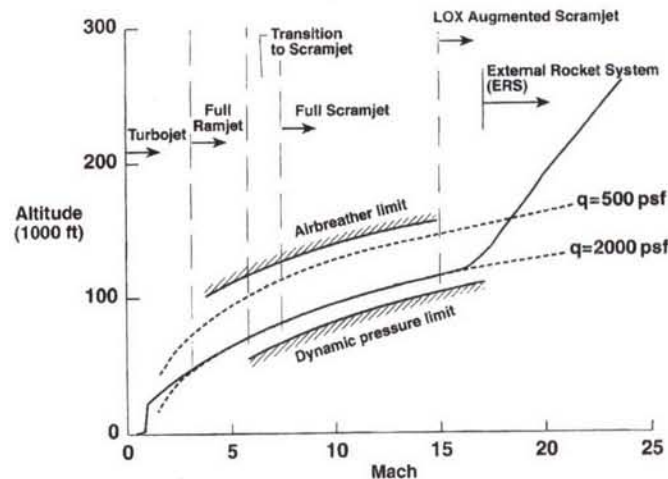


Figure 14 - Hypersonic airbreathing flight corridor

3.1 CIAM/NASA Flight Test

The Russian Central Institute of Aviation Motors (CIAM) performed a flight test of a CIAM-designed, hydrogen-cooled/fueled scramjet engine over a Mach number range of approximately 3.5 to 6.4 on February 12, 1998, at the Sary Shagan test range in Kazakhstan (Volland et. al. 1999). This rocket-boosted, captive-carry test of the axisymmetric engine reached the highest Mach number of any scramjet engine flight test at that time, and achieved 77 seconds of liquid hydrogen regeneratively cooled engine operation. The programme was conducted with NASA support and technical assistance from Langley Research Center. The engine used staged fuel injection through angled sonic holes and cavity flame holders, and was designed for dual-mode combustion. Analysis of the flight data indicated that an unexpected control sensor reading caused non-optimal fuelling of the engine, and flowpath modifications added to the engine inlet during manufacture caused markedly reduced inlet performance. Both of these factors contributed to the engine operating primarily in a subsonic combustion mode, with a peak combustion efficiency of 77.5%. Ground test data was obtained at similar conditions to flight, allowing for a meaningful comparison between the ground and flight experiments. The results of this comparison indicated that the differences in engine performance between ground and flight were small.

3.2 HyShot 2

The Centre for Hypersonics at the University of Queensland had routinely performed scramjet testing in shock tunnels since the early 1980's (Stalker et. al. 2006). Based on the desire to validate such testing for conditions in the Mach 7-8 regime, a sounding rocket based flight project known as HyShot was devised around 1997. This project involved two flight tests of a

simplified supersonic combustion experiment designed solely through shock tunnel testing. While the HyShot scramjet payload was elegantly simple and quite robust, significant issues associated with providing suitable scramjet flight test conditions with the available rocket needed to be overcome. The chosen solution to these issues resulted in a highly parabolic trajectory, with the scramjet experiment being conducted during an almost vertical re-entry (Paull et. al. 2002). Following a first launch failure on October 30th 2001, the University of Queensland conducted a successful second launch on July 30th, 2002.

Both HyShot flights took place at the Woomera Prohibited Area Test Range in central Australia. Each used a two-stage Terrier-Orion Mk70 rocket that generated a highly parabolic trajectory to boost the payload and the exhausted second stage Orion motor to an apogee in excess of 300km, as shown in Fig. 15. This combination of rocket and trajectory allowed the payload and attached second stage to re-enter the atmosphere with a Mach number in excess of 7.5 between 35 and 25 km altitude, thus supplying a range of conditions within the flight corridor of Fig. 14.

The HyShot payload included a nose-cone to shroud the scramjet flowpaths on the initial ascent, two scramjet combustors orientated back-to-back on a wedge forebody, plus hydrogen and nitrogen tanks, batteries, telemetry system, flight computer and other components. One combustor was hydrogen fuelled through 4 laterally spaced normal injectors, while the other combustor was unfuelled so as to obtain baseline (tare) conditions to compare against the fuelled flowpath throughout the flight. Figure 16 shows a photograph of the payload used for HyShot 2 (with the shroud removed). It was constructed predominantly of copper alloy for rapid dissipation of aerodynamic and combustion generated heat loads, with TZM (tungsten-zirconium-molybdenum) used for the highest heat flux regions that occur at the leading edges of both combustors.

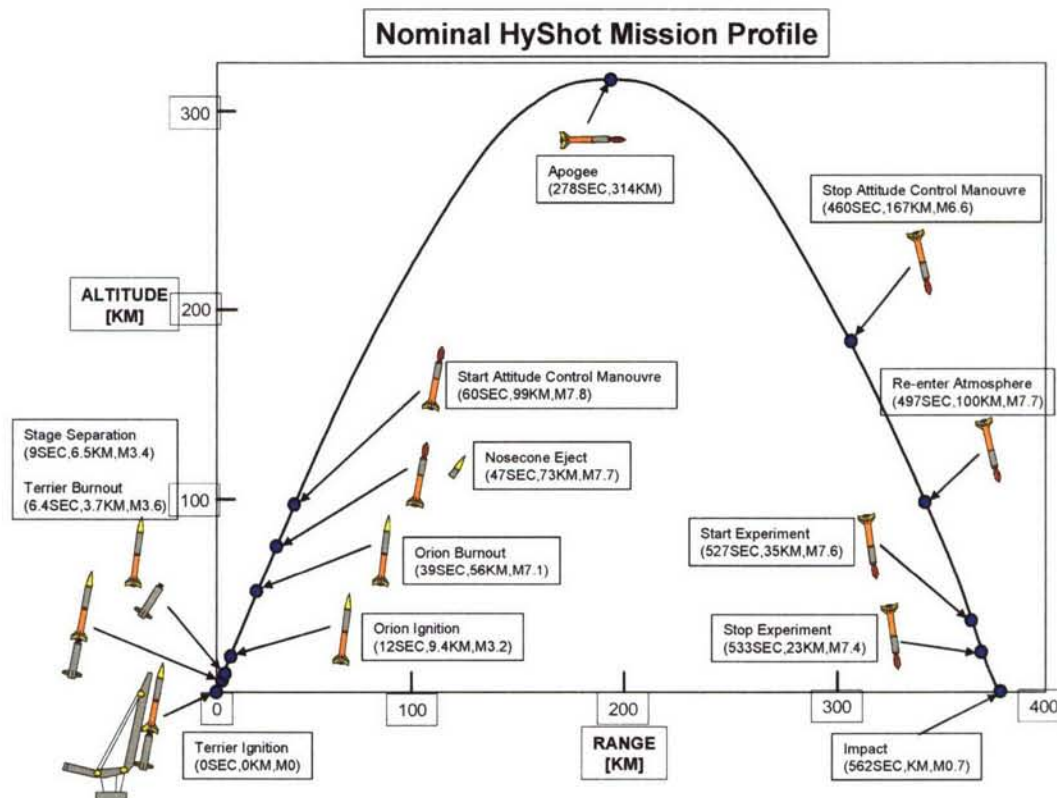


Figure 15 - HyShot flight profile



Figure 16 - HyShot payload

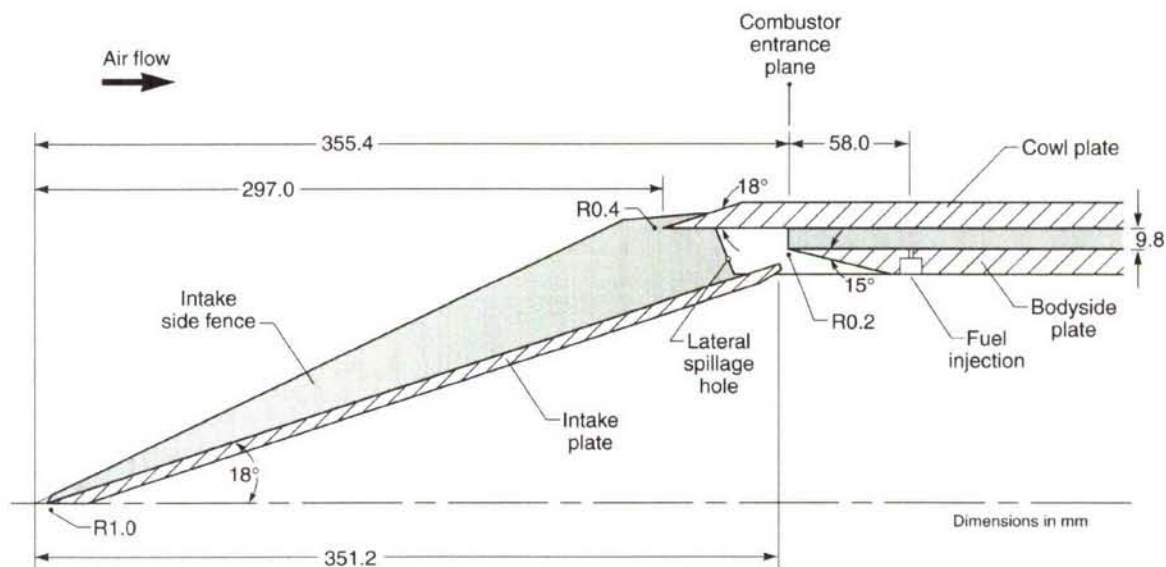


Figure 17 - Schematic of fuelled flowpath

The goal of the experiment was to supply uniform flow into the two rectangular combustors at conditions ranging between Mach 7.2 and 8.0, allowing for an angle-of-attack (α) variation of the payload between +5 and -5 degrees. Figure 17 shows a schematic of the fuelled flowpath. The intake consisted of a single 18 deg. wedge with a width of 100mm, a blunted leading edge, and highly swept side fences. The high wedge angle was necessary to ensure that the combustor entrance temperature and pressure were great enough to readily induce self-ignition of hydrogen. The rectangular combustor had a constant area 9.8 mm x 75 mm cross-section and a length of 300 mm (length/height = 30.61). The combustor cowl spanned the full width of the intake wedge and was situated such that the intake shock was upstream of its leading edge at all times. The flowpath

design incorporated a shock trap that was situated between the end of the intake wedge and the entrance of the combustor. This feature not only captured the cowl shock, but also bled off the intake boundary layer. The reduced width of the combustor (relative to the intake wedge) and lateral spillage holes in the side fences adjacent to the shock trap were designed to remove the fence boundary layers and corner flows. The angle-of-attack of the payload was defined as positive when the fuelled combustor was on the windward side, and negative when the fuelled combustor was leeward.

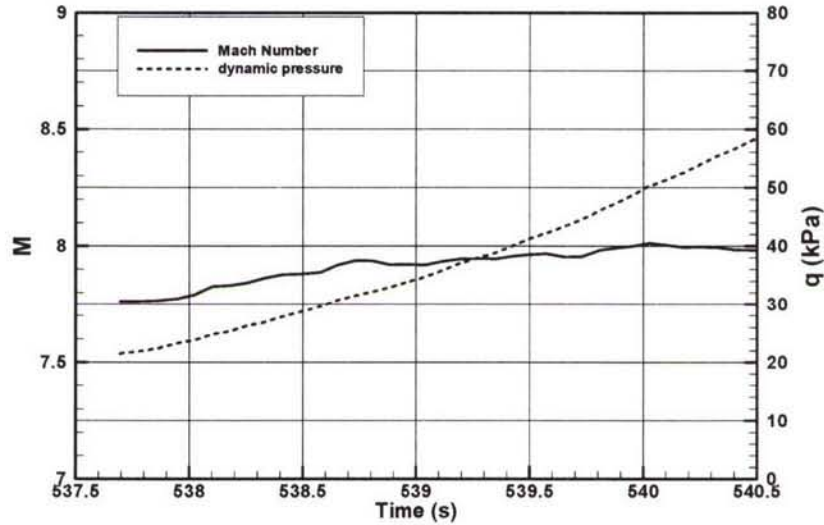


Figure 18 - Reconstructed Mach number (M) and dynamic pressure (q) histories

number	Time (s)	Flight Mach Number	Flight dynamic pressure (kPa)	Altitude (km)	angle-of- attack(deg.)
1	538.103	7.828	24.88	34.48	-5.012
2	538.179	7.831	25.33	34.31	5.540
3	538.734	7.938	31.55	33.05	-5.081
4	538.805	7.938	32.20	32.89	4.617

Table 1 – Flight parameters for analysed time slices

The flight produced a significant set of scramjet combustor data at varying duct entrance pressure, temperature and Mach number. Trajectory reconstruction was accomplished using onboard sensors alone (Cain et. al. 2004). Fuel flow was initiated at approximately $t = 536.5$ seconds after launch as the payload and attached Orion motor re-entered the atmosphere. Figure 18 shows the Mach number and dynamic pressure time histories during three seconds of the experimental window, and Table 1 lists four zero-yaw time slices used for analysis. Figure 19 shows a comparison of the fuelled and unfuelled combustion pressure distributions at windward conditions: i.e. when each duct was at a positive angle-of-attack of approximately 5 degrees. Note that all data is normalized by the combustor entrance pressure, in order to make meaningful comparisons. The equivalence ratio of the fuelled duct was approximately 0.34, and the pressure rise from combustion of the hydrogen fuel is clearly evident. Cycle analysis of this data indicated

that supersonic combustion occurred at these times slices during the flight, at a combustion efficiency for the fuel of 81% (Smart et. al. 2006).

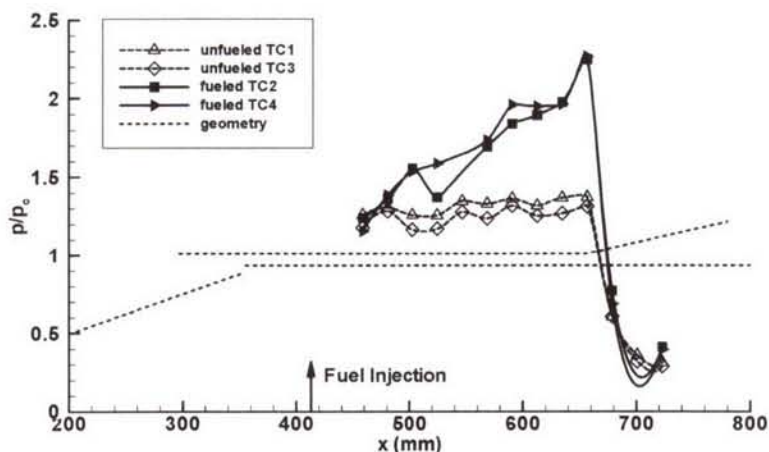


Figure 19 - Windward fueled and un-fueled combustor pressure distributions (x = axial distance from nose of payload)

The success of the HyShot 2 flight led to a significant interest in low cost scramjet flight-testing using sounding rocket boosters. Two further flights, HyShot 3 and 4 were conducted by The University of Queensland in March 2006; HyShot 3 for the British Company, Qinetiq, and HyShot 4, for the Japanese Aerospace Agency (JAXA). Further flights are planned.

3.3 Hyper-X

NASA's focused hypersonic technology program, called Hyper-X, conducted the most realistic flight tests of hypersonic airbreathing engines to date. Unlike either the CIAM flight test or HyShot 2, the Hyper-X flight vehicle separated from its booster to fly a controlled hypersonic trajectory under scramjet power. Two successful flights were conducted; the first at Mach 7 on March 27, 2004, and a second at Mach 10 on November 16, 2004. Both included 5+ seconds of hydrogen fuelled scramjet operation, followed by a series of hypersonic aerodynamic manoeuvres as the vehicle decelerated. The key results of the flights were that:

1. Airframe integrated scramjet powered vehicles can fly stable, controlled trajectories at hypersonic speeds.
2. Accelerating hypersonic flight is possible at Mach 7 using air-breathing propulsion.
3. Hypersonic cruise is possible at Mach 10 with a non-optimised vehicle/engine combination.
4. Ground test experiments, CFD analysis and other aerodynamic tools can be used to design scramjet powered flight vehicles.

The Hyper-X vehicle, a schematic of which is shown in Fig. 20, had significant heritage from the NASP program. It was a "smart scaled" version of a 200 ft operational vehicle (Rausch et. al. 1997) that could be flight tested within available budgets, while also demonstrating operation of a dual-mode hydrogen fuelled scramjet. The chosen 12 ft vehicle had a single airframe-integrated scramjet and was boosted to flight conditions using a modified Pegasus booster that was air-launched from a B-52 from Edwards AFB in California. The desired test conditions were 95,000 ft (~29.0 km) at Mach 7, and 110,000 ft (~33.5 km) at Mach 10, both of which correspond to a dynamic pressure of 1000 psf (~48 kPa). The flight sequence for the Mach 7 flight is shown in Fig. 21 (Volland et. al. 1998). The free-flying portion of the flight included separation from the booster, engine cowl opening, 5+ seconds of scramjet operation, fuel-off flight with the cowl open, and aerodynamic manoeuvres with the cowl closed. A similar sequence was conducted at Mach

10. The vehicles flown on the two flights were nominally of the same external shape, but had different thermal protection systems and different engine designs.

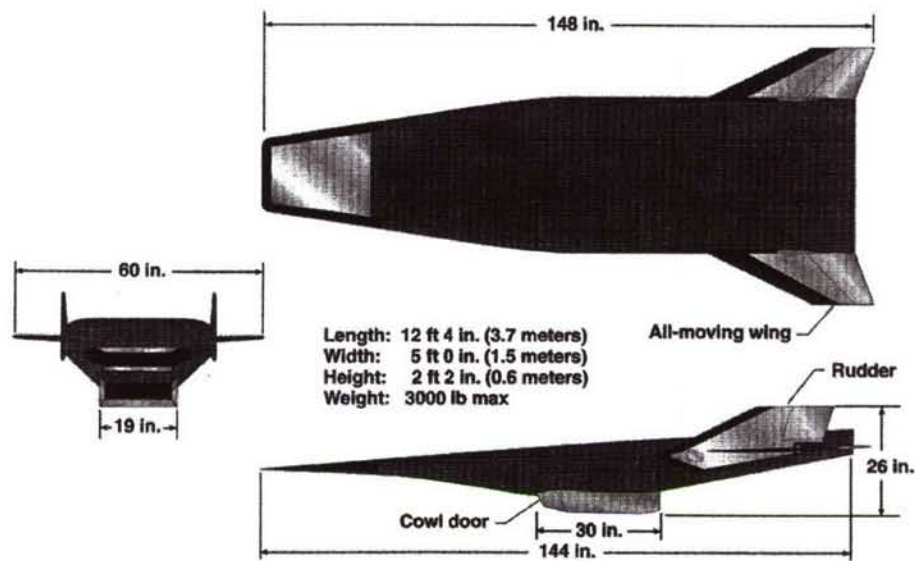


Figure 20 - Hyper-X vehicle configuration

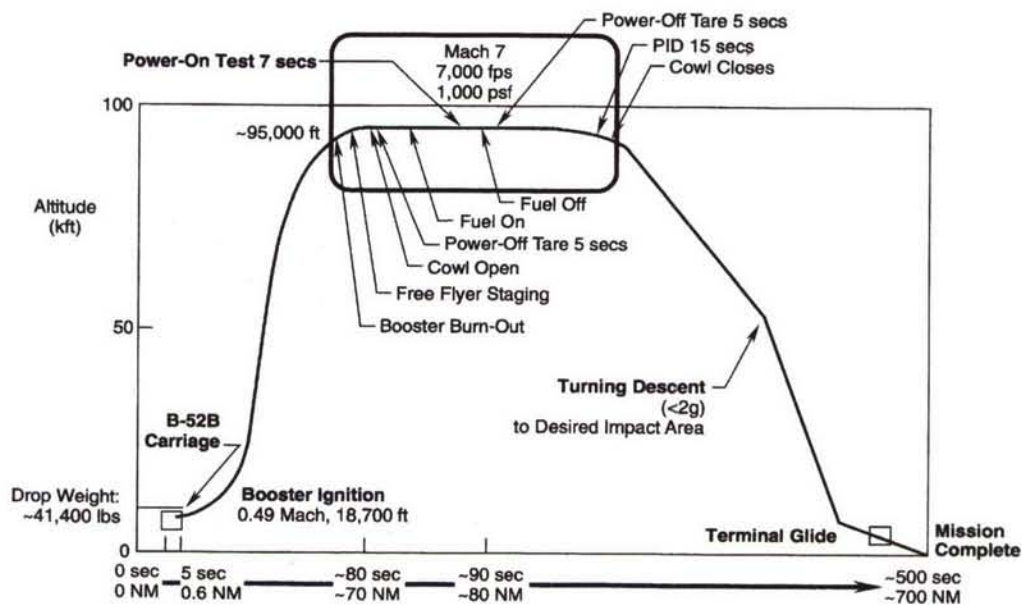


Figure 21 - Nominal Mach 7 Hyper-X flight trajectory

In terms of the scramjet flowpath, the Hyper-X vehicle enabled testing of a complete forebody, internal engine, and aftbody/thrust nozzle. The Mach 7 engine was developed through a long series of partial flowpath and subscale testing at NASA Langley Research Center, followed by a complete tip-to-tail flowpath simulation in the 8 foot High Temperature Tunnel (8-FT HTT), also at NASA Langley. A photograph of the engine, known as the Hyper-X Flight Engine (HXFE), is shown in Fig. 22. It was mounted upside down in the test section of the 8-FT HTT on a force balance with identical internal system components to those used in flight. The main objectives of this pre-flight testing were to validate the Mach 7 propulsion database and to verify the operation of system components. Not only were the engine operability and performance data acquired during

testing, but realistic estimates of the aero-propulsive vehicle force and moment increments due to both opening the cowl door and combustion were obtained (Huebner et. al. 2001).



Figure 22 - HXFE engine in 8-FT HTT (flow from right to left)

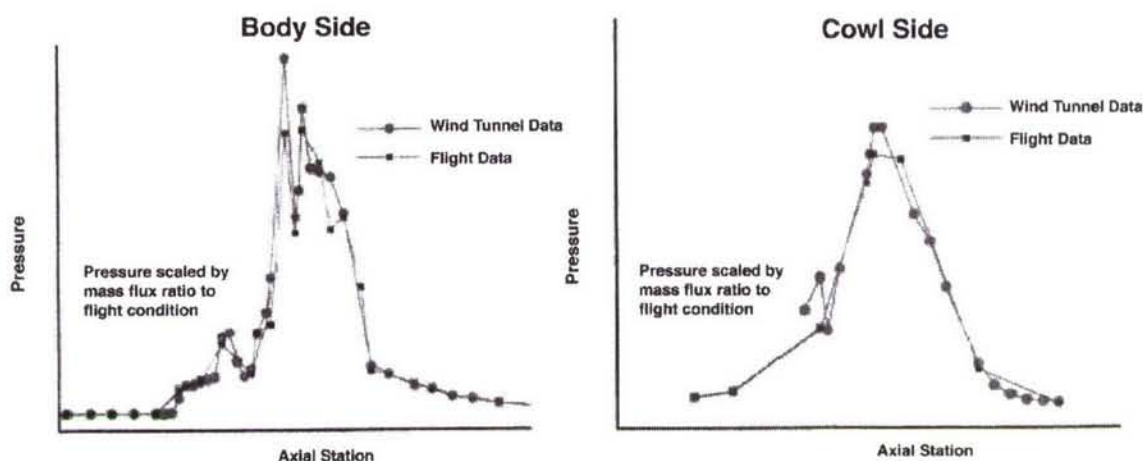


Figure 23 - Comparison of ground and flight data for the Hyper-X Mach 7 flight at design throttle level

Figure 23 shows a comparison of the body and cowlside pressure distributions in the Hyper-X engine between 8ft-HTT ground tests and flight, at the design throttle level (Ferlemann et. al. 2005). These results indicate very little difference between ground and flight data, which were closely matched in terms dynamic pressure and Mach number. The main difference between the two experiments was the flow contaminants in the 8ft-HTT (H_2O and CO_2), which appear to have little effect on the engine performance at these conditions and throttle level.

While the Mach 7 engine was able to be ground tested in long duration facilities, only impulse facilities can generate conditions to simulate Mach 10 propulsive flight on the ground. The ground tests to support development of the Mach 10 engine were done at the NASA HyPulse Shock tunnel situated at GASL's New York facility. This meant that only instantaneous testing was possible, and engine sequences such as piloting and fuel ramp-up could not be simulated. Despite this, the Mach 10 engine performed to expectation, as indicated in Fig. 24, which shows a comparison of prediction and flight pressure distributions on the bodyside of the Mach 10 engine taken from McClinton (2006).

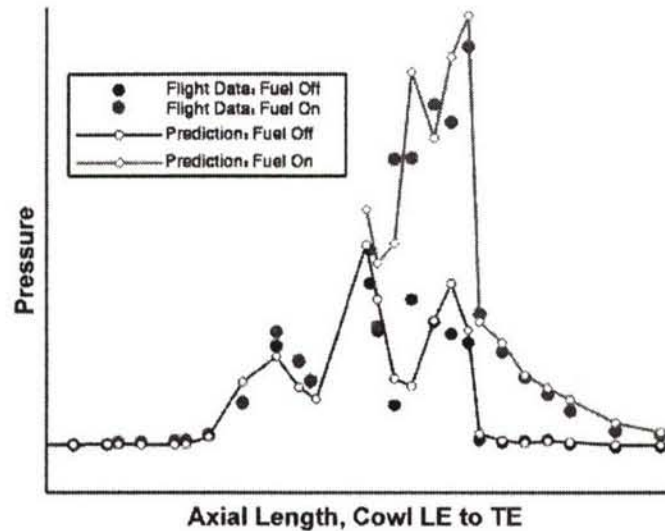


Figure 24 - Comparison of prediction to flight for the Hyper-X Mach 10 flight at design throttle position

Since Hyper-X, the United States Air Force has initiated the X-51 program, which is planned to include multiple flights of a liquid hydrocarbon missile-like configuration. The DARPA has funded the HyFly Program, which is based on the APL DCR configuration. Finally, a ten flight sounding rocket based programme called HiFIRE was recently initiated by the Defence Science and Technology Organisation (DSTO) of Australia and the United States Air Force. The goal of this programme is to develop the technology required for long duration scramjet flight at Mach 8.

4.0 Scramjet performance analysis

The performance of a scramjet engine, either uninstalled or when integrated on a hypersonic vehicle, is most easily determined by what is called stream thrust analysis. This technique conserves the fluxes of mass, momentum and energy on strategically placed control volumes to determine the propulsive forces on the vehicle. Figure 25 shows a schematic of a scramjet powered vehicle with a control volume surrounding all the airflow that passes through the engine. Airflow enters the control volume at the flight conditions, fuel is added to the air in the combustor and the flow exits through the vehicle nozzle. For ease of analysis, the flow exiting the control volume is usually represented by a flux-conserved one-dimensional average of the non-uniform exhaust plume. In the current analysis only the axial forces will be considered, however, similar relations can be developed for the transverse direction to determine the lift forces generated by the propulsion system.

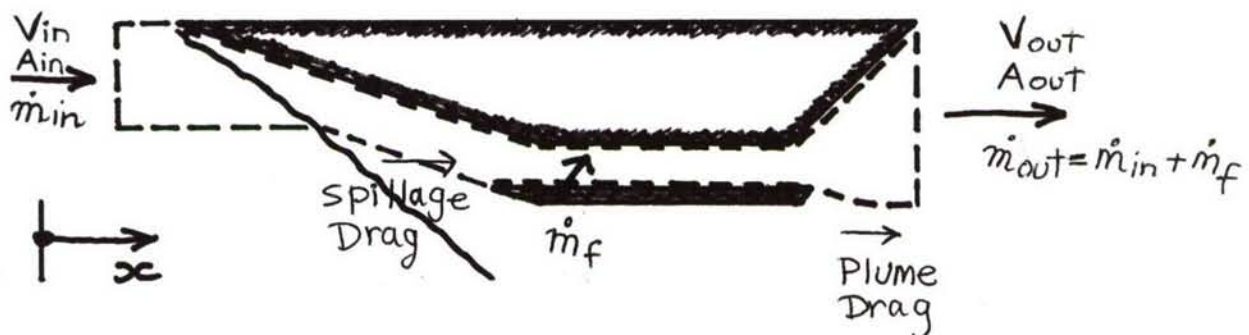


Figure 25 - Schematic of control volume used for scramjet performance analysis

Assuming for simplicity that fuel is added with no component of velocity in the streamwise direction, application of Newtons law to the control volume in Fig. 25 in the streamwise direction yields the following relation:

$$\dot{m}_{in}V_{in} + p_{in}A_{in} - (\dot{m}_f + \dot{m}_{in})V_{out} + p_{out}A_{out} + \sum F_{xs} = 0 \quad (1)$$

where $\sum F_{xs}$ = sum of the pressure and viscous forces on the top and bottom boundaries of the control volume.

It is customary to separate the additive drag due to inlet spillage and the nozzle plume from $\sum F_{xs}$ as follows:

$$\sum F_{xs} = F_{add} + F_{surface}$$

Re-arranging eqn. 1 yields:

$$F_{surface} = (\dot{m}_f + \dot{m}_{in})V_{out} + p_{out}A_{out} - \dot{m}_{in}V_{in} - p_{in}A_{in} - F_{add} \quad (2)$$

The left hand side of eqn. 2 is the thrust of the uninstalled engine, F_{un} . Using the definition of stream thrust, $F = pA + \dot{m}V$, we can express eqn. 2 as:

$$F_{un} = F_{out} - F_{in} - F_{add} \quad (3)$$

Equation 3 indicates that the uninstalled thrust of an engine can be determined with knowledge of the stream thrust of the air entering the engine, the additive drag, and the stream thrust exiting the engine nozzle. The flow enters the engine at ambient conditions and at the flight velocity, so determination of F_{in} reduces to a determination of the freestream capture area. Air spillage (and therefore spillage drag) decreases as the vehicle speed approaches the design point, and the plume drag varies depending on the amount of under-expansion in the nozzle. Both these are usually estimated through CFD analysis, or through rules-of-thumb based on empirical or experimental databases. Determination of F_{ex} requires an involved analysis that follows the air through the complete scramjet flowpath. Many authors have presented analyses to calculate F_{ex} for complete scramjet flowpaths with differing levels of sophistication and accuracy (Heiser & Pratt 1994, Pandolfi 1986, Pinckney et. al. 2004). The analysis presented here is in the form used by the present author.

4.1 Scramjet Component Analyses

Figure 26 shows a schematic of the internal flowpath of an airframe-integrated scramjet with particular reference stations highlighted. In keeping with the convention of Heiser & Pratt (1994), station 0 is in the freestream flow ahead of the engine, and a streamtube with area A_0 is captured and processed by the engine. Station 1 is downstream of the vehicle forebody shock and represents the properties of the flow that enters the inlet. Station 2 is at the inlet throat, which is usually the minimum area of the flowpath, and the length between stations 2 and 3 is referred to as the isolator. Station 3 represents the start of the combustor, and fuel and air is mixed and burned by the end of the combustor at station 4. The nozzle includes an internal expansion up to station 9, and an external expansion to station 10 at the end of the vehicle.

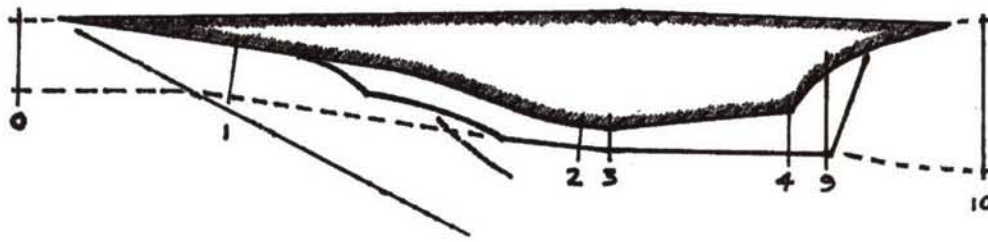


Figure 26 - Flow stations for engine analysis

It is appropriate to break the analysis needed to determine the stream thrust of the flow exiting the vehicle, and therefore the uninstalled thrust of the engine, into the three processes that make up the engine cycle; i.e. those of compression, combustion and expansion. While the compression and combustion processes can be blurred for some operating conditions, this convention will be adhered to here.

4.1.1 Compression

Efficient combustion of fuel requires that air be supplied to the combustor at a suitable pressure, temperature and mass flow rate. For a scramjet traveling at speeds greater than Mach 5 and at altitudes in the flight corridor of Fig. 14, this requires significant compression and heating of the air. For an airframe-integrated scramjet, both the vehicle forebody and inlet share this task. A multitude of different forebody/inlet configurations have been developed by many researchers (Van Wie 2001), each designed to generate a specified level of compression over a range of flight Mach numbers. The performance of such compression systems can be separated into two key parameters; (1) inlet capability, or how much compression is performed, and (2) inlet efficiency, or what level of flow losses does the inlet generate during the compression process. Meaningful discussions of inlet performance must include both parameters as, for example, a highly efficient inlet can be very easily designed if it is required to do little compression.

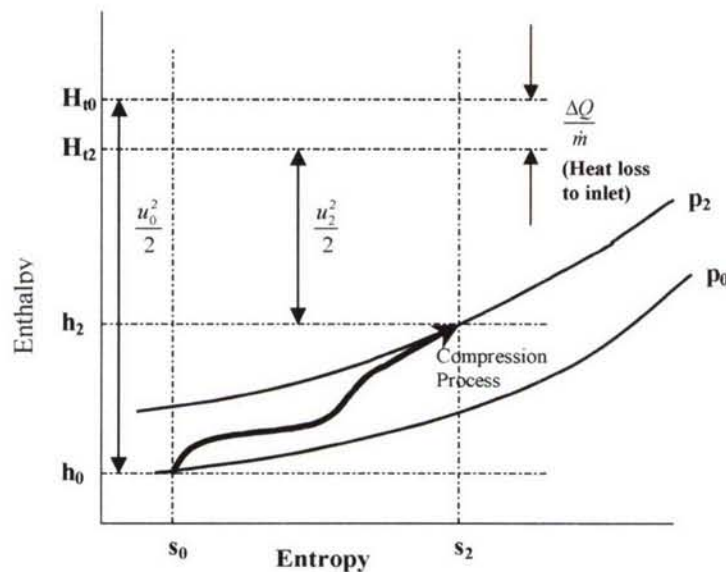


Figure 27 – Mollier diagram of inlet compression process

Performance analysis of scramjet inlets involves the determination of the flow conditions at the inlet throat (station 2 of Fig. 26). A common parameter used to quantify the efficiency of the forebody/inlet compression is the kinetic energy efficiency, η_{KE} . The usefulness of this parameter, compared to many others, is that it can be used for non-ideal gas processes, and that its value has been found to be relatively independent of Mach number for a given class of inlets. The definition of η_{KE} is simply the ratio of the kinetic energies of the flow before and after the compression, and is most easily described on a Mollier diagram, as shown in Fig. 27. Here the flow entering the engine is compressed from p_0 to p_2 . During the compression there is heat loss to the forebody/inlet structure, and:

$$\eta_{KE} = \frac{1/2u_2^2}{1/2u_0^2} = \frac{h_{t2} - h_2}{h_{t0} - h_0} \quad (4)$$

In some instances the adiabatic kinetic efficiency, $\eta_{KE,ad}$ is used. This parameter does not account for heat loss, and is defined as:

$$\eta_{KE,ad} = \frac{h_{t0} - h_2}{h_{t0} - h_0} \quad (5)$$

When conducting scramjet performance calculations, two common methods for determining the properties at the inlet throat are; (1) use an empirical relation for η_{KE} in combination with a number of other parameters, and (2) use CFD to perform a numerical simulation of the forebody/inlet flowfield. An empirical correlation for $\eta_{KE,ad}$ in terms of the ratio of throat Mach number to freestream Mach number, M_2/M_0 , is as follows (Waltrup et. al. 1982):

$$\eta_{KE,ad} = 1 - 0.4 \left\{ 1 - \frac{M_2}{M_0} \right\}^4 \quad (6)$$

This expression relates inlet efficiency to an inlet capability parameter, M_2/M_0 , so it satisfies our requirement for being a useful relation. However, in order to determine flow properties at the inlet throat, a temperature ratio, (T_2/T_0) , an average ratio of specific heats, γ_{av} , and an amount of heat loss to the vehicle must be also be specified. Figure 28 compares this correlation with a summary of reported inlet efficiency values for a range of inlet geometries. It appears that for first order accurate performance calculations, eqn. 6 is a reasonably choice for modeling scramjet compression processes.

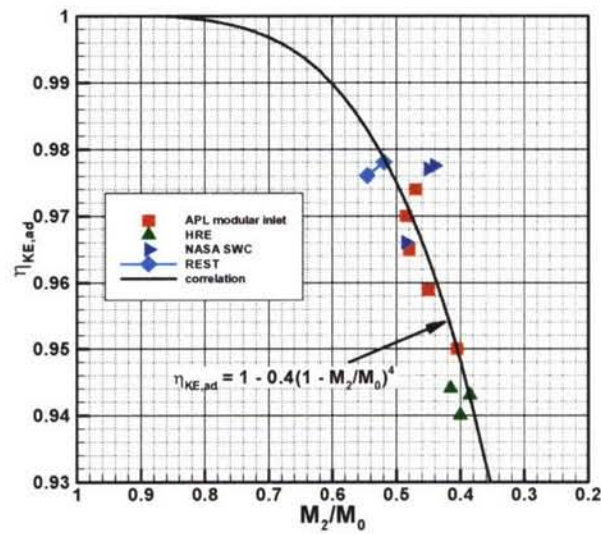


Figure 28 - Inlet efficiency data (subscript 4 corresponds to the inlet throat)

Since the mid-1990's, modern computers and CFD codes have developed to the point where the calculation of turbulent flows through hypersonic inlets can be performed on a routine basis. A more accurate model of the scramjet compression process for a particular configuration can therefore be obtained through multiple CFD calculations over the operational flight Mach number. An example of this is shown in Fig. 29, where the flux-conserved, one-dimensional averaged inlet throat properties and mass capture ratio are plotted for a 2-D forebody/3-D inlet combination based on CFD calculations over a range of inlet Mach number, M_1 (Smart & Tetlow 2006).

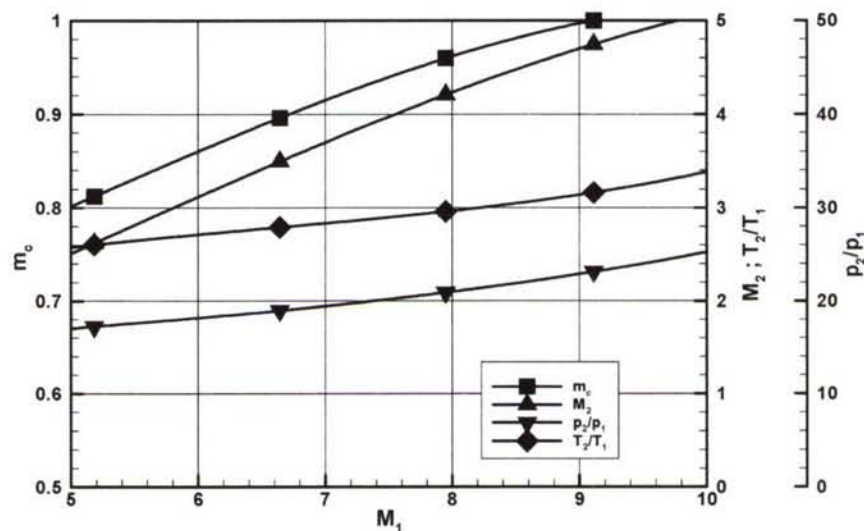


Figure 29 – CFD based Inlet capability parameters

In the design of hypersonic inlets there are some key issues that must be addressed in order to arrive at a useful configuration. These are:

1. Inlet starting limits
2. Boundary layer separation limits
3. Minimization of external drag
4. Performance at off-design Mach number

The process of establishing supersonic flow through the inlet, known as inlet starting, puts a significant constraint on the internal contraction ratio of hypersonic inlets. This can be overcome through variable geometry, however, the weight/complexity of such can significantly degrade the overall system performance of a scramjet engine. Figure 30 shows a plot of the internal contraction ratio limit for self-starting of a range of inlet configurations, as well as a theoretical starting limit developed by Kantrowitz & Donavon (1945), which is known to be conservative at hypersonic Mach numbers. In general, the self-starting limits of particular inlet classes are determined through experimental testing, and become more restrictive as the starting Mach number is decreased.

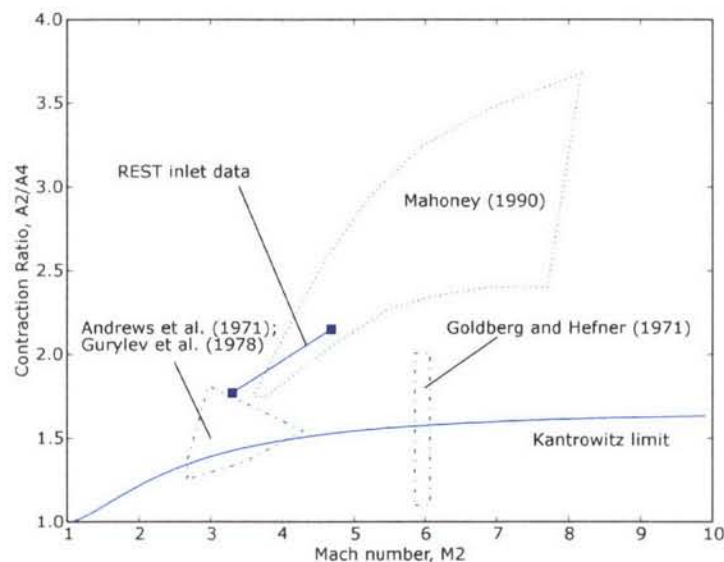


Figure 30 - Selected experimental data on starting limits with comparisons to the Kantrowitz limit (subscript 2 corresponds to the closure plane of the inlet; subscript 4 corresponds to the inlet throat)

The flow through any practical hypersonic inlet will be turbulent, and can be prone to boundary layer separation due to shock interactions. While minor boundary separation may be acceptable, large-scale boundary layer separation can create blockage of the engine and inlet unstart. Inlet flows are therefore required to satisfy established boundary layer separation limits (Korkegi 1975).

The minimization of external drag is an important aspect of the inlet design process. The external drag on the inlet will always be an important parameter when comparing the performance of different inlet configurations. Finally, most inlet design methods are based on a particular design Mach number, usually at the upper limit of the operational Mach number range. Adequate off-design performance; i.e. at Mach numbers lower than the design point, is required, otherwise the vehicle will never reach its design point.

4.1.2 Combustion

Analysis of the combustion process in a scramjet usually involves quasi-one-dimensional cycle analysis methods. While the real combusting flow in a scramjet is far from uniform at any cross-section throughout the engine, when used properly, these techniques provide an efficient means of modeling this region of a scramjet. While some methods simply jump from the start to the end of the combusting zone (Pandolfini 1986), the method presented in this article enables prediction of the pressure distribution in the entire region of the engine affected by combustion, therefore enabling comparison with experiment. These methods follow directly from the classical quasi-one-dimensional gasdynamics presented by Shapiro (1953).

At flight speeds below Mach 8, combustion in a scramjet engine can generate a large local pressure rise and separation of the boundary layer on the surfaces of the combustion duct. This separation, which can feed upstream of the point of fuel injection, acts to further diffuse the core flow in the duct, and will interact with the inlet, possibly causing an unstart of the engine. A short length of duct, called the isolator, is usually added to the scramjet flowpath upstream of the combustor to contain this phenomenon. In some engines the combination of the diffusion in the isolator and heat release in the combustor decelerate the core flow to subsonic conditions, in what is called dual-mode combustion. At speeds above Mach 8 the increased kinetic energy of the airflow through the engine means that the combustion generated pressure rise is not strong enough to cause boundary layer separation. Flow remains attached and supersonic throughout, and this is termed a pure scramjet. The quasi-one-dimensional analysis of pure scramjet flows is presented first, followed by analysis with the added complexity needed to deal with separated or dual-mode combustion flows.

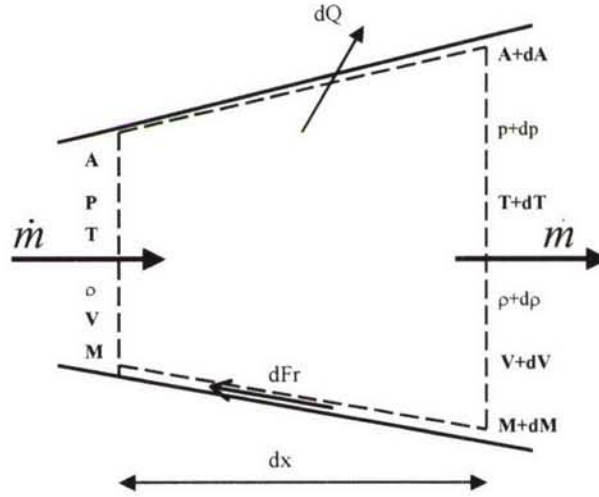


Figure 31 – differential element of combustor flow in a duct

A differential element of attached flow in a duct is shown in Fig.31. In this element, fuel and air are burning, and a friction force $dF_r = \tau_w A_w$ is applied by the walls, together with a heat loss in the amount dQ . For simplicity of analysis, the flow is assumed to be that of a calorically perfect gas with ratio of specific heats, γ , gas constant R , and constant pressure specific heat, c_p . Combustion heat release is modeled through the use of a heat of combustion, h_{pr} , and the change in total enthalpy of the element is:

$$dH_t = h_{pr} f_{st} d\phi - dQ \quad (7)$$

where f_{st} = stoichiometric fraction of fuel to air, and $d\phi$ = equivalence ratio of fuel that combusts in length dx .

The corresponding change in the total temperature of the flow is therefore $dT_t = dH_t/c_p$. The wall shear stress is related to a skin friction coefficient through $\tau_w = C_f \rho V^2/2$, and from the definition of the hydraulic diameter (D) of the duct, $A_w = 4A dx/D$. The differential conservation equations of mass, momentum and energy for the element, are therefore given by:

$$\frac{d\rho}{\rho} + \frac{dV}{V} + \frac{dA}{A} = 0 \quad (8)$$

$$\frac{dp}{p} + \frac{\gamma M^2}{2} \frac{4C_f dx}{D} + \frac{\gamma M^2}{2} \frac{dV^2}{V^2} = 0 \quad (9)$$

$$\frac{dT}{T} + \frac{\gamma-1}{2} M^2 \frac{dV^2}{V^2} = \left(1 + \frac{\gamma-1}{2} M^2\right) \frac{dT_t}{T_t} \quad (10)$$

Together with the equation of state for the gas and the definition of Mach number (in differential form):

$$\frac{dp}{p} - \frac{d\rho}{\rho} - \frac{dT}{T} = 0 \quad (11)$$

$$\frac{dM^2}{M^2} - \frac{dV^2}{V^2} + \frac{dT}{T} = 0 \quad (12)$$

we have five equations to relate the seven variables. Following Shapiro (1953), area change (dA/A) and total temperature change (dT_t/T_t) are treated as independent variables, and differential relations for all the others can be determined by elimination. The relation for Mach number is:

$$\frac{dM^2}{M^2} = \frac{2\left(1 + \frac{\gamma-1}{2} M^2\right)}{1 - M^2} \frac{dA}{A} + \frac{(1 + \gamma M^2)\left(1 + \frac{\gamma-1}{2} M^2\right)}{1 - M^2} \frac{dT_t}{T_t} + \frac{\gamma M^2\left(1 + \frac{\gamma-1}{2} M^2\right)}{1 - M^2} 4C_f \frac{dx}{D} \quad (13)$$

This relation may be integrated to determine the axial distribution of Mach number in ducts with specified area and total temperature distributions, along with a knowledge of C_f , and all the other 1-D flow properties of interest.

An example of the use of this methodology is plotted in Fig. 32, which shows the properties in a round combustor duct with an initial diameter of 0.06m and a divergence with area ratio of 2. In this instance the properties at the throat ($x_2 = 0.0$ m) are defined ($M_2 = 3.60$, $p_2 = 50$ kPa, $T_2 = 650$ K, $H_{t2} = 2.35$ MJ/kg) and hydrogen fuel ($h_{pr} = 119,954$ kJ/kg) is injected at $x_3 = 0.2$ m with an equivalence ratio of $\phi = 0.50$. The amount of fuel that is allowed to react with the air at a particular station is dictated by a mixing efficiency curve, $\eta_m(X)$, that takes the form:

$$\eta_m = \eta_{m,e} \frac{\mathcal{G}X}{1 - X} \quad (14)$$

where $\eta_{m,e}$ is the mixing at the end of the combustor, $X = (x - x_3)/(x_4 - x_3)$ and \mathcal{G} is an empirical constant of order 1 to 10 which depends of the rate of mixing (Heiser & Pratt 1994).

For the current example, $\eta_{m,e}$ was set to 0.8 and a value of $\mathcal{G} = 5.0$ was used. The heat release curve was therefore:

$$H_t = H_{t2} + h_{pr} f \phi \eta_m - dQ \quad (15)$$

Skin friction was calculated based on a $C_f = 0.002$ and heat loss to the structure (dQ) was calculated using Reynolds analogy.

Given the limitation of constant ratio of specific heats (γ) and gas constant (R) in the analysis, eqn. 13 is integrated in sections along the duct. In the isolator section upstream of fuel injection, values of $\gamma = 1.37$ and $R = 287$ J/kgK were used. In the combustor, the properties of the real fuel/air/combustion products mixture varies with length, but average values of $\gamma = 1.31$ and $R = 297$ J/kgK were used. In the isolator section of the duct the Mach number reduces and the pressure and temperature increase due to the action of friction on the duct surfaces. At the start of the combustor, flow properties are recalculated to be consistent with the values of γ and R used in the

combustor integration, while conserving fluxes of mass, momentum and total enthalpy across the boundary between the isolator and combustor. Fuel is also added, and combustion along the duct leads to a drop in the Mach number, an increase in the temperature, and the pressure varies smoothly in response to the competing effects of combustion and area increase. The peak pressure and temperature in the duct are $p/p_2 = 2.02$ and $T/T_2 = 2.65$. The analysis results in an estimate of the one-dimensional properties of the flow as it exits the combustor at $x_4 = 0.5$ m.

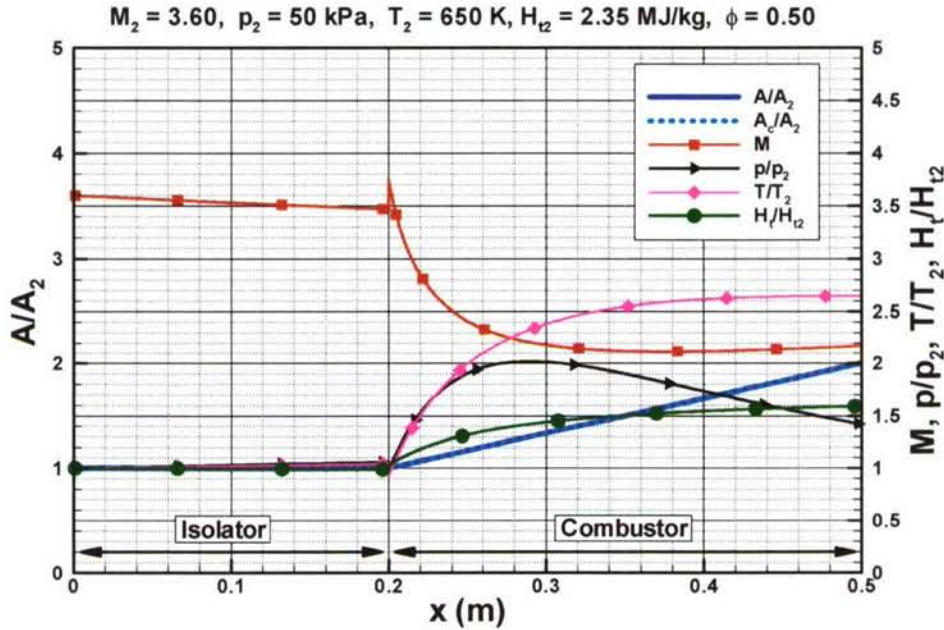


Figure 32 - Attached flow through an isolator and divergent combustor

For the situation where flow separation occurs in the combustion region, the preceding analysis does not provide a useful model of the real flow, as the area of the core flow, A_c , is less than the geometric area. The core flow area represents a new variable, hence an extra relation is needed to close the problem. Figure 33 shows a sketch of a supersonic duct flow that has been separated by either combustion or some other imposed back-pressure (Ortwerth 2001). The core flow (region I) experiences a pressure gradient in the form of an area constriction and shock train in the supersonic region, and an area increase once it is decelerated to subsonic conditions. The separated flow (region III) balances the pressure gradient by shear stress on its boundary with region II. The pressure gradient in the core flow must be equal to the pressure gradient that the shear can support in the separated region. Based on a large amount of experimental data at different Mach numbers, Reynolds numbers and duct geometries, the pressure ratio p/p_i over a length dx was determined by Ortwerth (2001) to vary as:

$$\frac{d(p/p_i)}{dx} = 4K\gamma(p/p_i)M^2 \quad (16)$$

where $4K = 44.5C_{f0}$ and C_{f0} = the friction coefficient at the initial separation point. This relationship essentially supplies a length scale required to achieve the full pressure rise.

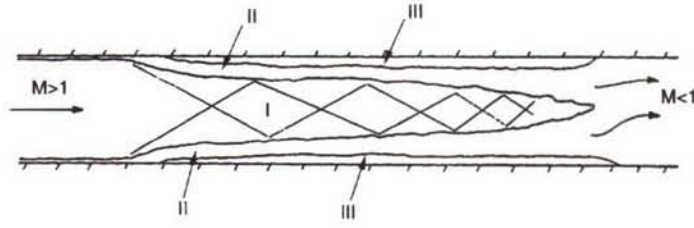


Figure 33 - Flow model for separation in a duct

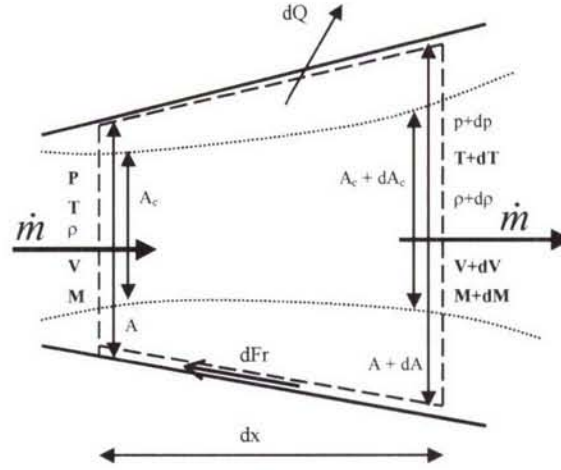


Figure 34 – Differential element of separated flow

A differential element of the separated flow in a duct is shown in Fig. 34. The main difference between this and Fig. 31 is that the core area (A_c) is less than the geometric area (A). The conservation equations all relate to the core area, but friction and heat loss are based on the geometric area. In this instance, the energy equation, equation of state and definition of Mach number are the same as for the attached flow, but the mass conservation and momentum equations are now:

$$\frac{d\rho}{\rho} + \frac{dV}{V} + \frac{dA_c}{A_c} = 0 \quad (17)$$

$$\frac{dp}{p} + \frac{\gamma M^2}{2} \frac{4C_f dx}{D} + \frac{\gamma M^2}{2} \frac{A_c}{A} \frac{dV^2}{V^2} = 0 \quad (18)$$

Equation 16 is the extra relation required to close the separated flow problem. After a significant amount of algebraic manipulation, a relation for Mach number equivalent to eqn. 13 is as follows:

$$\frac{dM^2}{M^2} = - \left(1 + \frac{\gamma-1}{2} M^2 \right) \left[\frac{dp/p}{\frac{\gamma M^2}{2} \frac{A_c}{A}} + \frac{4C_f \frac{dx}{D}}{\frac{A_c}{A}} + \frac{dT_t}{T_t} \right] \quad (19)$$

This must be integrated in conjunction with the following relation for A_c/A :

$$\frac{d(A_c/A)}{A_c/A} = \left[\frac{1 - M^2 \{1 - \gamma(1 - A_c/A)\}}{\gamma M^2 A_c/A} \right] \frac{dp}{p} + \left(\frac{1 + (\gamma - 1)M^2}{2 A_c/A} \right) 4C_f \frac{dx}{D} + \left(1 + \frac{\gamma - 1}{2} M^2 \right) \frac{dT_t}{T_t} \quad (20)$$

An example of the use of this methodology is plotted in Fig. 35, which shows the properties in the same round combustor duct as Fig. 32, but with reduced throat Mach number and increased fuel equivalence ratio. In this instance the properties at the throat are $M_2 = 2.65$, $p_2 = 50$ kPa, $T_2 = 650$ K and $H_{t2} = 1.59$ MJ/kg. Hydrogen fuel is injected at $x_3 = 0.2$ m once again, and is assumed to combust with the same mixing curve as before (eqn. 14), but with an increased equivalence ratio of $\phi = 0.81$. The same values of γ and R were also used for the isolator and the combustor. At these conditions the pressure rise from combustion separates the duct boundary layer (Korkegi 1975). The position at which separation occurs is iteratively chosen such that the flow may re-attach smoothly in the divergent section. Furthermore, if the core flow reduces to subsonic conditions in the separated region (as in this case), the flow must re-attach subsonically and then re-accelerate through a thermal throat at an axial position that can be calculated apriori, as outlined in Shapiro (1953).

Figure 35 shows that the separation point that satisfies these criteria is at $x = 0.988$ m. The core flow begins diffusing at this point at a rate dictated by eqn. 16, reaching a minimum area of $A_c/A_2 = 0.616$. Combustion of fuel acts to push the flow towards re-attachment, which occurs at $x = 0.284$ m with $M = 0.961$. The flow then re-accelerates through the thermal throat at $x = 0.295$ m. Note that in comparison with the attached flow example (Fig. 32), the pressure and temperature rise in this dual-mode combustion flow are considerably higher, peaking at $p/p_2 = 4.24$ and $T/T_2 = 3.64$. While it is recognized that this analysis involves the significant assumption of a perfect gas, it does however contain all the physical attributes that are exhibited by real flows. Similar analyses of combustion flows in thermodynamic equilibrium are presented in Auslander & Smart (1999).

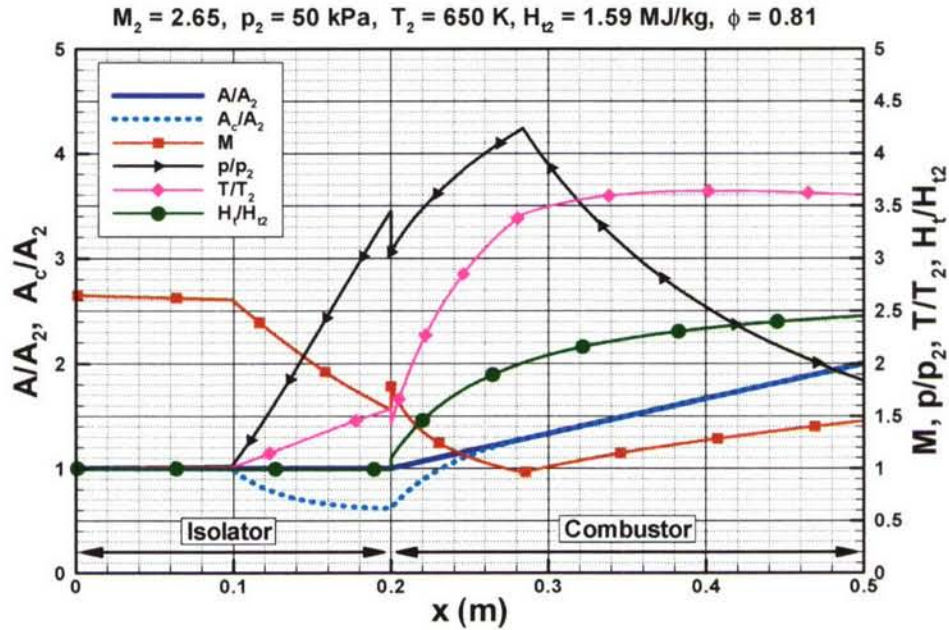


Figure 35 - Thermally throated, separated flow through a divergent duct

In the design of scramjet combustors there are some key issues that must be addressed in order to arrive at a useful configuration. These are:

1. Adequate mixing of fuel and air
2. Fuel ignition and flame holding
3. Operation over a range of inflow conditions

The perennial issue of fuel/air mixing can never be ignored in the design of a scramjet, and this issue becomes more difficult as the Flight Mach number increases. A multitude of fuel injection/mixing schemes have been examined by a multitude of researchers, including some interesting studies presented in Stalker et. al. (2006) and Northam et. al. (1991). Fuel ignition and flame holding are of course related to fuel mixing. Fuel injection schemes must not only generate fuel/air mixing, but enable ignition of fuel, followed by stabilization of a combustion flame. At lower flight Mach numbers ignition aids such as spark plugs and highly reactive fuel additives are used to overcome ignition problems, although fuel additives can affect the specific impulse of the engine if these are required on a continuous basis. In many instances it is desirable to operate a scramjet over a range of flight conditions, resulting in flow entering the combustor at a range of inflow conditions. Fuel scheduling from multiple injection sites is often used to increase the operational range of a scramjet combustor.

4.1.3 Expansion

The expansion process converts the potential energy of the combusting flow to kinetic energy and then thrust. In an airframe-integrated scramjet, this begins in the divergent sections of the combustor and internal nozzle, and continues over a large portion of the vehicle afterbody. The shape of the afterbody also determines the direction of the gross thrust vector relative to the vehicle's flight direction. An ideal expansion nozzle would expand the engine plume isentropically to the freestream pressure assuming chemical equilibrium, and this is the usual criterion that real nozzle flows are measured against. Loss mechanisms in practical expansion processes are due to:

1. Under-expansion
2. Failure to recombine dissociated species
3. Flow angularity
4. Viscous losses

The weight of a fully-expanding internal nozzle/aftbody would be prohibitive at most hypersonic flight conditions, hence under-expansion losses are usually traded against vehicle structural weight. Dissociation losses result from chemical freezing in the rapid expansion process in the nozzle, essentially locking up energy that cannot be converted to thrust. This problem can be exacerbated by inefficient compression, which leads to higher than necessary temperatures at the start of the expansion process. Flow angularity losses are a product of varying flow directions in the nozzle, and viscous losses are associated with friction on the internal nozzle and afterbody surfaces.

The aforementioned expansion losses are typically modelled using a nozzle efficiency parameter, η_N , which is applied as a gross thrust coefficient to the ideal stream thrust increment between the end of the combustor (station 4) and the end of the vehicle (station 10). The ideal stream thrust increment is calculated by isentropically expanding the flow at station 4 assuming chemical equilibrium to either, (1) a specified area based on an estimate of the size of the expanded plume, or (2) a specified pressure greater than or equal to the freestream pressure. Typical values for the nozzle efficiency range between $\eta_N = 0.85-0.95$. At the completion of this analysis, an estimate of the 1-D properties at the vehicle exit is obtained, and based on eqn. 3, an estimate of the uninstalled thrust of a scramjet can be calculated.

It would be fair to say that the design of nozzle expansion systems for airframe-integrated scramjet vehicles is one of the least mature aspects of overall design process. This may be due to the historical separation of the propulsion and airframe, with neither groups wanting to take full responsibility for the engine nozzle/vehicle afterbody. This difficulty is exacerbated by the fact that the character of the engine plume can vary greatly with flight Mach number and engine throttle level. The engine plume can also affect the performance of vehicle trim surfaces and flaps. Despite this, confidence that these issues can be solved for practical vehicles was significantly increased by the successful flights of the NASA's Hyper-X vehicle.

5.0 Scramjet applications

The “holy grail” of hypersonic airbreathing propulsion is its use as part of a system for reaching low earth orbit, either for satellites insertion or manned operations. At the current stage of scramjet technology development, single-stage-to-orbit systems are not viable, however many multi-stage options have been studied (Meht & Bowles 2001, Bowcutt et. al. 2002). Turbojets are a propulsion candidate for the initial phase of a flight to LEO, but are currently limited to Mach 3+. Scramjets are a desirable candidate for the middle phase, particularly if the upper limit of their operation can be stretched to Mach 10+. However, scramjet use in conjunction with turbojets is problematic, as the take-over Mach number of a scramjet designed to operate at Mach 10 and above is likely to be Mach 5-6, in the absence of significant variable geometry. An efficient liquid fuelled rocket is a desirable candidate for the last phase to LEO.

An example of a possible system for acceleration to low earth orbit is described here, based on a rocket-scramjet-rocket three-stage vehicle design to lift approximately 100 kg to LEO. The first stage is a solid rocket, chosen for its simplicity of operation, despite its low efficiency. The second stage is a scramjet powered hypersonic vehicle with an initial mass of 3000 kg that can operate between Mach 6 and 12. This is followed by a liquid fuelled rocket third stage to boost the payload to LEO.

5.1 Vehicle Description

Booster

The initial booster is required to achieve flight conditions suitable for operation of the scramjet from a ground launch. A preliminary sizing of this booster was made assuming solid fuel rocket motors, structural mass fraction $m_s/m_o = 0.18$, Isp of 270 seconds at sea level and 276 seconds in vacuum and aerodynamic data from a typical ballistic launch vehicle such as Ariane 3 (Isakowitz 1995). The requirements of the booster were that it place the 3000 kg scramjet powered second stage at an altitude of 27 km, travelling at Mach 6 with a flight path angle of $\zeta = 0.0^\circ$. An initial mass of $m_o = 10300$ kg was estimated from this preliminary analysis assuming an easterly, equatorial launch. Optimisation of the boost trajectory or use of a higher performing rocket would lead to a reduced m_o .

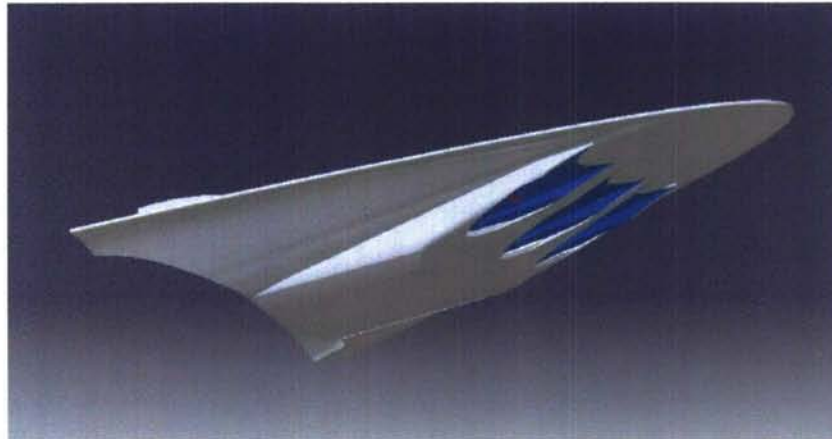
Scramjet Powered Hypersonic Vehicle

Waveriders are a class of hypersonic vehicles that have the capacity for high lift-to-drag ratio (L/D). These vehicles accomplish this by “riding” the shock wave they produce during flight, which theoretically remains attached to the sharp leading edges of the vehicle. These vehicles were taken beyond academic interest by researchers at the University of Maryland who optimised their shape to maximise $L/D(\text{Volume})^{2/3}/A_{\text{planform}}$, and accounted for viscous effects (Bowcutt et. al. 1987). Integration of scramjet propulsion systems into waverider-derived hypersonic vehicles has also been studied (O'Neill & Lewis 1992). The current concept involves the use of a scramjet-powered vehicle based on a waverider developed for Mach 14 flight (Gillum & Lewis 1997). From the predetermined start mass of 3000kg and the average density for a hydrogen fuelled hypersonic vehicle, including payload, of $124\text{kg}/\text{m}^3$ (Lewis 2001), the volume of the vehicle was 24.19 m^3 . Scaling up the waverider model to match this volume results in a vehicle with length = 12.59 m, span = 5.23 m and $A_{\text{planform}} = 39.05\text{ m}^2$.

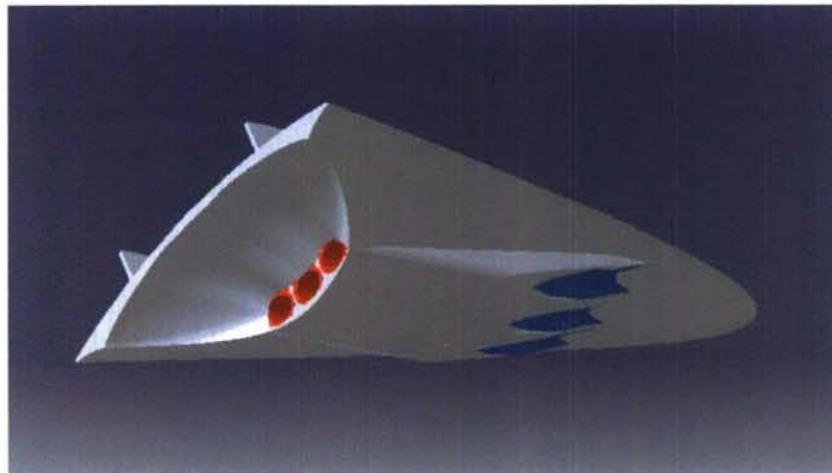
The experimentally determined aerodynamic coefficients of this waverider are listed in Norris (2006) for flight Mach numbers 6, 8, 10 and 14, indicating that the minimum vehicle drag occurs at $\alpha = -5^\circ$. These coefficients were used in this study for the scramjet-powered phase of the trajectory. In the force accounting methodology used here, the forebody drag of the vehicle was accounted to the propulsion system, whereas the external drag of the propulsion system was

accounted to the vehicle. Furthermore, installation of the scramjet modules was assumed to have little effect on the overall vehicle lift.

The scramjet propulsion system used in the study was based on the Rectangular-to-Elliptical Shape Transition (REST) Scramjet configuration (Smart 1999, Smart 2001). This is a three-dimensional, fixed geometry, scramjet flowpath that is integrated with the vehicle forebody, transitions from a rectangular capture area to an elliptical throat, and includes an elliptical combustor. The particular configuration used here was developed for flight between Mach 6 and 12 with hydrogen fuel. Two views of how multiple RESTM12 modules would appear installed on a waverider are shown as Figs. 36(a) and (b).



(a)



(b)

Figure 36 - Hypersonic waverider with RESTM12 scramjet propulsion system installed

Orbital stage

The orbital stage was a separate rocket that would be deployed from the scramjet vehicle payload bay and accelerate the payload from scramjet shut-down conditions to the required 200km circular orbit. A structural mass fraction of 0.15 was used for the orbital stage with $I_{sp} = 324s$. These values were taken from the upper stage of the Japanese H2 launch vehicle (Isakowitz 1995). From the mass, velocity, altitude and flight path angle at scramjet shutdown, the payload mass was approximated using Hohmann transfers. The orbital stage provided the propulsion to insert the payload into a low earth transfer orbit with an apogee altitude of 200km and then to circularize the orbit at 200km.

5.2 Trajectory Simulation

The software used for trajectory simulation was a Fortran based code, originally developed at the Space Systems Institute in Stuttgart, Germany. The dynamic equations were taken from Burkhardt (2001) and describe a 3 degree-of-freedom trajectory over a rotating earth model, using a 4th order Runge-Kutta integration technique. A spheroidal earth model was used to determine the radius of the Earth at given latitudes. A 4th order gravitational model (Regan & Anandakrishnan 1993) was implemented to approximate the Earth's gravitational field, and the atmospheric parameters were calculated using the Mass Spectrometer Incoherent Scatter Experiment 1993 (MSISE 93) atmosphere model (Tetlow 2003).

The boost flight segment was controlled by a launch elevation, azimuth and position. The scramjet flight phase was controlled using a parameter set of angle-of-attack as a function of time. The aim of the control strategy was to achieve as high an altitude and flight path angle as possible at a shut-off flight Mach number close to 12. The trajectory was also controlled to maintain dynamic pressure between 50 and 100kPa. Although several runs were performed to understand the dominant parameters governing the trajectory, no optimisation of the scramjet phase was performed in this preliminary study.

5.3 Scramjet Propulsion Database Generation

The propulsion module used for the example follows the form outline in section 4, and it was developed from the calculated performance of a fixed geometry, REST scramjet engine that has a design point of $M_0 = 12.0$, but remains operational down to $M_0 = 6.0$. This engine will be referred to here as the RESTM12 scramjet and is considered to be a near-term configuration that could be envisaged to fly within the 5-10 years.

During a trajectory calculation the trajectory program makes calls to the propulsion module to obtain the specific thrust, specific impulse, and equivalence ratio of the engine for a particular flight velocity, angle-of-attack and altitude. The RESTM12 scramjet is designed to operate at $q_0 \sim 50$ kPa in conjunction with a vehicle forebody compression equivalent to that generated by a 6° wedge. Analysis of the waverider vehicle forebody over the Mach 6-12 flight regime indicated that at $\alpha = 0^\circ$ it generates a pre-compression equivalent to an 8° wedge. Given this, the nominal angle-of-attack for the vehicle was assumed to be $\alpha = -2^\circ$. Hence the engine was installed on the vehicle so that the thrust vector of the engine was parallel with the velocity vector when the vehicle was at $\alpha = -2^\circ$. The operational angle-of-attack range for the engine was assumed to be ± 3 deg. about the nominal, so that the angle-of-attack limits for the vehicle were set to $\alpha = -5^\circ$ and $+1^\circ$. As already mentioned, the vehicle had minimum drag and zero lift at $\alpha \sim 5^\circ$.

A database was created for the RESTM12 flowpath using the compression, combustion and nozzle expansion models described in section 4. This was based on calculations performed for $M_0 = 6.0, 8.0, 10.0$ and 12.0 , at vehicle $\alpha = -6.0, -4.0, -2.0, 0.0$ and $+2.0$ degrees, and $q_0 = 50$ kPa. All calculations were performed with $\phi = 1.0$, except for the $M_0 = 6.0$ calculations, where the engine reached its operability limit at $\phi < 1.0$. This characteristic was due to the fact that the RESTM12 scramjet was designed with a contraction ratio and combustor divergence suitable for operation at $M_0 > 10$, and is one of the real world compromises that must be made in a fixed geometry engine.

The three propulsion parameters required by the trajectory code were the uninstalled specific thrust, $f = \Delta F / \dot{m}_0 = (F_{10} - F_0) / \dot{m}_0$, the specific impulse of the engine, $I_{sp} = \Delta F / (g^* \dot{m}_f)$, and equivalence ratio, $\phi = \dot{m}_f / (f_{st}^* \dot{m}_0)$. The calculations used in the database were performed for a single engine with a capture width, $w_{cap} = 0.15$ m; i.e. at wind-tunnel model scale. It was assumed that the propulsion parameters calculated in this way can be conservatively used for larger engines. A lower limit of $q_0 = 30$ kPa was placed on the use of the database due to kinetic

limitations related to low pressures entering the combustor. Three RESTM12 scramjet modules were used for the baseline trajectory calculation discussed in the next section, each with a width of $w_{cap} = 0.76$ m. This scale allowed smooth integration with the 12.59 m length vehicle.

5.4 Baseline LEO Trajectory

The solid rocket booster supplied the 3000 kg scramjet powered vehicle at an altitude $h = 27$ km, velocity $V = 1804.5$ m/s, and flight path angle of $\zeta = 0.0$ degrees. This corresponds to a flight Mach number $M = 6.01$ and dynamic pressure $q = 48.0$ kPa. An equatorial launch in an easterly direction was also assumed. Figure 37 shows M_0 , q_0 and α for a baseline 272.5 second scramjet powered acceleration that reached $M_0 = 11.73$ at scramjet shutdown. The dynamic pressure was controlled through variation of angle-of-attack to stay within the required range (50-100 kPa). Note that α was kept between -4.0 and -5.0 degrees to accomplish this, indicating that the high lift capability of the vehicle was not utilized. A key result of this preliminary analysis appears to be that high L/D is not required for hydrogen fuelled scramjets.

Figure 38 shows plots of vehicle drag and engine thrust over the trajectory, along with the vehicle mass. Positive net thrust (Thrust-Drag) is key to achieving useful ΔV with the available fuel. Figure 38 indicates that up to $M_0 \sim 11$ the vehicle maintained a strong level of net thrust, whereas above $M_0 = 11$ net thrust was diminishing. Figure 39 shows plots of vehicle altitude and velocity during the scramjet powered phase, indicating an altitude of $h = 37.15$ km and velocity of $V = 3745$ m/s at scramjet shutdown. The scramjet consumed 1356 kg of hydrogen fuel (45.2% of the vehicle starting mass) and covered 807.6 km, leaving a vehicle mass at the end of the scramjet phase of 1644 kg.

A fortunate aspect of the trajectory was that the vehicle was able to operate close to its minimum drag orientation for most of the scramjet powered flight. This was possible because of the low lift requirements of the vehicle. Furthermore, assuming a fuel density of 85 kg/m^3 consistent with slush hydrogen, 1356 kg of fuel corresponds to a volume of 15.95 m^3 , which is 65.9% of the entire vehicle volume. It would appear that a waverider most suitable for access-to-space applications should be optimised for maximum $(Volume)^{2/3} / A_{planform} / C_D$. Trajectory optimisation for maximum fuel efficiency was not performed here, but would result in reduced fuel consumption.

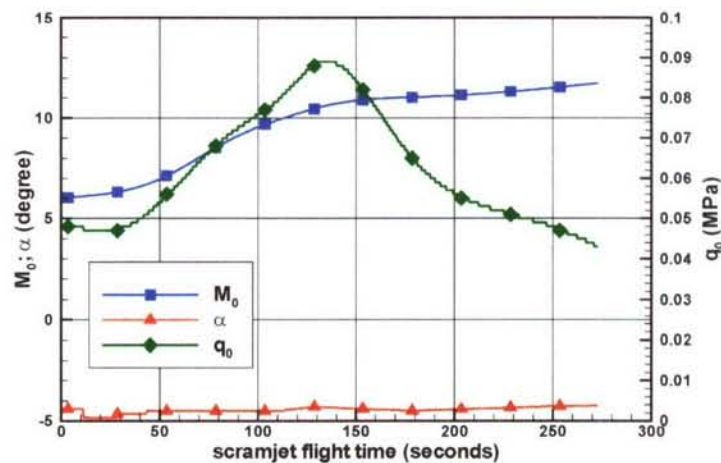


Figure 37 - Flight Mach number, angle-of-attack and dynamic pressure of baseline trajectory

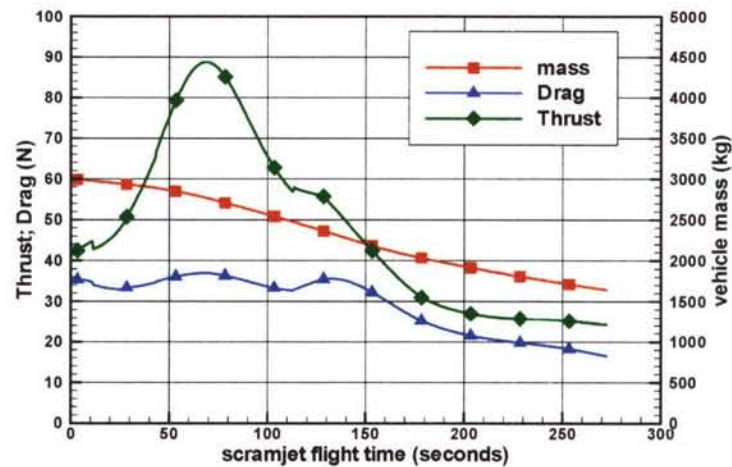


Figure 38 - Thrust, Drag and vehicle mass for the baseline trajectory

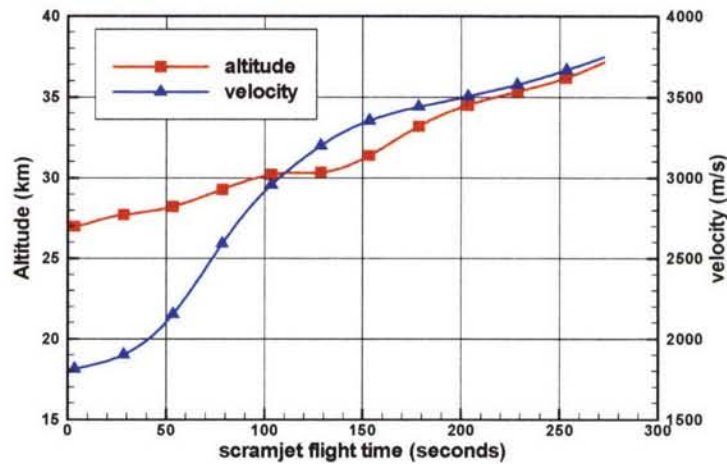


Figure 39 - Altitude and velocity of baseline trajectory

Analysis of the Hohmann transfers required to lift the final stage to a 200 km circular orbit indicated a final payload mass of 102.7 kg. Recalling that the estimated launch mass of the system was 10300 kg, the current analysis results in a payload fraction $m_p/m_0 = 0.0997 \sim 1\%$. This preliminary result is promising enough to consider refinements to the analysis (including trajectory optimization of boost and scramjet phases) and a higher performing booster. Greatest improvement in the scramjet phase would result from increased net thrust at Mach 10+. This could be achieved through higher engine thrust and/or reduced vehicle drag.

References

- Anderson, G.Y., McClinton, C.R. and Weidner, J.P., 2001, "Scramjet Performance", Scramjet Propulsion, Progress in Astronautics and Aeronautics, AIAA Washington DC, Chapter 6.
- Andrews, E.H., 2001, "Scramjet development and testing in the United States", AIAA paper 2001-1927.
- Andrews, E. H., McClinton, C. R., and Pinckney, S. Z., 1971, "Flowfield Starting Characteristics of an Axisymmetric Mixed-Compression Inlet," NASA TM-X-20n.
- Andrews, E.H. and Mackley, E.A., 1994, "Review of NASA's Hypersonic Research Engine Project", NASA TM 107759; also AIAA paper 93-2323.

Auslender, A.H., and Smart, M.K., 2000, "Comparison of Ramjet Isolator Performance with Emphasis on Non-Constant Area Processes", 2000 Joint Army-Navy-NASA-Air Force (JANNAF) Meeting, Monterey, California.

Barthelemy, R.R., 1989, "The National Aero-Space Plane Program", AIAA Paper 89-5001.

Billg, F.S., 1995, "Supersonic combustion ramjet missile", *Journal of Propulsion and Power*, 11(6), p1139-1146.

Bowcutt, K.G., Anderson, J.D., and Capriotti, D., 1987, "Viscous Optimized Hypersonic Waveriders", AIAA paper 87-0272.

Bowcutt, K., Gonda, M., Hollowell, S. and Ralston, S., 2002, "Performance, operational and economical drivers of reusable launch vehicles", AIAA paper 2002-3901.

Burkhardt, J., 2000, "REENT6D a Simulation and Optimization Tool for Re-entry Missions" IRS - Internal report IRS-01B7: Stuttgart.

Curran, E.T., 2001, "Scramjet engines: The first forty years", *Journal of Propulsion and Power*, 17(6), p1138-1148.

Cain, T., Owens, R. and Walton, C., 2004, "Reconstruction of the HyShot 2 Flight from Onboard Sensors" Fifth Symposium on Aerothermodynamics for Space Vehicles, Cologne, Germany.

Ferlemann, S.M., McClinton, C.R., Rock, K.E. and Volland, R.T., 2005, "Hyper-X Mach 7 scramjet design, ground test and flight results", AIAA paper 2005-3322.

Ferri, A., 1964, "Review of the problems in application of supersonic combustion", *Journal of the Aeronautical Society*, 64(645), p575-597.

Gillum, M.J., and Lewis, M.J., 1997, "Experimental Results on a Mach 14 Waverider with Blunt Leading Edges", *Journal of Aircraft*, 34(3), pp 296-303.

Goldberg, T. J., and Hefner, J. N., 1971, "Starting Phenomena for Hypersonic Inlets with Thick Boundary Layers at Mach 6," NASA TN-D6280.

Gurylev, V. G., and Mamet'yev, Yu. A., 1978, "Effect of Cooling of the Central Body on Start-Up Separation of the Flow at the Intake and the Throttling Characteristics of Air Scoops at Supersonic and Hypervelocity Velocities," *Fluid Mechanics-Soviet Research*, Vol. 7, No. 3.

Heiser, W.H. and Pratt, D.T., 1994, "Hypersonic Airbreathing Propulsion", AIAA Education Series.

Henry, J.R. and Anderson, G.Y., 1973, "Design considerations for the airframe-integrated scramjet", NASA TM X-2895.

Huebner, L.D., Rock, K.E., Ruf, E.G., Witte, D.W. and Andrews, E.H., 2001, "Hyper-X flight engine ground testing for flight risk reduction", *Journal of Spacecraft and Rockets*, 38(6), p844-852.

Hunt, J.L. and Rausch, V.L., 1998, "Airbreathing hypersonic systems focus at NASA Langley Research Center", AIAA paper 98-1641.

Isakowitz, S.J., 1995, "International Reference Guide to Space Launch Systems", AIAA.

Kantrowitz, A., and Donaldson, C., 1945, "Preliminary Investigation of Supersonic Diffusers," NACA WRL-713.

Korkegi, R.H., 1975, "Comparison of shock induced two- and three-dimensional incipient turbulent separation", *AIAA Journal* 13(4), p534-535.

Lewis, M.J., 2001, "Significance of Fuel Selection for Hypersonic Vehicle Range", *Journal of Propulsion and Power*, 17(6).

Mahoney, J. J., 1990, *Inlets for Supersonic Missiles*, AIAA Education Series, AIAA Washington, DC.

McClinton, C.R., 2006, "X-43 – scramjet power breaks the hypersonic barrier: Dryden lectureship in research for 2006", AIAA paper 2006-1.

Mehta, U.B., and Bowles, J.V., 2001, "A two-stage-to-orbit spaceplane concept with growth potential", *Journal of Propulsion and Power*, 17(6).

Norris, J.D., 2006, "Mach 8 High Reynolds Number Static Stability Capability Extension Using a Hypersonic Waverider at AEDC Tunnel 9", AIAA paper 2006-2815.

Northam, G.B., Capriotti, D.P., Byington, C.S. and Greenberg, I., 1991, "Mach 2 and Mach 3 mixing and combustion in scramjets", AIAA paper 91-2394.

O'Neill, M.K., and Lewis, M.J., 1992, "Optimized Scramjet Integration on a Waverider", *Journal of Aircraft*, 29(6), pp1114-1121.

Ortwerth, P.J., 2001, "Scramjet Vehicle Integration", *Scramjet Propulsion, Progress in Astronautics and Aeronautics*, AIAA Washington DC, Chapter 17.

- Pandolfini, P.P., 1986, "Instructions for using ramjet performance analysis (RJPA) IBM-PC Version 1.0", JHU-APL NASP-86-2.
- Paull, A., Alesi, H. and Anderson, S., 2002, "HyShot Flight Program and how it was developed", AIAA 02-4939.
- Pinckney, S.Z., Ferlemann, S.M., Mills, J.C. and Bass, L.S., 1994, "Program manual for SRGULL version 2.0", HX#829.1.
- Rausch, V.L., McClinton, C.R. and Crawford, J.L., 1997, "Hyper-X: flight validation of hypersonic airbreathing technology", AIAA paper 97-7024.
- Regan, F.J., and Anandkrishnan, S.M., 1993, "Dynamics of Atmospheric Reentry," AIAA Education Edition.
- Schweikart, L., 1998, "The Hypersonic Revolution – Case Studies in the History of Hypersonic Technology – Volume III", Air Force History and Museums Program, Bolling AFB, DC, 20332-1111.
- Shapiro, A.H., 1953, "The dynamics and thermodynamics of compressible fluid flow", John Wiley & Sons, New York.
- Smart, M.K., 1999, "Design of Three-Dimensional Hypersonic Inlets with Rectangular-to-Elliptical Shape Transition", Journal of Propulsion and Power, Vol. 15, No. 3, pp 408-416.
- Smart, M.K., 2001, "Experimental Testing of a Hypersonic Inlet with Rectangular-to-Elliptical Shape Transition", Journal of Propulsion and Power, Vol. 17, No. 2, pp 276-283.
- Smart, M.K., Hass, N.E. and Paull, A., 2006, "Flight Data Analysis of the HyShot 2 Flight Experiment", AIAA Journal, Vol. 44, No. 10, pp 2366-2375.
- Smart, M.K. and Tetlow, M. R., 2006, "Orbital delivery of small payloads using hypersonic airbreathing propulsion", AIAA paper 2006-8019.
- Stalker, R.J., Paull, A., Mee, D.J., Morgan, R.G. and Jacobs, P.A., 2006, "Scramjets and shock tunnels – the Queensland experience", Progress in Aerospace Sciences, 41, p471-513.
- Tetlow, M., 2003, "Commercial Launch Vehicle Design and Predictive Guidance Development," Ph. D. Dissertation, School of Mechanical Engineering, The University of Adelaide.
- Trexler, C.A. and Souders, S. W., 1975, "Design and performance at a Mach number of 6 of an inlet for an integrated scramjet concept", NASA TN D-7944.
- Van Wie, D. M., 2001, "Scramjet Inlets", Scramjet Propulsion, Progress in Astronautics and Aeronautics, AIAA Washington DC, Chapter 7.
- Voland, R. and Rock, K.E., 1995, "NASP concept demonstration engine and sub-scale parametric engine tests", AIAA paper 95-6055.
- Voland, R.T., Rock, K.E., Huebner, L.D., Witte, D.W., Fischer, K.E. and McClinton, C.R., 1998, "Hyper-X engine design and ground test program", AIAA paper 98-1532.
- Voland, R.T., Auslender, A.H. Smart, M.K. Roudakov, V.L., Semenov, V.L. and Kopchenov, V., 1999, "CIAM/NASA Mach 6.5 Scramjet Flight and Ground Test", AIAA paper 99-4848.
- Waltrup, P.J., Billg, F.S. and Stockbridge, R.D., 1982, "Engine sizing and integration requirements for hypersonic airbreathing missile applications", AGARD-CP-207, No. 8.
- Waltrup, P.J., 1987, "Hypersonic airbreathing propulsion: evolution and opportunities", AGARD CP-428, No. 12.
- Waltrup, P.J., 1990, "The dual combustor ramjet: a versatile propulsion system for hypersonic tactical missile applications", AGARD CP-527, No. 7.
- Webber, R.J. and MacKay, J.S., 1958, "An analysis of ramjet engines using supersonic combustion", NACA TN 4386.

von Karman Institute for Fluid Dynamics

RTO-AVT-VKI Lecture Series 2007

**ADVANCES ON PROPULSION TECHNOLOGY
FOR HIGH-SPEED AIRCRAFT**

March 12-15, 2007

CURRENT HYPERSONIC RESEARCH IN USA

R. Bakos
ATK GASL, USA

Current Hypersonic Research in the USA

Dr. Robert Bakos

ATK GASL

Robert.Bakos@ATK.com

INTRODUCTION

The potential benefit of an operational hypersonic system has driven continued research in the United States in basic and applied technologies. The goal is to progress beyond the demonstration of core principals, and begin to utilize hypersonic flight within the atmosphere to deliver revolutionary capabilities.

The X-43A program delivered clear and convincing evidence that the propulsive principles of hypersonic flight are understood. For the first time the test, analysis, and design tools that evolved over 40 years of research were brought together to yield a working hypersonic air-breathing vehicle. The hydrogen fuelled vehicle accomplished all of its validation objectives, performing flawlessly at Mach numbers near 7 and 10 in two successive flights. The engine produced thrust at Mach 7 in excess of drag to yield positive acceleration, and at Mach 10, produced sufficient thrust to balance drag, or cruise. As the prime contractor for NASA, ATK GASL had the unique perspective of seeing the complete program from start to finish. Although very important, these flights are only a first step on a long path to an operational capability.

There is more work to be done in the optimization and maturity of designs for hypersonic engines. As compared to rocket propulsion which currently achieve most of the hypersonic missions of interest, hypersonic air-breathing propulsion is extremely immature. This most common criticism of air-breathing propulsion together with an as of yet unjustified perception of high cost, has hindered funding for applications development.

Over the past 10 years, ATK-GASL has worked to advance hypersonic propulsion technologies by increasing maturity, identifying more practical, lower cost designs, and transitioning from ground test to flight test. Our objective is to develop a line of engine designs, aligned with envisioned mission requirements, and with a focus on manufacturability at an affordable cost in production. We have identified propulsion system components, integrations, as well as practical ground and flight test strategies to push the technological maturity, and accumulate in-flight operational experience.

An evaluation of the National Aerospace Initiative by a National Research Council committee in 2004 identified four critical and enabling technologies that must be matured to TRL 6-7 (System/Subsystems Prototype Evaluation in a Relevant/Operating Environment) to support future missile systems, aircraft systems and access to space systems:¹

- Air-breathing propulsion and flight test,
- Materials, thermal protection systems (TPSs), and structures,
- Integrated vehicle design and multidisciplinary optimization, and
- Integrated ground testing and numerical simulation/analysis.

Our research has focused to some degree on each of these areas. This lecture will review specific examples that have addressed these needs.

HYPERSONIC ENGINE RESEARCH PROGRESS

Depending on the mission scenario for the vision vehicle design, the propulsion cycle, engine configuration and the choice of fuel for the engine vary. Figure 1 shows a collection of hypersonic engine systems for which ATK GASL has played a significant role and that have been carried through significant ground tests or to flight test: the X-43A, HyTech, ATK TTRJ, and Dual Combustor Ramjet. These scramjet designs utilize a variety of inlet concepts ranging from planar two-dimensional to highly three dimensional designs. Likewise, combustor geometries also vary from high aspect ratio (width / height) rectangular to circular.

During the National Aerospace Plane (NASP) program era in the late 1980's to early 1990's, two-dimensional inlet / rectangular combustor geometries became the baseline for which significant tool and technology development was performed. The principle reasons for selection of this engine architecture were driven by the desire to maximize the airbreathing portion of the flight envelope for a Single-Stage To Orbit (SSTO) vehicle AND the need to build a flight vehicle in 5 years. These requirements drove the following considerations:

- Multi-Disciplinary Optimization (MDO) techniques necessary to optimize engine/vehicle integration demanded utilization of tools capable of rapid design iteration. Although Computational Fluid Dynamics (CFD) capabilities were maturing rapidly, analysis for two-dimensional designs was considered to be more advanced at the time than for other, more generalized shapes.
- High engine efficiency over a very wide Mach number range ($M = 0$ to $15+$) required significant variable geometry in both the inlet, combustor and nozzle section to optimize engine contraction ratio, combustion efficiency, and nozzle expansion ratio. The need to rapidly develop engines for a flight vehicle drove the architecture to two-dimensional planar which allows the most straightforward movement of engine walls to accomplish the needed variable geometry in a vehicle integrated configuration.

Since the NASP era, which ended over 10 years ago, several factors have changed the hypersonic landscape. Although SSTO is still the dream of some, most of the hypersonic community has adopted a more pragmatic approach that focuses on the following configurations and missions:

- A first stage of a Two-Stage-To-Orbit (TSTO) concept that utilizes either a turbine or rocket-based accelerator as well as a rocket-stage for orbital insertion. The fuel of choice varies, but again most vision applications do not require scramjet operation above about Mach 8-10.
- A cruise aircraft which uses similar, although much larger scale, ramjets or scramjets that again operate between Mach 3+ up to Mach 7 or 8.
- A hydrocarbon-fueled ramjet or scramjet powered long range cruise missile, boosted via a solid rocket to Mach 3-4 and with ultimate airbreathing speed capability between Mach 5 and 8.
- A gun-launched air-breathing powered projectile capable of very long range. Packaging of this configuration in gun-tube diameters and use of high density fuels presents unique challenges in the ramjet-scramjet design space.

The energy required for a ramjet or scramjet to ultimately accelerate a vehicle to Mach 5 or even Mach 10 from a takeover condition of about Mach 3 is a fraction of the requirement imposed by NASP. Therefore, the need for optimum engine efficiency via extreme engine flowpath geometry variations

gives way to other considerations of weight, surface area, volume, simplicity and affordability for the more pragmatic applications envisioned today.

Another factor that has changed the post-NASP landscape is the evolution of CFD and processing capability allowing MDO-based optimization of engine and vehicle configurations with much more general shapes. Significant effort is underway in the US and abroad to develop stream-line traced inlets and engine/airframe integrations with both superior inlet recovery and vehicle lift / drag characteristics. This capability has been enabled via development of CFD algorithms, computer processing capability and design automation tools to the point that development of geometries, grid generation and computation for generalized shapes now take a fraction of the time relative to two-dimensional geometries of the NASP-era.

These factors have also opened up the design space for combustors, and isolators which connect these unique inlets to the combustor. As the highest pressure, highest temperature component in any airbreathing engine, optimization of the combustor within performance, weight, surface area, volume, simplicity and affordability factors mentioned earlier is key to enabling practical scramjet systems.

Following the demise of NASP in 1994, evolution of the two-dimensional engine architecture design methods, tools and technology continued via both the NASA Hyper-X and the USAF HyTech programs. Today, we have demonstrated this technology in flight via the Mach 7 and 10 flights of the hydrogen fueled X-43A. Additionally, the HyTech program has demonstrated, via ground test, the viability of flight-weight two-dimensional hydrocarbon fuel-cooled scramjets. The next step, bringing these systems to flight, will occur via the USAF X-51 program with flights scheduled in late 2008 / early 2009.

During this period, 3-dimensional engine architectures continued to make advances with attention on more specific applications. The Johns Hopkins Applied Physics Laboratory continued development of the Dual Combustor Ramjet concept that utilizes a round scramjet combustor.² This concept has had extensive ground testing and was flight tested at Mach 5.5 conditions by ATK GASL in 2005. In the gun-launched area the ScramFire projectile was successfully flight tested in 2003.

X-43A

ATK GASL worked together with NASA to execute the design and fabrication and flight test of the X-43A flight vehicle and propulsion systems. Following in the footsteps of the NASP program, the X-43A engine design was derived from a vision 200-ft Global Reach vehicle.

Scaling to the 12-foot long X-43A vehicle (Figure 2) was executed by NASA using a series of Cycle code and CFD code methods.³ The propulsion system architecture is predominantly two-dimensional and allows for a movable cowl door that is opened to initiate and facilitate started supersonic flow through the engine. The smaller scale results in higher heat loads on a per-unit area basis which made the thermal/structural design of the engine challenging. The following discussion concerns the implementation of the engine design and the fuel supply system. The details of the X-43A mission are presented in reference [4]

The engine is manufactured as a self-contained unit Figure 3.⁵ It incorporates a rectangular flowpath, and is of airframe-integrated design where the vehicle forebody and afterbody provide external compression and expansion surfaces which are continuations of the internal compression and expansion surfaces within the engine. It operates on gaseous hydrogen fuel with a silane igniter; to provide sufficient run time the hydrogen and hydrogen/silane igniter mixture are stored at 8500 and 4500 psi, respectively. The Glidcop engine section is attached to a stainless steel strongback, which in turn connects it to the airframe. A key feature of the engine is the actuated inlet cowl door, which protects the internal flowpath during boost, opens for engine operation, and then closes again during

the vehicle descent from the test point. Both the cowl and the vertical leading edges of the engine are sharp-edged and water-cooled for thermal protection during boost and engine operation. Zirconia coating is used on the forward section of the engine cowl and in key places throughout the engine for additional thermal protection. The vehicle subsystems also incorporate a nitrogen purge system, which additionally provides cooling of certain vehicle subsystems during the flight test phase.

Results of the X-43A flight and ground tests yielded new confidence in the ability of design and analysis tools: cycle, computational, and test assets to effectively develop a hypersonic engine of desired performance. Figure 4 shows a comparison of engine pressures as measured in the NASA Langley 8-Foot High Temperature Tunnel as compared to flight data.³ The tunnel is combustion heated using methane fuel and the test gas is consequently vitiated with products of hydrocarbon combustion. Despite these test gas composition differences, the comparison shows the data to be very consistent. Although this level of agreement is encouraging, the configuration and operating condition dependence of this result must be further considered.

HyTech and X-51 Scramjet Programs⁶

The US Air Force HyTech and subsequent X-51 programs are focused on development and flight test of a scramjet engine with a storable liquid hydrocarbon fuel in an endothermic cycle. Supporting technologies including inlets, composite leading edges, heat exchangers, and flame-holding devices, were all developed early in the HyTech program. These developments were followed by a full-scale demonstration of the engine design in a heavy-weight, heat-sink flowpath called the Performance Test Engine (PTE), shown in Figure 5 at test in the ATK GASL Test Bay 6 Blowdown facility. General architecture of the engine is also shown in Figure 5 of a Direct Connect test article.

More recent efforts are focused on developing flight-weight engines that feature fuel-cooled walls operating in an endothermic cycle, Figure 6. Fuel is pumped from a holding tank through all four walls of the engine to provide cooling. In the process of cooling, the fuel (JP-7) is vaporized and eventually is partially cracked. This highly reactive vapor is then directed to any or all of the five fueling sites in the engine via flowcontrol valves capable of handling the high temperature gas. The practical limit of this process is coking limit of the fuel. Since coking within the cooling channels must be avoided at all costs, temperatures are controlled to values safely below the coking temperature. This limits the hydrocarbon fueled scramjet engine to approximately Mach 8.

Subsequent test of the HyTech engine were conducted in the Ground Demonstration Engine Number One (or GDE-1) also run at ATK-GASL and most recently in the GDE-2 engine tested at the NASA LaRC 8'HTT. The objective of these programs was to demonstrate the thermal response and the structural durability of the fuel-cooled construction. In GDE-1 the engine was operated in an "open loop" manner where separate fuel lines provided for fuel cooling and for combusted fuel. The fuel introduced to the combustor is first passed through a facility heater where the fuel is vaporized and partially cracked, simulating passage through the engine. This mode of operation was required since it was required that the engine be "over-cooled" initially until fuel distributions could be accurately determined. In each test series the engine was cooled at three times the expected flow rates and then at progressively reduced rates until a cooling flow rate was achieved that matched fueling requirements of the combustor. In the GDE-2 engine tests the fuel was standard JP-7 fuel in a closed-loop configuration at Mach 5 conditions to both cool engine hardware and fuel the engine's combustor.⁷

The X-51A flight program will carry the GDE engines through flight test, Figure 7. This flight program will demonstrate the operation of the endothermically fueled scramjet engine using a single flowpath and fixed-geometry inlet. The waverider derived vehicle will be launched on an ATACMS Booster to accelerate the test vehicle to a scramjet takeover Mach number of 4.5 with the scramjet engine further accelerating the vehicle to approximately Mach 7. The engine features a 9-in wide flowpath.

Dual Combustor Ramjet

The Dual Combustor Ramjet (DCR) propulsion system has been developed by John-Hopkins Applied Physics Laboratory. In the DCR, a subsonic combustion ramjet is used as the pilot to a scramjet engine, enabling efficient operation over a wider range of supersonic and hypersonic Mach numbers using logistically suitable fuels.⁸ This novel combination of subsonic and supersonic combustion in a combined flowpath (Figure 8) attacks the challenging problem of liquid fuel evaporation and combustion without regenerative fuel cooling as in the Hytech engine. The overall combined flowpath architecture can be packaged into a missile type configuration with a round combustor², and is a notable excursion from the generally two-dimensional configurations discussed previously.

Recently, a Dual Combustor Ramjet propulsion system was implemented in support of a flight test program at ATK GASL. The objective of this program was to develop a low-cost Free-Flight Atmospheric Scramjet Test Technique (FASTT). This concept uses sounding rockets and their mature launch support infrastructure to ferry scramjet powered payloads to hypersonic flight conditions.

One major objective of the program was to compare ground test engine performance and operability data for comparison to flight data. A freejet test article was built at the same scale as the flight engine and tested in the ATK GASL Test Bay 6 Blowdown Facility. The test article shown in Figure 9 was designed for multiple tests of approximately 30 seconds duration. A predominantly heat sink design approach was used with construction from heavy-weight copper and nickel alloys. Water cooling was necessary for certain high thermal load combustor regions.

The design requirements for the flight test called for on condition operation at approximately Mach 5.5 for 30 seconds. Throw weight considerations precluded copper construction, so a combination of high temperature nickel alloys and ablative linings were used for thermal management. Fuel was stored in a bladder system and pressure fed via regulated gas supply. The engine was instrumented for pressure and temperature measurement. Ignition was provided by a small solid-propellant gas generator that ignited the subsonic ramjet leg of the dual combustor.

The successful flight test will be described subsequently. From an engine perspective all objectives were met. Following separation from the booster system, and shroud disposal, fuel flow was initiated and the igniter system initiated combustion. Two levels of fuel flow were used. The initial rate was set near stoichiometric in the ramjet pilot combustor to assure robust ignition. This was fooled by a higher flow to achieve fuel rich conditions in the ramjet, as needed to fuel the supersonic combustor.

Correlation between flight to ground data underway. Preliminary comparisons show excellent agreement when heat losses are accounted in the different test articles.

Gun-Launched Scramjet

A series of Gun Launched scramjet designs were executed to demonstrate the feasibility of subscale gun-launch as a means to provide low-cost scramjet free-flight data⁹. Gun-launch was used to accelerate a projectile to scramjet take-over speeds and for flight in an atmospherically controlled ballistic range. The objective vehicle was a nominal 20-inch diameter missile operating over Mach 6-8. Pressure-Dimension (p-D) scaling rules were adopted to set conditions in the range to achieve comparable engine operation to the full scale vehicle in flight at altitude.

The engine design for the projectile was driven by the requirements for packaging within the constraints of a hypervelocity launch tube of 4" to 8" diameter, capability to withstand the gun set back acceleration, projectile stability in flight, and need for a self contained fuel system, and onboard instrumentation and telemetry.

Initial design iterations focused on a 2-dimensional derived annular configuration wrapped around a cylindrical centerbody as shown in Figure 10. These designs proved difficult to optimize for both performance and strength for the gun-launch environment. Subsequent successful designs like that shown in Figure 11 used multiple 3-dimensional engine modules positioned around the centerbody, allowing for more optimal structure to support compression in the projectile axis direction.

The projectile design had eight scramjet engines mounted around cylindrical centerbody. It included an onboard fuel storage and operating ethylene fuel system. The set-back accelerations in the gun-tube are in the range of 10,000 G, and were a significant driver on the projectile design. The overall integrated projectile was verified computationally including aerothermal and structural loads. The propulsion design was carried out using a mix of CFD and cycle codes and then verified experimentally in direct-connect wind tunnel tests.

Direct connect wind tunnel tests were performed to evaluate the combustor and isolator designs and to build a comparative performance database with which to compare flight data. The engine design was tested using a 7x scale model in the GASL Test Bay I direct-connect facility to determine modes of operation and fueling strategies. To correctly capture the performance of the engine, the facility conditions were set using pressure-dimension scaling, using the same methodology as between the range and the objective vehicle. Experiments showed that while the flow path and flame-holding strategies were adequate for the current application, the fuel injection pattern needed to be re-designed to improve engine performance. Subsequent testing with modified injection schemes validated the alteration.

NEW DIRECTIONS IN HYPERSONIC ENGINE RESEARCH¹⁰

The combination of revised requirement for hypersonic flight vehicles and the advancements in computing capability has resulted on a renewed focus on non-rectangular isolator and combustor geometries for near term practical scramjet propulsion systems. From a surface area and structural weight point of view, circular cross sections offer the most benefit. However, the performance characteristics of scramjet ducts are often characterized in terms of length / diameter due to the natural formation of shock trains and the fuel injection and mixing characteristics associated with isolator and combustor ducts, respectively. Without due care, the net result could be the requirement for a much longer circular vs. high aspect ratio (width / height) two-dimensional duct to obtain the same performance, thus negating the benefits of cross-section.

Isolator and Combustor Geometry Considerations

To examine flow area and structural weight benefits, a finite element analysis for a combustor duct operating at typical scramjet conditions with combined pressure and thermal stresses was performed. The scale of the duct utilized is typical of a missile-scale system. It should be noted that these trends are scale dependent, with slightly different trends exhibited at larger scales. The analysis ground rules and assumptions are summarized below:

- Flowpath area held constant at 10 in²
- Wall thickness held constant at 0.15 in
- 30% of material removed for cooling passages
- Material is Inconel 718
- Stress limit is 65 ksi (80% yield point strength at 1300°F)

- Deflection limit is 2% area change
- Pressure in flowpath is 100 psi
- Thermal Gradient is 400°F

The analysis results are shown in Figure 12. Also shown is the typical wall cross-section which represents a 0.15 inch thick cooled wall constructed of Inconel 718. From these results, it can be seen that circular cross-sections provide 13% less wetted or surface area to flow area than square and 25% less than a typical 3:1 aspect ratio rectangular duct. Reductions in wetted to flow area benefit from both a friction drag and heat transfer point of view. Similarly, circular ducts provide a 12% and 30% reduction in weight per length than square and 3:1 aspect ratio rectangular ducts, respectively. Benefits between elliptical versus rectangular ducts tend to diminish to about 5% in both surface area and weight as aspect ratio approaches 3:1. Another potentially more significant benefit of circular or very low aspect ratio elliptical ducts is the lack of a requirement for back structure. That is, the relatively thin cooled wall is able to support the required loads and deflections without exceeding stress limits. The addition of back structure can significantly increase weight per unit length (factor of 2) and is required for any high aspect ratio rectangular or elliptical duct. As mentioned previously, these results are scale dependent. The case shown represents an approximately 3.5 inch diameter duct. However, scaling studies performed to similar constraints have shown that circular ducts up to about 36 inches in diameter can be designed to meet similar requirements without back structure.

Although circular geometries show clear benefits in terms of wetted area and weight per unit length, care must be taken to manage overall length in order to achieve a system benefit. Performance characteristics for both isolators and combustors are often characterized in terms of Length / Diameter (L/D) or Length / Height (L/H). Example isolator and combustor characteristics are shown in Figure 13.

For the same duct constraints in the previous example and range of typical L/D or L/H, Figure 14 shows the trends for overall wetted surface area (surface area x length) as a function L/D for circular ducts or L/H for 3:1 aspect ratio elliptical or rectangular ducts. Recall that previously shown, circular and elliptical geometries result in reduced surface area per length. However, at comparable L/D or L/H, the total wetted area, due to length, actually increases by 1.5X for circular vs. 3:1 aspect ratio rectangular ducts. This clearly overwhelms the benefits previously shown from a surface area perspective and typically results in unmanageably long component lengths. However, the weight benefits derived from elimination of back structure could still favor the circular geometry for configurations where system benefit is more highly sensitive to weight than wetted area or length constraints. This wetted area and length effect can be largely mitigated through the use of high aspect ratio elliptical ducts which result in a 1.1X increase in surface area for 3:1 elliptical vs. rectangular ducts. However, recall the wetted surface area per length benefits were less pronounced between elliptical and rectangular, and again, both require back structure to meet stress requirements.

To take the maximum advantage of circular cross section geometries, one must decouple the engine performance from the duct L/D constraints. For combustion systems, this can be accomplished by the inclusion of in-stream fuel injection elements. A notional arrangement shown in Figure 15 accomplishes this decoupling by reducing the injection characteristic dimension or "gap" between the injection devices. The closer the gap, the shorter the combustor. However, care must be taken to properly balance overall combustor length against the additional stream drag imposed by the injector elements.

Another significant advantage of circular cross-section ducts and combustors, in particular, is their amenability to conventional manufacturing processes. Sections are readily machined via lathe, drill and wire electro discharge machining methods. Semi-finished sections can then be stacked on a

mandrel and welded together with minimal thermal distortion. Figure 16 shows an ATK manufactured cooled-combustor section which was fabricated and put into test less than 6 months after the design was initiated. Description of testing for this hardware is described in the following section.

Test Validation Activities

In order to evaluate performance and operability and to validate design tools for circular cross-section isolators and combustors. ATK GASL designed and fabricated a direct-connect isolator / combustor rig tested at the NASA Langley Research Center (LaRC) Direct Connect Scramjet Test Facility (DCSTF) in Norfolk Va. The configuration, named the Pilot Technology Development (PTD) rig, is shown installed in the DCSTF in Figure 17.

Both heavyweight heat sink and fuel-cooled hardware tested for a total of 72 minutes of combustion time over Mach 3.8 to 5.4 conditions and a range of dynamic pressures from 1000 to 3000 psf. Ignition and combustion were obtained on both ambient and heated fuel; the latter supplied initially by an external heater (open loop) and then via the fuel-cooled engine hardware for subsequent closed-loop testing. Conventional JP-10 fuel was used for most of the tests although subsequent testing on JP-7 showed negligible fuel sensitivity. Excellent combustion efficiency was obtained via a novel proprietary piloting and injection system design within 3 to 5 combustor L/D. Pre-combustion shock train lengths within the isolator section ranged from 3 to 8 L/D depending on flight condition and fuel equivalence ratio.

The flight-weight, fuel-cooled combustor was tested for a total of 23 minutes of hot (combustion) time, with individual tests of up to 2.5 minutes each to achieve thermal equilibrium. Combustor wall and fuel temperature measurements have been used to validate / calibrate both environment definition and heat transfer models. Post-test inspection shows the hardware is in excellent condition with no traces of either thermal distress nor fuel coking.

Following the highly successful PTD test series, ATK has designed, fabricated and tested a flight-weight fuel-cooled freejet engine utilizing a circular cross-section combustor mated to a rectangular, fixed geometry inlet. The engine in test at ATK GASL is shown in Figure 18 including a flight weight fuel pump. Demonstration of this engine and its critical subsystems establishes the near-term reality of lightweight, highly efficient, air-breathing engines capable of propelling vehicles at hypersonic speeds.

To support these near term goals, ATK's engine integrates several existing low-risk technologies to produce a near term high speed engine solution. The engine is fueled and cooled using an existing kerosene fuel, JP-10. Use of existing materials and established manufacturing processes allowed the ATK team to bring this high speed engine from concept to flight-weight hardware and subcomponents, to verification testing in just 2 years. The engine is capable of thrust-to-weight ratios of greater than 15 without the need for exotic materials.

RECENT PROGRESS IN HYPERSONIC FLIGHT TEST

Like the architecture of hypersonic engines, the Hypersonic Flight Test landscape has changed significantly from the NASP vision. The NASP concept was a fully reusable vehicle from the outset that would take-off from a runway and accelerate to orbital speeds without staging and return. An envelope expansion approach was to be used to achieve higher speeds incrementally while testing and validating the vehicle operating characteristics. This large "delta v" requirement drove the vehicle to be very large and the cost to be unaffordable. The envelope expansion flight development approach, although still most preferred, became impractical for even less capable vehicles just able to break into the hypersonic regime because of the relatively large vehicles and price tags they incurred.

Since the end of the NASP program, as more near term vehicle concepts and applications have been identified, a robust hypersonic flight test program in the US has been advocated by several advisory and research boards¹¹. In 2003, these activities culminated in the The National Aerospace Initiative (NAI). The NAI was started by the Director of Defense Research and Engineering, (DDR&E), with the objective to build a roadmap for combined Department of Defense and NASA resources and support a robust hypersonic development and flight demonstration program. The goal was to achieve incrementally increased flight Mach number per year, reaching Mach 12 by 2012.

The path to this objective was already paved by several on-going programs, such as X-43A, X-51A and HyFly. These focused on validation of design methods in flight utilizing air-launched rocket boosters to achieve hypersonic insertion conditions, thus allowing hypersonic air-breathing "payload" vehicles to be sized for powered flight over a relatively narrow speed range. To date none of these smaller vehicles have packaged landing or recovery equipment which is a notable shortcoming, but the overall program cost for these small vehicles can be kept modest despite the need for a new vehicle for each flight.

Ground to Flight Test Transition

Flight is the ultimate application of hypersonic propulsion development activities and therefore it is the only real test of the technology. The relatively high cost of flight test, coupled with the inability to easily recover and reuse flight test articles, has made extensive ground test the most appealing approach for practical technology development. Ground test in the hypersonic regime is compromised by limitations in facility size, energy, and test duration as well as vitiation of the test media. These issues have been at least partially understood and modeled to a degree such that development via ground test has continued. These practical considerations have driven most development programs to extract as much data and reduce as much risk as is practically possible in ground test, with flight test being held as an ultimate but necessary step.

The most appropriate point in a program to transition from ground to flight test is a crucial determination for hypersonic development. If an inexpensive approach to flight test were to be available, it would be possible to transition to flight test earlier in a development program. This would allow flight data to be compared with ground data, examine operability of key subsystems in flight, and feed back to the design activities for the future flight system, reducing risk and delivering a better optimized final product.

Cost for both Ground and Flight tests grow with the size, scale, and complexity of the test as indicated in Figure 19. For ground test, component tests of combustors or inlets are the least expensive. Complete engine tests are more expensive requiring larger facilities and having added complexity. Complete vehicle tests are more expensive still, and for hypersonic aero-propulsion there is little hope of large scale ground testing of hypersonic airplanes in the future. Large scale component testing, like an aircraft size combustor may be possible, but testing integrated performance will await ultimate flight test.

In flight a very similar story holds: size and complexity drive cost. The programs listed span recent, near-term, and envisioned flight programs. The Australian HyShot program is listed as the least expensive as it was a flying component (combustor) test. The ScramFire, FASTT and X-43A Programs were integrated vehicle tests of increasing scale and complexity. The X-51 program will attempt to fly for multiple minutes and accelerate over multiple Mach numbers. Long duration hypersonic cruise airplanes, and access to space vehicles are not currently planned for flight test, but will be significantly more complex and costly.

At what technical maturity level should the transition from ground to flight occur? At what scale should ground tests be run to prepare for flight? At some point in the future it will be necessary to leap forward from component and subscale ground tests to larger-scale more complex flight tests.

ATK GASL has conducted three flight test programs in the past 4 years. These programs ranged over two orders of magnitude in program complexity and cost. Each used a different flight test method and had widely different sophistication and completeness in the supporting ground programs. These programs serve as examples of the great variety of options that exist for flight test and the types and value of data that can be extracted.

ScramFire – Ballistic Range Flight Test Technique

The ballistic range test technique for scramjet-integrated vehicles provides a short-duration flight at actual altitude conditions¹². The vehicle is mounted in a gun and fired into a range, which is evacuated to match flight static pressure at altitude. Scaling is required since the range lacks static temperature control to match the temperature at altitude. The vehicle accelerates in the gun barrel and enters the range at the specified flight velocity. The on-board engine is then ignited and the vehicle proceeds under powered flight conditions until it impacts the far wall of the range. During this test time, data is taken via on-board and off board sensor systems to evaluate engine and vehicle performance.

Demonstrations of this flight test technique have been performed on a scramjet engine integrated into a cylindrical vehicle for Mach 6-8 flight conditions. To execute these tests a complete design and development of a scramjet-integrated projectile was undertaken including the verification of the structural design through FEM analyses, the verification of engine performance through engineering performance codes and wind tunnel data, and five flight tests in G-Range, a light gas gun facility at the Arnold Engineering Development Center (AEDC), Figure 20.

The cylindrical projectile and the integrated scramjet engine were designed specifically for this flight test demonstration program. The engines operated as dual-mode scramjets using ethylene fuel in a self-contained and actuated fuel supply system. The projectile is nominally 4-inch diameter and weighs approximately 20 lb. The projectile design included that of the internal and external flow lines, structure, telemetry system and associated onboard instrumentation, aerodynamic stability system, weight and balance. The projectile diameter is sized to fit in the AEDC G-Range four-inch launch tube and the structure is sized to survive launch loads. A picture of a projectile design is seen in 10.

The structural design is primarily driven by the high acceleration loads (10,000 G design condition) encountered during launch. As a result, the goal of the design was to achieve a simple structure capable of withstanding the launch loads. Consequently, the projectile is comprised of a minimum of overall components, including nonstructural components that include valves, telemetry system and associated instruments.

Onboard instrumentation and telemetry (TM) are employed to make direct measurements of engine performance in flight and transmit the information to a ground station for collection and post test analysis. The high g capable, miniaturized TM units include an 8 channel transmitter, encoder, signal conditioner, antenna, and power supply, Figure 21. The package included five pressure transducers, two projectile flight axis aligned accelerometers, and a battery voltage transducer.

Off-board instrumentation included IR, visible, and UV still imagery and spectral sensors spaced along the range to image both the projectile, the density field, and the emission of combustion products. Framing cameras were used in the visible and the IR to capture the time evolution of the flight.

Figure 22 shows a plot of axial acceleration at the projectile center of gravity versus flight time. This data contains residual high frequency response to the set-forward acceleration that occurs when the projectile leaves the gun muzzle. This vibration dominates the measurement during the early portions of the flight with amplitudes exceeding the range of the accelerometers. Subsequently, the axial acceleration data appears, in the mean, to rise from a low value to a higher value between 0.299 and 0.312 seconds, indicating acceleration due to scramjet operation. As indicated by annotations, the acceleration at 0.299 seconds closely matches the engine-off performance prediction. For comparison to the maximum acceleration measured, the stoichiometric engine performance is also shown as an annotation to the plot. The measured acceleration rises to approximately cruise conditions, in the mean, at 0.31 seconds. Late in the flight the projectile achieves significant incidence angle indicated on the right axis of the plot and determined from flash laser photographs along the range. This attitude results in a flight at angle of attack that ultimately causes inlet unstart. This is detected by on-board pressure measurements in the inlet (not shown). At this point the axial acceleration suddenly drops at 0.312 seconds.

Free Flight Atmosphere Scramjet Test Technique (FASTT)

This program set out to demonstrate the use of ground launched ballistic rockets as a low-cost solution to launch scramjet integrated vehicles to flight test conditions¹³. Such an approach can provide an affordable path for maturing hypersonic air-breathing components and systems in flight. Whereas the traditional approach to full-scale development has been to perform subscale and full-scale ground testing prior to full-scale flight testing, usually using an air-launched, fully-guided booster system, this approach takes a different path.

The FASTT approach uses an unguided, sounding rocket booster stack to carry a scramjet vehicle payload to desired insertion conditions in the atmosphere. There exists in the US are a broad range of launch assets along with a significant and mature infrastructure for launching, tracking, and transmission and reception of data. The combination allows for relatively affordable flight test of hypersonic test vehicles at small to moderate scale.

For the initial demonstrations, a two stage stack was selected with a separable payload vehicle. Launch operations were conducted at the NASA Wallops Flight Facility located on the Eastern shore of Virginia. A suppressed ballistic trajectory was chosen that inserts the payload at a velocity of approximately Mach 6 at near horizontal elevation angle. A scramjet engine powered payload was designed weighing approximately 300 lb, 11-inch diameter with an overall length of about 8 feet. The engine was derived from the Dual-Combustor Ramjet concept and fuelled with liquid JP-10. The engine and airframe was instrumented with approximately 150 transducers including pressure, temperature and redundant 3-axis accelerometers. The separated payload flies its own ballistic arc and over approximately 30 seconds transits less than 5000 ft altitude, such that the vehicle flight conditions are nearly constant.

The process is illustrated in Figure 23. The two stage booster stack is rail launched at suppressed elevation angle, Figure 24. The three sets of fins on the stack and payload are canted to impart a low-rate spin during flight to offset any thrust axis misalignment from the intended ballistic arc. Booster and payload data are transmitted to the tracking station throughout the flight. After the first stage lofts the vehicle and separates, an interstage delay allows the vehicle to execute a gravity turn toward horizontal before the second stage is ignited. The second stage accelerates the vehicle to the insertion conditions, and upon burnout, the payload vehicle is separated. To protect the engine from aerodynamic heating during ascent it is covered by a clamshell-type shroud. This shroud is deployed shortly after separation and the engine is ignited to execute the scramjet powered portion of the flight test. After the engine fuel is expended, the vehicle coasts until splashdown where no recovery is attempted.

The main features of the low-cost atmospheric flight test technique for scramjets are highlighted below:

- Low-cost sounding rocket boosters capable of carrying subscale hypersonic vehicles and scramjet engines to the required takeover conditions.
- Suppressed ballistic trajectory, with boost staging, to reach test conditions (altitude and Mach number) of nearly constant dynamic pressure, without the need for guidance, navigation, and flight control. This feature also avoids the requirement for a Flight Termination System, further simplifying the approach.
- Onboard instrumentation to measure engine pressures, temperatures, flow rates, heat flux, as well as health monitoring of critical systems.
- Data acquisition and telemetry system capable of conditioning measurement signals and transmitting data back to ground station.
- Electronic event sequencer to control in-flight events, including: separation events; shroud deployment; starting fuel flow; and engine ignition.
- Adapter flange for attaching scramjet engine and hypersonic vehicle payload to sounding rocket booster. This adapter will also incorporate a separation mechanism to initiate vehicle free-flight at the end of boost.
- Inlet shroud system that protects the payload inlets during the boost ascent phase. A shroud separation system deploys the inlet shroud after scramjet-payload separation, and prior to engine ignition.

In order to reduce the risks associated with flying a complex scramjet-integrated vehicle through an unproven trajectory with an unproven combination of flight hardware, surrogate payload missions were performed for booster performance testing and subsystems evaluation. Two surrogate payload missions were executed successfully and verified the booster capabilities and the full suite of payload instrumentation, power systems, and subsystems including the inlet shroud deployment, telemetry, and transponder tracking. Post-flight data analyses helped the flight test team to better understand launch vehicle tip-off and drag characteristics, and improved prediction capabilities to fine tune the successive launches to achieve the desired payload insertion point. In conjunction with a freejet ground test program that identified fueling schemes, demonstrated robust light-off, and provided a baseline engine data set to compare with flight data, flight vehicle airframe and fuel subsystems were integrated into flight hardware, and subsequently underwent successful preflight clearance testing.

The powered flight vehicle (Figure 25) was launched and inserted to free flight. Insertion occurred at an altitude approximately 10,000 ft lower than expected although at the correct Mach number. Figure 26 summarizes the pre-flight predictions and the achieved insertion conditions for the free flight vehicle (FFV). The discrepancy is not fully understood but appears to be a combination of rail tip-off and wind weighting. On-board systems performed as designed, and engine operation occurred including fuel-off tare, fuel ignition, throttle-up, and steady engine operation while critical engineering measurements were obtained. Sufficient measurements were taken for determination of engine cycle performance, and for comparison to ground test data. Preliminary comparisons to ground test measurements show good agreement. In flight the inlet eventually unstated, producing unstable coning flight in which the engine was not able to recover stable operation.

Figure 27 shows important flight measurements during the sequence of events from booster thrust tail-off through engine operation on a single plot. The acceleration peaked at ~65 sec and then dropped off

as the booster stage burned out. At 68.23 sec the vehicle deployed to free-flight, and 0.40 sec later the shroud was jettisoned. The Gas Generator (GG) pressure rose and steadied while the vehicle decelerated and a tare measurement was obtained for ~1.3 sec. By 70.0 sec the fuel flow rate was steady at the initial throttle setting however the GG pressure showed no sign of auto- ignition, until the sharp rise following the ignitor firing at 70.3 sec. The GG pressure steadied and a small delta acceleration was sensed. The fuel flow rate was increased to full flow rate and became steady by 71.1 sec and the GG pressure rose higher accompanied by a noticeable 2-g delta acceleration; however, the vehicle did not experience positive net acceleration resulting in a continuing slow decrease in flight Mach. The engine continued to burn until 73.1 sec when it experienced a disturbance from which it appears to initially have recovered, but then reverted to unsteady chugging, accompanied by acceleration tail-off. Subsequent analysis has identified a susceptibility to unstart of this particular inlet configuration that was flight tested.

The FASTT approach is an effective technique for testing small to modest sized hypersonic propulsion vehicles in free flight because the suppressed ballistic trajectory allows for test durations of 10 to 60 seconds with minimal variation of altitude, and through proper fueling control, minimal variation of dynamic pressure. Further investigation of launch initiation phenomena is required to better aim at the insertion point, or the flight experiment must be made less sensitive to insertion point. This may be accomplished through fuel controls, for example. The approach can also be extended by adding booster or vehicle flight controls if desired, however it will thereby take on greater complexity.

X-43A Flight Tests

The X-43A program set out to demonstrate hydrogen fueled scramjet operations in a fully integrated aircraft system at Mach numbers of 7 and 10. ATK GASL was the prime contractor to NASA for the execution of the program and had overall responsibility for the detailed design and manufacture and support to flight test of the vehicles. The research performance aspects of the engine and vehicle design were the responsibility of NASA. The program was well described by the keynote speaker for this lecture series.¹⁴ Here this activity will be briefly summarized for subsequent comparison and contrast with the gun-launched and FASTT approaches described previously.

The X-43A vehicle was a 12-foot long lifting body design, weighing about 3000 lb, with a fully integrated, hydrogen fuelled scramjet engine. The aircraft was designed statically stable and had full flight controls to maintain angle of attack and sideslip subsequent to separation from the booster stack, through engine cowl door opening, and engine start and shut-down. The vehicle also executed parameter identification maneuvers subsequent to scramjet function.

The boost system for X-43A was a modified Pegasus first stage that was air-dropped from the NASA B-52 (Figure 28). The Pegasus was fully controlled to execute a pull up from the air-launch altitude to the approximately 100,000 ft insertion point at Mach 7 or Mach 10. The vehicles were instrumented with over 300 transducers for pressure and temperature, and discrete local strain measurements. The flight management unit included accurate 3- axis measurements of translational acceleration and angular velocity, along with Global Positioning System (GPS) and control surface deflection measurements.

Flights 2 and 3 of the X-43A vehicles were successful in achieving all research objectives. Flight 2 at Mach 7 captured all engine and vehicle performance data and accelerometer data clearly indicated acceleration under scramjet power. Comparison of these data with the extensive ground tests database and predictive methodologies has shown all data to be within the stated uncertainties. The tunnel results including combustion heated, arc-heated, and shock heated all predict the flight results quite well without any systematic differences apparent. Flight 3 achieved a similar quantity and quality of data. Acceleration showed the vehicle to achieve cruise-level thrust at the peak of the fuel level of fuel

flow. Comparisons to ground test in shock heated tunnels confirm the ability of these facilities to measure engine performance consistent with flight.

Comparison of Flight Test Approaches

Executed by ATK GASL during an overlapping period from 1998-2005, the X-43A, FASTT and ScramFire programs offer a insight to the execution and outcome of flight test programs with vastly different budgets, test article scales, and flight test infrastructure.

As compared to the traditional self-powered, envelope expansion approach to aircraft flight development, all three programs are very different, but similar to each other. They rely on non-integrated propulsion to achieve hypersonic flight speeds and scramjet takeover. Without the need for significant self-acceleration capability and the required fuel volume that entails, these test systems can be built in relatively small packages, keeping one parameter which drives overall program cost low.

On the other hand, these approaches are sometimes characterized disparagingly as "point designs" since they operate over only a very small range of conditions. This view fails to capture the significance of the need for free-flight data to feed back to the modeling, simulation, and design tools that have not yet been adequately exercised in flight. Before the three flight tests described here, there existed no data on fully integrated scramjet powered vehicles. The CIAM hydrogen fueled ramjet/scramjet test in 1998 and the HyShot hydrogen fueled combustor test in 2002 each captured important but limited data on engine performance. In neither case was thrust measurement attempted or practical in a configuration where the test article stays attached to the boost vehicle.

The three flight programs are compared in Table 1 across a range of flight test approach figures of merit. Comparison and trade of these and other merits are important during the planning phase of a flight program, when the desires of the research team are being constrained by budget realities. The trades that occur and the impact on the program are briefly described next.

Flight Controls

Active flight control and software quickly accumulate costs. Consideration can be given to both the boost system and the test article. X-43A used full active controls on both elements, and also air-launched the booster from a manned airplane. Removing or simplifying controls reduces cost, and ground launch vs. air-launch avoids human rating systems for carriage on a piloted platform.

Ground Test Program Scope

Reducing or eliminating ground tests reduces costs with more reliance on computational simulations. Dynamic operability in flight can not be modeled, so eliminating ground tests incurs more risk. At a minimum and sufficient ground tests must be executed to assure the basic flight test objectives can be met. More robust ground campaigns as in the X-43A program bring value in comparison to flight test.

Experimental Design

Lower cost requires design adjustments, limits flexibility, and may cause some objectives to be sacrificed. To package a vehicle that can fly on an unguided stack requires the payload to be capable of being spun during boost which favors symmetric, non-lifting configurations. For gun-launch testing the test article must be capable of significant scaling to a small test article package, and be capable of withstanding the gun-launch G-forces. Conversely, cost-driven innovation can deliver dividends in packaging approaches that can deliver other dividends for the research program.

Risk

Lower cost ultimately requires acceptance of higher risk to the fundamental objectives. Adding iterations (more flights) and can lead to additional learning allowing more “unknown-unknowns” to become available for discovery

CONCLUSIONS

ATK GASL, with our NASA, DARPA, AFRL, and ONR sponsors and Contractor team partners, have been executing hypersonic engine research and transitioning from ground based research to flight test. We have examined a range of engine geometries since the end of the NASP program and with current missions focused on more narrow engine operating ranges and affordable, manufacturable designs for system applications, we have identified an engine architecture that offers robustness and simplicity. This engine is currently completing an extensive ground test program and flight test opportunities are on the horizon.

We have now executed flight programs over a range of complexity and costs that span two orders of magnitude. All flights programs included supporting ground test campaigns of varying scope and complexity. The flight programs met their intended objectives and delivered propulsion data needed to address key issues:

- Vehicle Acceleration – the final measure of propulsion effectiveness
- Ground to Flight performance comparisons, and predictive tool validation across multiple scales
- Design for integration and operability in flight

Remarkably good agreement has been seen between ground and flight data, although other Engine/vehicle designs may not be so robust. Future Flight Programs can baseline these successful programs, further refine approaches, and continue building a flight database.

ACKNOWLEDGEMENTS

The author would like to acknowledge the following organizations and individuals whose contractual support, referenced work, and individual contributions have formed the basis for this lecture:

Organizations: NASA, DARPA, AFRL, ONR

Individuals: S. Beckel, R. Foelsche, C. Gettinger, J. Garrett, J. Tyll, D. Modroukas, L. Keel, A. Castrogiovanni, R. Volland, C. McClinton, A. Siebenhaar, S. Ferlemann,

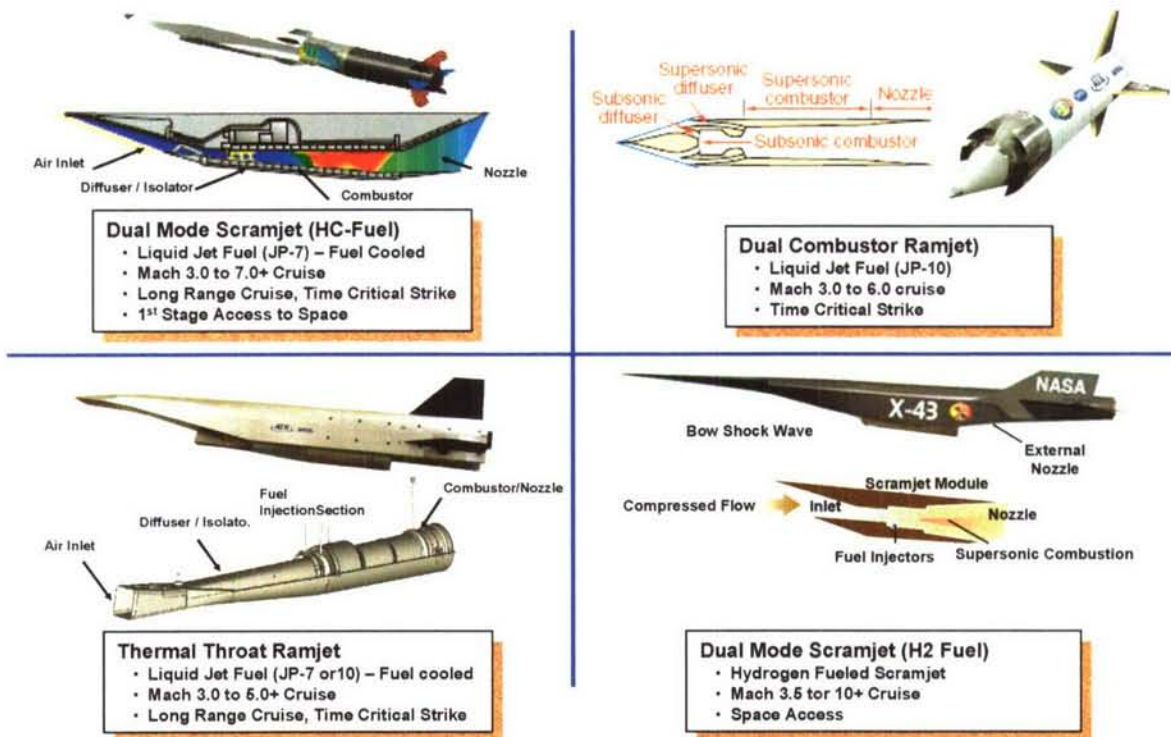


Figure 1. Hypersonic propulsion cycle and fuel choice depend on the speed range and intended mission among other parameters.



Figure 2. X-43A Engine and Fuel System were built as separate units and assembled to the vehicle. The fuel system delivered gaseous hydrogen and pyrophoric Silane for ignition.

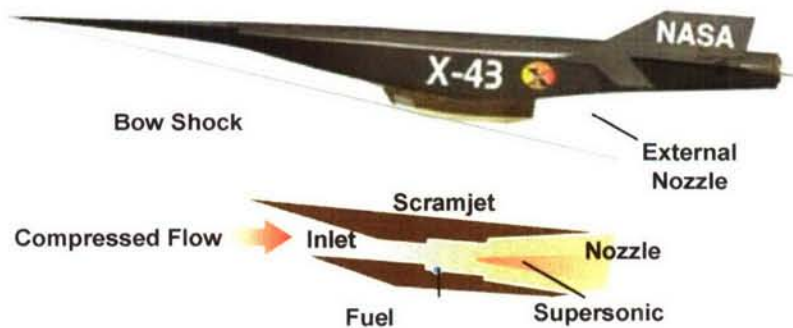


Figure 3: The X-43A Vehicle and predominantly two-dimensional propulsion flowpath

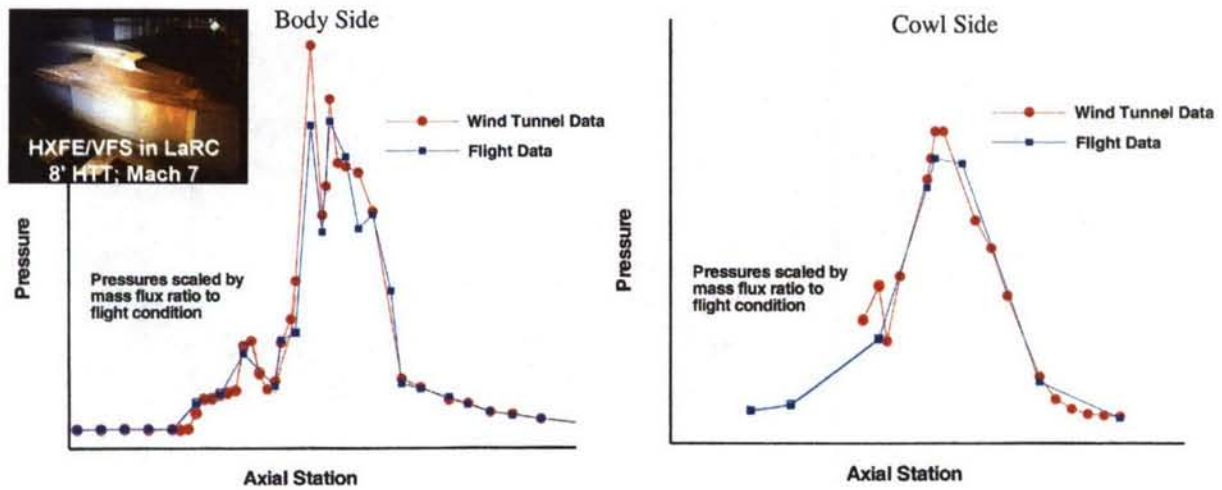


Figure4. Pressure data from the X-43A compared to flight data showed remarkably good agreement with ground test data from combustion heated, arc heated, and shock heated facilities.

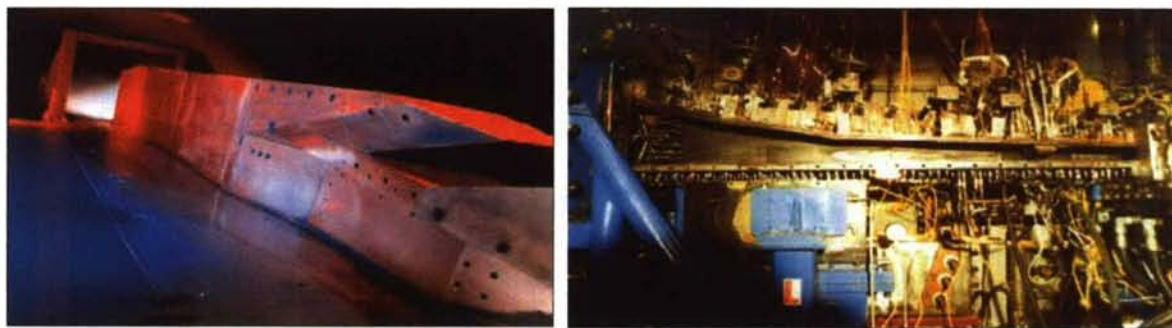


Figure 5. Inlet starting and performance of the USAF HyTech engine were demonstrated over the Mach 4-6 in the ATK GASL Leg 6 blowdown facility. The architecture of the engine is shown in the direct connect test article at the right.

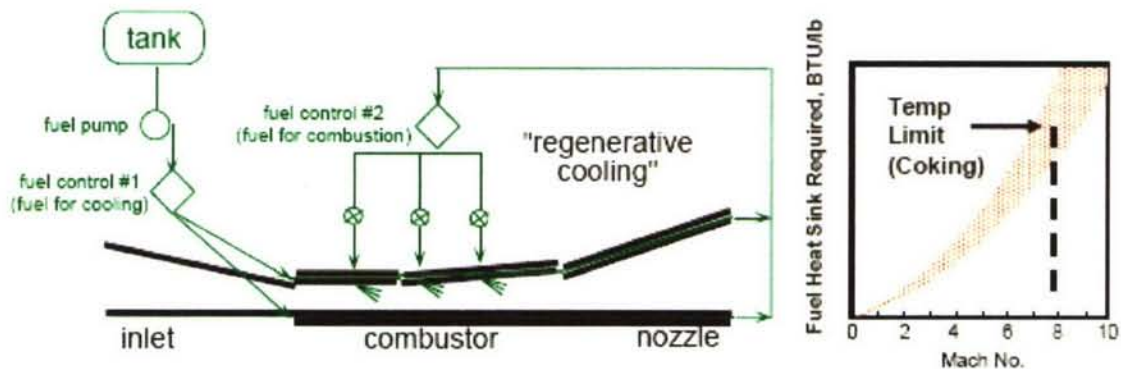


Figure 6. A schematic of a regenerative fuel cooled engine. As the flight Mach increases the thermal load increases. For liquid hydrocarbons the fuel coking limit occurs at about Mach 8.



Figure 7. The X-51A will flight test the US AF HyTech engine with first flight scheduled for 2009

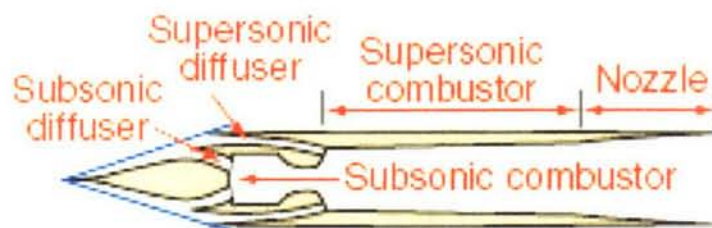


Figure 8 The Dual Combustion Ramjet (DCR) uses a subsonic combustor to pilot a supersonic combustor.

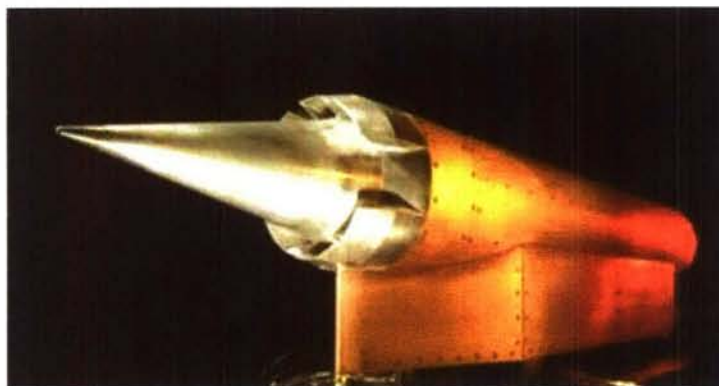


Figure 9. The DCR freejet test article installed in the ATK GASI test facility in preparation for testing at Mach 5.5.



Figure 10. Initial configurations for a gun-launched scramjet featured a predominantly annular engine design that did not offer sufficient strength for high G loads. A direct connect test rig was used subsequently to develop a fully 3D engine configuration



Figure 11. The gun-launched projectile design used eight scramjet wrapped around a cylindrical centerbody with fuel tank and delivery system.

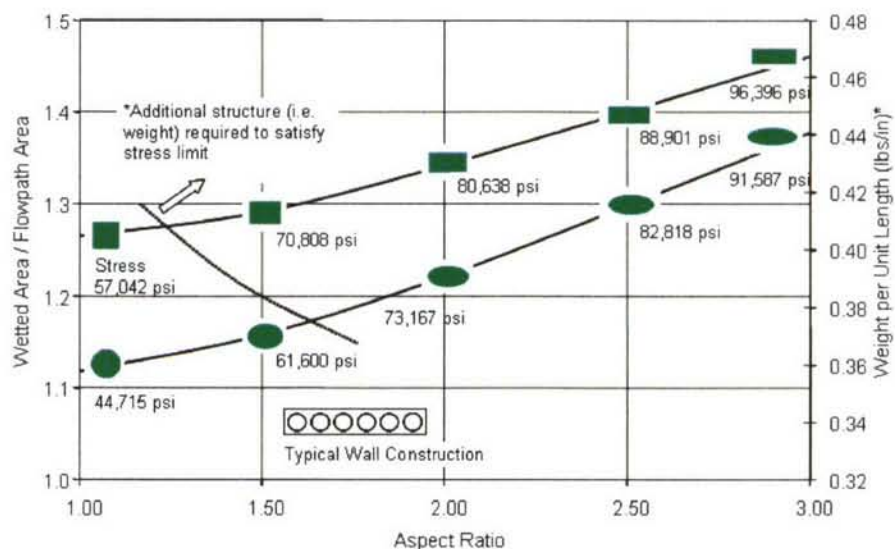


Figure 12: Wetted area and structural weight per unit length trends for two-dimensional and circular elliptical ducts

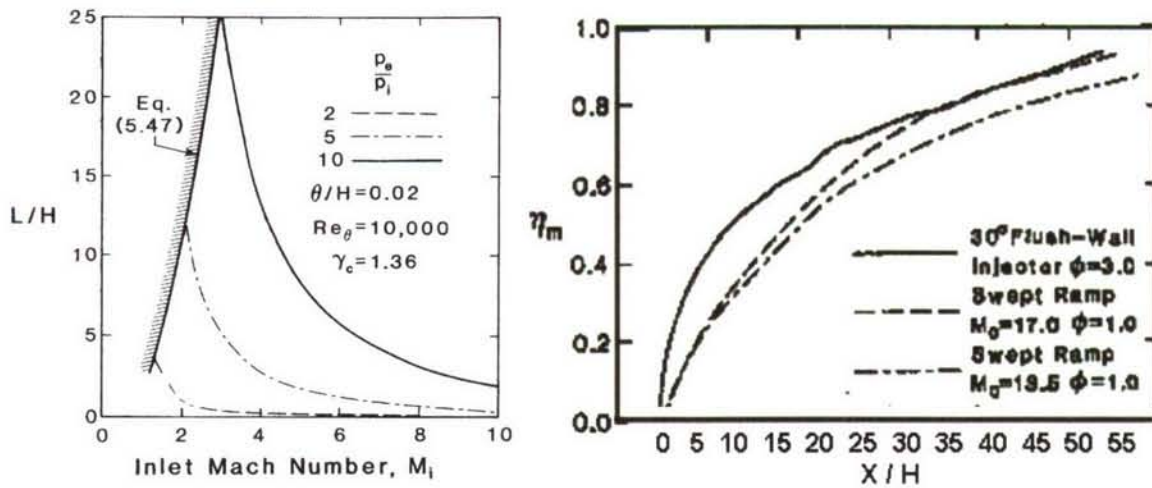


Figure 13: Isolator L/H requirements vs. inlet Mn for various pressure ratios and Combustor (fuel) mixing efficiency vs. normalized length

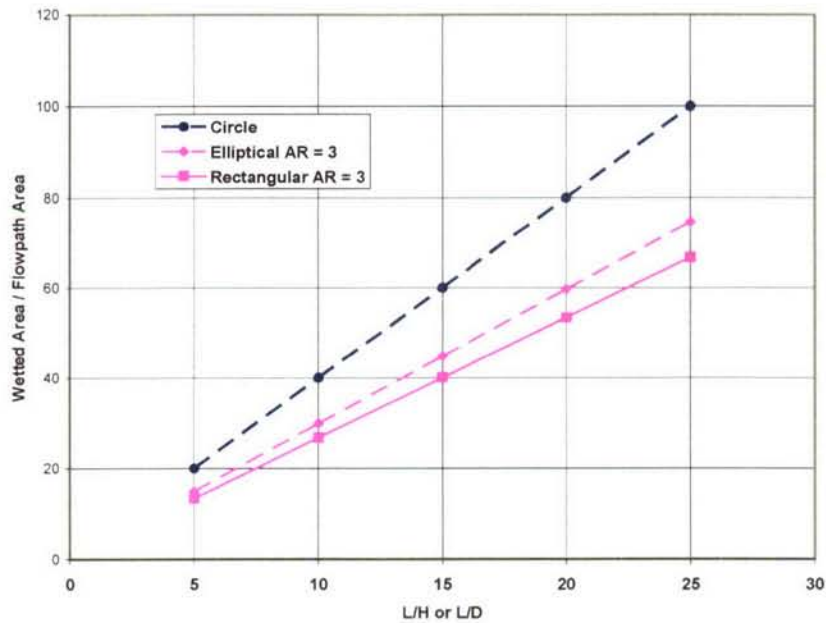


Figure 14: Total wetted surface area as a function of Length / Height or Length / Diameter for circular and high aspect ratio elliptical and rectangular geometries

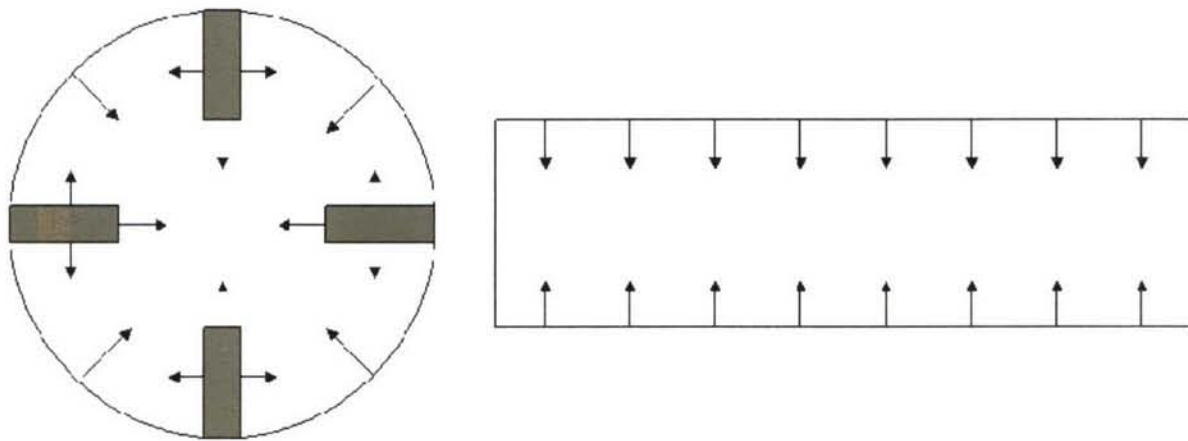


Figure 15: Alternate fuel injection strategies using in-stream fuel elements may be employed for circular ducts to achieve similar distribution characteristics to wall injected rectangular ducts.



Figure 16: ATK rapid prototyping processes applied to circular combustor geometries resulted in clean sheet design to fuel-cooled flight-weight hardware in less than 6 months

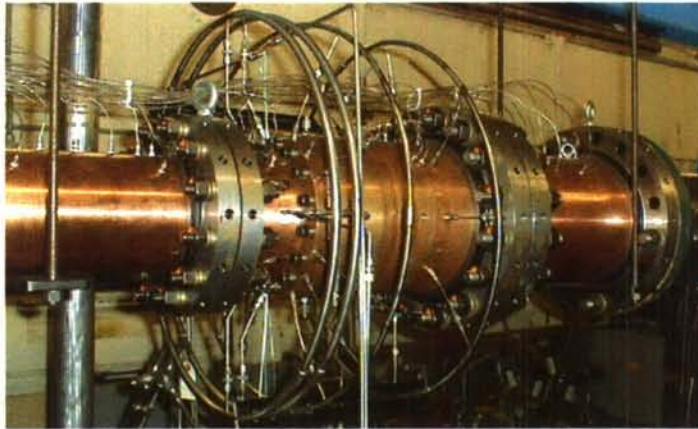


Figure 17: ATK circular cross section PTD rig installed in the NASA LaRC DCSTF

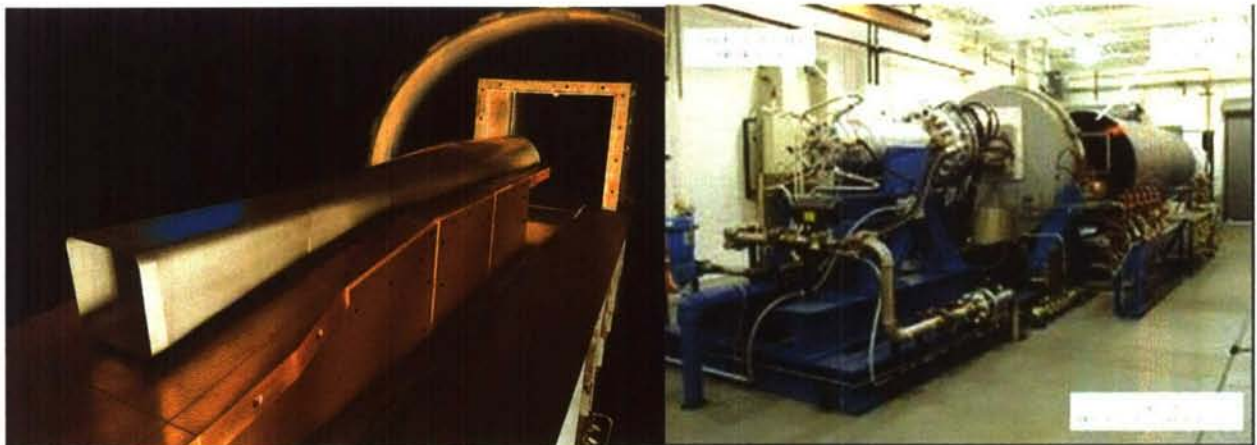


Figure 18: Flight-weight engine installed for freejet test in ATK GASL Test Cell 6

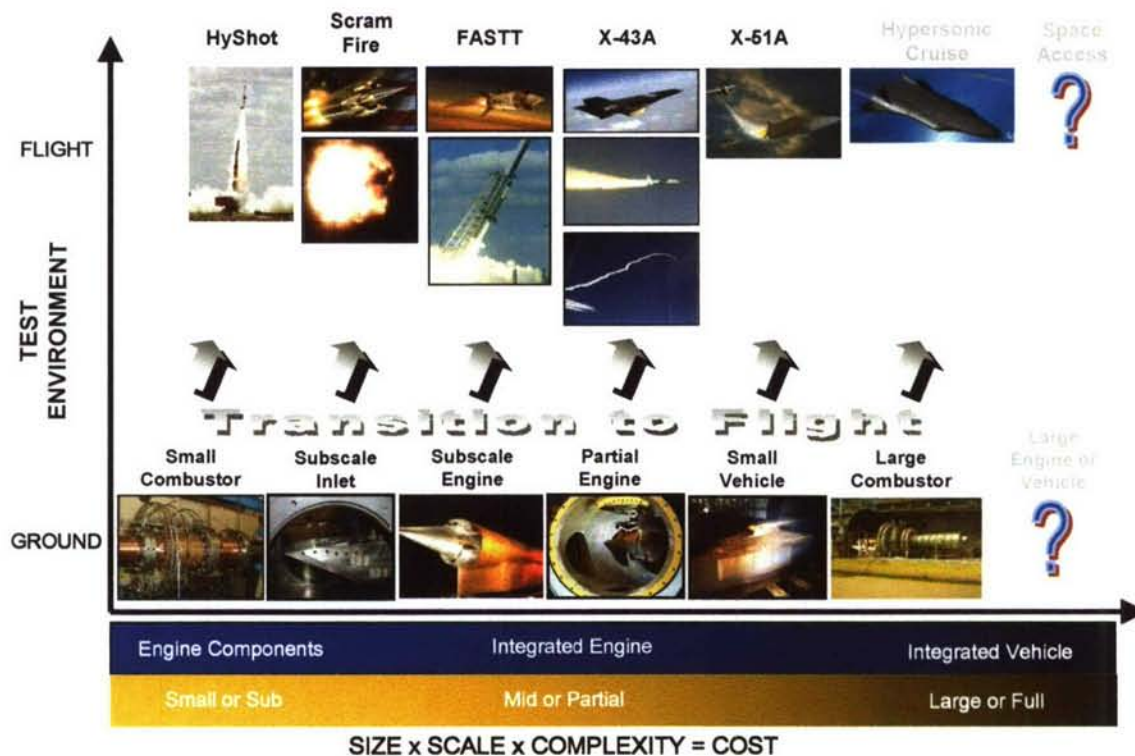


Figure 19. The transition from ground to flight test can occur at numerous points in the size, scale, and complexity domain. Less expensive flight test options foster earlier transition opportunities.

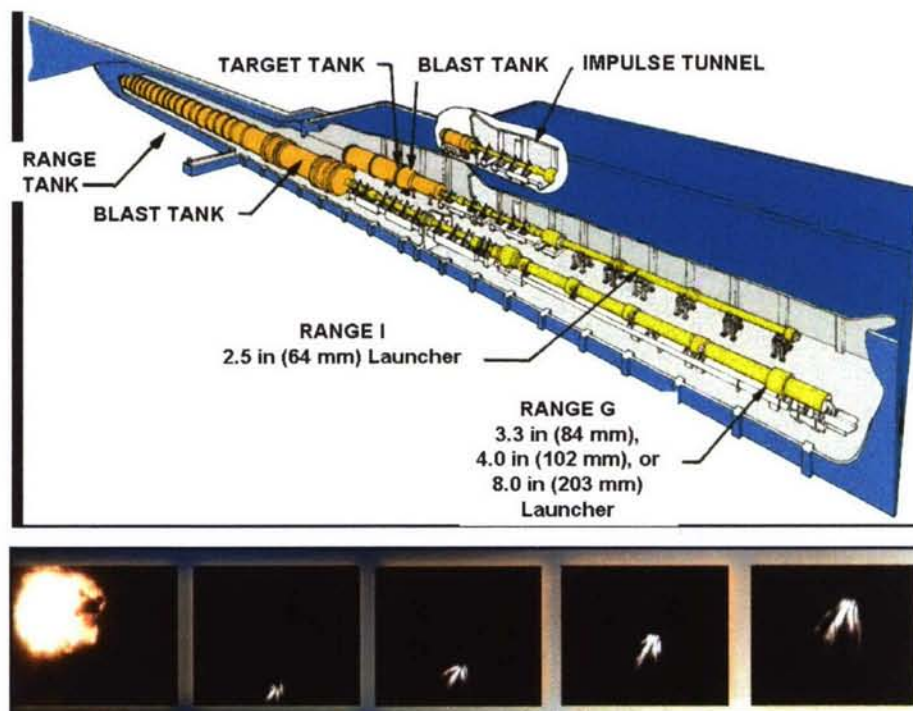


Figure 20. The Arnold Engineering Development Center, G-Range Facility. High speed video images of the Scramjet Projectile in powered flight in the range.

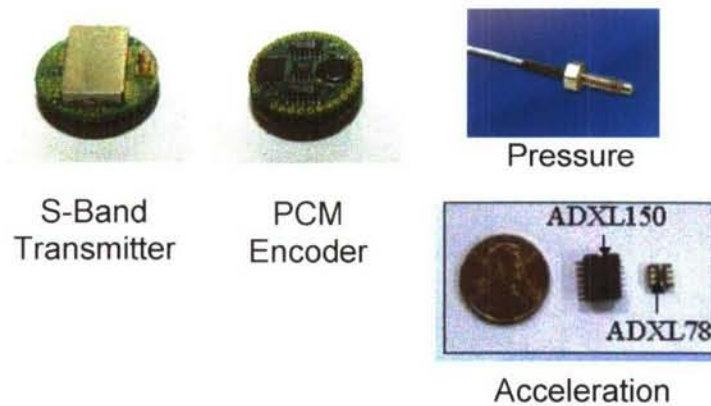


Figure 21. Eight Channel, G-hardened telemetry system, pressure sensors and accelerometers used for on-board measurements of the scramjet projectile.

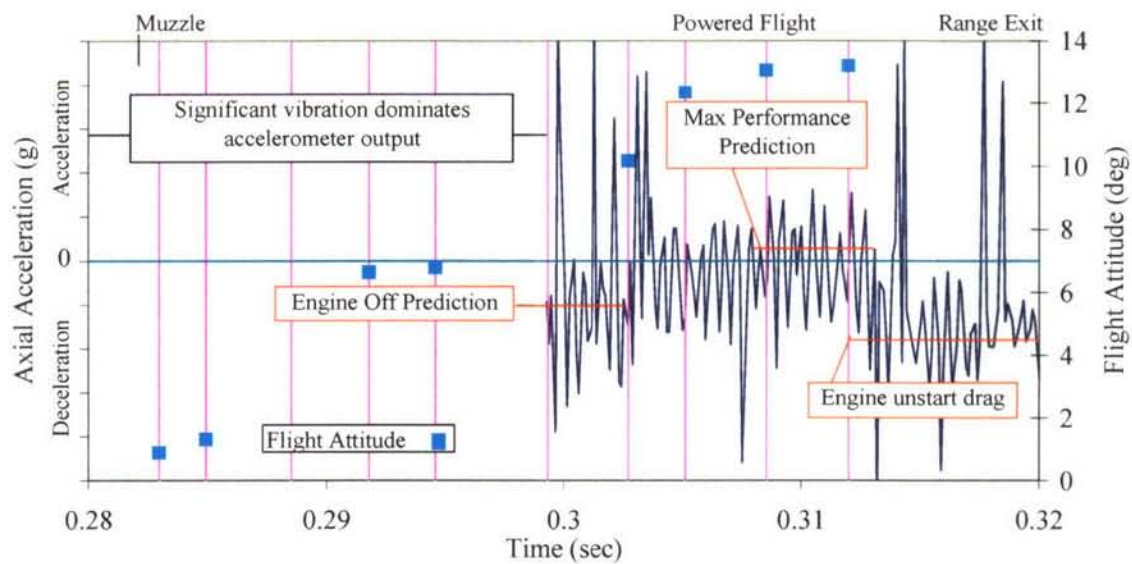


Figure 22. Acceleration measured in the projectile axial direction and flight attitude during launch and free flight. Predicted accelerations are shown for fuel off, fuel on, and engine unstart conditions.

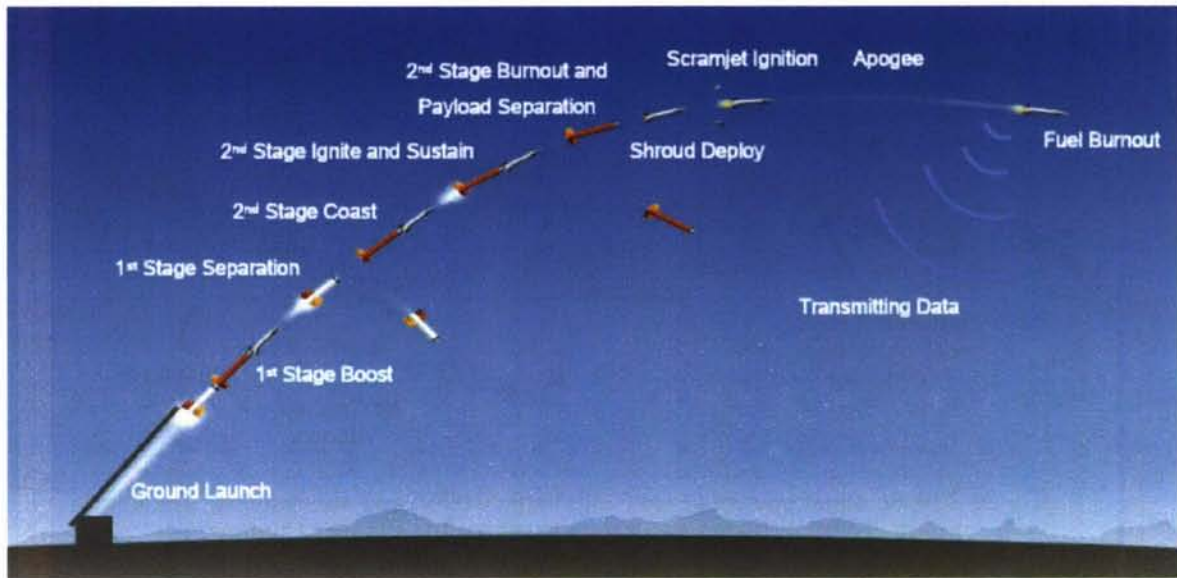


Figure 23. The FASTT approach uses sounding rocket boost system to carry a scramjet powered vehicle to hypersonic test conditions along a ballistic trajectory



Figure 24. The payload vehicle and two-stage booster stack are rail mounted and launched along a suppressed ballistic trajectory.

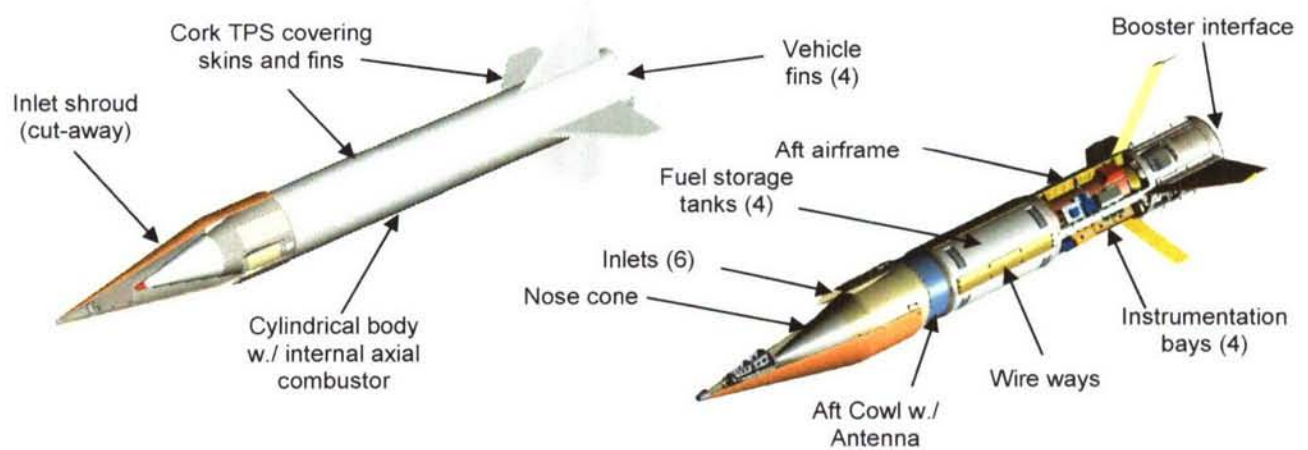


Figure 25. The Scramjet powered Free Flight Vehicle (FFV) and subsystems. The inlet shroud is deployed after separation exposing the engine to air flow.

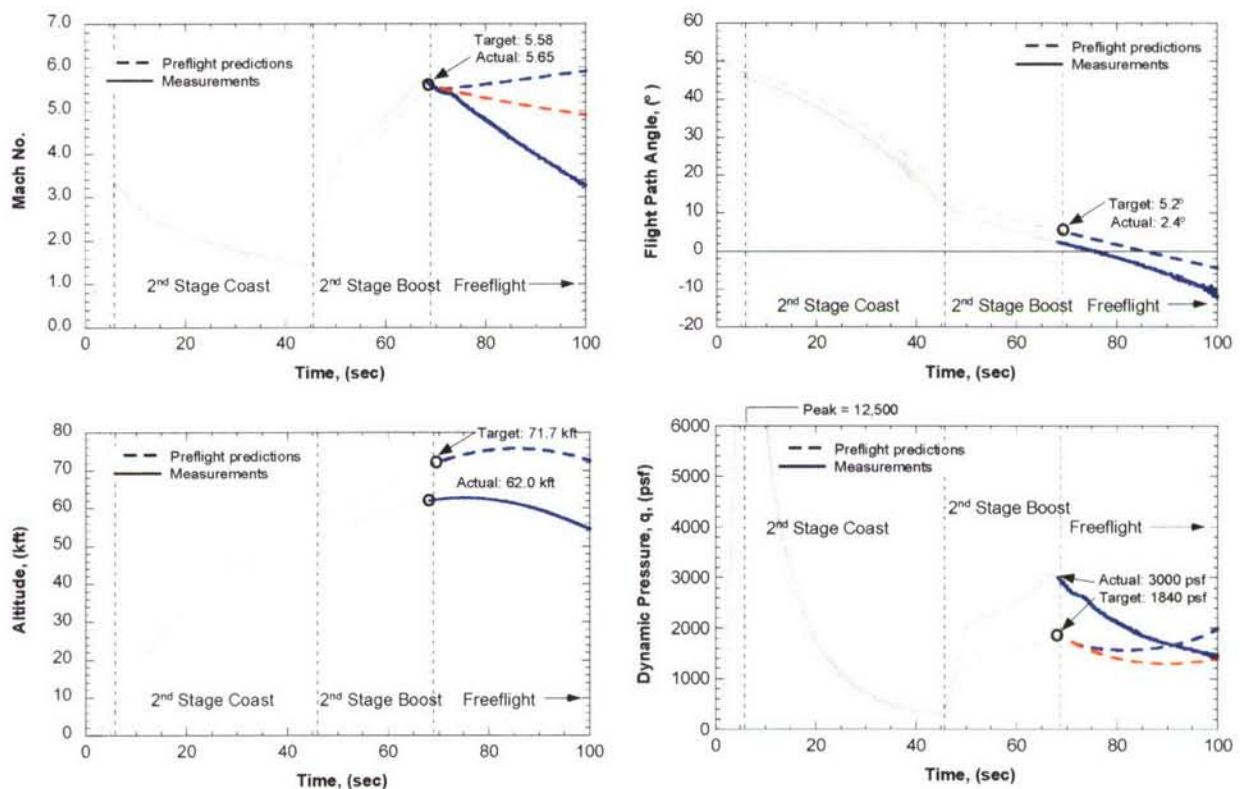


Figure 26. FFV trajectory data compared to preflight predictions. Left, top: flight deduced Mach No., right, top: flight path angle, left, bottom: altitude, right, bottom: calculated flight dynamic pressure.

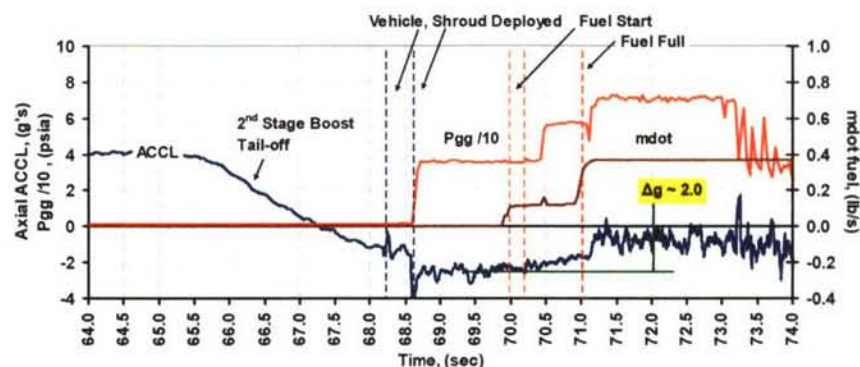


Figure 27: Axial acceleration, gas generator pressure, and fuel flow rate spanning from booster thrust tail-off through inlet unstart.

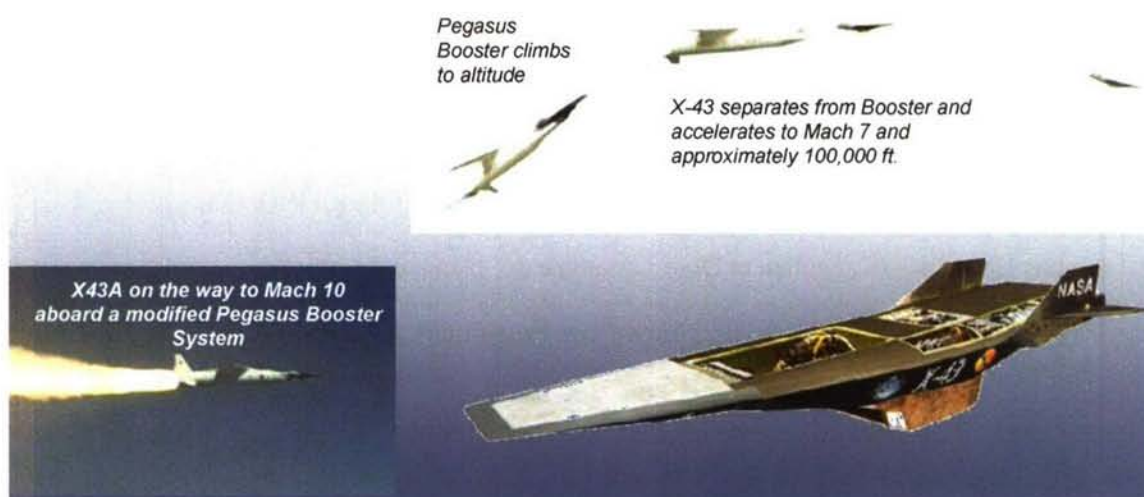


Figure 28. The X-43A vehicle and boost system on the way to Mach 7 for separation and flight test.

	Flight Mach	# Flights	Test Article Mass (lbm)	Inlet Span (in)	Test Duration (s)	Boost Insertion Mode	Flight Controls	Accel. Measured	# Data Channels (On-Board)	Off-Board Data	Ground Test Program	Success Criteria Met	Program Cost Range (\$M)
 X-43A	7, 10	3 1 Failed 2 Designs	3000	19	10	Air-Launched Controlled Boost	Active Vehicle and Engine	Yes	300+	Long Range Imaging	Inlet, DC FJ, Vehicle	All	\$100-\$200
 FASTT	5.5	3 2 Surrogates	300	10	10	Ground Launch Ballistic Boost	Event Sequence Timer	Yes	150+	Long Range Imaging	DC & FJ	All (Engine Unstart Captured)	10-\$15
 ScramFire	6 to 8	9 1 Failed 3 Surrogates 3 Designs	20	4	<0.1	Gun Launch In Range Chamber	Inertial Off/On Valve	Yes	8	Multiple Close Range Imaging	DC	All	\$1-\$2

Table 1. Comparison of technical and programmatic parameters from three different hypersonic flight programs

REFERENCES

- [1] EVALUATION OF THE NATIONAL AEROSPACE INITIATIVE, Committee on the National Aerospace Initiative, Air Force Science and Technology Board, THE NATIONAL ACADEMIES PRESS, Washington, D.C., 2004
- [2] ² Siebenhaar, A., and Bogar, T., The Impact of Round Combustors on TBCC Propulsion and Hypersonic Cruise Vehicles, AIAA-2006-7986
- [3] ³ Ferlemann, S., McClinton, C., Rock, K., and Volland, R., Hyper-X Mach 7 Scramjet Design, Ground Test and Flight Data, AIAA 2005-3322
- [4] ⁴ McClinton, C. X-43–Scramjet Power Breaks the Hypersonic Barrier, Dryden Lectureship in Research for 2006, AIAA 2006-0001
- [5] ⁵ Harsha, P., Keel, L., Castrogiovanna, A., Sherrill, R., X-43A Design and Manufacture, AIAA-2005-3334
- [6] ⁶ Boudreau, A., Hypersonic Air-Breathing Propulsion Efforts In the Air Force Research Laboratory, AIAA-2005-3255
- [7] ⁷ Pratt & Whitney Rocketdyne Press Release: July 27, 2006, Canoga Park CA.
- [8] ⁸ Johns Hopkins APL Technical Digest, Volume 26, Number 4 (2005)
- [9] ⁹ Tyll, J., Erdos, J., Bakos, R., Low-Cost Free-Flight Testing of Hypersonic Airbreathing Engines, ISOABE 2001-1072
- [10] ¹⁰ Beckel, S., Garrett, J., Gettinger, C., Technologies for Robust and Affordable Scramjet Propulsion, AIAA-2006-7980.
- [11] ¹¹ Aerospace Science and Technology Update, Dr. Ronald M. Sega, Undersecretary of the Air Force, November 2005.
- [12] ¹² Bakos, Successful Transition from Hypersonic Ground Test to Flight Test, AIAA Reno 2007
- [13] ¹³ Foelsche, R., Beckel, S., Charletta, R., Betti, A., Wurst, G., and Bakos, R., Flight Results from a Program to Develop a Freeflight Atmospheric Scramjet Test Technique, AIAA-2006-8119.
- [14] ¹⁴ McClinton, C.M. High Speed/Hypersonic Aircraft Propulsion Technology Development, VKI-RTO Lecture Series 2007

von Karman Institute for Fluid Dynamics

RTO-AVT-VKI Lecture Series 2007

**ADVANCES ON PROPULSION TECHNOLOGY
FOR HIGH-SPEED AIRCRAFT**

March 12-15, 2007

HYPERSONICS RESEARCH IN AUSTRALIA

M. Smart¹; R. Stalker¹; R. Morgan¹; A. Paull²
¹The University of Queensland & ²Defense Science and
Technology Organisation, Australia

Hypersonics Research in Australia

Michael Smart, Ray Stalker and Richard Morgan

Centre for Hypersonics,

The University of Queensland,

Brisbane, Australia. 4072

Allan Paull

Applied Hypersonics Group

Defense Science and Technology Organisation

Pullenvale, Brisbane, Australia, 4069

1. Introduction

Research into hypersonic flow phenomena has been conducted by numerous groups within Australia for over 40 years. The genesis of all the modern day work can be traced back to the return of the then Dr Ray Stalker from England, to take a faculty position in the Physics Department of the Australian National University, Canberra, in 1962. Dr Stalker had a keen interest in the aerodynamics of bodies travelling at speeds up to orbital velocity, and had devised a concept for generating such velocities in the laboratory through the use of a shock tunnel driven by free-piston compression. In the following years, Dr Stalker developed numerous facilities utilizing this concept, called free-piston shock tunnels, culminating in the commissioning of the T3 shock tunnel in 1968. A small group of researchers exploited the unique capabilities of T3, which was the first facility in which the product of test section density and model size, combined with the test section velocity, was such that the aerodynamic thermochemical phenomena generated at these elevated velocities were large enough to be measured. Bluff body shapes received early attention, as these shapes are typical of re-entry vehicles, and changes in the flow patterns due to dissociation thermochemistry were observed and analysed. Noting the interest in entry into the atmosphere of Mars, the bluff body studies were extended to include carbon dioxide flows, and because entry into the atmospheres of the large planets would involve ionisation, the effect of ionisation thermochemistry on bluff bodies was investigated. Dissociation thermochemical effects related to gliding re-entry vehicles also received attention, by studying the flow over an inclined flat plate, over a delta wing, and in the laminar boundary layer on a flat plate. The interaction of this boundary layer with a shock wave was also studied.

Sufficient experience had been gained with T3 by 1980 to begin research on scramjet engines, which offer the prospect of propelling an aircraft at these very high velocities. By this time Professor Stalker had taken a chair at The University of Queensland in Brisbane, and began leading a small group of researchers in pioneering work on the performance of scramjet engines at speeds in excess of 2.5 km/s. This team visited T3 for a number of weeks each year until 1987, when a larger shock tunnel facility known as T4 was commissioned at The University of Queensland. Since 1987 the primary mission of T4 has been to study scramjets. Scramjet models tested in T4 have progressed from simple generic models of a constant area combustor with a simplified fuel injector, to sophisticated models that involve the complete scramjet flowpath. Much of this work contributed to the successful scramjet flight experiment that was conducted by The University of Queensland in 2002.

Interest in hypersonics at The University of Queensland has expanded beyond scramjet engines to include the study of phenomena associated with flight in planetary atmospheres other than earth. This has resulted in the commissioning of the X3 expansion tube, which is able to generate higher freestream static pressure at a given Mach number than a reflected shock tunnel like T3 or T4, by use of an unsteady expansion. A strong computational group is also involved in hypersonics research at The University of Queensland, developing computational codes that are

used to assist in the understanding of the scramjet and planetary re-entry experiments, as well as the operation of the T4 and X3 facilities.

This article describes some key aspects of the hypersonics research that has been performed at The University of Queensland. A short description of the operation of the T4 shock tunnel is followed by a discussion of some scramjet component research conducted in T4, and a description of research on complete scramjet flowpaths. A short summary of the HyShot 2 flight experiment is also included. Discussion of the planetary re-entry research associated with X3 is next, and the article closes with a description of future plans. It should be noted that other groups within Australia are currently involved in hypersonics research, particularly those at the Australian Defence Force Academy at the University of New South Wales (ADFA) and the Defence Science and Technology Organisation (DSTO). Description of the work of these groups is not included in this article.

2. The free piston shock tunnel T4

T4 is shown in general arrangement in Fig. 1(a). A free piston is used to compress and heat the shock tube driver gas. A piston with a mass of 92 kg is normally used and, referring to the figure, is launched from the right-hand end of the compression tube, which is 26 m long and 228 mm in diameter, and initially contains the shock tube driver gas. The piston is driven along the compression tube by the expansion of air initially contained in the piston driver reservoir, which has a volume of 1.2 m³ and a maximum working pressure of 14 MPa. The piston acquires kinetic energy as it is driven along the compression tube, and this energy is then passed to the shock tube driver gas as the piston slows down on approaching the left-hand end of the compression tube. The driver gas is adiabatically compressed to pressures which are a multiple of the initial pressure in the piston driver reservoir. A high pressure diaphragm, located at the left-hand end of the compression tube, spontaneously ruptures when the shock tube driver gas reaches a predetermined pressure. This initiates conventional operation of the shock tube, which is 10 m long and 75 mm in diameter. The resulting shock wave in the test gas traverses the length of the shock tube and reflects from its left-hand end, where it ruptures a thin Mylar diaphragm to initiate the flow of test gas through the nozzle and test section. The shock heated test gas thus becomes the supply gas for the nozzle and test section flow, with a nozzle supply pressure which can somewhat exceed 50 MPa on a routine basis. This limit has recently been raised to 90 MPa.

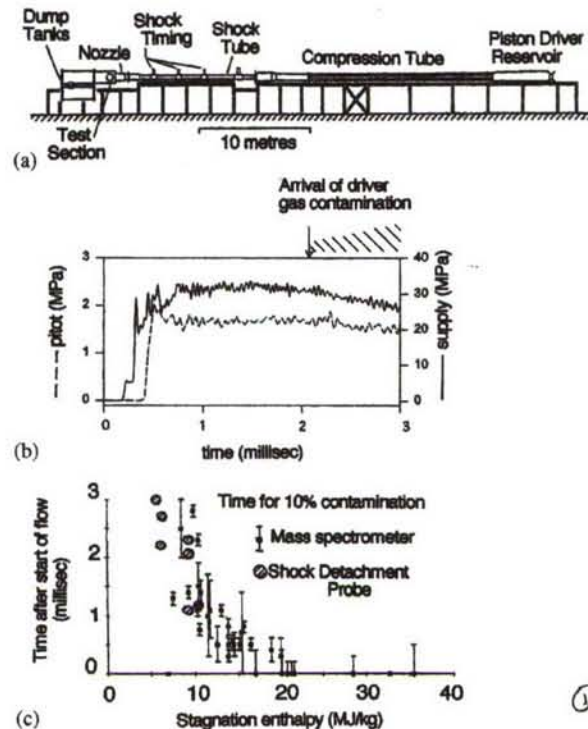


Figure 1 - Free piston shock tunnel T4 at the University of Queensland: (a) general arrangement, (b) typical records of Pitot pressure, and nozzle supply pressure, (c) test time limit due to driver gas contamination

2.1 Test times – driver gas contamination of the test flow

Typical records of test section Pitot pressure and nozzle supply pressure are shown in Fig. 1(b). A rule of thumb used in shock tunnel research is that the test flow must traverse three model lengths in order for the mainstream and boundary layer flows to effectively reach a steady state. The stagnation enthalpy of the figure (8 MJ/kg) yields a flow velocity of about 3.5 km/s, indication that the flow would reach a steady state on a model 1 m long in 0.9 ms. Thus, the Pitot pressure record indicates that a steady-state flow persists for about 1.3 ms or 4.5 model lengths. However, the figure also shows the arrival of driver gas contamination of the test flow and, if the experiment in the shock tunnel demands uncontaminated test flow, then steady flow persists for only 0.5 ms, or 1.8 model lengths, and only test results obtained in this time can be accorded unqualified acceptance. Thus, the useful test time in a shock tunnel may be determined by driver gas contamination, rather than by the time for which the nozzle supply pressure remained unchanged.

Measurements of the time to contamination in T4 are presented in Fig. 1(c). The measurements were first made using a time of flight mass spectrometer (Skinner 1994), and later with a shock detachment probe (Paull 1996). The latter was developed as a simple instrument for routine monitoring of the test flow, and works by choking a duct when the specific heat of the flow gas increases beyond a critical value. It will be noted that the 10% contamination test time is reduced to zero for stagnation enthalpies in excess of 15 MJ/kg. It is thought that this may be due to turbulent mixing at the interface between the test gas and the driver gas in the shock tube. The peculiarities of the shock tunnel site demanded a length to internal diameter ratio of the shock tube of 133, instead of the value of 80-100 used in normal shock tunnel practice, and the extra length may have allowed extra mixing to take place. Notwithstanding this effect, it will be seen below that the test times available at stagnation enthalpies somewhat less than 15 MJ/kg have proven adequate for scramjet research.

2.2 Fuel supply

Hydrogen fuel is used for almost all the tests performed to date, although both ethylene and gaseous kerosene have been recently used. Fuel is supplied to a model in the test section from a room temperature reservoir. For safety reasons, the capacity of the reservoir is limited so that if it were fully combusted in the test chamber it would reach a maximum working pressure of 10 MPa. The supply of fuel to the test section is controlled by a quick acting solenoid valve, which is slaved to the recoil of the compression tube to open and start fuel injection on the model approximately 10 ms before flow is initiated in the test section. Thus a constant rate fuel flow is established on the model before the test flow arrives. Fuel is injected through pre-calibrated orifices at the model, and the fuel flow is monitored by pressure transducers located as near to the injection orifices as is conveniently possible.

3. The two-dimensional combustion wake

The addition of fuel to a supersonic airstream in a duct, and the mixing and combustion which follows, will generate an increase in pressure along the duct. This pressure increase is at the heart of a scramjet, and leads to thrust generation in the expansion nozzle which follows the duct. To develop a knowledge of scramjets, it is important first to develop some understanding of the means of generating this pressure increase. This was done by studying combustion wake phenomena in relation to the pressure rise in a duct of rectangular cross section with a central injector spanning the duct, as shown in Fig. 2(a), to produce a flow which was essentially two-dimensional. The two-dimensional configuration was chosen because it offered relative simplicity for interpretation of experimental results, while recognizing that this configuration may not be the most efficient one in terms of providing maximum combustion in minimum combustion chamber length.

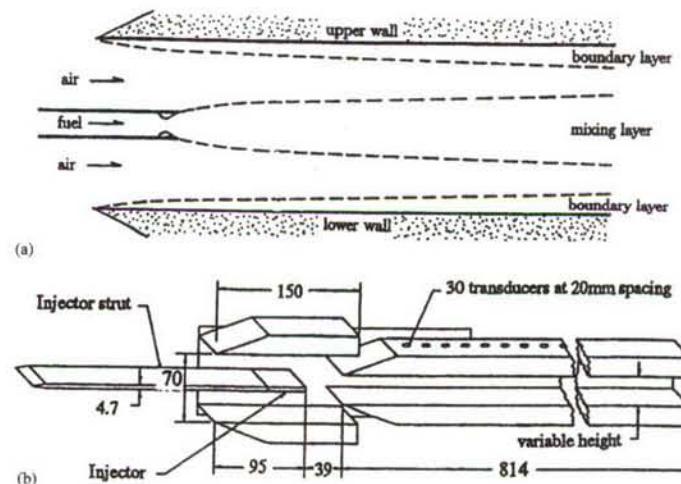


Figure 2 - Combustion wake studies: (a) schematic of 2-D combustion duct, (b) typical experimental duct with side plate removed (dimensions in mm)

3.1 Wake independent of duct height

The mechanism by which the duct pressure rise is produced was investigated experimentally using the configuration of Fig. 2(b) (Wendt et. al. 1999). The precombustion pressure in the duct was 61 ± 5 kPa, the Mach number was 4.4 ± 0.2 , the stagnation enthalpy was varied from 5.6 to 8.9 MJ/kg and the associated air velocity varied from 2.9 to 3.5 km/s, while hydrogen fuel was supplied from a room temperature reservoir at a velocity of 2.3 ± 0.1 km/s. Duct heights of 30, 50 and 70 mm were used, and the fuel flow rate was maintained at a value corresponding to an equivalence ratio of one with a 30 mm duct height.

The inset on the top right of Fig. 3 shows typical pressure distributions obtained when hydrogen fuel was injected into air and nitrogen. These were obtained under conditions corresponding to a precombustion temperature of 1480 K. The difference in the pressure distributions is ascribed to combustion, which clearly causes the fuel-air wake to produce a much greater pressure rise than the fuel-nitrogen wake. As indicated by the straight lines on the figure, the pressure increases linearly with distance downstream. Estimates of the ignition length for a hydrogen air mixture (Huber et. al. 1979) indicate that this length is less than an order of magnitude less than the length of the duct, indicating that the growth of the wake is governed by the process of mixing between hydrogen and air, rather than the reaction process.

A numerical analysis of this flow (Wendt et. al. 1999), based on the two-dimensional model of Fig. 2(a), found that the growth of the wake displacement thickness was responsible for the combustion induced increase in pressure along the duct and, the growth in displacement thickness was independent of the height of the duct. Figure 3 shows that, using the same combustion wake, a reasonable prediction can be made of the pressure rise along the duct by subtracting the sum of the displacement thicknesses of the wake and the boundary layers on the walls of the duct from the duct cross-sectional area, implying that as the duct height reduces, the mainstream experiences greater contraction and the pressure rise is increased. This model breaks down for the 30 mm duct at a temperature of 1230K, where it over-predicts the pressure rise but, for the less extreme conditions, it is possible to regard the development of the wake as decoupled for the associated pressure rise.

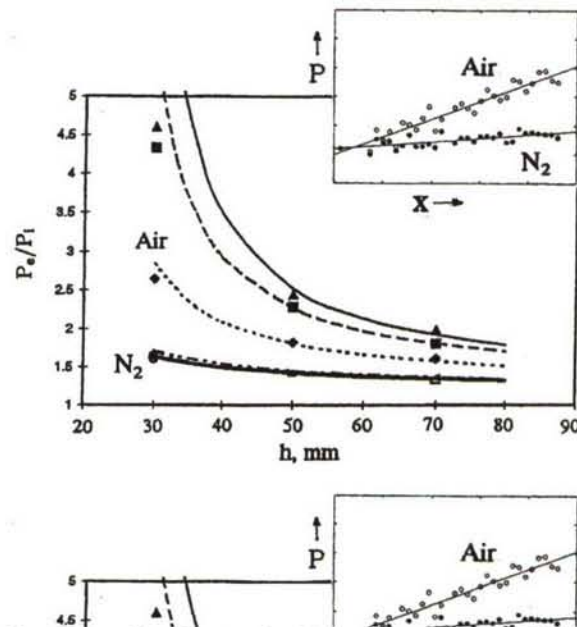


Figure 3 - Displacement effect of combustion wake (P_e = exit pressure; P_i = precombustion pressure; x = distance from injector; h = duct height; T = precombustion temperature; u = precombustion air velocity)

3.2 Scaling of supersonic combustion

Scaling studies are not only important for extrapolating from laboratory experiments to flight, but they can be helpful in revealing the dominant phenomena in a flow system. Experiments were done to compare the pressure distributions in the two ducts shown schematically in Fig. 4(a) (Pulsonetti 1997). To ensure the same composition of test gas entering the two ducts, the large duct was supplied with oblique shock recompressed flow from a Mach 8 shock tunnel nozzle and the small duct was supplied directly from a Mach 4 nozzle. The ducts were geometrically similar, but different in size by a factor of 5, the large duct height being 47 mm, and the small duct 9.4 mm. Precombustion pressures in the large duct varied from 25 to 10 kPa, and from 101 to 32 kPa in the

small duct, while the precombustion Mach number was 4.4 ± 0.2 , and the hydrogen fuel equivalence ratio was 1.3 ± 0.2 .

At each flow condition, the values of the product of the duct precombustion pressure and the duct height was the same for the two ducts. The results presented in Fig. 4(b) show that, by setting this product to be the same, identical normalized pressure distributions in the large duct and the small duct are obtained when the distance downstream of injection is scaled by the duct height. Thus, binary scaling applies to these flows, implying that small-scale experiments can be used as models of larger scale flows.

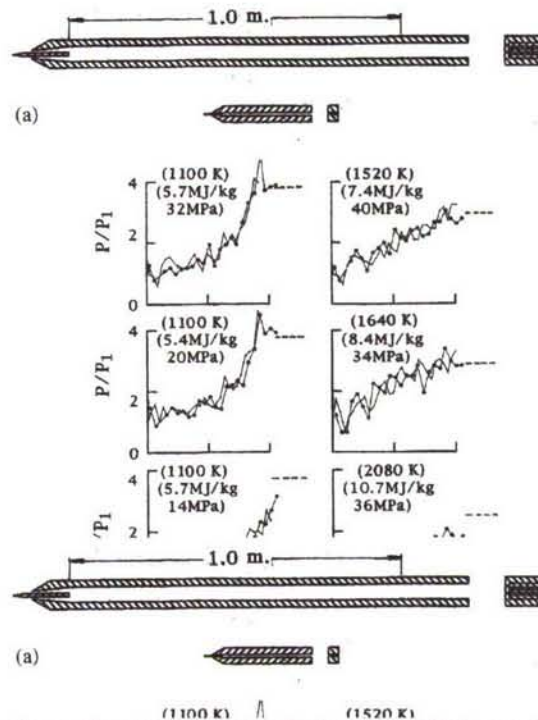


Figure 4 - Scaling of supersonic combustion: (a) sketch showing relative scale of two combustion ducts, (b) pressure distributions (P_1 = precombustion pressure, P_c = theoretical peak pressure, x = distance from injector, h = duct height)

The pressure distributions on the right-hand side of the figure indicate the effect of varying the precombustion temperature while the precombustion pressure remains approximately constant, as indicated by the nozzle reservoir pressure on the figure. The linear pressure distributions, with the pressure gradient reducing as the precombustion temperature increases, indicate mixing controlled growth of the combustion wake, as in Fig. 3. It might be noted that Fig. 3 is also associated with linear pressure distributions at precombustion temperatures as low as 1230K.

The left-hand side of Fig. 4(b) indicates the effect of varying the precombustion pressure, as indicated by the values of nozzle reservoir pressure on the figure, while maintaining the precombustion temperature at 1100 ± 50 K. The gradient of the pressure rise along the duct is somewhat reduced as the precombustion pressure falls, but the most notable feature of these pressure distributions is that they do not exhibit the linear characteristic of those at higher temperatures. This non-linearity is consistent with the expected rapid increase in the flow length for reaction, which occurs as the mainstream temperature falls to about the temperature of these pressure distributions. At these temperatures the reaction length is sufficiently large that, in comparison with the mixing controlled flows on the righthand side of Fig. 4(b), the combustion release of energy is delayed, allowing more mixing and creation of radicals to take place, before a delayed but rapid energy release and relatively steep pressure rise. Thus, the pressure distributions on the left-hand side of Fig. 4(b) represent examples of reaction-controlled combustion.

Reaction-controlled combustion wakes were observed in other experiments. It was found (Casey et. al. 1992) that raising the precombustion pressure at a precombustion temperature of 1200K in the large duct would lead to the expected reduction in the combustion energy release delay but, as less mixing had then occurred, the combustion pressure rise was reduced. With a 25 mm duct height and precombustion pressures exceeding 150 kPa, the combustion energy release delay was further reduced (Stalker et. al. 1996), but the pressure rise was such as to suggest substantial combustion energy release and hence enhanced mixing. This may have been associated with the occurrence of a normal shock which was observed in the fuel rich part of the wake (McIntyre et. al. 1997). Other experiments (Buttsworth 1994) have shown that the interaction between a shock wave and a wake can lead to enhanced mixing.

An approximate combustion pressure rise may be calculated by using a Rayleigh analysis (Hall 1951), with the square of the Mach number much greater than one both before and after the heat addition zone, to yield

$$p_c / p \approx 1 + (\gamma - 1) \Delta Q / a^2 \quad (1)$$

where p_c = downstream pressure, ΔQ = combustion heat release, a = speed of sound and γ = ratio of specific heats.

Equation 1 with $\Delta Q = 3.45$ MJ/kg and $\gamma = 1.3$ provides an estimate of the resultant pressure levels if all the oxygen in the air entering the duct is burnt, and this level is shown in Fig. 4(b) for each pair of pressure distributions. The duct lengths are just sufficient for complete combustion, except at the highest precombustion temperature, where it is expected that the combustion energy release was limited by partial dissociation of the combustion products.

4. Force measurement

After a significant series of component experiments, some of which have been described here, Prof. Stalker and the group at The University of Queensland began to experiment with complete scramjet configurations. These involved the integration of the inlet, combustion duct and thrust nozzle into one complete model. The obvious measurement to initially make on such models is the net thrust (or drag) as this is the essential measure of installed scramjet performance. Such measurement demanded the development of a new shock tunnel measurement technique.

In the shock tunnel, flow is initiated and forces are rapidly applied to the model, causing stress waves to occur that will, by reflection and re-reflection, traverse the length of the model many times before the model comes into stress equilibrium. It follows that the few flow model lengths of test time available in a sub-orbital shock tunnel were, in general, not sufficient for the model to come into stress equilibrium, and therefore that the overall forces acting on a model could not be measured by available force balance methods, since these treated the model as a rigid body.

Fortunately, the stress waves which were the source of this difficulty can themselves be exploited to measure the force on the model. This is done by placing strain gauges on the model support system and recording the time history of the strain produced by the stress waves passing into the supports. Deconvolution of the strain records then would yield the forces on the model. For measurement of the thrust or drag of a slender body, supported from a downstream sting, a single strain gauge, recording the strain time history of stress waves passing into the sting, would yield a satisfactory measurement.

The relation between the strain measured in the sting, $u(t)$, and the axial force on the model $y(t)$, can be described by the integral:

$$y(t) = \int_0^t G(t - \tau)u(\tau)d\tau \quad (2)$$

where $G(t)$ is a pre-determined impulse response function, and t and τ are time. The impulse response function can be determined numerically or by experiment, for example, by measuring the strain history resulting from application of a sudden increase in axial load on the model. The deconvolution of the integral of eqn. 2 to yield the axial force history, $u(t)$, from the recorded strain history, $y(t)$, is accomplished by a numerical procedure using a personal computer.

The method was first applied to measurement of the drag on a relatively short cone, with 15° semi-vertex angle (Sanderson & Simmons 1991). In this case, the internal stress waves in the model were unimportant, but the stress wave balance was established as a viable method of measuring axial force. Subsequent measurements of drag were made on a 5° semi-vertex angle cone which was 425mm long (Tuttle et. al. 1995, Tuttle 1996), where the internal stress wave reflections were significant, and yielded results consistent with theoretical estimates. The sensitivity of the method to the distribution of drag producing forces on the model was investigated numerically during this project leading to the conclusion that measured drag was independent of the force distribution on the cone.

The numerical investigations just referred to included a case where the drag force was concentrated at the tip of the cone. The fact that this did not influence the measured drag was exploited to conduct an investigation of the effect of nose blunting on the drag of a 5° semi-vertex angle cone (Porter et. al. 1994). The tests were done at a stagnation enthalpy of 15 MJ/kg with a test flow in which driver gas contamination occurred, but was less than 30% of the test flow by molar concentration. It was found that the drag remained at a constant value when the radius of the blunt nose remained less than 0.12 times the radius of the base of the cone. This indicates that a moderate degree of nose bluntness could be used to accommodate nose tip heat transfer effects on scramjet inlets without directly affecting the drag.

The stress wave force balance has also been used with a two-dimensional straight thrust nozzle in an exercise aimed at determining the influence of skin friction on thrust (Tuttle 1996). The nozzle had plane sidewalls, was 300 mm long and 54 mm wide, and had two thrust surfaces which were symmetrically disposed about the nozzle center-line, each with a divergence angle of 11° . The nozzle was supported by a two sting system, and was otherwise freely suspended immediately downstream of a fixed combustion duct, which supplied flow to the nozzle. Provision was made for fitting the thrust surfaces with transducers. Thus, the measured net thrust could be compared with the thrust obtained from measured pressure distributions to assess the thrust loss due to skin friction. It was found that this thrust loss was 20% +/- 5% of the pressure thrust, and was consistent with approximate estimates using a skin friction coefficient of 3×10^{-3} . These estimates indicated that approximately half the skin friction drag was associated with the nozzle walls, and therefore the skin friction drag on the thrust surfaces was roughly 10% of the pressure thrust. However, the presence of combustion in the combustion duct did not measurably affect the skin friction drag, indicating that the combustion thrust increment, obtained by subtracting the fuel-off pressure thrust from the fuel-on pressure thrust, is not measurably affected by skin friction.

The stress wave balance method was extended to simultaneously measure three components of force (Mee et. Al 1996), and was used for experimental measurement of the lift, drag and pitching moment on a 15° semi-vertex angle cone 220 mm long, at angles of incidence which varied from 0° to 5° . Results were consistent with theoretical calculations, and led to use of the three-component stress wave balance for scramjet experiments.

5. Integrated scramjet force measurements

With the development of the stress wave balance for measuring axial force, it became possible to measure the thrust/drag performance of integrated scramjet configurations. The axisymmetric scramjet model shown in Fig. 5(a) was chosen for initial experimentation (Paull et al. 1995). The model is shown with half the cowl removed. It consisted of an axisymmetric center-body, with six combustion chambers and associated intakes arranged about its periphery. These intakes consisted of compression ramps formed by the splitters which separate the combustion chambers.

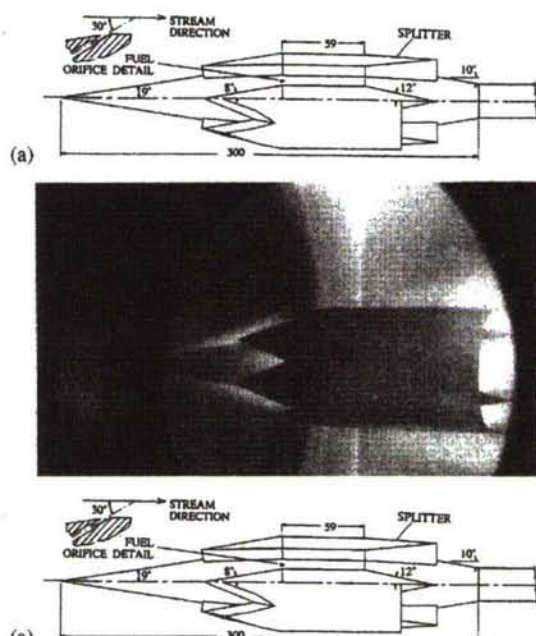


Figure 5 - Integrated scramjet model: (a) model details (dimensions in mm), (b) time integrated photograph of model (3MJ/kg)

5.1 Model design

Experiments with integrated scramjet configurations are more demanding of shock tunnel performance than the component experiments described so far. This is illustrated in the design of the scramjet model. In order to avoid the possibility of thermal choking at the lower end of the sub-orbital velocity range, a post combustion Mach number of approximately 2 was chosen which, with a constant area combustion duct and a heat release corresponding to stoichiometric combustion of hydrogen, implied a precombustion Mach number of approximately 4. This Mach number is a result of the inlet compression process. For a scramjet in atmospheric flight, where the static temperature is fixed, it would be necessary for the inlet compression process to yield precombustion temperatures and pressures which are high enough to assure ignition and burning of the fuel but, because the shock tunnel can supply an airflow at any reasonable freestream temperature, the temperature requirement can be relaxed. The function of the scramjet inlet compression process in a shock tunnel is therefore to raise the precombustion pressure to a suitable multiple of the freestream pressure. Choosing a value of 10 for this multiple, representing a reasonable thermal cycle efficiency, and an inlet compression process which took place through three oblique shocks, resulted in a freestream Mach number of 6 and an inlet contraction ratio of 4.8. Detailed intake considerations reduced the inlet contraction ratio to 4.4. The thrust nozzle expansion ratio is, through geometrical considerations, related to the inlet contraction ratio and, with the value of the inlet contraction ratio just quoted, the expansion ratio of the thrust nozzle was 5.8.

The value of the precombustion pressure must be sufficient for the combustion reaction and associated heat release to take place. For the hydrogen air reaction, Fig. 4 indicates that the value

of the product of precombustion pressure and combustion chamber length should be approximately 15 kPa m. The length of the combustion chamber, at 0.06m, was limited by the model size, which was itself limited by the shock tunnel test time, and this combustion chamber length led to a required precombustion pressure of 250 kPa. Unfortunately, the shock tunnel nozzle supply pressure was limited to 40 MPa for these experiments and, with a freestream Mach number of 6, the precombustion pressure was limited to 100kPa. Thus the limitation of the shock tunnel nozzle supply pressure led to a precombustion pressure which was insufficient to sustain complete hydrogen air combustion. Or, to put it another way, the demands made by this integrated scramjet experiment exceeded the shock tunnel performance levels.

However, by using hydrogen fuel mixed with silane (SiH_4) as an ignition promoter, it was possible to reduce the pressure required for combustion. The results of central injector constant area combustion duct experiments with hydrogen-silane fuel mixtures (Morris 1989) indicated that, at the expected minimum scramjet model precombustion temperature of 800 K, the required value of the product of precombustion pressure and combustion chamber length was approximately 3 kPa m with a fuel mixture which included between 20% and 5% of silane by molar concentration. Assuming that, as with hydrogen fuel, the mode of injection would not significantly affect the combustion lengths, it was concluded that a fuel consisting of 13% silane and 87% hydrogen would undergo complete combustion heat release within the combustion chamber length at a precombustion pressure of 100 k Pa.

Relatively large increases in pressure occur through the inlet compression process, and the boundary layers must be able to negotiate these pressure increases without separation. Therefore, the Reynolds numbers on the forecone of the model should be high enough to ensure transition to a turbulent boundary layer. A study of transition on a flat plate in the shock tunnel (He and Morgan 1994) had yielded a transition Reynolds number which varied from 2.5×10^6 to 1.0×10^6 as the stagnation enthalpy increased. The corresponding forecone Reynolds numbers were 2.7×10^6 to 1.2×10^6 over the same range of stagnation enthalpies and this, together with the disturbances to the boundary layer generated by the compression shocks, indicated that transition to a turbulent boundary layer would occur on the forecone. Figure 5(b) shows the scramjet model in operation in the shock tunnel. Flow luminosity on the forecone arises from flow compression by the conical shock formed on the forecone. The absence of the regions of high luminosity which would be associated with the strong shock waves resulting from choking is an indication that the inlet compression process is performing as designed. The high luminosity seen at the downstream end of the cowl is associated with the combustion region, and is thought to be due to silicon released during the combustion process.

5.2 Performance of the model

The performance of the scramjet model in shock tunnel tests is presented in Fig. 6 in terms of the net thrust Coefficient, C_{TN} . Two continuous lines are displayed, with associated experimental points, showing the comparison between experimental and theoretical values of the axial force, both with fuel injection and without fuel injection. The theoretical values were obtained by adding the calculated inviscid and viscous axial forces acting on the inlet, combustion chambers and the thrust nozzle. The consistency between the axial forces calculated in this manner and the measurements served as a check on the validity of the calculation. Fig. 6 also displays two broken lines. The lower one on the figure represents the fuel off drag, and is fitted by eye to the associated experimental points. This broken line was used to yield values of the drag coefficient, C_D , for the upper broken line, which was obtained from theoretical calculations of the forces on the engine. These calculations yield values of the net thrust coefficient which are generally consistent with the experimental results, with a tendency to somewhat underpredict the drag at stagnation enthalpies exceeding 4 MJ/kg. A positive thrust was obtained only at stagnation enthalpies below this level.

At stagnation enthalpies below 3.0 MJ/kg, unsteadiness in the thrust began to appear, and attempts to increase the thrust, either by further lowering the stagnation enthalpy or by increasing the fuel equivalence ratio led to choking of the scramjet inlet. This is unlikely to have been due to thermal choking of the combustion chambers, as eqn. 1 indicates that insufficient heat release is taking place, so the choking is attributed to boundary layer separation in the engine due to the combustion pressure rise.

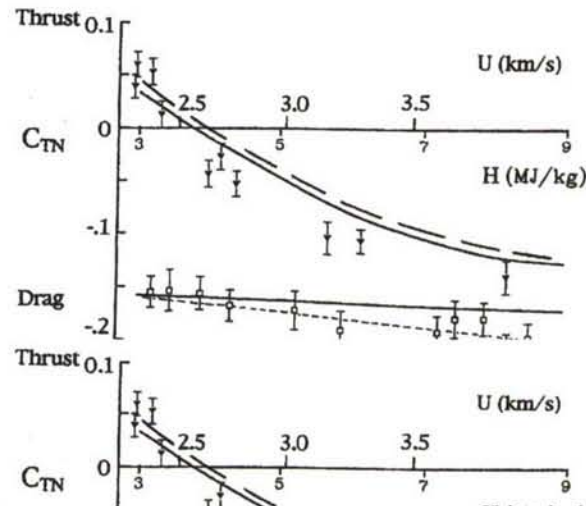


Figure 6 - Performance of the axisymmetric scramjet model in the shock tunnel (U = velocity, H = stagnation enthalpy)

5.3 Hydrogen fuelled scramjet models

The use of a silane-hydrogen mixture as fuel did indeed reduce the value of the pressure \times combustion chamber length parameter required for essentially complete combustion, but it also increased the mixture molecular weight with respect to hydrogen, and therefore had the disadvantage that it reduced the fuel specific impulse. In an attempt to show experimentally that this reduction could be avoided, a scramjet model was designed in which combustion of hydrogen fuel would be encouraged, without the need for an ignition promoter (Stalker & Paull 1998). Figure 7 shows detail of one half of the model, which was symmetrical about the plane AA' in the figure. This symmetry was necessary because, at the time the experiments were done, the force balance could only operate with axial loads. An inlet contraction ratio of 5.2 was used, with the aim of producing a local region of high temperature and pressure and, to minimize choking tendencies when combustion occurred, was followed by a divergent combustion chamber. Hydrogen fuel injection took place at the minimum cross-section. It was found that, although the model flow started and ran during the shock tunnel test time with no fuel injection, the flow choked when the fuel flow was initiated before the shock tunnel flow, but ran when the fuel flow was initiated after initiation of the shock tunnel flow. A possible explanation for the choking effect may be that the injected fuel interacted with the shock tunnel nozzle starting flow to establish a choked flow which was subsequently maintained by combustion. Using the delayed fuel injection technique, it was possible to establish a steady flow with hydrogen combustion.

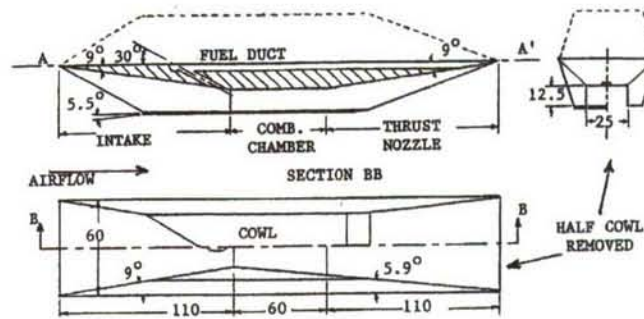


Figure 7 - Hydrogen fuelled scramjet cruise model (dimensions in mm)

In experiments at a stagnation enthalpy of 3.5 MJ/kg and a Mach number of 6.4, the thrust with combustion increased with equivalence ratio, and became equal to the drag as the equivalence ratio approached unity, thus achieving the cruise condition of net zero thrust or drag. By comparison with results of pressure measurements in a combustion duct thrust nozzle combination, it was conceded that combustion was taking place in the thrust nozzle (Stalker et. al. 2004, Stalker & Paull 1998) but as indicated by a measured fuel specific impulse of 835 seconds, a portion of the fuel did not burn. Thus, although the use of an ignition promoter had been avoided, the fuel specific impulse of hydrogen fuel had not been fully realized. It is worth noting that the fuel off drag coefficient was 0.183, which is similar to the drag coefficient of the axisymmetric scramjet model discussed above, and was again divided approximately equally between inviscid and viscous drag.

6. Inlet injection and radical farming

The integrated scramjet force measurements indicated that mixing and combustion of hydrogen could not be completed at the precombustion pressures and combustion duct lengths of the experiments in section 5. Not only did this limitation lead to development of the shock tunnel to increase operating pressure levels, but it also encouraged experiments on two concepts; one designed to reduce combustion duct lengths for complete combustion, and the other to explore a mode of combustion different from the diffusion flame modes considered so far.

The first of these concepts involved injection of fuel on the inlet. Inlet injection has clear advantages in allowing mixing of hydrogen with air at the relatively low temperatures of the inlet before the mixture enters the combustion duct and ignites, thereby ensuring that the combustion process in the combustion duct is not delayed by the necessity for mixing. However, it was important to ensure that ignition did not occur prematurely, and thereby cause drag on the inlet due to the resulting combustion pressure increase. Experiments involving surface pressure measurements and shadowgraph flow visualization were done with injection through surface orifices in the inlet. The scramjet walls were at room temperature and the stagnation enthalpy was 3.0 MJ/kg (Gardener 2001). No evidence of inlet combustion was detected, but combustion was observed in the combustion duct. Experiments were also done with hydrogen injected through orifices in an inlet surface which was heated to 500 K (Kovachevich et. al. 2004), and no evidence of inlet combustion was detected either by surface pressure measurements or by interferometric imaging.

The second concept combined inlet injection with a technique to promote early ignition of the fuel-air mixture called "radical farming" (Odam 2004). This technique is illustrated in Fig. 8(a), which represents a two-dimensional scramjet configuration. The shocks or compression waves which make up the inlet compression process are arranged to form a local region of elevated pressure and temperature, near the entrance to the combustion duct, where the production of the chemical radicals, which are a first stage in the overall combustion process, will be encouraged. This region is called the radical farm, and is isolated from the walls of the combustion duct by a lower pressure, cooler flow. The radical farm is terminated by the expansion waves from the

corner at the combustion duct entrance, but the radicals remain “frozen” in the flow until they meet another region of elevated temperature and pressure, where combustion continues. The benefit of radical farming is that, because of the exponential dependence on temperature of the rate of radical formation, the regions of elevated temperature and pressure in the radical farms provide accelerated development of the ignition process.

Experiments were done with the two-dimensional configuration of Fig. 8(a). The model was 75 mm wide, and was fitted with sideplates to ensure two-dimensional flow. Pressure measurements were taken in the model midplane, along the inlet, combustion duct and thrust nozzle, together with measurements along three transverse lines to check that the flow was two-dimensional. Typical pressure distributions are displayed in Fig. 8(b), and show that vigorous combustion occurred within the length of the combustion duct. Using the inlet flow conditions, a mean precombustion temperature of 700 K is obtained for the case of Fig. 8(b), a temperature which has been found to be too low for combustion in other experiments with constant area combustion ducts. Thus radical farming offers considerable improvement in the ignition characteristics of a hydrogen-fuelled scramjet.

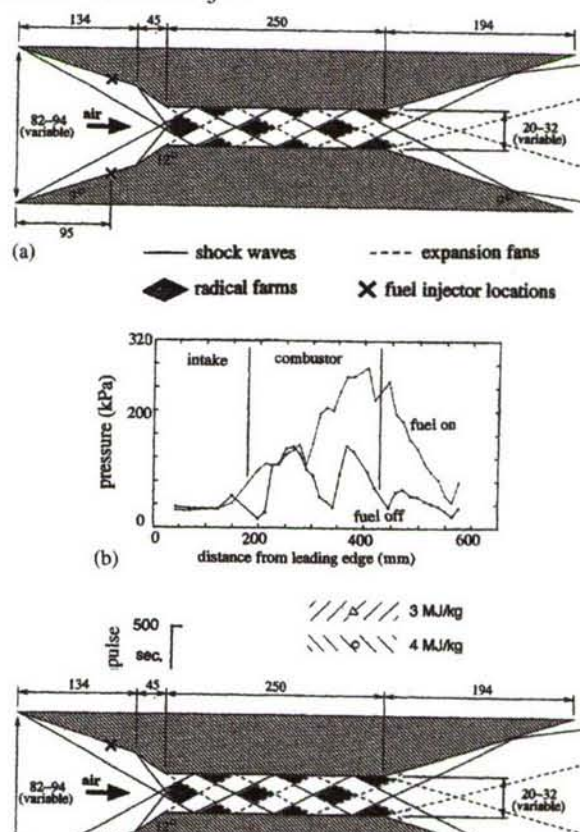


Figure 8 - Experiments on radical farming (dimensions in mm)

Integration of the measured pressure distributions was used to obtain a two-dimensional inlet drag and nozzle thrust, and this was combined with skin friction calculations for all interior surfaces (including the interior of the side plates) to obtain an interior flowpath net thrust. Using measured values of the injected fuel mass flow, this net thrust could be converted to a net specific impulse, which is presented in Fig. 8(c). The inlet contraction ratio was varied by adjusting the spacing between the upper and lower halves of the scramjet model, as shown in Fig. 8(a), and at each contraction ratio, the equivalence ratio was increased until choking occurred. At a stagnation enthalpy of 3 MJ/kg, the equivalence ratio for choking fell from 0.65 to 0.35 as the contraction ratio was increased from 2.9 to 4.1 and at 4 MJ/kg, it fell from 0.85 to 0.40. Estimates indicated that, as the contraction ratio changed, the radical farms persisted without major changes in their

dimensions, suggesting that combustion processes in the model were essentially independent of the contraction ratio. This is in contrast to the more conventional scramjet, where the inlet contraction ratio determines the precombustion temperature, which strongly influences the combustion process. Fig. 8(c) confirms this independence by presenting points which were obtained by taking the mean of 2-4 measurements of the net specific impulse near the choking limit at each value of the contraction ratio. As represented by the cross-hatched zones, the net specific impulse values tended to remain constant as the contraction ratio was varied at both the stagnation enthalpies tested, indicating that combustion heat release was not significantly affected by the changes in contraction ratio. It may also be observed that the net specific impulse values, though small, are all positive, indicating that positive net thrust was obtained for the internal flowpath of this scramjet model.

7. Skin friction reduction by boundary layer combustion

The importance of skin friction drag in reducing the net thrust with an integrated scramjet configuration focussed attention on a means of reducing skin friction in turbulent boundary layers. Noting that the Reynolds stresses in a turbulent boundary layer play the role of viscosity, and that they are density dependent, it was thought that they could be reduced by raising the temperature, thus reducing the effective viscosity. In addition, the reduction in density would increase the width of the boundary layer streamtubes, and these two effects of increasing the boundary layer temperatures would both tend to reduce the skin friction.

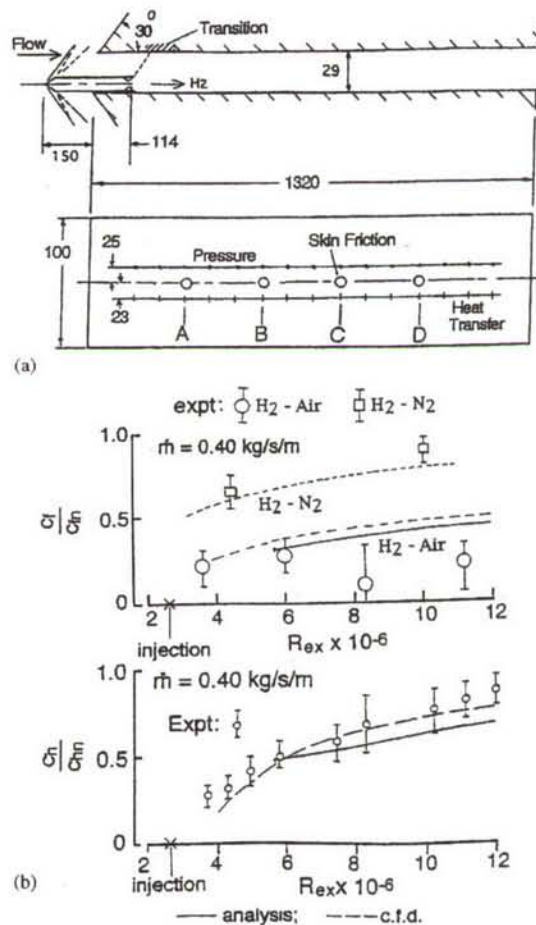


Figure 9 - Turbulent skin friction reduction by boundary layer combustion; (a) Experimental duct details (dimensions in mm); (b) skin friction and heat transfer measurements (C_f, C_{fm} = skin friction coefficient with and without hydrogen injection, C_h, C_{hn} = Stanton number with and without hydrogen injection, \dot{m} = hydrogen mass flow)

This concept was tested by doing experiments with the rectangular duct configuration shown in Fig. 9(a) (Goyne et. al. 2000) at a stagnation enthalpy of 7.8 MJ/kg and a pre-injection pressure, temperature and Mach number of 50 kPa, 1500K and 4.5, respectively. Hydrogen was injected from a room temperature reservoir, at a Mach number of 1.8, through a slot at the wall which spanned the 100 mm dimension of the duct cross-section. Thus, the flow over the surface downstream of the slot was nominally two-dimensional. As shown in the figure, this surface was instrumented to measure pressure and heat transfer, while four skin friction gauges were used to measure skin friction at the indicated station. The height of the duct was such that combustion could be confirmed by an increase in the pressure rise along the duct length. Results from the experiments are presented in Fig. 9(b) for an injected hydrogen mass flow of 0.40 kg/s per metre width of the slot. Large reductions in skin friction are apparent for hydrogen injection and combustion, with the skin friction coefficient then only one quarter of the skin friction coefficient with no injection. To confirm that this effect was due to combustion, experiments were done with nitrogen test gas under the same test conditions. Although the figure shows a reduction in skin friction, due to the reduction in boundary layer densities caused by hydrogen mixing, the reductions in skin friction are much less than when combustion of the injected hydrogen took place. Figure 9(b) also displays heat transfer measurements showing that near fuel injection, the Stanton number with fuel injection is much less than the Stanton number without fuel injection and rises towards no injection values well downstream. This reduction in heat transfer takes place in spite of the combustion heating of the boundary layer. It occurs because, by virtue of Reynold's analogy, the reduced skin friction coefficient implies a reduced Stanton number, and this effect is only partially offset by the additional combustion related heat transfer close to injection. Further downstream, more of the injected hydrogen is burned and combustion heat release has a greater relative influence on heat transfer.

The experimental results in Fig. 9(b) were compared with predictions of a numerical simulation (Goyne et. al. 2000, Brescianini 1993) and a theoretical analysis (Stalker 2005). The numerical simulation employed finite rate chemistry, a κ - ϵ turbulence model, a parabolic Navier-Stokes code, and assumed a uniform pressure over the surface on which the boundary layer was formed. It was generally consistent with the experimental results in predicting a reduction in skin friction in the absence of hydrogen combustion, and a large reduction in the skin friction with combustion. The low values of measured skin friction coefficient at the two downstream stations are thought to be an effect of the pressure gradients along the wall acting on the reduced wall friction. The combustion induced heat transfer reduction was also predicted satisfactorily.

The theoretical analysis (Stalker 2005) used a model of the turbulent boundary layer formulated by Van Driest, which represents the effect of temperature induced density changes in the boundary layer on the skin friction on a flat plate. The Van Driest model was extended by incorporating the changes in temperature and density resulting from the injection of hydrogen along the surface from an upstream slot. Combustion of the hydrogen with oxygen was assumed to take place instantaneously when the two came into contact, regardless of the temperature. This allowed the distribution across the boundary layer of the species mass fractions and the stagnation enthalpy to be determined by using the Shvab-Zeldovich scheme for coupling of these variables. The density could then be obtained as a quadratic relation in the boundary layer velocity, as in the analysis of Van Driest, but with coefficients which were different to those of Van Driest. This expression was used to yield the momentum thickness, which was differentiated with respect to the downstream distance to obtain the skin friction. As shown in Fig. 9(b), this analysis yields results which are in approximate agreement with results from the numerical simulation and the experiments.

The analysis has been employed to determine the effect on skin friction and heat transfer on a flat plate for flight velocities up to 6 km/s. It yielded values of skin friction drag which were less than half of the fuel-off skin friction drag, together with a net reduction in heat transfer when the

combustion heat release in air was less than the stagnation enthalpy. The mass efficiency of hydrogen injection, as measured by effective specific impulse values was approximately 2000 seconds. Clearly, if boundary layer combustion of hydrogen can be realized over a sufficiently wide range of freestream conditions, it can be an important factor in increasing penetration of integrated scramjet configurations into the sub-orbital regime.

8. The HyShot 2 flight experiment

The ultimate test of shock tunnel predictive capability is a direct comparison of shock tunnel data with data obtained in flight with the same experimental configuration and the same flow conditions. Although examples existed where flight data for external aerodynamics was compared with shock tunnel data (Krek & Stalker 1992), flight data involving supersonic combustion did not exist in the late 1990's, thus eliminating the possibility of a comparison with shock tunnel data. However, this situation changed when two sounding rocket flights became available to The University of Queensland for supersonic combustion experiments.

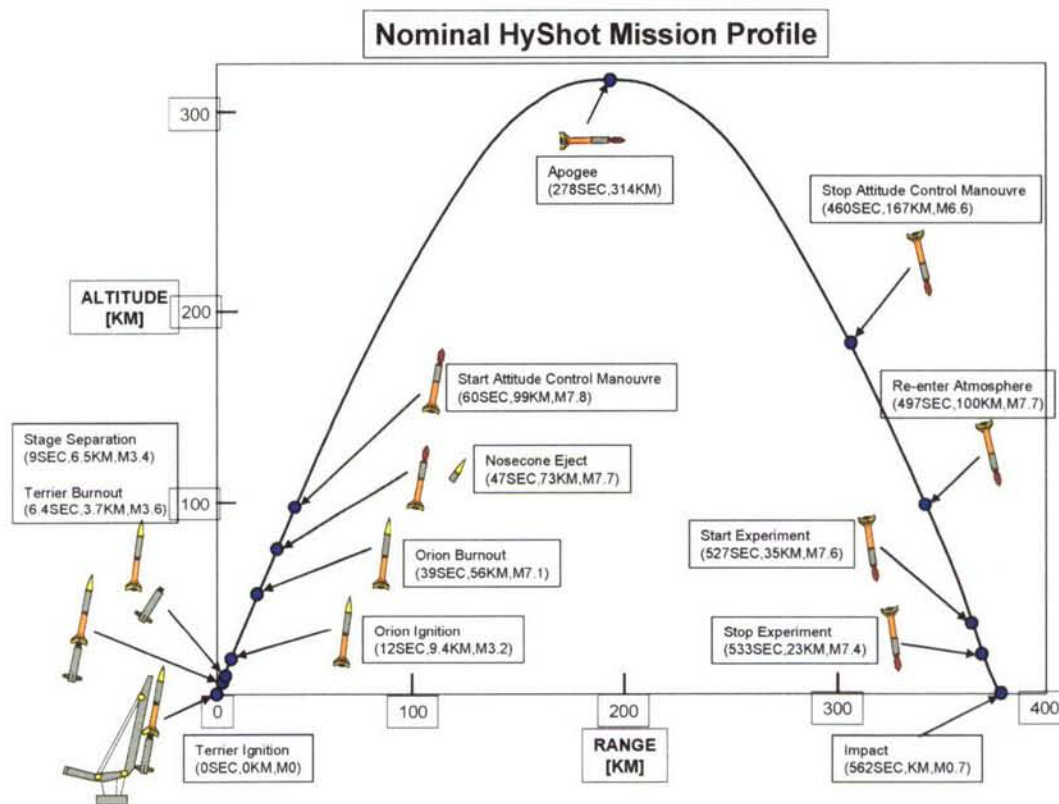


Figure 10. HyShot flight profile

The sounding rockets were two-stage Terrier-Orion combinations, and were supplied by Astrotech Space Operations Inc. of the USA. As shown in Fig. 10, the flight began with ignition, followed by burnout and separation of the Terrier first stage, and subsequent ignition and burnout of the Orion second stage. The burnt out Orion remained attached to the experimental payload, in order to provide aerodynamic stability on re-entry to the atmosphere. The resulting flight vehicle then followed a parabolic trajectory, ascending to an altitude of 314 km before descending towards the atmosphere. While executing this manoeuvre, a control jet was activated in a "bang-bang" mode to realign the flight vehicle so that it re-entered the atmosphere with the experimental model pointing downwards. Re-entry was accomplished with a steep trajectory, allowing the experiment

to take place over a planned period of 7 seconds as the vehicle passed from 35 km to 23 km in altitude (Paull et. al. 2002, Smart et. al. 2006).

A photograph of the experimental model is shown in Fig. 11, with a schematic of the fuelled flowpath in Fig. 12. The aim of the experiment was to establish a correlation between the conditions for supersonic combustion of hydrogen fuel in the shock tunnel and in flight, and the experiment was therefore designed to be as simple as possible. A two-dimensional flow configuration was chosen, consisting of two identical flow paths, symmetrically disposed about the center-line, both of which were instrumented for pressure measurement. By arranging that fuel was injected into only one of the two combustion ducts, it was possible to compare fuel-on with fuel-off pressure distributions, and thus to make a flight to shock tunnel comparison of the effect of the hydrogen fuel mixing and combustion processes.



Figure 11. HyShot 2 payload

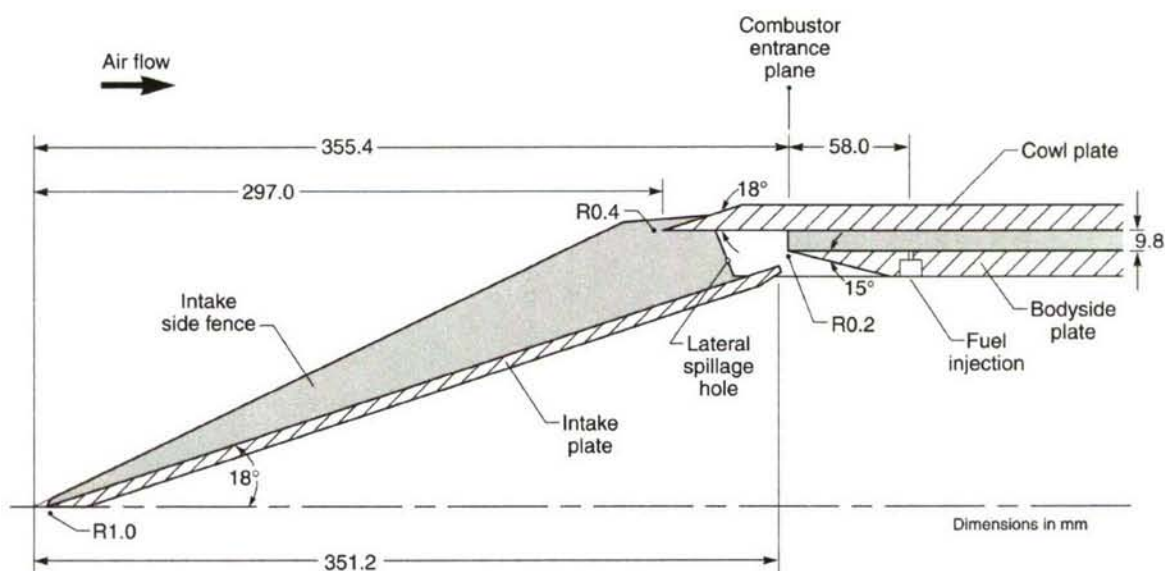


Figure 12. Schematic of fueled flowpath in the HyShot 2 payload

The inlet consisted of a single 18 deg. wedge with a width of 100mm, a blunted leading edge, and highly swept side fences. The high wedge angle was necessary to ensure that the combustor entrance temperature and pressure were great enough to readily induce self-ignition of hydrogen. The rectangular combustor had a constant area 9.8 mm x 75 mm cross-section and a length of 300 mm (length/height = 30.61). The combustor cowl spanned the full width of the intake wedge and was situated such that the intake shock was upstream of its leading edge at all times. The flowpath design incorporated a shock trap that was situated between the end of the inlet wedge and the entrance of the combustor. This feature not only captured the cowl shock, but also bled off the intake boundary layer. The reduced width of the combustor (relative to the inlet wedge) and lateral spillage holes in the side fences adjacent to the shock trap, were designed to remove the fence boundary layers and corner flows. The angle-of-attack of the payload was defined as positive when the fuelled combustor was on the windward side, and negative when the fuelled combustor was leeward.

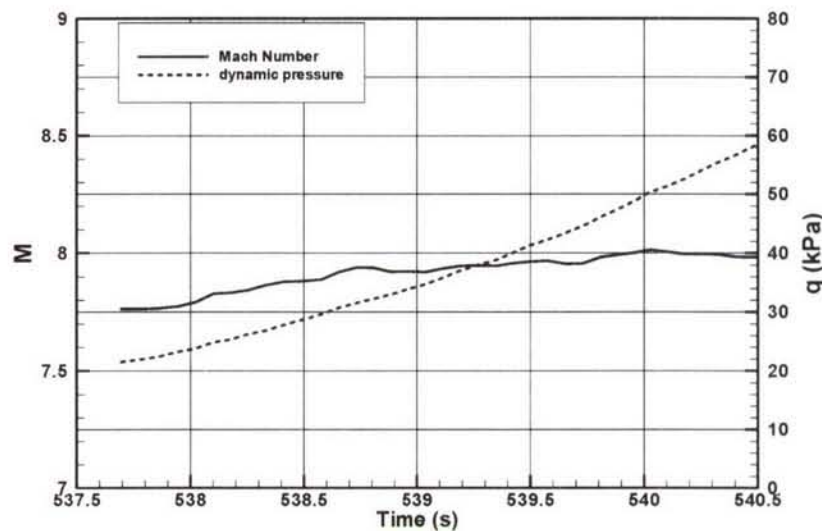


Figure 13. Reconstructed Mach number (M) and dynamic pressure (q) histories

number	Time (s)	Flight Mach Number	Flight dynamic pressure (kPa)	Altitude (km)	angle-of- attack(deg.)
1	538.103	7.828	24.88	34.48	-5.012
2	538.179	7.831	25.33	34.31	5.540
3	538.734	7.938	31.55	33.05	-5.081
4	538.805	7.938	32.20	32.89	4.617

Table 1 – Flight parameters for analyzed time slices

The flight produced a significant set of scramjet combustor data at varying duct entrance pressure, temperature and Mach number. Trajectory reconstruction was accomplished using onboard sensors alone (Cain et. al. 2004). Fuel flow was initiated at approximately $t = 536.5$ seconds after launch as the payload and attached Orion motor re-entered the atmosphere. Figure 13 shows the Mach number and dynamic pressure time histories during three seconds of the

experimental window and Table 1 lists four zero-yaw time slices used for analysis. Figure 14 shows a comparison of the fuelled and unfuelled combustion pressure distributions at windward conditions: i.e. when each combustion duct was at a positive angle-of-attack of approximately 5 degrees. Note that all data is normalized by the combustor entrance pressure, in order to make meaningful comparisons. The equivalence ratio of the fuelled duct was approximately 0.34, and the pressure rise from combustion of the hydrogen fuel is clearly evident. Cycle analysis of this data indicated that supersonic combustion occurred at these times slices during the flight, at a combustion efficiency for the fuel of 81%.

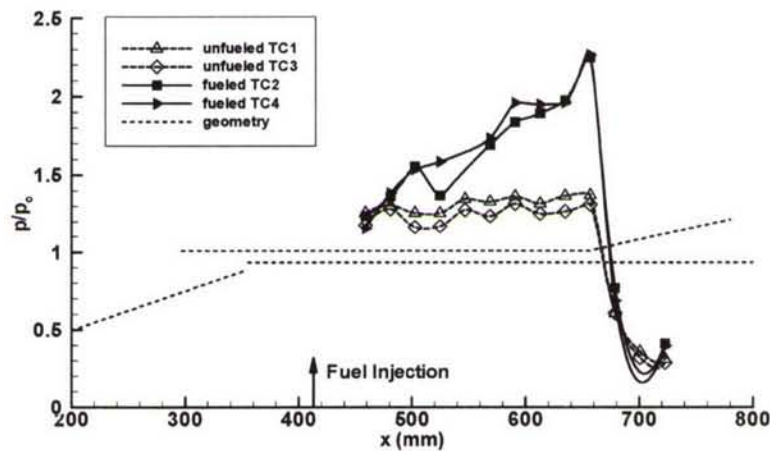


Figure 14. Windward fueled and un-fueled combustor pressure distributions (p = duct pressure, p_c = combustor entrance pressure, x = axial distance from nose of payload)

One of the important motivations for the HyShot flights was validation of short duration ground testing for scramjet development. As a first step towards this, a series of pre-flight experiments were conducted at The University of Queensland in the T4 shock tunnel to determine the expected performance of the flight payload. These experiments were documented in Paull et. al. (2000), and four of these shock tunnel runs are compared here with the presented flight time slices.

The model used for the pre-flight ground tests was designed to generate similar combustor entrance conditions to flight at Mach 7.6, while using an existing Mach 6.5 shock tunnel nozzle. This dictated the use of an experimental model with a 17° wedge intake (compared to 18° in the flight payload) and shock tunnel nozzle exit conditions with higher freestream pressure and temperature than flight. The 300 mm length combustor and fuel injectors were identical to flight, except that fuel injection took place 40 mm downstream of the combustor entrance (compared to 58 mm in flight), and the ground test model had an increased number of combustor pressure taps. A final difference between the ground and flight hardware was that the nozzle expansion was situated on the bodyside of the combustor in the ground test model (compared to the cowlside for the flight hardware).

Figure 15 shows a comparison between ground and flight data for the fuelled combustor at windward conditions. Both ground and flight data showed a clear pressure rise due to supersonic combustion of hydrogen, and Fig. 15 confirms that both ground and flight had similar pressure distributions along the combustor. It is interesting to note, however, that despite the fact that the ground data had a higher equivalence ratio than flight (0.47 compared to 0.34), both ground and flight generated very similar normalized pressure levels up to the last pressure tap in the ground

model. Additional ground experiments are planned with a model and test conditions identical to the flight experiment.

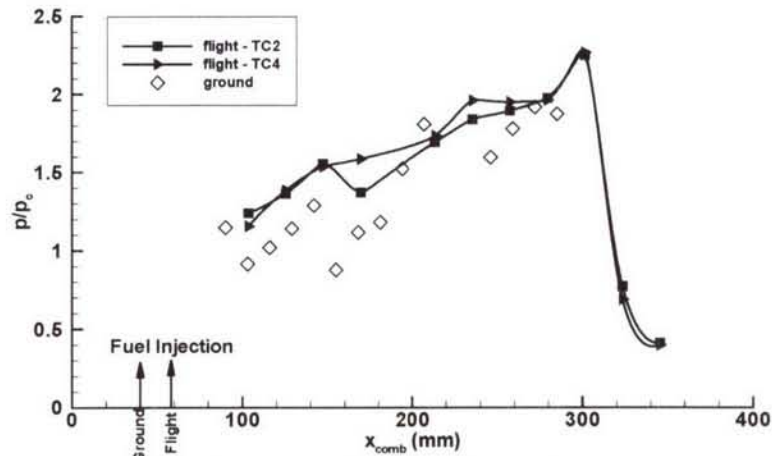


Figure 15 - Flight-to-ground comparison at windward conditions

9. Super-orbital studies

Since shock tunnels were first used for the study of high speed flow phenomena, attempts to enhance performance have concentrated on driver design. Many driver techniques have been tried with varying degrees of success. In recent years the free piston driver technique, has been the preferred option for most high enthalpy facilities. However, both reflected and non-reflected shock tunnels are limited, independently of driver considerations, in the total enthalpy which they can simulate because all the energy is added across a shock. This causes a radiation limit for reflected shock tunnels, and a highly dissociated plasma for non reflected tunnels at very high shock speeds. For practical purposes of aerodynamic testing, such facilities are limited to earth orbital velocities and below.

Many practical flight applications occur at superorbital speeds, such as the return of the Apollo capsules from the moon, the entry of space probes into the atmospheres of the gas giants, and the reentry of sample return missions to Earth from space. The heat shields for these missions have been designed with access to scarce experimental data, which has led to the use of conservative design techniques, and safety factors much larger than normal in the weight watching aerospace world (Gnoffo 1999). The expansion tube concept first proposed by Ressler and Bloxham (1952) offers the potential to increase both the total enthalpy and total pressure of shock tunnel flows, and also to reduce the levels of free stream dissociation and ionisation.

A schematic of an expansion tube is shown in Fig. 16. Only part of the energy is added to the flow through a shock wave, and acceleration to hypervelocity conditions is achieved by means of an unsteady expansion fan. In this way energy and total pressure is added to the flow, at the expense of test time, without the flow dissociation which would occur if all the energy were to be added across a single shock wave. The largest expansion tube in operation at The University of Queensland, X3, is 65 m long, has a bore of 182.6mm and a total mass of 44 tonnes. It was originally commissioned as a two piston facility with a 500mm diameter launch tube delivering the secondary piston of mass 360 kg to the driver. It is currently being rebuilt with a single piston of 500 mm diameter. The driven section may be configured up to 40 m in total length, with provision for secondary and tertiary diaphragms along the tube with 1 m axial resolution. Adjustable diaphragm location is necessary to get optimized lengths for different operating conditions due to changes in the wave processes which determine the development of useable flow. A Mach 10

steady flow nozzle is being fabricated for X3 to give high total pressure conditions for scramjet testing.

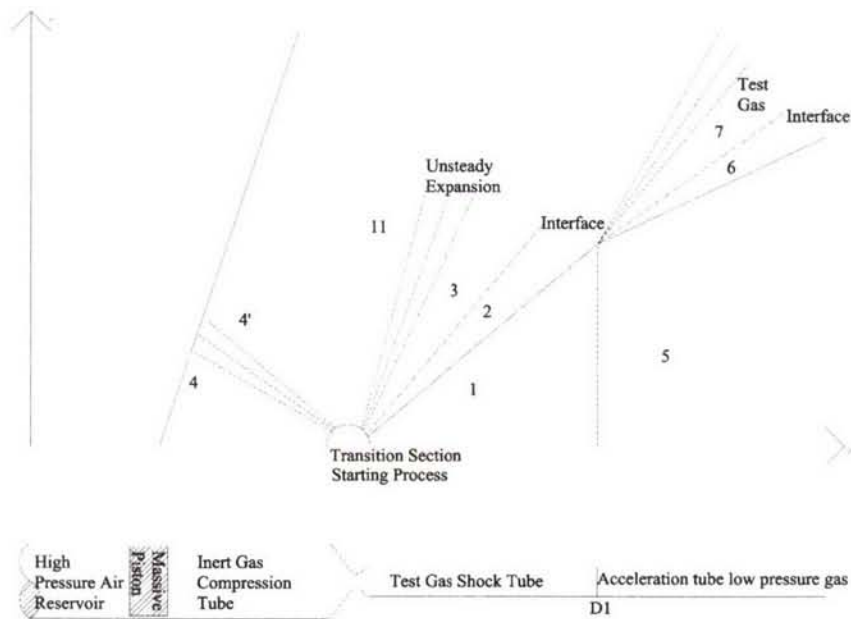


Figure 4.3.1: Schematic of a Generic Expansion Tube with x-t Diagram

Figure 16 - Schematic of the expansion tube an x-t diagram

In Fig. 17, the simulation capability of The University of Queensland expansion tubes (X1, X2 and X3) is shown in terms of density x length (ρL) and total pressure (P_0), together with the requirements for several important classes of mission, including a large moon return vehicle, the FIRE capsule (representative of small unmanned capsules), a Titan aerocapture ballute, and the Muses C sample return project. The University of Queensland expansion tube facility envelope is not complete, but includes selected points across the spectrum, showing how it meets the requirements of a large range of applications.

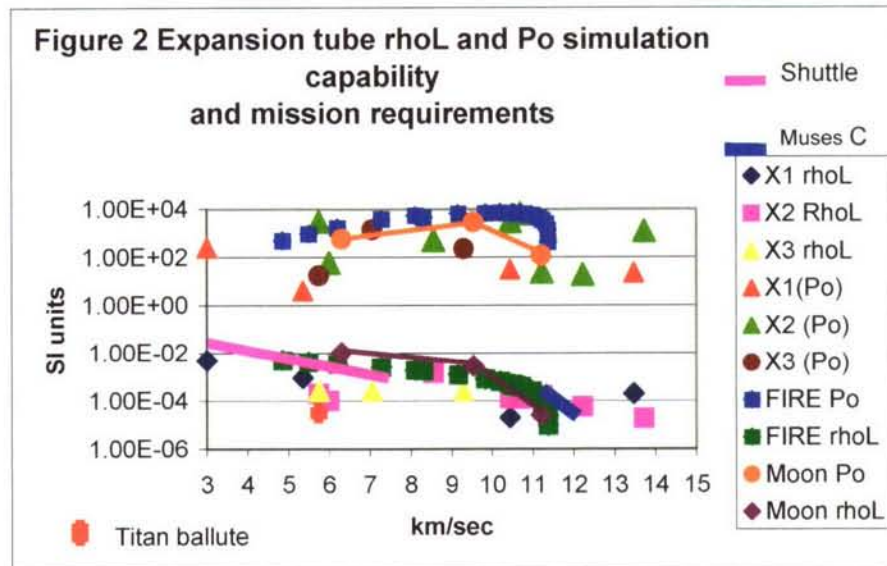
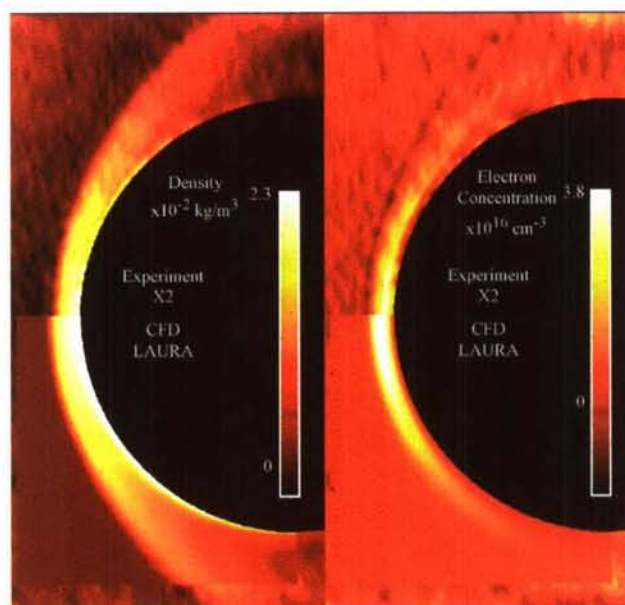


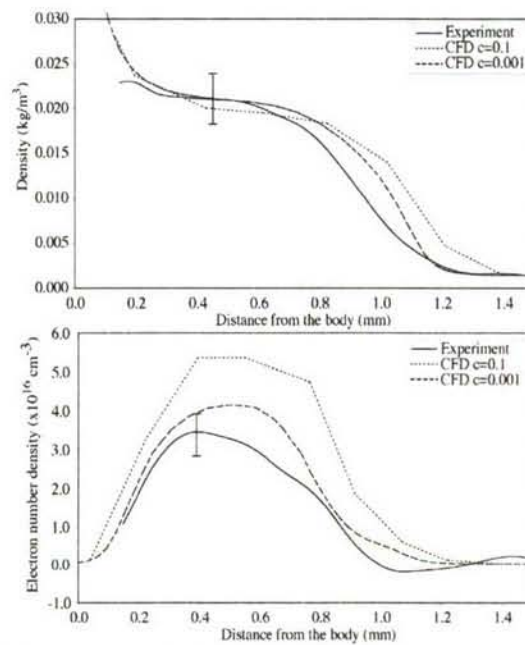
Figure 17 - Expansion tube rhoL and Po simulation

The possibility of simulating the aerodynamics of entry into the Jovian atmosphere is exciting, because of the very large velocities involved, which are ~ 50 km/sec. Whilst shock speeds of such levels can be created in the laboratory, the shock-heated gas is in the form of an unsteady plasma, with no useable test time suitable for aerodynamic purposes (Sharma & Park 1990). However, Stalker & Edwards (1998) noted that by substituting the helium content of the hydrogen-helium mixture of Jupiter for neon, a similarity between shock tunnel flows and flight could be obtained at speeds of the order of 10 km/sec. Inger (2003) used this principle in the X2 expansion tube to investigate the effects of ionisation on blunt body shock standoff.

At very high speed flows, ionisation becomes a significant factor in determining the gas state in blunt body flows, and the ability to create such flows in the laboratory and quantify the ionisation level is extremely useful. McIntyre et. al. (1997,2003), have developed interferometry techniques to do this, and some of the results are shown in Fig. 18(a). Figure 18(b) shows a comparison of the data with an analysis from the NASA LAURA code (Gnoffo 1999). The detailed agreement with the computations is evident, illustrating the utility of such experiments.



(a) Holographic measurements of density and ionisation levels



(b) Comparison of CFD analysis and measurements
Figure 18 – Blunt body flows with ionization

Flow behind steps can be very important in sustained hypersonic flight, and the associated separated flow regions can give high heat transfer values on reattachment. Such effects can occur at control surfaces and attachment points of structural members. In figure 19, separated flow behind a step was reproduced by Hayne (2003, 2004) for a flow of air with an equivalent flight speed of 7750 m/s. Interferometry and thin film heat transfer measurements were used to quantify the extent of the separated flow region. Time resolved traces of the separation region were used to confirm that steady flow was established, and the steady heating levels are displayed in the figure. Also shown are the results of CFD, which show good agreement over the range for which they were computed. The results of these tests give confidence that the facility can now be used for the study of a wider range of more challenging separated flows, including leeward flows on re-entry capsules, and simulated gaps in the space shuttle tile insulation.

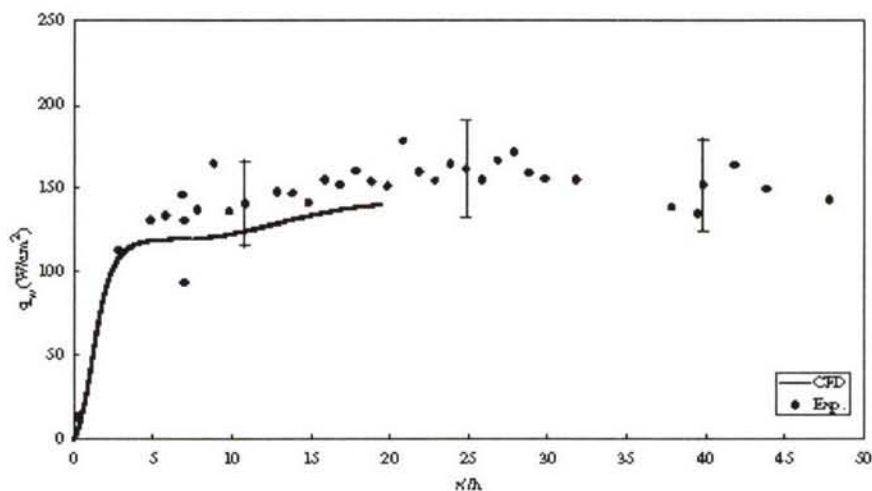


Figure 19 - Separated flow behind flat plate, velocity = 7750 m/s (q_w = heat transfer to wall, x = distance from step, h = step height)

The use of expansion tubes for simulating flows at very high speeds has been demonstrated. There is plenty of scope for using these facilities as new generations of spacecraft are developed, such as moon return vehicles, aerocapture heat shields and ballutes, and waverider designs. Instrumentation is available to record specific data from tests to give useful information about surface heating and skin friction levels, three components of force, density and ionisation levels and some radiation measurements.

10. Future plans

Hypersonics research in Australia is alive and well. The success of the HyShot flights has led to a significant interest in low cost scramjet flight-testing using sounding rocket boosters. In November 2006, an agreement was signed between the Defence Science and Technology Organisation (DSTO) of Australia and the United States Air Force, to support a 10-flight test program called HIFiRE. The goal of this program is to develop the technology required for long duration scramjet flight at Mach 8. The University of Queensland is responsible for the payloads to be flown on three of the ten flights; designated HyShot 5, 6 and 7. The plan for these flights is as follows:

HyShot 5 - A free-flying hypersonic glider

HyShot 5 will be a hypersonic glider designed to fly at Mach 8. It will separate from its rocket booster in space and perform controlled manoeuvres as it enters the atmosphere. This flight will not have a scramjet attached. Both an up-and-down trajectory similar to HyShot 2, and a more horizontal "depressed" trajectory are being considered for the flight. The goal of the flight is to learn about the control of hypersonic vehicles in the upper atmosphere.

HyShot 6 - A free-flying Mach 8 scramjet

HyShot 6 will use an up-and-down trajectory similar to HyShot 2, but the scramjet engine will separate from the rocket and enter the atmosphere on its own at about Mach 8. It will be a payload of around 250 kg, over twice the size of the HyShot 2 payload. The goal of the flight is to measure actual thrust levels of the scramjet over five seconds of scramjet engine operation. A three-dimensional scramjet flowpath developed at The University of Queensland will be flown.

HyShot 7 - Sustained Mach 8 Scramjet Powered Flight

HyShot 7 is the culmination of the other two flights. It will be a scramjet-powered vehicle and its design will make use of the information learned from HyShot 5 and 6. A depressed trajectory will be used for this flight and the goal is to fly the scramjet-powered vehicle horizontally for up to a minute at Mach 8. The engine structure will reach a thermally steady-state condition in this period, so this flight is a proof-of-concept for long duration scramjet flight.

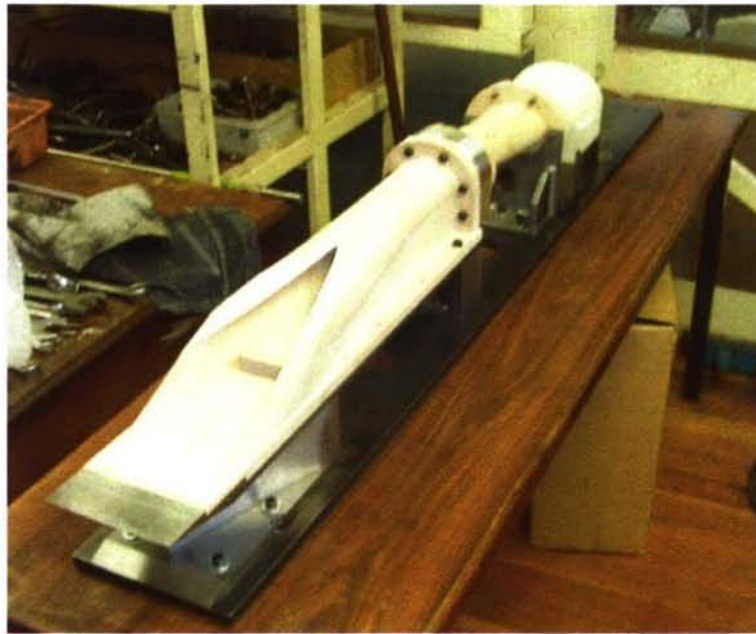


Figure 20 - REST engine model for T4

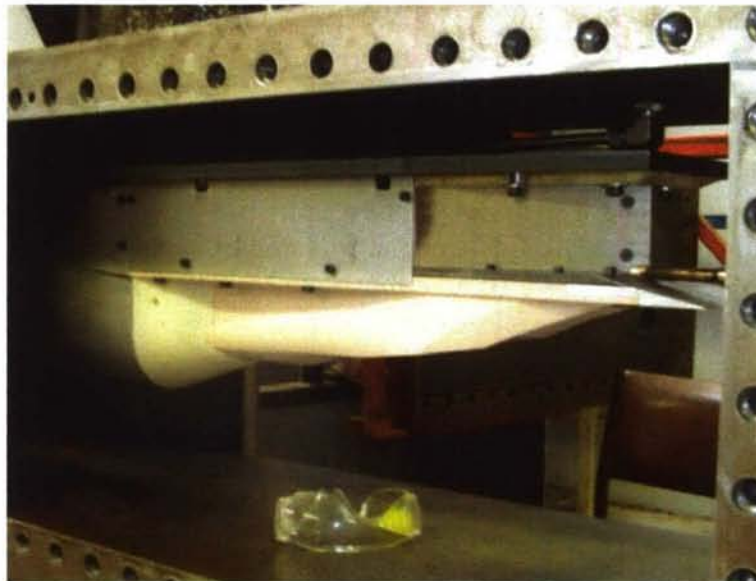


Figure 21 - REST engine mounted in the T4 test section

Preliminary testing of a candidate 3-D scramjet flowpath for HyShot VI has begun in T4. The engine includes a Rectangular-to-Elliptical Shape Transition (REST) inlet (Smart 1999,2001) and a divergent combustor with elliptical cross-section. Figures 20 and 21 show 2 photographs of the shock tunnel model used in the experiments, which was fabricated from high strength plastic. The short duration of the test-time in T4 allows the use of such fabrication techniques, which cannot be used for longer duration testing or flight. Figure 22 shows some preliminary test data for the engine. The test flow conditions were equivalent to Mach 8 flight at 30 km altitude, which corresponds to a dynamic pressure of 0.5 atmospheres, and the fuel was gaseous hydrogen. The bodyside pressure distributions in Fig. 22 indicate a clear pressure rise due to combustion in the combustor and nozzle.

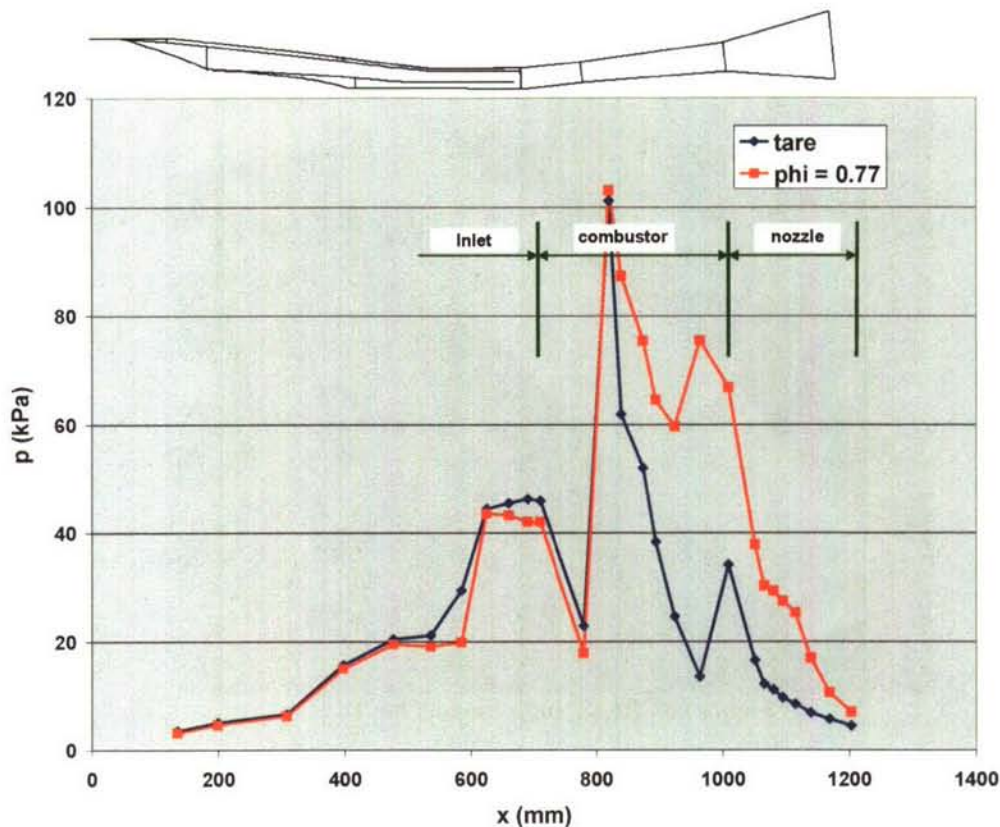


Figure 22 - Preliminary REST engine data at Mach 8 (p = duct pressure, x = distance from leading edge of the model, ϕ = equivalence ratio)

Together with the flight experiments, the Centre for Hypersonics at The University of Queensland will continue to conduct fundamental research on scramjet flowpaths, with particular emphasis on Flight Mach numbers of 10 and above, and super-orbital flows that are affected by radiation.

References

- Brescianini, C., 1993, "An investigation of the wall injected scramjet", PhD thesis, The University of Queensland.
- Buttsworth, D.R., 1994, "Shock induced mixing and combustion in a scramjet", PhD thesis, The University of Queensland.
- Cain, T., Owens, R. and Walton, C., 2004, "Reconstruction of the HyShot 2 Flight from Onboard Sensors" Fifth Symposium on Aerothermodynamics for Space Vehicles, Cologne, Germany.
- Casey, R.T., Stalker, R.J. and Brescianini, C., 1992, "Hydrogen combustion in a hypersonic airstream", *Aeronautical Journal*, 96(955), p200-202.
- Gardner, A.D., 2001, "Upstream porthole injection in a 2-D scramjet model", M.Sc thesis, The University of Queensland.
- Gnoffo, P.A., Weilmuenster K.J., Hamilton, II, H.H., Olynick, D.R., Ventatapathy, E., 1999, "Computational aerothermodynamic design issues for hypersonic vehicles", *AIAA J. Spacecraft and Rockets*, Jan-Feb, vol.36, No 1, pp21-43.
- Goyne, C.P., Stalker, R.J., and Paull, A., 2000, "Hypervelocity skin friction reduction by boundary layer combustion of hydrogen", *Journal of Spacecraft and Rockets*, 37(6), 740-746.
- Hall, N.A., 1951, "Thermodynamics of fluid flow", Prentice Hall, New York, p169-171.
- Hayne, M.J., Mee, D.J., Morgan, R.G., Gai, S.L. and McIntyre, T.J. 2003, "Heat transfer and flow behind a step in high enthalpy superorbital flow", *The Aeronautical Journal*, vol. 109(1073), pp. 435-442.
- Hayne, M.J., 2004, "Hypervelocity Flow Over Rearward-Facing Steps", PhD Thesis, The University of Queensland.

He, Y. and Morgan, R.J., 1994, "Transition of compressible high enthalpy boundary layer flow over a flat plate", *Aeronautical Journal*, 98(972), p25-34.

Huber, P.W., Schexnayder, C.J. and McClinton, C.R., 1979, "Criteria for self-ignition of supersonic hydrogen-air mixtures", NASA TP 1457.

Inger, GR; Higgins, C; Morgan, R., 2003, "Generalized Nonequilibrium Binary Scaling for Shock Standoff on Hypersonic Blunt Bodies", *Journal of Thermophysics and Heat Transfer*. V17, No 1

Kovachevich, A., Paull, A. and McIntyre, T., 2004, "Investigation of an intake injected hot wall scramjet", AIAA paper 2004-1037.

Krek, R.M., and Stalker, R.J., 1992, "Experiments on space shuttle orbiter models in a free piston shock tunnel", *Aeronautical Journal*, 96(957), p249-259.

McIntyre, T.J., Houwing, A.F.P., Palma, R.C., Rabbath, P.A.B. and Fox, J.S., 1997, "Optical and pressure measurements in shock tunnel testing of a model scramjet combustor", *Journal of Propulsion and Power*, 13(3), p388-394.

Mcintyre T.J., Wegener, M.J., Bishop, A.I., Rubinsztein-Dunlop, H., 1997, "Simultaneous two-wavelength holographic interferometry in a superorbital expansion tube facility", *Applied Optics* 36, pp.8128-8134.

McIntyre TJ, Bishop AI, Rubinsztein-Dunlop H, Gnoffo P.A., 2003, "Experimental and numerical studies of ionizing flow in a super-orbital expansion tube", *AIAA Journal* Vol. 41, No. 11, pp 2157-2161.

Mee, D.J., Daniel, W.J.T., Simmons, J.M., 1996, "Three-component force balance for flows of millisecond duration", *AIAA Journal*, 34(3), p590-595.

Morris, N.A., 1989, "Silane as an ignition aid in scramjets", PhD thesis, The University of Queensland.

Odam, J., 2004, "Scramjet experiments using radical farming", PhD thesis, The University of Queensland.

Paull, A., Stalker, R.J., and Mee, D.J., 1995, "Experiments on supersonic ramjet propulsion in a shock tunnel", *Journal of Fluid Mechanics*, 296, p150-183.

Paull, A., 1996, "A simple shock tunnel driver gas detector", *Shock Waves Journal*, 6(5), p 309-312.

Paull, A., Frost, M. and Alesi, H., "HyShot-T4 Supersonic Combustion Experiments", report for NAG-1-2113, University of Queensland, 2000.

Paull, A., Alesi, H. and Anderson, S., 2002, "HyShot Flight Program and how it was developed", AIAA 02-4939.

Pulsinetti, M.V., 1997, "Scaling laws for scramjets", PhD thesis, The University of Queensland.

Sanderson, S.R., and Simmons, J.M., 1991, "Drag balance for hypervelocity impulse facilities", *AIAA Journal*, 29(12), p2185-2191.

Sharma, S.P. and Park, C. 1990 (1), "Operating characteristics of a 60-cm and 10-cm electric arc-driven shock tube – Part 1: the driver", *J. Thermophys and heat transfer*. 4, pp. 259-265.

Sharma, S.P. and Park, C. 1990 (2), "Operating characteristics of a 60-cm and 10-cm electric arc-driven shock tube – Part 2: The driven section", *J. Thermophys and heat transfer*. 4, pp. 266-272.

Ressler, E.L., and Bloxson, D.E. 1952., "Very high Mach number flows by unsteady flow principles", Cornell University Grad. Sch. of Aero. Eng. limited distribution monograph.

Skinner, K.A., 1994, "Mass spectrometer of hypersonic combustion", PhD thesis, The University of Queensland.

Smart, M.K., 1999, "Design of Three-Dimensional Hypersonic Inlets with Rectangular-to-Elliptical Shape Transition", *Journal of Propulsion and Power*, Vol. 15, No. 3, pp 408-416.

Smart, M.K., 2001, "Experimental Testing of a Hypersonic Inlet with Rectangular-to-Elliptical Shape Transition", *Journal of Propulsion and Power*, Vol. 17, No. 2, pp 276-283.

Smart, M.K., Hass, N.E. and Paull, A., 2006, "Flight Data Analysis of the HyShot 2 Flight Experiment", *AIAA Journal*, Vol. 44, No. 10, pp 2366-2375.

Stalker, R.J., Morgan, R.G. and Paull, A., 1996, "A shock tunnel investigation of scramjet performance with partially premixed combustion", AIAA paper No. 96-4534.

Stalker, R.J. and Edwards, B.P., 1998 "Hypersonic Blunt Body Flows in Hydrogen-Neon Mixtures", AIAA 36th Aerospace Sciences Meeting and Exhibit, Reno NV, Jan. 12-15, Paper 98-0799.

Stalker, R.J. and Paull, A., 1998, "Experiments on cruise propulsion with a hydrogen scramjet", *Aeronautical Journal*, 102(1011), p37-43.

Stalker, R.J., Truong, N.K. Morgan, R.G. and Paull, A., 2004, "Effects of hydrogen-air non-equilibrium chemistry on the performance of a model scramjet thrust nozzle", 108(1089), p575-584.

- Stalker, R.J., 2005, "Control of hypersonic turbulent skin friction by boundary layer combustion of hydrogen", *Journal of Spacecraft and Rockets*, 42(4), 577-587.
- Tuttle, S.L., Mee, D.J., and Simmons, J.M., 1995, "Drag measurements at Mach 5 using a stress wave force balance", *Experiments in Fluids*, 19, p336-341.
- Tuttle, S.L., 1996, "Measuring thrust and drag in a hypersonic impulse facility", PhD thesis, The University of Queensland.
- Wendt, M.N., Jacobs, P.A. and Stalker, R.J., 1999, "Displacement effects and scaling of ducted supersonic flames", *Combustion & Flame*, 115(4), 593-604.

von Karman Institute for Fluid Dynamics

RTO-AVT-VKI Lecture Series 2007

**ADVANCES ON PROPULSION TECHNOLOGY
FOR HIGH-SPEED AIRCRAFT**

March 12-15, 2007

*SOME FUNDAMENTAL GASDYNAMIC AND PHYSICAL-CHEMICAL ASPECTS
OF COMBUSTION IN HIGH VELOCITY FLOW*

V.I. Kopchenov
CIAM, Russia

*Some fundamental gasdynamic and physical-chemical aspects
of combustion in high velocity flow
(Abstract)*

presented by Dr. V.I. Kopchenov

*Authors: L.V. Bezgin, Dr. O.V. Gouskov, M.K. Danilov,
Prof. A.B. Vatazhin, Dr.Sc. A.M. Starik, Dr. N.S. Titova*

The active interest to the problem of combustion in high velocity flow was initiated by pioneering works of A. Ferri (USA) and E.S. Schetinkov (USSR) in 1957-1958 years (see, for example, [1,2]). These publications have given rise to impetuous advance in fundamental and applied investigations. The bibliography of these investigations is quite extensive to be presented in this report. As the example, the detailed reviews of previous investigations [3,4] can be recommended. The book [5] with reviews of investigations have been made in Australia, France, Germany, Russia, Japan, USA allows to obtain information concerning the state of the art in this area.

Some fundamental aspects of combustion in high velocity flow, which were in the scope of interests of author and his colleagues, are discussed in this presentation. The primary attention is given to the investigations of gasdynamic and physical-chemical processes at the combustion of hydrogen in high velocity flow. Numerical simulation is the main tool of these investigations. However, the numerical simulation was performed in the close relations with experimental research. The available published data of experimental investigations were also used. The numerical simulation is based on the full or parabolized Navier-Stokes equations and detailed schemes of chemical kinetics with account for turbulent mixing process. The turbulent combustion, as a rule, is considered in quasi-laminar approach.

Part 1. The mixing process in high velocity flow was considered as limiting the efficiency of diffusion combustion, and as one of the problematic question. Effective mixing enhancement methods were studied. One of them is concerned with the dividing of the hydrogen jet, injected into the air flow, on two smaller jets. This effect is realized due to special design of the nozzle for hydrogen injection. The capability of the secondary air flow to provide the mixing enhancement was also analyzed. The secondary air flow was generated by special design of the trailing part of the strut for hydrogen injection. The computational research and experimental verification of these mixing enhancement methods were made.

The peculiarities of the physical-chemical processes were analyzed and the possible reasons of combustion efficiency decrease were revealed. The analysis of the losses structure at the combustion allows to define the role of the so called losses on the dissociation. This type of losses is concerned with the equilibrium state, which is realized at the combustion. If high level of temperature is attained at the combustion, the equilibrium is shifted from the final product of reactions (water) to the intermediate products (radicals OH, O) and this is the real reason of the decrease of heat released into the flow at the combustion. The chemical composition of the combustion products is freezing at fast expansion and the process of recombination is not finished. Therefore the essential part of the heat, which could be potentially released into the flow at the combustion, is not utilized. Some possibilities to increase the efficiency of the heat release into the flow at the combustion with the aid of duct shaping were evaluated.

Part 2. The questions concerned with gasdynamic flow structure in the duct at the thermal throttling variation have aroused considerable interest. The investigations of the combustion regime in the shock-train system (and especially, the pseudo-shock combustion regime) have a long history, which has begun in the 70th years of the past century (see, for example, [6-10]).

Some results of gasdynamic flow structure investigations at the variation of thermal duct throttling are presented for the model duct. The cylindrical tube of constant area having the slightly expanding trailing part was considered. The computational investigations have allowed to explain the well known experimental evidence and to relate them with gasdynamic structure peculiarities. The influence of the tube wall temperature on the flow performances was studied. For model 2D duct, it was shown that the gasdynamic flow structure can be very sensitive to small changes of the duct thermal throttling. Particular attention has been given to the combustion regime known as combustion in pseudo-shock. The essential feature of this combustion regime is that flow at the duct entrance is supersonic one; it becomes subsonic in heat release zone with following acceleration to sonic conditions at the cross-section of transition from constant area section to trailing expansion section. The complicated interaction of the shock train system with the wall boundary layer is realized in this case. The comparison of numerical simulation results with experimental data is presented [11].

Part 3. The resolution of the problem of ignition and flame stabilization requires also to account for the gasdynamic flow structure. The situation was analyzed for the flow regime, when the temperature at the duct entrance is lower than this one necessary for self-ignition, but the total temperature is certainly sufficient to provide the ignition. It was shown that the existence of base face of the strut for the hydrogen injection, providing the self-ignition in base region, does not assure the flame stabilization in the main stream at these gasdynamic conditions. At the same time, if to initiate (for these flow conditions at the duct entrance) the combustion in pseudo-shock, then the flow structure generated in this case allow to maintain the stable combustion without any additional means for ignition and flame stabilization. The unsteady process of initiation and transition to the stable process of combustion in the regime of pseudo-shock was investigated. The possibility of unsteady phenomenon occurrence for the self-sustaining combustion regime in pseudo-shock is demonstrated. The situation was also analyzed when the temperature at the duct entrance is high to provide the self-ignition, however the time residence of fuel – air mixture in duct is small. In this case, the self-ignition is realized in the system of shocks, which are formed in supersonic flow. The essential feature of this process is that the self-ignition takes place at the comparatively high level of preliminary mixing of hydrogen and air due to ignition delay. This example shows that shock induced combustion can play important role in high velocity flow.

Part 4. The theoretical analysis was performed in CIAM to estimate the MHD methods possibility for the high velocity flow control. The MHD control was proposed as the alternative to traditional gasdynamic methods of flow control in order to provide the essential increase of the technical devices performances (see, for example, [12-14]). The realization of this control method implies the solution of two problems. The first problem concerns the generation of conducting media and requires, in many cases, special technical decisions. This question is not considered in this presentation. The second problem was studied in our work. The efficiency of MHD control is estimated at the assumption that the required level of conductivity can be provided. Particular attention has been given to the evaluation of irreversible losses with the use of MHD control. The concept of combined compression inlet was proposed. The flow deceleration in this inlet is realized in the external system of shocks and then in the MHD generator installed inside the internal duct. The results of inlet efficiency estimations are presented taking into account the additional irreversible losses inherent to MHD control. It is shown that MHD control allows also to influence on the combustion in high velocity flow. The positive effect manifests itself in decrease of ignition delay length and in reliable flame stabilization, and it is concerned with pressure and temperature rise in MHD generator. The positive effects are accompanied by negative factors. The pressure ratio rise in inlet is followed by essential decrease of the total pressure recovery coefficient. The evaluation of total balance of the forces acting on the aerodynamic body with the internal duct, where the heat supply to the

flow takes place, shows that, MHD control causes the essential improvement of aerodynamic forces (pressure and skin friction forces) input. However the negative effect, concerned with additional MHD force, acting on the body, which carries the magnetic field, can essentially decrease and even exceed (in absolute value) the gain (due to MHD control of the flow) in aerodynamic force.

Part 5. Since a reliable ignition and flame stabilization in high velocity flow still remain a challenge, the study of capability to use some new concepts is of immediate interest. Previously, the novel methodology of combustion control by excitation of vibrational and electronic states of reactive molecules was proposed in CIAM. The fundamentally new physical and chemical models were developed for the description of both excitation of reactive species molecules and combustion with taking into account the excited molecules [15-18]. Using the developed models, some problems on combustion in high velocity flow at the preliminary excitation of internal degrees of freedom of the main species (vibrations of hydrogen molecules, electronic states of oxygen molecules) were considered in 2D formulation. Much attention is given to the question of decrease of the power input necessary to initiate the combustion process. The local influence on the flow is considered as one way to attain this goal. The problem on combustion initiated by the shock (generated by the wedge) in premixed hydrogen-oxygen flow at the preliminary laser-induced excitation of oxygen molecules upstream the wedge is considered in this presentation as the first example. The second example demonstrates the necessity to take into account the nonequilibrium effects at the excitation of molecular vibrations of reactive molecules behind the shock generated by the wedge. The nonequilibrium vibrations excitation results in increase both the induction zone behind the shock and transition zone to detonation shock formation in comparison with traditional thermally equilibrium chemical kinetic model. At the same time, the local excitation of hydrogen molecules vibrations before the shock provides essential decrease of the induction and transition (to detonation shock) zones.

Acknowledgments. Authors thank Dr. V.Ju. Alexandrov, Dr. K.E. Lomkov, Dr. Yu.S. Mnatsakanyan, Dr. A.N. Prokhorov, Dr. A.S. Roudakov, Prof. A.M. Kharitonov, Dr.Sc. A.V. Lokotko, Dr. A.V. Tchernyshev, Dr. V.N. Avrashkov, Prof. V.M. Levin for the fruitful cooperation.

References

1. Ferri A., Libby P.A., Zakkay V. Theoretical and Experimental Investigations of Supersonic Combustion. Proceedings of the International Council of the Aeronautical Sciences. Third Congress, Stockholm, 1962, Spartan, New York, 1964, pp.1089-1155.
2. Schetinkov E.S. Research of Performances and Operational Conditions of Ideal Ramjet at Very High Flight Velocities. (NII 1 Report. 1957). Published in "Rocket – Space Engines and Power Plants. Pioneers of Rocket Technique. E.S. Schetinkov. No.2 (157). Moscow, 2000, pp.91-148.
3. Billig F.S. Research on Supersonic Combustion. J. of Propulsion and Power, 1993, V.9, No.4, pp.499-514.
4. Curran E.T. Scramjet Engines: the First Forty Years. J. of Propulsion and Power, 2001, V.17, No.6, pp.1138-1148.
5. Scramjet Propulsion. Ed. by E.T. Curran and S.N.B. Murthy. Progress in Astronautics and Aeronautics. 2000, V.189, Published by AIAA, Inc., 1293 p.
6. Schetinkov E.S. About Piecewise 1D Models of Supersonic Combustion and Pseudoshock in Duct. Physica Goreniya i Vzriva, 1973, Vol. 9, No. 4, pp. 473-483.
7. Waltrup P.J., Billig F.S. Structure of Shock Waves in Cylindrical Ducts. AIAA J, 1973, Vol. 11, No. 10, pp. 1404-1408.
8. Zimont V.L., Levin V.M., Mescheryakov E.A. Combustion in supersonic flow at the existence of pseudoshock. Physica Goreniya i Vzriva, 1978, Vol. 14, No. 4. pp. 23-36.
9. Tretyakov P.K. Pseudoshock Combustion Regime. Physica Goreniya i Vzriva, 1993, Vol. 29, No. 6, pp. 34-38.
10. Matsuya G., Ichikawa N., Kumasaka T., Takita K. Pseudo-Shock Wave and Mode Transition. ISABE 2003—1151, 2003.
11. Rizhov Y.A., Avrashkov V.N., Levin V.M., Kopchenov V.I., Gouskov O.V. Experimental and Numerical Simulation Research of Hydrogen Burning at the Duct. EUCASS (European Conference for Aerospace Sciences), 2005, Moscow, Russia.
12. Bityurin V.A., Zeigarnik V.A., Kuranov A.L. On a Perspective of MHD Technology in Aerospace Applications. AIAA Paper, 1996, 96-2355.
13. Frishtadt V.L., Kuranov A.L., Sheikin E.G. The MHD System Use on the Hypersonic Flight Vehicles. Journal of Technical Physics, 1998, V.68, No.11, pp.43-47.
14. Bityurin V.A., Bocharov A.N., Lineberry J.T. MHD Aerospace Applications. Proc. Intern. Conf. on MHD Power Generation and High Temperature Technologies, Beijing PRC, 1999, V.3, pp.793-814.
15. A.M. Starik, N.G. Dautov. On a Possibility of Promotion of Combustion for H_2-O_2 Mixtures by Vibrational Excitation of Molecules. Doklady Physics, 1994, V.39, pp.424-429.
16. Starik A.M., Titova N.S. Low-Temperature Initiation of the Detonation Combustion of Gas Mixtures in a Supersonic Flow under Excitation of the $O_2(a^1\Delta_g)$ State of Molecular Oxygen. Doklady Physics, 2001, V.46, No.9, pp.627-632.
17. Starik A.M., Titova N.S. Kinetic Mechanisms of Initiating Hydrogen-Oxygen Mixture Combustion Through the Excitation of Electronic Degrees of Freedom of Molecular Oxygen by Laser Radiation. Technical Physics, 2003, V.48, No.3, pp.334-343.
18. Loukhovitski B.I., Starik A.M., Titova N.S. Activation of Chain Processes in Combustible Mixtures by Laser Excitation of Molecular Vibrations of Reactants. Combustion, Explosion, and Shock Waves, 2005, V.41, No.4, pp.386-394.

List
of main publications with presented results

1. Gouskov O., Kopchenov V., Lomkov K., Roudakov A., Semenov V. CFD in the Preparation and Data Processing of Scramjet Testing on Hypersonic Flight Beds. AIAA-96-4562, 1996.
2. Roudakov A., Kopchenov V., Semenov V., Gouskov O. Flight Experimental and Computational Investigations of Scramjet Gasdynamics and Combustion. Proceedings of the Third European Symposium on Aerothermodynamics for Space Vehicles. ESA SP-426, 1998, pp.59-67.
3. Kopchenov V., Lomkov K., Miller L., Krjukov V., Rulev I., and oth. Scramjet CFD Methods and Analysis. Part 1. Scramjet CFD Methods. Numerical Simulation of the Flow in Scramjet Duct. AGARD-LS-194, 1993, pp.4-1 - 4-20.
4. Kopchenov V., Lomkov K., Zaitsev S., Borisov I. Scramjet CFD Methods and Analysis. Numerical Simulation of Supersonic Mixing and Combustion Applied to Scramjet Combustor. AGARD-LS-194, 1993, pp. 8-1 - 8-30.
5. Bezgin L., Ganzhelo A., Gouskov O., Kopchenov V., Laskin I., Lomkov K. Numerical Simulation of Supersonic Flows Applied to Scramjet Duct. ISABE 95-7082, 1995, pp.895-905.
6. Bezgin L.V., Burico Yu.Ya., Ganzhelo A.N., Gouskov O.V., Zaitcev S.A., Kopchenov V.I., Laskin I.N., Lomkov K.E. CFD in Hypersonic Propulsion System Investigation and Design. Aviation-2000. Prospects. International Symposium Proceedings. Zhukovsky, Russia. August 19-24, 1997, pp.701-708.
7. Bezgin L.V., Ganzhelo A.N., Gouskov O.V., Kopchenov V.I. Numerical Simulation of Viscous Non-Equilibrium Flows in Scramjet Elements. ISABE 97-7131, 1997, pp.976-986.
8. Kopchenov V.I., Lomkov K.E. The Enhancement of the Mixing and Combustion Processes Applied to Scramjet Engine. AIAA 92-3428, 1992.
9. Gouskov O.V., Kopchenov V.I., Nikiforov D.A. Flow Numerical Simulation in the Propulsion Elements of Aviation Space System within Full Navier-Stokes Equations. VII International Conference on the Methods of Aerophysical Research. Proceedings, Part 1, Novosibirsk, 1994, pp.104 - 109.
10. Gouskov O.V., Kopchenov V.I., Numerical Simulation of Duct Flow at Supersonic Entry Conditions. VIII International Conference on the Methods of Aerophysical Research, Proceedings, Part 3, Novosibirsk, 1996, pp.84-89.
11. Kopchenov, V.I., Lomkov, K.E. Numerical Simulation of the Supersonic Combustion Enhancement and the 3D Scramjet Combustor Design with Account of Nonequilibrium Chemical Reactions. High Speed Aerodynamics, V.1, No.1, 1997, pp.43-53.
12. Kopchenov V.I., Lomkov K.E., Mnatsakanyan Yu.S., Prokhorov A.N., Shutov A.A. Computational Estimation of Influence of Injector Nozzle Shape on Mixing in Supersonic Flow and Comparison with Experimental Data. Intern. Conf. on the Methods of Aerophysical Research, Proceedings, Pt. 3, Novosibirsk, 2000, pp.67-74.
13. Gouskov O.V., Kopchenov V.I., Lomkov K.E., Mnatsakanyan Yu.S., Prokhorov A.N., Shutov A.A. Numerical and Experimental Investigation of Supersonic Mixing and Combustion. AIAA 2001-1821, 2001.
14. Kharitonov A.M., Lokotko A.V., Tchernyshyev A.V., Kopchenov V.I., Lomkov K.E., Rudakov A.S. Mixing Processes of Supersonic Flows in a Sketchy Model of a Rocket Scramjet Engine. Intern. Conf. on the Methods of Aerophysical Research, Proc., Pt. 3, Novosibirsk, 1996, pp.195-200.
15. Kharitonov A.M., Lokotko A.V., Tchernyshyev A.V., Kopchenov V.I., Lomkov K.E., Rudakov A.S. Mixing Processes of Supersonic Flows in Model Duct of a Rocket Scramjet Engine. AIAA 2000-0559, 2000.
16. Gouskov O.V., Kopchenov V.I. Investigation of Ignition and Flame Stabilization behind the Strut in Supersonic Flow. AIAA 2002-5226, 2002.

17. Gouskov O.V., Kopchenov V.I. Investigation of Influence of Pylon back Face on Mixing and Ignition Process of Hydrogen Jet. Conf. on the Methods of Aerophysical Research, Proc., Pt. 3, Novosibirsk, 2000, pp.57-62.
18. Gouskov O.V., Kopchenov V.I. Numerical Investigation of Flow Structure in the Channel at Supersonic Conditions at the Entrance. Aeromechanics and Gas Dynamics. 2001, No.1, pp.28-39.
19. Gouskov O.V., Kopchenov V.I. About the Influence of the Wall Temperature on the Combustion of Hydrogen Jet in Channel at the Supersonic Conditions at the Entrance. Chemical Physics, 2004, V.23, No.4, pp.52-60.
20. Gouskov O.V., Kopchenov V.I. About the Combustion Regimes in the Channel at Supersonic Conditions at the Entrance. In "Scientific Support of Aviation Engines Development". Ed. by V.A. Skibin and V.I. Solonin. 2000, V.1, Section "Research in Hypersonic and Aerospace Engines", pp.255-258.
21. Gouskov O.V., Danilov M.K., Kopchenov V.I. Investigations of Flow Features in Model Combustor at Supersonic Flow Conditions at the Entrance Corresponding to $M_f=6$. In "CIAM 2001-2005. The Main Results of Scientific and Technical Activity". Ed. by V.A. Skibin B.A. V.I. Solonin, M.Ya. Ivanov. 2005, V.1, Section "Propulsion of Hypersonic and Aerospace Flying Vehicles", pp.205-211.
22. Bezgin L.V., Kopchenov V.I. Optimization of the Flow Path of Model Scramjet Taking into Account Complicated Gasdynamic Flow Structure and Nonequilibrium Chemical Reactions. In "CIAM 2001-2005. The Main Results of Scientific and Technical Activity". Ed. by V.A. Skibin B.A. V.I. Solonin, M.Ya. Ivanov. 2005, V.1, Section "Propulsion of Hypersonic and Aerospace Flying Vehicles", pp.200-205.
23. Gouskov O.V., Danilov M.K., Kopchenov V.I. Some Gasdynamic Aspects of Combustion in Supersonic Flow. EUCASS (European Conference for Aerospace Sciences) Proceedings, 2005, 4-7 July, Moscow, Russia, 7pp.
24. Skibin V.A., Roudakov A.S. CIAM Hypersonic Engines. Memories about Future. Aerospace Herald, 2003, No.4, pp.29-31.
25. Alexandrov V.Yu., Gouskov O.V., Danilov M.K., Jirnov D.B., Kopchenov V.I., Mnatsakanyan Yu.S., Prokhorov A.N., Roudakov A.S., Semenov V.L. Investigation of Operational Process, Development and Testing of Combustion Chambers of High Velocity Ramjets. Conversion in Mashine-Building, 2005, No.4-5, pp.49-59.
26. Kopchenov V.I., Roudakov A.S., Semenov V.L., Grigoriev N.V., Kondratov A.A., Tsiplakov V.V. Experience and Future Trends of Flight Tests of Hypersonic Engines. Conversion in Mashine-Building, 2005, No.4-5, pp.59-65.
27. Skibin V.A., Prokhorov A.N. Engine for Future. Science World, 2006, No.11, pp.76-79.
28. Vatazhin A.B., Gouskov O.V., Kopchenov V.I. The Investigation of Supersonic Flow Deceleration by Magnetic Field. Proc. of Intern. Conf. on MHD Power Generation and High Temperature Technologies, Beijing PRC, 1999, V.3, pp.875-882.
29. Vatazhin A., Kopchenov V., Gouskov O. Numerical Investigation of Hypersonic Inlets Control by Magnetic Field. The 2nd Workshop on Magneto-Plasma Aerodynamics in Aerospace Applications. Moscow: Institute High Temperature of RAS (IVTAN), 2000, pp.56-63.
30. Bityurin V.A., Vatazhin A.B., Gouskov O.V., Kopchenov V.I. Hypersonic Flow over Spherical Nose at the Presence of Magnetic Field. Fluid Dynamics, 2004, No. 4, pp.169-179.
31. Vatazhin A.B., Gouskov O.V., Kopchenov V.I., Likhter V.A. Problem of Deceleration of Supersonic Conducting Channel Flow by a Magnetic Field. Fluid Dynamics, 1998, No. 5, pp.169-181.
32. Vatazhin A.B., Gouskov O.V., Kopchenov V.I. Peculiarities of Deceleration of 2-D Hypersonic Flow of Conductive Gas in Channel on Regime of Electric Energy Generation. Proceedings of Math. Institute named V.A. Steklov, 1998, V.223, pp.153-162.

33. Vatazhin A.B., Gouskov O.V., Danilov M.K., Kopchenov V.I. Research of Possibility of MHD Flow Control in Hypersonic Inlets. *Aeromechanics and Gas Dynamics*, 2002, No. 2, pp.3-15.
34. Vatazhin A.B., Danilov M.K., Gouskov O.V., Kopchenov V.I. Magnetogasdynamic Control of Supersonic Flow over Aerodynamic Bodies: Possibilities and Undesirable Effects. *Fluid Dynamics*, 2006, No.2, pp.138-148.
35. Bezgin L.V., Kopchenov V.I., Starik A.M., Titova N.S. Numerical Investigation of Detonation Shock Formation in the Supersonic Flow of Mixture H₂/O₂ at Nonequilibrium Molecular Excitation of Reagents. *Physics of Combustion and Explosion*, 2006, V.42, No.1, pp.1-9.
36. Bezgin L.V., Kopchenov V.I., Starik A.M., Titova N.S. Some Aspects of Oblique Detonation Wave Initiation in a Supersonic Flow. In "Pulsed and Continuous Detonation", Ed. by G.Roy, S.Frolov, J.Sinibaldi. Moscow, Torus Press Ltd., 2006, pp. 308-316.
37. Bezgin L.V., Kopchenov V.I., Starik A.M., Titova N.S. Initiation of a Detonation Wave by Resonant Laser Radiation in a Hydrogen – Oxygen Mixture Flowing about a Wedge. *Zhurnal Tekhnicheskoy Fiziki*, 2007, V.77, No.1, pp.42-49.
38. Bezgin L.V., Kopchenov V.I., Starik A.M., Titova N.S. Modeling of Oblique Detonation Wave Initiation in H₂-O₂ Mixture by Excitation of Molecular Vibrations of Reactants. In "Combustion and Atmospheric Pollution", Ed. by G.D. Roy, S.M. Frolov, A.M. Starik. Moscow, Torus Press Ltd., 2003, pp.306-311.

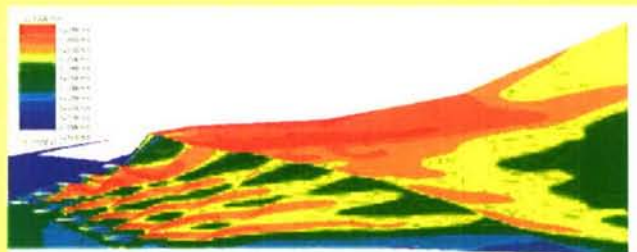
MAIN PROBLEMS

- Mixing in high velocity flow
- Efficient heat release into the flow at combustion
- Gasdynamic flow structure in channel at combustion
- Ignition and flame stabilization in high velocity flow
- Channel shape influence

Non traditional control methods

- MHD flow control
- Internal degrees of freedom excitation of reactive molecules

Part 1. Diffusive combustion regime in high velocity flow

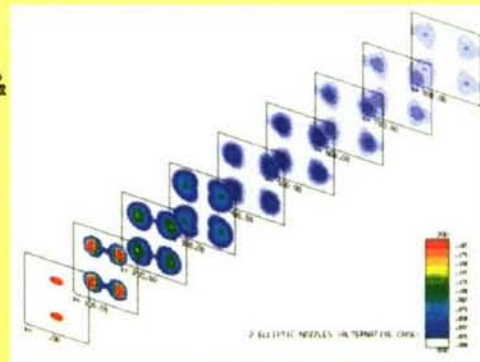
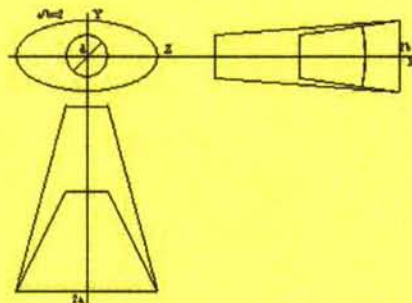


Temperature field

Main problems:

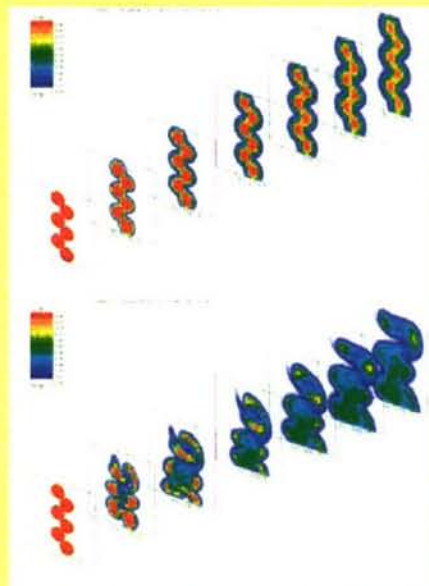
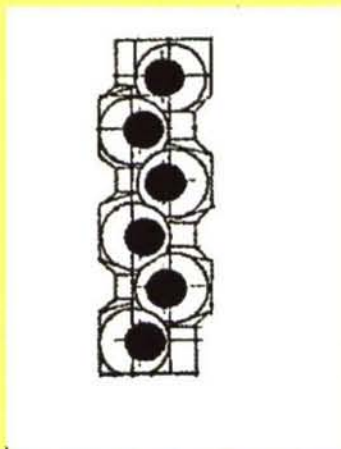
- Mixing and combustion enhancement
- Combustion efficiency
- Structure of losses at the combustion
- Losses on the dissociation

Mixing and combustion enhancement with the aid of fuel nozzle shaping

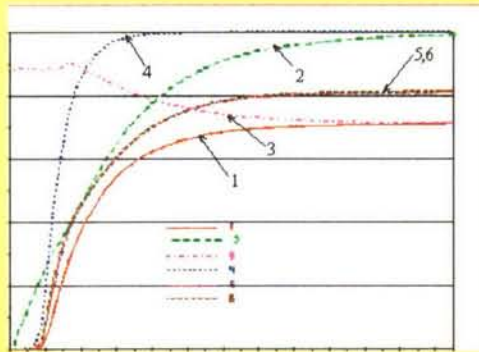


Effect of jets dividing

Mixing enhancement with the aid of special shaping of trailing part of the strut for fuel injection



Structure of the losses at the combustion



➤ Curve 1 – combustion efficiency.

➤ Curve 2 – mixing efficiency

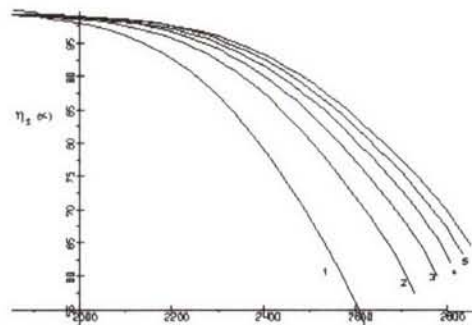
➤ Curve 3 – quality of equilibrium

➤ Curve 4 – degree of equilibrium

Combustion efficiency and its constituents along the channel length

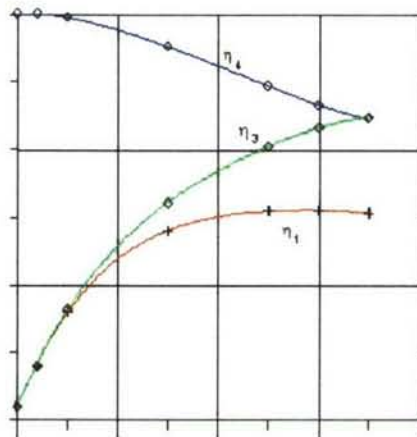
Losses on Dissociation (equilibrium quality)

High level losses at temperatures greater than 2200 K



The quality of equilibrium in hydrogen-air mixture for air/fuel equivalence ratio 0.9 and different pressures.
Curves 1..6 - $P=0.1, 0.3, 0.5, 0.7, 0.9$ and 1.1 bar.

Structure of the losses at the combustion

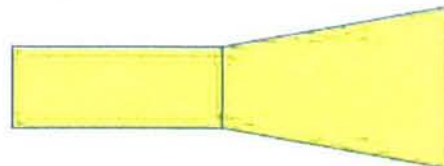


•Curve 1 – combustion efficiency

•Curve 3 – quality of equilibrium

•Curve 4 – degree of equilibrium

Influence of channel trailing part expansion on the losses constituents



Rational channel shaping with account for complicated wave structure and nonequilibrium chemical reactions



a



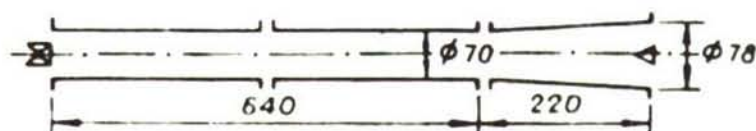
b



Temperature field for base configuration (a) and modified configuration (b). Longitudinal force for base (dashed line) and modified channel shape (red curve)

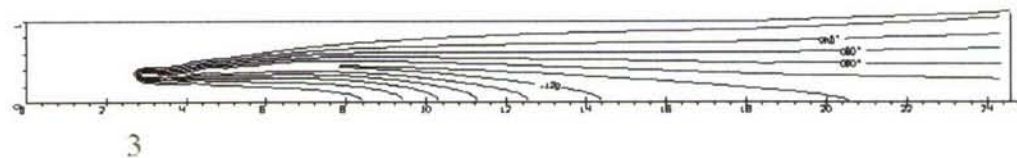
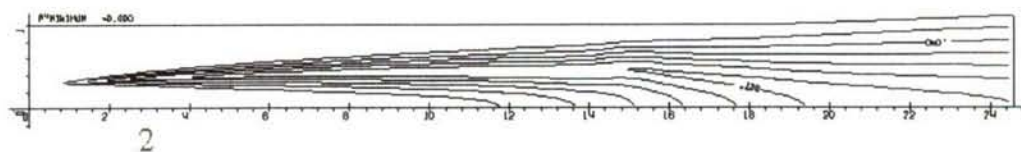
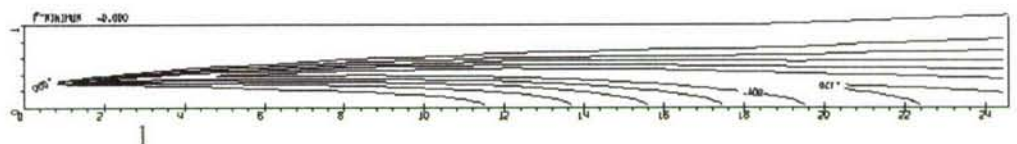
Part 2

Research of gasdynamic flow structure in the channel at the variation of heat throttling

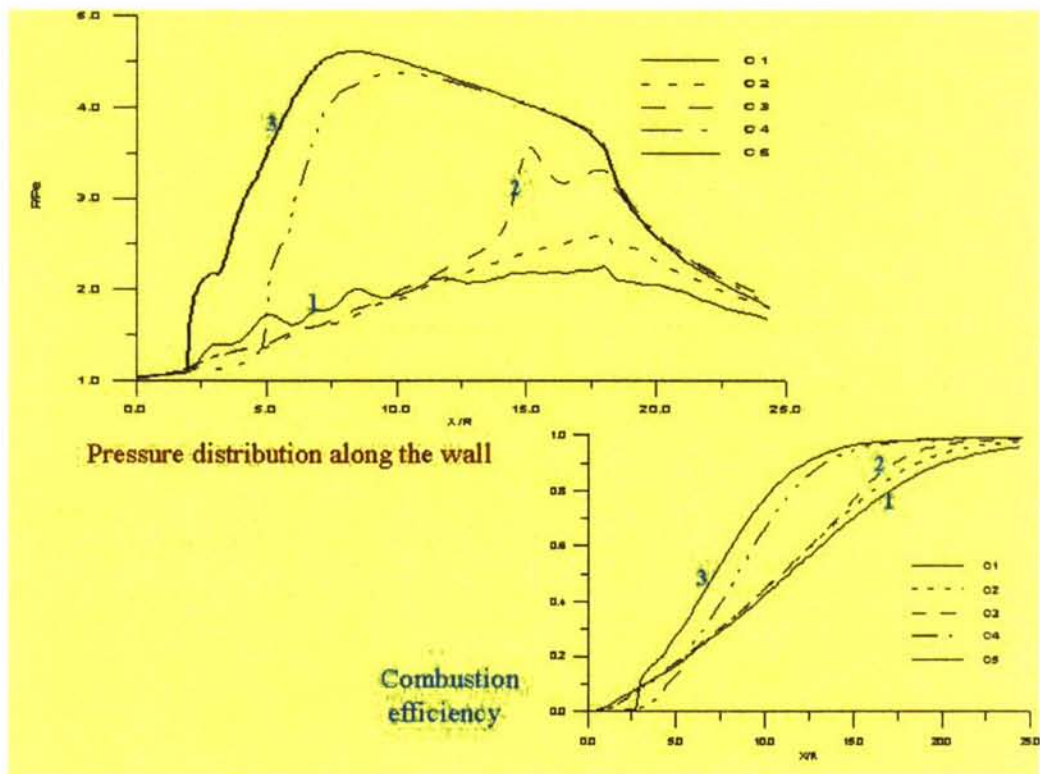
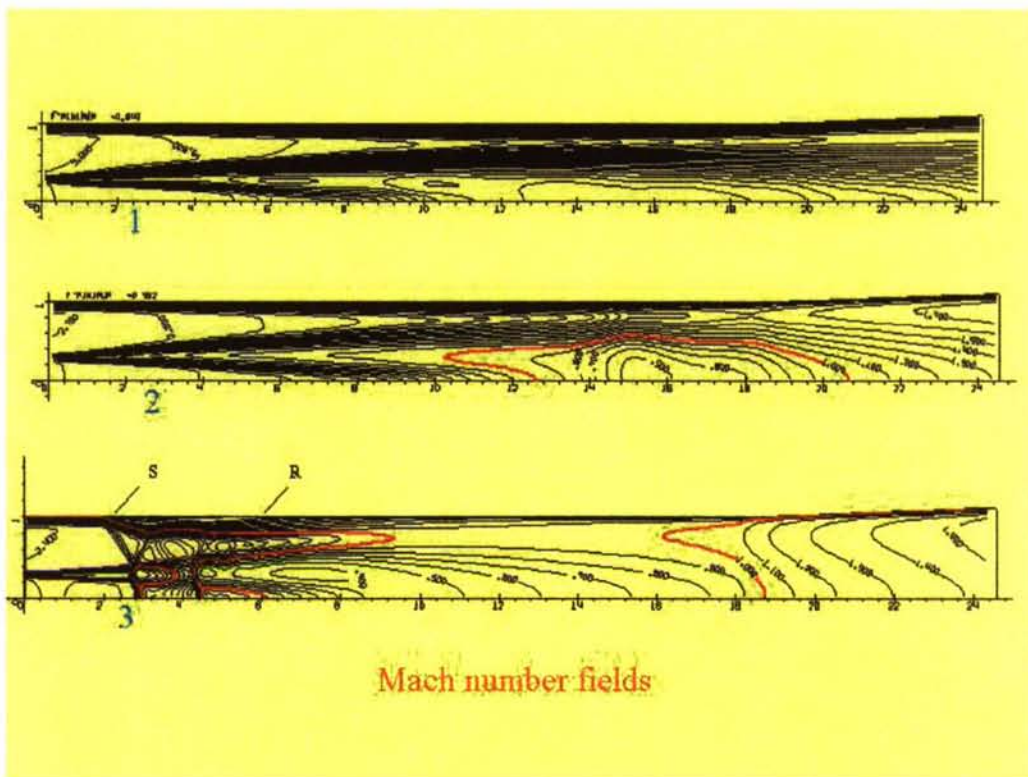


Air flow:

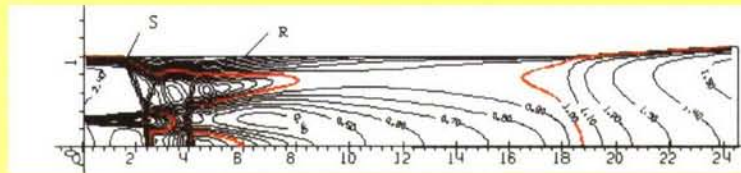
- 1 - $M=3.9$, $P=1$ atm, $T=1150$ K
- 2 - $M=2.8$, $P=1$ atm, $T=1150$ K
- 3 - $M=2.5$, $P=1$ atm, $T=1150$ K



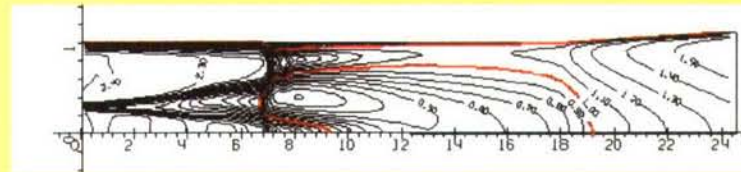
Mass fraction fields



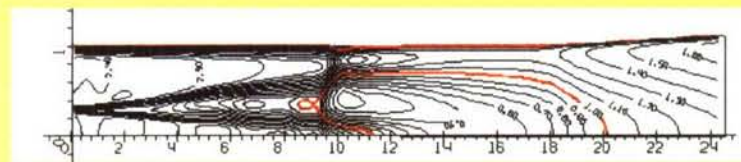
Influence of the wall temperature on the flow structure



Adiabatic wall



$T_w = 1000 \text{ K}$



$T_w = 250 \text{ K}$

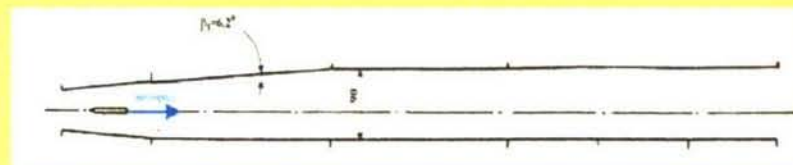
Mach number fields

Investigation of gasdynamic flow structure in channel at the variation of heat throttling

Air stream: $T^* = 1660 \text{ K}$, $P^* = 15 \text{ bars}$, $M = 2.5$

Hydrogen jet: $T^* = 300 \text{ K}$, $M = 1.0$

Air to fuel equivalence ratio $\alpha = 1.8 - 2.5$



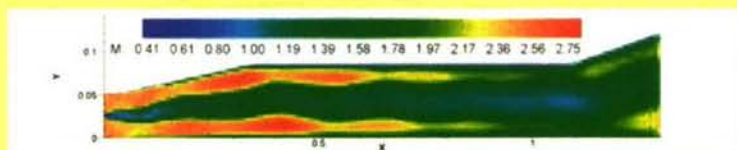
Channel scheme

FUTURE STEPS

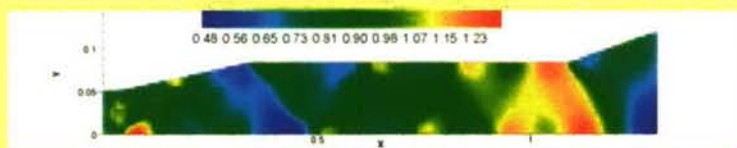
Experimental investigation is needed

- Adaptation of spectral diagnostic methods
- Development and adaptation of special devices to realize the desirable methods of influence on the flow at the real flow conditions
- Physical experiments and experiments on the model devices with simulation of real flow conditions

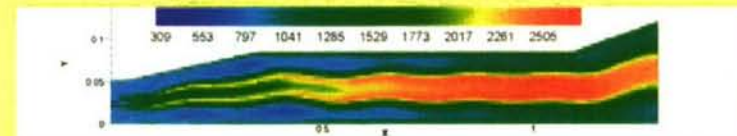
Combustion at supersonic conditions air to fuel equivalence ratio 2.5



Mach number field

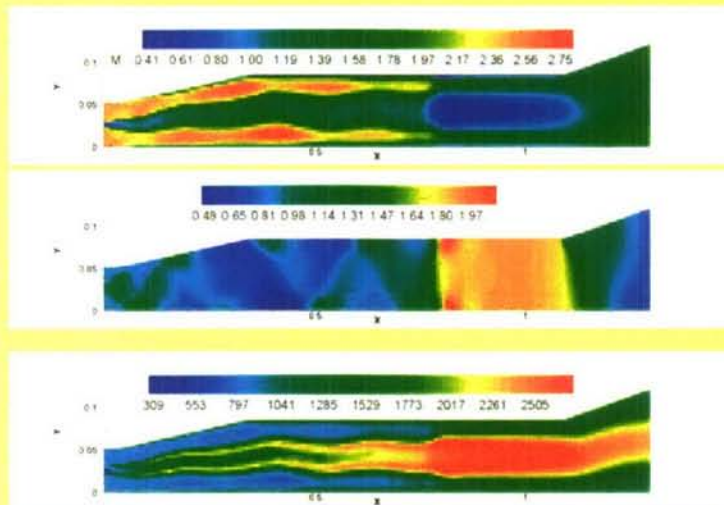


Pressure field



Temperature field

Transition combustion regime air to fuel equivalence ratio 2.25

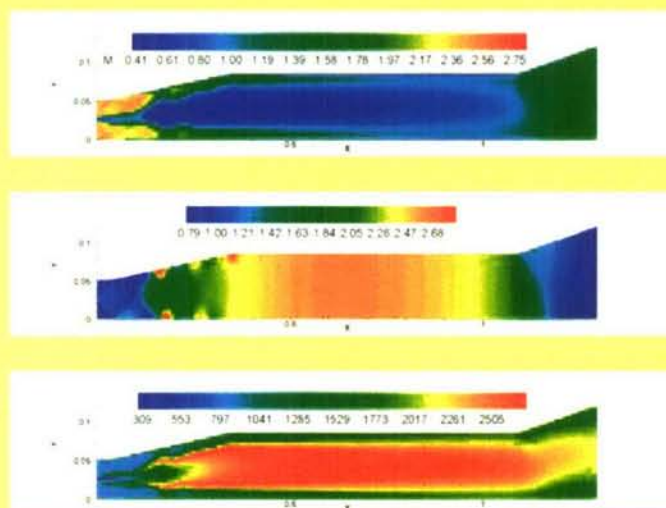


Mach number field.
Arising
of subsonic zone

Pressure field

Temperature field

Pseudo-shock combustion regime air to fuel equivalence ratio 1.8



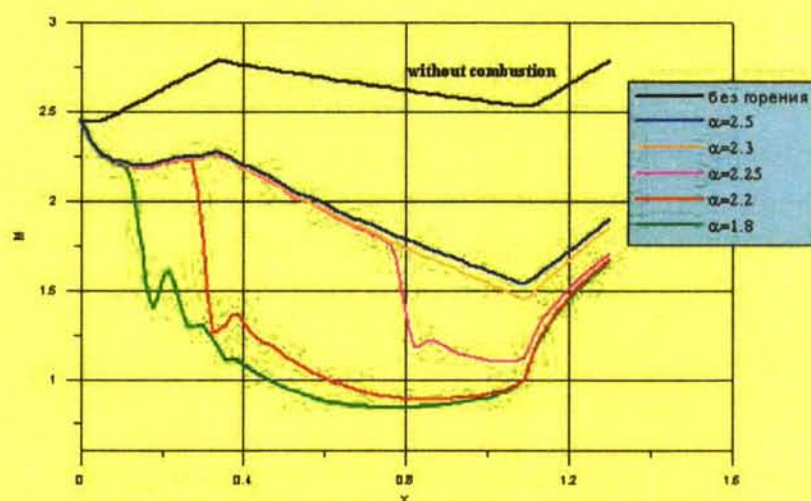
Mach number field.

**Transition from
supersonic to
subsonic (averaged
over cross-section)
flow**

Pressure field

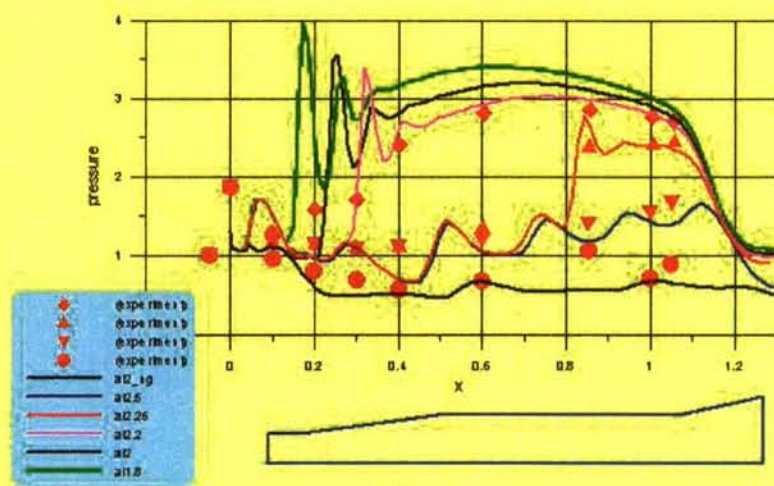
Temperature field

Combustion regimes in the channel at the variation of air to fuel equivalence ratio (2.5 - 1.8)



Averaged over the cross-section Mach number distribution along the channel

Comparison of computational and experimental data



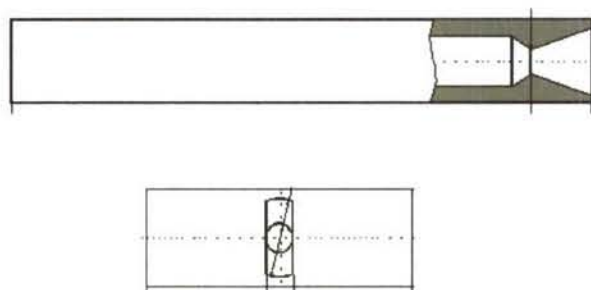
Pressure distribution along the channel wall

Part 3. Ignition and flame stabilization in high velocity flow

- High static temperature, small residence time
(ignition and stabilization by shocks)
- Low static temperature, high total temperature
(ignition and flame stabilization in self-sustained
gasdynamic structure after initiation of pseudo-shock
combustion regime)
- Low total temperature (igniters and cavities or steps / base
regions of pylons / high temperature jets)
- Alternative methods (excitation of internal degrees of
freedom of molecules of the main reagents)

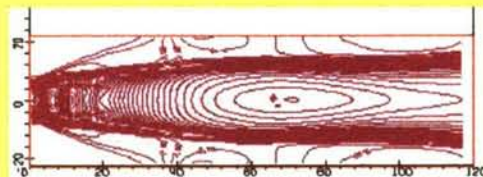
Experimental investigation and numerical simulation

Flame stabilization by the strut base region

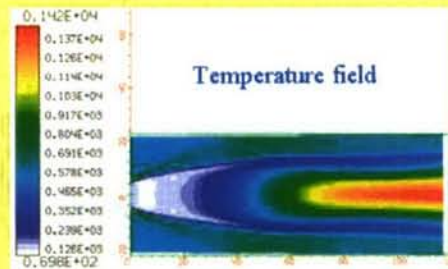


Ignition and flame stabilization in supersonic flow (ignition is provided in strut base region)

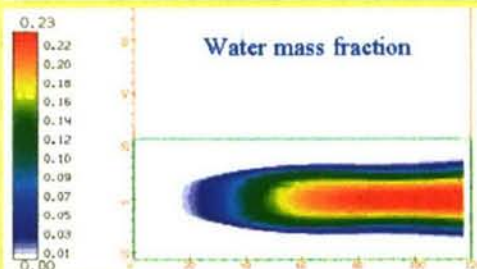
Mach number field



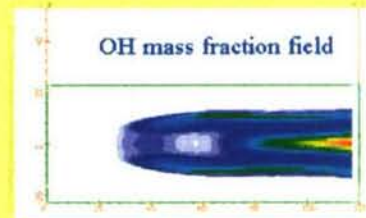
Temperature field



Water mass fraction

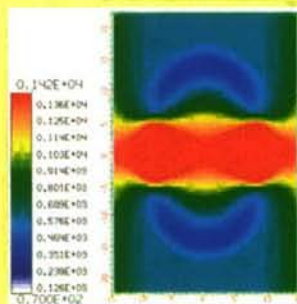


OH mass fraction field

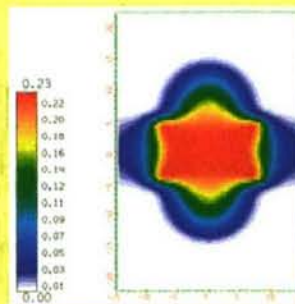


Ignition and flame stabilization in supersonic flow (ignition is provided in strut base region)

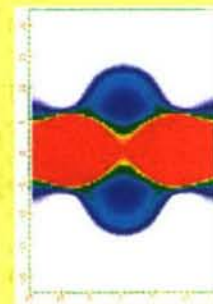
(ignition is provided in strut base region)



Temperature field



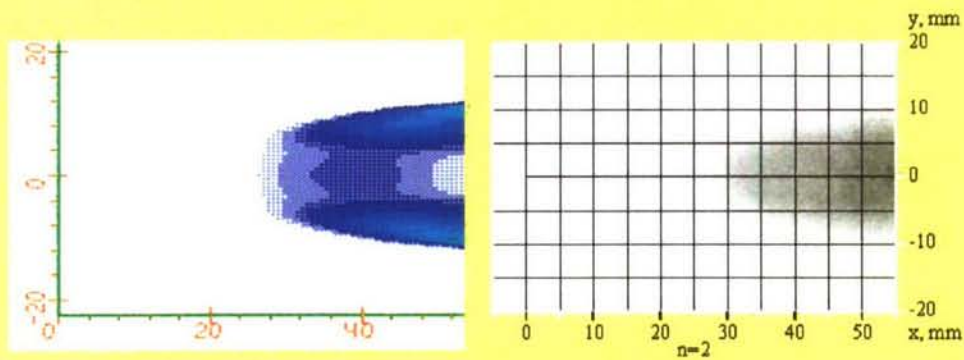
Water mass fraction field



OH mass fraction field

Combustion is observed only in the wake
of strut base face

Comparison with the experiment

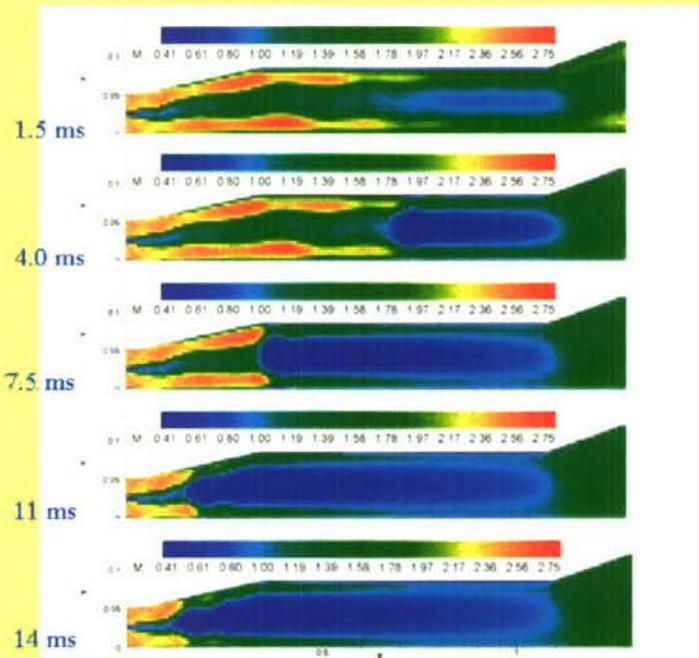


Calculation

Experiment

OH mass fraction field

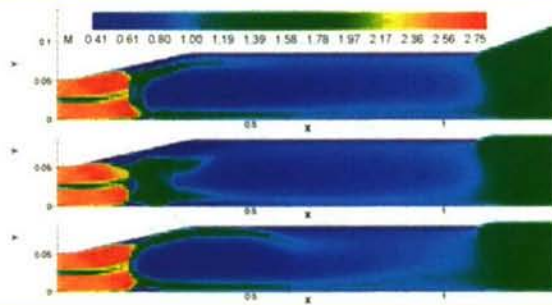
The starting process and self-sustained structure formation



Process of starting
(by pilot flame)

Mach number
field

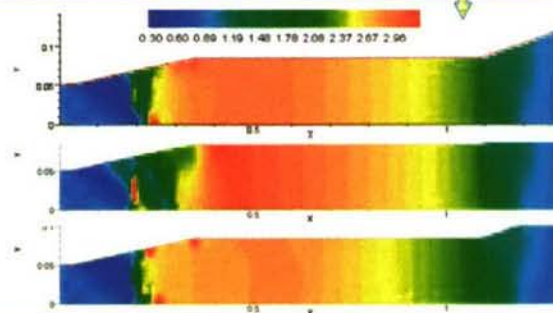
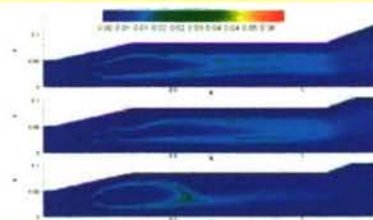
Unsteady effects after switching off pilot flame



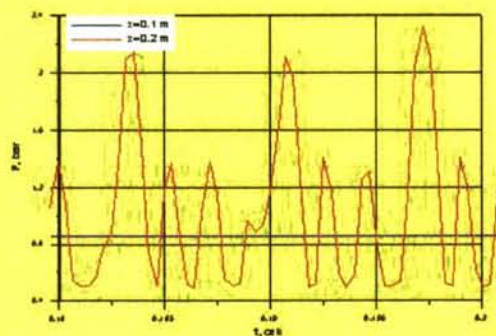
Mach number field

Pressure field

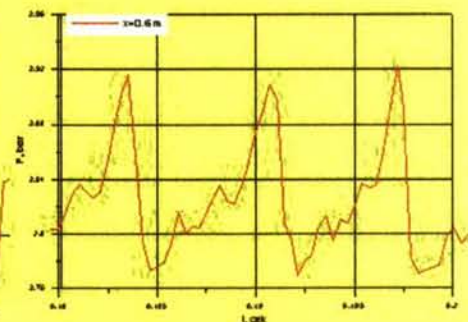
OH mass fraction field



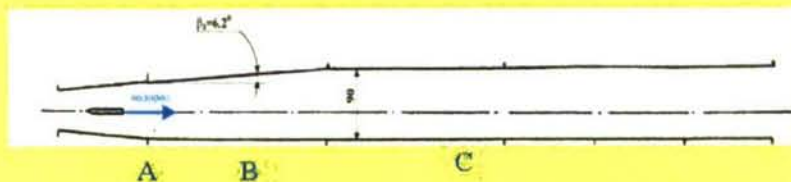
Pressure oscillations in time



Pressure at points A (upstream the pseudo-shock head) and B (downstream the head of the pseudo-shock)



Pressure at point C



Ignition and flame stabilization in high velocity flow (by shock system)



Temperature field



Water
mass fraction field

Part 4. MHD control in high velocity flow



- High velocity flow deceleration
- MHD flow control in inlet
- Influence of MHD control on the forces balance
- Positive effects and their “cost”

Mathematical and physical model

- Full averaged Navier-Stokes equations with MHD terms
- Differential model of turbulence
- Electrodynamic equations
- Detailed schemes of chemical kinetics for hydrogen combustion in air

Dimensionless parameters

MHD interaction parameter $S = \sigma B^2 L / \rho u$

Load parameter $K = E / u B$

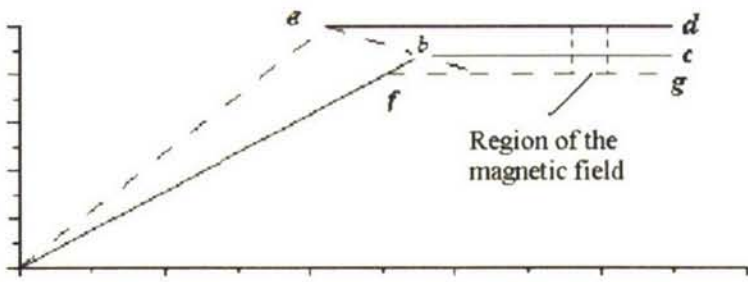
Hall parameter $\beta = e \tau B / m$

MHD

CONTROL OF HIGH VELOCITY FLOW



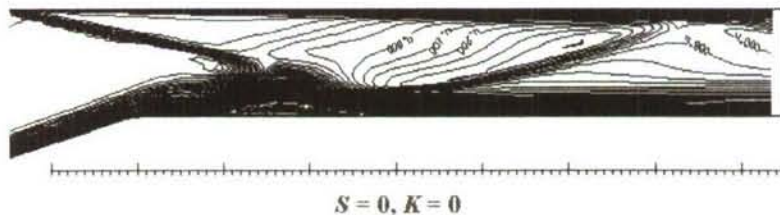
1
 2
 3
 4
 5
 6
 7
 8
 9
 10
 11
 12
 13
 14
 15
 16
 17
 18
 19
 20
 21
 22
 23
 24
 25
 26
 27
 28
 29
 30
 31
 32
 33
 34
 35
 36
 37
 38
 39
 40
 41
 42
 43
 44
 45
 46
 47
 48
 49
 50
 51
 52
 53
 54
 55
 56
 57
 58
 59
 60
 61
 62
 63
 64
 65
 66
 67
 68
 69
 70
 71
 72
 73
 74
 75
 76
 77
 78
 79
 80
 81
 82
 83
 84
 85
 86
 87
 88
 89
 90
 91
 92
 93
 94
 95
 96
 97
 98
 99
 100
 101
 102
 103
 104
 105
 106
 107
 108
 109
 110
 111
 112
 113
 114
 115
 116
 117
 118
 119
 120
 121
 122
 123
 124
 125
 126
 127
 128
 129
 130
 131
 132
 133
 134
 135
 136
 137
 138
 139
 140
 141
 142
 143
 144
 145
 146
 147
 148
 149
 150
 151
 152
 153
 154
 155
 156
 157
 158
 159
 160
 161
 162
 163
 164
 165
 166
 167
 168
 169
 170
 171
 172
 173
 174
 175
 176
 177
 178
 179
 180
 181
 182
 183
 184
 185
 186
 187
 188
 189
 190
 191
 192
 193
 194
 195
 196
 197
 198
 199
 200
 201
 202
 203
 204
 205
 206
 207
 208
 209
 210
 211
 212
 213
 214
 215
 216
 217
 218
 219
 220
 221
 222
 223
 224
 225
 226
 227
 228
 229
 230
 231
 232
 233
 234
 235
 236
 237
 238
 239
 240
 241
 242
 243
 244
 245
 246
 247
 248
 249
 250
 251
 252
 253
 254
 255
 256
 257
 258
 259
 260
 261
 262
 263
 264
 265
 266
 267
 268
 269
 270
 271
 272
 273
 274
 275
 276
 277
 278
 279
 280
 281
 282
 283
 284
 285
 286
 287
 288
 289
 290
 291
 292
 293
 294
 295
 296
 297
 298
 299
 300
 301
 302
 303
 304
 305
 306
 307
 308
 309
 310
 311
 312
 313
 314
 315
 316
 317
 318
 319
 320
 321
 322
 323
 324
 325
 326
 327
 328
 329
 330
 331
 332
 333
 334
 335
 336
 337
 338
 339
 340
 341
 342
 343
 344
 345
 346
 347
 348
 349
 350
 351
 352
 353
 354
 355
 356
 357
 358
 359
 360
 361
 362
 363
 364
 365
 366
 367
 368
 369
 370
 371
 372
 373
 374
 375
 376
 377
 378
 379
 380
 381
 382
 383
 384
 385
 386
 387
 388
 389
 390
 391
 392
 393
 394
 395
 396
 397
 398
 399
 400
 401
 402
 403
 404
 405
 406
 407
 408
 409
 410
 411
 412
 413
 414
 415
 416
 417
 418
 419
 420
 421
 422
 423
 424
 425
 426
 427
 428
 429
 430
 431
 432
 433
 434
 435
 436
 437
 438
 439
 440
 441
 442
 443
 444
 445
 446
 447
 448
 449
 450
 451
 452
 453
 454
 455
 456
 457
 458
 459
 460
 461
 462
 463
 464
 465
 466
 467
 468
 469
 470
 471
 472
 473
 474
 475
 476
 477
 478
 479
 480
 481
 482
 483
 484
 485
 486
 487
 488
 489
 490
 491
 492
 493
 494
 495
 496
 497
 498
 499
 500
 501
 502
 503
 504
 505
 506
 507
 508
 509
 510
 511
 512
 513
 514
 515
 516
 517
 518
 519
 520
 521
 522
 523
 524
 525



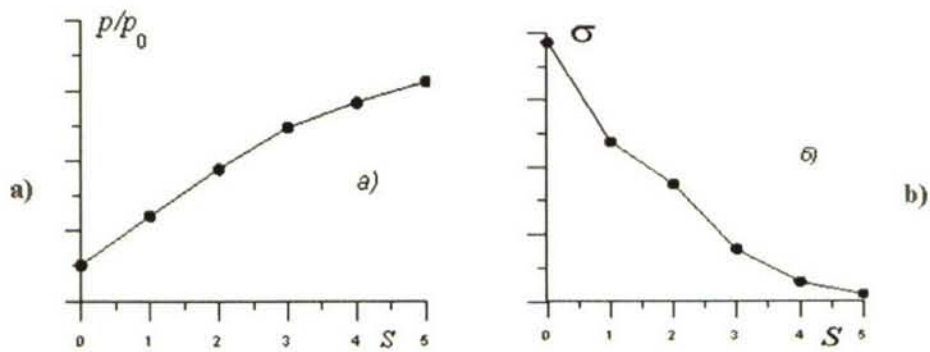
Principal inlet scheme

一、
二、
三、
四、
五、
六、
七、
八、
九、
十、
十一、
十二、
十三、
十四、
十五、
十六、
十七、
十八、
十九、
二十、

Mach number fields

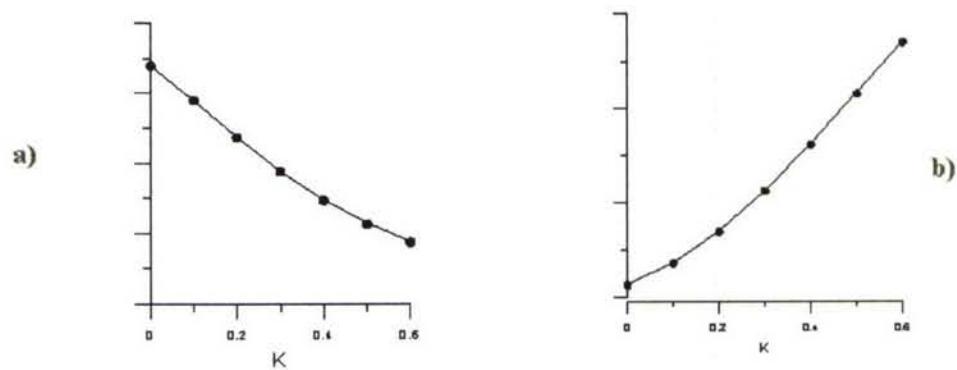


MHD control and inlet performances



Exit / entrance pressure ratio (a)
and total pressure recovery coefficient (b)
vs MHD interaction parameter S

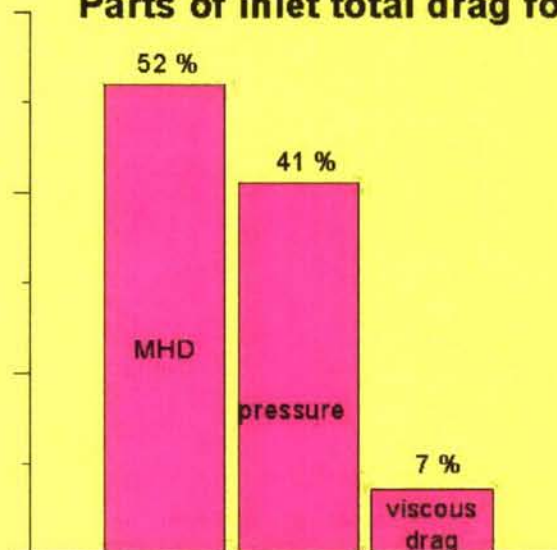
MHD control and inlet performances



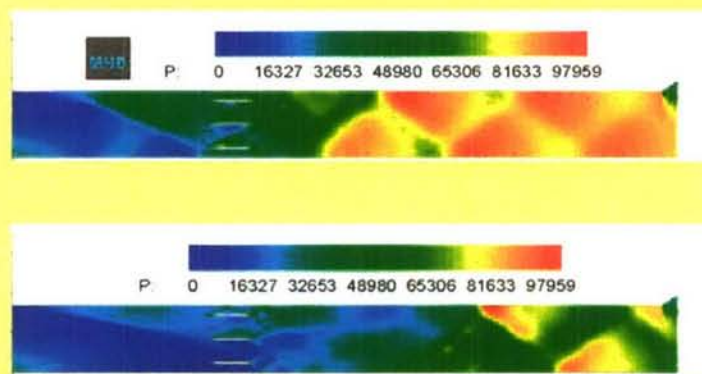
Exit / entrance pressure ratio (a)
and total pressure recovery coefficient (b)
vs load parameter K

MHD control and inlet performances

Parts of inlet total drag force

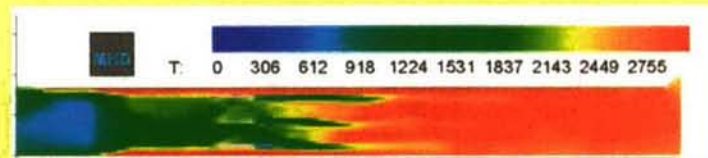


Flow in the channel with combustion MHD control influence



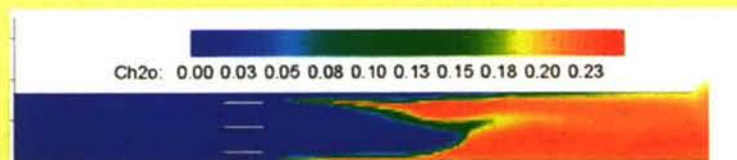
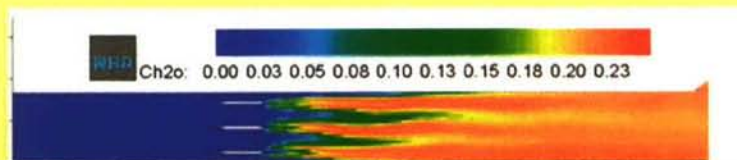
Pressure fields
with MHD control and at its absence

Flow in the channel with combustion MHD control influence



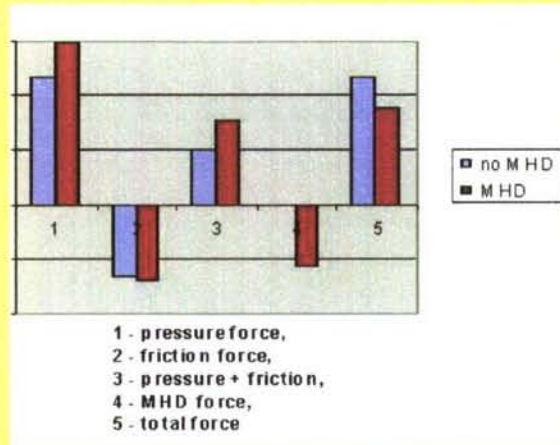
Temperature fields
with MHD control and at its absence

Flow in the channel with combustion MHD control influence



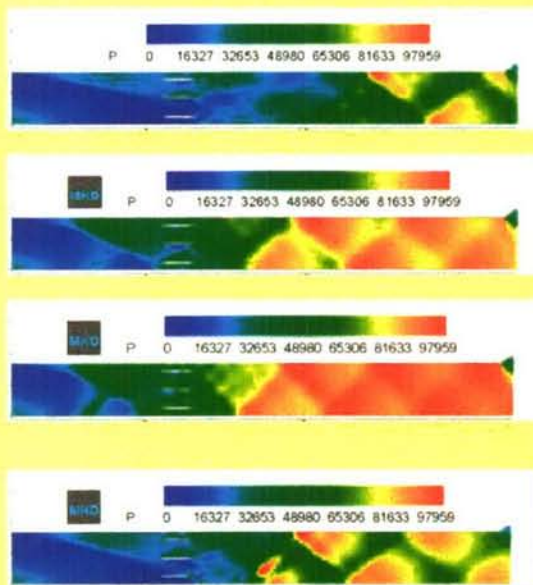
Water mass fraction fields
with MHD control and at its absence

Influence of the MHD control on the forces balance



Positive effect of MHD control on the aerodynamic forces balance (pressure and skin friction).

MHD force negative input has a dramatic effect on the total balance.



S=0

S=2

S=3

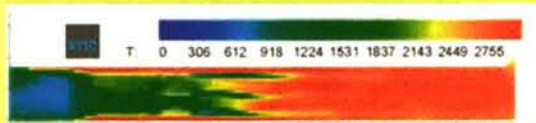
S=2 K=0.5

MHD flow control in the channel with combustion at the variation of parameters defining the MHD influence on the flow

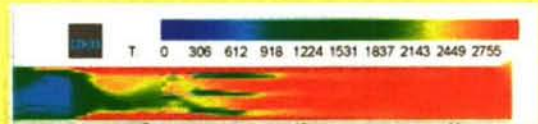
Pressure fields



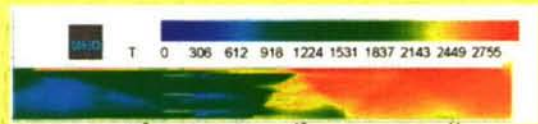
$S=0$



$S=2$



$S=3$



$S=2, K=0.5$

MHD flow control
in the channel
with combustion
at the variation of
parameters
defining the MHD
influence on the
flow

Temperature fields



$S=0$



$S=2$



$S=3$



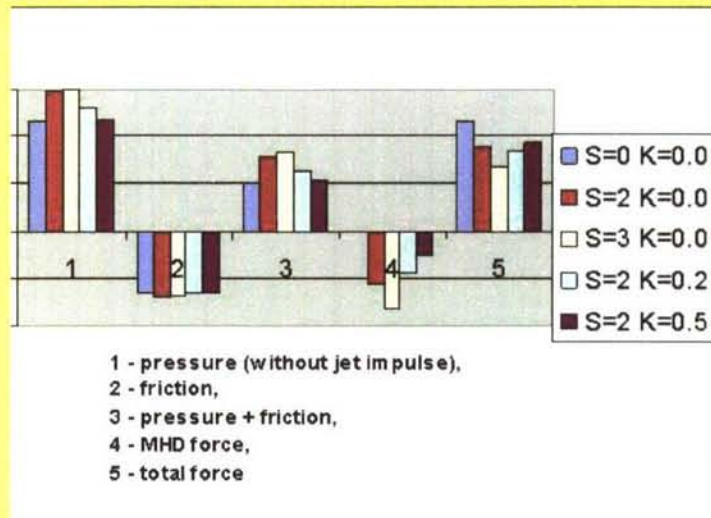
$S=2, K=0.5$

MHD flow control
in the channel
with combustion
at the variation
of parameters defining
the MHD influence
on the flow

Water mass fraction fields

Influence of the MHD control on the forces balance

MHD dimensionless parameters variation



Conclusion

- Numerical investigation of internal and external supersonic MHD flows was carried out
- MHD method allows the possibility to control the deceleration of the flow and exit to entrance pressure ratio in inlet, ignition and flame stabilization at the combustion in high velocity flow
- It is shown that MHD control has a favorable effect on the aerodynamic force (pressure and friction forces sum). The additional magnetic constituent of drag force exceeds (in absolute value) the positive effect in aerodynamic force.

Part 5

COMBUSTION CONTROL

EXCITATION OF INTERNAL DEGREES OF FREEDOM

(VIBRATIONAL AND ELECTRONIC STATES)

OF REACTIVE MOLECULES



Energetic efficiency of different methods of excitation

Excitation of N_2 molecule to vibrational level $N_2(v=1)$ - 0.29 eV

Activation of O_2 molecule to electronic level $O_2(a^1\Delta_g)$ - 0.98 eV

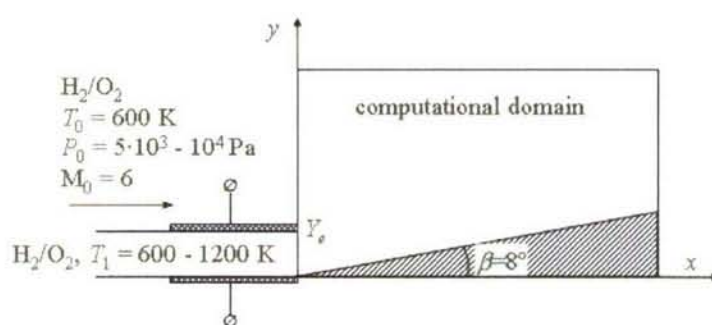
Formation of atoms at the dissociation of O_2 molecule - 5.1 eV

Formation of ions O^+ , O_2^+ , N^+ - more then 12 eV

CIAM INVESTIGATIONS

- Preliminary excitation of vibrational degrees of freedom of reactive molecules (H_2 , H_2O , O_3) in electrical discharge or by resonance laser excitation
- Activation of O_2 molecules in electrical discharge to obtain electronically excited oxygen molecules
- Preliminary activation of electronic states of O_2 molecules by laser resonance radiation
- Laser-induced combustion due to photodissociation of reactive molecules (O_3 , O_2)
- Principle of local influence

The effect of nonequilibrium excitation of molecular vibrations behind shock front



Schematic of the flow and computational domain

The effect of nonequilibrium excitation of molecular vibrations behind shock front

- Kinetic model: 9 reversible chemical reactions
(H_2 , O_2 , H , O , OH , H_2O).

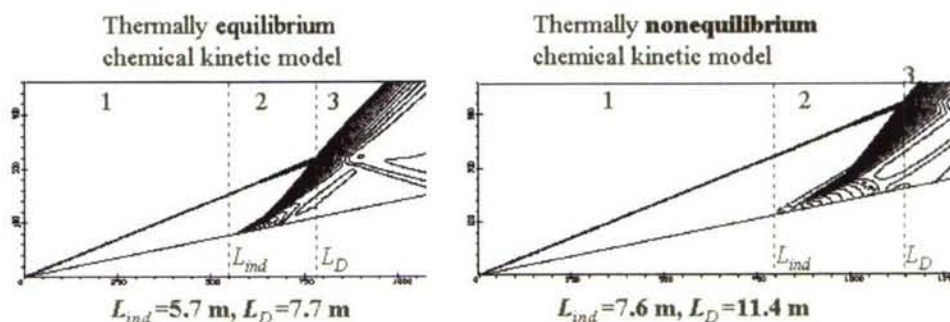
- Two models were considered :

In thermally equilibrium chemical kinetic model it is assumed the equilibrium between translational, rotational, and vibrational degrees of freedom.

In thermally nonequilibrium chemical kinetic model it is assumed that the rotational and translational degrees of freedom of molecules are in the thermodynamic equilibrium, and the local Boltzmann distribution with its own vibrational temperature exists in each mode. The processes of intermode V-V'-exchange and V-T-relaxation are included in this model. Reaction rate constants are the functions of translational and vibrational temperatures. (*Starik and Dautov, Doklady physics, 1996*)

The effect of nonequilibrium excitation of molecular vibrations behind shock front

Pressure fields in the flow of $\text{H}_2/\text{O}_2 = 2/1$ mixture ($P_0 = 5 \cdot 10^3$ Pa, $T_0 = 600$ K, $M_0 = 6$)



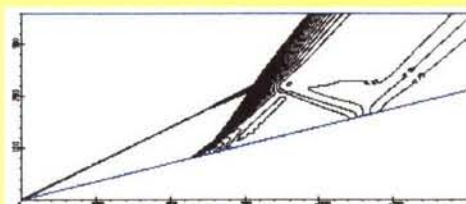
- ☐ In thermally nonequilibrium kinetic model the induction and transition zone lengths are essentially larger than those in the thermally equilibrium model.
- ☐ It is necessary to account for the nonequilibrium effects in molecules vibrations excitation at the detonation initiation

Detonation shock formation on the wedge

Free stream conditions: $M=6$, $P=0.05$ bar, $T=600$ K
Stoichiometric mixture H_2 / O_2

Thermally **equilibrium** chemical
kinetic model

Preliminary excitation of vibrations
of H_2 molecules
Excitation region $Y_{ex}=25$ sm



Pressure



Excitation region $Y_{ex}=5$ sm



Temperature



Temperature



Reaction-step mechanism for H_2/O_2 mixture with electronically excited O_2 molecules

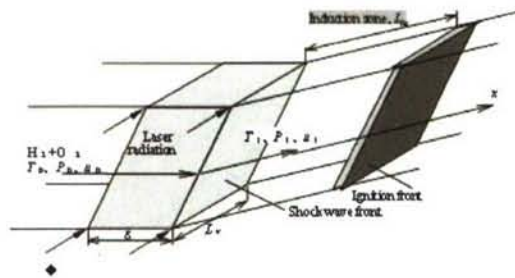
Excitation of O_2 molecules from the main $X^3\Sigma_g^-$
to first $a^1\Delta_g$ and second $b^1\Sigma_g^+$ electronic states

76 reversible chemical reactions with H_2 , $O_2(X^3\Sigma_g^-)$,
 $O_2(a^1\Delta_g)$, $O_2(b^1\Sigma_g^+)$, OH , H_2O , HO_2 , H_2O_2 , O_3 , $O(^3P)$,
 $O(^1D)$, H species

Electronic-electronic exchange between $O_2(a^1\Delta_g)$,
 $O_2(b^1\Sigma_g^+)$ and $O_2(X^3\Sigma_g^-)$ molecules and $O(^3P)$, $O(^1D)$
atoms

Quenching processes for excited particles $O_2(a^1\Delta_g)$,
 $O_2(b^1\Sigma_g^+)$, $O(^1D)$.

Shock Induced Combustion in Supersonic Flow



$$\tau_I = W_I^{-1}$$

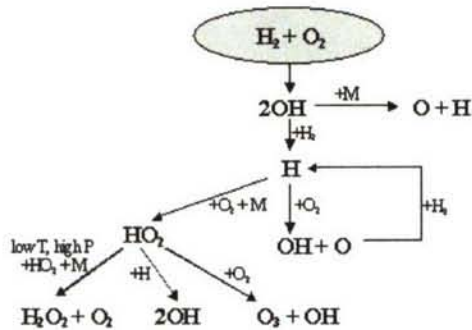
$$\tau_I \ll \tau_R, \tau_V$$

$$\delta \ll L,$$

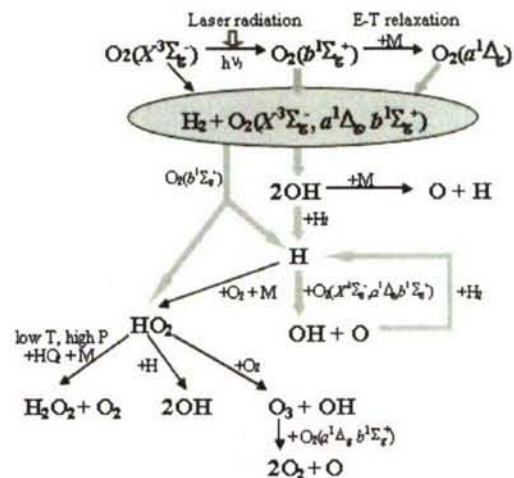
- ◆ Flow Scheme of Laser Shock- Induced Combustion
- ◆ Model for laser irradiation zone
- ◆ Chemical kinetics mechanism

Kinetic Mechanisms of Combustion Initiation in H_2+O_2 Mixture

1. Without preliminary excitation

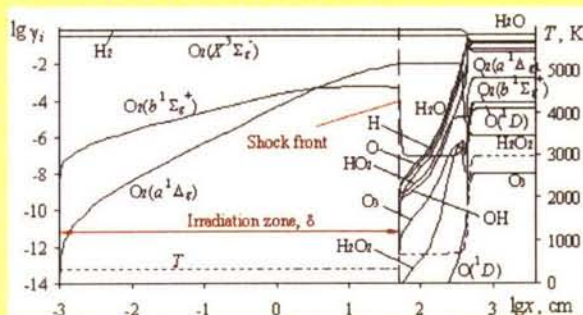


2. Under preliminary excitation of $b^1\Sigma_g^+$ electronic state of O_2 by laser radiation with $\lambda_f=762$ nm

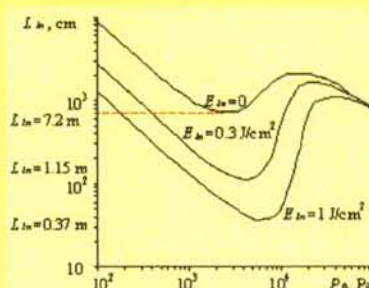


Initiation of Combustion in Supersonic Flow

Evolution of species mole fractions (solid lines) and gas temperature (dotted line) in the irradiation zone and in the reacting zone behind inclined shock


$$\begin{aligned} H_2/O_2 &= 2/1, \\ T_0 &= 300 \text{ K}, P_0 = 10^3 \text{ Pa}, M_0 = 6, \beta = 25^\circ \\ \lambda_T &= 762 \text{ nm} \\ J_0 &= 10 \text{ kW/cm}^2 \\ \delta &= 0.5 \text{ m} \end{aligned}$$

Induction zone length as a function of initial pressure


$$H_2/O_2=2/1$$

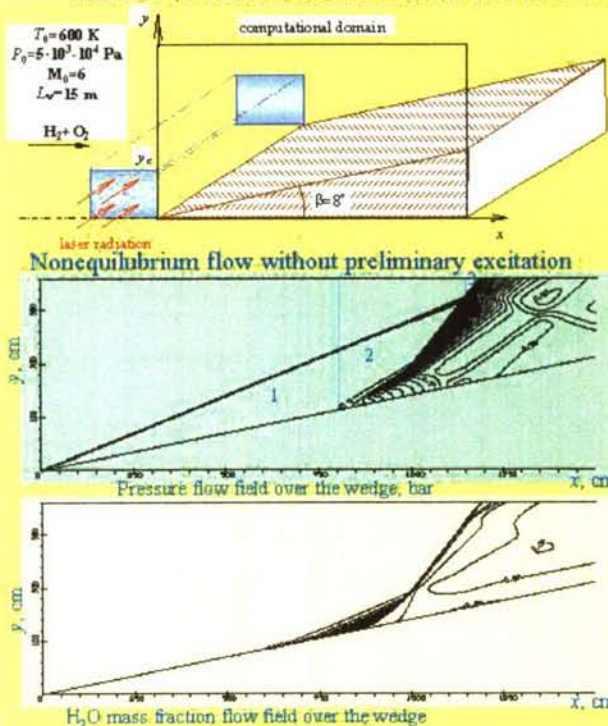
$$T_0=300\text{ K}, M_0=6, \beta=30^\circ$$

$$\lambda_f=762\text{ nm}$$

$$E_{in}=I_0 \cdot \tau_p, \quad \tau_p = \frac{\delta}{u_0}$$

The reduction in L_{in} value due to irradiation at $\lambda_i = 762 \text{ nm}$ for $E_{in} = 1 \text{ J/cm}^2$ may reach a factor of 20-50.

Laser-induced combustion behind the shock on the wedge



The principal scheme of the flow under exposure of the reacting mixture to the resonant laser radiation

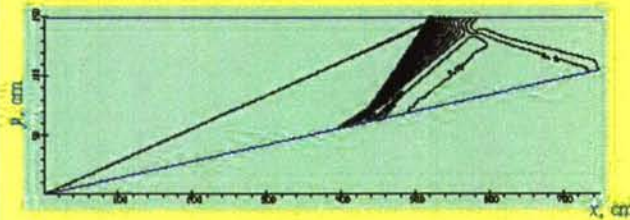
- 1 – the induction region
- 2 – the transition region
- 3 – the detonation region

Free stream conditions

$M=6, P=0.05 \text{ bar}, T=600 \text{ K}$

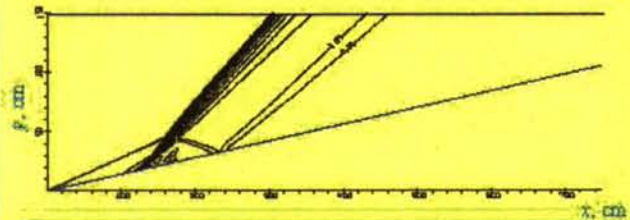
**Vibrational – translational
equilibrium in the free stream,
 $T_j(0)=T(0)$ ($j=1, \dots, 6$)**

Laser-induced combustion behind the shock on the wedge

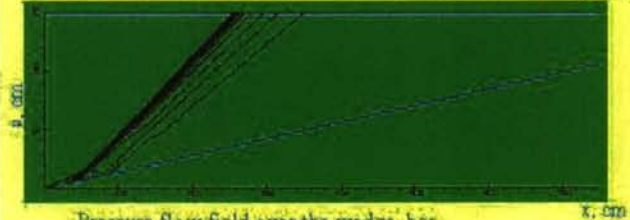


Absence of excitation

$H_2/O_2=2/1$
 $M_0=6$, $P_0=10^4$ Pa
 $T_0=600$ K, $\beta=8^\circ$
 $L_m=4$ m
 $L_d=5.2$ m



$E_s=0.01$ eV/molecule, $Y_{ex}=0.5$ m
 $L_v=15$ m, $L_m=1$ m, $L_d=1.6$ m
 $I_0=10$ kW/cm², $l_p=45$ cm,
 $\lambda_f=762$ nm
 $[O_2(a^1\Delta_g)]=2.46 \cdot 10^{15}$ cm⁻³
 $[O_2(b^1\Sigma_g^+)]=3.8 \cdot 10^{13}$ cm⁻³

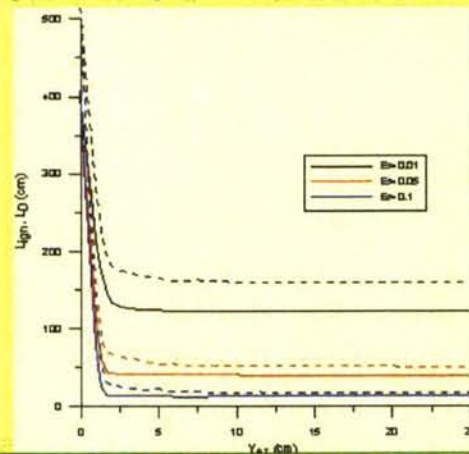


$E_s=0.05$ eV/molecule, $Y_{ex}=0.5$ m
 $L_m=0.23$ m, $L_d=0.5$ m
 $I_0=40$ kW/cm², $l_p=58$ cm,
 $\lambda_f=762$ nm
 $[O_2(a^1\Delta_g)]=1.24 \cdot 10^{16}$ cm⁻³
 $[O_2(b^1\Sigma_g^+)]=3.52 \cdot 10^{13}$ cm⁻³

Pressure flow field over the wedge, bar

Laser-induced combustion behind the shock on the wedge

Dependencies of induction zone and combustion zone lengths (solid and dashed curves) on the radial distance of the irradiation region, Y_{ex} , under exposure of supersonic flow to laser photons with $\lambda_f=762$ nm in front of the wedge apex for different values of absorbed energy E_s .



$H_2/O_2=2/1$ mixture

$M_0=6$, $T_0=600$ K, $P_0=10^4$ Pa, $\beta=8^\circ$

1 - $E_s=0.01$ eV/molecule

2 - $E_s=0.05$ eV/molecule

3 - $E_s=0.1$ eV/molecule

At $E_s=0.01$ eV/molecule and $Y_{ex}=2$ cm the induction zone length is approximately 100 cm. For $E_s=0.1$ eV/molecule the induction zone length is approximately 10 cm.

For generation of the detonation shock in a supersonic flow of H_2+O_2 mixture over the wedge it is sufficient to excite the oxygen molecules in a narrow near-axis region, i.e. in a thin layer adjacent to the wedge. It makes possible to control the detonation in supersonic flow by small energy deposited in the gas.

von Karman Institute for Fluid Dynamics

RTO-AVT-VKI Lecture Series 2007

**ADVANCES ON PROPULSION TECHNOLOGY
FOR HIGH-SPEED AIRCRAFT**

March 12-15, 2007

LAPCAT: HIGH-SPEED PROPULSION TECHNOLOGY

J. Steelant
ESA-ESTEC, The Netherlands

LAPCAT: HIGH-SPEED PROPULSION TECHNOLOGY

J. Steelant

ESA-ESTEC,

Division of Propulsion and Aerothermodynamics

Keplerlaan 1, 2200AG Noordwijk,
Netherlands

Johan.Steelant@esa.int

ABSTRACT

In spring 2005, the EC kicked-off a 3 years long project called LAPCAT: Long-Term Advanced Propulsion Concepts and Technologies to initiate research on propulsion concepts for sustained hypersonic flight. The project, composed of a consortium of 12 partners from industry, research institutions and universities, is coordinated by ESA-ESTEC.

The ambitious mission goal is to reduce travelling time of long-distance flights, e.g. Brussels to Sydney, to about 2 to 4 hours. Therefore advanced propulsion concepts and technologies need to be developed. This requires a new flight regime with Mach numbers ranging from 4 to 8. At these high speeds, classical turbo-jet engines need to be replaced by advanced airbreathing engines. Different combined cycles, i.e. TBCC and RBCC, are evaluated both on system and fundamental research level in combination with a corresponding vehicle system study.

At the writing of this article, the project has passed its midterm review and its achievements up to this point will be highlighted here.

1.0 INTRODUCTION

Tendencies in aeronautics clearly show a continuous increase in air traffic. Based on IATA statistics the international passenger traffic growth increased with 6.8% in February 2006 over 2005 which continues on pace with forecast. Even for long-distance flight such as from Europe to Asia Pacific, IATA's five year forecast shows an annual average growth of 5.9% between 2005 and 2009. This is primarily due to the explosive economic growth in Asia and in particular in China. These long-distance flight taking easily flight times of 16 hours or more to connect two major intercontinental cities, would become more attractive when travel-time would be reduced drastically such that a final destination can be reached within 4 hours or less.

However, with present aircraft and propulsion designs, we're getting close to the optimal design and margins for further improvement are getting smaller. Only drastic changes in aircraft configuration, propulsion concepts and flight velocities are able to achieve these goals.

New aircraft configurations and related propulsion engines presently studied for classical flight Mach numbers around $M=0.9$ look into e.g. blended wing-body configuration for aerodynamic performance and multiple engines mounted on top of the wings close to its trailing edges to improve propulsion efficiency. These interesting developments will decrease further fuel consumption up to 30% but will not enable the shortening of travel times.

New aircraft development seems to be stalled with respect to flight speed, despite the proven technical possibility shown by the supersonic Concorde. Opponents to supersonic transport development always point to the large specific fuel consumption of Concorde which undeniable is roughly twice the value

of present commercial aircraft. However, one should not forget that the specific fuel consumption, sfc , obtained for the first turbojet driven aircraft, e.g. Comet in 1951 were only 20% lower. Since then fuel consumption reduction for aero-engines has been drastically driven throughout time by technology e.g. cooling techniques, new alloys, improved thermodynamic cycles by increased pressure ratios and TIT, etc... As the Olympus 593 engine was based on the Olympus design of 1950 for the Canberra and later for the Avro Vulcan in 1956, it is hence impossible to compare its sfc with e.g. the latest Trent's of R&R or the GE90-family when half a century of technology development has not been implemented in these Olympus engines.

Before given an overview of the LAPCAT goals, some basic considerations about supersonic vs. subsonic flight and its potential for evolution will be discussed. Finally some first results obtained so far within the LAPCAT project will be discussed.

Nomenclature

ATR	Advanced Tactical Fighter
CG	Center of Gravity
CP	Center of Pressure
EoS	Equation of State
ER	Equivalence Ratio
HHV	Higher Heating Value [MJ/kg]
HSCT	High Speed Civil Transport
I_{sp}	Specific Impulse [s]
LHV	Lower Heating Value [MJ/kg]
\dot{m}	air mass flow [kg/s]
\dot{m}_f	fuel mass flow [kg/s]
MTF	Mid Tandem Fan
NGLT	Next Generation Launcher Transportation
OPR	Overall Pressure Ratio
RBCC	Rocket Based Combined Cycle
RTA	Revolutionary Turbine Accelerator
RTD	Research and Technology Development
SST	Supersonic Transport
sfc	Specific Fuel Consumption [kg/s/daN]
TIT	Turbine Inlet Temperature [K]
TBCC	Turbine Based Combined Cycle
VCE	Variable Cycle Engine

Subscripts

a	ambient
cc	combustion chamber
j	jet condition
∞	cruise flight point

2.0 MOTIVATION AND ASSESSMENT

Reducing travel times by going supersonic has only sense on long-distance flights. Range is hence an important figure of merit to evaluate high-speed aircraft concepts. It is strongly dependent on total available fuel mass and its consumption throughout the itinerary, i.e. from taxiing, speed-up cruise and final descent manoeuvres. Among these different parts, cruise represents a major portion of the needed fuel. The range achieved during cruise can be easily derived from the Bréguet range equation:

$$R = \frac{H}{g} \eta \frac{L}{D} \ln \left[\frac{1}{1 - W_F / W} \right] = \frac{V_\infty}{g \text{ sfc}} \frac{L}{D} \ln \left[\frac{1}{1 - W_F / W} \right] \quad (1)$$

where:

R	Range [m]
H	the fuel energy content [J/kg]: 120 (LHV) and 142 (HHV) MJ/kg for H_2 , 43.5 (LHV) and 47MJ/kg (HHV) for kerosene, 50.0 (LHV) and 55.5MJ/kg (HHV) for Methane
g	gravity constant [m/s^2]
η	the overall installed engine efficiency
sfc	specific fuel consumption [$kg/s/N$]
V	flight velocity [m/s]
W	total take-off mass [kg]
W_F	fuel mass [kg]

The range depends linearly on the energy content H in the fuel which can be increased with a factor of 2.7 by switching e.g. from kerosene to hydrogen.

The aerodynamic performance given by L/D in eq. (1) depends primarily on the Mach number and was analyzed by Küchemann [1] who formulated a general empirical relationship referred to as the “ L/D barrier”:

$$\left(\frac{L}{D} \right)_{\max} = \frac{4(M_\infty + 3)}{M_\infty} \quad (2)$$

Further studies optimized waverider designs taken into account viscous effects resulted in better L/D ratio resulting in a shifted L/D barrier (Anderson [2]):

$$\left(\frac{L}{D} \right)_{\max, \text{viscous}} = \frac{6(M_\infty + 2)}{M_\infty} \quad (3)$$

For an increasing Mach range the values are decreasing asymptotically to a value of 4 or 6:

M_∞	0.9	2	4	6	8	10
$L/D_{\max, \text{euler}}$	17.3	10	7	6	5.5	5.2
$L/D_{\max, \text{viscous}}$	19.2	12	9	8	7.5	7.2
η	0.25	0.4	0.57	0.67	0.73	0.77

Table 1: Aerodynamic L/D barrier and overall installed engine efficiency in function of flight Mach number

This decrease of aerodynamic performance with increasing Mach number would inherently exclude long-range supersonic flight as it would be economically not viable. However, the overall propulsion efficiency, defined as

$$\eta = \frac{T \cdot V_\infty}{m_f' H} = \frac{V_\infty}{\text{sfc} H} \quad (4)$$

increases with Mach number for turbojets and ramjets as will be explained further. A first approach, suggested by R.G. Thorne according to [1], is given by:

$$\eta = \frac{M_0}{M_0 + 3} \quad (5)$$

To better understand the increase of the overall efficiency η of an aircraft engine, one can split the term thermodynamically into a thermal and propulsion efficiency $\eta = \eta_t \eta_p$, given approximately for a single jet by:

$$\eta_t = \frac{m'(V_j^2 - V_\infty^2)}{2m_f H} \quad \eta_p = \frac{2V_\infty}{V_j + V_\infty}$$

The thermal efficiency of either compressor or ram-based engines can be approached as a Brayton cycle and hence its efficiency is mainly driven by the combustor temperature T_{cc} to intake temperature T_a ratio. This ratio would be at its optimal point when operating the combustor close to the stoichiometric value. However, for turbojets or turbofans, the rotary turbine components limit this ratio due to material yield strengths to a value of about $T_{cc}/T_a=6$ or $\eta_t = 47\%$.

Typical values for propulsion efficiency of a modern engine at $M_\infty=0.85$ is 48% for a turbojet and 77% for a turbofan with a bypass ratio of 6. The overall efficiency in cruise results into values of 20% to 37% and increases above 40% for larger bypass ratios [3].

For ram- and scramjets, the combustion temperature is not limited by rotary components. Hence higher equivalence ratios are easier to reach and $ER=1$ is presently used in scramjet flight experiments. Hence, the thermal efficiency can reach values as high as $\eta_t = 60-70\%$. The propulsion efficiency is clearly better as the jet/flight velocity difference is rather small resulting into a $\eta_p = 70-90\%$ leading to an overall efficiency of $\eta = 42-63\%$. This large η_p implies that a massive intake needs to be foreseen, which can occupy the complete frontal section of the aircraft in order to provide the necessary thrust given by $T = m'(V_j - U_\infty)$.

As shown above, both factors η and L/D have reverse dependencies on flight Mach number and for a first assessment the combined value $\eta L/D$ can be considered in first order to be constant, i.e. a value of about 3 to 4, at worst only 40% smaller for careful designs. This means that the range is more or less independent of the flight speed and is then only determined by the relative fuel fraction W_f/W and the fuel type.

However, one point of caution should be raised. This general analysis is purely based on the Bréguet range, i.e. cruise flight. However, aircraft's operation and handling largely depends on this performance at take-off and during acceleration. In particular the latter is increasingly more dominant for higher Mach number flights. For example, a practical flight at Mach 5, such as the LAPCAT A2 vehicle, reveals that the acceleration and deceleration entails about 50 minutes each compared to a 2.8h flight. At higher Mach numbers, these phases are becoming even more dominant in the propulsion optimization process not only due to the longer speed-up and slow-down phases, but also to the relatively shorter cruise phase.

Another important point, also highlighted by Cain and Walton [4], is how far one can extend or extrapolate parameters for subsonic transport to supersonic or even hypersonic transport. So far, this first order approximation does not include the effect of changes in structural mass fractions that may be required to cope with the high heating loads during flight. Also the requirement that the plane needs to operate over a wide range of flight Mach numbers, i.e. from take-off to cruise, will demand for a

largely flexible engine, most likely as a variable cycle engine, which sequentially will penalize the concept by a larger engine mass fraction. Related to this is the need for fully integrated design of engine and airframe to obtain a global maximum in efficiency whereas up to now engine and airframe can and are being designed and optimized quite separately.

Despite these concerns, it is worthwhile to assess the performance of a wide range of existing aircraft in the light of the above described logic. Data were mainly obtained from websites of a/c manufacturers or others. Hence, these might not necessarily represent the true values but should rather be taken as indicative.

The specific fuel consumption (sfc) is plotted versus a non-dimensional range defined as R/R_g in fig. 1. R_g is the ultimate anti-nodal point for a final destination, i.e. 20,000km. The Concorde is very competitive in range compared to the aircraft designed in the same period (60's and 70's) e.g. Comet, DC-9,... despite a larger sfc. Ranges for subsonic aircraft designed in the 90's have almost doubled, e.g. MD-11, B767,... This is of course related to the improved aerodynamics, availability of light-weight and high-temperature materials, lower sfc due to higher bypass ratios, higher TIT, etc. Similar improvements can be applied to a successor of the Concorde to improve its sfc or range for the same flight speed: implementation of a bypass ratio of 0.5 to 1 or higher instead of presently none, application of more advanced cooling concepts for turbine blades, use of light-weight heat resistant materials, use of a Variable Cycle Engine rather than using an afterburner or reheat, etc...

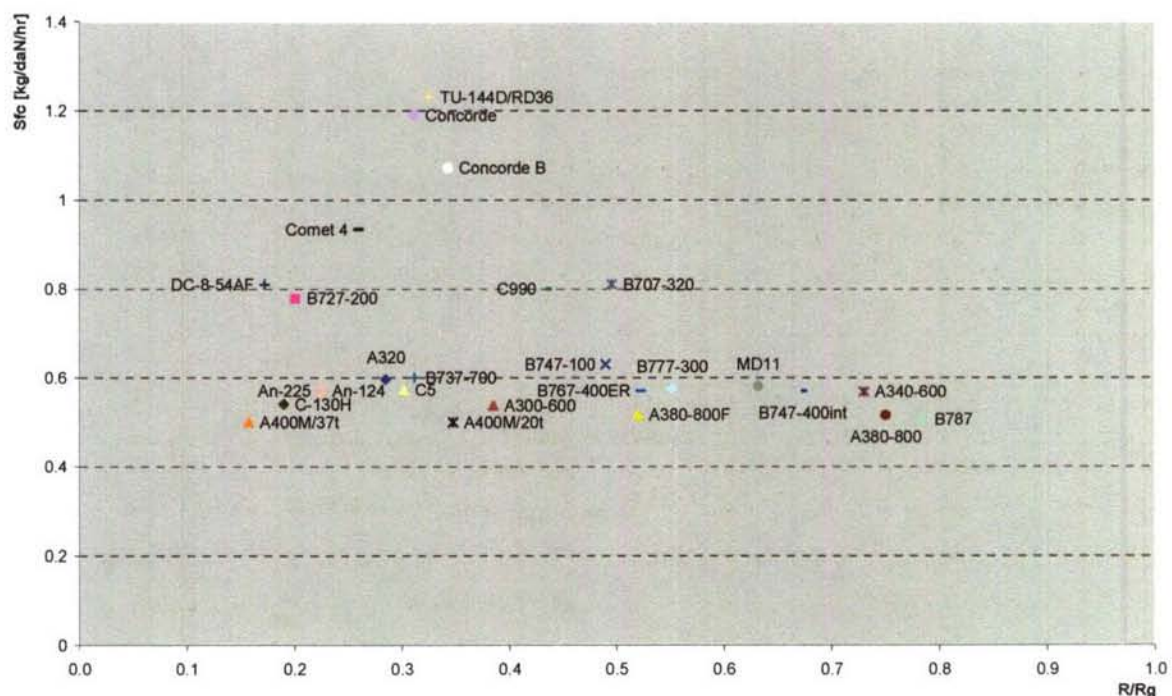


Fig.1: Indicative specific fuel consumption values for various sub- and supersonic aircraft in function of non-dimensional range. A400M is given for two different payloads.

The positive effect of the cruise speed on the overall propulsion efficiency is clearly depicted on fig. 2. Equation (5), represented as a full line, clearly fit the efficiencies of the first designs of their kind for subsonic, e.g. Comet-4 and supersonic commercial vehicles, e.g. Concorde. The formula (5) seems to bound a lower limit. The earlier mentioned 20% efficiency for turbojet and its evolution towards values above 40% for large bypass turbofans seems to be confirmed by the trend observed for commercial aircraft. With respect to fig. 1, this efficiency doubling results inherently in a doubling of the range. Not surprisingly, efficiencies have in particular improved for the heavily used subsonic

aircraft. This is entirely due to massive resources made available to improve this range of aircraft in their aerodynamics' design and engine fuel consumption and not due to intrinsic physical limitations for supersonic transport vehicles.

The aircraft indicated below this line are all supersonic transport vehicles. In order to sustain supersonic flight, these aircraft are equipped with engines which require to be run with afterburning, which is of course thermodynamically inefficient (low η_l). Concorde and TU-144D are however equipped with high thrust engines enabling to sustain supersonic flight without afterburner.

Further improvements were in the planning which would have led to a further efficiency increase away from the lower limit given by eq. 4. Indeed, less known to the public is the start of studies to improve the performance of the Concorde four months after the start of scheduled services in 1976. This project should lead to the Concorde B model. Among modifications on aerodynamics, systems, weight, fuel tanks, the modification on the propulsion unit consisted of replacing the low-pressure compressor by a compressor with increased diameter and the low pressure turbine assembly by a two-stage turbine (fig. 3). The installation of a discharge system to increase the margin of air flow through the engine would result in an increase in air flow which reaches 25 % on takeoff and 35 % during approach. The thrust gains obtained at takeoff and at transonic speeds also make it possible to remove the reheat (afterburner) system with its very heavy fuel consumption and significant addition to the noise generated by the powerplant.

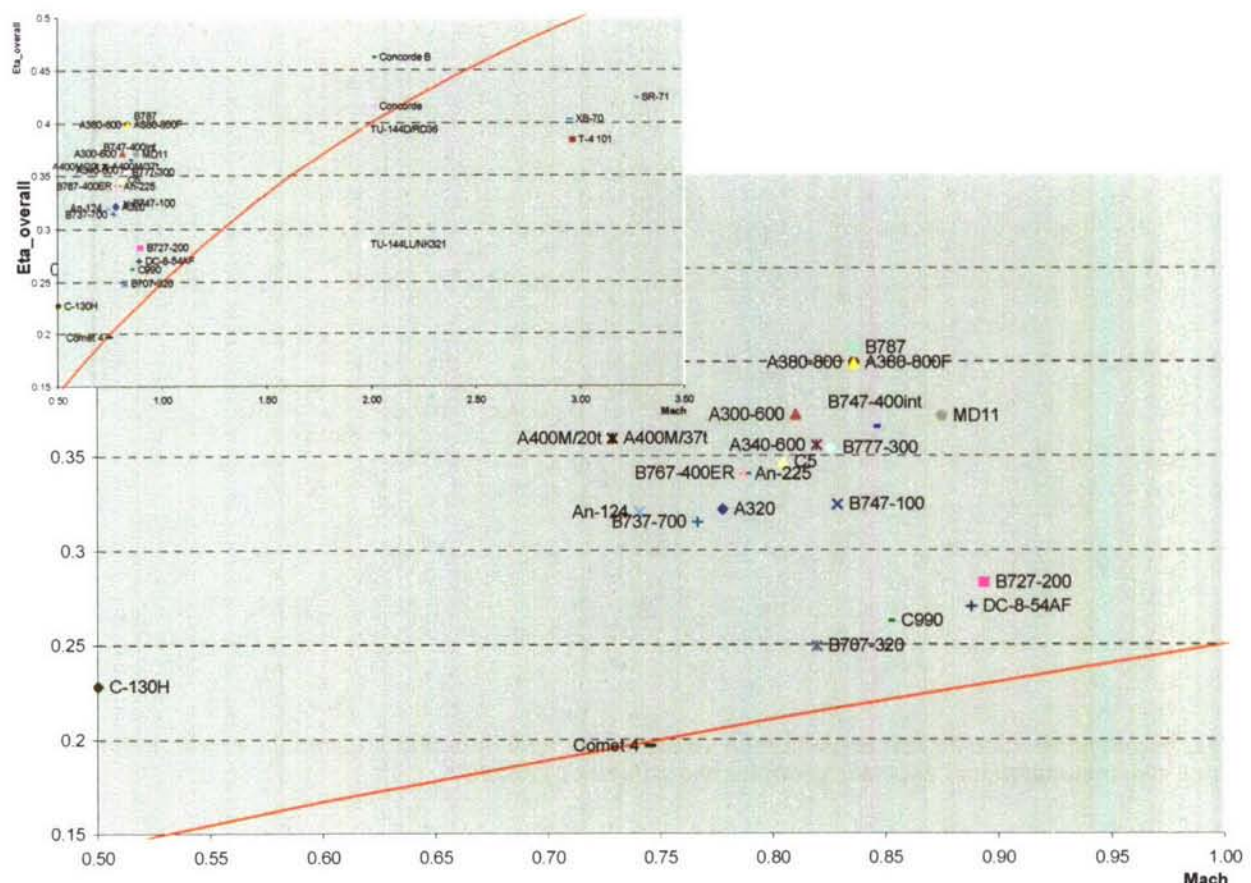


Fig.2: Indicative overall engine efficiencies for various sub- and supersonic aircraft in function of flight Mach number. Eq. (4) is given by full line.

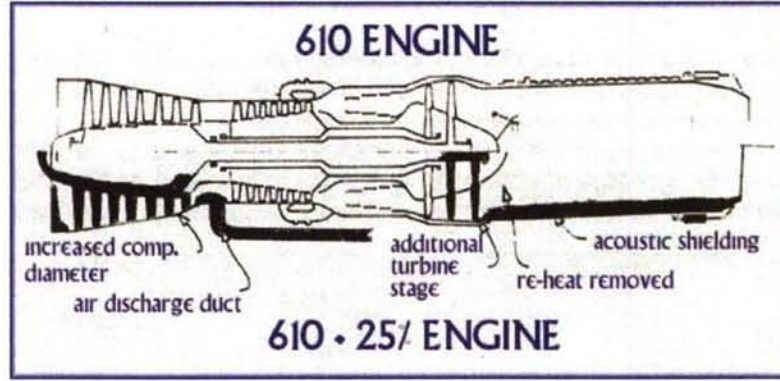


Fig. 3: Suggested improvements (lower part) to the original Olympus (upper part) engine shortly after the Concorde introduction with higher thrust and lower sfc, avoiding the use of an afterburner [5].

Presently, within the military aircraft development, there is an objective to equip their fighters with high-thrust engines to avoid the use of afterburner not only for sustained supersonic flight but also to accelerate through the high-drag transonic flight regime. Examples are the Eurofighter Typhoon and The F-22 raptor. The latter incorporates a pair of new, higher thrust-to-weight turbofan engines, the Pratt & Whitney F119-PW-100, which is designed for efficient supersonic operation without afterburner (called supercruise). The F119 engine develops more than twice the thrust of current engines under supersonic conditions, and more thrust without afterburner than conventional engines with afterburner. Of course, limited data is available related to sfc, bypass ratio, TET, OPR, ... to plot them relatively to the other data.

In [1], a weight breakdown analysis is described for which the total take-off weight W is split into different parts. Items including wings, undercarriage, services and equipment are proportional to the overall weight, i.e. $c_1 W$. Other items are proportional to payload $c_2 W_p$ including fuselage weight, furnishings and the payload itself, hence $c_2 > 1$. Finally we have the engine and fuel weight W_E and W_F . This results into:

$$W = c_1 W + c_2 W_p + W_E + W_F$$

Combined with eq. (1) one can obtain:

$$\frac{W_p}{W} = \frac{1}{c_2} \left[\exp \left(-R \frac{H}{g} \eta \frac{L}{D} \right) - c_1 - \frac{W_E}{W} \right] \quad (6)$$

Evaluating W_E/W from a large range of data (fig. 4), setting this value to 0.05 seems to be a good average. The factors c_1 and c_2 largely depend on the use of state-of-the-art structural materials and are retained here as variable parameters. In fig. 5, the payload fraction W_p/W , i.e. passengers or cargo, for multiple existing aircraft is plotted against the non-dimensional range. These data have been fitted by adapting the structural parameters c_1 and c_2 , along with the propulsion and aerodynamic performance parameter $\eta L/D$ of eq. (6) according to the values given in table 2.

	$\eta L/D$	c_1	c_2
A	4	0.3	2.25
B	5	0.25	2.00
C	5.5	0.2	1.90
D	6	0.15	1.75
E	3	0.35	2.75

Table 2: Parameter sets used for evaluation of future trends

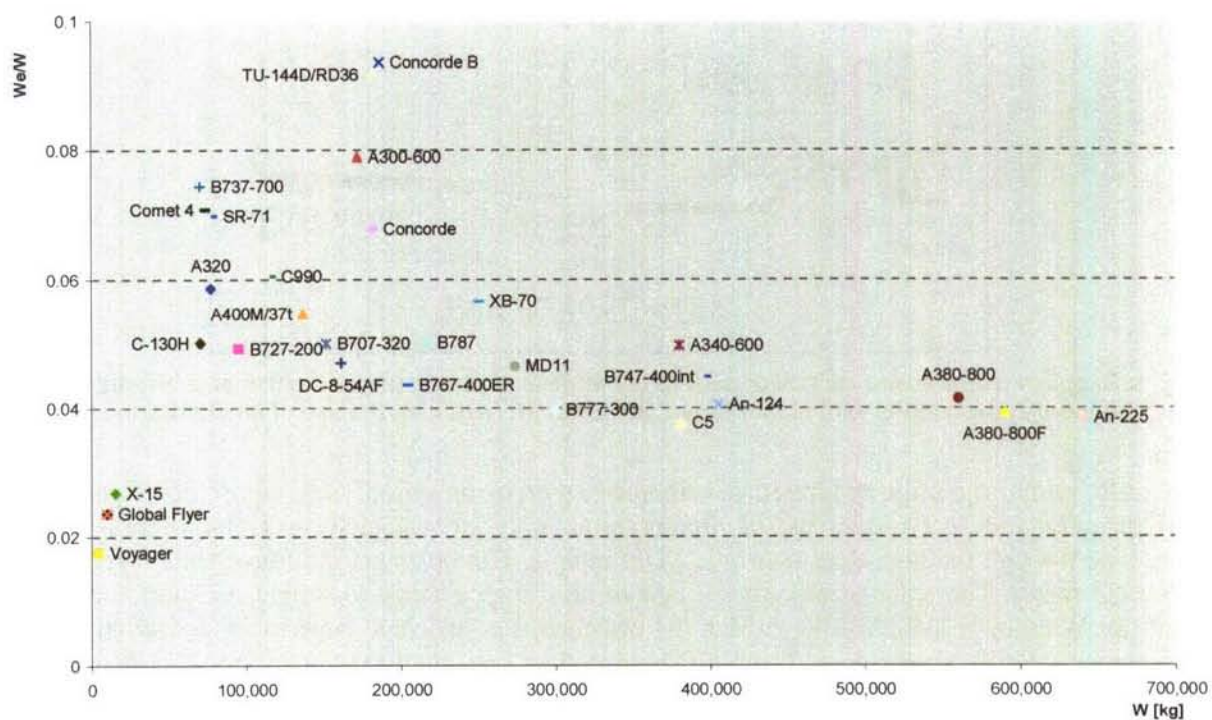


Fig. 4 Indicative engine fraction for various aircraft

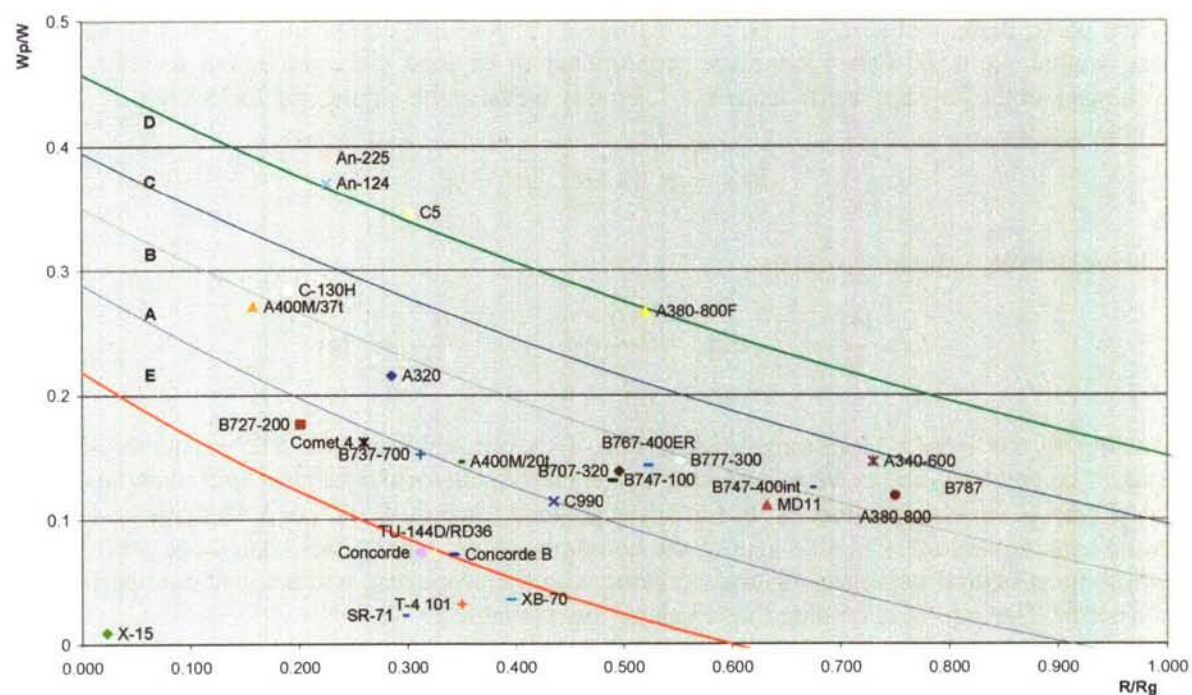


Fig. 5: Indicative payload fraction in function of non-dimensional range for various aircraft. Full lines A to E are based on eq. (6) for structural, propulsion & aerodynamic parameter variation.

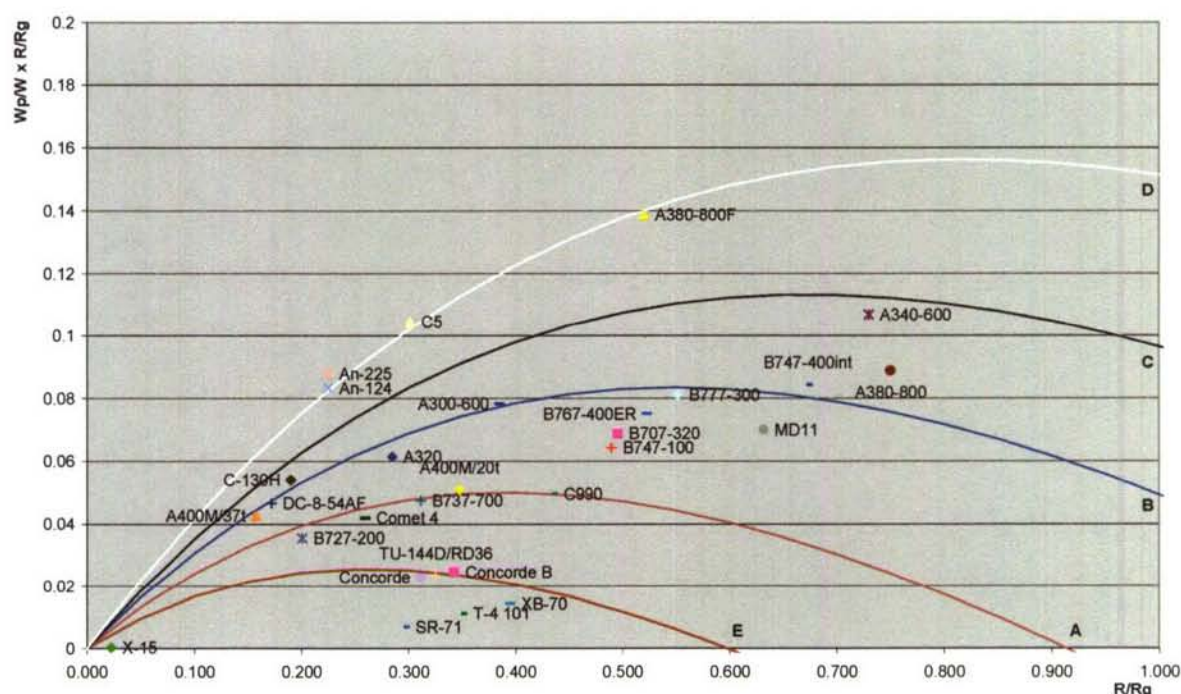


Fig. 6: Seat-km: figure of merit comprising both payload and range for various aircraft

Generally speaking, the payload fraction increases from A to D due to the improved structural and propulsive parameters and demonstrate the technological evolution introduced into the newer airplanes. The line E is definitely lower for the supersonic aircraft which is due to the lower $\eta L/D=3$ versus 4 for the subsonic ones achieved in the same era. Small changes on the aerodynamics, as proposed for Concorde B in 1976, combined with efficiencies of recent engines developed for supersonic fighters, indicate that a recent SST might achieve a performance which lies in between lines A and B.

Another important figure of merit for aircraft is seat-kilometre produced which can be expressed as $W_g/W \times R/R_g$. This is shown in figure 6 along with the fittings discussed previously. Also here the tendencies are well represented by the equations with higher values for the more recent airplanes and the lowest for the obsolete commercial SST.

The still remaining parameter to be discussed is the use of hydrogen as fuel. Studies have been performed in Europe (e.g. Cryoplane) and Russia, but little information is available on the aircraft performance. However, making use of the suggested correlations, the influence of hydrogen as a fuel can be easily assessed. In figs. 7 and 8, the previous parameter settings A, D and E have been applied for a hydrogen aircraft, denoted respectively AH2, DH2, EH2. This is a first approximation as the larger required volume for hydrogen storage will induce a higher drag which is not accounted for. The dashed lines clearly indicate that aircraft have a larger potential in range with still an interesting payload capacity, including SST. Aircraft of lower performance, according to A, have now a potential equivalent for the ultimate range to aircraft of type D by switching to hydrogen. This opens up the potential to reach anti-nodal destination with optimum seat-km already for conservatively designed aircraft.

This motivated the LAPCAT-team to tackle the final technological challenge within aviation: can man travel to the other side of the world within a relatively short time of two to four hours?

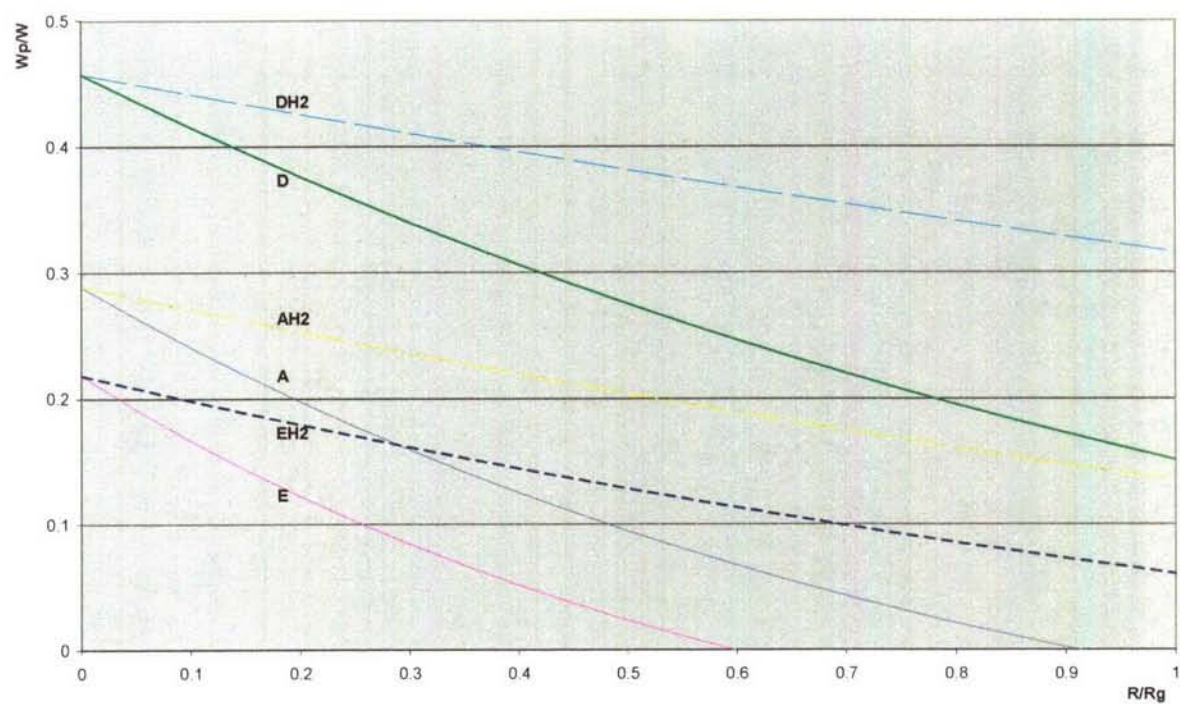


Fig. 7: Payload fraction dependence on fuel type: Kerosene (full), hydrogen (dashed).

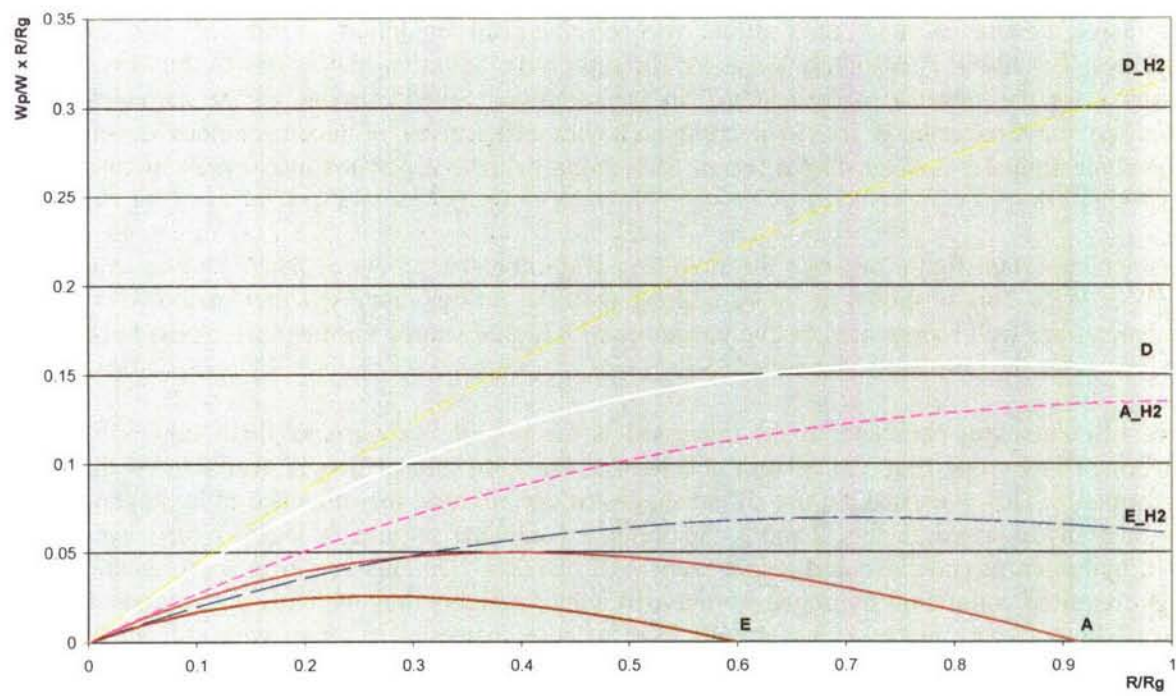


Fig. 8: Seat-km dependence on fuel type: kerosene (full), hydrogen (dashed)

3.0 LAPCAT: PROJECT DESCRIPTION

3.1 High-Speed Propulsion: Introduction

Two types of air-breathing engines for high-speed aircraft have so far been successfully developed: The turbojet and the ramjet. The turbojet, based on active compression, has reached a high state of development and is widespread within the aeronautical world, mainly due to its accelerated appearance in the mid 40's. A supersonic application of turbojets in commercial aviation is the well-known Olympus 593 engine of Snecma/Rolls-Royce used for the Concorde. Another particular application is the reconnaissance aircraft Blackbird SR-71 with an integrated P&W J58 turbojet which has an afterburner fed in part by air vented from the compressor.

The ramjet, based on ram-compression, has found extensive applications in missiles and some experimental aircrafts. The technological transfer towards commercial aviation has been hampered so far due to the lack of an economical driver for setting up a novel and expensive development cycle with adaptation of or new high-speed wind tunnel facilities and flying test beds. The largest stumbling block, however, is the environmental concern (noise) of supersonic planes.

Moreover, thermal aspects limit the flight Mach number for both airbreathing types as well as the flight duration. Even at moderate pressure ratios, turbojets become impractical beyond Mach 3 when using conventional materials and classical thermodynamic cycles. Ramjets are considered feasible up to Mach 7. Beyond this, the increasing stagnation enthalpy prohibits further acceleration of the jet flow due to endothermic dissociation of the combustion products. The consequence is a high loss of energy in the exhaust due to a large amount of unreacted species.

Precooling the airflow as is done by the Japanese ATREX engine only partly alleviates the thermal limit for turbojets. Thermal limits for ramjets, however, are alleviated by keeping supersonic flow conditions in the combustion chamber (scramjets) with corresponding lower static temperature. Major challenges are the reduction of the higher viscous losses and achieving a high combustion efficiency in spite of lower mixing rates and smaller residence time in the combustion chamber. Scramjets have received a great deal of analytical, computational and experimental attention, especially in the USA. The major drive was in connection with the National Aero-Space-Plane (NASP) project from 1984-1995. Recently an experimental flight project with the X-43A or Hype-X has been concluded in the US. A self-accelerated scramjet flight at $M=7$ took place on the 27th of March 2004 as a first step, followed by a Mach=10 flight on November 16, 2004. In France, the "Prométhée" program focuses on a scramjet cruise vehicle using storable propellants. The University of Queensland (Australia), in collaboration with a number of international partners including DLR (Germany) and QinetiQ (UK) performed flight and ground tests for scramjet engines under the HyShot program. Their supersonic combustion flight test in 2002 lasted for 5 seconds during vertical descent at Mach 7.6. At flight altitudes from approximately 35km down to 23km, hydrogen supersonic combustion data were successfully collected. The US-Australian Hypersonics Research Program, HIFiRE, calls for 10 flight tests over five year in the field of hypersonics. Three flights are dedicated towards a scramjet powered waverider above Mach 8.

Ram-based engines cannot accelerate from zero to operating speed without the presence of an integrated accelerator. A TBCC integrates a gas turbine within the ram-duct, whereas a RBCC is based on an integrated rocket engine. The J58 engine of the SR-71 (USA) and also the proposed engine for the Sänger first stage (Germany) are examples of a TBCC. The Revolutionary Turbine Accelerator (RTA) once under development in the USA for the X-43B scramjet flight test program is expected to self accelerate up to Mach 4+. At Jaxa, the Air Turbo Ramjet of a precooled Expander Cycle (ATREX), designed for operation at Mach 6, has completed static conditions at sea-level. All these concepts vary widely in purpose and timeline and hence in vehicle and propulsion concept, development strategy and technology demonstrator.

3.2 LAPCAT: Objectives

In Europe, continuous effort for basic high-speed airbreathing propulsion research has been made at many institutions. However, these efforts are scattered and strongly specialized. The LAPCAT offers the opportunity to practice the indispensable cooperation on European level and to integrate specialized findings into a system to assess the overall relevance and benefits. During the project, system design tools are developed as well as rules and guidelines for conceptual development of system which have not been in place before. The capability to systematically guide a system development process through interface management and to assess its output will be enhanced.

The baseline mission requirement is to reduce travelling time of long-distance flights, e.g. Brussels to Sydney, in about 2 to 4 hours. This requires a new flight regime with Mach numbers ranging from 4 to 8. At these high speeds, classical turbo-jet engines need to be replaced by advanced airbreathing propulsion concepts and hence related technologies need to be developed.

As objectives, two major directions at conceptual and technological level are considered: ram-compression and active compression. The latter has an upper Mach number limitation but can accelerate a vehicle up to its cruise speed. Ram-compression engines need an additional propulsion system to achieve their minimum working speed. Key objectives are the definition and evaluation of:

- different propulsion cycles and concepts for high-speed flight at Mach 4 to 8 in terms of turbine-based (TBCC) and rocket-based combined cycles (RBCC) in fig. 9
- critical technologies for integrated engine/aircraft performance, mass-efficient turbines and heat exchangers, high-pressure & supersonic combustion experiments and modelling.

A sound technological basis will be determined for long-term (20-25 years) to advance innovative propulsion concepts. The most critical RTD-building blocks will be identified employing analytical, numerical and experimental tools to address issues of the following road-map:

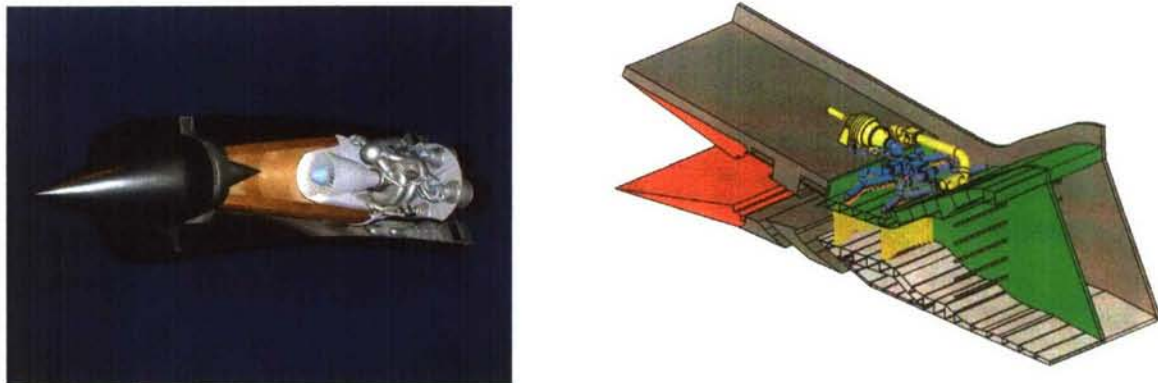


Fig. 9: Turbine Based (Sabre-engine: courtesy REL) versus Rocket Based Combined Cycle (Prepha: courtesy SNECMA).

- Two airbreathing engines for selected reference vehicle(s) and trajectory point(s).
- Dedicated combustion experiments for supersonic and high-pressure combustion, including potential fuels and its interaction with flow-field turbulence.
- Modelling and validation of combustion physics on the basis of chemical kinetics and fuel spray vaporization models and turbulence affecting the combustion.

- Aerodynamic experiments for major engine components (intakes, nozzles, full engines), and establishment of data for interaction of vehicle and propulsion aerodynamics.
- Evaluation and validation of advanced turbulence models to evaluate unsteady, separated flow regimes and to develop transition models based on intermittency related parameters.
- Performance prediction of contra-rotating turbines and light cryogenic fuel heat exchangers.

The three years lasting project will result into:

- Definition of requirements and operational conditions for high-speed flight at system level
- Dedicated experimental data-base specific to high-speed aerodynamics for supersonic and high-pressure combustion and flow phenomena.
- Setting-up and validating physical models supported by numerical simulation tools to address supersonic and high-pressure combustion, turbulence and transition phenomena.
- Feasibility study of weight performance turbine and heat exchanger components

The team consists of 12 partners out of 6 European countries and is coordinated by the European Space Research and Technology Centre ESTEC-ESA in the Netherlands. This involves four industries EADS-Astrium (D), Reaction Engines (UK), Snecma (F) and Cenaero (B); four research institutions being ESA-ESTEC (NL), DLR (D), CIRA (I) and VKI (B) and finally the universities of Rome (I), Stuttgart (D), Southampton (UK) and Oxford (UK).

4.0 PRELIMINARY RESULTS

In order to specify realistic conditions for both the detailed experimental and numerical campaigns, several vehicle systems studies were performed. Two different designs were conceived for a Mach 4 to 5 range on the basis of turbine based combined cycles, either using hydrogen or kerosene as a fuel. This approach was taken in order to capitalise as far as possible on the vast experience now available from turbojet design and operation. For the Mach 8 range, a single vehicle concept was designed on the basis of a rocket based combined cycle where the airbreathing part is done consecutively by a hydrogen fuelled ejector rocket, ramjet and finally scramjet.

The initial work on RBCC mainly concentrated on deriving first performance figures to be used in the context of vehicle pre-design and analysis. This was accomplished by providing net I_{sp} figures over a wide flight Mach number range such that absolute dimensioning could be avoided in the initial absence of requirements derived from a vehicle concept.

4.1 Vehicle and Propulsion System Studies based on TBCC

The project objective was to examine two turbine based cycle (TBCC) engine concepts for high Mach number (4 – 5) flight in the context of future civilian transportation. The experience accumulated from turbojet design and operation is huge and this should obviously form the basis of the next generation of engines if at all possible.

Using the engine concepts, vehicles were defined and their aerodynamic performance optimised. These were incorporated into trajectory models together with subroutines of the engine performance to derive scaled performance and formed the basis of estimating vehicle size and mass. The nominal mission was to fly economically from Brussels to Sydney in approximately 4 hours.

4.1.1 Hydrogen Precooled Turbo-Ramjet

The first study focused on a precooled Mach 5 engine, named Scimitar, employing a cycle based on the Reaction Engines SABRE spaceplane engine and fuelled by liquid hydrogen. The Scimitar engine

must have good subsonic and supersonic performance if it is to be a practical engine for a new generation of hypersonic aircraft. This would allow it to operate from normal airports and over-fly inhabited regions without the nuisance and political problems which limited Concorde's effectiveness. These characteristics have been successfully incorporated into the Scimitar design (fig. 10) by incorporating a high bypass fan into the bypass duct which encloses the core engine and is otherwise needed to match the intake air capture flow to the engine demanded flow over the supersonic Mach number range. The bypass fan is driven by a hub turbine using flow diverted from the core engine nozzle. The flow then discharges into the bypass and mixes with the bypass flow. More details on the engine and its thermodynamic cycle are given by A. Bond [6].

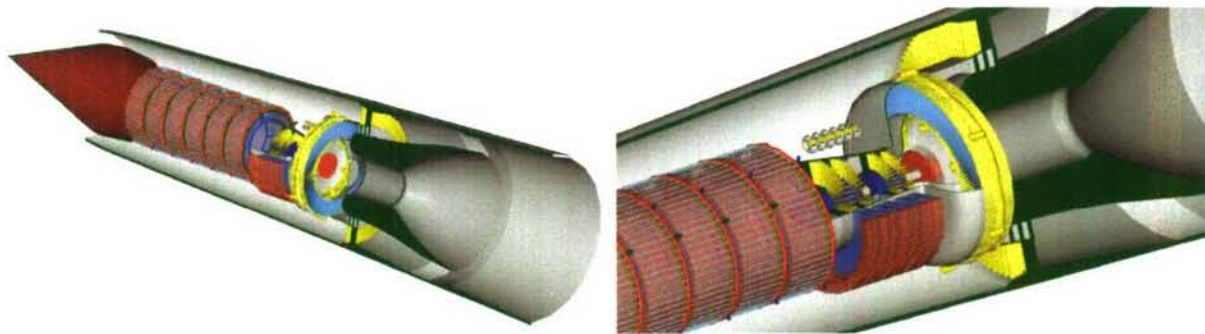


Fig. 10: Scimitar: pre-cooled Turbofan-Ramjet engine for LAPCAT A2 cruiser.

Due to their central role to the concept of the pre-cooled engine two technologies are being addressed at experimental level: a lightweight heat exchanger and contra-rotating turbine.

The air pre-cooler is a metallic tubular matrix with the captured intake air in cross flow over a helium cooled small diameter (1.0mm) tube bank. The Scimitar power cycle depends on maintaining a constant top-cycle helium temperature at around 1000K. The preburner is needed to heat the helium leaving the pre-cooler exit at low flight Mach numbers when the captured air enthalpy, and therefore the helium temperature also, is low. The pre-cooler heat exchanger is a smooth plate Silicon Carbide surface in order to minimise the pressure loss on the combustor gas side. It is intended to design, manufacture and test heat exchanger technology associated with the high temperature part of the engine cycle.

The design of the tubular surface test items has been done and oxidation trials of Inconel 718 tube material has been completed. Strength problems have been identified at high temperature with the metallic materials and further manufacturing contracts have been placed to address these. The SiC technology is in the early stages of development.

It is intended to design, build and test a stator-less contra-rotating model turbine which is aerodynamically similar to the real turbine driving the turbocompressor of the Scimitar engine concept. The real turbine runs on high pressure (200 bar) hot (1000K) helium with a power output of over 60 MW. It is impractical from a cost aspect to carry out aerodynamic testing on representative components on the real fluid at this preliminary design stage. The model will therefore be run on a low pressure high molecular weight gas which can simulate the high pressure helium used in the engine. REL prepared an initial scoping design for the turbocompressor of the real engine for which VKI have optimised the aerodynamics. CENAERO has performed 3-D optimization of the VKI design for Helium flow. 3-D optimization for the Argon scaled model is currently underway.

The test program will begin in 2008 and demonstrate that very efficient ultra-compact turbines are feasible for applications in hypersonic aerospace engines. The Scimitar engine analysis suggests that it can produce efficient supersonic and subsonic flight and meet the anticipated noise regulations for normal airport operation.

An important side result is the critical role of environmental impacts, specifically NO_x, contrails and Ozone damage. These may prove to be one of the most significant potential obstacles to scheduled hypersonic civil aviation and a literature search showed that they played a large part in the USA's decision in the early 1970s not to pursue a Concorde-like aircraft at that time. The Scimitar engine as configured in the current design would be unacceptable for its NO_x production although some options exist for reducing the NO_x at a performance penalty. Future studies need to include these problem at the outset to avoid naïve results and the expenditure of considerable resources on studying projects which are ultimately not viable. The studies in this area are complete for the current project.

4.1.2 Hydrogen Mach 5 Cruiser

4.1.2.1 Vehicle

The LAPCAT A2 vehicle flying at Mach 5 was carried out by Reaction Engines. The preliminary results of this analysis are encouraging. The vehicle study is complete at initial project study level and indicates that a 400ton, 300 passenger vehicle could achieve antipodal range without marginality. The concept is particularly interesting for this mission requirements as a trajectory optimization allowed to fly almost continuously over sea and avoiding sonic boom impact when flying over land.

The proposed aircraft Configuration A2 is shown in Figures 11-12. The vehicle consists of a slender fuselage with a delta wing carrying 4 engine nacelles positioned at roughly mid length. The vehicle is controlled by active foreplanes in pitch, an all moving fin in yaw and ailerons in roll. This configuration is designed to have good supersonic and subsonic lift/drag ratio and acceptable low speed handling qualities for takeoff and landing. A leading edge sweep angle of 55 deg was chosen as roughly equivalent to the Concorde value and known to be the minimum necessary to generate a stable separated vortex at high AOA. A thickness/chord of 3% was selected as typical of supersonic cruise vehicles. An achievable takeoff wing CL of 0.59 gives a minimum wing area of 900 m² for a takeoff mass of 400 tonnes. A fuselage diameter of 7.5 m was chosen to trade a small increase in drag for a saving in fuselage mass. The resulting fuselage is much longer than existing aircraft at 139m.

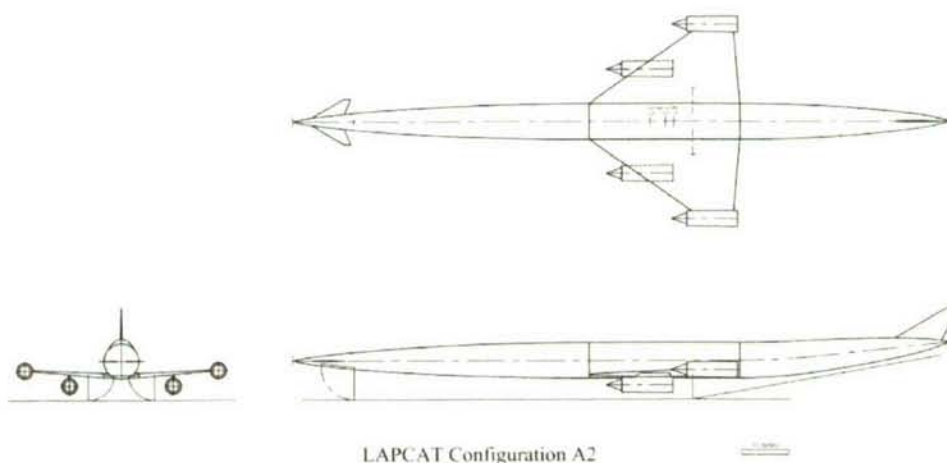


Fig. 11: LAPCAT A2: configuration for a Mach 5 TBCC vehicle based on hydrogen



Fig. 12: Artist's impressions of LAPCAT A2. Left: Mach 5 hydrogen fuelled cruiser for 300 passengers with a MTOW of 400tons; right LAPCAT A2 compared with A380.

The flight deck and passenger compartment (arranged in two decks) occupies a length of about 32 m and is located over the wings on the vehicle centre of gravity. Unlike conventional airliners hydrogen storage within the wings is not feasible since the wing volume is too small. Consequently the liquid hydrogen occupies the remainder of the fuselage volume and is split into two large pressurised tanks either side of the passenger compartment. This permits circular cross section tankage which minimises insulation and pressure vessel mass.

The vehicle has 4 engines (for redundancy), which are mounted in separate axisymmetric nacelles on the wing. Currently two engines are located on the wingtips whilst the remaining two are located within inboard nacelles located under and ahead of the wing leading edge. Physically separating the nacelles reduces the possibility of a mechanical failure in one engine causing damage to the adjacent engine, and also causes less aerodynamic disruption when an engine is shutdown or unstarts. Carrying the engines on the wing gives good CP/CG matching and is structurally efficient, whilst the alternative option of mounting the engines on the fuselage incurs the penalty of a large boundary layer diverter and acoustic fatigue of the fuselage skins. Locating the engines at the rear of the fuselage would pull the vehicle centre of gravity too far back. The wing tip mounted engines generate a large yawing moment if one is shutdown however calculations indicate that the all moving fin is capable of controlling the vehicle since it is acting at a large moment arm.

Normally the engines of supersonic cruise vehicles are mounted underneath the wing towards the trailing edge which permits the designer to capitalise on precompression and allows the nozzle to discharge aft of the wing trailing edge. However at Mach 5 the wing shock wave is at an angle of only 8.9 deg relative to the wing lower surface, which would necessitate moving the nacelle aft until the intake face was behind the wing trailing edge. Therefore this approach is structurally impractical and would scrape the nacelles on the runway during takeoff rotation. Consequently the nacelles are positioned with the intake face ahead of the wing shock wave in relatively freestream conditions, which has the added advantage that no wing boundary layer has to be dealt with. The inboard nacelles are mounted underneath the wing to reduce wing skin acoustic fatigue damage. The main disadvantage of the inboard nacelle location is that the nacelle cross section is introduced ahead of the wing maximum thickness which is counter to normal area ruling practice and will increase transonic wave drag.

4.1.2.2 Routes

Commercial civil transport aircraft, flying subsonically, normally follow a "great circle" route between the airports of departure and arrival, once they are clear of local traffic. However in the case of supersonic aircraft there is the complication of the "sonic boom", or ground overpressure produced by

supersonic flight. Various tests show broad agreement that an overpressure below 50 Pa is tolerable for regular overflights of populated areas (although there appears to be no safe level which will eliminate complaints). Unfortunately practical civil transports produce overpressures above this level. For example Concorde generated an overpressure of about 93 Pa, which restricted supersonic flight to over water regions only and effectively reduced its commercial viability. Current overpressure estimates for the LAPCAT configuration A2 vehicle suggest that at the start of Mach 5 cruise the overpressure will be about 85 Pa under the ground track, reducing to about 70 Pa at mid cruise. Therefore preliminary route planning for the LAPCAT vehicle has assumed that supersonic flight is only possible over regions of very low population density (oceans and the North and South Poles). The possibility of overflying desert regions (eg: central Australia or the Sahara) has been ignored although this may be feasible following international negotiation. This philosophy will give a "worst case scenario" for the range requirement – in the event that the vehicle will be able to fly over land the distances traveled will obviously be smaller.

The Brussels to Sydney route was adopted as the baseline mission. This was seen as a sensible starting point in that it requires extreme range and would greatly benefit from hypersonic speeds in significantly reducing flight times. Nevertheless, other potential routes of interest are evaluated in table 3. Some of the routes are depicted in the figs. 13 to 16.

Route	Subsonic aircraft	Mach 5 aircraft
Brussels – Sydney	22.25 hours ¹	3.8 hours ^{2,6}
Brussels – Los Angeles	10.0 hours	2.5 hours ²
Brussels – Tokyo	10.75 hours	2.5 hours ²
Brussels - New York	7.5 hours	1.6 hours
Brussels - Beijing	8.9 hours	4.9 hours
Brussels - Delhi	7.2 hours	5.3 hours
Paris - Kourou	7.9 hours	1.7 hours
Los Angeles - Tokyo	9.75 hours	2.0 hours
Los Angeles - Sydney	13.4 hours	2.6 hours
Los Angeles - Singapore	15.7 hours	3.0 hours
Los Angeles - Delhi	14.3 hours	7.5 hours

Table 3: Approximate Flight Times: 1) Includes 2 hour refuelling stop; 2) Assumes supersonic overflight of the Bering Straits; 3) No wind (jet stream) effects; 4) No "airport flight stacking" (i.e. straight in approaches); 5) Nominal ascent/descent times and distances; 6) Detailed trajectory modelling indicates 4.6 hours due to longer ascent/descent times than initially forecast.

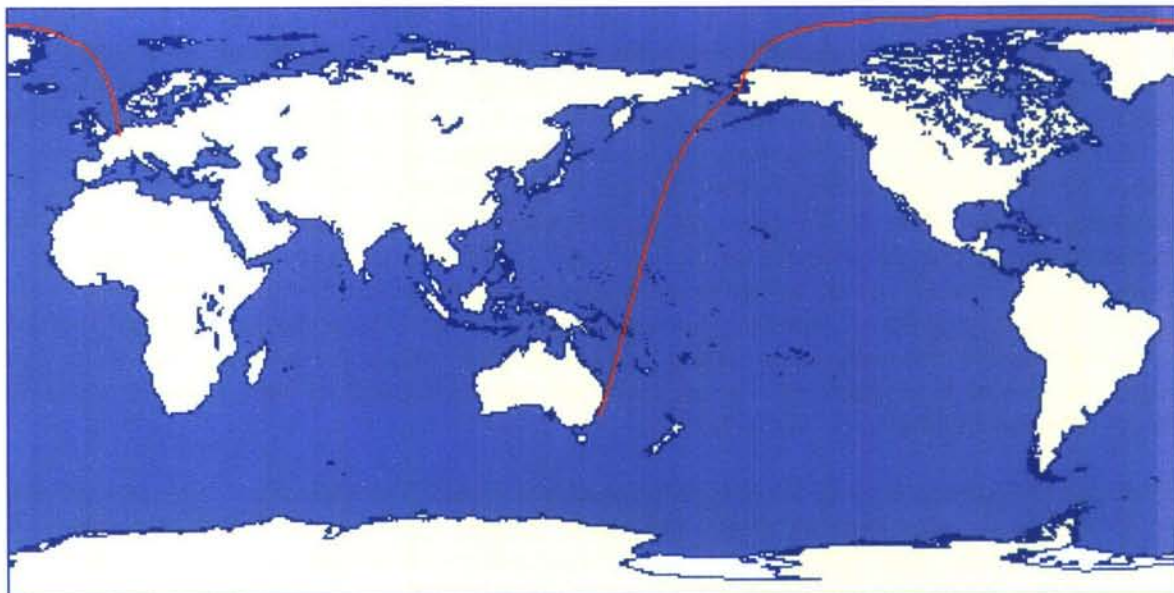


Figure 13: Brussels to Sydney via Bering Strait (18,728 km)

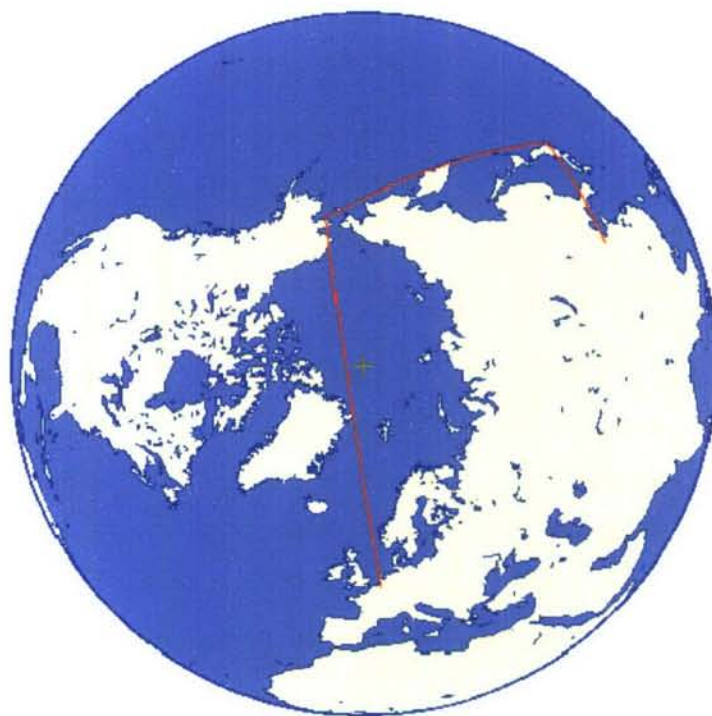


Figure 14: Brussels-Beijing via Nome and Tokyo (14,100 km)



Figure 15: Los Angeles-Sydney (12,071 km)



Figure 16: Los Angeles-Delhi via Singapore (18,256 km)

4.1.2.3 Development plan and economics

To address the relatively high technical risk of this project it is proposed that the development program proceed in a step by step basis in 3 phases, namely Concept Validation (2 years), Technology Demonstration (3 years) and System Development (8 years). At the end of each program stage the project would be reviewed before deciding whether to proceed with the next stage. An arbitrary start date of 2010 has been assumed which implies an Entry Into Service date at the beginning of 2023.

The predicted engine development cost in 2006 prices is 8,147M€ and vehicle development cost 14,454M€ to give a total development cost of 22,601M€. The first vehicle production cost is 979M€. Assuming an 85% learning factor and a total production run of 100 vehicles implies an average vehicle sale price of 639M€ (including full development cost recovery).

The estimated annual operating cost per vehicle is 553.8M€ of which the liquid hydrogen fuel comprises 83%. This assumes hydrogen derived from electrolysis of water however hydrogen derived from steam reforming of hydrocarbons would be about 1/3rd the cost which would roughly halve the annual operating cost.

The A2 vehicle should carry about 148,000 passengers per year assuming 2 flights per day, 90% availability and 75% load factor. This implies an average one way ticket price to Australia of 3940€ in 2006 prices. This compares with a current Business class ticket of around 4060€ and First class ticket of 5075€. Therefore in principle the A2 vehicle could capture all of the current business and first class traffic due to the greatly reduced journey time of 4.5 hours compared to the current 22 hours (assuming subsonic carriers do not drop their prices in competition). The ticket prices would roughly halve (2000€) if the hydrogen is produced by steam reforming. This analysis assumes no hydrogen subsidy, however in reality it is likely that the first generation of hydrogen fuelled aircraft would be subsidised to promote the switch to a more environmentally friendly fuel.

Unlike Concorde the A2 vehicle has exceptional range (both subsonic and supersonic) and is therefore able to service a large number of routes whilst simultaneously avoiding supersonic overflight of populated areas. Its good subsonic performance enables it to service conventional subsonic overland routes thereby increasing its sales potential to airlines.

4.1.3. Kerosene Variable Cycle Engine

An parallel study carried out by DLR-Sart [7,8] focuses kerosene as a fuel in order to explore the performance of this fuel in preference to hydrogen since its supply infrastructure is well established.

In section 2, it was identified that turbfans are most efficient in subsonic flight whereas turbojets are better suitable for supersonic flight as their dry thrust drops far more slowly than that of a fan with increasing vehicle airspeed. A supersonic aircraft would profit of an engine which combines both performances: one for supersonic cruise flight and the other for take-off and landing as well for subsonic cruise over densely populated areas. This demands for a Variable Cycle Engines (VCE) might offer a good compromise for such applications where the specific thrust is low at low altitude flight and subsonic cruise, but is forced high during supersonic cruise and acceleration.

In [8], Sippel made a comprehensive overview of VCE which is repeated here. Recently the US was aggressively pushing this technology for military and space function (RTA, Revolutionary Turbine Accelerator) [9, 10]. The cycles are based on a suitable arrangement of the fan stages and variable bypass flows. The MTF (Mid Tandem Fan) type VCE engine has been studied in Europe by Rolls Royce and Snecma in the early 1990ies [11].

Based on development work for the GE-21 [12], the YF120 is a variable cycle engine capable of adjusting its bypass ratio to the optimum for a given flight regime [13]. The F-120 can be seen as one of the most advanced jet engines ever flown in the YF-22 and YF-23 ATF test airplanes. Another VCE project has been the Revolutionary Turbine Accelerator (RTA) as the TBCC demonstration project in the NGLT program of NASA (fig. 17). Designated as the GE57 by General Electric (GEAE), the RTA engine represents a unique variable cycle engine where internal flowpath changes allow for high I_{sp} throughout the flight trajectory for an accelerator vehicle [9,10].

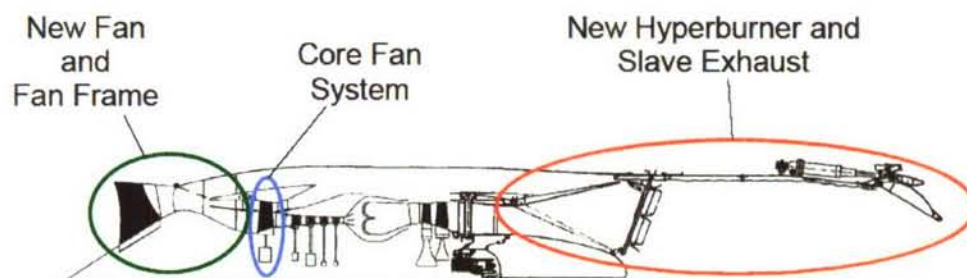


Fig. 17: General Electric RTA-1 (GE-57) cut view [9]

Three different variants of advanced variable cycle engines have been conceptually designed for the LAPCAT supersonic airliner. All are double bypass turbofans principally similar to the RTA-1 design, however adapted to the mission and thrust requirements of the LAPCAT-M4. The major differences of the three concepts are in the number of fan or compressor stages and their OPR. A RAM burner is integrated with the convergent divergent nozzle in all variants. The different concepts are evaluated in depth by Sippel [8]. The discussion below is however limited to the one selected as most optimal for the M=4.5 vehicle.

The LAPCAT VCE-214 is a variable cycle incorporating a two stage fan with large blades mounted on the low pressure spool. The first bypass flow is controlled by the first variable area bypass injector (VABI). This device is followed by the core section, starting again with a single stage fan (core driven fan stage CDFS). After the second VABI the four stage core compressor delivers the remaining air into the combustion chamber. A single stage HPT is followed by a single stage LPT and the bypass flow is again controlled by an aft VABI to achieve mixing with the core flow in the complete flight regime.

The more complicated lay-out of the VCE allows an adaptation of the different compressors more or less independently of each other. This feature can be used at higher supersonic Mach numbers. Around Mach 2.5 these engines are switching to an operation mode in which the first fan is transitioning to windmilling. At Mach 3 the low pressure spool is in full windmilling, thus temperature and pressure of the incoming air is no longer altered by this component. The turbofan is operating in double bypass mode with small bypass ratios λ_1 and λ_2 and still at its maximum TET of 1950K and a OPR of 28 without reaching the compressor exit temperature limitation of 1000 K. The first VABI is opened with λ_1 approaching 0.85. The VABI2 is kept slightly open. The core engines of VCE will be closed beyond the Mach 3.5 trajectory point and the complete air-flow is directed through the bypass duct to the RAM chamber. Technical solutions for the practical design of such a TBCC might become very challenging. Some preliminary proposals will be investigated in later LAPCAT work. A thermal environment around 1050 K for the windmilling LP-Fan during the several hours of RAM cruise could raise problems. In case of the turbojet these design challenges might become even tougher and a switch to two separate flow passes might be necessary. The RAM cycle performance is presented in reference [14]. The maximum combustion temperature is limited to 2100 K as for the afterburner. This high value is used during the acceleration phase and can be significantly reduced when reaching the cruise flight. Depending on the remaining airliner weight, the combustion temperature is reduced in steady cruise to values between 1850 K and 1700 K. The lower thermal loads ease somewhat cooling concerns because no cryogenic fluid for active cooling is available. Further optimisation is ongoing related to the engine and the intake design. The latter is performed numerically by CENAERO.

4.1.3. Kerosene Mach 4.5 Cruiser

4.1.3.1 Vehicle

The preliminary design of the LAPCAT-M4 vehicle [14] is based on a critical recalculation of a 1990 NASA Langley and Lockheed study [15] of a 250-passenger, Mach 4 high-speed civil transport with a design range of 6500 nautical miles (12045.8 km). The LAPCAT mission range Brussels to Sydney is highly ambitious and by almost 40 % larger than NASA's 12000 km, which requires a re-design.

The new supersonic cruise airplane has to be considerably enlarged compared to the earlier NASA design to meet its ambitious range requirement. To keep the wing loading in an acceptable range the wing size has been increased to 1600 m² (+ 36%). The span grows almost proportionally by 16 %, while the total length reaches 102.78 m which is only slightly longer (+ 8.8 %) than the earlier HSCT proposal. The general arrangement of the generic airplane geometry is illustrated in Figure 18. The LAPCAT-M4 employs similar to the NASA concept a blended wing-body with a modified nose, a highly swept inboard wing panel, and a moderately swept outboard wing panel (see fig. 18). The

inboard wing panel is swept 78° , allowing the flow component normal to its leading edge to remain subsonic even at the Mach 4.5 cruise condition. The outboard wing panel is swept 55° but its exact, possibly curved form has not been defined yet. The total wing is inclined with a positive angle of attack of approximately 2.75° . Note that this angle and the wing's airfoil are not optimized yet and might be adapted in the future, if required.

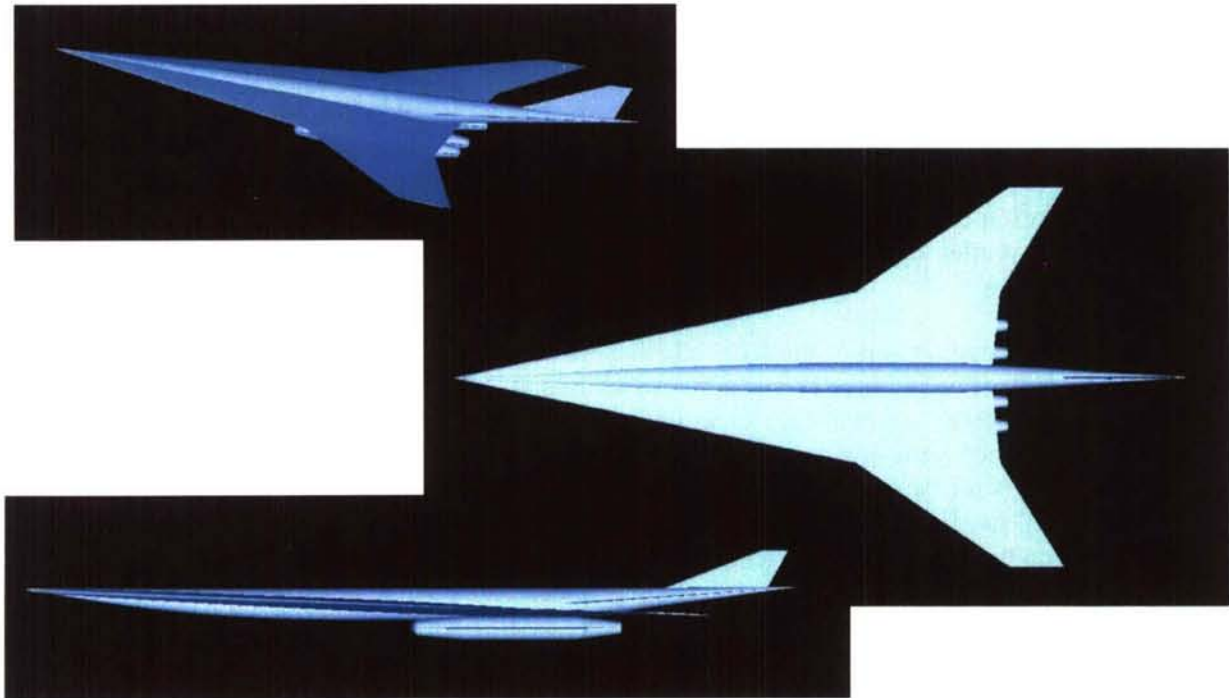


Fig. 18: Preliminary Mach 4.5 kerosene fuelled aircraft for 200 passengers with a MTOW of 720 tons.

The forebody of the concept is slender and elliptical in cross section. The wing-mounted struts of the main landing gear should retract into the engine nacelles and are housed between the inlet ducts as in [15]. The two-wheeled nose gear is mounted on the bulkhead forward of the crew station and retracts forward. The four advanced turbo-RAM-jet engines are mounted in two nacelles on the wing lower surface adjacent to the fuselage. The location of the engine and nacelles is still open for adaptation if required by trim as long as they remain under the wing. The axial-symmetric geometry and the size of the air-intakes, nacelles and nozzles as shown in Figure 18 are not representative of the actual LAPCAT design. A rectangular shape of the air-intake with vertical ramps as in [15] is the preferred design option.

Fuel is carried in integral wing tanks and in a single aft fuselage tank. It is further assumed that the vehicle uses thermally stabilized jet fuel (TSJF) because the existing airport infrastructure is designed around conventional jet fuel. A single vertical stabilizer is attached to the upper part of the aft fuselage. The large, slightly inclined wing might help to achieve a good maximum L/D of 7.8 at a small angle of attack and cruise Mach number 4.5 according to preliminary DLR-analysis. Actually, a high L/D is essential to achieve the ambitious range requirement.

The total take-off mass of the supersonic cruise airplane has been iterated in the first loop to the huge value of 720ton, which is well beyond any supersonic passenger aircraft built to date. The dry mass is estimated at 184.5ton and the structural index is at a for airplanes low 36.8%. According to current data the HSCT would be able to transport about 200 passengers with their luggage. More data on the LAPCAT-M4 airliner design is published in reference [8, 14].

4.1.3.2 Routes

The complete flight trajectory of LAPCAT-M4 from take-off, via ascent, acceleration to the supersonic cruise, descent and landing approach has been simulated using control algorithms described in [14]. The calculation ends after depletion of nominal propellants with descent to sea-level altitude. The vehicle follows almost the orthodrome, however, with some deviations to avoid some densely populated areas, adding about 200km to the shortest great circle route (fig. 19). It's no objective in LAPCAT to prove if the chosen track is actually acceptable for supersonic high altitude flight. Nevertheless, the propulsion system performance should be assessed under realistic operational conditions. Thus, a significant portion of the trajectory (from Brussels in eastern direction up to Volgograd) is assumed to be flown in subsonic cruise.

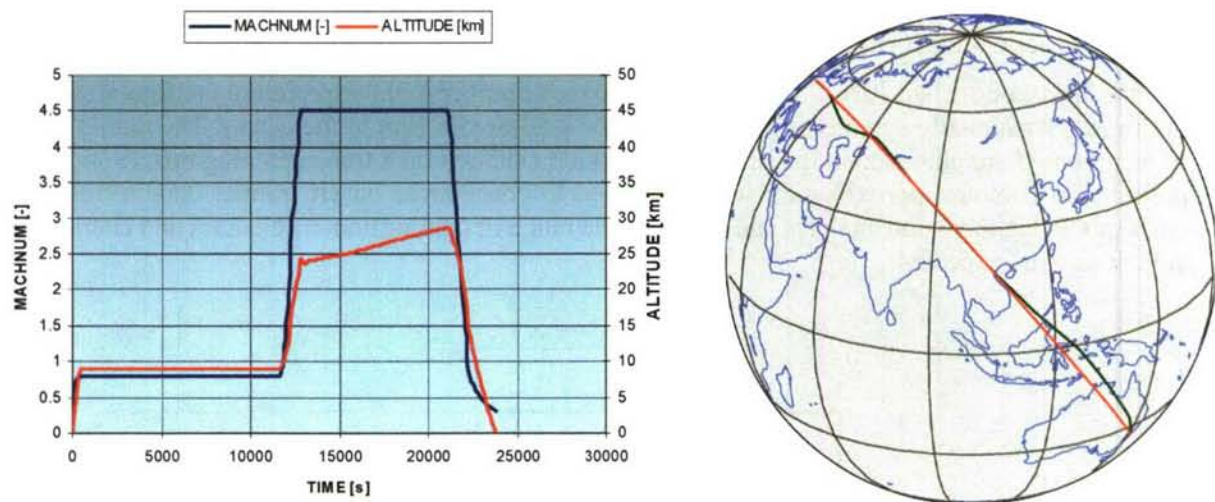


Figure 19: Brussels to Sydney: flight profile and route (16,700 km)

Under these hypotheses LAPCAT-M4 with the available 484.8ton of JP-fuel does not fully reach its final destination Sydney but at least arrives after 15,989 km in central Australia (145.9° E; 26.4° S). Flight time is 23,811s (6.6h). It has not been intended to further enlarge the vehicle to finally fulfil the mission goal. Such work could be the subject of a separate study while LAPCAT focuses on propulsion system research. Simulations show that if a direct acceleration to Mach 4.5 already over the European continent would be acceptable, the HSCT could reach its final destination of Sydney.

Therefore, the obtained results demonstrate the principle feasibility of a TBCC-powered ultra long-haul supersonic airliner. The VCE-214 engine variant with relatively high OPR shows the best performance of all investigated types as long as potentially different engine masses are not taken into account [8].

4.2 Vehicle and Propulsion System Studies based on RBCC

In parallel to TBCC propelled vehicles, Rocket Based Combined Cycles are evaluated for the two vehicle concepts. As the thrust to weight ratios for rockets are far higher (~60-100) than turbojets (~3), they might be a good alternative for the acceleration phase despite their higher sfc. The objectives of rocket based combined cycles are:

- Identification and preliminary definition of system-related parameters for high-speed aircraft and propulsion unit RBCC

- Preliminary design and dimensioning of RBCC engines coupled with vehicle and a reference trajectory
- Evaluation and comparison of RBCC engines
- Trade-off of technical and economic characteristics of RBCC engines
- Comparison of RBCC engine performance with that of TBCC engines

The preliminary design and dimensioning of RBCC engines coupled with vehicle and a reference trajectory was addressed after the first vehicle designs for M4 (kerosene) and M8 (hydrogen) became available. For each of the vehicles, a basic RBCC concept was derived, and tools and rules for dimensioning the RBCC were developed.

4.2.1. Kerosene RBCC engine for Mach 4.5 cruiser

For the kerosene-fuelled RBCC for cruise flight Mach number 4.5, the preferred configuration turned out to be a rotationally symmetric concept with the separated rocket in the center. The ramjet consists of a contoured annulus around the center block which exhausts on a truncated plug nozzle (fig. 20). A preliminary contour approximation was developed to concentrate on HC ramjet combustion on the basis of CFD combustion analysis and to assess the range of combustion efficiencies and characteristic velocities to be expected.

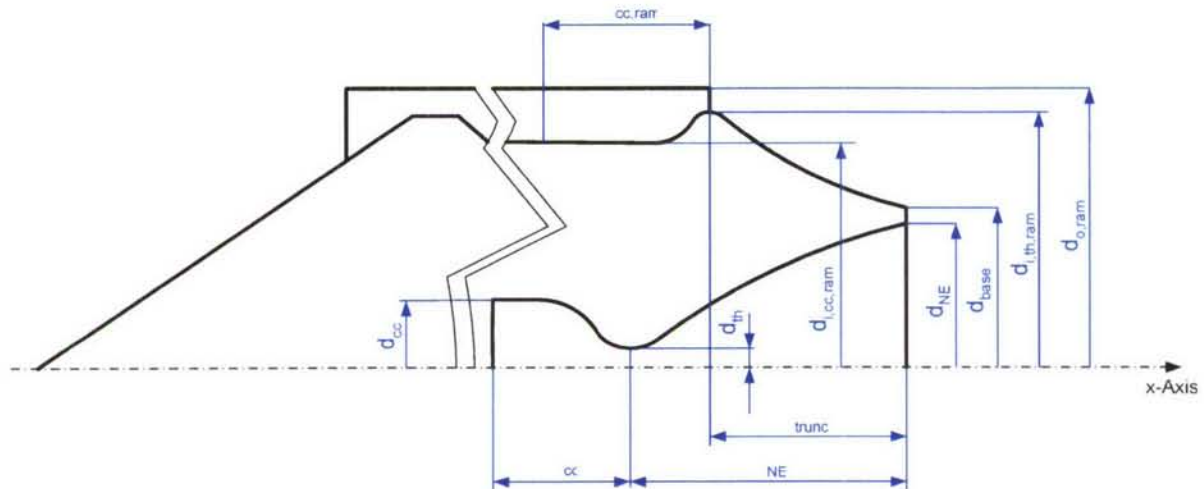


Figure 20: Contour parameters of rotationally symmetric kerosene-fuelled RBCC engine for M4.5 vehicle

The evaluation showed that for the given mission kerosene as fuel was unfeasible, but that the mission can theoretically be achieved using a hydrogen-fuelled RBCC. Also, the performance-sensitive factors have been highlighted and their influence on the net I_{sp} of the RBCC was shown. It turned out that the net I_{sp} performance values of the RBCC are highly dependent on an efficient combustion and nozzle expansion process.

4.2.2. Hydrogen RBCC engine for Mach 8 cruiser

The hydrogen-fuelled RBCC for Mach 8.0 is a planar design with a sophisticated intake system, and rockets integrated into struts. The struts separate short scramjet combustors, for which maximum length and divergence could be determined from basic gas dynamic relations. Also it turned out that it was feasible to design a side-wall injection concept such that the combustor would be sufficiently penetrated with the fuel jet for mixing. The nozzle consists of a single expansion ramp nozzle of the Sanger type and was tentatively demonstrated to be efficient for the proposed vehicle type. After one

year the settings for the basic RBCC cycle input parameters were refined by conducting systematic parametric studies, and by taking into account the latest CFD results about the physics of supersonic combustion from the specialized work packages, allowing a more realistic setting without performance loss at the operational point. Currently, the RBCC engine model for the M8 vehicle is extended to include ramjet combustion and thermal choking to enable the examination of a mixed ramjet-scramjet configuration with different fuel injection positions and side wall struts in the remainder of the system.

The most important issue encountered was the difficulty in compartmentalizing work and developing interfaces between RBCC components as well as between the organizations working on it since an RBCC propulsion system is inherently a highly integrated one. This was addressed by assuming the role of overall engine system responsible via developing guidelines and requirements to component design, and through pursuing decisions on design paths to take within the LAPCAT team.

One important driving parameter was the combustor length, and the drivers' definition for its dimensioning. Regardless of the intricate supersonic mixing and combustion processes the system design team could determine from practical gas dynamic and manufacturing considerations that the scramjet combustion chamber should not exceed a maximum length allowing for a slight divergence to give margin for design issues other than the mixing process. By cooperation with specialized CFD analyses, the assumed model input parameters could be refined in a series of parametric studies to represent more realistic values.

A basic concept for the SERN nozzle and the contouring criteria was defined such that the concept was valid for both the subscale experiments and the fullscale M8 vehicle design. The same applied for the definition of a flexible intake geometry for parametric testing but still representative for the fullscale M8 vehicle. Both intake and nozzle work logic is described below.

The TRL of RBCC propulsion is low and a high degree of uncertainty exists on its actually achievable performance in ejector-rocket and SCRAM-mode. Therefore, an iterative approach in defining the thrust requirements and subsequent calculation of the mission performance has been chosen. All variants studied are based on LH2 propellant and on LOX as the oxidizer in rocket mode. Hydrocarbon propellants had also been regarded at an early phase but fuel consumption was found tremendously high due to the poor specific impulse in ejector-rocket operation mode. Therefore, all hydrocarbons were dropped quite early in the study as a feasible propellant for LAPCAT-M8. The following paragraphs give a brief overview on the evolution process.

4.2.3. Hydrogen Mach 8 Cruiser

The dimensioning of the propulsion system components allowed the definition of the lower part of the latest generic LAPCAT-M8 airplane geometry as illustrated in Figure 10 through Figure 12. The upper section of the vehicle is dependent on the necessary volume for fuel tanks and the SERN expansion ratio intended to be as far adapted as possible. The vehicle span is influenced by the intake width which is directly proportional to the required thrust. LAPCAT-M8 as a generic airplane is designed as a lifting body with a simple 2D-geometry in the central air-intake part, easing not only the conceptual lay-out but also CFD and experimental investigations (fig. 21). The total length is 101.2 m with a total span of 41.58 m. Its height mounts up to 19.5 m. The outboard region converges rapidly to the "wingtips", so that the leading edge sweep angle is about 82°. The stabilizer located in the tail part of the lifting body and two vertical fins, slightly inclined outboards, are to be used for aerodynamic trim and control. Their respective sizes are not yet designed by flight dynamic and stability requirements.

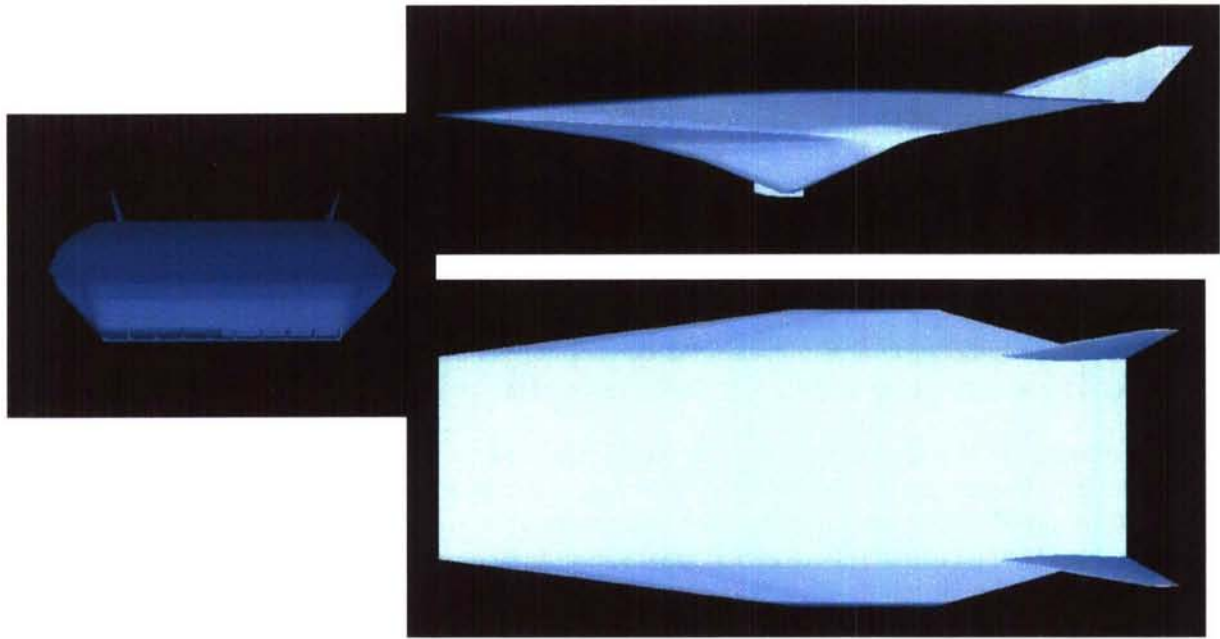


Fig. 21: Preliminary design of a Mach 8 cruiser based on a hydrogen RBCC engine

The engine operational sequence supposes ejector-rocket mode up to $M = 2.5$, a pure RAM operation up to $M = 5$, and subsequently a transition to SCRAM-jet. In its current configuration based on the best available consistent data the airbreathing hypersonic airliner is not able to reach or come any close the LAPCAT mission requirement. The total amount of required LH2 and LOX-propellant is 669ton. Though using ultra light-weight structural design in high load and very high temperature environment, its empty weight mounted still to 267ton with an incredibly large take-off mass of 944ton.

As the RBCC requires a rocket ejector operation at low Mach number flight, its low performance along with the availability of reliable data, results in very high fuel consumption during the acceleration phase. Its performance is highly critical to overall feasibility. Large scale SCRAM propulsion is yet to be demonstrated. This version of a Mach 8 hypersonic RBCC airliner could reach intercontinental range of up to 9500km. LAPCAT-M8 flight performance calculation should not be interpreted as a proof of its feasibility. Intention is to show “best case” performance and identify critical points.

4.3 Combustion Experiments

Dedicated combustion experiments are clearly needed for both TBCC & RBCC concepts in order to evaluate and check the performance and characteristics at specific conditions for supersonic combustion and high-pressure combustion, to evaluate the performance and achievements for potential fuels, either hydrogen or hydrocarbons (HC) and potential oxidizers (air or liquid oxygen), including the investigation of reaction products and hence the impact on emission requirements, to evaluate the chemical kinetics and its interaction with the flow-field turbulence, its impact on ignition delay and flame stabilization, to evaluate potential injection systems with emphasis on mixing and combustion efficiencies and to set-up a database for modelling and validation purposes in these areas where detailed and dedicated experiments are lacking.

So far, experimental data obtained in supersonic combustion experiments performed in the M11 connected tube facility at DLR Lampoldshausen have been evaluated for differently shaped strut

injectors (fig. 22). The main aim was to describe as precise as possible the entry conditions of the flows (pressure, temperature, flow rate, ..) and provide experimental data of physical values which are accessible from CFD solutions such as, wall pressure distributions taken with static pressure measurements, temperature profiles from CARS measurements and velocity data from PIV. Additionally, qualitative information about the position of shock waves as well as the mixing intensity at some position downstream of the injector were deduced from flow visualisation studies.

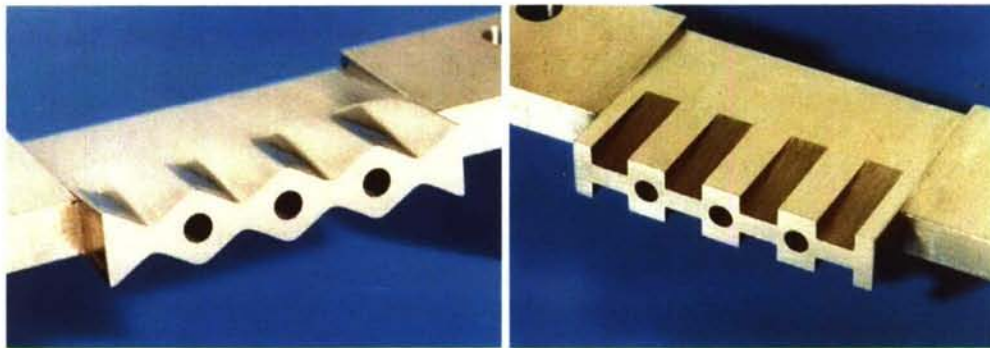


Fig. 22: Different strut injectors tested in M11-facility: left WAVE and right USCER injector

The campaign of testing a complete airbreathing engine in the High Enthalpy Shock Tunnel Göttingen (HEG) is in process. Recent experience gained by designing new operating conditions in HEG have been used to significantly improve the test conditions to be used for the testing in the framework of LAPCAT. Two generic scramjet configurations were selected for the ground based testing in HEG. These two configurations allow comparing the efficiency of two types of fuel injector configurations (perpendicular porthole injection and wall injection using vortex generators). Further, a flexible wind tunnel model with detailed surface instrumentation and optical access was designed and built (fig. 23).

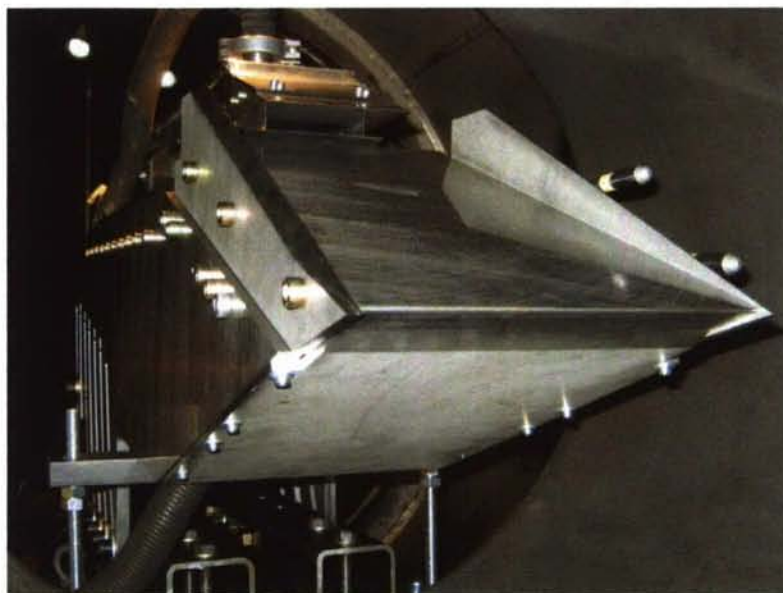


Fig. 23: Full M=8 engine model mounted in the HEG shock tunnel with optical access

In the framework of high pressure combustion experiments with focus on the HC disintegration processes, the ITLR shock tube at the University of Stuttgart (fig. 24) has been equipped with a fast-response fuel injector [16]. An extensive set of "cold" experiments (i.e. with the shock tube not in operation) has been conducted, aimed at characterizing the injection procedure with respect to

triggering, delay times, spray duration and fuel injection pressure. The latter was varied over the range 10 - 50 MPa. Subsequently, the injection system has been tested with the shock tube in operation ("hot" experiments) with timing, spray duration, and fuel injection pressure similar to those employed in the "cold" experiments. As the trigger source, a pressure transducer - located 60 mm from the end wall - is used, which supplies a voltage signal in correspondence of the passage of the incident shock wave. These "hot" experiments were performed for purpose of validating the spray injection technique with respect to reproducibility of the spray, timing of the experiments, and the achievement of steady-state firing conditions. Currently, fluid disintegration experiments are being performed under supercritical and subcritical conditions, employing dodecane (as exemplary hydrocarbon fuel) in argon. The results are visualised by means of flashlight shadowgraphy.

The objective of these experiments is twofold:

- to provide quantitative data on binary fluid disintegration;
- to relate our experimental results (e.g. spray angle, spray penetration length, disintegration regime) to literature data on pure-component fluid disintegration and standard atomization, in order to assess the differences between one-component and binary systems.

It is noteworthy noticing that the analysis of quantitative data and subsequent formulation of empirical correlations for the different break-up regimes has been limited, to date, to one-component systems. This limitation is motivated by the additional difficulties introduced by the occurrence of mixture effects. Due to the enhanced solubility of argon in dodecane at high pressure conditions, the critical pressure of the mixture can be increased considerably above the critical pressure of pure dodecane, depending on the chamber temperature. This leads to some difficulties in analyzing and classifying the experimental results, since the critical point of the binary mixture cannot be known a priori. In order to overcome such difficulties, the development of dedicated software is envisaged, aimed at calculating the fluid-phase equilibrium composition of the binary system dodecane/argon as function of chamber pressure and temperature.

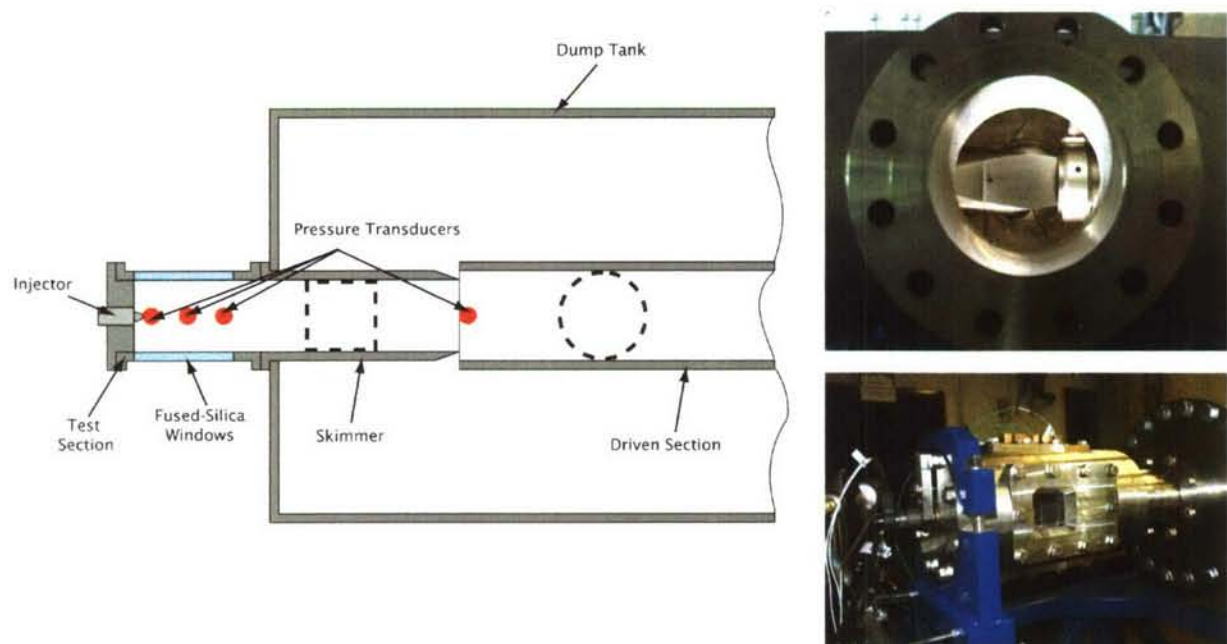


Fig. 24: Shock tube test set-up for investigation of HC disintegration in sub-, trans- and supercritical conditions.

The M3 test facility (fig. 25) at the German Aerospace Center, DLR in Lampoldshausen, designed for the operation with H₂/O₂ (cryogenic or ambient) has been refurbished to allow the use of hydrocarbon

fuel such as methane. For this purpose, a new injector head and feed lines have been designed and built. Moreover, software dedicated for the test bench operation with CH₄ has been developed for the design and the operation of the new hardware. The acceptance tests for operation with LOX/CH₄ have been successfully done. Reliable igniter performance has been demonstrated and first hot runs at representative conditions have been done.

The operation of the laboratory burner provides gas mixtures at representative composition and thermodynamic conditions to develop and test optical diagnostic approaches. Spectroscopy of the flame's emission due to chemi-luminescence and thermal radiation has been analyzed for pressures up to 1 MPa. Quantitative thermometry of the hot gases using CARS-spectroscopy has been started in the CH₄/O₂-flames. Based on the CARS-spectra obtained in the laboratory flames a decision on probe molecules was achieved. For the characterization of the ignition transient and stationary spray combustion software tools are developed to analyze shadowgraphs and high speed recordings of the flame emission.

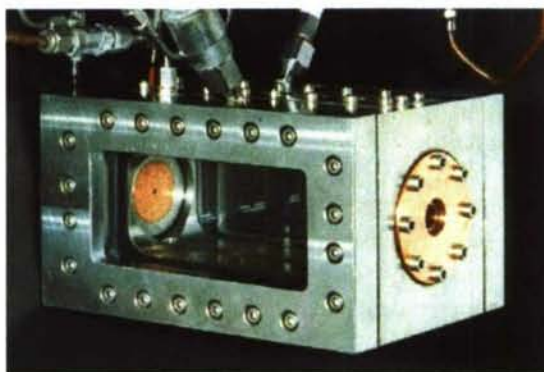


Fig. 25: M3 test facility with optical access

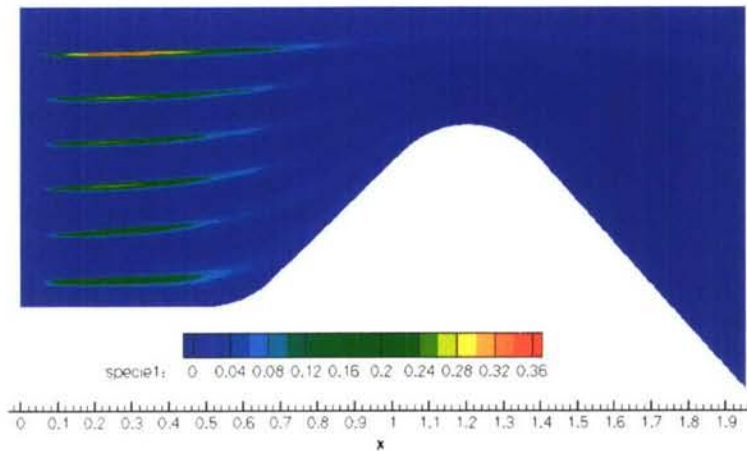
The intensive literature study and the validation predictions yielded the Leeds mechanism as the most promising candidate mechanism for O₂/CH₄ combustion for further reductions towards a kinetic scheme short enough to become applicable in 3D CFD tools. Within the previous period the mechanism was updated using the recently published data. Additionally, the reactions and reaction rate constants are modified such that they are better suited for our range of parameters which is much broader than the original one. Therefore, the modified mechanism has been extensively and successfully validated by performing verification predictions over the entire range of application using the experimental data base established within the frame of the project. First attempts towards a skeletal mechanism have been performed and the validation predictions are underway but not yet finished.

4.4 Combustion Modelling and Validation

The goal is to investigate physics of supersonic combustion and to develop new tools to enhance numerical simulations. In fact, numerical simulations performed by means of RANS (Reynolds Averaged Numerical Simulations) or LES (Large Eddy Simulations) are fundamental in designing SCRJ combustors; in particular, by focusing on the unsteadiness of the flow, Large Eddy Simulations (LES) can help in understanding how to improve mixing, flame anchoring and combustion efficiency in supersonic reacting flows. A proper reduced kinetic scheme for H₂/air and kerosene/Air is mandatory to correctly reproduce combustion temperature and species in not prohibitive CPU times. In particular, H₂/air kinetics has been examined using different schemes. Development of the RANS codes and of the LES code is proceeding apace.

The extension and validation of the existing axisymmetrical EADS code Rocflam-II towards LOX/HC (Hydrocarbons, i.e. Kerosene and Methane) chemistries has been finished. The necessary fluid data

and reaction schemes have been selected and implemented. The reaction model in Rocflam-II consists of a tabulated equilibrium chemistry with a PPDF (*presumed probability density function*) approach to



model turbulent combustion. Code validation has been carried out on available sub- and generic fullscale engines. The code has been further adapted and applied to an Air/Kerosene Ramjet engine. Here, liquid kerosene droplets are injected into a gaseous air surrounding, simulating atmospheric conditions at a sea level altitude of ca. 25 km. The air is already compressed and heated up in an inlet previously, so the combustion process will take place under subsonic conditions.

Fig. 26: Ramjet Combustion Modelling for Kerosene-Air: mass fractions contours of Jet-A.

CIRA selects the code C3NS-PB as starting platform, consisting of two different modules: A pressure-based module (C3NS-PB) and a density-based module (C3NS-DB). The pressure-based module is able to describe the flow of a 3D, unsteady, turbulent, chemically reacting mixture of ideal gases. A thermodynamic model able to properly describe propellants injection in high pressure LOx/HC rocket thrust chambers has been developed and implemented.

Two different approaches (compressibility factor formulation and analytical formulation) have been selected: the accuracy and robustness of both approaches have been preliminary assessed through comparison with experimental data available in literature. Furthermore, the compressibility factor formulation has been implemented in the flow solver and a suitable test case has been selected to test the capabilities of the model in typical rocket operating conditions (supercritical injection pressure, transcritical injection temperature): the CFD simulations have shown a good agreement with experimental data (fig. 27). A basic turbulent combustion model (Eddy Dissipation concept) has been also implemented in the code.

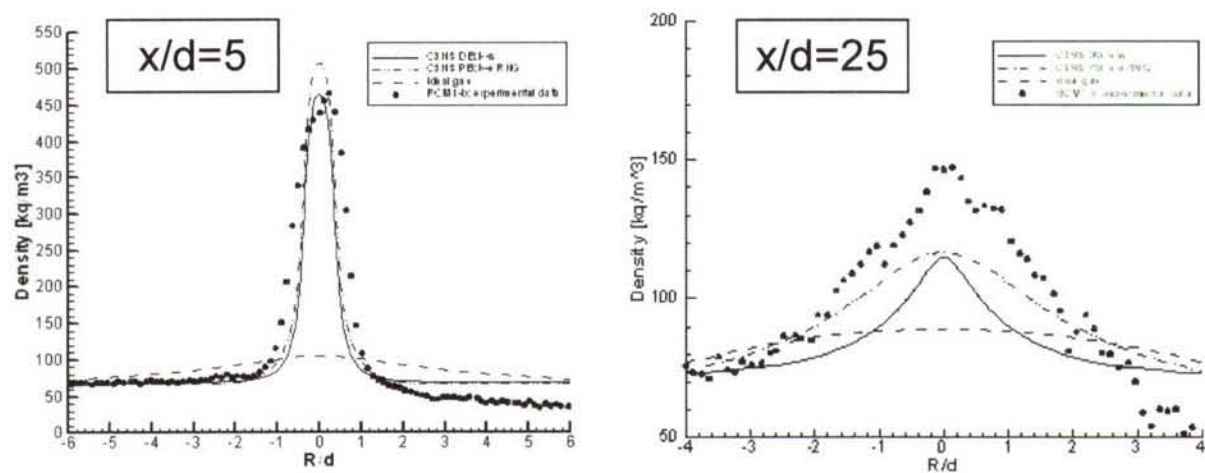


Fig. 27: Influence of thermodynamic (real gas EOS on the basis of compressibility factor) and turbulence modelling: Radial density profiles at different axial stations

In order to simulate supersonic combustion processes in scramjet engines, the following upgrades and developments of the density-based module have been done:

- code extension to a generic multi-component mixture of reacting gases;
- input capabilities have been generalized to allow the input of generic number of species and reactions, with their corresponding physical-chemical properties;
- thermodynamic and transport models have been modified to analyse mixtures of thermally perfect gases;
- a new set of boundary conditions have been introduced in order to simulate mass injections with a specified composition.

A laminar combustion model for a gaseous hydrogen/air mixture has been implemented in the DLR Tau code. It is based on an existing extension of aerothermodynamic description of the re-entry flight of space vehicles. Partition functions for individual species and appropriate mixture rules are used to compute the thermodynamic and transport properties. This offers the possibility of future model extensions (e.g. multi temperature models to account for thermal nonequilibrium). Appropriate Dirichlet and von Neumann boundary conditions for the species mass fractions at fully catalytic and non catalytic walls have been implemented. Transport coefficients are computed for the individual species. Suitable mixture rules are then used to obtain the mixture viscosity, heat conductivity and diffusion coefficients. Basic test cases have been used to verify correct implementation and results for laminar reactive flow. Two reaction rate schemes with different level of complexity are implemented in the code.

The model has been further extended with an assumed PDF method to account for the influence of the turbulent flow in Scramjet combustors on the chemical production rates. The assumed PDF approach has been chosen from many available turbulent combustion models for the following reasons:

- Wide range of applicability for premixed, non-premixed and partially premixed combustion and different Damköhler numbers,
- Limited computational cost, high robustness and straightforward implementation,
- Convergence acceleration techniques can be used because the PDEs for the needed temperature and concentration variances have the same form as the Navier-Stokes equations (contrary to e.g. multi-dimensional PDEs used for transport PDF methods that need to be solved with particle methods),

The complete supersonic combustion model in TAU was validated and tested using experimental benchmark results for a supersonic coaxial burner which produces a lifted flame at typical scramjet flow conditions (fig. 28). The flame lift-off distance and flame structure could be well reproduced by the numerical investigation of this test case using the DLR Tau-Code. Application to a full-engine scramjet simulation can be found in [17].

The study concerning the applicability of several hydrogen/air reaction mechanisms for scramjet applications has been completed. Seven detailed (9-species, 19- to 27-step), one reduced (7-step, 7-species) and one global kinetic scheme (in the last 6 month) have been investigated. The basic result is that at critical conditions close to the ignition limit of hydrogen (this corresponds to low flight Mach numbers of a scramjet) only detailed mechanisms are able to accurately predict the ignition delay correctly. However, there are also significant differences between the detailed kinetic schemes and the best suited mechanisms for scramjet simulations are identified.

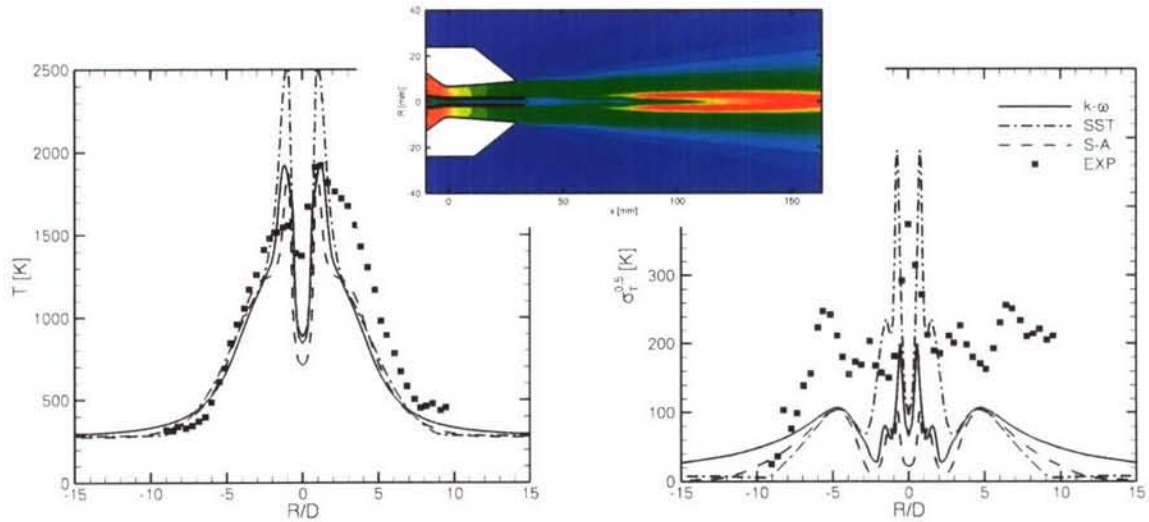
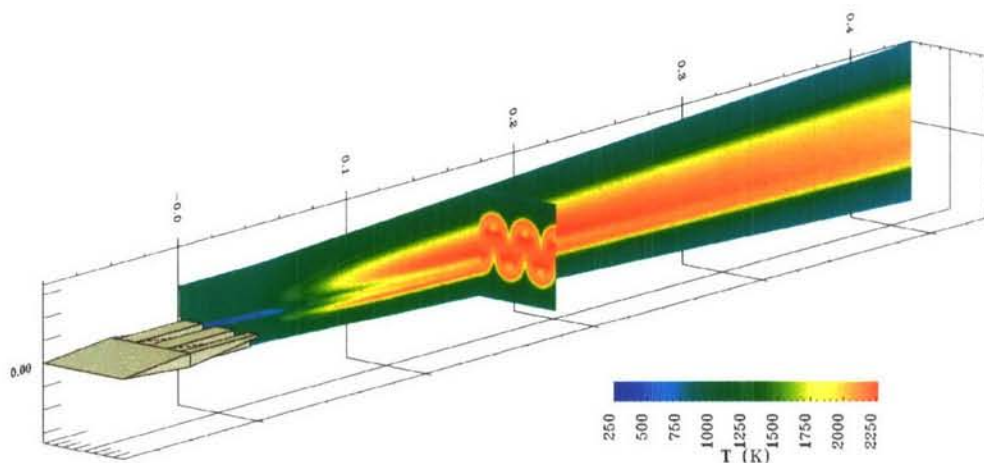


Fig. 28: Radial distribution of temperature (left) and standard deviation of temperature (right) 50 mm downstream of the nozzle exit (middle).

Next different lobed strut injector concepts have been investigated. In case of axial fuel injection methods for mixing enhancement are required to enable a short combustor length and to reduce the skin friction drag. Possibilities for mixing enhancement may be based on the use of shock waves or on the production of strong streamwise vorticity. The last concept has been investigated numerically using the TASC3D code. The strength and size of the vortices induced may be modified by changing the strut geometry. Different lobed strut injectors are compared in a cold non-reacting mixing study with respect to their mixing efficiencies and losses in total pressure. Aim is to produce vortices which cover large parts of the combustor cross section. A comparison with experimental data for one strut geometry has demonstrated the numerical accuracy of the code. At low flight Mach numbers of a scramjet (7 to 8 as in LAPCAT) detached flames are possible in case of axial fuel injection. Thus the degree and speed of mixing has a strong influence on the ignition delay too. The next step in this investigation will be to extend the studies to hot reactive flows with combustor inlet conditions, corresponding to the LAPCAT flight Mach number.



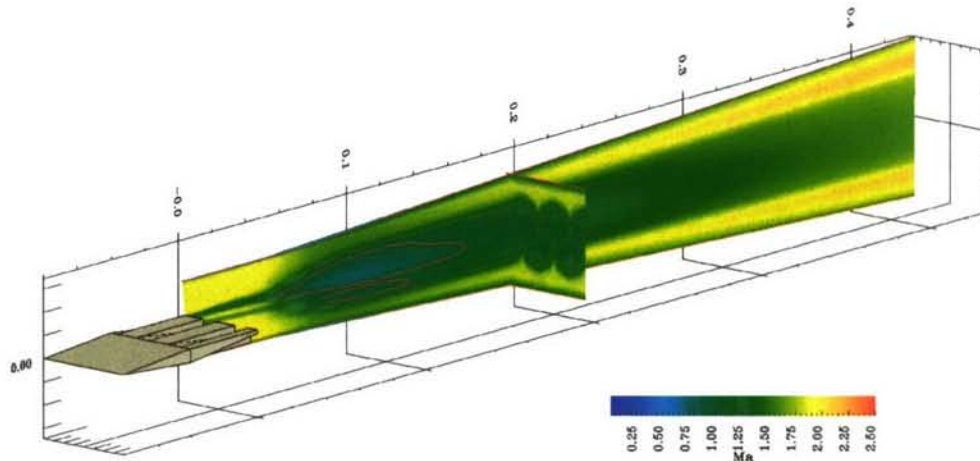


Fig. 29: Flame stabilization of a lifted flame for a lobed strut injector based on a multi-variate assumed PDF closure plotted with contours of temperature and Mach.

In parallel simulations of the HyShot flight experiment have been performed. While the simulation of the inlet and suction region of the engine is completed, the combustor simulations are still work in progress. They are performed using the multi-variate assumed PDF (probability density function) approach and finite-rate chemistry. First simulations demonstrated a strong influence of the chosen inflow and boundary conditions on the flame.

Results obtained by LES simulation (fig. 30) indicate combustion may be made to take place in a short distance (about 1 m or so) by supersonic injection of hydrogen inside the supersonic airstream [18]. The ISCM LES SGS model has been validated using the NASA-Langley data of the supersonic combustion experiment carried on for the NATO RTO, AV-10 a few years ago [19]. In this context, much attention has been put on scaling laws for the mixing and chemistry of supersonic combustion. Although not originally contemplated, scaling laws were examined in order to produce a rough but workable first cut for the combustor length. In fact, combustor length shapes vehicle length, especially that where cross section is maximum, thereby affecting strongly overall weight at take-off.

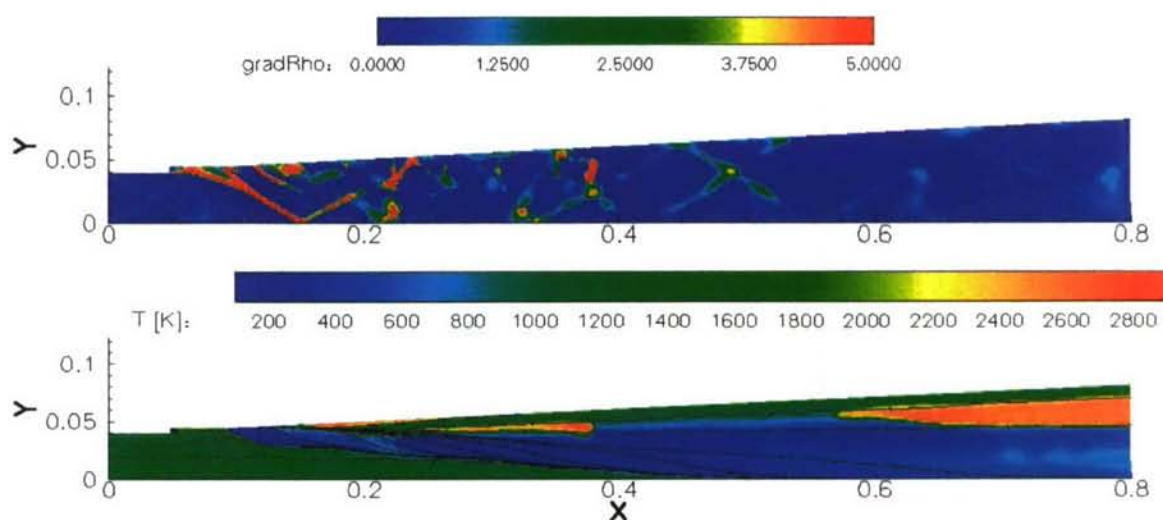


Fig. 30: Density gradient and temperature contour plots obtained with LES-ISCM turbulent combustion model [18].

The conclusions reached so far from theory and simulations indicate that at low air inlet temperature (about 1000 K) combustion length, L , is controlled by the interplay between convection, turbulent mixing and kinetics. As a first approximation, flame anchoring may be predicted according to the Damköhler number scaling $p \cdot L = \text{constant}$. At air T of order 1400 K and higher, kinetics is fast, so that combustion length is dominated by mixing time. Scaling in this regime becomes more complex: in fact, a relationship has been derived that predict flame length and anchoring based on the airstream velocity, angle of fuel injection and fuel jet momentum. This relationship has been tested using the NASA-Langley test case and predicts well the distance from injector where flame is observed to anchor. The actual distance is, in fact very short (of order 1 m). This result allows sizing a combustor realistically. Because the combustor length is short, total vehicle length may now be also determined.

4.5 Design and Aerodynamics of Propulsion Components

For high-speed transportation vehicles powered by air-breathing engines achieving a positive aeropropulsive balance is crucial for the success of the whole system. Along the last 40 years, almost all attempts to fly a scram-jet propelled vehicle have failed due to largely underestimation of the vehicle total drag with respect to the allocated thrust. One of the lessons learned of such experiences is that the vehicle design requires an optimized propulsion airframe integration resulting in an extremely coupled development procedure of the system components, namely the intake, combustion chamber, thrust nozzle and airframe. However, this last statement is not easy to realize since there is no ground facility in the world which allow testing a real sized vehicle under flight conditions including operating engines and furthermore, till today no scaling rules are available at all. According, the only successful flight of a vehicle propelled with a scram-jet, e.g. the X-43, has been done with a vehicle sized to a scale compatible with the size of the ground based facilities used for its design. As like other areas of the hypersonic technology, here the potential of the CFD tools for ground to flight extrapolations is coming on request. To accomplish with that mission CFD tools require dedicate validation experiments, hence specific tasks focus on the carefully design and experimental testing of intakes, nozzles and the interaction with the external flow to be used for CFD validation. Furthermore, being the loss of thrust due to earlier nozzle flow separations and the vehicle total drag the main issues required to be predicted, important efforts are assigned to test advanced turbulence models (fig. 31). Finally, since one of the major potential show-stoppers of intakes is the transition of the incoming boundary layer from laminar to turbulent, specific efforts are allocated to fix from the very beginning of the intake operation turbulent flow.

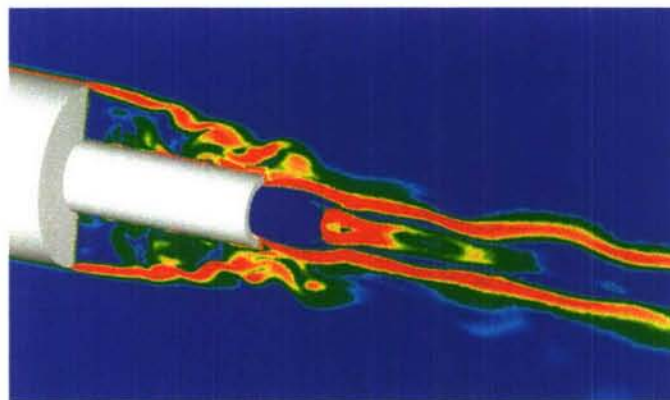


Fig. 31: Base drag estimation by advanced turbulence models: simulation of unsteady turbulent phenomena in base flow regions.

For the definition of the required experimental models it was decided not to use any generic intake or nozzle / base flow but those resulting from the vehicle system parameters studies. Accordingly, two highly flexible wind tunnel models, allowing many configurative variations have been designed and are today under construction: one for the intake (fig. 32) and one for the nozzle flow/external flow interaction problematic (fig. 33). Both models have been designed taking into account the nominal flight conditions resulting from the project system study but also accounting for the facilities capabilities. Several types of CFD turbulence model have been evaluated with respect to geometrical configuration constraints and numerical dissipation. It turns out a clear advantage for the highly developed models even they require large computational resources. The capabilities of different turbulence models for the simulation of unsteady turbulent phenomena have been investigated. The study has shown that the superior results of Detached Eddy Simulation models against Unsteady Reynolds Averaged Navier-Stokes models and the deep insight into the unsteady flow physics are purchased by a significantly higher complexity of the computation.

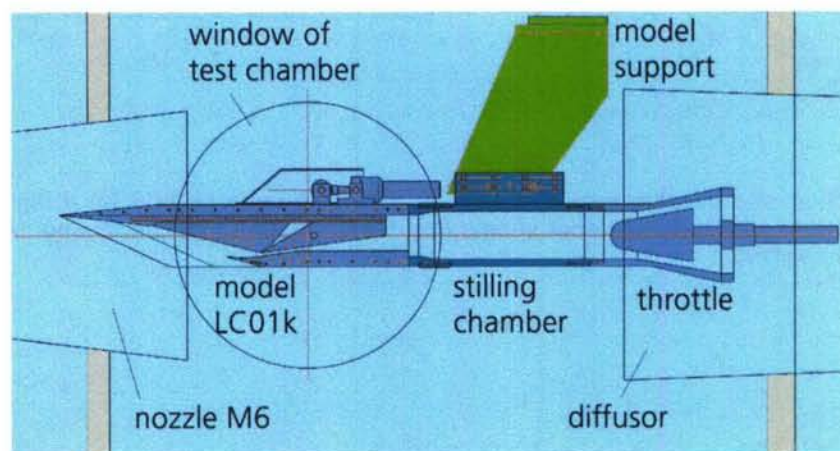


Fig. 32: Intake model without forebody for M8 vehicle.

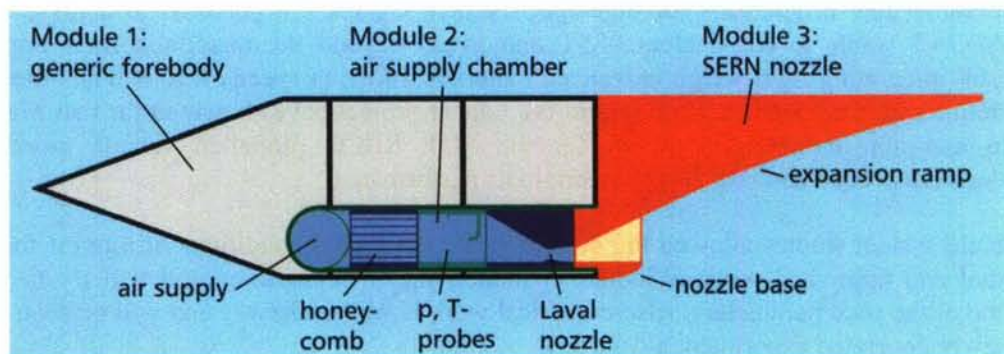


Fig. 33: Concept of a Single Expansion Ramp Nozzle and Base Flow experimental model

Furthermore, large eddy simulation models have been found by comparison with direct numerical simulation (fig. 34), to be accurately enough tools for the prediction of supersonic shock induced laminar-turbulent boundary layer transition. It has been shown that it is possible to have self-sustained transition to turbulence in a shock-induced separation bubble provided the pressure rise over the bubble is high enough. The design of turbulence devices for forcing turbulent flow is underway.

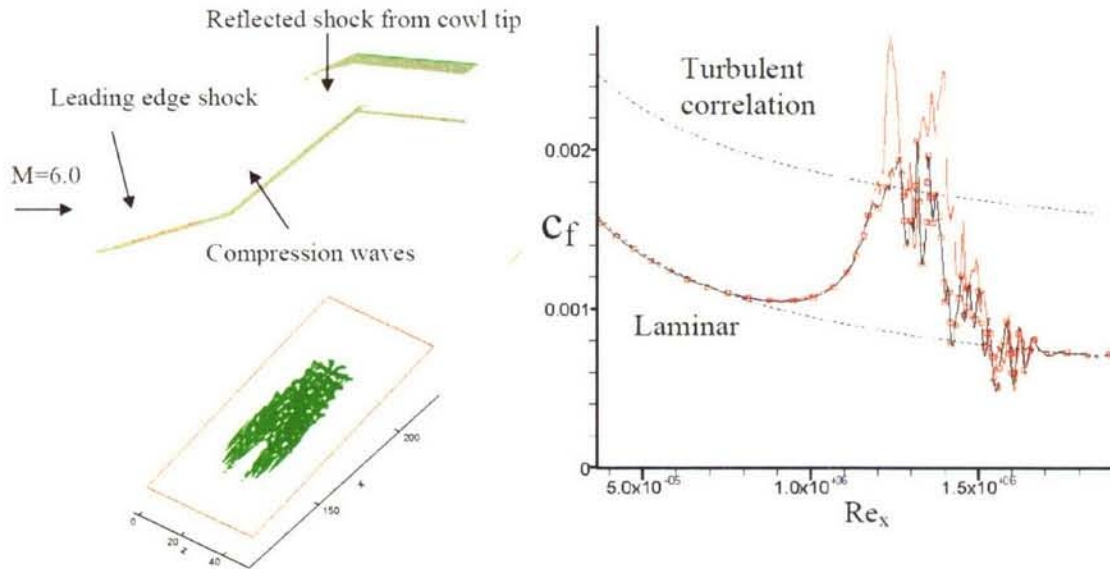


Fig. 34: Skin friction of a passing turbulent spot on an intake ramp by LES for a flight Mach=6; Left: configuration with turbulent spot shape; Right: skin friction induced by spot: legend: symbols LES; full line DNS.

5.0 CONCLUSIONS

Based on general trends in the evolution of aircraft performance and the possible aerodynamic and propulsive achievable efficiencies for high-speed vehicles, there's a potential to achieve antipodal range. LAPCAT wants to (re)-evaluate SST and to go beyond the material's limit imposed for Concorde by integrating light-weight advanced materials allowing speeds 4 to 8 times the speed of sound. Preliminary parametric studies within the Lapcat project have shown so far that Mach 4-5 is achievable and not marginal. However, for the M=8 RBCC propelled vehicle more detailed investigations are needed and ongoing to ascertain its performance.

These vehicle system studies allowed the definition of operational conditions of interest for detailed experimental and numerical work. Windtunnel models are in preparation and will try to reveal or justify some of the used parameters. Also numerical work is well underway and will be soon validated with the newly generated experimental database.

Acknowledgements

The work was performed within the 'Long-Term Advanced Propulsion Concepts and Technologies' project investigating high-speed airbreathing propulsion. LAPCAT, coordinated by ESA-ESTEC, is supported by the EU within the 6th Framework Programme Priority 1.4, Aeronautic and Space, Contract no.: AST4-CT-2005-012282. Further info on LAPCAT can be found on the web-site <http://www.esa.int/techresources/lapcat>.

This consolidated overview would not have been possible without the inputs received from the many partners, in particular A. Bond and R. Varvill (REL), A. Götz (EADS-Astrium), J.-M. Conrardy (SNECMA), G. Paniagua (VKI), S. Pierret (CENAERO), K. Hannemann, J. Longo, O. Haidn, M. Sippel and P. Grün from DLR, S. Borreca and S. Borrelli (CIRA), G. Lamanna (U. Stuttgart), C. Bruno (U. Rome), N. Sandham (U. Southampton), A. Matthews (U. Oxford) and many others in the team.

The survey of Mr. O. Mouton (TU-Delft) on aircraft performance data and the discussion with Prof. P. Hendrick of the ULB is greatly appreciated.

References

- [1] Küchemann D., The Aerodynamic Design of Aircraft, Pergamon Press, 1978.
- [2] Anderson J., Introduction to Flight, 4th ed. McGraw-Hill, 2000.
- [3] Penner J. E. et al., Aviation and the Global Atmosphere – A special report of IPCC Working Groups I and III, Cambridge University Press, 1999.
- [4] Cain T. and Walton C., The Sustained Hypersonic Flight Experiment, 12th AIAA Int. Space Planes and Hypersonic Systems and Technologies, 15-19 December 2003, Norfolk, Virginia.
- [5] <http://www.concordesst.com/concordeb.html>
- [6] Bond A., Turbine Based Combined Cycles, Advances on Propulsion Technology for High-Speed Aircraft, RTO-AVT-VKI Lecture series, March 12-15, 2007.
- [7] Sippel M., Klevanski J. and Steelant J., Comparative Study on Options for High-Speed Intercontinental Passenger Transports: Air-Breathing- vs. Rocket-Propelled, IAC-05-D2.4.09, 2005.
- [8] Sippel M., Research on TBCC Propulsion for a Mach 4.5 Supersonic Cruise Airliner, 14th AIAA Int. Space Planes and Hypersonic Systems and Technologies, AIAA 2006-7976, 06-09 November 2006, Canberra, Australia.
- [9] Bartolotta P., McNelis N. and Shafer D.G.: High Speed Turbines: Development of a Turbine Accelerator (RTA) for Space Access, AIAA 2003-6943, December 2003
- [10] McNelis N. and Bartolotta P.: Revolutionary Turbine Accelerator (RTA) Demonstrator, AIAA 2005-3250, May 2005.

- [11] Timnat, Y.M.: Advanced Airbreathing Propulsion, Chapter 10 Civil Engines for Supersonic Aircraft, 1996
- [12] Morris, S. J., Geiselhart K.A. and Coen P.G.: Performance Potential of an Advanced Technology Mach 3 Turbojet Engine Installed on a Conceptual High-Speed Civil Transport, NASA Technical Memorandum 4144, November 1989.
- [13] Brazier M.E. and Paulson R.E.: Variable Cycle Engine Concept, ISABE 93-7065, 1993.
- [14] Sippel, M.; Klevanski, J.: Definition of the LAPCAT Reference Vehicles LAPCAT-M4 and LAPCAT-M8, Issue:1, Rev. 0, LAPCAT Del. No. D.2.2.1, SART TN-005-2005, DLR-IB 647-2005/11, February 2006
- [15] Domack C. S., Dollyhigh S. M., Beissner F. L., Geiselhart K. A., McGraw M. E.; Shields E.W. and Swanson E.E.: Concept Development of a Mach 4 High-Speed Civil Transport, NASA Technical Memorandum 4223, 1990.
- [16] Stotz I., Lamanna G., Weigand B. and Steelant J., 'Double-Diaphragm Shock Tube (DDST) for Hydrocarbon Disintegration Studies', 14th AIAA/AHI Space Planes and Hypersonic Systems and Technologies Conference, AIAA-2006-8109, 06-09/11 2006, Canberra, Australia.
- [17] Karl S., Hannemann K., Steelant J. and Mack A., 'CFD Analysis of the HyShot Supersonic Combustion Flight Experiment Configuration', 14th AIAA/AHI Space Planes and Hypersonic Systems and Technologies Conference, AIAA-2006-8041, 06-09/11 2006, Canberra, Australia.
- [18] Ingenito A., Bruno C., Giacomazzi E. and Steelant J., 'Supersonic Combustion: Modelling and Simulation', 14th AIAA/AHI Space Planes and Hypersonic Systems and Technologies Conference, AIAA-2006-8035, 06-09/11 2006, Canberra, Australia.
- [19] Drummond J. P., Diskin G. S. and Cutler A. D., "Fuel-Air Mixing and Combustion in Scramjets", Technologies for Propelled Hypersonic Flight, NATO Research and Technology Organization, Working Group AVT 10, Final Report, January 2001.

von Karman Institute for Fluid Dynamics

RTO-AVT-VKI Lecture Series 2007

**ADVANCES ON PROPULSION TECHNOLOGY
FOR HIGH-SPEED AIRCRAFT**

March 12-15, 2007

HIGH SPEED JET NOISE

V.F. Kopiev
TsAGI, Russia

High speed jet noise

Victor F. Kopiev

Central Aerohydrodynamics Institute (TsAGI), Acoustic Division
105005 Moscow, Radio str.17, Russia

vkopiev@mx.iki.rssi.ru

INTRODUCTION

Recent advances in computational aerodynamics have encouraged the attempts of direct numerical simulation of the aero-acoustic processes in supersonic jets. However, despite significant efforts being spent, this approach has not given any definite results in solving the problem up to now. The main obstacle is the wide range of spatial and temporal scales which have to be accounted for in order to fully solve aero-acoustic problems. This range ensures that the task still lies outside the limits of modern computational capabilities for high Reynolds number. This is why there is much current interest directed at search of mechanisms which are the main source of acoustical radiation. The relative input of each mechanism is not clear as yet, though it is indeed necessary to know a concrete radiation mechanism for developing the methods of noise control, numerical methods of noise prediction etc.

It is now generally accepted that one of the main mechanisms of acoustic radiation in a supersonic jet can be identified with packets of instability waves propagating downstream within the mixing layer of the jet [1]. This follows from the generally accepted assumption [2] that supersonic jet noise is generated by large-scale turbulence which, in turn, can be represented as a sum of spatially developing waves. Tam's method is based on two fundamental principles: 1) the main part of mixing noise is radiated by instability waves evolving downstream from the nozzle edge; 2) near the nozzle edge the initial amplitudes of instability waves of all the harmonics, in the range of Strouhal numbers being of interest, are the white noise. Thus, the unknown parameter of the theory is only one constant which is a power of the white noise. This constant within the limits of such an approach can be obtained from the experiment data. Assumption (1) is based on the idea that the instability wave as the most growing one must significantly increase in its evolution to the zone of maximum. It substantially exceeds other disturbances in this zone and is the principal and effective radiation source if its velocity remains supersonic (Fig.1). Moreover instability wave despite increasing continues to be wave packet in zone of maximum that means nonlinear rolling up of shear layer typical for subsonic jet does not begin. Assumption (2) is based on ideas on the absence of the characteristic length scale near the nozzle edge where the instability waves originate.

It should be noted that there are alternative approaches for supersonic jet prediction [3] recently further developed in [4]. Therefore the answers, which are "vitally important", are: do the instability waves really exist and radiate noise? Does the instability wave mechanism dominate each other? Do the amplitudes of instability waves smoothly distributed near orifice or some scales of disturbances are dominated, etc. It is clear that the knowledge about this mechanism and its dynamic features is the first and necessary condition of the elaboration of noise control strategy and has a direct importance for the flight vehicles future elaboration. Along with the experimental validation available, obtained for $St=0.2$ previously [5], the direct validation of the instability wave theory in the round jet was recently realized by

azimuthal decomposition technique [6] in the region of $Sh \sim 0.1-0.35$ to be sure that this mechanism really exists and dominates any other. Azimuthal modes are directly under consideration in Tam theory and their relative amplitudes could give careful instrument for theory development and unique possibility of comparing the theory and its principal concepts with the results of the experiments.

Supersonic jet noise consists of three main components. They are the turbulent mixing noise, the broadband shock associated noise and the screech tones. The latter two noise components are generated only when the jet is imperfectly expanded and a shock cell structure is formed in the jet plume. This lecture considers perfectly expanded jets and turbulent mixing noise alone.

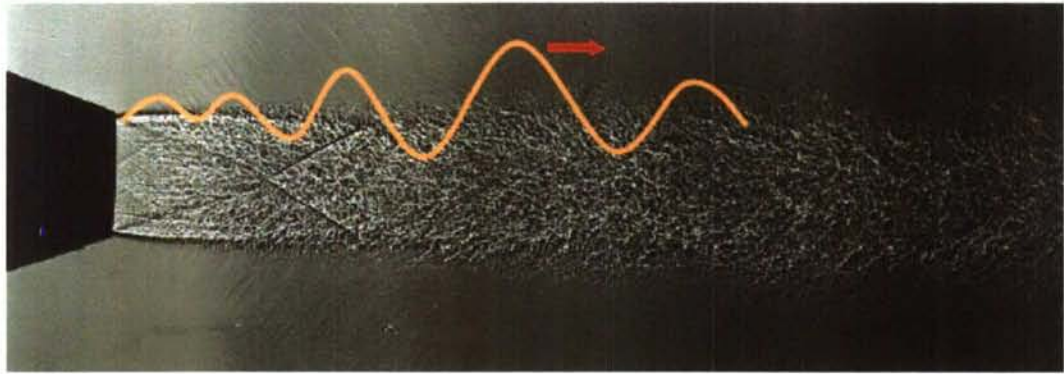


Figure 1: Supersonic jet and scheme of instability wave packet

Thus in the present work we consider the main principles of Tam instability wave theory for mixing noise and new approach to verification this theory on the basis of the experimental data obtained with the use of the azimuthal decomposition technique (see review of the problem in [7]), Fig.2. In the first part of the work we consider the instability wave concept for the simplest 2D shear layer. In the second part the looking over the Tam's theory details was conducted. This analysis gives the main background for comparison with experiment. In the third experimental part of this work the method of azimuthal decomposition, which helps to measure directly the azimuthal harmonic amplitudes and directivities, is used for the well-shaped convergent-divergent axisymmetrical nozzle designed for exit Mach number $M=2$. The method is used for careful acoustic measurements.

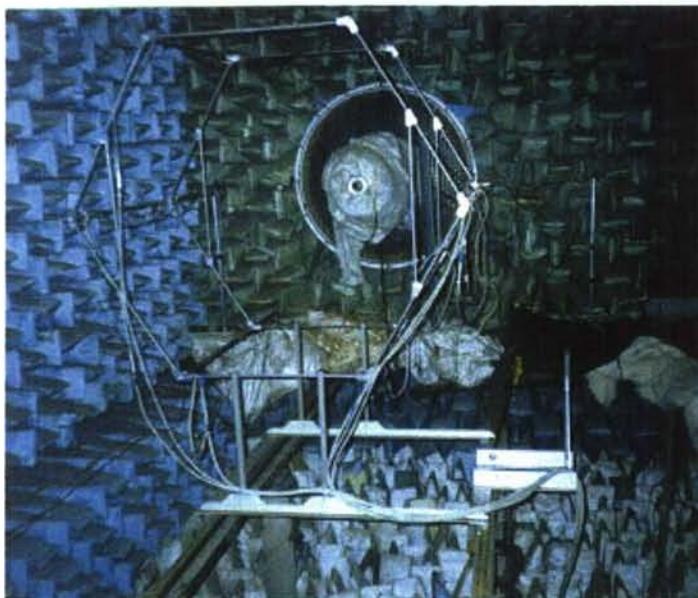


Figure 2. Microphone array in anechoic chamber for azimuthal decomposition technique

A comparison between the theory predictions and the measurement data shows that for all azimuthal harmonics $n = 0, 1$ and 2 , which contribute the main part to the jet noise, the theory predictions are in agreement with measurement data. It concerns the directivity of sound radiation, frequency dependence of radiation peak and amplitude scales of sound radiation for different harmonics in frequency ranges. It means that the experimental results have confirmed two main hypothesis of Tam's theory: i) the main source of sound in supersonic fully expanded jet are the instability waves; ii) the instability waves have an amplitude of the same order in the region of their origination in wide frequency range and for different harmonics. Therefore the instability waves could be considered as objects for direct noise control in supersonic jet.

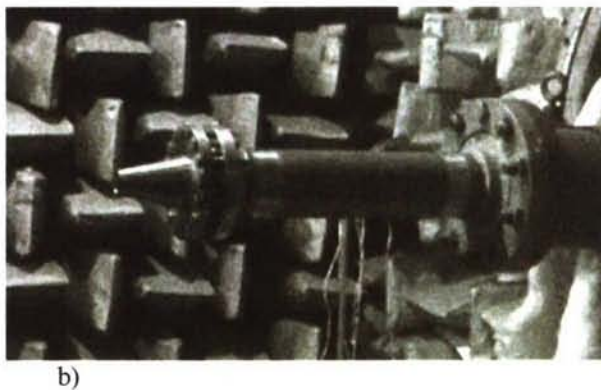
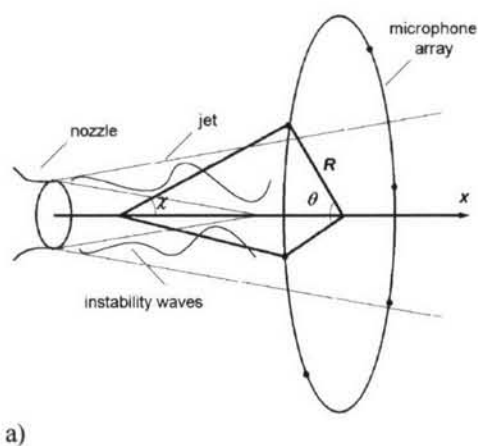


Figure 3. Scheme of experiment (a); supersonic nozzle (b).

AZIMUTHAL MODE MEASUREMENTS

We briefly discuss in this chapter the measurements of supersonic round cold jet noise following the paper [8], where the method of azimuthal decomposition for noise measurements was firstly used. This technique gives a possibility of measuring the noise of each azimuthal mode separately. In experiment the mixing noise of supersonic cold jet from convergent-divergent conical nozzles of design Mach number $M=2.0$ was studied. The experimental program consisted of measuring the azimuthal mode intensity in different frequency ranges by a six-microphone array. The results for the special “well shape nozzle” to measure the mixing noise only is considered to the end of the lecture.

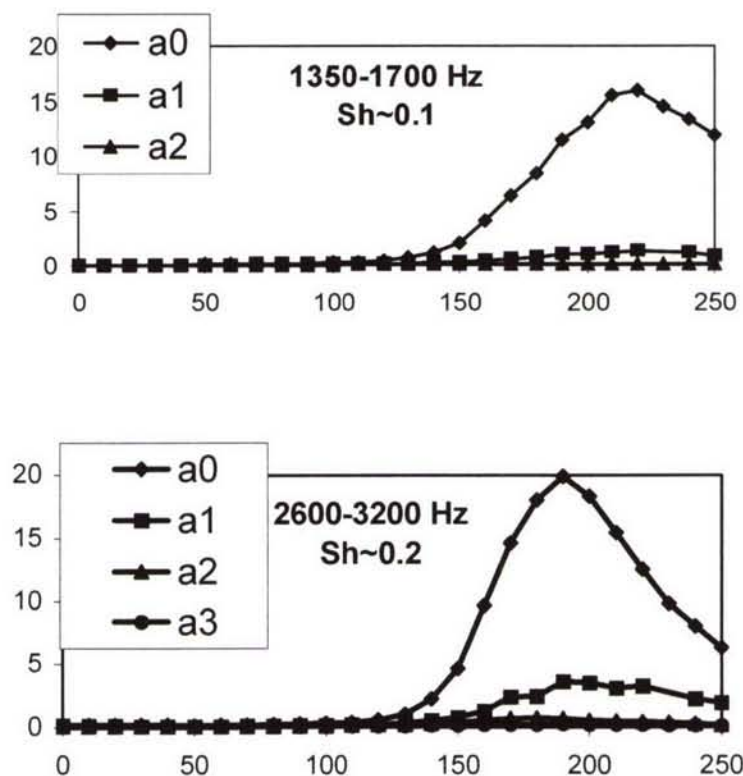


Figure 4. Directivity of azimuthal modes in two frequency ranges: a) $Sh \sim 0.1$, domination of axisymmetrical mode; b) $Sh \sim 0.2$, appearing first ($n=1$) azimuthal mode in far field.

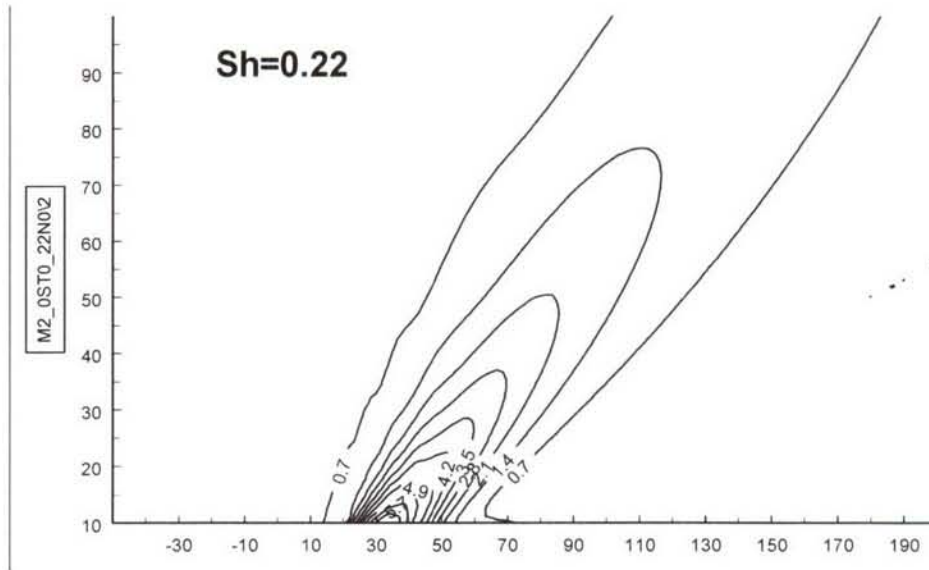


Figure 5. The sound pressure levels created by instability wave packet in the near field of supersonic cold jet at $M=2$, $St=0.22$ for azimuthal harmonic $n=0$.

The microphone array moves along jet axis z from 0 to 250 cm covering the cylindrical surface around the jet. The nozzle orifice position corresponds to the section $z=50$ cm. The scheme of the experiment is presented in Fig.2-3. We present only low frequency results for jet noise azimuthal decompositions up to $St \sim 0.3$. The more careful discussion of the problem will be presented below.

Fig.4 presents the powers of four azimuthal modes $a_0^2, a_1^2, a_2^2, a_3^2$ (where subscript corresponds to the number of azimuthal harmonic) as the result of azimuthal noise decomposition. We see that only axisymmetric radiation dominates in the low frequency range, the first mode appears only for $Sh \sim 0.2$. So, only a few first azimuthal modes give a contribution to the round jet noise. The second and the third modes are absent in this range. The supersonic jet noise directivity has a strong maximum in downstream direction. Prediction of supersonic jet noise based on Tam's theory presents on Fig.5. This regime with intensified axisymmetrical mode was used for directivity comparison in [6].

Since the instability waves are the main element of the theory we consider their main features in simplest situations in some details.

INSTABILITY WAVE PROBLEM

Vortex sheet waves

Vortex sheet model corresponds to the initial part of shear layer near the nozzle. This part of shear layer is one of the most important one due to its strong instability and great sensibility to the outer disturbances. The problem of designing the advanced propulsion system requires the high velocity jets of complex configuration to be investigated. For such jets the representation of the shear layer in the form of vortex sheet is a substantial simplification. We will discuss some approach to the instability wave concept, restricting ourselves by 2D problem and begin from the eigen solution for the vortex sheet separated the uniform flow from the surrounding gas [9-11].

Consider the simplest model of the mixing layer, i.e. a vortex sheet model. Let (x, y) be Cartesian system of coordinates with the x -axis oriented along the main flow. In the region I ($y > 0$) where the fluid is at rest and in the region II ($y < 0$) of the uniform flow with the velocity V_0 , the disturbances of the potential ϕ are governed by the wave equation and by the convective wave equation, respectively

$$\frac{\partial^2 \varphi_1}{\partial t^2} - \Delta \varphi_1 = 0, \quad y > 0 \quad (1)$$

$$\frac{D^2 \varphi_2}{Dt^2} - \Delta \varphi_2 = 0 \quad y < 0, \quad (2)$$

$$\frac{D}{Dt} \equiv \frac{\partial}{\partial t} + V_0 \frac{\partial}{\partial x}$$

At the vortex sheet $y = 0$ the boundary conditions of pressure continuity

$$\frac{\partial \varphi_1}{\partial t} = \frac{D \varphi_2}{Dt} \quad (3a)$$

and of boundary displacement continuity

$$\frac{D}{Dt} \frac{\partial \varphi_1}{\partial y} = \frac{\partial}{\partial t} \frac{\partial \varphi_2}{\partial y}. \quad (3b)$$

are to be fulfilled.

For disturbances of $\exp(-ikct - i\alpha x)$ type (c is the sound velocity) the solutions of Eqs. (1), (2) are as follows: $\varphi_1 \sim e^{-\gamma y}$, $\varphi_2 \sim e^{\beta y}$, where functions γ and β are the following:

$$\gamma = \sqrt{\alpha^2 - k^2}, \quad \beta = \sqrt{(1 - M_0^2)\alpha^2 - 2M_0\alpha k - k^2}$$

The branches of the functions γ and β are selected according to the radiation condition: (i) the field must diminish at $y \rightarrow \pm\infty$ for every fixed t ; (ii) the field must be produced by sources on the vortex sheet (causality).

It is easy to show that this condition at $k = k_1 + ik_2$ ($k_1 > 0$) is satisfied only by the solutions of the type of $k_2 > 0$, $\text{Re } \gamma > 0$, $\text{Re } \beta > 0$. The case $k_2 = 0$ is considered to be the limit of $k_2 \rightarrow +0$.

The dispersion relation determining the flow eigen-oscillations is as follows:

$$D_0(k, \alpha) = (k + \alpha M_0)^2 \gamma + k^2 \beta = 0 \quad (4)$$

The cuts of the function γ are realized from the branch points $\alpha = \pm k$ along the lines $\text{Re } \gamma = 0$. The cuts of the function β are realized from the branch points $\alpha = \frac{k}{1 - M_0}$, $\alpha = -\frac{k}{1 + M_0}$ along the lines

$\text{Re } \beta = 0$, Fig. 6. The solution of equation (4) can be considered on four sheets of the Riemann surface of the function $D_0(k, \alpha)$: I. $\text{Re } \gamma > 0$, $\text{Re } \beta > 0$, II. $\text{Re } \gamma < 0$, $\text{Re } \beta > 0$, III. $\text{Re } \gamma > 0$, $\text{Re } \beta < 0$, IV. $\text{Re } \gamma < 0$, $\text{Re } \beta < 0$. We are interested in the solution on the first sheet only, where the branches of the functions γ and β are selected according to the radiation conditions said above, that is $\text{Re } \gamma > 0$, $\text{Re } \beta > 0$.

The solutions of equation (4) in the complex plane α and at the real $k > 0$ depend on the flow Mach number [9-11]. At $M_0 < 2$ only two complex roots are available on the first sheet:

$$\frac{\alpha_{1,2}}{k} = \left[-\frac{M_0}{2} \mp i \sqrt{-\left(\frac{M_0^2}{4} + 1\right) + \sqrt{1 + M_0^2}} \right]^{-1} \quad (5a,b)$$

In this equation the upper sign (α_1 -wave) corresponds to Kelvin-Helmholtz instability (Fig.6 a,b).

At $2 < M_0 < 2\sqrt{2}$ the complex roots (5) remain. Besides, the root

$$\frac{\alpha_3}{k} = -\frac{2}{M_0} \quad (6)$$

transfers from the second (third) sheet to the first (forth) one (Fig.6c). This root appearance is associated with overlap of the cuts of the functions γ and β .

At $M_0 \rightarrow 2\sqrt{2}$ two complex roots of the type of (5) approach the real axis. Thus at $M_0 > 2\sqrt{2}$ there are three real roots. Two of them are as follows:

$$\frac{\alpha_{1,2}}{k} = \left[-\frac{M_0}{2} \pm \sqrt{\left(\frac{M_0^2}{4} + 1 \right) - \sqrt{1 + M_0^2}} \right]^{-1} \quad (7)$$

The third root is defined by Eq.(6) (Fig.6d). Thus for the vortex sheet model the flow becomes steady at $M_0 > 2\sqrt{2}$ relative to 2-D disturbances. In such flow there are three neutrally stable waves determined by Eqs.(6), (7).

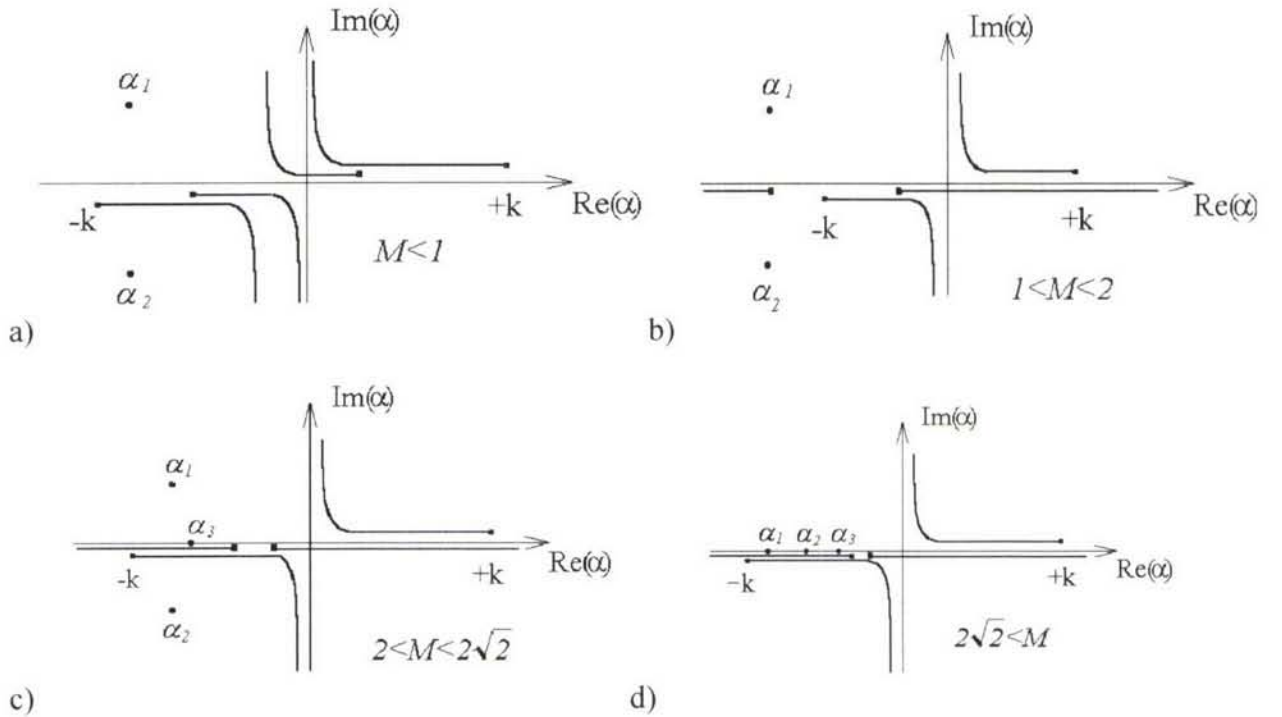


Figure 6. Possible positions of the roots α of the dispersion equation (4) on the complex plane of α according to M

At very large M the expressions for the roots are simplified and are as follows:

$$\frac{\alpha_1}{k} = -1 + \frac{1}{2M_0^2} + O(M^{-3}), \quad \frac{\alpha_2}{k} = -\frac{1}{M_0 - 1} - \frac{1}{2M_0^2} + O(M^{-3}), \quad \frac{\alpha_3}{k} = -\frac{2}{M_0} \quad (8)$$

Thus the root α_1 displaces at large M along the real axis to the branch point of the function γ and the root α_2 displaces to the branch point of the function β .

To excite the eigen solutions (5)-(7) in initial value problem we must to consider the incidence field not orthogonal to them. For the scattering of plane acoustic wave these solutions are not excited [9-11]. Vortex sheet modes are excited in the more special problems where some non-uniformity is existed: (i) point source near the vortex sheet, (ii) plane wave scattering on the half plane, etc. Even in these problems to capture the instability pole with nonzero imaginary part some special technique based on causality principle is to be used. The limit regime as $t \rightarrow \infty$ could be realized for the convective instability system only [12-13]. The causality principle for such systems strongly differs from usual technique of small dissipation. The causal solution of initial value problem is based on Fourier transformation with complex k ($Im k \rightarrow \infty$) with subsequent analytical continuation $Im k \rightarrow 0$.

Point source near vortex sheet

Consider the sound source located over the vortex sheet $y_0 = L$ of $\exp(-ik_0 ct)$ type switched on at $t > 0$ (initial value problem). There were many questions connected with statement of oscillation problem for the system of unconfined increase [14-16] which is incorrect according to Hadamar [17]. The other problem connects with using of Fourier transformation technique for unstable system. These problems were resolved following some ideas adopted from plasma physics and plasma instabilities [12-13]. Thus, the vortex sheet as oscillation system is supposed to be a realization of some system of confined increase with convective type of instability.

Consider the second problem in more details (Fig.7). The boundary conditions are formulated above (3a)-(3b).

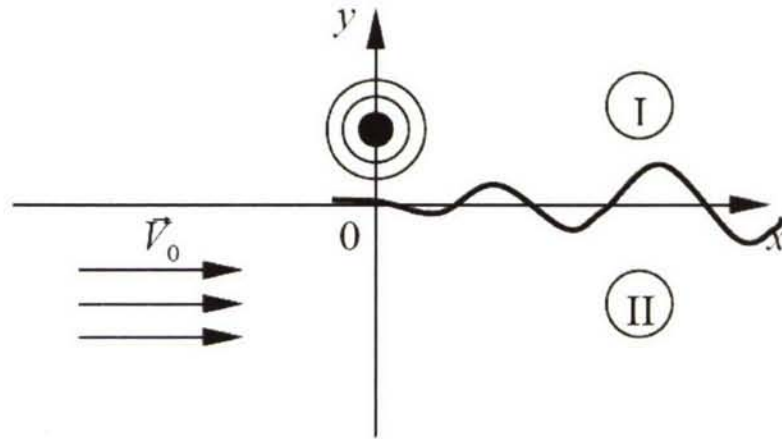


Figure 7. Sound source under the vortex sheet

For the Fourier transformation of the solution in the region I we obtain

$$\varphi(\alpha, y) = \int_{-\infty}^{\infty} \varphi \exp(i\alpha x) dx$$

$$\varphi(x, y) = \frac{1}{2\pi} \int_C \frac{A(\alpha, k_0)}{\gamma} \exp(-\gamma(y+h) - i\alpha x) d\alpha \quad (9)$$

$$A(\alpha) = \frac{k_0^2 \beta - (k_0 + M\alpha)^2 \gamma}{k_0^2 \beta + (k_0 + M\alpha)^2 \gamma}, \quad (10)$$

Integrand in Eq. (9) includes the pole corresponding to the Kelvin-Helmholtz instability. The instability wave is equal to the residue in the denominator (10) at point (5b). If the contour C coincided with real

axis it would not include the instability wave [18]. In correct solution the contour C is obtained from condition of analytical continuation from complex k_0 having large imaginary part to $\text{Im } k_0 \rightarrow 0$ (this procedure localize the position of the singularities in the α -plane, corresponding to the causal solution, Fig.8) [20-23].

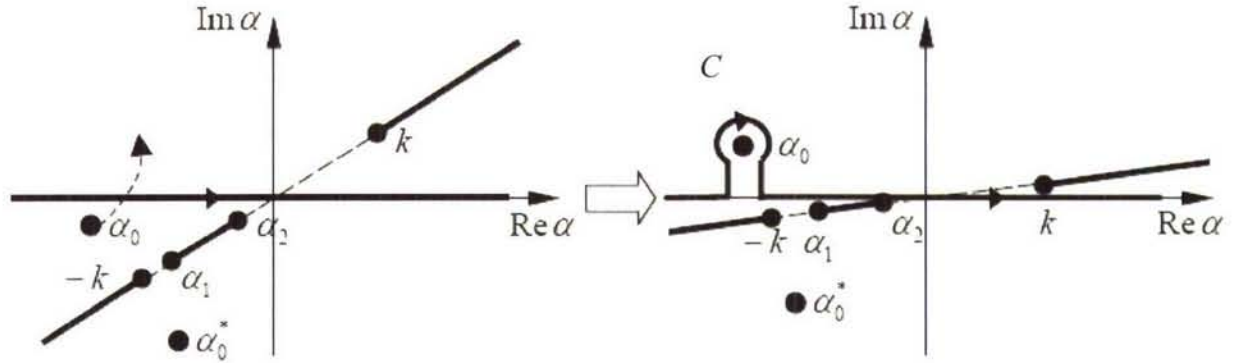


Figure 8 Localization of all peculiarities in $A(\alpha)$ (a) for the $\text{Im } k_0 \rightarrow \infty$, b) for $\text{Im } k_0 \rightarrow 0$.

Scattering of plane wave by semi-infinite screen

Suppose that plane wave is incident on the trailing edge from the supersonic stream (Fig.9). It is some image of instability wave generation in the turbulent jet due to the disturbances in the flow. We suggest that full Kutta-Zhukowsky condition is applied at the trailing edge. Reviews of Kutta conditions in different situations one could find in [24-25]. This problem is solved with the Wiener-Hopf technique.

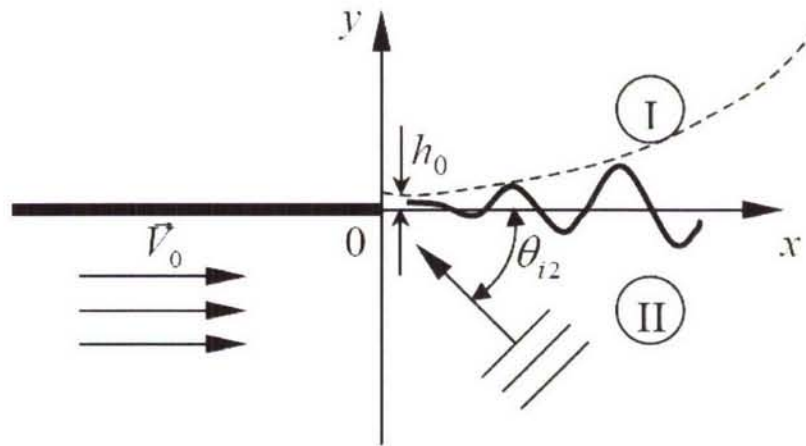


Figure 9. Plane wave incidence on the trailing edge

The capture of Kelvin-Helmholtz instability realized accordingly the same procedure (Fig.8b). The instability wave arises as the residue input in the pole α_0 . Full solution contains the incident wave and diffraction field that along with instability wave satisfy the Kutta condition near the edge. Therefore the instability wave initial amplitude h_0 is determined by the incident wave properties only.

Instability wave in a mixing layer

For slowly divergent free shear flows such as 2D mixing layer the rate of spread ε could be considered as a small parameter (Fig.10). Then the shear layer thickness $H(\varepsilon x)$ is a function of slow variable εx .

This selection of inner variables effectively ensures that the lowest-order solution is identical with that of the classical locally parallel-flow approximation.

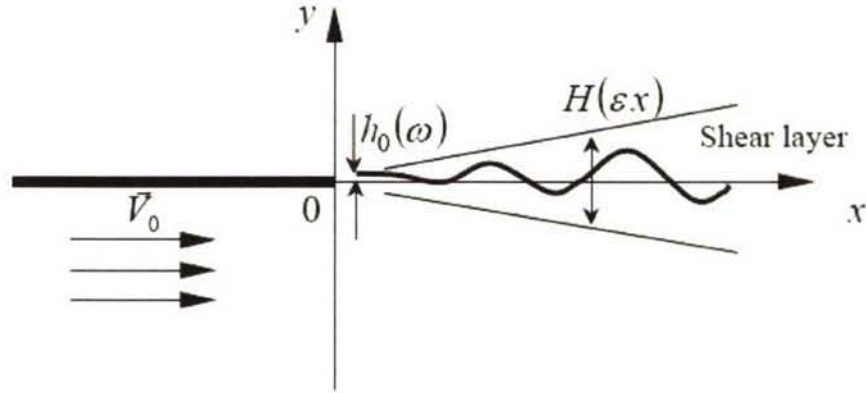


Figure 10. Plane wave incidence on the trailing edge with slowly divergent shear layer

Thus we suggest the instability wave has initial amplitude $h_0(\omega)$ near the edge where the shear layer is close to the vortex sheet. These amplitudes are free parameter in the theory considered later. We consider the initial amplitudes of the instability waves correspond to the diffraction of some incidence disturbances on the plate. The region near the edge gives start to instability wave packet. The amplitude of the packet grows exponentially in the downstream direction while shear layer is thin. After shear layer achieves some value the amplitude of wave packet begins to decrease. This evolution of the wave packet amplitude in downstream direction was considered carefully in the paper [26]. The global solution for noise radiated by wave packet was built there also.

TAM'S THEORY

Inside the jet the mean flow changes very slowly in the axial direction as compared to the radial direction. Therefore in the mixing layer of a supersonic jet the flow near the nozzle has a vortex sheet character and spreading rate of the jet in the downstream direction is very small so that this large disparity in the rate of spatial change in the two directions provides a natural small parameter for a multiple-scales expansion. Vortex sheet instability considered above gives the starting points for the instability wave generation and noise radiation in the supersonic jet. In addition 2D vortex sheet problem explains main difficulties which should be overcome to build the correct causal solution.

Governing Equations

Instability waves in the high-speed axisymmetrical jet and the acoustic radiation generated by these waves are considered. The linearized equations are used for their description. In addition, it is assumed that viscosity and heat conductivity play no significant role in the instability wave evolution.

The disturbances are described by the following equations

$$\frac{\partial \vec{v}}{\partial t} + (\vec{V}_0 \nabla) \vec{v} + (\vec{v} \nabla) \vec{V}_0 = -\frac{1}{\rho_0} \nabla p \quad (11)$$

$$\frac{\partial p}{\partial t} + (\vec{V}_0 \nabla) p + \gamma P_0 \nabla \vec{v} + \gamma p \nabla \vec{V}_0 = 0 \quad (12)$$

where \vec{V}_0 , P_0 , ρ_0 are mean flow velocity, pressure and density, \vec{v} , p are the disturbances of velocity and pressure, $\gamma = C_p/C_v$ is specific heat ratio. Equation (11) is the momentum equation, equation (12) is a combination of equations of continuity, energy and gas law.

The axial symmetry of the mean flow permits searching the solutions of the Eqs (11)-(12) in the form of separate azimuthal harmonics $\exp(in\varphi)$ in cylindrical coordinates r, φ, z with z -axis directed along the jet. Assuming that the instability wave is generated by an external harmonic in time source we search for the solution in the form of $\exp(-i\omega t)$. Then the equations (11)-(12) can be written in the form

$$-i\omega v^r + V \frac{\partial v^r}{\partial r} + U \frac{\partial v^r}{\partial z} + v^r \frac{\partial V}{\partial r} + v^z \frac{\partial V}{\partial z} + \frac{1}{\rho_0} \frac{\partial p}{\partial r} = 0 \quad (13)$$

$$-i\omega v^\varphi + V \frac{\partial v^\varphi}{\partial r} + U \frac{\partial v^\varphi}{\partial z} + \frac{2}{r} V v^\varphi + \frac{in}{r^2 \rho_0} p = 0 \quad (14)$$

$$-i\omega v^z + V \frac{\partial v^z}{\partial r} + U \frac{\partial v^z}{\partial z} + v^r \frac{\partial U}{\partial r} + v^z \frac{\partial U}{\partial z} + \frac{1}{\rho_0} \frac{\partial p}{\partial z} = 0 \quad (15)$$

$$-i\omega p + V \frac{\partial p}{\partial r} + U \frac{\partial p}{\partial z} + \gamma p_0 \left(\frac{1}{r} \frac{\partial}{\partial r} r v^r + in v^\varphi + \frac{\partial v^z}{\partial z} \right) + \gamma p \left(\frac{1}{r} \frac{\partial}{\partial r} r V + \frac{\partial U}{\partial z} \right) = 0 \quad (16)$$

where V and U are the r and z - components of the mean flow velocity, v^r, v^φ, v^z are the r, φ and z components of the velocity field disturbances.

The mean flow in the high-speed jet is characterized by a slow variation of parameters in the longitudinal direction, i.e. $\frac{\partial}{\partial z} = 0(\varepsilon) \frac{\partial}{\partial r}$, where $\varepsilon \ll 1$ is the small parameter. This permits searching the solution of the problem with the use of perturbation methods. In [27] the solution of this task using the method of matched asymptotic expansions is obtained. For this purpose the internal and the external regions were separated. The internal region is the jet interior and its vicinity and the external field is the whole space outside the jet.

Two approximations in terms of parameter ε are obtained in the internal region. The disturbances are written down as follows

$$p = A(s) \cdot [p_0(r, s) + \varepsilon p_1(r, s) + 0(\varepsilon^2)] \cdot \exp(i\phi) \quad (17)$$

where $s = \varepsilon z$ is the "slow" longitudinal coordinate, $\frac{\partial \phi}{\partial z} = \alpha(s)$, α is the local wave number. Thus, fast and slow variations relative to the longitudinal coordinate z are separated in the disturbances. In the main approximation, retaining the terms of $O(1)$ order we get from equations (3)-(6) a simple differential equation relative to the pressure disturbance:

$$\frac{1}{r} \frac{\partial}{\partial r} \frac{r}{\rho_0 \bar{\omega}^2} \frac{\partial p}{\partial r} - \left(\frac{\alpha^2}{\rho_0 \bar{\omega}^2} + \frac{n^2}{\rho_0 r^2 \bar{\omega}^2} - \frac{1}{\gamma P_0} \right) p = 0 \quad (18)$$

where $\bar{\omega} = \omega - \alpha U$. This equation is solved under finiteness condition at $r = 0$ and under condition of $p \sim H_n^{(1)}(i\lambda r)$ at $r \rightarrow \infty$, where $H_n^{(1)}$ is Hunkel function of the n -th order of the first kind, $\lambda = \sqrt{\alpha^2 - \omega^2/c_0^2}$, $c_0 = \sqrt{\gamma P_0/\rho_0}$ is the sound velocity outside the jet and the cuts of function $\lambda(\alpha)$

are determined in such a way, that $\text{Re } \lambda > 0$ over the whole list of Rieman's surface (this corresponds to p decrease at $r \rightarrow \infty$).

A solution of the spectral task (18) is local wave-number α and eigen-function $p(r)$ in each jet cross-section $z = \text{const}$, that is longitudinal coordinate z enters the equation (18) as a parameter. However, solution of Eq.(18) is not sufficient for determining the instability wave even in the main approximation. The point is, that the solutions of spectral task (18) are determined with the accuracy up to arbitrary multiplier $A(s)$. To relate the amplitudes $A(s)$ in different jet cross-section, the following approximation in terms of ε is used.

The terms of $O(\varepsilon)$ order in equations (13)-(16) give the so called solvability equation or, in other words, amplitude equation

$$I_1(s) \frac{dA}{ds} + I_2(s) A = 0 \quad (19)$$

where I_1 and I_2 are the integrals over the radial coordinate r from the terms p_0 and \bar{v}_0 of 0-th order in the expansion (17). The solution of Eq.(19) is expressed in the following form:

$$A(s) = A(0) \cdot \exp \left(- \int_{I_1}^{I_2} ds \right) \quad (20)$$

The equation (20) connects the solutions of the spectral task (18) obtained in different jet cross-sections. This completely determines the shape of the instability wave in the jet.

In contrast to the internal region only one approximation in terms of ε should be obtained in the external region (outside the jet). In this approximation equations (13)-(16) are reduced to the wave equation in the static medium.

$$c_0^2 \nabla^2 p + \omega^2 p = 0 \quad (21)$$

With the use of Fourier transform in terms of the longitudinal coordinate, solution of this equation can be presented in the following form

$$p = \int_{-\infty}^{\infty} g(\eta) H_n^{(1)}(i \lambda r) \exp \left(\eta z + \frac{\pi}{2} \right) dz \quad (22)$$

$$g(\eta) = \int_{-\infty}^{\infty} Q(z) \exp(-i \eta z) dz \quad (23)$$

Equations (22)-(23) is a general form of the wave equation solution in the cylindrical coordinates and expresses the acoustic field outside the jet through density $Q(z)$ of the sources located on the jet axis. The source density $Q(z)$ determining the acoustic field outside the jet can be expressed through amplitude function $A(z)$ obtained as the result of the internal task solution. It was shown [27] that

$$Q(z) = A(z) \quad (24)$$

if the solutions of equation (18) are normalized in such a way, that $p_0(r, s) \rightarrow H_n^{(1)}(i \lambda r)$ at $r \rightarrow \infty$ in each jet cross-section.

The amplitude equation role in the method.

We discuss now the amplitude equation role in the method considered. There are two aspects in this consideration. First, only the amplitude equation permits connecting the disturbance amplitudes in different jet sections. The wave packet has the following form

$$p = \text{const} \sqrt{\frac{1}{I_1(s)}} \cdot \exp\left(-\int_0^s \frac{I_0}{I_1} ds\right) \cdot \exp\left(i \int_0^s \alpha ds\right) \quad (25)$$

and is determined by three multipliers. The first two multipliers are determined by the amplitude equation and only the third one is determined by the imaginary part of wave number α . To solve equations (18) describing the disturbances in different jet sections such a normalization is chosen in the present work, that for each jet section $P = H_n^{(1)}(i\lambda r)$ in the region outside the jet. However since equations (18) are linear any other normalization could be chosen for their solutions. The normalization change is automatically taken into account through change of integrals I_0 and I_1 in amplitude equation (19). Due to complexity of amplitude equation, two first multipliers containing the integrals I_0 and I_1 are often omitted to simplify Tam's method [28-30]. This means that the wave packet is presentation in the form $p = \exp(i \int \alpha dz)$. In this case wave packet form will depend on the normalization of equation (18) solutions, i.e. the solution becomes absolutely arbitrary, in essence.

The second aspect in the amplitude equation role is the quantitative effect of the amplitude equation on the wave packet form and, hence, the radiation directivity. To evaluate this effect the predictions were made in which the amplitude equation was not solved and the wave packets were presented in the form of $p = \exp(i \int \alpha dz)$. It will be shown that without amplitude equation the prediction does not match to the

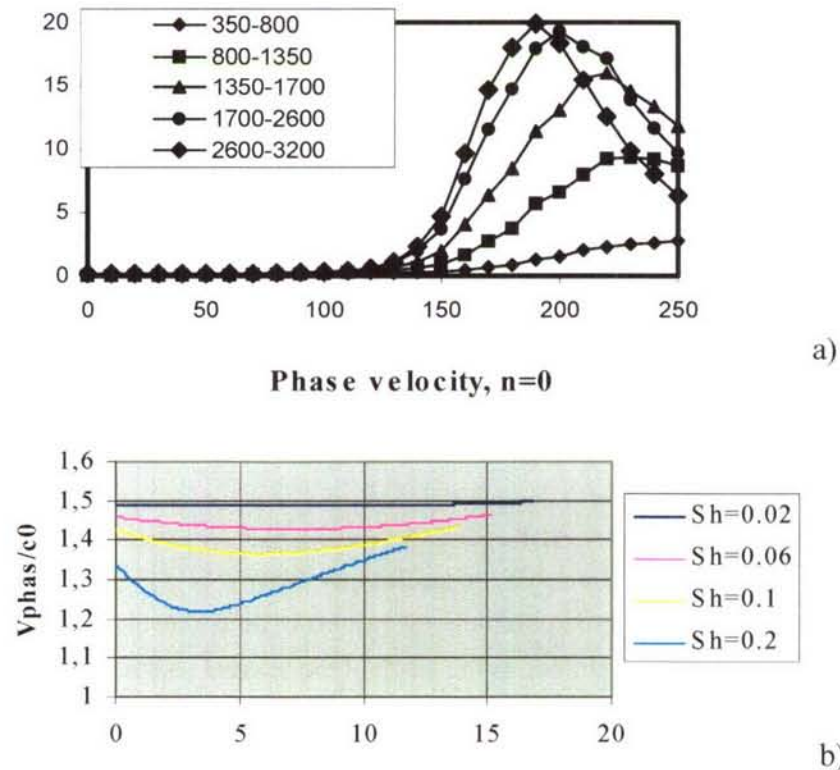


Figure 11. Measurements of axisymmetrical azimuthal mode in jet noise a) and decreasing of phase velocity for . Displacement of maximum upstream as frequency increase.

experiment data. Really, the phase velocity of the wave in the maximum point is decrease as Sh increase (Fig.11b) but in experiment the maximum is displaced in upstream direction (Fig.11a).

DIRECT MEASUREMENTS OF NOISE AZIMUTHAL STRUCTURE

To exclude the noise sources not associated with the Tam's mechanism from experiment, special efforts were made [31]. First, the well shaped convergent-divergent axisymmetrical nozzle designed for exit Mach number $M=2$ was fabricated. The notion of a "well shaped nozzle" included the requirement of flow uniformity at the nozzle exit as well as the property of velocity monotony on the nozzle wall, providing the boundary layer non-separation at any Reynolds numbers.

To avoid the appearance of shock-associated noise in the experiment (Fig.12), the design regime of issuing for well shaped nozzle was controlled with the use of visualization. Fig.13 presents the visualization results for fully expanded regime and under-expanded regime. The fine tuning of fully expanded regime was realized proceeding from the requirement of a complete absence of shocks in the jet. Due to the impossibility of simultaneous performance of the acoustic measurements and visualization on account of the interference introduced by optical equipment, the following scheme of the experiment was chosen. First, with the use of visualisation the necessary monitoring of the system of air supply, which assured the design issue regime, were chosen, and then the optical equipment was taken away from the anechoic chamber and the acoustic experiment was carried out.

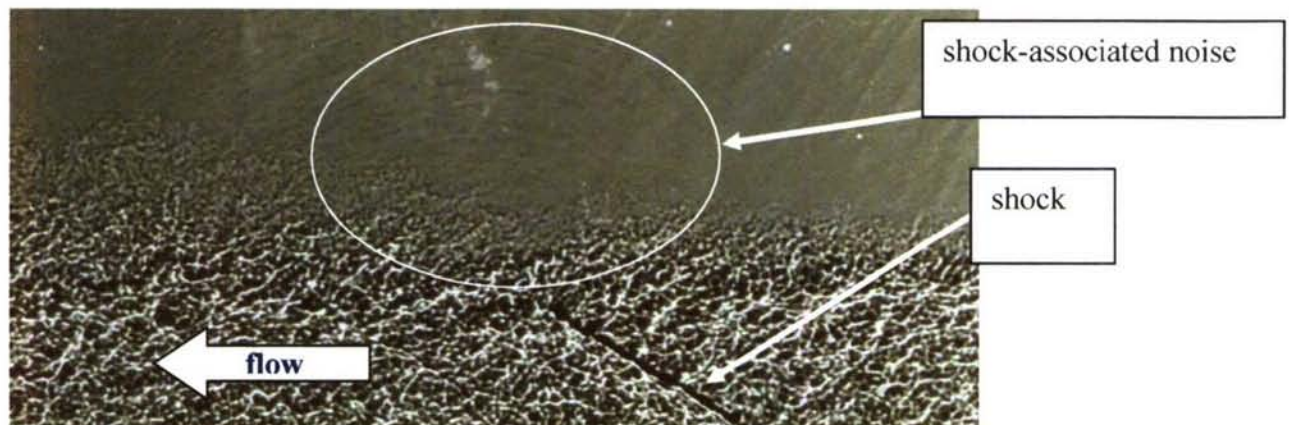


Figure 12. Fully expanded jet from conical convergent-divergent nozzle. Shock-associated noise component exists even for designed regime due to weak shocks structures in the jet (the shadowgraph was kindly given by Dr. V.G. Pimshtein). It was recently measured in azimuthal decomposition experiment (Kopiev, Zaitsev & Karavosov 2002).

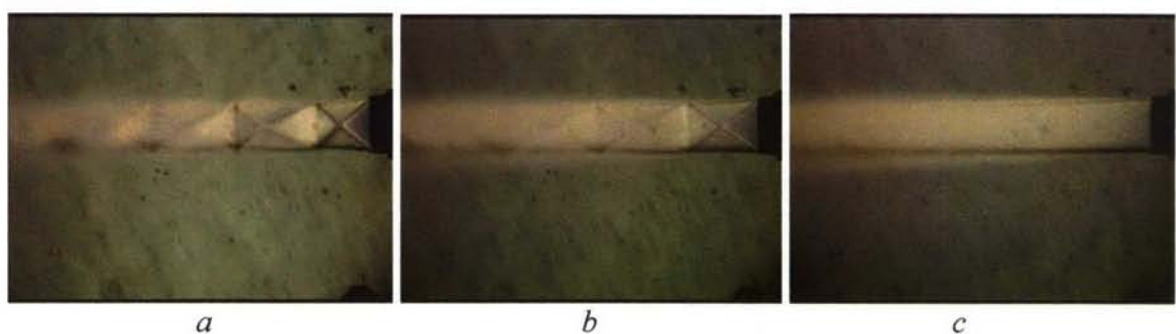


Figure 13 Selected pictures from movie: under-expanded (a,b) and fully expanded (c) regimes.

The technique of azimuthal decomposition of the sound field of supersonic jet with the use of a 6-microphone array (Fig.2) is described in detail in the review paper [7]. This technique gives a possibility of direct measuring the noise of each azimuthal mode separately. In experiment the mixing noise of

supersonic cold jet from convergent-divergent nozzles ($d=3\text{cm}$, $d_{crit}=2.31\text{cm}$) of design Mach number $M=2.0$ (it corresponds to jet velocity $V=540\text{ m/s}$, for cold jets the reservoir temperature equals to ambient temperature $T\sim 300^\circ\text{K}$) was studied. The experimental program consisted of measuring the azimuthal mode intensity in different frequency ranges by a six-microphone array. For acoustic measurements an array of $\frac{1}{4}$ " ICP microphones (Bruel&Kjaer, type 4935) was used. These microphones provided good phase-matching characteristics. The microphone array moves along jet axis z from 0 to 240 cm. The signals from microphones were supplied to Dynamic Signal Acquisition Board NI4472. The nozzle orifice position corresponds to the section $z=20\text{ cm}$. The scheme of the experiment is presented in Fig.3.

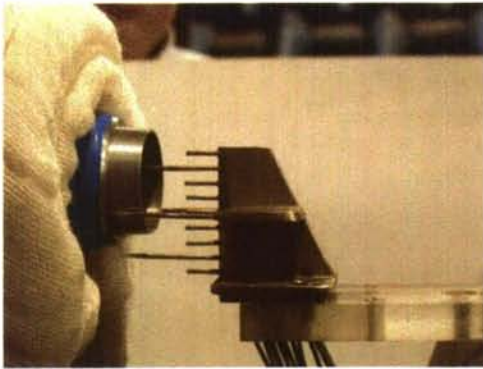
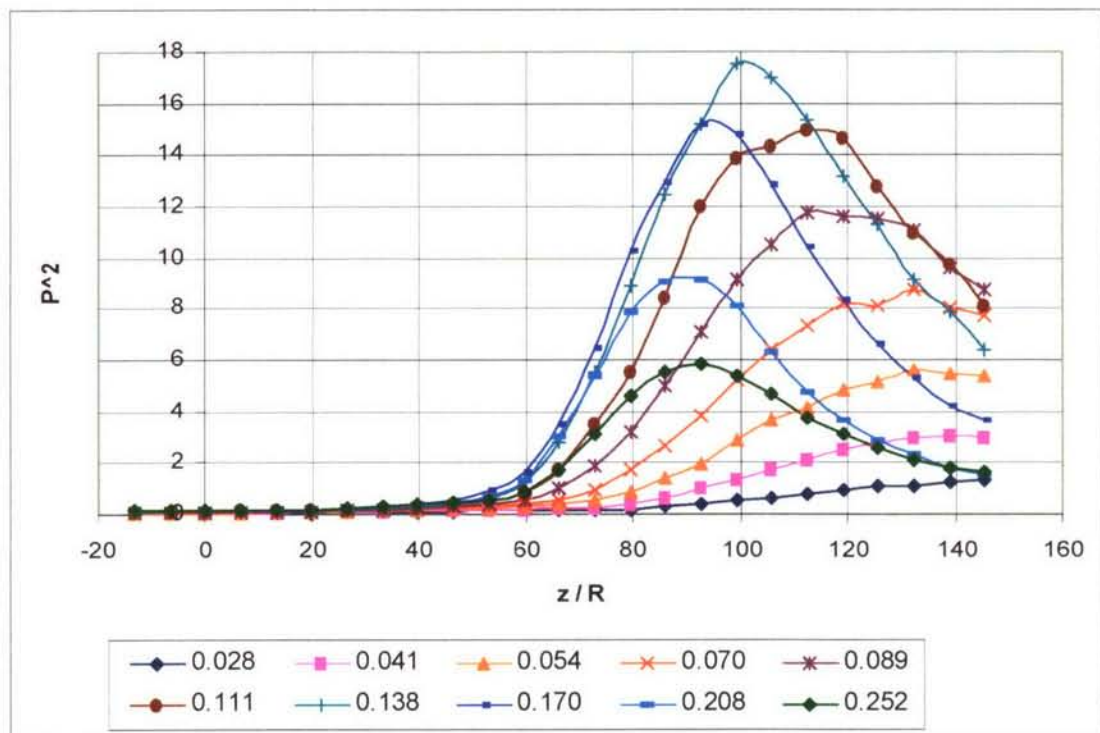
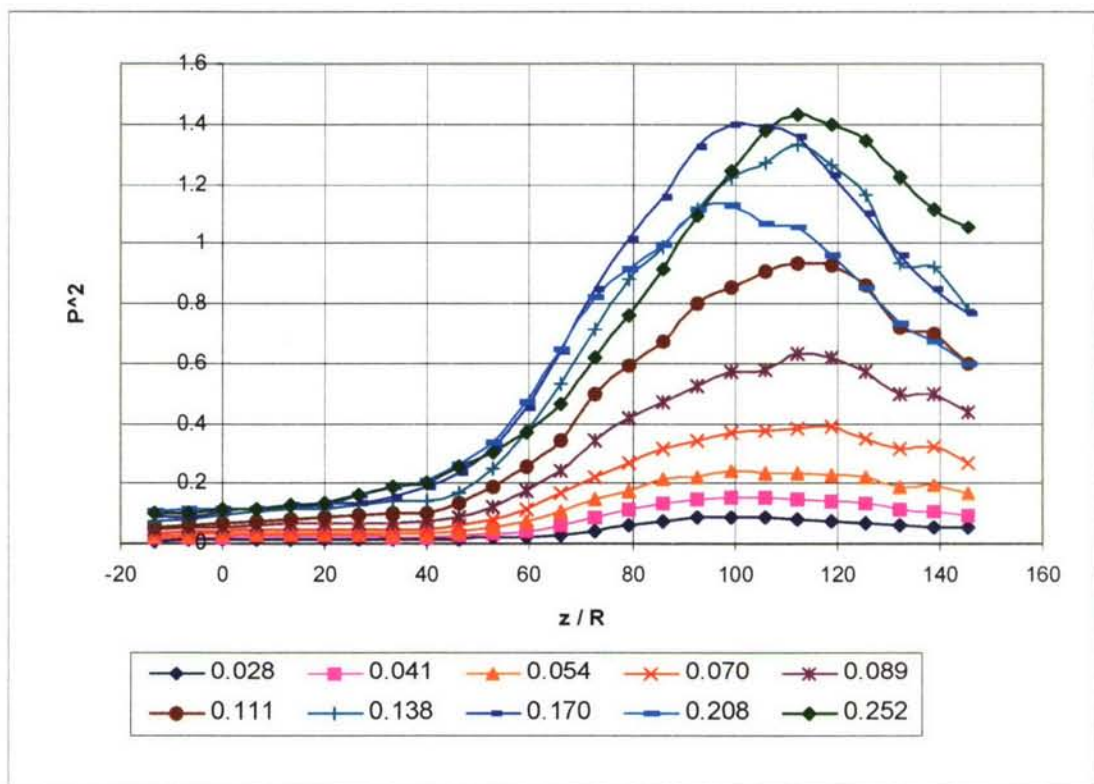


Figure 14. Mean flow measurements.

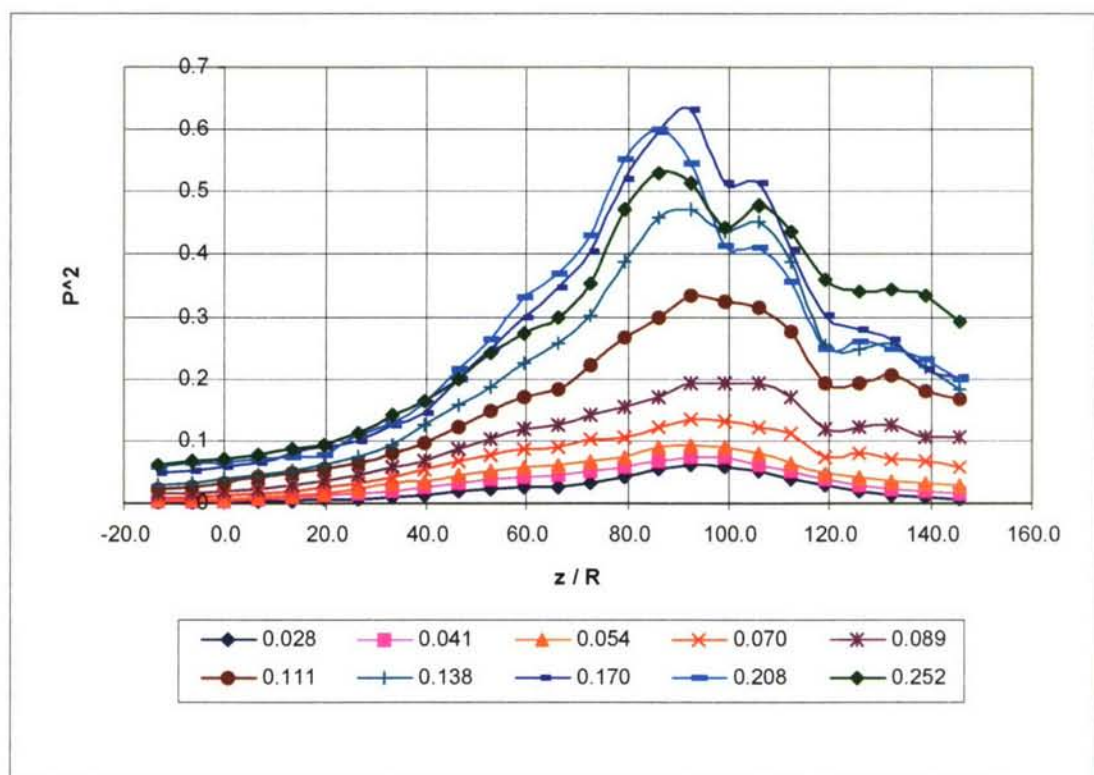
Fig.15 presents the powers of three azimuthal modes a_0^2 , a_1^2 , a_2^2 (where subscript corresponds to the number of azimuthal harmonic) as the result of azimuthal noise decomposition. We see that only axisymmetric radiation dominates in the low frequency range. So, only a few first azimuthal modes give a contribution to the round jet noise. The second and the third modes are small in this range. The peak in axisymmetrical ($n=0$) mode directivity displaced upstream as Strouhal number increase. We present only low frequency results for jet noise azimuthal decompositions up to $St\sim 0.3$.



a)



b)



c)

Figure 15. Measured acoustic pressure level in different frequency ranges for harmonics a) $n=0$, b) $n=1$, c) $n=2$. Harmonic $n = 0$ contributes most of all in total pressure level.

The local Mach number in a jet was calculated from the data obtained with the use of stagnation pressure tube behind the normal shock and the data from static pressure probe before the shock (Fig.14) accordingly known formula [32].

Mean flow parameters underline the acoustic pressure prediction

The mean flow in the program was specified with the use of analytical expressions and for obtaining the non-steady disturbances the numerical solution of differential equations was made. The axial component of the mean flow velocity was determined as follows:

$$U = U_0, \quad r < H$$
$$U = U_0 \exp\left[-\frac{\ln 2}{B^2}(r - H)^2\right], \quad r > H$$

where U_0 is the velocity on the jet axis, B is the half-width of the mixing layer, H is the jet core size in the initial size. Thus, the axial velocity in the mean flow was determined by three functions: $U_0(z)$, $B(z)$, $H(z)$ where z is the longitudinal coordinate, which were calculated using the semi-empirical theory described in the handbook [32]. A comparison of measured and calculated velocity at the axis of the jet is presented in Fig.16. The temperature field in the mean flow was specified using Crocco-Busemann's equation and the radial component of the velocity in the mean flow was found from the equation of continuity.

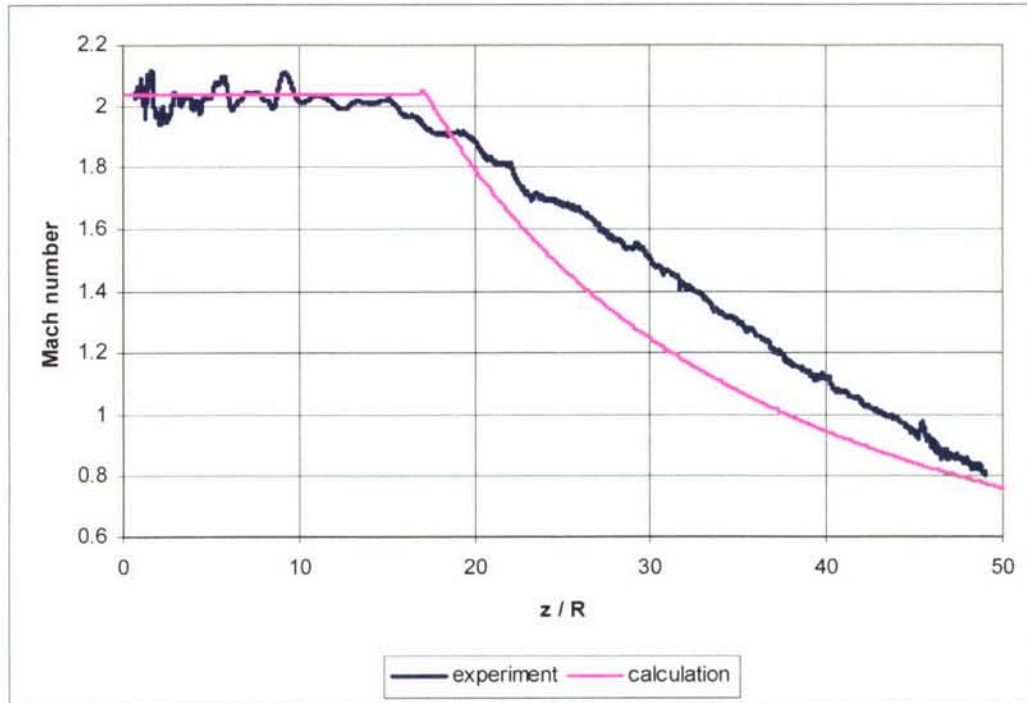


Figure 16 Comparison of measured and calculated mean flow axial velocity at the axis of the jet.

PREDICTION AND MEASUREMENT COMPARISON

The measurement results for well shaped nozzle are compared with the theory predictions. For predicting the jet near field the numerical program was worked out based on the instability wave theory considered above. For comparing with the predictions, the results of acoustical measurements in three frequency ranges were chosen for three azimuthal harmonics $n = 0$, $n = 1$ and $n = 2$. It is seen in Fig.17, where the measurement data are presented, that the largest contribution in the sound pressure level over all the frequency ranges is given by harmonic $n = 0$, a less contribution is given by harmonic $n = 1$ and still less contribution is given by harmonic $n = 2$. According to this observation, the most significant in the prediction and measurement comparison is harmonic $n = 0$.

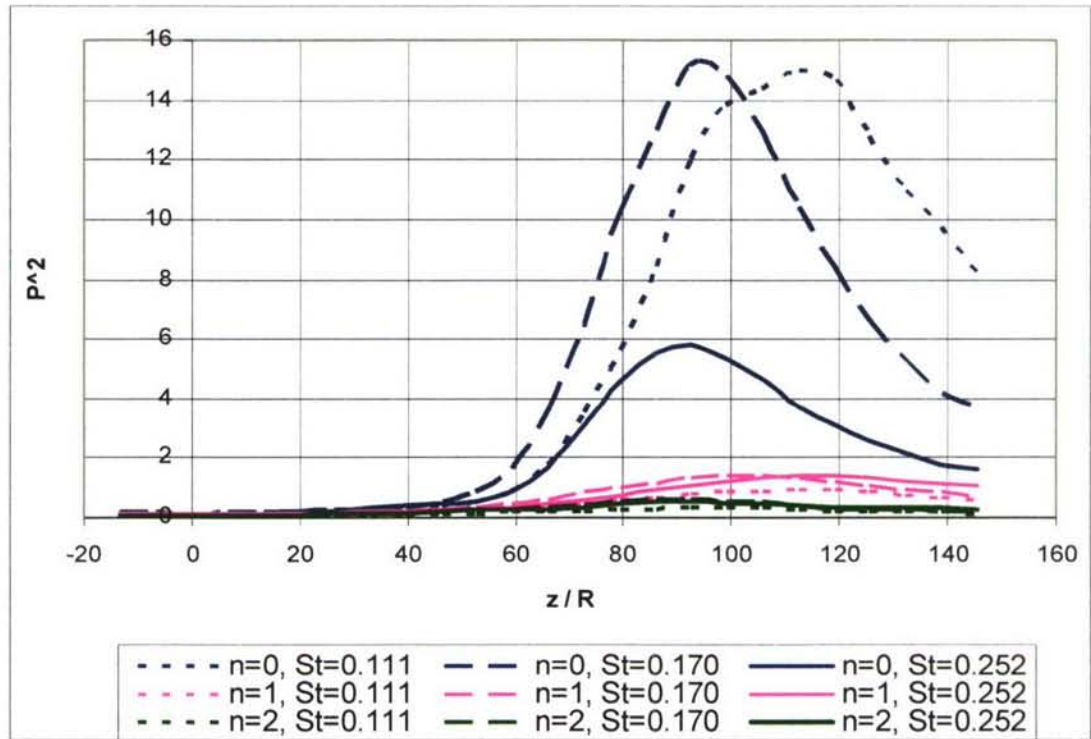


Figure 17. Measured acoustic pressure level in three frequency ranges for harmonics $n=0$, $n=1$ and $n=2$. Harmonic $n = 0$ contributes most of all in total pressure level.

Fig.18-21 presents a comparison between the prediction and measurement data related to acoustic radiation of a cold jet with $M = 2.04$ for three frequency ranges and three azimuthal harmonics. In doing so, its own normalization was chosen in each frequency range at which the radiation levels would coincide at the maximum point for predictions and measurements. Fig.22 presents relative values of pressure disturbances in the initial part of the mixing layer, corresponding to this normalization. According to the Tam's theory [2] the pressure disturbances near the nozzle edge is a white noise in time and space (in the azimuthal direction). In this case the pressure disturbance level in this region must be the same for different harmonics and frequency ranges. It is seen in Fig.22 that this value varies in dependency on harmonics and frequency. Nevertheless, this variation can be considered is rather small as compared with the dispersion of near field acoustic pressure (Fig.17).

It follows from Fig.18-21 that the directivity characteristics predicted and measured are similar but the predicted peak of sound pressure is located more closely to the nozzle than in the measurements. This can indicate a less phase velocity in the instability wave or a larger extension of the radiation source in the real jet, in comparison with the numerical model. The most likely cause of this can be not very accurate description of the mean flow velocity profile in the initial jet part. The point is that integral I_0 (25) in many respects determining the wave packet form appears to be very sensitive to the velocity profile form [6]. At the same time it should be taken into account that the distance from the nozzle to the radiation peak location is twice as large as the distance from the jet axis to the measurement array. This means that the discrepancy of the peak locations $\frac{\Delta x}{R} = 10 - 20$ corresponds to the discrepancy in 2-4 degrees in the directivity pattern. Therefore there is a good reason to believe, as a whole, that the prediction results are in agreement with measurement data.

Consider the amplitude equation role on the wave packet form and, hence, on the radiation characteristics. To evaluate this effect the predictions were made in which the amplitude equation was not solved and the wave packets were presented in the form of $p = \exp(i \int \alpha dz)$ and compared with experiment and prediction accordingly full Eq. (25).

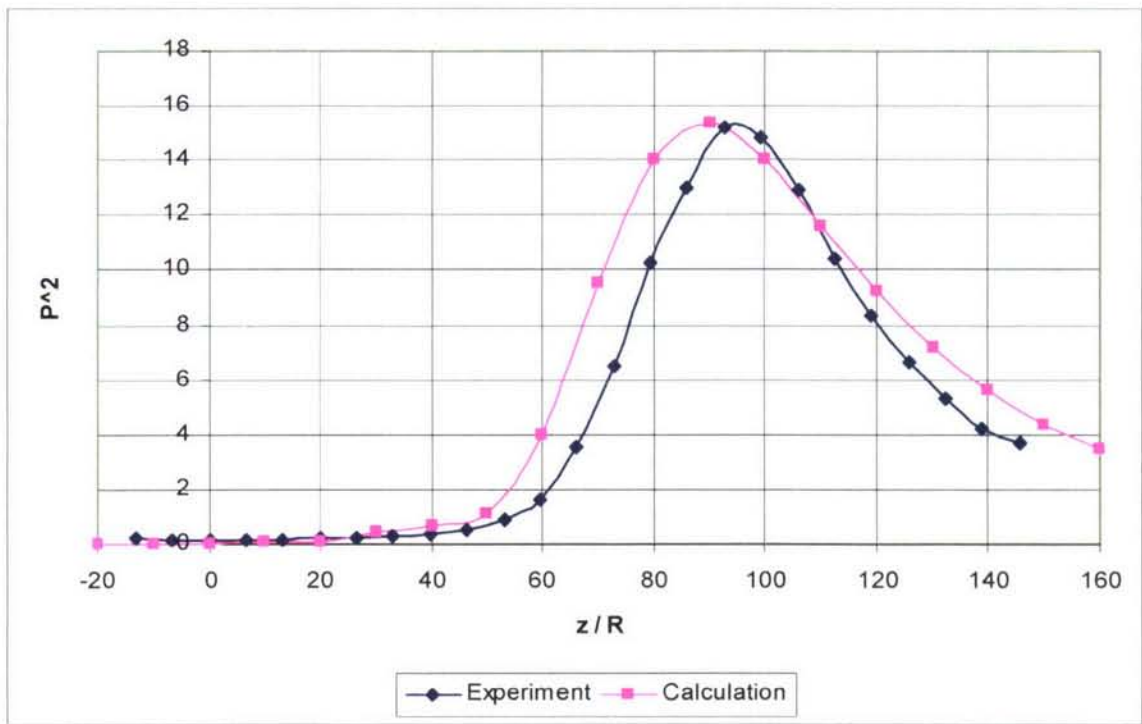


Figure 18. Comparison of the predicted and measured acoustic pressure levels. $n = 0$, $St = 0.17$.

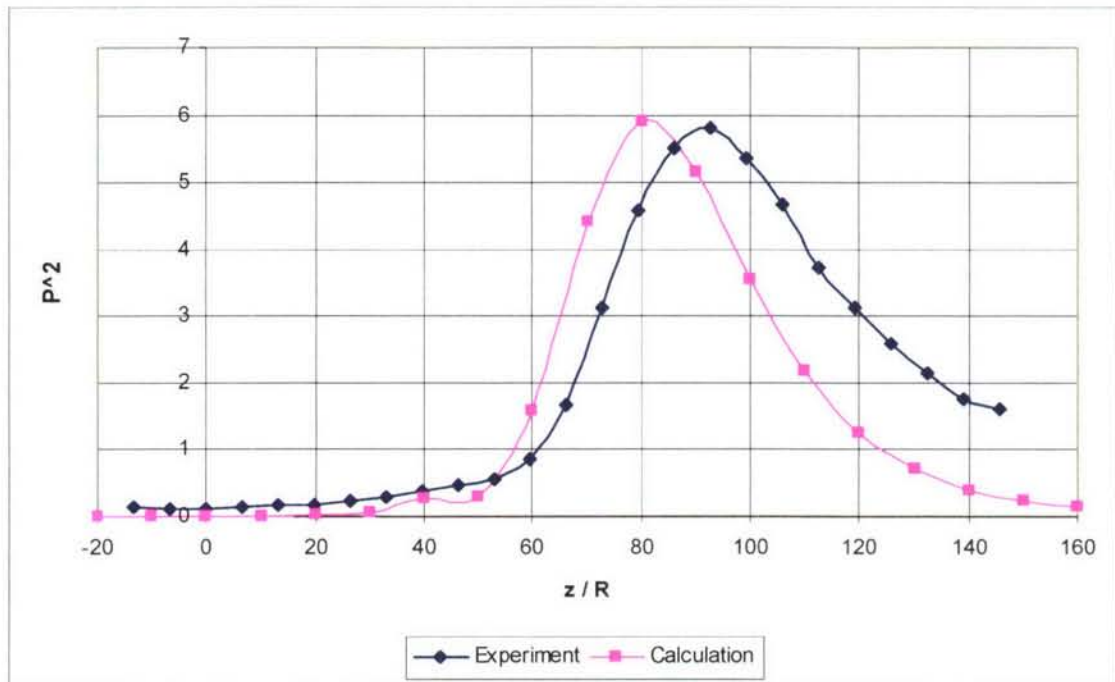


Figure 19. Comparison of the predicted and measured acoustic pressure levels. $n = 0$, $St = 0.252$.

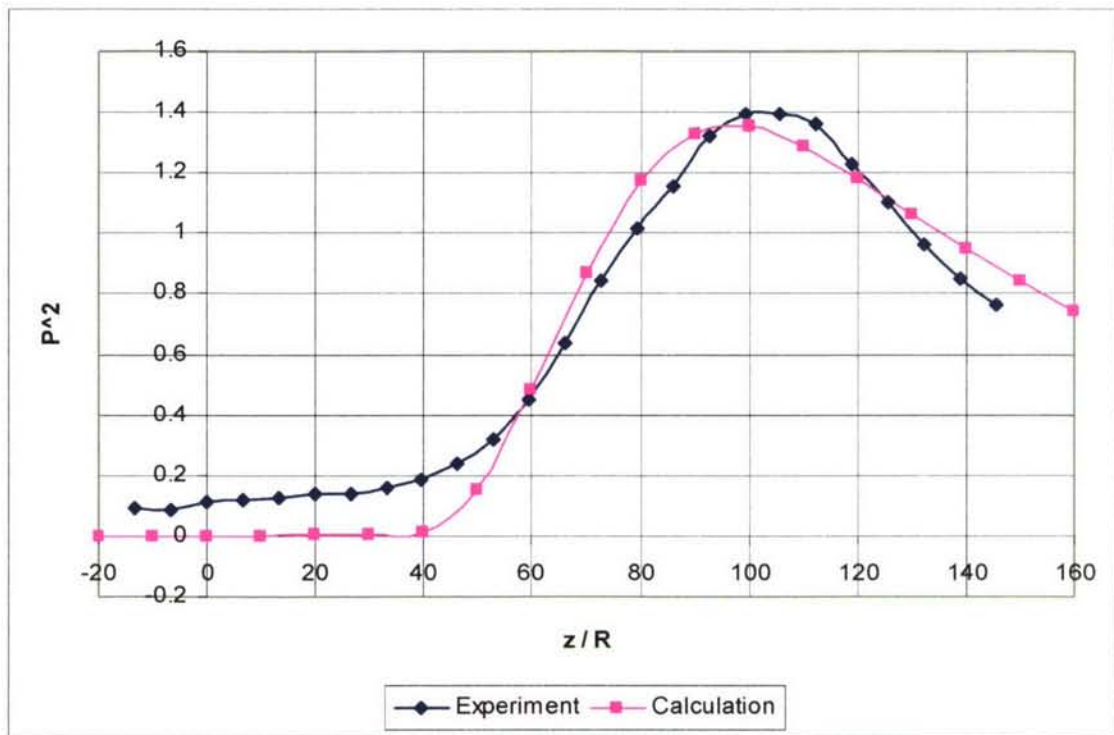


Figure 20. Comparison of the predicted and measured acoustic pressure levels. $n = 1$, $St = 0.17$.

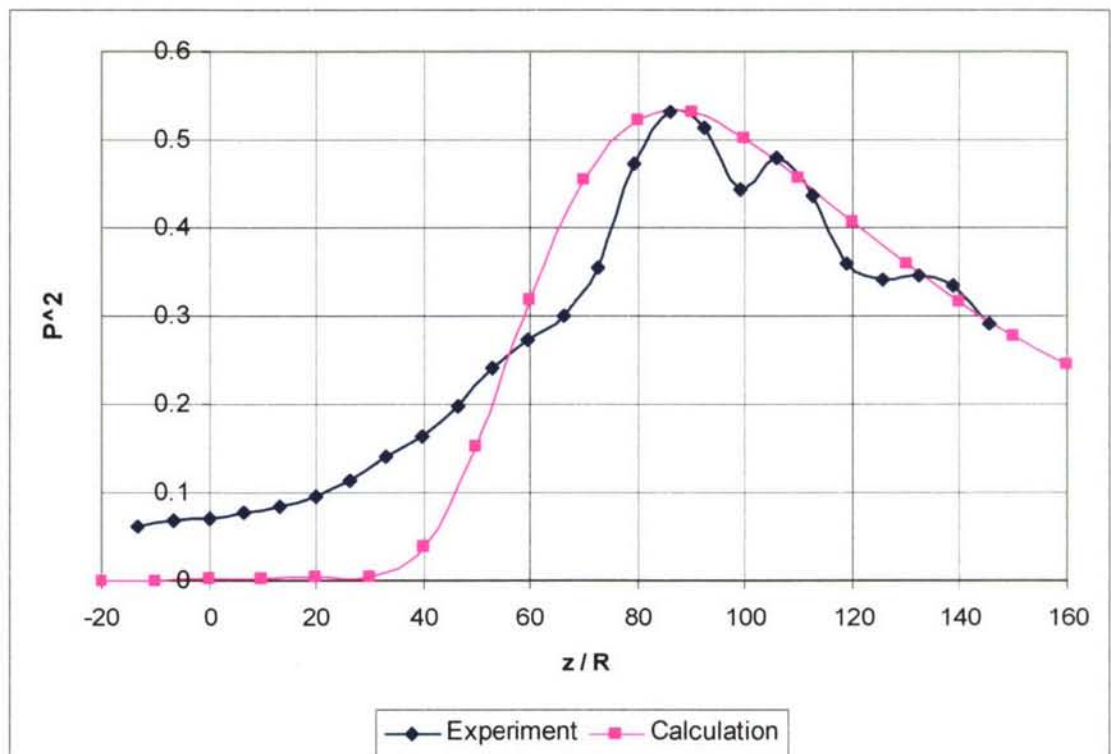


Figure 21. Comparison of the predicted and measured acoustic pressure levels. $n = 2$, $St = 0.252$.

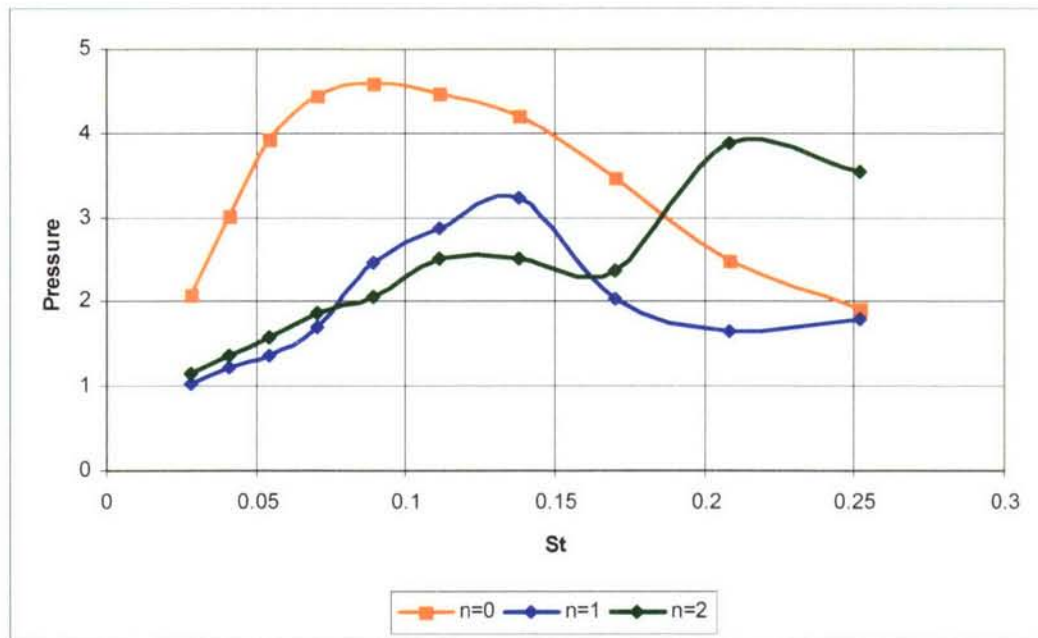


Figure 22. Relative values of pressure disturbances in the initial part of the mixing layer adjusted to acoustic measurements. Dispersion of these data is much less than near field acoustic level.

The wave packets in these prediction were of less extension and the radiation peak was closer to the nozzle than in the full predictions and even more so in the experiments. We see (Fig.7a) that in experiment the maximum in radiation directivity shifts upstream, as the frequency increases. Thus the calculation without amplitude equation is in disagreement with measurement data.

As a whole a conclusion is to be made that the amplitude equation is the essential part of the method and determines the solution in the main approximation.

PROSPECTS

We considered the instability wave model for high speed (supersonic) jet mixing noise. We discussed the verification of instability wave mechanism of noise radiation for supersonic jet. A comparison between the theory predictions and the measurement data shows that the instability waves are the real sources of noise generation in supersonic jet and their control means in fact the noise control.

Consider one possible strategy based on instability wave resonant coupling suggested in [31] which could have a direct importance for the flight vehicles future elaboration. For a round jet with a non-uniform mixing layer, all the Kelvin-Helmholtz eigen-modes are azimuthal harmonics, which are proportional to $\exp(in\phi)$ and have an amplitude which varies in axial direction in a manner which can be ascertained in principle. Independence of each azimuthal harmonic from any other means that knowledge of the amplitude of a given harmonic, near the nozzle exit, entirely determines the amplitude of the wave packet and sound radiation by this harmonic. Given that, at least for $St < 0.3$, harmonics of high azimuthal numbers are poor sources of sound, we can conclude that total noise due to a non-uniform round jet is determined by the harmonics with small azimuthal numbers arising in the total disturbance near the nozzle exit.

Coupling vibrators

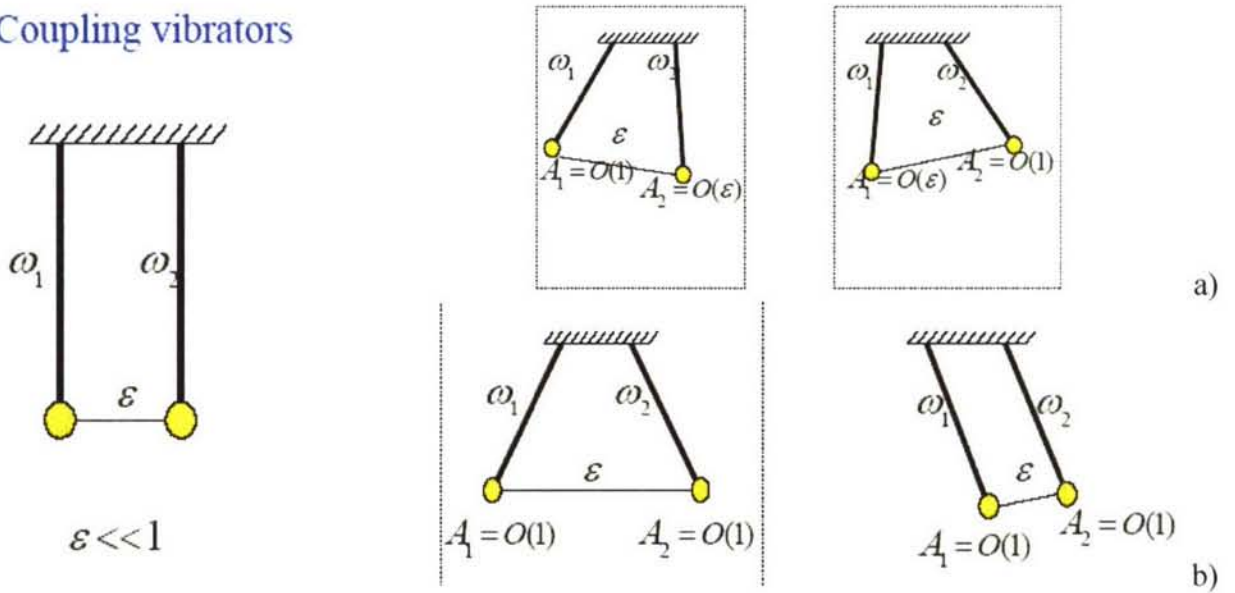


Figure 23. Coupling vibrators

The situation changes dramatically for a jet having a nozzle of a corrugated shape [31]. Clearly, the jet cross-section remains corrugated only for initial part of the jet. The effect of the mixing layer is to reduce the corrugation, ensuring that the jet cross-section becomes circular downstream. Nevertheless, even a weak corrugation, in the initial part of the jet, can strongly affect the disturbance behavior. It was shown that different azimuthal harmonics of a corrugated vortex sheet (an appropriate model for the initial part of a jet) are coupled. In other words, the eigen-modes consist not of a single harmonic but of a mixture of different harmonics (similarly two vibrators with weak coupling: if the eigen frequencies differ, then the weak coupling does not change the eigen forms, Fig.23a, but if the eigen frequencies are close to each other then the weak coupling leads to resonant interaction and strongly changes the shapes of eigen oscillations). Thus, in the case of resonant coupling, this mixture includes two different harmonics in the first approximation in corrugation parameter, a so-called strong mixture of two harmonics.

For example, for a corrugated jet with a lobe number $s = 8$ the 1st and the 7th harmonics are in resonant coupling. It means that there are two abnormal spatial instability eigen-waves within such a jet. Each of them is a strong mixture of the 1st and the 7th harmonics in the initial part of the jet. However, by the point at which the cross-section of the jet has become circular, one of them will have become a pure 1st harmonic whilst the other will have become a pure 7th harmonic. Note, that the latter eigen-mode is not an effective source of sound.

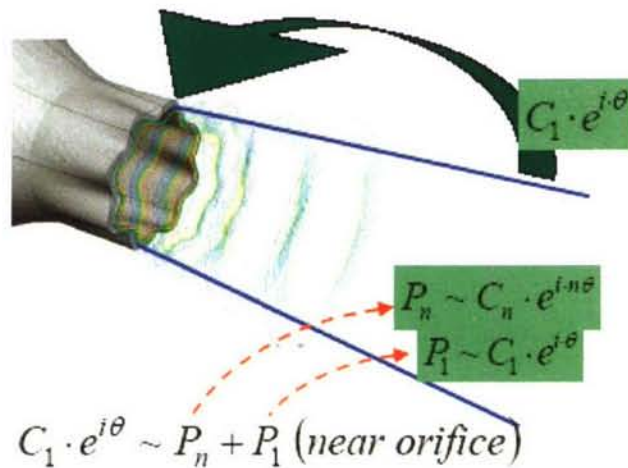


Figure 24 Transformation of radiating part into non radiating one

Thus, an excitation of the disturbances near the nozzle exit in the form of the 1st harmonic generates not one instability wave, as in the case of round jet, but two abnormal instability waves. They combine to give only the 1st harmonic at the nozzle exit cross-section and in some combination of the 1st and 7th harmonics downstream (where the later is non radiating, Fig.24).

Hence, the splitting of the initial disturbance into two eigen-oscillations leads to the situation where part of the initial disturbance is transformed into a non-radiating mode. Moreover, if the initial disturbance is made up of a mixture of the first and the seventh harmonics exactly corresponding to the seventh eigen-oscillation for a corrugated vortex sheet, then such an initial disturbance completely transforms downstream into the seventh azimuthal harmonic and will not radiate at all.

The question related to preparing a required mixture of azimuthal harmonics in the nozzle exit plane and the role of chevrons, or other distortions, in solving this task are left to future investigations.

ACKNOWLEDGEMENTS

The authors would like to express his deep gratitude to Drs. S.A. Chernyshev, M.Yu. Zaitsev and N.N. Ostrikov for fruitful discussions. The work is partly realized with the support of Russian Foundation of Basic Research (RFBR 05-01-00670, 05-01-08052ofi_a)

References

- [1] Tam, C. K. W. "Jet Noise Generated by Large-Scale Coherent Motion" in "Aeroacoustics of flight vehicles. Theory and practice" ed. H. Hubbard, v. 1, pp. 311-390 ASA/AIP, 1991
- [2] Tam, C.K.W. & Chen, P. (1979) A statistical model of turbulence in two-dimensional mixing layers. J Fluid Mech., Vol. 192, pp. 303-306.
- [3] Ffowcs Williams J.E., Maidanik G. The Mach wave field radiated by supersonic turbulent shear flow. J. of Fluid Mech., 1965, v.21, p.641-657
- [4] Bailly C., Candel S., Lafon P. Prediction of supersonic jet noise from a statistical acoustic model and a compressible turbulence closure. J. of Sound and Vibr. 1996, v.194 (2), 219-242
- [5] Troutt T.R., Mc Laughlin D.K., "Experiments on the flow and acoustic properties of a moderate Reynolds number supersonic jet", J. Fluid Mech., 116, 123 – 156 (1982).
- [6] V.F. Kopiev, S.A. Chernyshev, M.Yu. Zaitsev, V.M. Kuznetsov, Experimental validation of instability wave theory for round supersonic jet, 2006, AIAA-2006-2595
- [7] Kopiev V.F., "Azimuthal decomposition of turbulent jet noise and its role for diagnostics of noise sources", VKI Lecture Series 2004-05 "Advances in Aeroacoustics and Applications", 2005, VKI.
- [8] Kopiev V.F., Zaitsev M.Yu., Karavosov R.K. On azimuthal structure of supersonic jet noise. Proceedings of Tenth International Congress of Sound and Vibration ICSV10, Stockholm, Sweden, 2003, v.2, p.637-644
- [9] J.W. Miles. On the reflection of sound an on interface of relative motion. JASA, 1957, v.29, N2, p. 226-228.
- [10] H.S. Ribner. Reflection, transmission and amplification of sound by a moving medium JASA, v.29, 1957, N4, p. 435-441.
- [11] J.W. Miles. On the disturbed motion of a plane vortex sheet. 1958, J. Fluid Mech., v. 4, p.538-552.
- [12] P.A. Sturrock. Kinematic of growing waves. Phys. Rewiew, 1958, v. 112, N 5, p. 1488-1503.
- [13] R.J. Briggs. Electron-Stream interaction with plasmas. MIT, Cambridge, 1964.

- [14] G. Birkhoff. Helmholtz and Taylor instability. Proc. Symp. App. Math. Soc. v. 13, p. 55-76, 1962.
- [15] K.M. Case. Hydrodynamic stability and the initial value problem. Proc. Symp. Appl. Math. Am. Math. Soc. v. 13, 1962, p.25-33.
- [16] P.N. Shankar. On the evolution of disturbances at an inviscid interface. 1981, J. Fluid Mech. v. 108, p. 159-170.
- [17] R.D. Richtmyer Principles of advanced mathematical physics. V.1, Springer 1978.
- [18] P. Gottlieb. Sound source near a velocity discontinuity. JASA, 1960, v. 32, N9, p. 1117-1122.
- [19] M.S. Howe. Transmission of an acoustic pulse through a plane vortex sheet. 1970. J. Fluid Mech. v. 43, p. 353-367.
- [20] C.K.W. Tam Directional acoustic radiation from a supersonic jet generated by shear layer instability. J. of Fluid Mech., 1971, v.46, p.757-768.
- [21] N. Hardisty. The instability due to acoustic radiation striking a vortex sheet on a subsonic stream, Proc.R.Soc Edinburgh (a), 1973, v.71, p. 141-149.
- [22] M.A. Mironov. Effect of periodical volume source on the flow with 2D tangential discontinuity. Acoust. Zhurn (translated in Acoust. Phys), 1975, v.21, n1, p.79-85.
- [23] Howe M.S. A review of the theory of trailing edge noise. J. Sound Vib. 1978, v.61, 437-465
- [24] Crighton D.G. The Kutta condition in unsteady flow. Ann.Rev. Fluid Mech, 1985, v.17, 411-445
- [25] Tam, C.K.W. & Burton, D.E. (1984) Sound generated by instability waves of supersonic flows: Part1. Two-dimensional mixing layers. J. Fluid Mech., Vol. 138, pp. 249-272.
- [26] Tam, C.K.W. & Burton, D.E. (1984) Sound generated by instability waves of supersonic flows: Part2. Axisymmetric jets. J. Fluid Mech., Vol. 138, pp. 273-295.
- [27] Tam C.K.W., Chen P. Turbulent mixing noise from supersonic jets. AIAA Journal, vol. 32, No. 9, p. 1774-1780, 1994.
- [28] Millet C., Casalis G., Selection of acoustic modes in the vicinity of supersonic jets. AIAA paper 2002-2452, p. 1-7
- [29] Morris, P.J. & Bhat, T.R.S. (1993) Supersonic elliptic jet noise. AIAA Paper 93-4409
- [30] Kopiev V.F., Ostrikov N.N., Chernyshev S.A., Elliot J.W., "Aeroacoustics of supersonic jet issued from corrugated nozzle: new approach and prospects", International Journal of Aeroacoustics, 2004, 3 (3), pp. 199-228
- [31] Abramovich G.N. Applied gas dynamics. Moscow, Nauka, 1969, 824p.

von Karman Institute for Fluid Dynamics

RTO-AVT-VKI Lecture Series 2007

**ADVANCES ON PROPULSION TECHNOLOGY
FOR HIGH-SPEED AIRCRAFT**

March 12-15, 2007

*LH₂ AS ALTERNATIVE FUEL FOR AERONAUTICS –
STUDY ON AIRCRAFT CONCEPTS*

A. Westenberger
Airbus, Germany

LH2 AS ALTERNATIVE FUEL FOR AERONAUTICS - STUDY ON AIRCRAFT CONCEPTS

A. Westenberger

Airbus
Germany

ABSTRACT

A project under the title “Cryoplane – Liquid Hydrogen Fuelled Aircraft System Analysis”, Contract G4RD-CT-1999-00192, has been started within the 5th Framework program of the European Commission in April 2000.

36 partners from industry, research and academia contributed to this project covering aircraft configuration, systems & components, propulsion, safety, environmental compatibility, fuel sources & infrastructure, transition

Total project time was 26 months.

The objectives of the project were to develop a conceptual basis for unlimited applicability, safety, and full environmental compatibility, and to undertake medium/long term scenarios for a smooth transition from kerosene to hydrogen in aviation. This system analysis covers all relevant technical, environmental, societal and strategic aspects providing a sound basis for initiating larger scale activities preparing for the development and introduction of Liquid Hydrogen as an aviation fuel.

The project helped in mastering the necessary technology and provided a comprehensive analysis of the complex interrelated aspects. It looked into the technical feasibility, safety and environmental compatibility of the concept and produced technical solutions and tools. It worked out possible strategies for a smooth transition to the new fuel.

The results of the project confirmed that liquid hydrogen, from the technical side, could be an alternative future fuel. Because of today's high hydrogen production costs and the missing infrastructure it remains not attractive for operation at this time.

This report presents the major results of the assessments made under “WP2 – Aircraft Configurations” and the remarkable messages of the other work packages of the project.

NOMENCLATURE

CMR	Cryoplane Medium Range
CO2	Carbondioxide
A/C	Aircraft
COC	Cash Operation Costs
DOC	Direct Operating Costs
H2	Hydrogen
H2O	water

LCA	Life Cycle Analysis
LH2	Liquid H2
MTOW	Maximum Take-Off Weight
MWE	Manufacturer's Weight Empty
NOx	Nitrogen Oxide
OWE	Operating Weight Empty
p. a.	per annum
Pax	Passenger
RK	Reference a/c Kerosene
WP	Work Package

INTRODUCTION

Air traffic has enjoyed strong growth over a long time, and it is predicted that such growth will continue at rates of 4 – 5 % p.a. over the next decades. Assuming continuing worldwide economic growth, saturation of air traffic is not yet in sight.

It is generally accepted that the emission of greenhouse gases, most notably of long-living carbon dioxide (CO₂), resulting from industrial activities, cannot be allowed to continue increasing if adverse global climate change is to be avoided.

Air traffic today contributes about 3% to the anthropogenic greenhouse effect. This number may change due to increase of air traffic and the decrease of the major CO₂ producers of today.

LH2 could be an alternative to the hydrocarbon fuel like cheap kerosene or any other “designed” hydrocarbon fuel.

It could be a fuel suitable for aircraft to be produced from renewable energy and offering extremely low emissions (zero CO₂, very low NO_x). It has the potential to eliminate the dependency of aviation upon dwindling crude oil resources and to reduce dramatically, the contribution of aviation to the anthropogenic greenhouse effect. Use of liquid hydrogen hence could allow sustainable growth of aviation at high rates (typically 4-5% per year) with an extreme low impact on the environment.

The project “Cryoplane – Liquid Hydrogen Fuelled Aircraft System Analysis” included the assessment of all aspects relevant to form an overall judgment and defined technical concepts for initializing realization.

The whole project was structured into 8 technical work packages.

WP1 (Project Management)

WP2 Aircraft Configuration

WP3 Systems and Components

WP4 Propulsion

WP5 Safety

WP6 Environmental Compatibility

WP7 Fuel Sources and Infrastructure

WP8 Transition Scenarios

WP9 Trade-off: Slush

Overall aircraft configurations have been identified, which meet the requirements of efficient and safe operation in all aircraft categories, from “Business Jets” to “Very Large Long Range Aircraft” (600 and more seats). Their performance has been analyzed and compared to conventional aircraft.

Based on an overall architecture for the fuel system, which was adapted to those tank arrangements required for different aircraft categories, the technical feasibility and availability of suitable components has been assessed.

Detailed analyses of „conventional“ and “unconventional” engines have been done.

Safety aspects specific to aviation have been assessed, coming to the overall conclusion that hydrogen fuelled aircraft certainly will be as safe as conventional aircraft.

Assessments on H₂ production (including extensive LCA), infrastructure and ground-handling facilities and procedures were as well part of this exercise.

With respect to environmental compatibility, great benefits have been identified. According to extensive computer simulations, also the contrails produced by hydrogen-fuelled aircraft will contribute less to anthropogenic greenhouse effect compared to the conventional case. (Source: WP 6 of [2])

This report gives an overview of the project.

TECHNICAL WORKPACKAGES

According to the introduction WP2 to WP9 are technical work packages. WP1 was only related to project management.

Objective of the WP2.

In order to prove the possibility of the use of H₂ as an alternative fuel from the aircraft industrial side the exercise of this project was related to the range of aircraft categories, which are in general in commercial operation.

One objective at the beginning of this project was to identify aircraft configurations, which meet the requirements of efficient and safe operation in all aircraft categories, from “Business Jets” to “Very Large Long Range Aircraft”. Their performance and DOC should be analyzed and compared to conventional aircraft.

Based on data coming from the other work packages configurations of the selected aircraft categories have been worked out. Aircraft performances have been calculated and compared with conventional aircraft.

The work on Aircraft configurations WP2 was split into two main groups of tasks; the conventional und unconventional configurations.

Conventional aircraft configurations have been evaluated for those categories, which were selected before, whereas unconventional categories were worked out in a more general way.

Results

The “Cryoplane - System Analysis” has shown that hydrogen could be a suitable alternative fuel for the future aviation. Nevertheless, due to the missing materials, parts, components and engines further R&D work has to be performed until hydrogen can be used as an aircraft fuel. According to estimations made during this project the earliest implementation of this technology could be expected in 15 to 20 years, under the condition that the research work will continue on a certain level.

From the operating cost point of view hydrogen remains not attractive under the today's condition, while kerosene is much cheaper than hydrogen and production/infrastructure is completely missing.

Following features have resulted from comprehensive calculation and parametric studies for the above listed range of aircraft categories. Due to the bigger wetted surface the energy consumption would increase by 9% to 14%. The OWE may increase by roughly 23% by having additional tank structure, while the difference of the MTOW will vary between plus 4.4% to minus 14.8% depending on the aircraft configuration and mission. All this will result in an increase of the operating costs by 4% to 5% caused by fuel only.

Various unconventional configurations have been assessed. An advantage of the selected configurations relative to conventional configurations could not be identified.

Detailed analysis of “conventional” engines has confirmed that a hydrogen engine will be as efficient as a kerosene engine in terms of energy consumption. Substantial improvements in NO_x emissions by lean combustion have been quantified on the basis of experimental data. Small but not negligible benefits have been found for unconventional engine configurations, utilizing the liquid hydrogen's cooling capacity.

A heat exchanger was identified as one novel feature of the fuel supply system. It is needed to heat up the liquid hydrogen to a temperature, which is suitable to the injection into the combustion chamber. Different design principles have been assessed. Result has confirmed the feasibility, but further research is needed for validation of the design itself and its implementation into the power plant.

Requirements and regulations for ground handling and servicing have to be reviewed and adapted. Airworthiness requirements may be amended according to the specific behavior of LH₂ and the technical design solutions.

All kind of accidental incidents and results of emergency landings have been identified and analyzed. Technical design solutions and/or possible changes of operating procedures have been identified.

Conservative life cycle analysis, based on the data taken from the detailed analysis of the different production, transportation, storage and consumption methods (oilfield to jet propulsion) of H₂ and kerosene performed and compared. The result showed in any case a lower CO₂ production in case of H₂ use. But the high potential is the production of H₂ by renewable energy.

According to extensive computer simulations, contrails produced by hydrogen-fuelled aircraft will contribute less to anthropogenic greenhouse effect compared to the conventional case. The H₂ fuelled main engines may produce 2,6 times more H₂O as kerosene fuelled engines. H₂O is a greenhouse gas, which will remain only very short time, about half a year, in the upper atmosphere whereas CO₂, which is emitted by a kerosene engine, remains about 100 years in place.

Assessments based on conservative calculations have confirmed that the use of hydrogen would reduce aircraft emissions to a minimum. It needs to be validated that the water emission of hydrogen fuelled aircraft propulsion has low impact to the atmosphere as predicted.

Global scenarios for a soft transition to the new fuel have been quantified and checked for practicality in detail by considering Sweden as the leading region during transition to hydrogen.

WP2 – Aircraft Configuration

General

In order to get comparable data from each configuration assessment, design requirements have been established. The fundamentals have been selected as the basis of 1990 with the technology level of 2010. Design rules describing all necessary features like interior layout, weights, performance etc. have been established. Economical conditions of 2010 have been considered for the calculation of DOCs. Family concepts have been worked out for each configuration (Picture 2). The 200 Seater medium range aircraft has been selected as an example aircraft, for which the basic systems' studies were made.

Conventional Configurations

For a selection of transport aircraft, ranging from regional turboprops to very large, long-range jet aircraft (*Picture 1*), a comparison has been made between kerosene and LH2 fuelled versions. The tank layout turned out to be the driver for the design on configurations as LH2 requires 4 times more storage volume than kerosene for the same energy content and must be stored under overpressure. This precludes the use of wing tanks. The optimal choice for the tank layout depends on the aircraft category. For seven categories of aircraft, three basic tank layouts are now being proposed. For "Small Regional Aircraft" and "Business Aircraft" tanks are arranged aft of the aft pressure bulkhead only. For "Regional aircraft up to 100 seats" (turboprop as well as jet) and "Short/Medium Range Aircraft" tanks are arranged behind the aft pressure bulkhead and on top of the fuselage. For "Long Range Aircraft" and "Very Large Long Range Aircraft" (VLLR) tanks are proposed aft of the rear pressure bulkhead and between the cabin and the cockpit. Although these solutions seem to be so diverse as to be conflicting, they are in line with each other as will be explained in the following.

Small Regional Aircraft and Business Aircraft

The simplest solution, the tank behind the aft pressure bulkhead, is only feasible from a center of gravity location consideration when the fuel weight fraction is small. Hence it is applicable only to the "Small Regional Aircraft". However, this concept was used for the "Business Aircraft" as well, for lack of an alternative. To reduce the impact of the single tank on the center of gravity, a wider fuselage was adapted than usual. An exploratory study revealed yet an excessive center of gravity travel, probably requiring a combination of fly-by-wire and a very large horizontal tail, or operational restrictions to the center of gravity. As a result, the aircraft will suffer from increased trim drag and reduced maximum lift.

Regional 100-Seater Aircraft.

For larger fuel fractions and thus range, the fuel in the aft tank must be balanced by a more forward tank. For the "Regional aircraft up to 100 seats" (turbo-prop and turbo-jet) and "Short/Medium Range Aircraft" the fuselage diameter is too small to enable a catwalk parallel to and beside the forward tank, to serve as the cockpit-cabin connection. This forces the tank on top of the fuselage, thereby creating a weight and profile drag penalty. Special attention must be paid to disk burst, as this might lead to an explosion of the LH2 in the top tank. Therefore a dry bay may be created. As a consequence, this configuration is less efficient as the other solutions. It is expected that the top tank does not pose a threat to the passengers in case of fire, as the LH2 will boil off, evaporate and rise upwards.

Short and Medium Range Aircraft

Picture 2 shows the aircraft and family designs, which was based on market requirements

1st Step: Basic version 185 passengers (dual class) 4000 nm design range

2nd Step: Stretch version 218 passengers (dual class) 3300 nm design range

3rd Step: Second step with developed MTOW for 4000 nm design range

4th Step (option only): 1st step with reduced MTOW and engine thrust reduction,

The design philosophy for fuselage assumed the requirements for the fuselage cross section of the 6-abreast single aisle design. This type of cross section is well balanced in terms of comfort / flexibility and freight. On the Cryogene fuselage the top of the cross section is flattened off in the pressurized cylindrical section for reason of tank integration at minimum wetted area.

The first approach a/c CMR-200 -driven by hydrogen fuel - is based on a high wing design for reason of the following considerations:

- use of the box volume - being available anyway – as part of the overall integrated fuel system and as a benefit from this

- close coupled tank without fuel piping in the pressurized cabin.

As a side condition it is assumed that the wing fuel volume should not be under 30% of the total, because it is estimated that otherwise the volume / system ratio would be out of balance.

The condition to provide 30% of the total fuel volume in the wing defines a very large area (233 m²).

Calculation of the drag polar showed that this configuration has a penalty of 17,5% compared with the conventional aircraft.

To improve the situation, the Cryoplane configuration - in a second approach - was redefined. In principle, the low wing (170 m²) of the kerosene aircraft (RK-200) was combined with the fuselage of the initial Cryoplane aircraft (CMR-200). However, as it makes no sense to carry LH2 fuel in the small wing (volume/system unbalance) the tail cone of the fuselage was reshaped to provide the additional volume required for total fuel.

The second-approach configuration of the CMR1-200 a/c, driven by hydrogen fuel, is based on a low wing design and is characterised by a close coupled wing tank on top of the fuselage, by a tail tank and by the absence of fuel piping in the pressurized cabin.

This configuration showed a penalty on the drag polar of 3,5 % against the conventional A/C.

The weight comparison led to following results:

MWE/pax

- Cryoplane a/c: longer fuselage, higher wing weight, additional fuselage tank structure, LH2 tanks 29% higher MWE vs kerosene version

MTOW/pax

- Cryoplane a/c: ~60% lower fuel weight compensates the higher structural weight and leads to 3.3% lower MTOW vs kerosene version at design range (4000 nm)

(Propulsion+Fuel) /pax

- Cryoplane a/c: Same Propulsion weight, ~60% lower fuel weight 46% lower (propulsion+fuel ratio) vs kerosene version

(Propulsion+Fuel+Tanks) /pax

- Cryoplane a/c: Same Propulsion weight, ~70% lower fuel weight, additional tank structure 23% lower (Propulsion+Tanks+Fuel) ratio vs. kerosene version,

For the payload range the design point is the same on both versions 185 pax / 4000 nm. However, the hydrogen aircraft is extremely sensitive to payload variations and exchanging payload for LH2 fuel has a severe effect on range. In consequence of this, the payload – range flexibility on an individual LH2 aircraft is fairly limited, in particular, as for this type of aircraft the fuel volume is not defined by stretched versions. This is specific to the actual LH2 configuration – fuel tanks on top of the fuselage – , because fuel volume increases automatically when the fuselage is lengthened.

Contrary to this, the fuel volume on a conventional kerosene aircraft is defined by the requirements of stretched family members, but – of course – it can be used also for payload/range flexibility on the basic version, if required.

Again, the design point is the same on both versions 218 pax, 4000 nm Payload – range effects, of course, are the same as described under the basic versions. It is worth mentioning, however, that the CMR1-300 has available some extra fuel volume from its stretch, whereas the fuel volume on the RK-300 was already designed into the basic version.

Economics – Fuel Price Assumption: As hydrogen-fuelled aircraft are in an early stage of development there is quite a number of years ahead until this type of aircraft could enter service.

It may be that there will be various reasons to develop the LH2 technology for aeronautical use, like political initiatives in order to protect the environment locally and or globally, increase of kerosene price. As this analysis should not depend on vague speculations, political initiatives have not been taken into consideration.

Therefore, an estimate of future price trends on LH2 / kerosene fuel was established and this was made the reference for basic COC / DOC trends of LH2 and kerosene aircraft. When comparing the cross over points of the fuel cost curves and the COC curves it is found that the year of cross over is identical – for all practical purposes (2037 / 2038).

It may be assumed, therefore, that in terms of economic performance the H2 version CMR1–200 is almost identical to the reference kerosene aircraft RK–200.

As it is assumed that the aircraft price is dependent on the aircraft OWE, and as the H2-variant is some 26% heavier than the kerosene version the cross over point of the DOC curves – relative to fuel and COC - move two years farther into the future (2040).

An energy (block – fuel) comparison came to the result that the energy used by the H2 version on one hand and the kerosene version increases by 6% to 10% on the H2 side, depending on the mission range and on the member of the family considered.

The LH2 aircraft takes off at a higher weight than the kerosene version on short ranges. However, the difference between the two is decreasing as stage length is increasing, and at design range the LH2 MTOW is even slightly below that of the kerosene aircraft.

This results from the effect that the mission-weights of both versions come closer to each other at longer ranges in consequence of that the LH2 fuel is less heavy than kerosene.

Long Range Aircraft and Very Long Range Aircraft.

For the “Long Range Aircraft” and “Very Large Long Range Aircraft” the tank can be placed in the front and aft part of the fuselage. The very large long-range aircraft is very similar to the one shown, except a three-deck layout in order to remain within the 80x80x80 box.

Further Discussion

Finally a check on the various solutions, an extensive parametric study was performed on the allowable combinations of fuselage cross-section, passenger capacity and design range. It appeared that all designs confirm their validity.

All aircraft designs have been compared to check their consistency. The tank layouts have already been discussed. The design weights show a remarkable trend of almost constant OWE versus MTOW fraction of 0.68, i.e. independent of aircraft category or size (*Picture 10*).

The consistency in operational cost penalty to be paid for the improvement in emissions has been investigated. Considering the fact that no technology jump is required for implementation of LH2, aircraft prices have been estimated on basis of empty weight only and no additional development costs have been incurred. The production price of LH2 was assumed to come down from a high factor 5 more expensive than kerosene now to equal in 2037, based on the same energy content. The energy consumption increase of LH2 aircraft is dependent on aircraft category due to the efficiency of the various tank layouts.

All these considerations combined lead for a 1000 nm mission to a 25 % higher DOC now, decreasing to a break-even point in 2040. Obviously, this outcome is heavily dependent on fuel price development of both fuel types.

Unconventional Configurations

A score of configurations has been screened on their suitability for LH2 application. It surfaced very soon that none exhibits those characteristics that met the requirement of carrying volume. Only one configuration, “the twin boom”, was promising. As a comparison, the blended wing body (BWB) was studied as well in the of Medium Range Aircraft category. In the end it appeared that none is superior to the conventional configuration. For the twin boom configuration the large external tanks, leading to high profile and interference drag.

At the end it turned out that all for all unconventional configurations, selected for this study, no advantage against the conventional configurations was obvious.

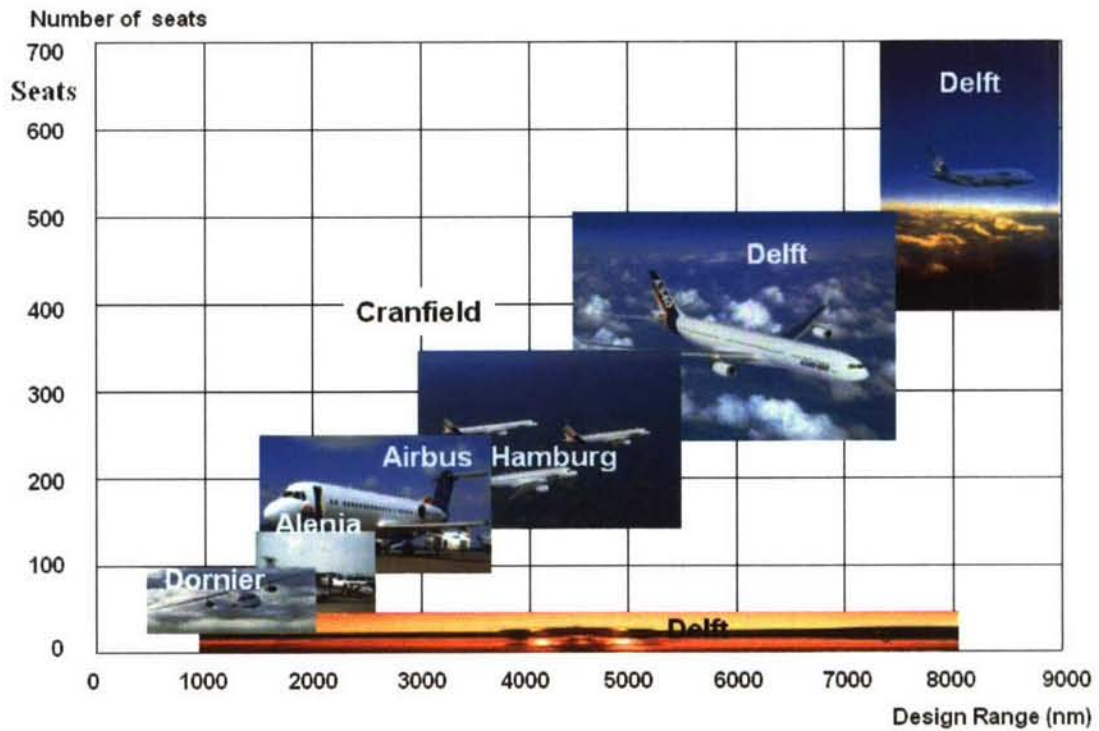
General conclusions

Various tank layouts appeared to be optimal depending on aircraft category. Crucial element is balancing of the aircraft’s center of gravity. Due to the large and heavy tanks, aircraft empty weight will go up by some 25% compared to kerosene aircraft. However, due to the light LH2 maximum take-off weights will go down. As a consequence of the bulky tanks the energy consumption increases as well, resulting in a 25 % increase in DOC as of today for a 1000 nm mission. When LH2 production cost drops to the level of kerosene price, DOC’s for LH2 and kerosene fuelled aircraft may reach a crossover point at about 2040.

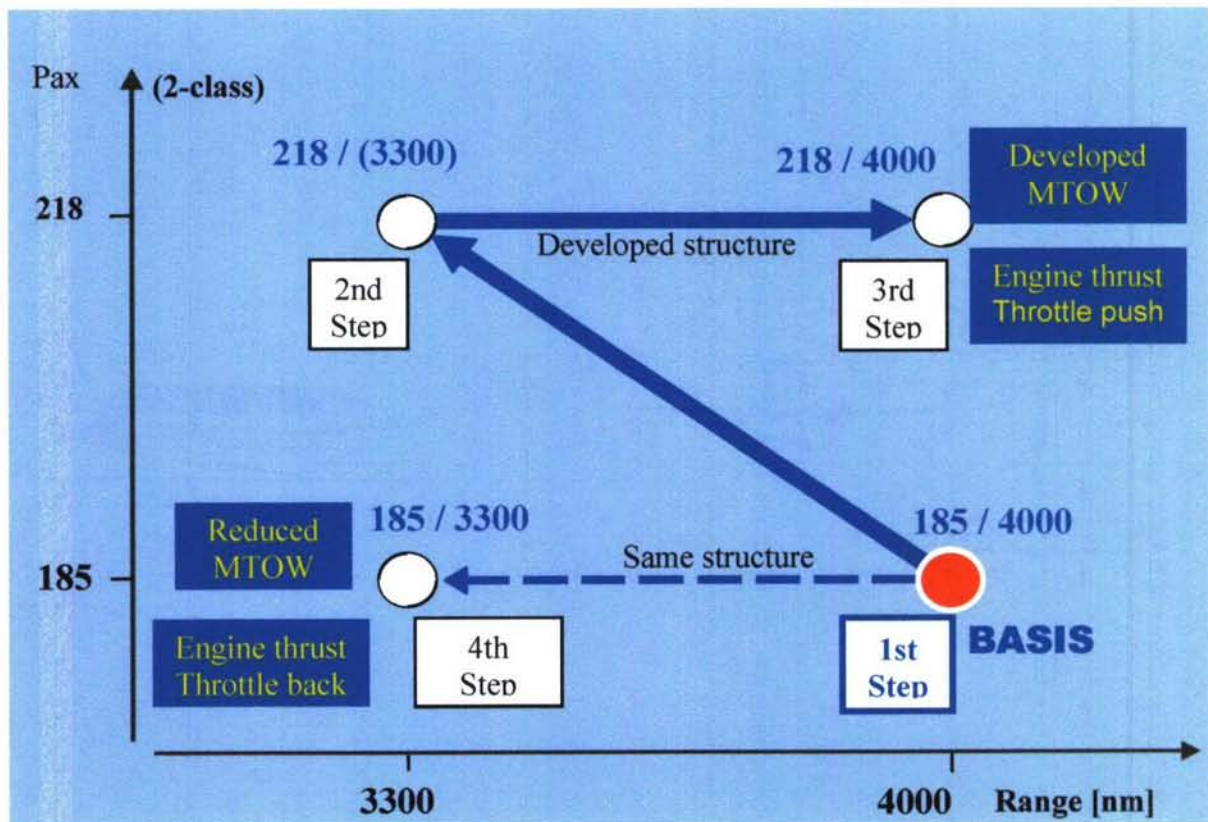
6. - References.

- [1] 1. - "Liquid Hydrogen Fuelled Aircraft – System Analysis (CRYOPLANE)", Part B, Proposal No. GRD1-1999-10014. 14th June 1999. 5th Framework Program of the European Communities Contract No. G4RD-CT-2000-00192.
- [2] 2. Westenberger, A., "Liquid Hydrogen Fuelled Aircraft – System Analysis (CRYOPLANE)", Final Technical Report, Revision 1.
- [3] 3. Prenzel, E., "Liquid Hydrogen Fuelled Aircraft – System Analysis (CRYOPLANE)", TFR2.2.4, Aircraft Configuration - Short/Medium Range Aircraft, Revision 1, 30.09.01.
- [4] 4. Slingerland, R., "Liquid Hydrogen Fuelled Aircraft – System Analysis (CRYOPLANE)", WFR2, Aircraft Configuration, Revision 1, 18.07.02.

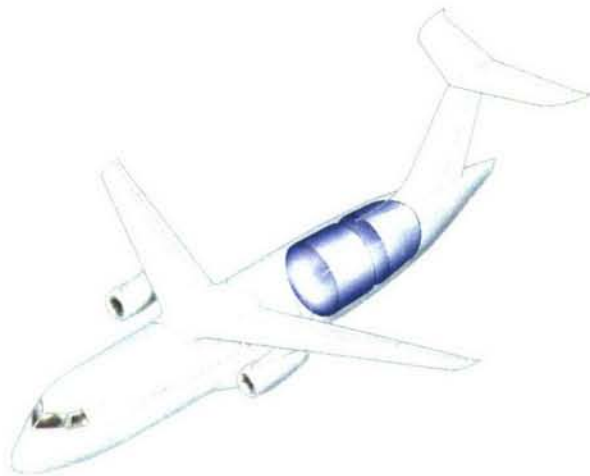
Figures



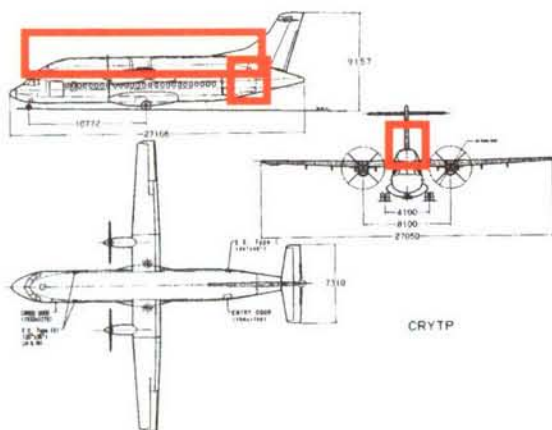
Picture 1: Range of Aircraft Categories, which have been subject of this Project. Dornier, Alenia, Airbus Deutschland, Cranfield and TU Delft have been the partners within this work package)



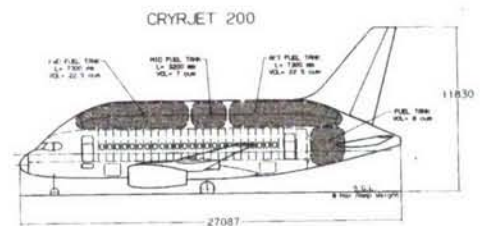
Picture 2: Family Concept for S/M range Aircraft



Picture 3: Small Regional Aircraft.



Picture 4: Regional Turboprop Aircraft



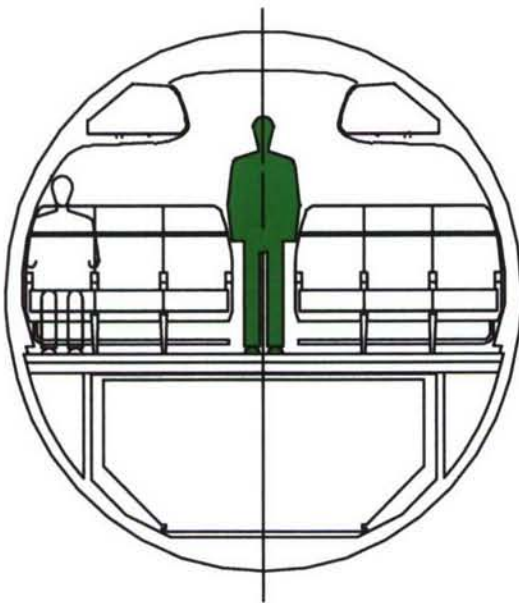
Picture 5: Regional Jet Aircraft



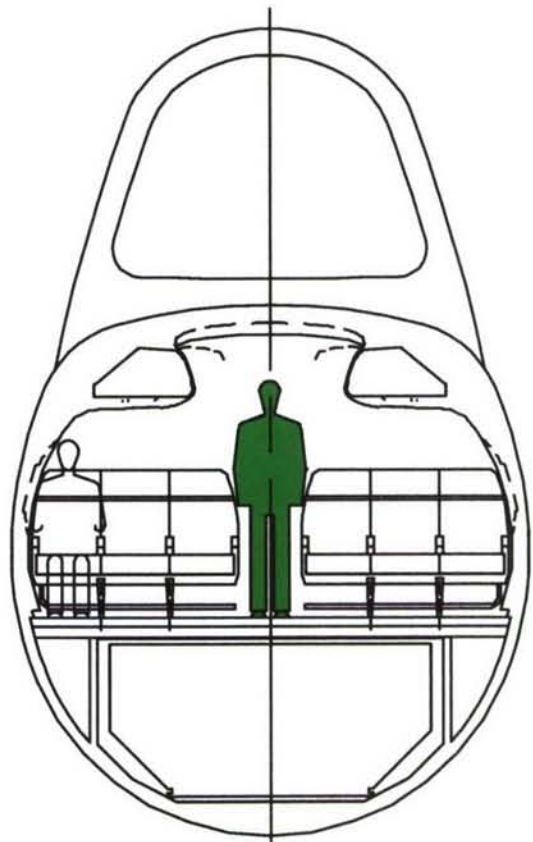
Picture 6: S/M Range A/C First proposal



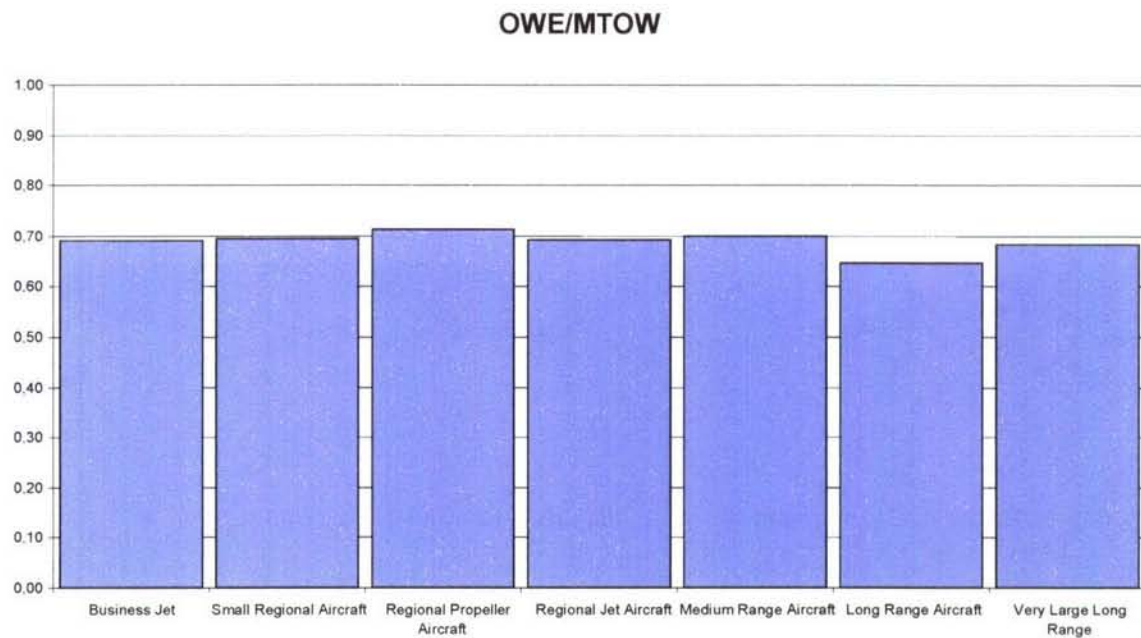
Picture 7: Revised configuration



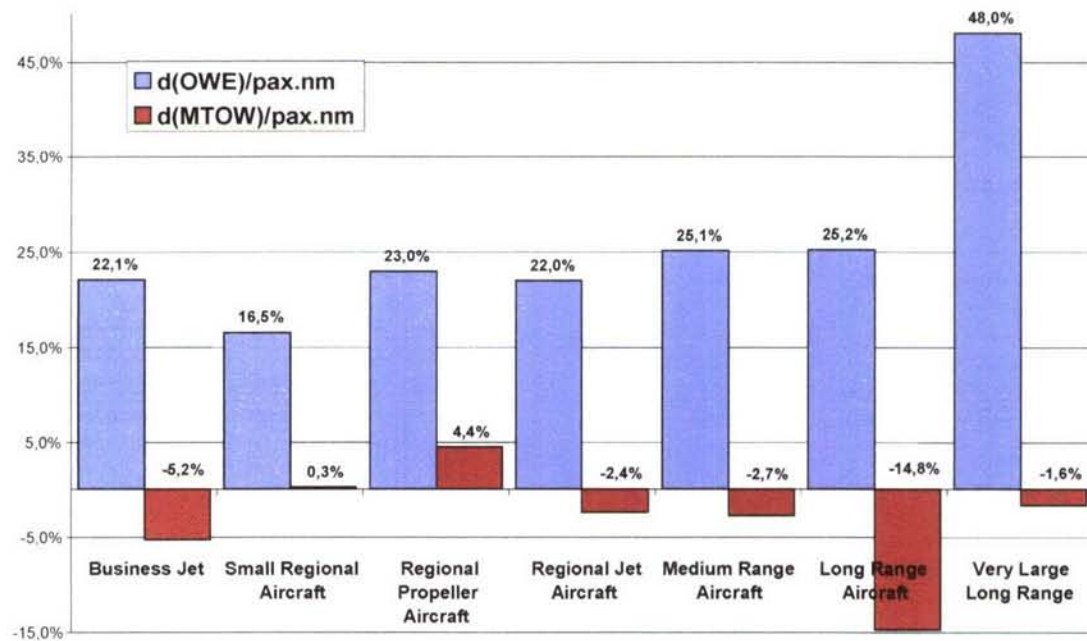
Picture 8: Cross section R-200



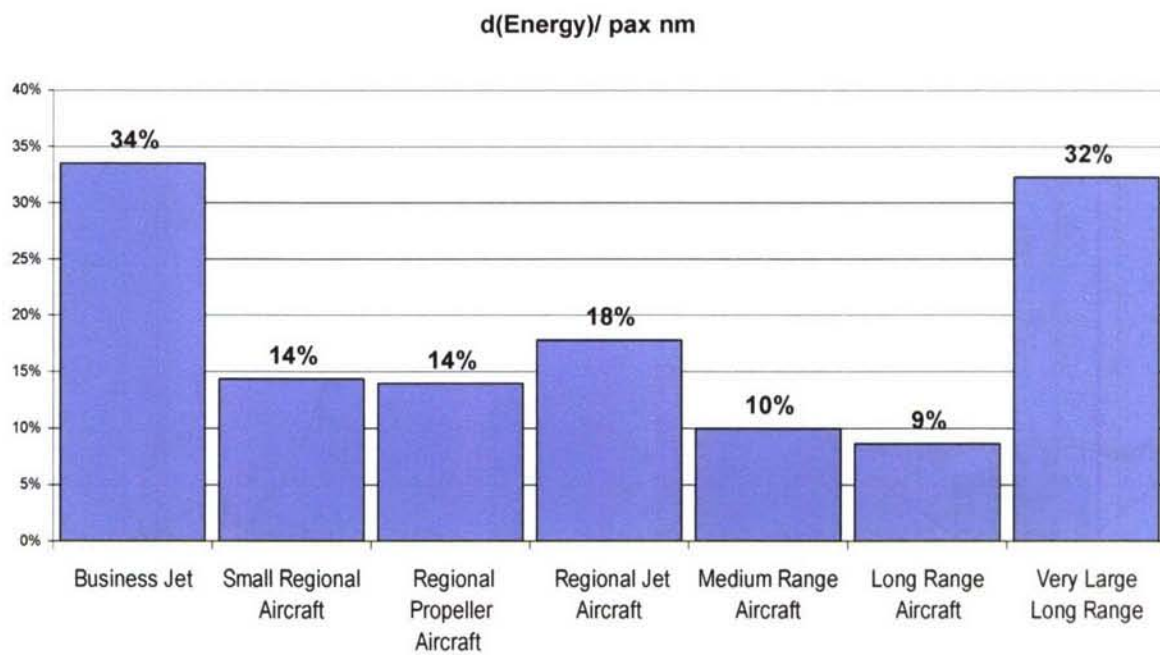
Picture 9: Cross section of RCK(1)-200



Picture 10: Fraction of OWE/MTOW.

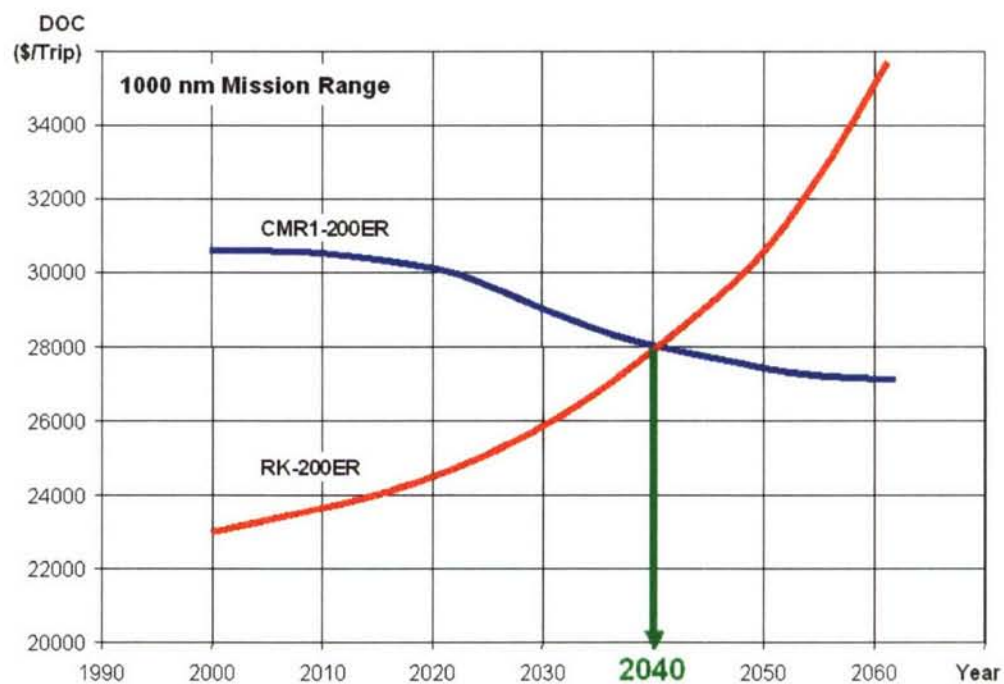


Picture 11: Dependencies between operating weight empty and max. take off weight, when H2 is applied on the Aircraft.

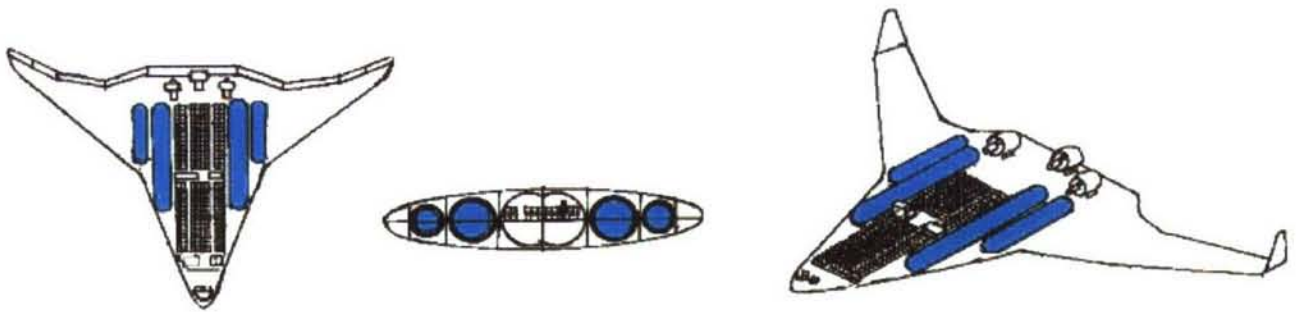


Picture 12: Change of energy consumption for H2 fuelled aircraft.

Economics – DOC Comparison



Picture 13: Calculated break even point in case of RK-200ER and CMR-200ER



Picture 14: Blended Wing Body

Presented by

Andreas Westenberger
Airbus



LH_2 as Alternative Fuel for Aeronautics – Study on Aircraft Concepts

Results of the FP5 Project “Cryoplane – System Analysis”
Advances on Propulsion Technology for High-Speed Aircraft – VKI; Belgium

LH_2 – Liquefied Hydrogen



Content

- Vision
- Hydrogen Today
- History
- Project Description
- Configurations
- Sytsems
- Propulsion
- Environment



The Vision

The vision is:

To achieve long term continuing growth of civil aviation until every man and woman on earth can fly as often and as far as they want, and when doing so, do no harm to other human beings , or to the environment.



© Airbus 2006. All rights reserved. Airbus is a registered trademark of Airbus Industrie.

November 2006

Page 3



Overview hydrogen infrastructure

Energy Source

- Natural Gas
- Oil
- Biomass
- Nuclear Power
- Renewables

Production

- Reforming
- Electrolysis

Distribution

- Pipelines
- Cryogenic Tankers
- Gaseous Tankers
- Ship
- Rail

Storage

- Liquid Storage
- High pressure
- Metal Hydride



© Airbus 2006. All rights reserved. Airbus is a registered trademark of Airbus Industrie.

November 2006

Page 4



The market of hydrogen

Worldwide more than **54 Mt** is produced and consumed per year.

54Mt H₂ equals in terms of energy 151Mt Kerosene

75% for the ammonia industry
8% for the production of methanol
1% for hydrogen as an energy carrier

Furthermore H₂ plays an important role in the following industries like:



Fertilisers



Plastics



Nuclear power stations



Refineries



Semiconductors



Aerospace

The production costs

The costs of H₂ depends on several aspects like the way it is produced, the amount and the distance of transportation.

Technique	Costs	
Natural Gas Reforming	3-4	Cent/ kWh
Electrolysis / Hydropower	9-15	Cent/ kWh
Electrolysis / Windpower	8-25	Cent/ kWh
Electrolysis / Solarpower	33-75	Cent/ kWh
Biogas Reforming	4-9	Cent/ kWh

DWW



H₂ = 33,33 kWh/kg

Electrolysis process needs **300ml demineralised water per kWh H₂**

The cost of the liquefaction process is between **0,35 Cent to 3€ per kg**, depending on the size of the liquefier. (**3 t/day to 40 t/day**)

Since fuel cells have an electrical energy efficiency of almost 50%.
2kWh of H₂ -> 1kWh of electrical power

Hydrogen gas stations for automobiles June 2006



LBST



November 2006

Page 7

H₂ liquefaction worldwide

More than 50 t/day LH₂ in production.
Distribution infrastructure existing.

More than 20 t/day LH₂ in production
Distribution infrastructure existing.

No liquefiers for H₂ existing.
Hydrogen is produced and consumed
on site in many industries by reforming
of natural gas.

No liquefiers for H₂ existing.
Built up due to natural gas resources feasible.

No liquefiers for H₂ but for helium existing.
Built up due to He infrastructure practicable.



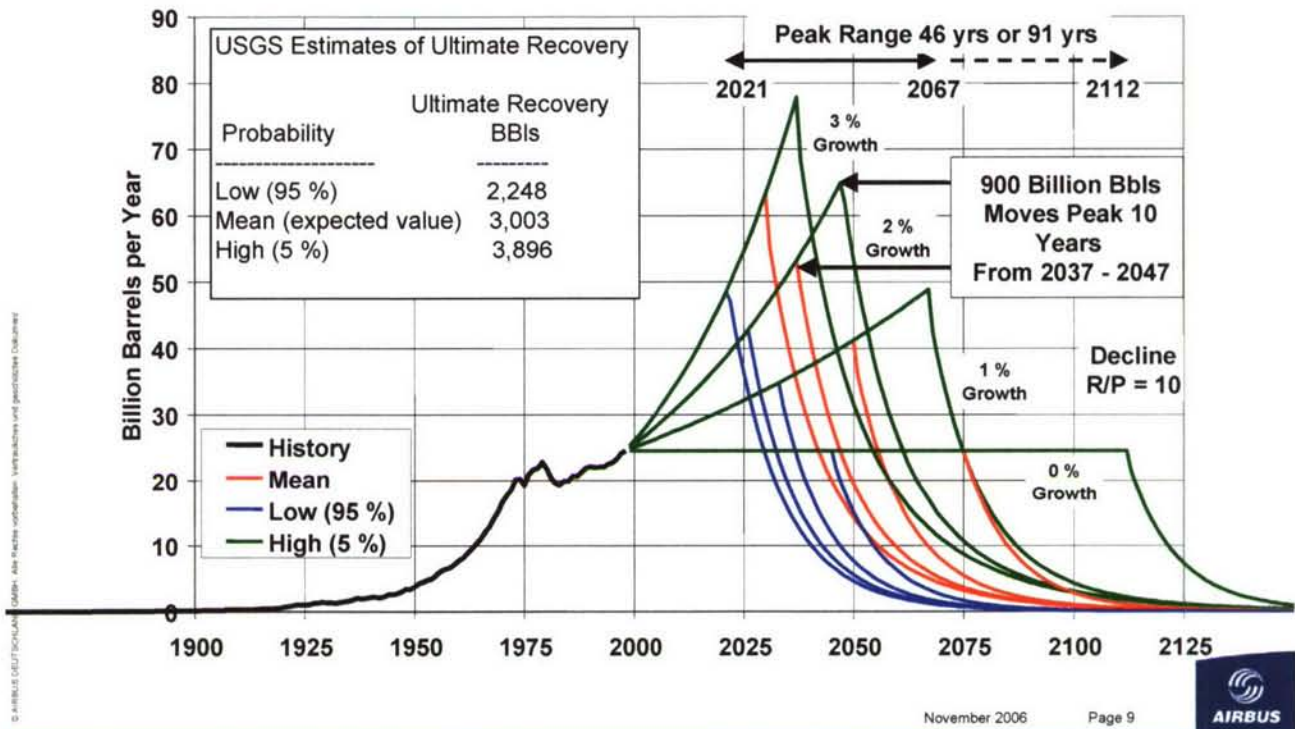
November 2006

Page 8

Indications - Oil peak scenarios

• Oil production: different scenarios

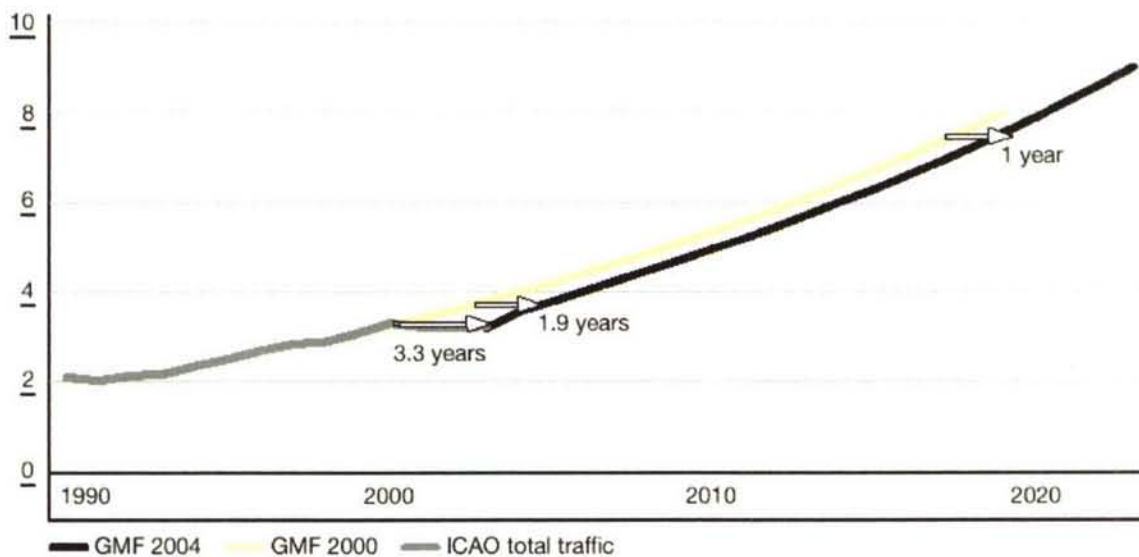
Source: USGS



Market of commercial aircraft

World annual traffic

Trillions RPKs



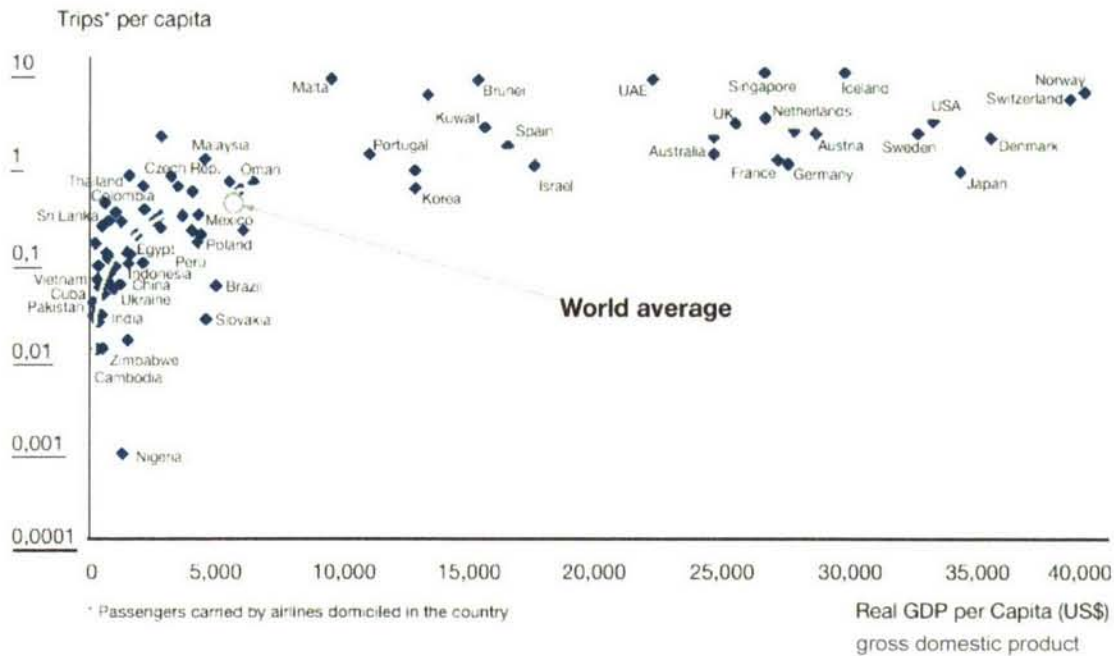
November 2006

Page 10



Is driven by wealth ...

Large potential for future growth in air travel



© Airbus, ICAO, UN, World Bank, OECD, IMF, Eurostat, CIA, etc.

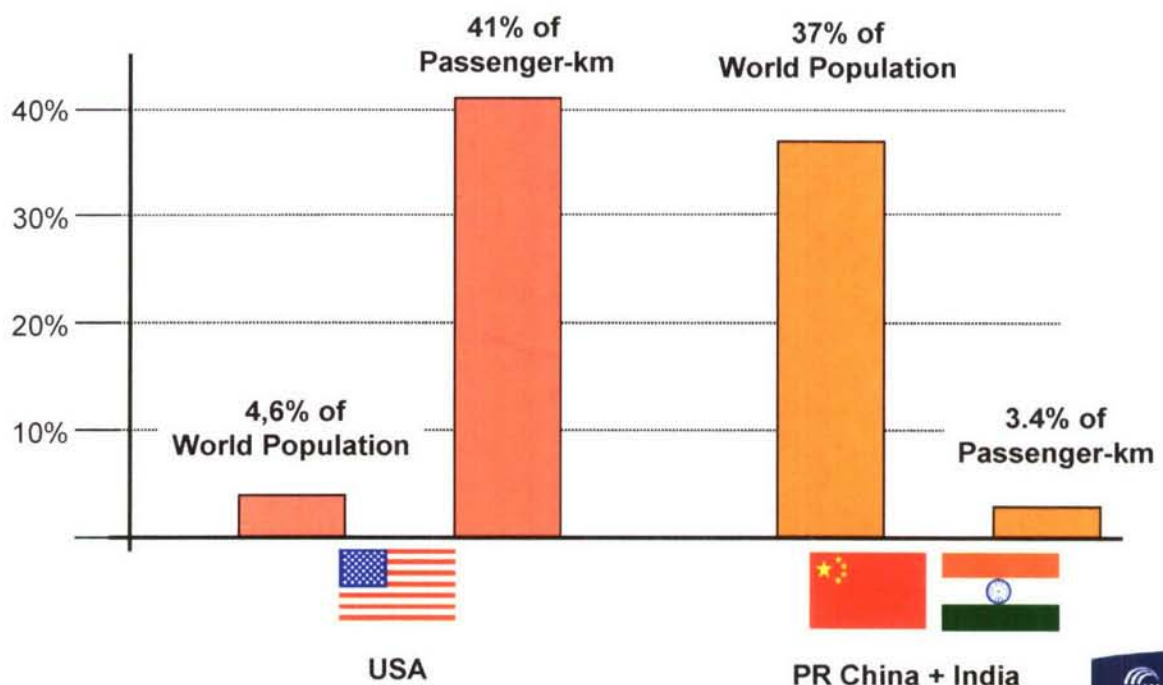
November 2006

Page 11



Traffic an Population

Status: 1994



© Airbus, ICAO, UN, World Bank, OECD, IMF, Eurostat, CIA, etc.

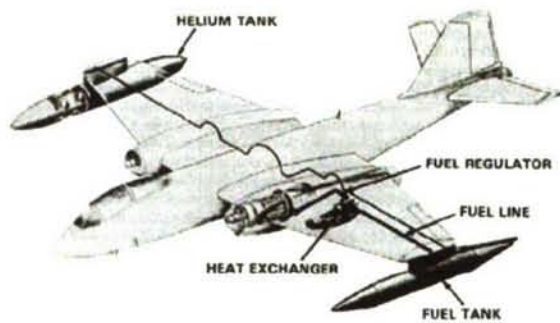
Prepared by DASA Airbus HK 26 11 199

November 2006

Page 12



History (1)



© AIRBUS DEUTSCHLAND GMBH - Alle Rechte vorbehalten. Vertraulich und geschütztes Dokument

- 1937 Dr. v. Ohain rig-tests He-S-2 experimental turbojet engine on hydrogen
- 1955 Report of NACA -Lewis Flight Propulsion Laboratory on the potential of hydrogen
- 1957 US Air Force B 57 bomber flight tests
- 1950ies Lockheed studies on Mach 2.5 reconnaissance airplane
- 1970ies Studies by NASA Ames; Institute of Gas Technology; Linde/Union Carbide Corporation, Lockheed, and others; civil transport aircraft, safety aspects
- 1988 First flight of Tupolev Tu 155 Laboratory aircraft; proves principal feasibility of transport aircraft flying on Liquid Hydrogen and Liquid Natural Gas, respectively (LNG is main interest of Russia)
- 1990 Daniel Brewer publishes "Hydrogen Aircraft Technology"

November 2006

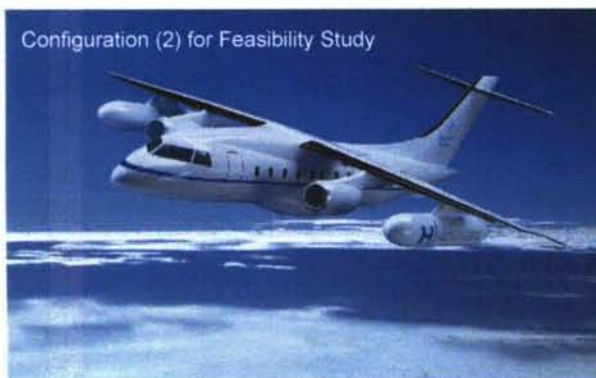
Page 13



History (2)



Configuration (1) for Feasibility Study



Configuration (2) for Feasibility Study

© AIRBUS DEUTSCHLAND GMBH - Alle Rechte vorbehalten. Vertraulich und geschütztes Dokument

- 1990 German-Russian Cooperation (DASA, Tupolev, Kuznetsov and others) initiated
- 1990/93 German-Russian "Feasibility Study" - CRYOPLANE based on A310 defined
- 1992/96 EQHPP Combustion Chamber Tests
- 1994/99 EU/INTAS Tank Tests(Tupolev, with DA and Air Liquide)
- 1994/99 APU Tests (FH Aachen, with DA and Allied Signal)
- 1995/98 German/Russian studies for Demonstrator Aircraft based on Do 328
- 1996/99 ISO/TC 197 WG4 "Airport Hydrogen Refuelling Facility"
- 1998 Daimler Benz DASA Top Management orders Project Manager to initiate a European R&D Program „System Analysis“
- 1999 Project preparation Cryoplane

November 2006

Page 14



Cryoplane – System Analysis



Project within 5th Framework Program of European Commission, targeted at "Sustainable Growth".

Comprehensive systems analysis to provide decision basis for future technology development..

Covers configuration, systems & components, propulsion, safety, environmental compatibility, fuel sources & infrastructure, transition

36 partners from industry, research and academia, from 11 European countries.

Total project time 26 months.

Start of project: 1. April 2000

Final meeting in May 27th and 28th, 2002

Page 15



Work Packages

Work Package

Task Owners

- | | |
|--|---|
| 1 Project Management | Airbus*, MTU |
| 2 Aircraft Configuration | DUT, Airbus*, Alenia, CIRA, Fairchild Dornier, Cranfield Uni CoA |
| 3 Systems and Components | Air Liquide, Airbus*, Thales, TUHH, Grimm, SNECMA, JRC Ispra, Delft UT, Advanced, MI Developments, MTU, Techspace Aero. |
| 4 Propulsion | Cranfield Uni SME, UP Madrid, FH Aachen, SNECMA, DIEHL Aeronautics |
| 5 Safety | JRC Ispra, SNECMA, BAM, CIRA, Airbus* |
| 6 Environmental Compatibility Assessment | Uni Thessaloniki LAP, DLR, Ui Oslo, Fraunhofer IFU, Uni Thessaloniki LHTEE |
| 7 Fuel Sources, Infrastructure | TUHH, JRC Ispra, Linde, Air Liquide, Cranfield Uni CoA |
| 8 Transition Scenarios | FOI, TU Berlin, Shell Hydrogen, JRC Ispra |
| 9 Trade-off Slush Hydrogen | MagnaSteyr, Airbus* |

* (Airbus includes all Airbus entities)

November 2006

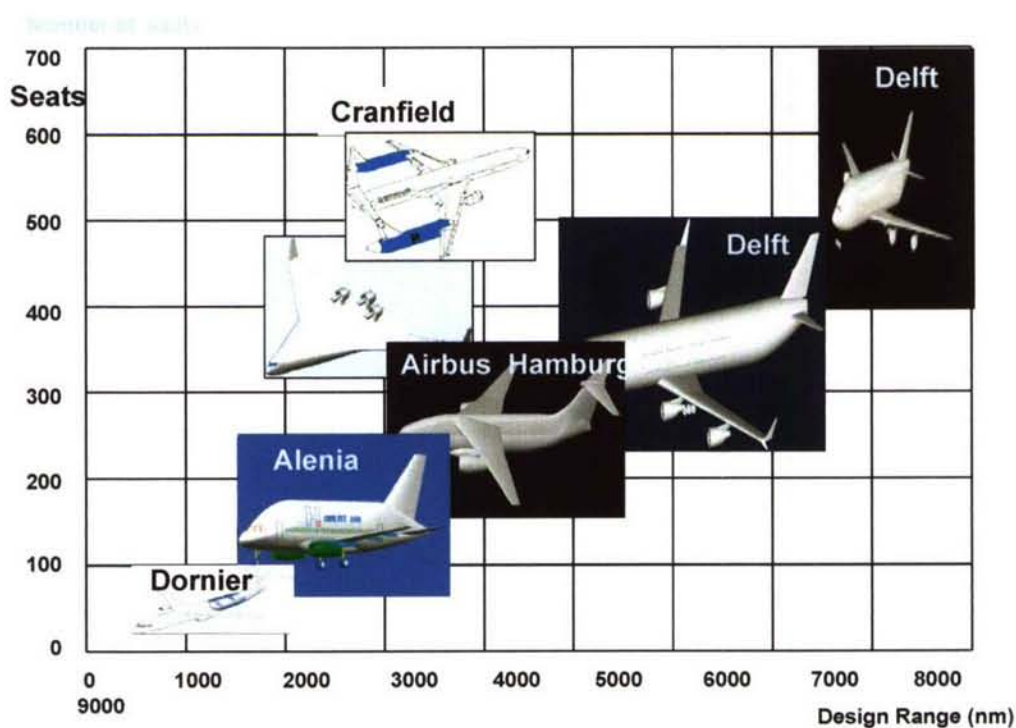
Page 16



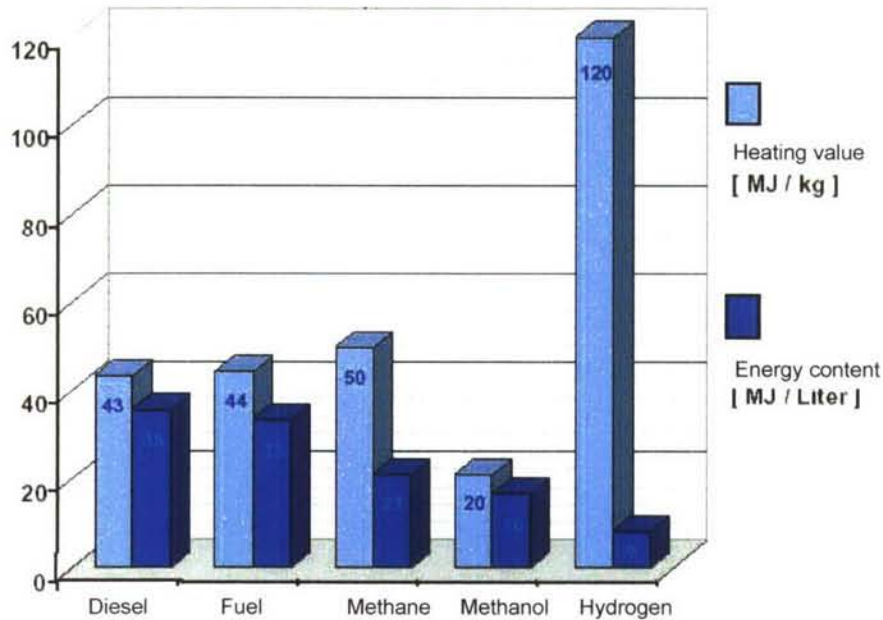
Aircraft Configuration

- WP on configurations is split into two main groups of tasks
 - Conventional aircraft configurations
 - Unconventional aircraft configurations
- Objectives:
 - To prove the possibility of the use of H_2 as an alternative fuel in different aircraft categories
 - To meet the requirements of efficient and safe operation from „Business Jets“ to „Large Long Range Aircraft“
 - To analyze the performance and the DOC compared to conventional aircraft

Aircraft Configuration



Comparison of Fuels



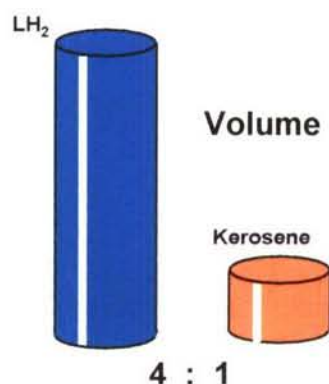
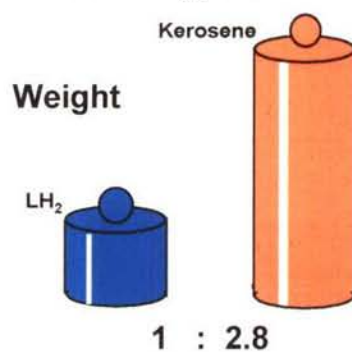
November 2006

Page 19



Conclusion for the use of H₂ on the Aircraft

Fuel masses of same energy content



- Burning hydrogen produces water - the cycle is closed.
- Hydrogen offers a high energy content per mass, hence promises payload or range increase for aircraft.

But

- For aviation, hydrogen must be cooled down to the liquid state (LH₂, -253°C) for reasons of volume and weight of tanks.
- LH₂ needs
 - 4 times greater volume than kerosene
 - Very good insulation of tanks, pipes
 - Tanks under some differential pressure
 - Spherical or cylindrical tanks
 - New aircraft configuration

November 2006

Page 20



To be Considered for Change on Aircraft

Systems

Fuel System: Tanks, Pipes, Valves, Pumps, Vents....

Fuel Control System : Sensors, Control Box....

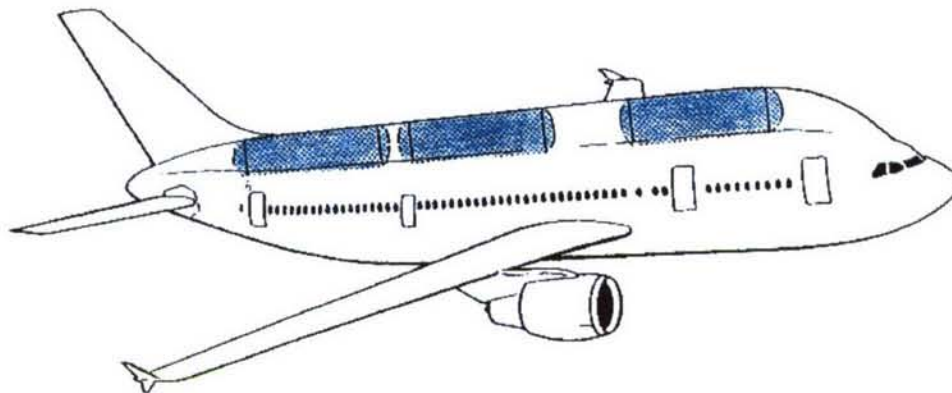
Fire Protection :Sensors, Ventilation, Control Box...

Airframe

Tank support, local strenghtening fuselage, fairings

Fuselage stretch to accomodate increased payload

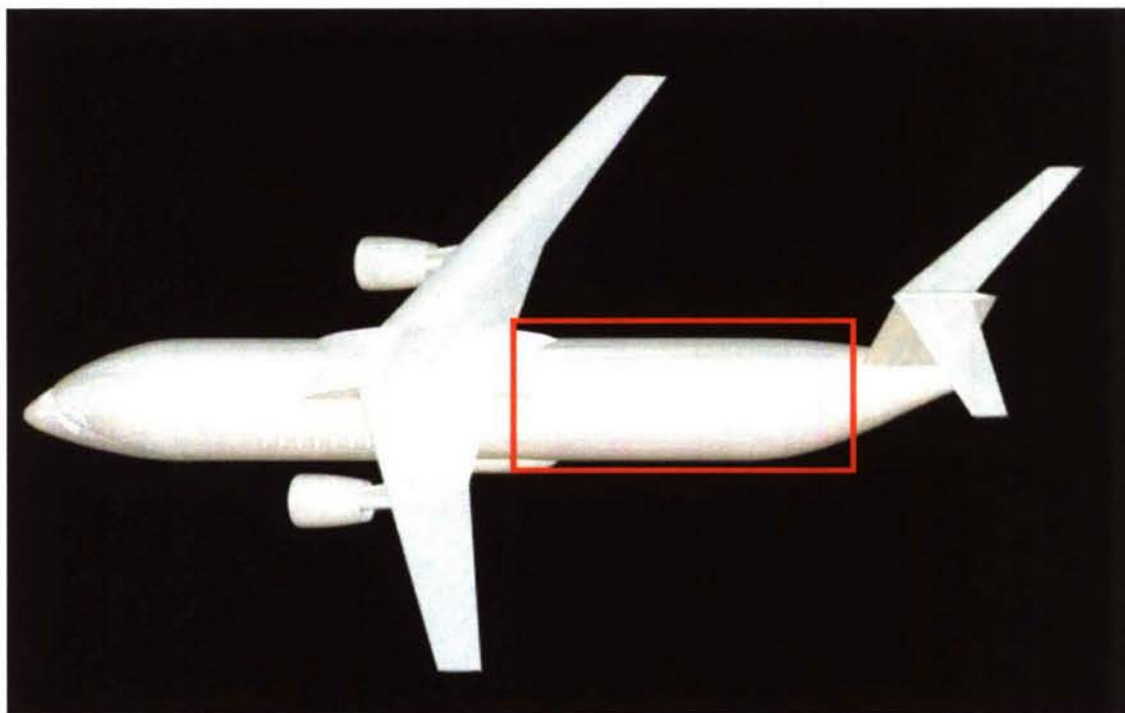
Strengthening of wing structure




Powerplant

High Pressure Pump, Heat Exchanger,
Fuel Flow Control Valve, Combustion Chamber
Control Box, Oil Cooler

Business Jet – 12 pax – 3500 nm



 Liquid Hydrogen Tank

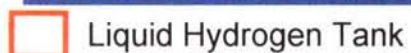
© 2000 Blackwell Science Ltd, *Journal of Internal Medicine* 247: 395–401



Page 23



© 2000 Blackwell Science Ltd, *Journal of Internal Medicine* 247: 319–326

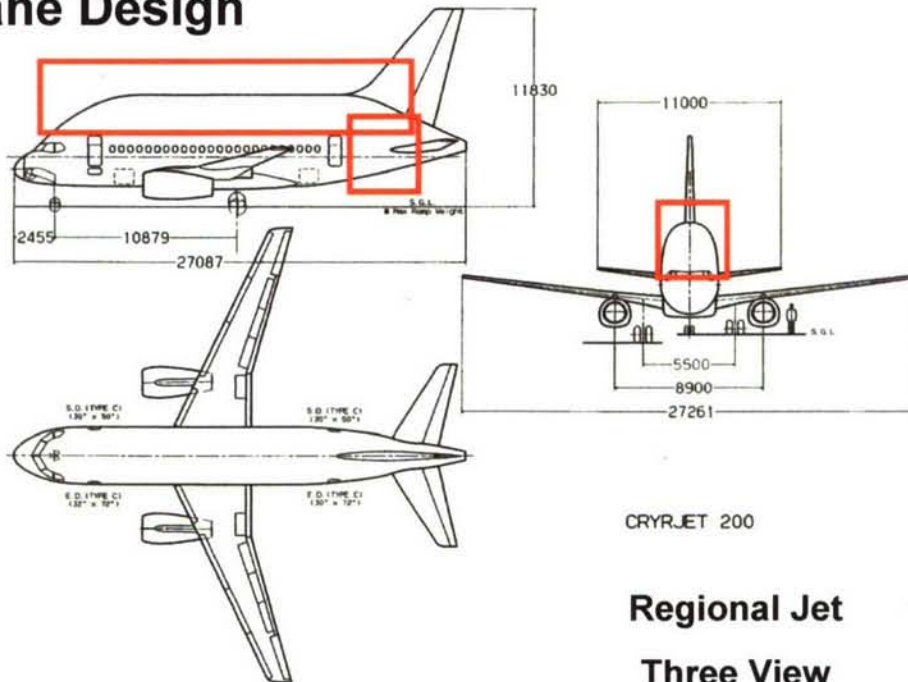


Page 24




Standard Regional Aircraft – 70 pax – 2000 nm

Cryoplane Design



CRYJET 200

Regional Jet Three View

 Liquid Hydrogen Tank

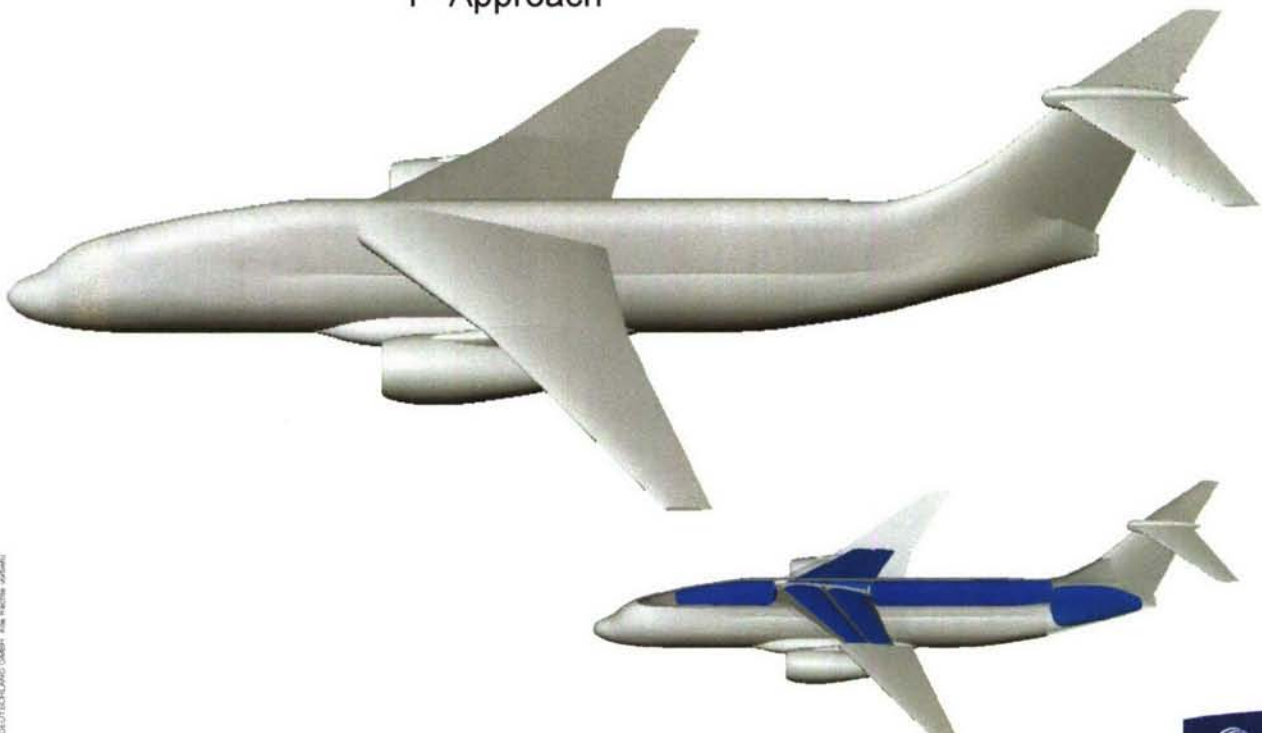
November 2006

Page 25



Medium Range Aircraft – 185 pax – 4000 nm

1st Approach

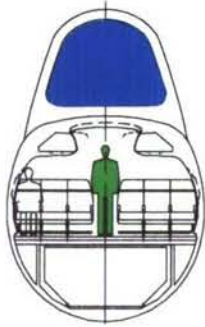


November 2006

Page 26



Medium Range Aircraft – 185 pax – 4000 nm



2nd Approach

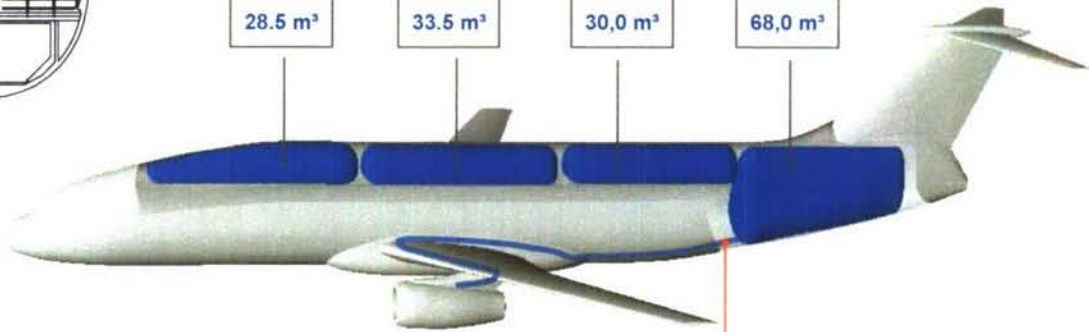
4 fuselage tanks reach
160 m³ tank volume
(incl. 10 m³ unusable tank volume)

28.5 m³

33.5 m³

30,0 m³

68,0 m³



Engines' fuel supply pipes
are outside of pressurized fuselage

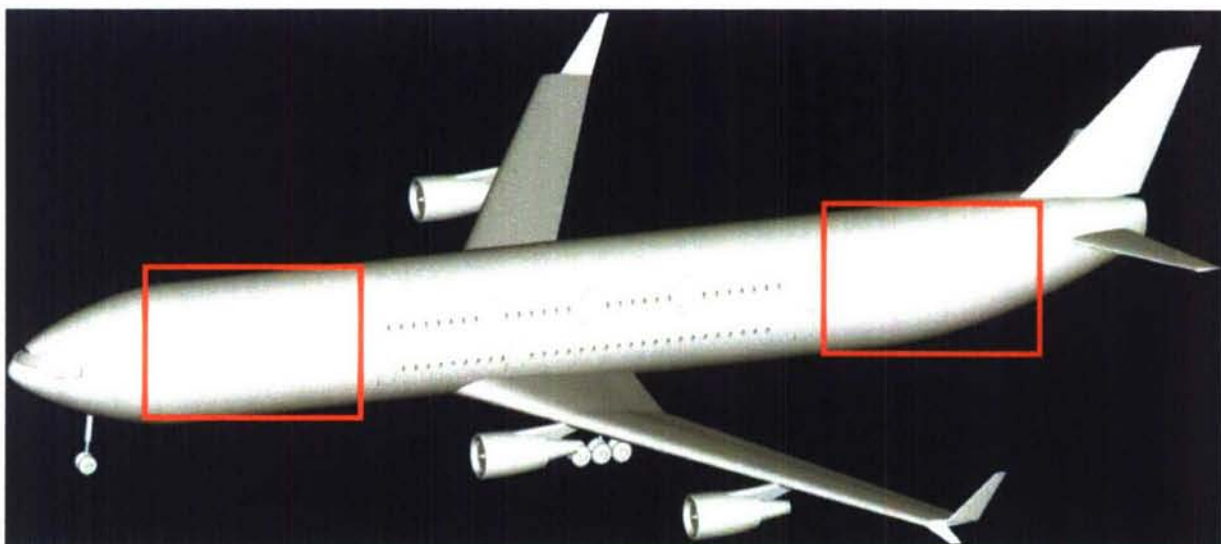
© Airbus (S) 2006. All rights reserved. Airbus is a registered trademark of Airbus Group. Airbus is a registered trademark of Airbus Group.

November 2006

Page 27



Long Range Aircraft – 380 pax – 8500 nm



Liquid Hydrogen Tank

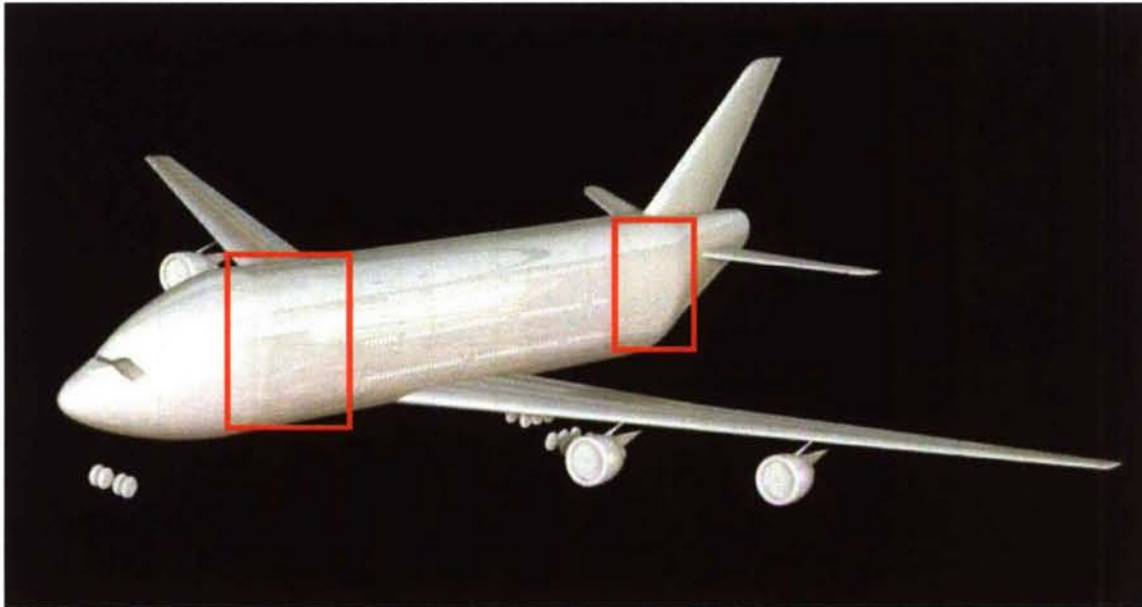
© Airbus (S) 2006. All rights reserved. Airbus is a registered trademark of Airbus Group. Airbus is a registered trademark of Airbus Group.

November 2006

Page 28



Large Long Range Aircraft – 550 pax – 8500nm



 Liquid Hydrogen Tank

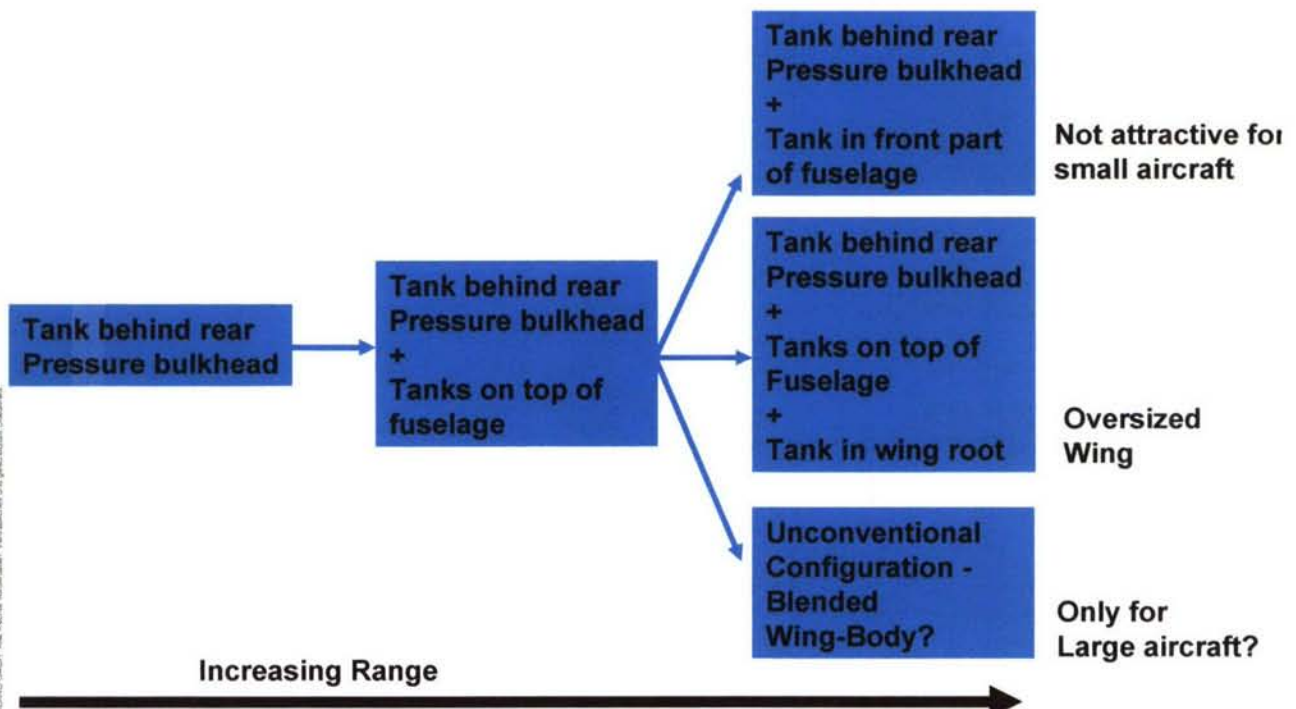
© AIRBUS DEUTSCHLAND GMBH - Alle Rechte vorbehalten. Vertrauliches und geschütztes Dokument

November 2006

Page 29



Summary of Configurations



Prepared HG Klug July 2001 on the basis of "System Analysis"

© AIRBUS DEUTSCHLAND GMBH - Alle Rechte vorbehalten. Vertrauliches und geschütztes Dokument

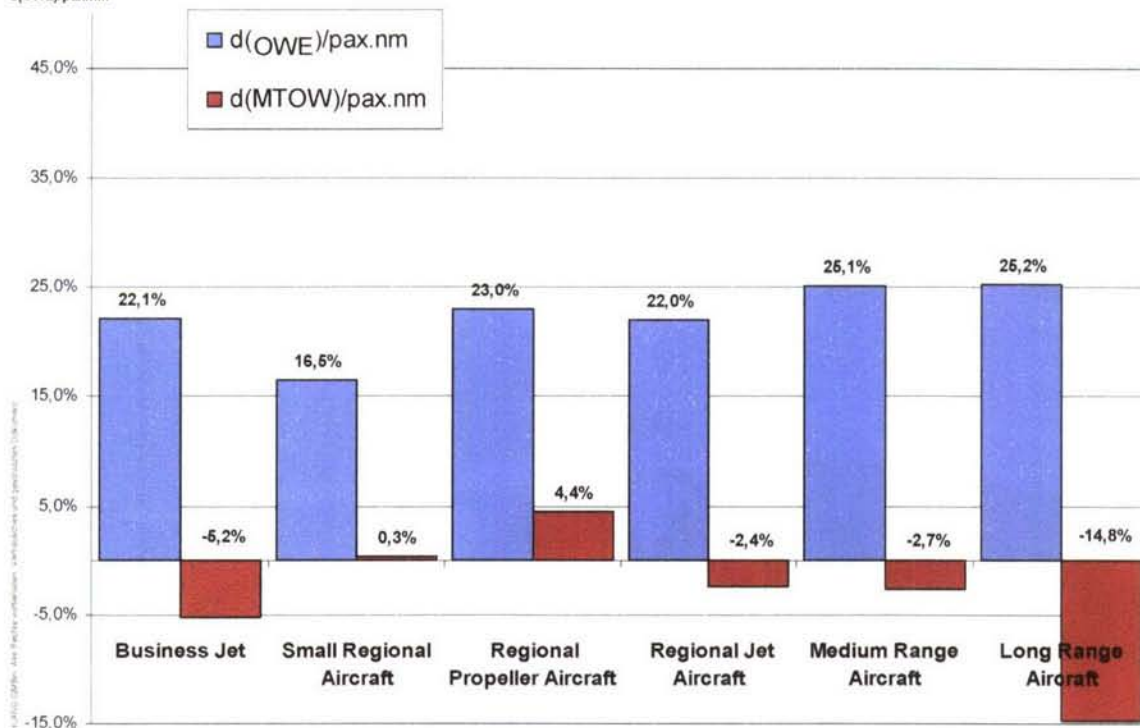
November 2006

Page 30



OWE – Operating Weight Empty MTOW – Max. Take Of Weight

d(OWE)/pax.nm



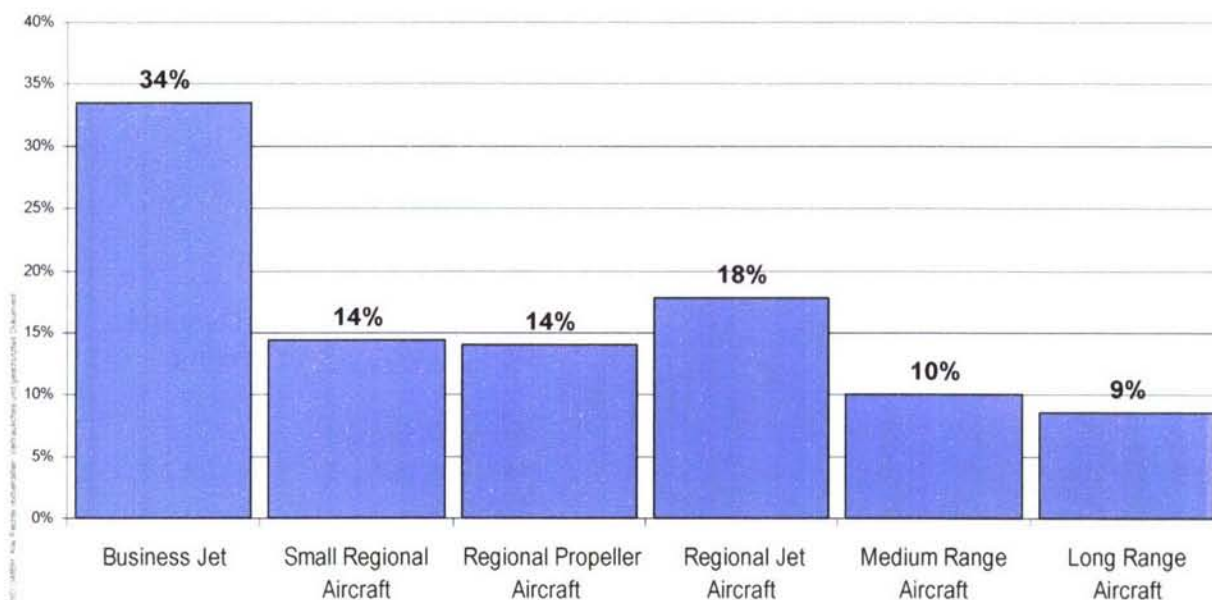
November 2006

Page 31



Change in Energy Consumption

d(Energy)/ pax nm

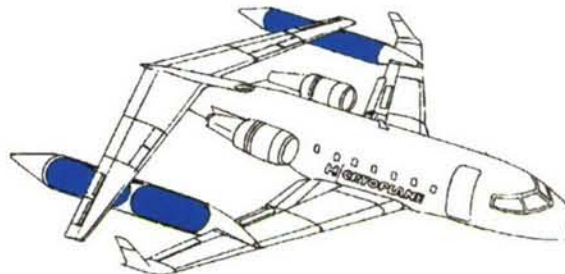
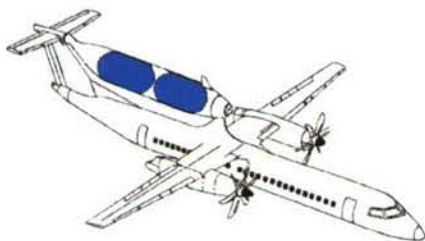
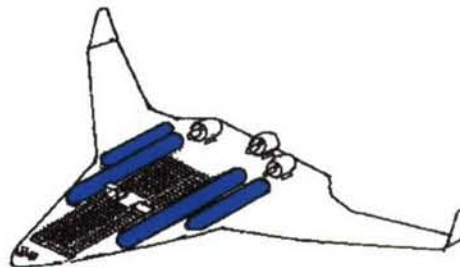
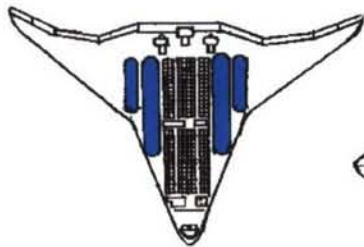


November 2006

Page 32



Unconventional Configurations



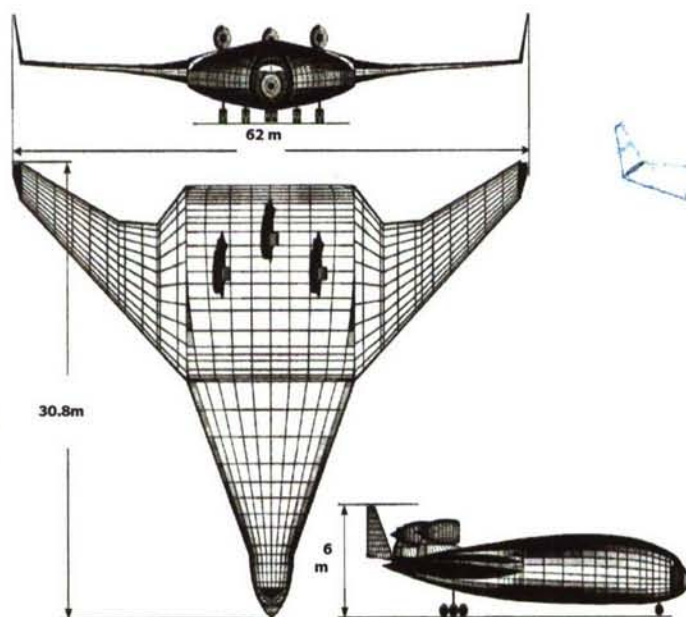
© AIRBUS DEUTSCHLAND GMBH - Alle Rechte vorbehalten. Vertriebs- und gesteuerte Dokumente.

November 2006

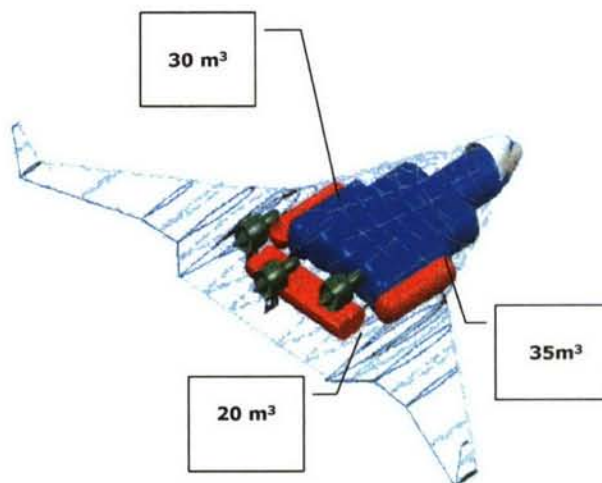
Page 33



Unconventional Configurations



TOTAL Useable Volume 193 m³



© AIRBUS DEUTSCHLAND GMBH - Alle Rechte vorbehalten. Vertriebs- und gesteuerte Dokumente.

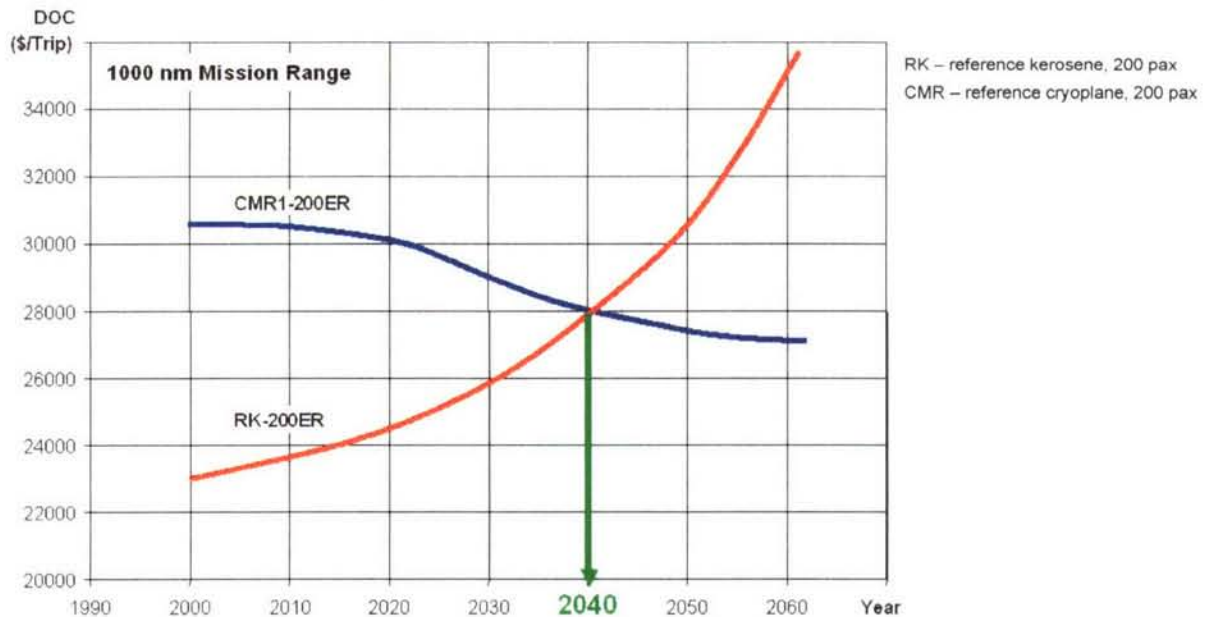
November 2006

Page 34



Economics

Economics – DOC Comparison



- Calculated break even point in case of RK-200ER and CMR-200ER
- Conclusion is based on medium scenario and data from 2001

November 2006

Page 35



Conclusion on Configurations

- Practical configuration available for all categories of airliners
- No “standard configuration” for all categories of airliners
- Max TO Weight of long range aircraft some 15% smaller than for kerosene
- Operating Weight Empty increased by some 20-25%
- Specific energy consumption increased by 8-15%
(more wetted area, higher mean flight weight)
- Unconventional configurations to be revisited. Better integration of new technology needed.

November 2006

Page 36



Systems



Tanks

Structural material: Steel? Aluminium-Lithium? Composites?

Insulation: Closed cell foam? Foam, perlite powder under vacuum?

"Super vacuum insulation"? Refrigerated screen?

Challenges: Heat loss/pressure operating cycle; stratification; sloshing; heat bridges (structural support).....



Pumps

Low Pressure Pump: Inlet pressure >1...1.2 bar (cavitation!);

Head appr. 3 bar; appr. 13 000 rpm; variable speed electric motor, gear box.

High Pressure Pump: Inlet pressure appr. 4 bar; head appr. 80 bar at TO; 150 000 rpm; driven from Engine Accessory Box; 86 kW



Heat Exchanger

Necessary to ensure gaseous/"fluid" state at injection; installation in hot gas stream behind turbine first choice; "intermediate compressor cooling" would improve engine efficiency.

Challenge: Heat exchanger skin temperature cannot avoid frosting/icing

© Airbus Deutschland GmbH - Alle Rechte vorbehalten. Vertrauliches und geschütztes Dokument

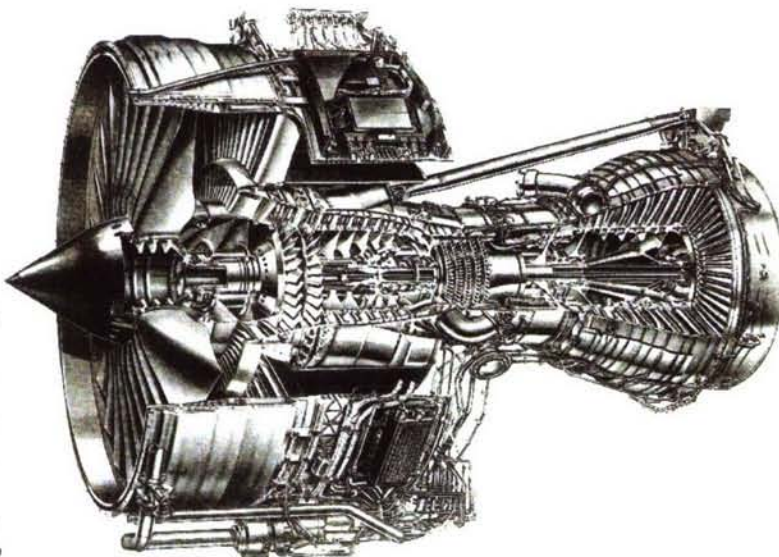
Source: SNECMA/AirLiquide/TU München/Airbus Deutschland - "System Analysis 2000/2002"

November 2006

Page 37



Engines (1)



New for the Hydrogen Engine:

High Pressure Fuel Pump

Heat Exchanger

Fuel Flow Control Valve

Fuel Distribution Pipes

Fuel Nozzles

Combustion Chamber

Engine Controller

Oil Cooler

Purging System?

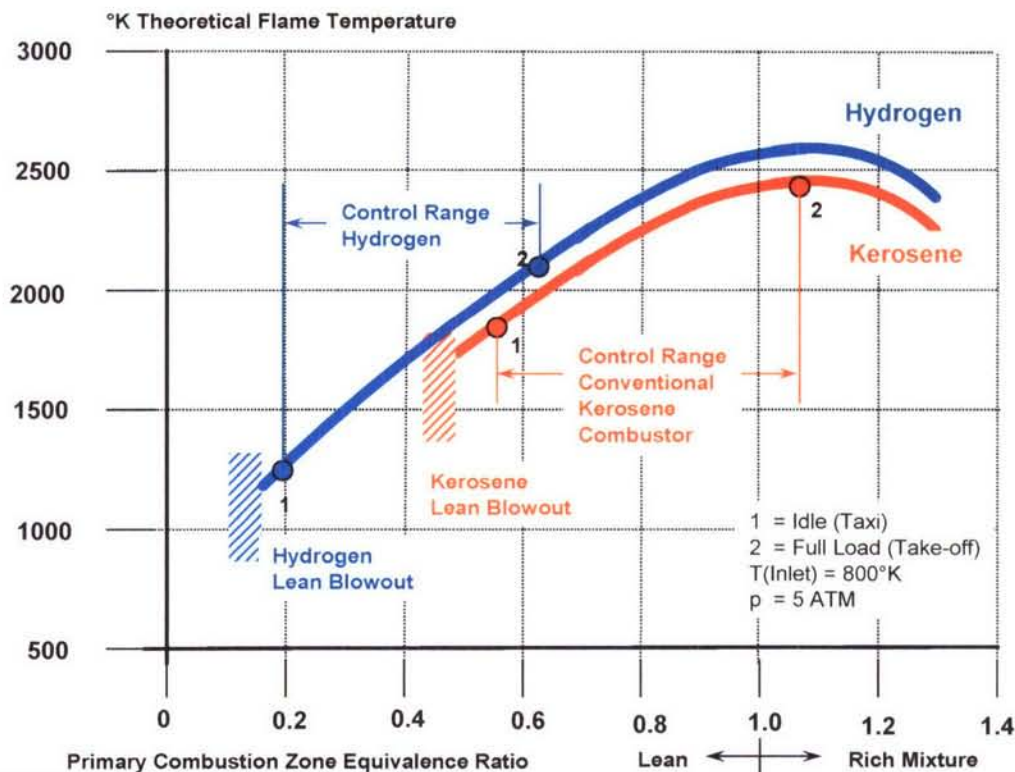
© Airbus Deutschland GmbH

November 2006

Page 38



Engines (2)



Prepared by DASA Airbus HK 8.12.1999

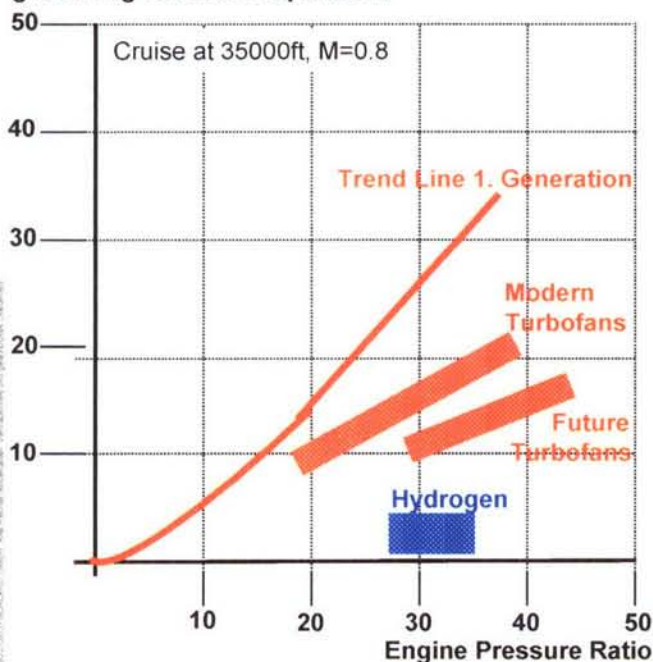
November 2006

Page 39



Engines (3)

Emission Index
g NO_x / kg Kerosene equivalent



- EQHHP =Euro Quebec Hydro Hydrogen Pilot Project, sponsored by EC and the province of Quebec, Canada

- Low Nox combustion technology 1992 - 1996

- Participants: Pratt&Whitney Canada, United Technology Research Center, DLR, Allied Signal, Daimler Benz Aerospace, FH Aachen

Tests:

- Generic nozzle tests (steady state combustion)
- Nozzle array tests (steady state combustion)
- Transient combustor tests

Conclusions:

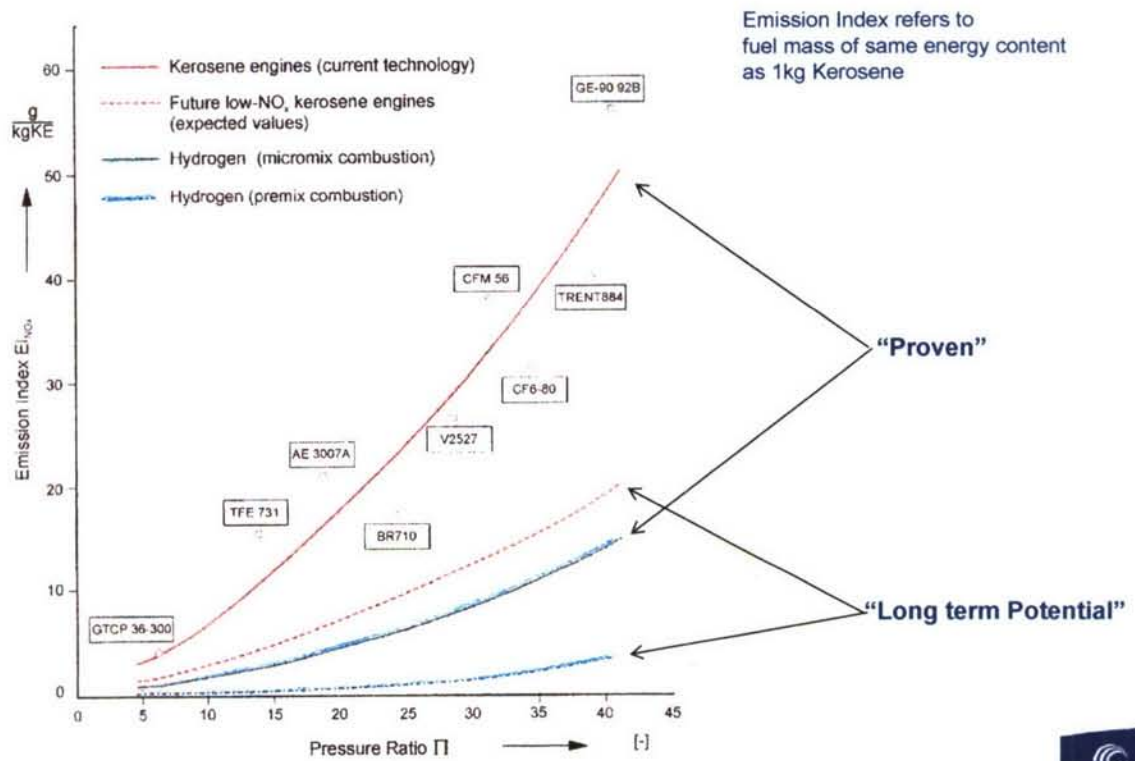
- Optimized High Swirl Nozzles offer very significant reduction in NO_x compared to kerosene engines
- Premixing offers extremely low NO_x emissions
- Safe operation feasible also for premix system

November 2006

Page 40



Engines - NOx Emissions at Take-off

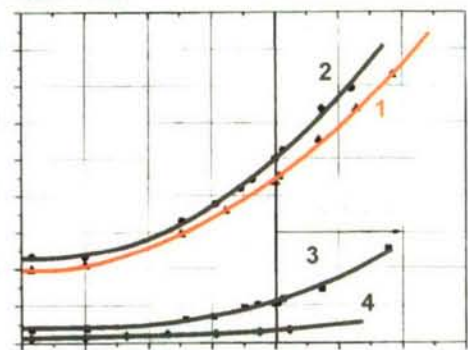
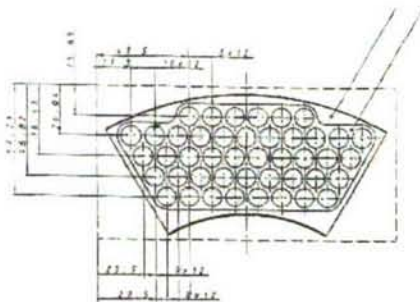


Source: FH Aachen, "System Analysis 2000/2002"

November 2006 Prepared by: Flug Sep



Engines - Micro Mix Combustion Chamber, FH Aachen



APU AlliedSignal GTCP 35-300

- 1 Kerosene, Original Combustion Chamber
- 2 Hydrogene, Nozzles exchanged
- 3 Hydrogen, Micro-Mix Chamber
- 4 Hydrogen, improved Micro-Mix Chamber

Source: FH Aachen

November 2006

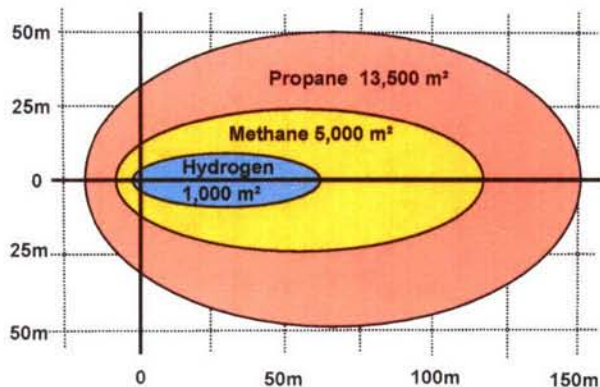
Page 42



Safety – General Aspects

Danger Zones of Spilled Liquid Gases

Example: 3.3m³ Liquid Gas Spilled - 4m/sec Wind



- Psychological problem primarily.
- In free atmosphere, hydrogen rises quickly, hence small danger zone if hydrogen leaks out/ is spilled.
- Hydrogen will burn at concentrations significantly below the limit for detonation.
- No detonation in free atmosphere.
- Will not form a fire carpet.
- Fast burning, very low heat radiation.
- Not toxic. Combustion products not toxic.

Practical Experience:

- Large scale test over decades, involving millions of laymen: *Town Gas* contained appr. 50% hydrogen.
- "Worst case tests" for car tanks successful (BAM Berlin/ BMW).
- Side-by-side tests at University of Miami prove clear safety advantage of hydrogen vs. gasoline.
- Excellent safety record for LH2 related tanks/ tank trailers/test installations.



Page 43

Comparative Safety Tests

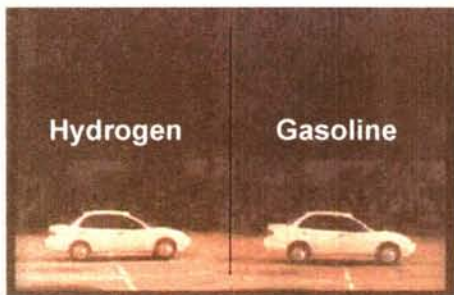


Photo 1: Time 0 min. 0 sec - Hydrogen powered vehicle on the left. Gasoline powered vehicle on the right.



Photo 2: Time 0 min. 3 seconds - Ignition of both fuels occur. Hydrogen flow rate 2100 SCFM. Gasoline flow rate 680 cc/min.



Photo 3: Time 1 min. 0 sec - Hydrogen flow is subsiding. view of gasoline vehicle begins to enlarge.



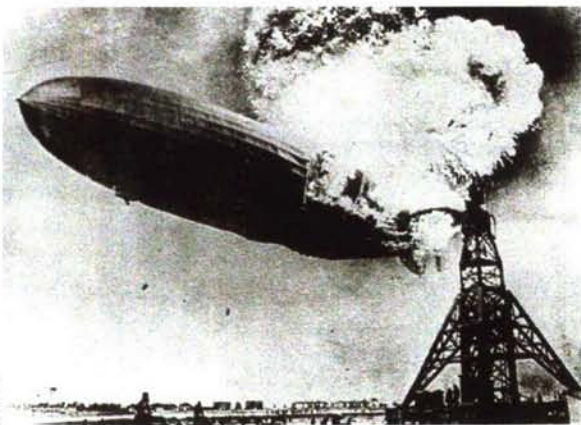
Photo 6: Time 2 min. 20 sec - Deflagration in the interior. following frame shows flames exiting around edges of trunk lid.



November 2006

Page 44

History



- German Airship "*Hindenburg*" destroyed 06.5.1937 at Lakehurst, USA, during landing.
- Airship contained about 200.000 m³= 18.000 kg of gaseous hydrogen.
- According to latest research, static electricity set fire to highly flammable impregnation of fabric cover .



- Airship floating at 60 m over ground when fire started.
- No explosion, but 1 minute of fire until airship settled on ground.
- 97 persons on board (crew plus passengers)
- 62 persons surviving!

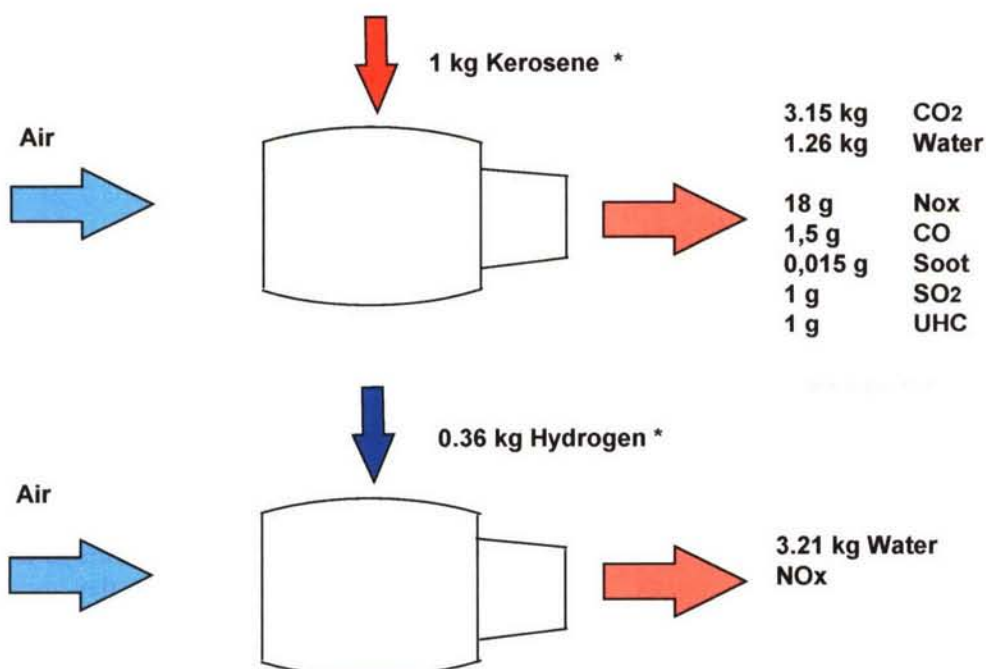
November 2006

Page 45

AIRBUS

Environment - Combustion Products - Kerosene vs. H₂

* Fuel masses of identical energy content



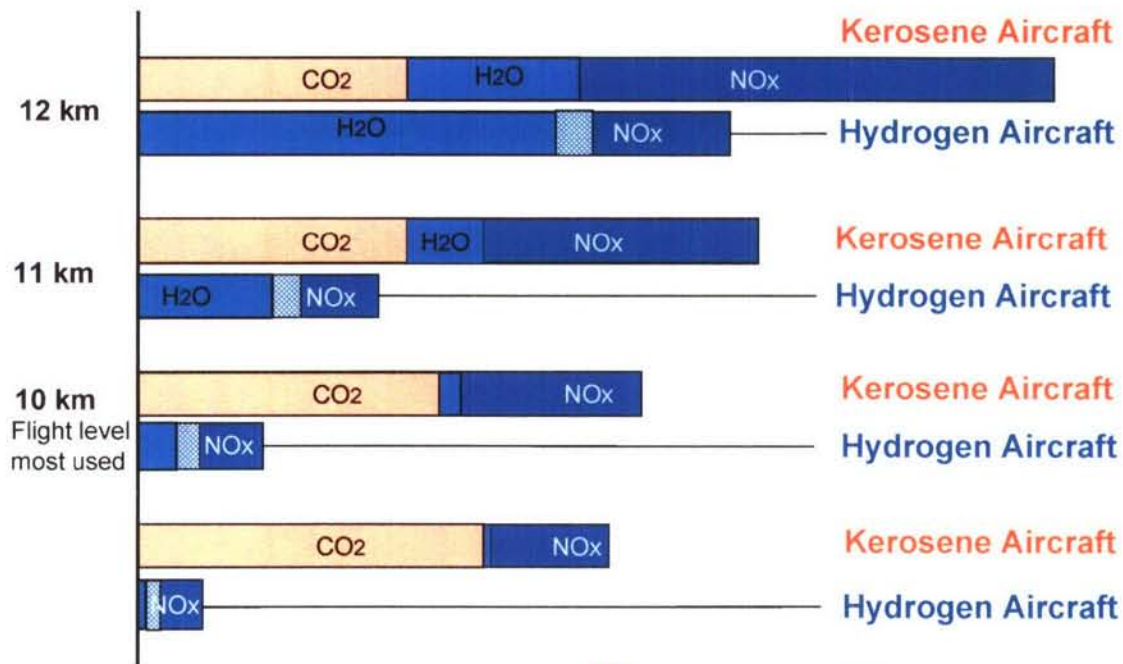
November 2006

Page 46

AIRBUS

Comparison on Green House Emissions

Simplified Parametric Analysis based on GWP Concept



© Airbus 2006. All rights reserved. Airbus and the Airbus logo are registered trademarks of Airbus Industrie.

November 2006

Page 47



Infrastructure



- During tests, demonstration and early operation: LH2 could be dispensed from conventional tank trailer (above).
- Long term solution: Production and storing of LH2 at airport, distribution by pipeline system (below).
- Servicing/refuelling of aircraft at terminal. Refuelling within normal turn-around time (see experience with refuelling of cars!)
- Current view: Aircraft designed for 12 hrs on ground before spilling hydrogen. Thereafter: catalytic combustion or collection/recooling/recirculation by ground vehicles/system.
- LH2 production capacity in Europe today: 19 t per day; USA: 170 t per day. Full intra-European air traffic would require some 30.000 t per day!
- Long transition time to build up infrastructure.

© Airbus 2006. All rights reserved. Airbus and the Airbus logo are registered trademarks of Airbus Industrie.

November 2006

Page 48



**„Prediction is extremely difficult.
Especially about the future."**

Niels Bohr

Thank you for your attention

© AIRBUS DEUTSCHLAND GMBH. Alle Rechte vorbehalten. Vertrauliches und geschütztes Dokument.

November 2006

Page 49



© AIRBUS DEUTSCHLAND GMBH. All rights reserved.
Confidential and proprietary document.

This document and all information contained herein is the sole property of AIRBUS DEUTSCHLAND GMBH. No intellectual property rights are granted by the delivery of this document or the disclosure of its content. This document shall not be reproduced or disclosed to a third party without the express written consent of AIRBUS DEUTSCHLAND GMBH. This document and its content shall not be used for any purpose other than that for which it is supplied.

The statements made herein do not constitute an offer. They are based on the mentioned assumptions and are expressed in good faith. Where the supporting grounds for these statements are not shown, AIRBUS DEUTSCHLAND GMBH will be pleased to explain the basis thereof.

AIRBUS, its logo, A300, A310, A318, A319, A320, A321, A330, A340, A350, A380, A400M are registered trademarks.



© AIRBUS DEUTSCHLAND GMBH. Alle Rechte vorbehalten. Vertrauliches und geschütztes Dokument.

November 2006

Page 50

Gases

Values of gaseous, conventional and alternative fuels

Units	chem. Formula	density at 0° C and		main constituents	boiling temperature at 1013mbar °C	calorific value		ignition temperature °C	theoretical need of air kg/ kg	ignition limits		
		kg/ m³	min. max.			Waight-%	MJ kg fuel			MJ m³ fuel-air-mixture for lambda=1,2	volume %gas in air	lower upper
liquid gas		2.25			-30	46.1	3.11	400	15.5	1.5	15	
town gas		0.56	0.61	50H, 8CO, 30CH ₄	-210	ca 30	ca 2.73	560	10	4	40	
natural gas		ca	0.83	76C, 24H	-162	47.7						
water gas		0.71		50H, 38CO		15.1	2.8	600	4.3	6	72	
blast furnace gas		1.28		28CO, 59N, 12CO ₂	-170	3.2	2.17	600	0.75	ca 30	ca 75	
sewage gas				46CH ₄ , 54CO ₂		27.2	3.62					
carbon monoxide		1.25		100CO	-191	10.05	3.22	605	2.5	12.5	75	
methane		0.72		75C, 25H	-162	50	2.88	650	17.2	5	15	
acetylene	C ₂ H ₂	1.17		93C, 7H	-81	48.1	3.66	305	13.25	1.5	80	
ethane	C ₂ H ₆	1.36		80C, 20H	-88	47.5		515	17.3	3	14	
ethene	C ₂ H ₄	1.26		86C, 14H	-102	47.1		425	14.7	2.75	34	
propane	C ₃ H ₈	2		82C, 18H	-43	46.3	3.09	470	15.6	1.9	9.5	
propene	C ₃ H ₆	1.92		86C, 14H	-47	45.8		450	14.7	2	11	
butane	C ₄ H ₁₀	2.7		83C, 17H	-10	45.6	3.11	365	15.4	1.5	8.5	
butene	C ₄ H ₈	2.5		86C, 14H	-5	45.2			14.8	1.7	9	
hydrogen		0.09		100H	-253	120	2.81	560	34	4	77	
disilane	Si ₂ H ₆											
methane hydrate	CH ₄ x 5.75 H ₂ O											

© Airbus Helicopters 2006. All rights reserved. Airbus Helicopters is a registered trademark of Airbus Helicopters.

Fluids

Values of liquid conventional and alternative fuels

Values of liquid conventional and alternative fuels																	
	chem. Formula	density		main constituents Weight-%	boiling temperature		enthalpy of evaporation		calorific value		ignition temperature	theoretical need of air	ignition limits		RON ⁽¹⁾	CaN ⁽²⁾	
		kg/ l			°C	kJ/kg	MJ/kg	°C	kg/ kg	volume % gas in air				min.		max.	
		min.	max.		min.	max.	min.	max.	min.	max.			untere	obere		min.	max.
motor fuels	normal	0.715	0.732	86C, 14H	25	215	377	502	42,7		300	14,8	0,6	8	92	14	
	super	0.73	0.78	86C, 14H	25	215	419		43.5		400	14,7			98	8	
aviation fuels		0.72		85C, 15H	40	180			43.5		500		0.7	0.8			
kerosene	Jet A1	0.77	0.83	87C, 13H	170	260			43		250	14,5	0,6	7.5		40	55
diesel	Normal	0.815	0.855	86C, 13H	180	360	ca.	250	42.5		250	14,5	0,6	6.5			
crude oil		0.7	1	80-83C, 10-14H	25	360	222	352	39,8	46,1	220	14,3	0,6	0.65			
heavy oil		0.95		86C, 13H	175	450			40	41		13,7				34	44
pentane	C ₅ H ₁₂	0.63		83C, 17H	36		352		45,4		285	15,4	1,4	7,8			
hexane	C ₆ H ₁₄	0.66		84C, 16H	69		331		44,7		240	15,2	1,2	7,4			
n-heptane	C ₇ H ₁₆	0.68		84C, 16H	98		310		44,4		220	15,2	1,1	6,4			
iso-octane	C ₈ H ₁₈	0.69		84C, 16H	99		297		44,6		410	15,2	1	6			
benzene	C ₆ H ₆	0.88		92C, 8H	80		394		40,2		550	13,3	1,2	8	98	10	
toluene	C ₇ H ₈	0.87		91C, 9H	110		364		40,8		530	13,4	1,2	7			
xylene	C ₈ H ₁₀	0.88		91C, 9H	144		339		40,8		460	13,7	1	7,6			
aether		0.72		64C, 14H, 22O	35		377		34,3		170	7,7	1,7	36			
acetone		0.79		62C, 10H, 28O	56		523		28,5		540	9,4	2,5	13			
ethyl alcohol	C ₂ H ₅ OH	0.79		52C, 13H, 35O	78		904		26,8		420	9	3,5	15	> 100	8	
methanol	CH ₃ OH	0.79		38C, 12H, 50O	65		1110		19,7		450	6,4	5,5	26	> 110	3	
brown coal creosote		0.85	0.9	84C, 11H	200	360			40,2	41,9		13,5					
mineral coal creosote		1	1.1	89C, 7H	170	330			36,4	38,5							
ammonia	NH ₃														110		
silane	trialane Si ₃ H ₈				53												
	tetra silane Si ₄ H ₁₀				108												
bio diesel		0.878		77C, 12H, 11O	182	338					13,8					48	65

1) research octane number
2) cetane number

© Airbus Helicopters 2006. All rights reserved. Airbus Helicopters is a registered trademark of Airbus Helicopters.

von Karman Institute for Fluid Dynamics

RTO-AVT-VKI Lecture Series 2007

**ADVANCES ON PROPULSION TECHNOLOGY
FOR HIGH-SPEED AIRCRAFT**

March 12-15, 2007

GASEOUS AND PARTICULATE EMISSIONS
WITH JET ENGINE EXHAUST AND ATMOSPHERIC POLLUTION

A.M. Starik
Central Institute of Aviation Motors, Russia

Gaseous and particulate emissions with jet engine exhaust and atmospheric pollution

A.M. Starik

Central Institute of Aviation Motors
Aviamotornaya St., 2, Moscow, 111116, Russia

e-mail: star@ciam.ru

ABSTRACT

The features of nonequilibrium processes in combustor, postcombustor flow, and in the plume of gas-turbine engines which are responsible for the formation of gaseous pollutants, mainly, SO_x , NO_x , CO_x , HO_x , HSO_y , HNO_y , and ions as well as for processes that give rise various sorts of volatile and nonvolatile (with soot core) aerosols and ice particles are considered. The results of numerical simulation as well as experimental studies of these processes are reported.

Key words: nonequilibrium physico-chemical processes, combustor, plume, pollutants, ions, aerosols, atmosphere.

INTRODUCTION

The aviation is the source of gaseous and particulate emissions into the atmosphere. The number of species emitted by jet engine is much enough and depends on a kind of a fuel and on an engine design. The emission from aviation engines is significantly smaller (in a factor of 40-50) than that from surface sources. However, because the emissions of aircraft engines occur in the atmospheric regions (high troposphere and low stratosphere), which are very sensible to various perturbations, the problem of aviation effect on atmospheric processes and climate change has come into great importance [1].

The impact of aviation on the atmosphere is under way through the complex of interconnected processes. In present, there are no any standard limitations for the concentrations of gaseous and particulate pollutants emitted by aircraft engines at cruise altitudes. Nevertheless, it is believed that emissions of different gaseous species and aerosols by aviation engines are of reverence to the impact of aviation on atmospheric chemistry, ozone depletion, and climate [1-3]. Numerous model investigations showed that gaseous species, mainly NO_x , HO_x , CO_x , SO_x , organics, emitted from aircraft engine as well as combustion and newly formed in the exhaust plume aerosols may influence significantly the total ozone concentration, cloudiness, Earth's radiation budget, and climate.

The ozone layer is a term that refers to the distribution of ozone that is naturally formed in the stratosphere. This layer protects life on Earth from harmful levels of solar ultraviolet radiation. Climate is defined as the typical behavior of the atmosphere, the aggregation of the weather, and is generally expressed in terms of averages and variances of temperature, precipitation and other physical properties. Climate is being affected by human activities that emit radiatively active substance such as greenhouse gases or aerosol particles. Greenhouse gases in the atmosphere absorb infrared radiation, especially in the "atmospheric window" region from 8 to 12 μm , that would otherwise escape to space. This trapped radiation warms the atmosphere, creating a positive radiative forcing which in turn warms the Earth's surface. Aerosols, on the other hand, scatter or absorb solar radiation and prevent it from reaching the Earth. This has a net cooling effect. Together, emissions of greenhouse gases and aerosols destroy the existing radiative balance of the atmosphere and alter the heating and cooling rate of the Earth.

In view of the aviation impact on the atmosphere, the following gaseous species can play the most important role: NO_x ($\text{NO} + \text{NO}_2$), HNO_y ($\text{HNO}_2 + \text{HNO}_3$), SO_x (SO_2 , SO_3), H_2SO_4 , HO_x (OH , HO_2 , H_2O), CO_x (CO , CO_2), and nonmethane hydrocarbons. The elements of NO_x and HO_x groups participate in the catalytic cycles of ozone destruction and the abundance of the species HNO_2 , HNO_3 , and NO_2 as well as H_2O can result in a broadening of the polar stratospheric cloud formation areas due to appearance of additional HNO_3 and H_2O in Polar Regions. The element of CO_x group (especially CO_2) and hydrocarbons are greenhouse gases and affect the Earth's radiative balance.

Besides the gaseous species, aircraft engines emit aerosol particles and aerosol precursors. Soot and metal particles are directly emitted by aircraft engines. Soot particles are believed to be the most important aviation aerosols impacting contrail and cirrus cloud formation. As Lohmann and Feichter pointed out in a recent review of the global indirect aerosol effects [3], black carbon, which is a major constituent of carbonaceous particles emitted from incomplete combustion processes, contributes to the direct aerosol radiative effect by absorption of visible radiation which results in a net reduction in shortwave radiation and thus a negative forcing at the surface [3]. At the top-of atmosphere, carbonaceous particles exert a positive forcing. This effect can be amplified if absorption of solar radiation by carbonaceous particles occurs within cloud droplets. Since aerosol particles are predominantly a complex internal mixture of chemical substances, the effects of coating insoluble black carbon particles with soluble organic or inorganic species may have a strong effect on the cloud condensation nuclear (CCN) activation of those particles. The knowledge of the coating effects is in turn a prerequisite for an adequate treatment of carbonaceous particles in global climate models.

The newly formed in the exhaust plume aerosols are mainly the sulfate volatile aerosol particles. The formation of sulfate ($\text{H}_2\text{O}/\text{H}_2\text{SO}_4$) liquid small droplets (diameter of 1-10 nm) is generally caused by emission of condensable gases such as water vapor (H_2O) and gaseous H_2SO_4 or SO_2 and SO_3 which can be converted to H_2SO_4 . Besides oxidized sulfur in different forms (SO_x , H_2SO_4) and water vapor, aerosol precursors emitted by aviation engine include chemi-ions, HNO_3 , and unburned hydrocarbons (organics). A number of modeling studies have demonstrated that the emission of sulfur oxides (SO_2 , SO_3) and, especially, of sulfate aerosol particles can considerably affect the surface area of the sulfate stratospheric aerosol layer. Moreover, the emission of sulfate aerosol particles into the stratosphere caused by the fleet of supersonic high-speed civil transport aircraft, known as HSCTs, can result in ozone depletion.

In order to obtain the required information about pollutants emitted by aircraft engines it is needed to conduct the investigations on the following topics: (1) formation of SO_x , HSO_y , NO_x , HNO_y , HO_x , $\text{C}_x\text{H}_y\text{O}_z$ species, ions, and soot particles during the burning of high-order hydrocarbons (aviation kerosene) with air in aero-engine combustor; (2) evolution of gaseous and particulate species (soot particles) in the postcombustor flow of jet engine; (3) generation of ionic clusters and binary $\text{H}_2\text{O}/\text{H}_2\text{SO}_4$ (or ternary $\text{H}_2\text{O}/\text{H}_2\text{SO}_4/\text{HNO}_3$, $\text{H}_2\text{O}/\text{H}_2\text{SO}_4/\text{organics}$) volatile aerosols in aircraft plume, formation of the coverage onto soot particle surface, and condensation of water vapour on activated large soot particles; (4) freezing of soluble material accumulated on the surface of soot particles and contrail formation.

The general objective of this paper is to discuss the nonequilibrium processes in the combustor and in the postcombustor flow of gas-turbine engine that are responsible for gaseous pollutant formation and processes that give rise various sorts of volatile and non-volatile (with soot core) aerosols and ice particles in the plume.

FORMATION OF GASEOUS SPECIES, CHEMI-IONS, AND SOOT PRECURSORS IN AVIATION COMBUSTOR

In present, for commercial aircraft engines the aviation kerosene is used as a fuel. Aviation fuels are comprised of numerous hydrocarbons such as n-paraffins, iso-paraffin, naphtene (cycloparaffin),

aromatics, alkenes, and sulfur in a trace amount [4]. Table 1 lists the properties and average composition of the typical aviation fuels. Different surrogate blends have been proposed to model the ignition/combustion of aviation fuels [4]. For example the possible JP-8 surrogate consists of 5% iso-octane, 5% methyl cyclohexane, 5% m-xylene, 5% cyclooctane, 15% butyl benzene, 15% tetradecane, 10% hexadecane, 5% butyl benzene, 5% tetralin, 5% l-methyl naptalen, and 5% 1, 2, 4, 5-tetramethyl benzene. The complexity associated with the chemical composition of kerosene-type fuels is well recognized [5], and a detailed computational consideration of all of the fuel components of kerosene would be prohibitive. Doute et al. [6] report a chemical analysis of 79-mol % alkanes, 10-mol % cycloalkanes, and 11-mol % aromatics for the fuel utilized in their investigation of kerosene flames. As was shown in [5] the chemical structure of n-decane and kerosene flames is marked similarities. Thus the chemical composition of kerosene may be modeled by a surrogate blend comprising 89-mol % n-decane and 11-mol % aromatic fuel, example, benzene, toluene, ethyl benzene, and naphthalene.

Table 1. Typical aviation fuel properties

Property	JP-4	JP-5	JP-7	JP-8 (Jet A/A-1)	RP-1
Approx. formula	$C_{8.5}H_{17}$	$C_{12}H_{22}$	$C_{12}H_{25}$	$C_{11}H_{21}$	$C_{12}H_{24}$
H/C ratio	1.99	1.87	2.02	1.91	1.98
Boiling range	140-460	360-495	370-480	330-510	350-525
Freeze point	-80	-57	-47	-60 JP-8/Jet A-1; -50 Jet A	-55
Avg. composition					
Aromatics, vol %	10	19	3	18	3
Naphthenes	29	34	32	20	58
Paraffins	59	45	65	60	39
Olefins	2	2	—	2	—
Sulfur, ppm	370	470	60	490	20

The kinetic model for kerosene surrogate blend should be supplemented by reaction mechanisms of S- and N-containing species and chemi-ions (CIs) formation. Aviation kerosene contains between 0.001% and 0.3% sulfur per mass. Sulfur is present in the fuel as a compound of aromatic groups of hydrocarbons. During the oxidation, the various S-containing species (in the fuel lean flame, mostly SO_x ($x=1, 2, 3$) and HSO_3) forms. The kinetic model should describe rather accurately the proportions between SO_2 , SO_3 , and HSO_3 . Such a model was developed by Starik et al. [7]. The point is that the most particles forming in the exhaust plume behind aircraft at cruise are liquid and contain sulfuric acid [8], and some condensable hydrocarbons [9]. The formation of volatile aerosols in the aircraft plume depends on the concentration of gaseous O, OH, SO_2 , SO_3 , H_2SO_4 , and on CIs emitted by the engine. The concentrations of OH, SO_3 , and H_2SO_4 at core engine exit depend on the non-equilibrium chemistry in the combustor and in the postcombustor flow from the combustor through the turbine and the expansion nozzle to the engine exit [10, 11].

N-containing species are generated due to oxidation of air nitrogen in the high temperature region inside a combustor. The main species formed in an aviation combustor are NO and NO_2 . The following mechanisms is believed to be responsible for NO_x production: (1) extended Zel'dovich mechanism; (2) "prompt NO" or Fenimor mechanism; (3) NO_2 mechanism; (4) N_2O mechanism; (5) NNH mechanism. The extended Zel'dovich mechanism involves the oxidation of N_2 by O_2 : $N_2+O=NO+N$, $N+O_2=NO+O$ and reaction of N atoms with OH radicals $N+OH=NO+H$. The Fenimor mechanism passes via HCN: $CH+N_2=HCN+N$, $O+HCN=NO+CH$ and occurs, mostly, in a fuel rich flame. The N_2O mechanism is the summation of NO production in the course of reactions with N_2O :

$\text{N}_2\text{O} + \text{CO} = \text{NCO} + \text{NO}$, $\text{N}_2\text{O} + \text{H} = \text{NH} + \text{NO}$, $\text{N}_2\text{O} + \text{O} = 2\text{NO}$. The NO_2 mechanism specifies the NO production in the course reactions with NO_2 : $\text{NO}_2 + \text{CO} = \text{NCO} + \text{NO}$, $\text{NO}_2 + \text{OH} = \text{HO}_2 + \text{NO}$, $\text{NO}_2 + \text{H} = \text{OH} + \text{NO}$, $\text{NO}_2 + \text{O} = \text{NO} + \text{O}_2$, $\text{NO}_2 + \text{M} = \text{NO} + \text{O} + \text{M}$. The NNH mechanism involves the reactions with HNO and N_xH_y species.

Besides the NO and NO_2 formation, the kinetic mechanism of N-containing species production should describe also the formation of N_2O , HNO, HNO_2 , HNO_3 , NO_3 , N_xH_y , proportions between NO and NO_2 and between NO_x ($\text{NO} + \text{NO}_2$) and NO_y ($\text{NO}_y = \text{NO}_x + \text{N}_2\text{O} + \text{NO}_3 + \text{HNO}_y$). The ratio of NO_2 to NO_x concentration was measured in the exhaust plume for several aviation engines and varies from 5% to 25% [12]. The NO_y/NO_x concentration ratio is close to 0.01 [13]. The quantitative information about HNO_2 and HNO_3 emissions from aircraft is extremely important for atmospheric chemistry, formation of polar stratospheric clouds, and prediction of the aviation effect on the atmosphere. For the aviation combustor operating in a diffusion mode, the Zeldovich and Fenimore mechanisms are mainly responsible for NO formation. Also the NO_2 mechanism plays a noticeable role in the NO_x production inside the combustor. It is worth noting that NO and NO_2 production inside the aviation combustor are in a strong interconnection. The N_2O and NNH mechanisms give smaller contribution in NO formation [14].

In order to predict the emissions of NO_x , CO_x and unburned hydrocarbon (UHC) the two different approaches has been developed. One of them is based on semi-empirical formulas so-called correlation models that include the pressure and temperature of the gas at the combustor inlet as well as the residence time for the gas inside the combustor (see, for example [15]). The other one is based on the use of multi-reactor models, which calculate the concentrations of NO_x , CO_x , HO_x , UHC, and the other species in the each individual reactor by using the detailed kinetic reaction mechanism [14]. Note that this approach may be used also to predict the emissions of S-containing species and CIs. To construct the reactor model, the information on fields of the temperature and other flow parameters inside the combustor is required. To obtain these fields the three-dimensional (3D) numerical simulation of turbulent combustion using the CFD code with the equilibrium chemical model may be applied. Fig.1 shows the temperature field inside the typical aviation combustor (this combustor is similar to that for PC-90A turbo-jet engine) computed using standard STAR-CD software [14].

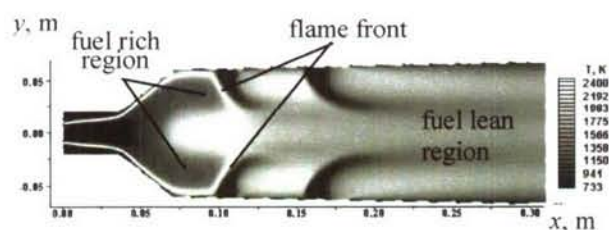


Fig. 1. The temperature field inside the conventional aviation combustor.

The simulations have demonstrated that predicted NO_x emission index strongly depends on the applied kinetic reaction mechanism. This illustrated by the data on the measured and computed using the different kinetic models [16-18] the NO_x emission index EINO_x ($\text{EINO}_x = G_{\text{NO}_x} / G_f$, where G_{NO_x} , G_f are the mass flow rates of NO_x and fuel, respectively) for typical aviation combustor operating in a diffusion mode (gas residence time of 6.7 msec, the pressure of 10^6 Pa) for two values of the temperature at the combustor inlet $T_{\text{air}} = 600$ and 660 K presented in Fig.2. One can see that only the prediction using the DS reaction mechanism is consistent with experimental data. The widely applied GRI-Mech 3.0 and Konnov 0.4 reaction mechanisms underestimate the NO_x emission considerably. Furthermore, the GRI-Mech 3.0 and Konnov mechanisms underestimate the NO_2/NO_x

ratio (the predicted value of this ratio is as small as 1%). The DS reaction mechanism predicts the NO_2/NO_x ratio of 5-10% that is consistent satisfactorily with experimental data.

For modern gas-turbine engines the values of EINO_x vary from 12 to 40 g/kg fuel. In order to lower significantly the NO_x emission up to $\text{EINO}_x=5-8$ g/kg the lean premixed and prevaporised (LPP) technology has been proposed. In LPP combustor a homogeneous burning of lean fuel/air mixture (equivalence ratio 0.6-0.5) takes place. In this case, the maximal temperature inside the combustor does not exceed 2100 K that is significantly smaller than that for traditional diffusion combustor ($T=2400$ K). This reduces the rate of NO_x production in the course of Zeldovich mechanism. However, the LPP combustor exhibits the worse re-light and blow-out characteristics as compared to conventional diffusion combustor.

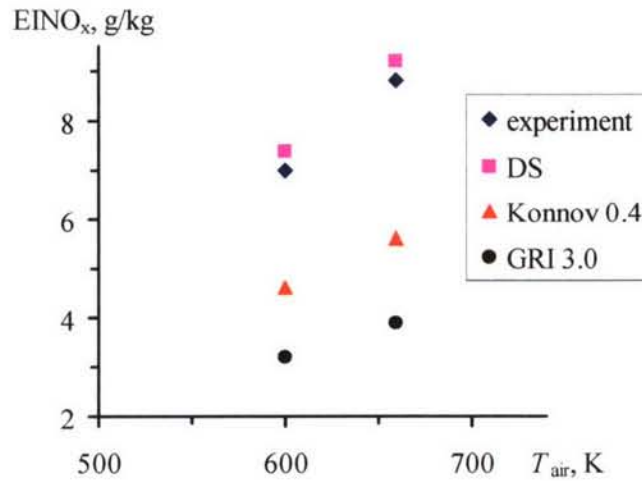


Fig. 2. Measured and predicted using different kinetic mechanisms (GRI 3.0, [16], Konnov 0.4 [17], and DS [18]) NO_x emission index, EINO_x , as a function of the combustor inlet temperature.

Besides SO_x and NO_x species, the CO , CO_2 and unburned hydrocarbons (C_xH_y) form inside the combustor. The emission indices for various species depends on the engine power setting. The computations carried out by using the multi-reactor model [14] exhibited that the decrease in power setting results in a strong increase of EICO and $\text{EIC}_{\text{C}_x\text{H}_y}$ and, conversely, in decrease of NO_x and CO_2 emissions. The value of EISO_2 does not depend markedly on power setting. Table 2 lists the predicted emission indices for NO_x , CO , C_xH_y , SO_2 , SO_3 , species, as well as the values of residence time pressure and temperature of the air at the combustor inlet for different power settings at $\text{FSC}=0.04\%$.

Table 2.

Parameters Power setting	P , MPa	T_{air} , K	EINO_x , g/kg	EICO , g/kg	$\text{EIC}_{\text{C}_x\text{H}_y}$, g/kg	EISO_2 , g/kg	EISO_3 , g/kg
100% $\tau_{res} = 13.63$ ms	2.14	755	36.4	0.72	0.06	0.783	0.0199
85% $\tau_{res} = 13.78$ ms	1.88	727	29.2	11.3	1.2	0.781	0.0213
30% $\tau_{res} = 14.78$ ms	0.89	591	12	76.7	12.9	0.748	0.0256
7% $\tau_{res} = 17.14$ ms	0.41	485	8.7	105	18.8	0.723	0.0205

The important precursors of volatile aerosol particles are CIs, which form in the combustor during the combustion of hydrocarbon fuel with air via radical-radical and ion-molecular reactions [7, 19]. CIs may induce the nucleation of volatile aerosols and promote the growth of aerosols via ion-assisted

coagulation [20]. Another possible mechanism of CIs influence on volatile and nonvolatile (with soot core) particle formation is connected with ion-soot interaction. CIs may attach to soot particles, induce the charge, and as a consequence enhance the water uptake by soot particles [21].

It should be noted that the most studies on ion formation were conducted for flames [19]. Ion composition strongly depends on the fuel/air equivalence ratio, ϕ , and on the type of fuel (hydrogen, hydrocarbons, aviation kerosene, etc.). The most frequently used technique to measure an ion concentration in flame is massspectrometry [19]. Numerous types of positive and negative ions such as $C_2H_3O^+$, $C_3H_3^+$, CH_3^+ , HCO^+ , $C_3H_5O^+$, $C_3H_7O^+$, H_3O^+ , H_2O^+ , O_2^+ , NO^+ , NO_2^+ , HCO_2^+ , HCO_3^+ , CO_3^+ , CO_4^+ , O_2^- , OH^- , NO_2^- , NO_3^- , CN^- were observed in hydrocarbon/air flames. In fuel rich flames, heavy hydrocarbon ions $C_{13}H_9^+$, $C_{19}H_{11}^+$, $C_{22}H_{12}^+$, $C_{55}H_{19}^+$, as well as positively charged fullerene molecules may form [22]. Measurements behind the aviation combustor demonstrated the presence of $C_xH_yO^+$ and $C_xH_yO^-$ ions as well as SO_3^- , SO_4^- , and HSO_4^- ions [23]. In order to understand the mechanisms and principal pathways of ion formation the experimental data should be supplemented by numerical simulation. In this light, rather complicated kinetic models for charged species formation during combustion of various fuels have been developed [7, 24].

The processes of ion formation inside the aero-engine combustors are more complicated than those in flames. The modern combustor operates in a diffusion mode. In this case, the fuel/air mixture composition differs considerably in various regions of combustor. Therefore, a number of different ions can form inside the combustor. The gas residence time for combustor (5-10 ms) is much smaller than that for flame (~ 100 ms). The total ion concentration of $\sim 2 \cdot 10^8 \text{ cm}^{-3}$ at the exit plane of aero-engine combustor was measured recently by Haverkamp et al. [25]. However, inside the combustor, the concentration of ions and electrons may be estimated only by computations. To simulate the processes of charged gaseous species formation inside an aviation combustor one have to apply approximate combustion models, for example, Flame Let model [26]. In our computations this model was supplemented by the ion kinetics developed in [7, 24]. To calculate the flow parameters inside the combustor (these parameters are needed as input ones for the Flame Let model) with outlet pressure of 10^6 Pa and temperature $T_c = 1540 \text{ K}$ the 3D numerical simulation of turbulent combustion using the standard STAR-CD software with the equilibrium chemistry was conducted [27].

Inside the combustor the maximal concentration for the most abundant ions in flames, $C_2H_3O^+$, is observed in the fuel rich region located ahead of the flame front (see Fig. 1) and attains $10^{11} - 10^{12} \text{ cm}^{-3}$. In this region, the maximal concentration for negatively charged species is appeared for electrons and HCO_2^- ions. However, at the combustor exit the concentrations of these species are negligible. In the fuel lean zone of combustor at the exit section only NO^+ , H_3O^+ , SO_3^- , HSO_4^- or NO_3^- ions remain to be abundant. The predicted total concentration of positive (negative) ions in the combustor outlet is around $2 \cdot 10^8 \text{ cm}^{-3}$ [27] that is in a good agreement with measurements [25]. It is worse noting that the ion composition strongly depends on the value of fuel sulphur content (FSC). The principal scheme of ion formation in hydrocarbon flames and inside the combustor is presented in Fig.3.

Soot particles form in the fuel rich zone of combustor due to clustering and heterogeneous surface growth of primary soot precursors such as polyene molecules, and polyaromatic hydrocarbons [28]. In accordance to modern models, the pyrene molecules which consist of four aromatic rings are the main soot precursors. The particle inception with radius of approximately 1 nm is constructed from PAH. In the fuel rich zone of combustor the concentration of pyrene molecules can be as large as $10^{12} - 10^{14} \text{ cm}^{-3}$ and concentration of primary clusters (particle inception) attains $10^{11} - 10^{12} \text{ cm}^{-3}$. It should be noted that combustion exhausts are the typical dusty plasma. It consists of various molecular gases, ions, electrons, carbon clusters, and soot particles. Therefore, in order to predict the charge and size distribution of soot particles it is needed to take into account the plasma-chemical processes occurring inside the combustor. Figure 4 shows the principal scheme of soot particle formation.

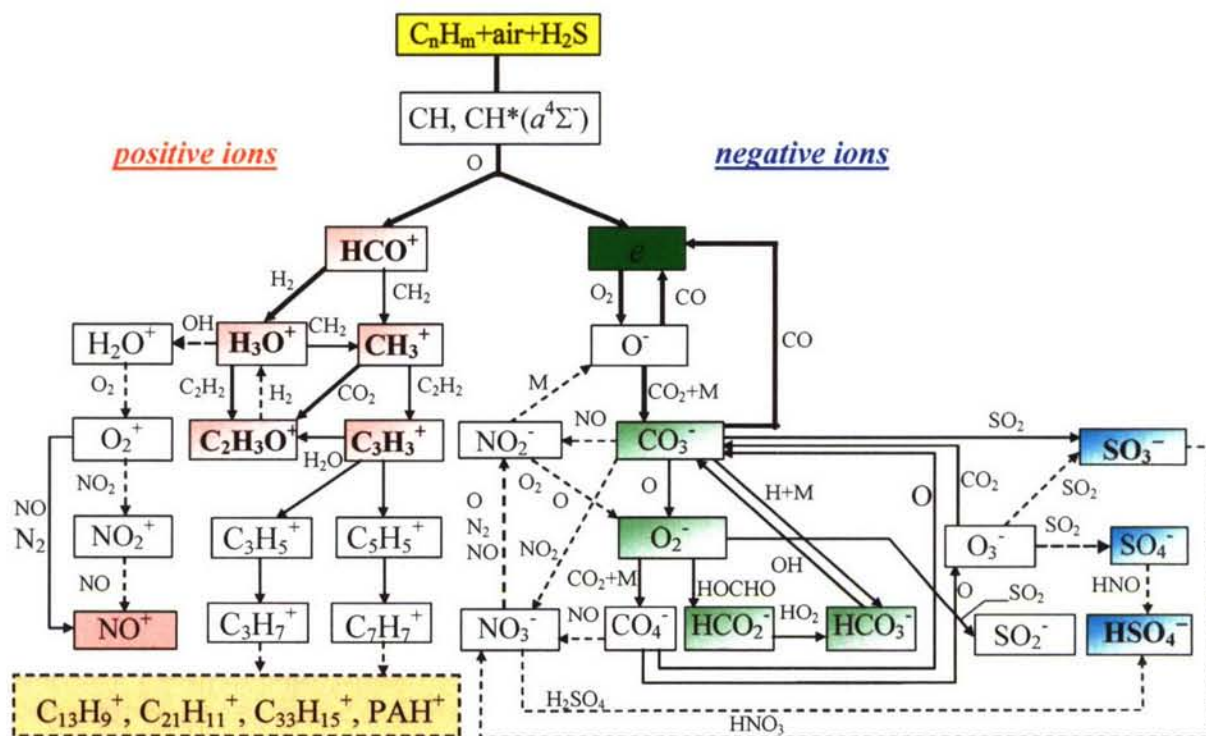


Fig. 3. Principal scheme of ion formation in hydrocarbon+air flame.

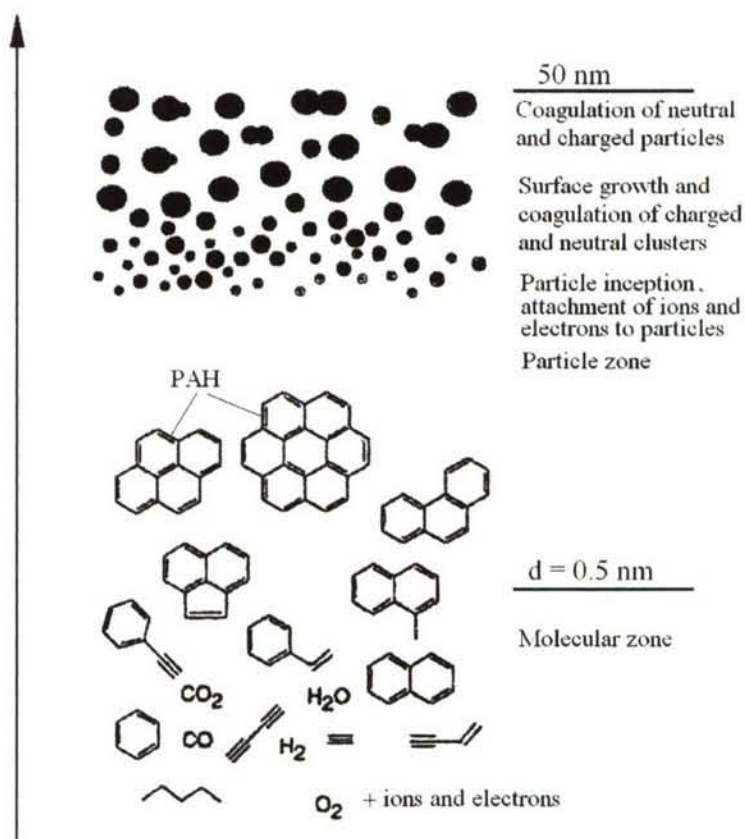


Figure 4. A rough picture for soot formation in combustion plasmas.

Ions and electrons originated in the fuel rich zone of combustor attach to small clusters and soot particles. As a result primary neutral clusters and particles acquire a significant charge [21]. Charged clusters with opposite polarities coagulate more rapidly than neutral ones. The charged cluster induces the image charge on a neutral particle. Therefore, for charge-neutral cluster (particle) interaction the appearance of the image force enhances the cluster coagulation [29] and, as a consequence, facilitates the formation of soot particles [30]. Fig. 5 depicts the predicted charge distribution of clusters with different sizes formed from the neutral monodisperse primary precursors of initial concentration $N_0=10^{11} \text{ cm}^{-3}$ with radius $a_0=1 \text{ nm}$ at time instants $t = 0.1$ and 5 ms . One can observe that at an initial stage even small size clusters are principally charged negatively due to the strong electron attachment. At the latter time instant the charge distribution becomes to be more symmetrical and the size of clusters increases. Even small clusters with radius $a = 4 \text{ nm}$ may acquire the charge $Q=4-5e$ (e is an elementary charge). Larger size soot particles with $a \approx 40 \text{ nm}$ acquire the charge of $(15-30)e$ in the region placed directly ahead of the flame front [21].

The existence of a charge on the cluster (or soot particle) surface enhances the uptake of the molecules having a permanent dipole momentum by cluster and soot particle. For example, the attachment coefficient for H_2O molecules to the cluster with $a = 4 \text{ nm}$ and $Q=5e$ is by a factor of 10 larger at $T=2000 \text{ K}$, $P=10^6 \text{ Pa}$ than that for neutral cluster. Calculations showed that a noticeable proportion of soot particles ($\sim 10\%$) having a relatively large charge can accumulate the water soluble compounds inside a combustor. Thus, this fraction of soot particles may be activated to act as contrail nuclei with in an engine.

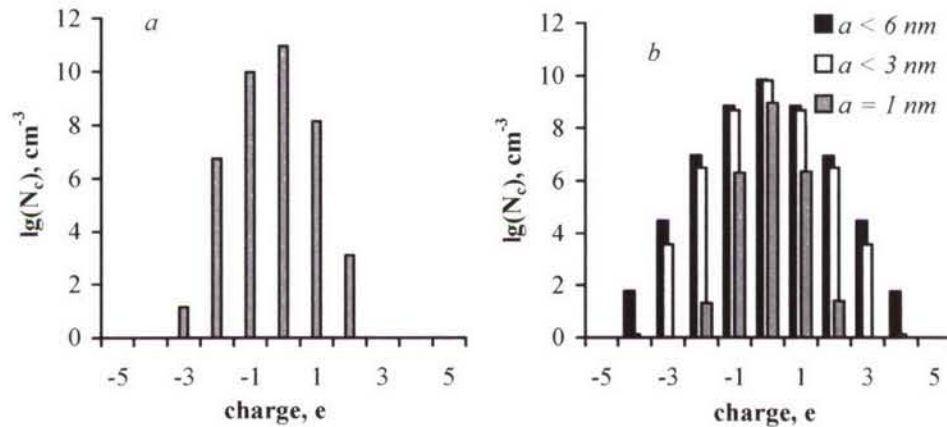


Figure 5. Predicted charge distribution of clusters with radii smaller than given value at $N_0=10^{11} \text{ cm}^{-3}$ and $a_0=1 \text{ nm}$ at the conditions in the fuel rich region of combustor for time instants of 0.1 ms (a) and 5 ms (b).

The analysis of the IR-Fourier spectra of combustor-generated soot particles exhibited that combustor soot consists of two different fractions: a main fraction containing, mostly, amorphous carbon and a fraction of impurities specified by a complex structure and a noticeable amount of water soluble compounds such as organic sulfates, S-containing ions, and organic molecules on the surface of soot particles. It was observed that $\sim 13.5 \text{ wt } \%$ of water soluble fraction may be appeared on the soot particles within a combustor [30, 31]. The main fraction is supposed to form from neutral clusters or particles with a small charge, $Q \leq 2e$. These particles can not accumulate polar molecules within a combustor and are hydrophobic. Conversely, the fraction of impurities demonstrates the high level of hydrophilicity [30, 31].

NONEQUILIBRIUM PROCESSES IN TURBINE AND NOZZLE FLOW

Rapid expansion of hot gases with a complex composition through the turbine and nozzle (the residence time is $\sim 5\text{-}7$ ms) causes the nonequilibrium chemical transformation and ion-soot attachment due to change of temperature and pressure [10, 11, 32]. The typical values of temperature at combustor exit for modern engines are $\sim 1300\text{-}1800$ K and at the nozzle exit $\sim 450\text{-}650$ K. The pressure in these sections for cruise regime varies in the range $0.8\text{-}1.2$ MPa and in the range $10\text{-}20$ kPa, respectively.

In present, to investigate the nonequilibrium processes in the postcombustor flow of jet engines the numerical simulation is used. The computation of the evolution of the chemical composition of combustor exhaust gases in the turbine and nozzle flow for modern aero-engine at cruise of *B-747* aircraft (Mach number $M_0=0.8$ and altitude $H=10.8$ km) based on the quasi-one dimensional (Q1D) model [7] showed that the mole fractions, γ_i , vary considerably for most of the mixture components with minor variations only for H_2O , O_2 , N_2 , and CO_2 . The variations of the γ_i values are most pronounced for strong oxidizers such as O , OH , and HO_2 , as well as for NO_3 and for the species of the N_xH_y group. The effective mass emission index of OH amounts to 5.4 g/kg at combustor exit and 66 mg/kg at engine exit. At engine exit, most of the initially formed OH radicals are depleted by reactions with NO , NO_2 , SO_2 and others, leaving a mole fraction of about 10^{-6} , and this explains why measurements so far found hardly significant traces of OH at engine exit [33]. From measurements of HNO_2 , HNO_3 , NO , and NO_2 in aged exhaust plumes, OH emission indices of 60 to 400 mg/kg have been derived using models describing the chemistry in the diluting plume, starting from engine exit [34]. This fits reasonably with the present model results. The small amount of OH emitted from the engine exit implies small ($<1\%$) additional sulfur conversion to H_2SO_4 after engine exit. It should be noted that the concentrations of HNO_2 and HNO_3 in the turbine affect each other.

Significant SO_2 oxidation occurs throughout the turbine and nozzle resulting in up to 10% oxidation of the total SO_x to $(\text{SO}_3+\text{H}_2\text{SO}_4)$ at the engine exit. The NO_3 and HNO_2 concentrations also increase significantly within the postcombustor flow but stay below 1% of the sum of NO and NO_2 species, as found in measurements [34]. Concentrations of sulfur species SO_2 , SO_3 , and H_2SO_4 at the engine exit strongly depend on FSC. Note that even for $\text{FSC}=0$ the marked amount of gaseous H_2SO_4 and HSO_4^- ions may be abundant in the nozzle exhaust. This is caused by the presence of S-containing species, mainly COS , H_2S , SO_2 , in the atmospheric air, which is supplied to the combustor. For $\text{FSC}=0$ the concentration of the gaseous H_2SO_4 achieves $2.5 \cdot 10^8 \text{ cm}^{-3}$. The abundance of gaseous H_2SO_4 in the engine exhaust at $\text{FSC}=0\%$ leads to formation of small sulfate volatile particles (with diameter $d \leq 1$ nm) in the plume (see below). During expansion of combustion exhausts throughout the turbine and nozzle, the concentrations of different gaseous species may vary significantly. This is clearly seen from the data presented in Table 3.

Table 3. Predicted species molar fractions at the different sections of the modern gas-turbine engine at $\text{FSC}=0.04\%$

Parameters and species	Combustor	Turbine	Bypass flow	Mixer	Nozzle
T , K	1414	774	375	480	473
P , kPa	2080	167	101	167	166
O_2	1.26(-1)	1.26(-1)	2.00(-1)	1.82(-1)	1.82(-1)
H_2O	4.96(-2)	4.96(-2)	5.77(-5)	1.25(-2)	1.25(-2)
SO_2	7.68(-6)	7.33(-6)	3.79(-9)	1.83(-6)	1.84(-6)
SO_3	1.56(-7)	4.89(-7)	0	1.22(-7)	3.99(-8)
H_2SO_4	4.36(-11)	2.47(-8)	5.06(-13)	6.20(-9)	8.89(-8)
N_2	7.79(-1)	7.79(-1)	8.00(-1)	7.94(-1)	7.94(-1)
NO	4.80(-4)	4.78(-4)	1.00(-11)	1.20(-4)	1.20(-4)
NO_2	1.68(-5)	1.66(-5)	6.03(-12)	4.18(-6)	4.22(-6)
HNO_2	9.65(-8)	2.39(-6)	0	5.99(-7)	6.01(-7)

CO	1.61(-5)	1.28(-5)	2.28(-7)	3.38(-6)	3.38(-6)
CO ₂	4.44(-2)	4.44(-2)	3.09(-4)	1.13(-2)	1.13(-2)

Decrease of FSC value results in the change of ion composition both at the combustor and at the nozzle exit. The concentration of ions grows with the FSC increase. The total number density of positive (negative) ions at the engine exit may vary in the range $2 \cdot 10^7 - 2 \cdot 10^8 \text{ cm}^{-3}$. For the free sulfur fuel the concentration of NO_3^- and NO_2^- ions becomes noticeable and is comparable with the concentration of HSO_4^- ions.

During expansion through the turbine and nozzle, soot particles may change their charge as a result of continuous charging and discharging events in a bipolar ion environment. To simulate the processes of the soot particles charging in the turbine and nozzle flow the Q1D code with coupled gas phase ion and neutral species kinetics, and kinetics of accumulation of a charge on soot particles with different radii was developed [32]. The computations performed for cruise regime of *B-747* aircraft showed that ion-soot interaction in the postcombustor flow leads to evolution of soot particles charge just in the high pressure turbine of the engine.

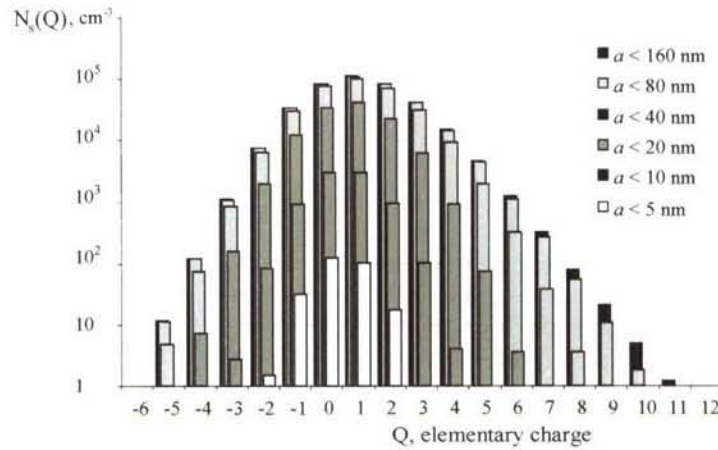


Fig. 6. Predicted charge distribution of soot particles with different radii, a , and total concentration $N_s^0 = 8 \cdot 10^6 \text{ cm}^{-3}$ at the nozzle exit of *RB-211* engine at cruise regime of *B-747* ($M_0=0.8$, $H=10.8 \text{ km}$).

At the nozzle exit the rather small soot particles with $a \leq 10 \text{ nm}$ may accumulate only two elementary charges. Large particles with $a \approx 60 \text{ nm}$ may accumulate the elementary charges of 4-5. Due to smaller mass of positive ions (NO^+ , H_3O^+) as compared with that for negative ions (HSO_4^- , NO_3^-), which are abundant at combustor exit, the concentration of positively charged soot particles are larger than negatively charged ones. The proportions of neutral, positively and negatively charged soot particles depend on the fraction of charged soot particles in combustion products. The predicted charge distribution of soot particles (the median radius of lognormal size distribution is 25 nm , and geometrical deviation is 1.57), $N_s(a)$, at the nozzle exit of *RB-211* engine at *B-747* aircraft cruise regime of are presented in Fig. 6.

FORMATION OF AEROSOL PARTICLES IN AIRCRAFT PLUME

There are a number of gaseous pollutants, ions, aerosol precursors, charged and neutral soot particles in the engine exhaust. Cooling of hot exhaust gases ($T \approx 600 \text{ K}$) caused by mixing with co-flow atmospheric air ($T_a = 200-220 \text{ K}$) leads to an occurrence of a complex of nonequilibrium processes resulting in transformation of chemical composition of exhaust gases, formation of ionic clusters, mostly, $\text{HSO}_4^-(\text{H}_2\text{SO}_4)_n$ ($n=1 \dots 3$), $\text{NO}_3^-(\text{HNO}_3)_n(\text{H}_2\text{O})$, $\text{HSO}_4^-(\text{HNO}_3)_n$, $\text{HSO}_4^-(\text{SO}_3)$, $\text{H}_3\text{O}^+(\text{H}_2\text{O})_m$, $\text{H}_3\text{O}^+(\text{CH}_2\text{O})(\text{H}_2\text{O})_m$, $m=1 \dots 9$, generation of liquid volatile $\text{H}_2\text{O}/\text{H}_2\text{SO}_4$ small aerosol particles with

diameter $d \leq 10$ nm, production of large particles with soot core coated by liquid soluble materials or by freezed solution [35-38]. The size of soot particles and ice particles are in the range 10 nm – 1 μ m. Fig. 7 shows the size distribution of volatile ($d \leq 10$ nm) and non-volatile particles in the plume of ATTAS aircraft [35]. The microphysical processes which are responsible for volatile and non-volatile aerosol particle formation in the aircraft plume are rather complicated. The schematic of these processes are presented in Fig. 8.

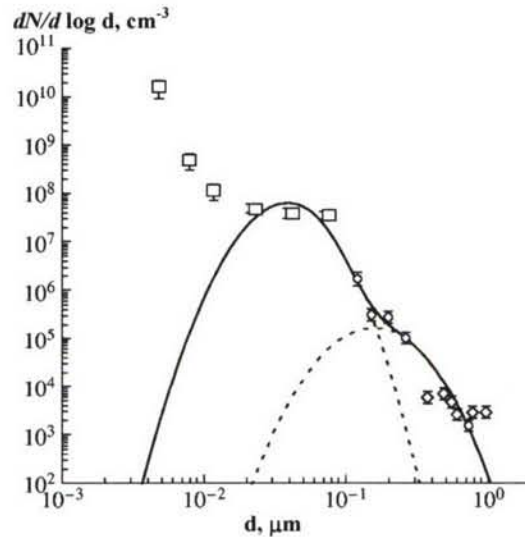


Fig. 7. Size distribution of aerosol particles (d is the particle diameter) in the plume of ATTAS aircraft. Dashed, dotted, and solid lines correspond to the mode of primary soot particles, mode of agglomerated particles, and total distribution of soot particles. Measurements: squares, rhombuses, and circles.

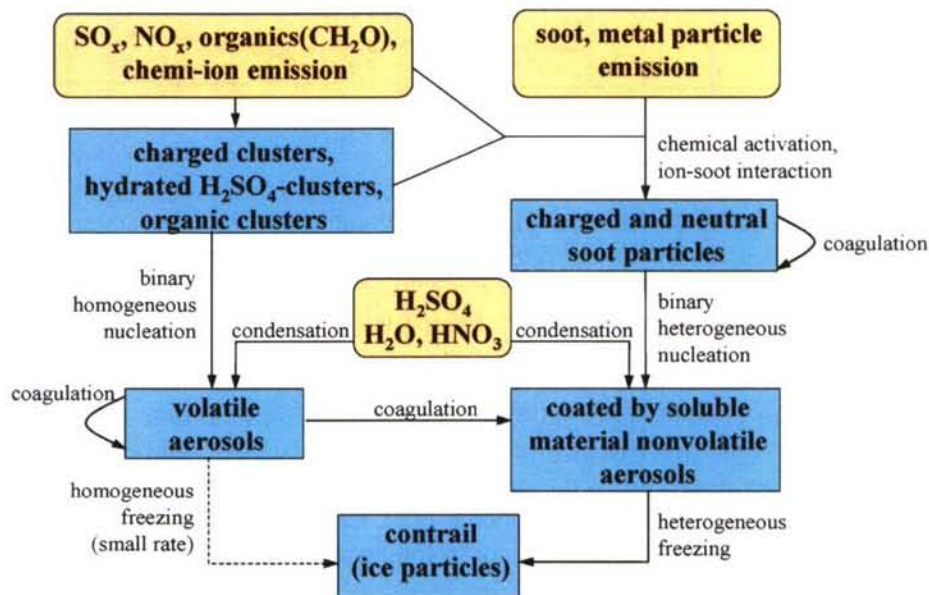


Fig. 8. The schematic of processes being responsible for aerosol particle formation

Despite of a number of experimental and numerical investigations of the microphysical processes in the plume many questions are still unresolved. Up to now there is lack of quantitative consistent between computed and observed data on volatile aerosols particle concentration in the plume. Moreover, the main mechanisms of formation of relatively large volatile particles with $d > 5$ nm are not still undetermined. Two hypotheses were proposed to improve the agreement between simulation and

in-situ measurements of number density of large-size volatile aerosols. First, it was hypothesised that abundance of SO_3 additionally to SO_2 at the nozzle exit results in a growth of the size and number density of volatile aerosol particles [40]. Previous analysis prescribed the SO_3 concentration at the nozzle exit as a free model parameter and did not take into account the presence of HSO_3 and H_2SO_4 species at the nozzle exit besides SO_3 . However, as it was shown above these species may be abundant at the nozzle exit as a result of a strong oxidation of SO_2 and SO_3 in the turbine and nozzle flow.

As compared to the case where only SO_2 is abundant at the nozzle exit, the analysis demonstrated that the presence of SO_3 , HSO_3 , and H_2SO_4 species in the nozzle exhaust leads to an increase of H_2SO_4 partial pressure, nucleation rate, sulfur conversion efficiency, intensification of coagulation processes, change of the particle size distribution, and an increase of the number of large-size volatile aerosols in the near field plume. Fig. 9 depicts the evolution of the $\text{H}_2\text{O}/\text{H}_2\text{SO}_4$ volatile aerosol number density, N_a , with different diameters along *B-747* aircraft plume axis at cruise for $\text{FSC}=0\%$ and 0.04% when all S-containing species are present in the nozzle exhaust and when only SO_2 is abundant at the nozzle exit. Markedly, that even for $\text{FSC}=0\%$ the abundance of SO_3 and H_2SO_4 which are produced in a combustor due to burning the hydrocarbon fuel with atmospheric air containing sulfur species, results in a formation of sulfate aerosols in the plume (at $100\text{ m} - 150\text{ m}$ distance from nozzle exit). But diameter of these volatile particles does not exceed 1.2 nm and concentration of the particles with $d > 1\text{ nm}$ is around 10^4 cm^{-3} . When only SO_2 is abundant at the engine exit there are no any sulfate aerosols in the plume [38].

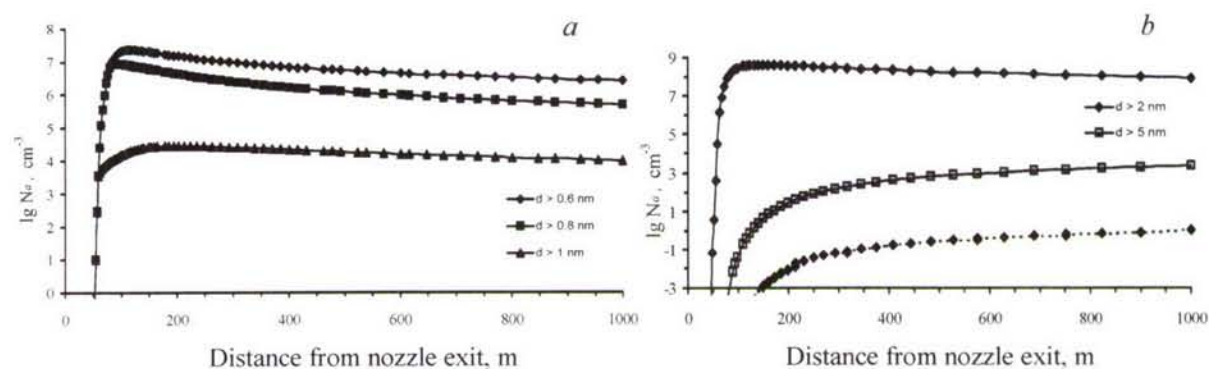


Fig. 9. Predicted evolution of the number density of volatile $\text{H}_2\text{O}/\text{H}_2\text{SO}_4$ aerosol particles with particle diameters larger than a given size d along the plume axis of *B-747* for two cases of initial S-containing species abundance at the engine exit: all S-containing species are present (solid curves) and only SO_2 is abundant (dotted curves) at $\text{FSC}=0\%$ (a) and $\text{FSC}=0.04\%$ (b).

At the mediate fuel sulfur content ($\text{FSC}=0.04\%$) the concentration of sulfate aerosol particles with $d \geq 5\text{ nm}$ stays below 10^4 cm^{-3} at a distance of 1000 m from nozzle exit, and remains so even when SO_3 , HSO_3 , and H_2SO_4 are produced in the engine. If only SO_2 is abundant at the nozzle exit, the concentration of such aerosols is negligible. Schöder et al. measured concentration of about 10^6 cm^{-3} of relatively large volatile particles with $d > 5\text{ nm}$ in the near field plume of the ATTAS aircraft for $\text{FSC}=0.026\%$ [41]. These results could not be explained by the formation of sulfate aerosol precursors (SO_3 , HSO_3 , H_2SO_4) in the combustor.

The second idea is connected with emitted condensable hydrocarbons and CIs, which were considered to be responsible for the generation of the observed large volatile aerosols in the aircraft plume [9]. In these study the unified mechanism to form volatile particles is supposed to be coagulation between charged clusters. The key questions in this theory are following: what sorts of ions may be generated and what amount of these ions may be abundant at the nozzle exit. In order to explain measurements

[41] the concentration of ions at the engine exit should be as large as $2 \cdot 10^9 \text{ cm}^{-3}$. However, this value of ion concentration is believed to be too large and is not produced in modern aero-engines.

In-situ flight measurements exhibited the existence of volatile sulfate aerosol particles with $d=2\text{-}5 \text{ nm}$ at 15-20 m distance from nozzle exit. However, the Q1D models predict the formation of sulfate aerosols in the plume axis at 35-40 m distance. The appearance of sulfate particles at the short distance from engine exit is caused by the turbulent diffusion of aerosol particles from the boundary streamline ($\bar{r}=1$) dividing the engine core flow and bypass flow to the axis of the plume. Fig.10 shows the location of the nucleation region in the plume of B-747 aircraft at cruise predicted by two-dimensional 2D model for turbulent plume of bypass engine.

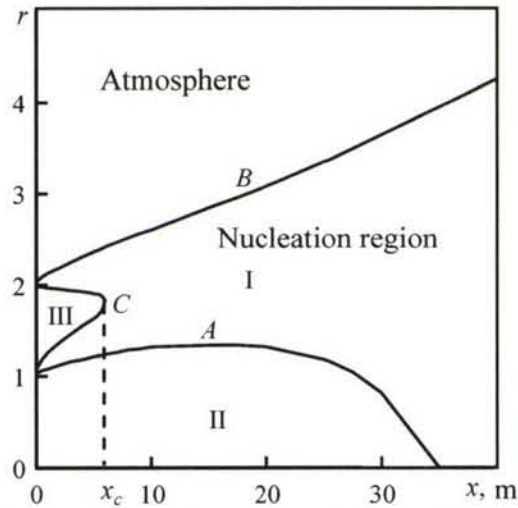


Fig. 10. Location of nucleation region in the plume of B-747 aircraft at cruise for FSC=0.04 % predicted by 2D model (\bar{r} is the normalized radius of the plume, A depicts the boundary of the engine core flow, B depicts the boundary of the plume)

The amount of volatile aerosol particles depends on the fuel sulfur content, type of combustor, parameters at the combustor inlet, engine design, and flight altitude. Figure 11 presented by Schumann *et al.* [37] shows the variation of sulfate aerosol particle emission index PEI (PEI defined as the number of aerosol particles forming due to burning of 1 kg fuel) for different subsonic aircrafts (engines) as a function of FSC measured in-situ during a various European campaigns (Sulfur 5,6,7; SNIF; SUCCESS; POLINAT).

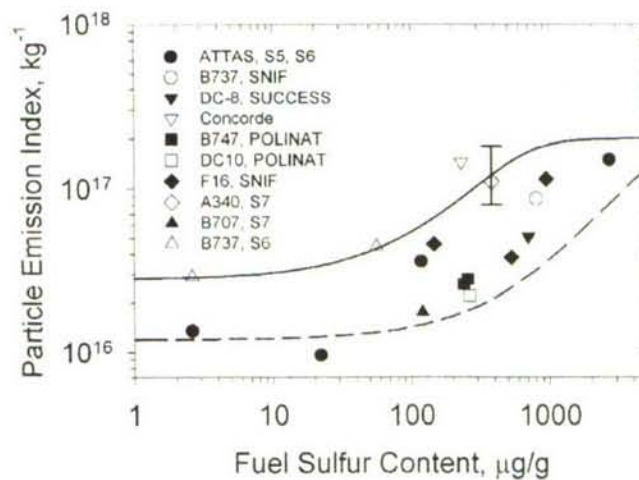


Fig. 11. Particle number emission index (PEI) of detectable volatile particles in noncontrail plumes versus FSC from various measurements normalized to plume age 3s.

Aerosol microphysical and chemical processes are similar in subsonic and supersonic aircraft plumes. The aerosol changes will differ because soot emission levels, aerosol formation potential, and plume dilution properties vary with engine type and atmospheric conditions at cruise altitudes. Significant increases in stratospheric aerosol are expected for the operation of a large fleet of supersonic aircraft, at least for non-volcanic periods.

As was mentioned above, soot particles emitted from engine consist of two fractions. One of them, the fraction of impurities, has hydrophilic properties and involves the activated particles. The second one is the main fraction and involves non-activated hydrophobic particles. These particles may be partly activated due to a deposition of solvable material on their surfaces in the plume. The simulation exhibited that general mechanisms responsible for such a process are the coagulation of soot particles with volatile sulfate aerosols and heterogeneous binary ($\text{H}_2\text{O}/\text{H}_2\text{SO}_4$) nucleation [30, 43]. It turned out that small size particles with diameter $d \leq 15$ nm are activated, generally, due to coagulation process and larger particles ($d > 15$ nm) are activated due to heterogeneous nucleation [30]. Depending on FSC, 5-15 % amount of soot particles of hydrophobic fraction may be activated in the plume. The activation degree grows with the FSC increase.

The other pathway of soot particle activation deals with the existence of charged soot particles in the plume. The computations show that various ionic clusters, mainly $\text{HSO}_4^-(\text{H}_2\text{SO}_4)_m$, $\text{HSO}_4^-(\text{HNO}_3)_{m-1}$ ($m=1\dots3$), $\text{H}_3\text{O}^+(\text{CH}_2\text{O})(\text{H}_2\text{O})_m$, and $\text{H}_3\text{O}^+(\text{H}_2\text{O})_n$ ($n=1-6$) form in the plume. Their concentration at 10 m distance from engine exit may be as large as 10^6-10^7 cm^{-3} [30]. Due to dilution of the plume and attachment of ionic clusters to soot particles their concentration decreases rapidly with the plume age increase and at 50 m distance drops to 10^4-10^5 cm^{-3} that is consistent with measurements [35]. Nevertheless, the significant charge continues to be on the particle surface even to 100 m distance from the engine exit. Heterogeneous binary $\text{H}_2\text{O}/\text{H}_2\text{SO}_4$ nucleation on the surface of charged soot particles occurs much faster than on the neutral one.

Coated by water solution soot particles at atmospheric supersaturation conditions can condense a significant amount of water vapor that leads to an increase of their size. This is illustrated by Fig. 12 and Fig. 13, which depict the evolution of the radius of soot particles and concentration of sulfuric acid in particles the solution coating soot particles along the plume of B-747 aircraft for particles with different initial radii (R_0) at lognormal distribution of fresh soot particles.

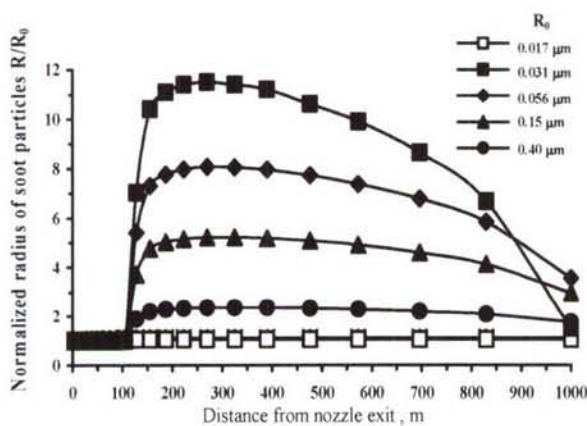


Fig. 12. Evolution of normalized soot particle radius along the plume of B-747 aircraft at cruise for different initial radius values of fresh soot particles, R_0 .

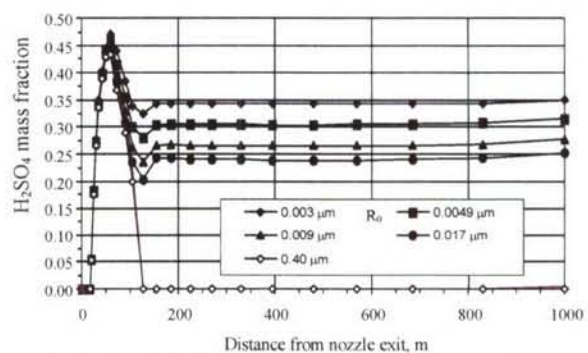


Fig. 13. Evolution of H_2SO_4 concentration in the solution accumulated on the surface of soot particles with different initial radii, R_0 , along the plume of B-747 aircraft at cruise.

One can see that only relatively large soot particles can accumulate a significant amount of water molecules on their surface. The concentration of H_2SO_4 in the $\text{H}_2\text{SO}_4/\text{H}_2\text{O}$ solution is smaller than 10% only for particle with $R_0 > 25\text{--}30\text{ nm}$. Therefore, only these large particles can freeze. That is why the amount of ice particles observed in the plume ($N_{ice} \approx 10^3\text{--}10^4\text{ cm}^{-3}$) is significantly smaller than the number density of fresh soot particles emitted by engine ($N_s \approx 10^5\text{--}10^6\text{ cm}^{-3}$) [37].

Soot emissions for current aircraft engines are specified under the International Civil Aviation Organization (ICAO) using smoke number measurements. The smoke number is dominated by the largest soot particles collected onto a filter. Sampling soot particles smaller than about 300 nm on such filters becomes inefficient. Correlations between smoke number and soot mass concentrations may be used to estimate the soot mass EI from ICAO certification data. A mean value has been estimated to be approximately 0.04 g/(kg fuel) for the present subsonic fleet. Soot emissions depend strongly on engine types, power settings, and flight levels, additional information is generally needed to relate smoke number to emissions under flight conditions.

The diameter of soot particles emitted by aircraft engines are in the 10 nm – 100 nm range and the values of particle emission index depending on the engine type for subsonic transport aircraft vary from $1.8 \cdot 10^{14}$ - $3 \cdot 10^{15}\text{ kg}^{-1}$ [37]. The soot mass (EI_{soot}) and number emission indices (PEI_{soot}) at cruise for different fleet and smoke numbers (SN) were reported by Schumann et al. [37] and are presented in Table 4.

Table 4. Soot Mass and Number Emission Indices at Cruise and Smoke Numbers^a

Aircraft	$\text{EI}_{\text{soot}}, \text{g kg}^{-1}$	$\text{PEI}_{\text{soot}}, 10^{15} \text{ kg}^{-1}$	SN at 100%	SN at 30%
B707	0.5±0.1	1.7±0.3	54.5	n.a.
ATTAS	0.1±0.02	1.7±0.35	46.3	10.9
A310	0.019±0.01	0.6±0.12	5.8	n.a.
B737	0.011±0.005	0.35±0.07	4	2.5
B747		0.27, 0.45	16.0	n.a.
DC10		0.46	11.4	1.6
A340	0.1±0.003	0.18±0.05	12.6	1.0

^a EI_{soot} and PEI_{soot} : soot mass and number emission indices per unit mass of fuel burned; smoke number (SN) at two power settings: 100% and 30%.

Thus, besides gaseous species such as H_2O , CO_2 , NO , NO_2 , SO_2 , SO_3 , CO , and HNO_2 , HNO_3 , OH , N_2O in a trace amount, aircraft plume is the source of small volatile sulfate aerosol particles, neutral and charged soot particles, which may be partly activated as CCN, as well as ice particles at the conditions of contrail formation (H_2O vapour supersaturation over the water surface is necessary to form a contrail).

AIRCRAFT ENGINE EMISSIONS AND ATMOSPHERIC PROCESSES

As is believed the most important gaseous pollutants impact on the ozone concentration in the atmosphere are NO , NO_2 , H_2O . Modeling studies showed that emissions of NO_x by aircraft into the stratosphere may result in ozone depletion. In contrast, the NO_x emissions into the troposphere lead to an increase of ozone concentration [2]. The quality of the effect of NO_x emissions on the atmospheric ozone depends on the surface area of sulfate stratospheric aerosol layer and polar stratospheric clouds.

In the published in 1998 paper [44] four independently formulated two-dimensional chemical transport models with sulfate aerosol microphysics are used to evaluate the possible effects of sulfur emissions from supersonic high-speed civil transport aircraft (HSCT) operating in the stratosphere in 2015. The aircraft emission scenarios employed in the estimations represented 500 aircrafts operating in the year 2015 and burning $82 \times 10^9\text{ kg}$ of fuel annually, with the geographical fuel use distribution derived in [45]. The HSCT aircraft cruise at Mach 2.4, which a cruise altitude of 18-21 km. Engine emissions are specified by an emission index. The results were presented for two values of EINO_x , 5

and 15 g/kg. An EINO_x of 5 g/kg represents a significant reduction in emission index from current supersonic aircraft (values of about 12-20 g/kg are typical), though technological advances in the last several years have shown that an EINO_x of 5 g/kg is achievable. EIH_2O of 1230 g/kg is used in all calculations. The EISO_2 was taken to be 0.4 g/kg, based on projections that sulfur content in jet fuel will decline from its current average value of 0.8 g/kg.

All models have shown much larger increases in aerosol surface area when aircraft sulfur was assumed to be emitted as particles of 10 nm diameter rather than as gas phase SO_2 . If it was assumed an emission index for SO_2 of 0.4 g (kg fuel burned) $^{-1}$ in 2015, maximum increases in stratospheric sulfate aerosol surface area range from 0.1 $\mu\text{m}^2\text{cm}^{-3}$ to 0.5 $\mu\text{m}^2\text{cm}^{-3}$ with sulfur emitted as SO_2 gas and from 1.0 $\mu\text{m}^2\text{cm}^{-3}$ to 2.5 $\mu\text{m}^2\text{cm}^{-3}$ with sulfur emitted as particles. Model differences in calculated surface area were deemed to be due mainly to differences in model transport. Calculated annual average ozone perturbations due to aircraft emissions with $\text{EINO}_x=5$ g/kg, $\text{EIH}_2\text{O}=1230$ g/kg, and $\text{EISO}_2=0.4$ g/kg varied from -0.1% to 0.6% at 45°N for sulfur emission as SO_2 gas and from -0.4% to -1.5% with sulfur emission as 100% particles. The variation in the ozone concentration due to HSCT emissions of SO_2 and sulfate particles of 10 nm diameter predicted by Atmospheric and Environment Research (AER) 2D model [44] is shown in Figure 14.

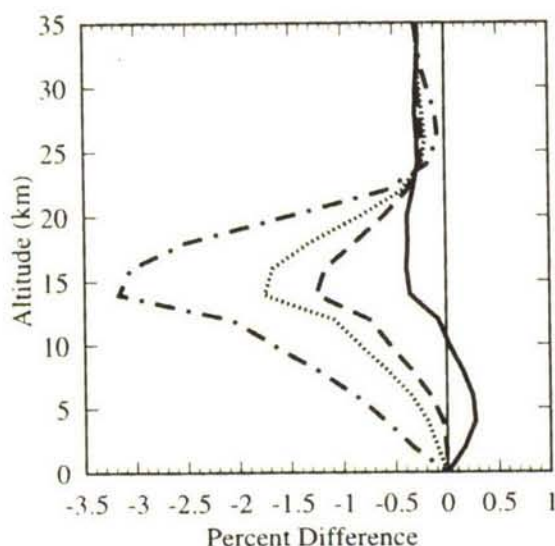


Fig. 14. Calculated percent change in the ozone concentration depending on the altitude due to HSCT emissions with a scenario: 500 aircrafts operate at cruise ($M=2$, $H=18$ km), $\text{EINO}_x=5$ g/kg, $\text{EIH}_2\text{O}=1230$ g/kg, $\text{EISO}_2=0.4$ g/kg, $[\text{Cl}_y]=3$ ppbv. The solid line represents a case with no SO_2 emissions, the dashed line represents a case with SO_2 gas emissions only, the dotted line represents a case with emissions 90% as SO_2 gas and emitted as 10%. Sulfate aerosols ($d=10$ nm), dot-dashed line represents a case with emissions of 100% sulfate aerosol particles ($d=10$ nm).

The authors of this paper strongly recommended for future analysis of HSCT impact on ozone to take into account in assessment calculations, the chemical and microphysical processes within the plume and far wake for accurate atmospheric modeling. IPCC (1999) pointed out that the future aerosol impact will depend on trends in fuel consumption, fuel sulfur content, engine soot emissions, and the efficiency with which fuel sulfur is transformed into aerosols behind the aircraft. Any aerosol increase will be enhanced if future air traffic operates at higher altitudes, because of longer atmospheric residence times of the emission products. Any climate change causing reduced temperature and increased humidity at flight levels would enhance aerosol and contrail formation.

Thus, the emissions of sulfate aerosol particles by aircrafts can significantly influence on the surface area of stratospheric aerosol layer and as a result on the radiative forcing as well as on the total ozone concentration. This exhibits the necessity of reasonable limitation on sulfate aerosol particles emitted. For modern aviation fuels the typical value of FSC does not exceed 400 μg or 0.04%. Therefore, we

can suggest for prospective jet engines the limitation standard for sulfate aerosol particle emission index of $(1-2) \cdot 10^{16} \text{ kg}^{-1}$.

The main source of carbon-containing particles in the atmosphere is the combustion of natural fuel and biomasses on the Earth's surface. Every year, up to 12 Tg of soot are emitted to the atmosphere [2]. The estimated value of soot emissions by aircraft for the year of 1992 is several orders of magnitude smaller 10^{-3} Tg. However, the role of surface sources at a height of 10 km may be insignificant because of a high activity of soot aerosols as CCN, their precipitation and washing from the lower troposphere. On the other hand, a constant increase in the frequency of aircraft flights gives grounds to predict an increase in the mass concentration of aviation soot aerosols exactly at a height of 10 km in northern latitudes. At the specified index of soot emission 0.04 g/kg , in the middle latitudes of the Northern Hemisphere, the annual maximum increase in the mass concentration of soot particles can reach 0.6 ng/m^3 [2].

According to the ICAO data, by 2050, a five-tenfold increase in the intensity of commercial flights is expected [2]. During the accumulation of soot particles in the troposphere owing to an increase in fuel consumption by aviation, the region covered with contrails is also increased. According to the prognosis given in [46], this region will be increased from 0.06 (1992) to 0.23% (2050), and, accordingly, the radiation effect of contrails will be increased by a factor of four (from 3.5 mW/m^2 to 14.8 mW/m^2). Unfortunately, the radiation effect of cirrus clouds initiated by aviation still remains to be estimated [2]. Even the sign of this effect has not been determined yet. However, it is clear that soot particles, unlike sulfate aerosols, can cause heating that leads to the cooling of the vertical temperature profile in the atmosphere, the slowing down of evaporation, and, correspondingly, to a decrease in cloud formation. Therefore, additional studies are necessary to estimate the effect of soot emissions by aviation on cloud formation and precipitation and to estimate the dependence of this effect on the physicochemical properties of aviation soot aerosols. Nevertheless, it is believed that in order to minimize the impact of aircraft flights on the atmosphere and especially on climate the limitation standard should be introduced for the soot particle emissions from prospective aircraft engines.

REFERENCES

1. D.J. Wuebbles, A. Jain, J. Edmonds, D. Harvey, K. Hayhoe, Global change: state of the science. *Environmental Pollution*. 1999, 100, 57-86.
2. D. W. Fahey, U. Schumann, S. Ackerman, P. Artaxo, O. Boucher, M. Y. Danilin, B. Kärcher, P. Minnis, T. Nakajima and O. B. Toon, in *Aviation and the Global Atmosphere, A Special Report of IPCC (Intergovernmental Panel on Climate Change)*, ed. J. E. Penner, D. H. Lister, D. J. Griggs, D. J. Dokken and M. McFarland, Cambridge University Press, Cambridge, UK. 1999, 65-120.
3. U. Lochman, J. Feitcher *Atmos. Chem. Phys.* 2005, 5, 715-737.
4. R.P. Lindstedt and L.Q. Maurice A detailed chemical kinetic model for aviation fuels. *J. Propulsion and Power*. 2000, 16, 187-195.
5. L.Q. Maurice, Detailed chemical kinetic model for aviation fuels, Ph. D. Thesis, Univ. Of London, Imperial College, Mechanical Engineering Dept., London, England, UK, 1996.
6. C. Doute, J.-L. Delfan, R. Akrieh, and Vocell, *Comb. Sci. Technol.* 1995, 106, 327-341.
7. A.M. Starik, A.M. Savel'ev, N.S. Titova, and U. Schumann, *Aerosp. Sci. Technol.* 2002, 6, 63-81.
8. U. Schumann, J. Ström, R. Busen, et al., *J. Geophys. Res.* 1996, 101, 6853-6899.
9. B. Kärcher, F. Yu, F.P. Schröder, and R.P. Turco, *Geophys. Res. Lett.* 1998, 25, 2793-2796.
10. S.P. Lukachko, I.A. Waitz, R.C. Miake-Lye et al., *J. Geophys. Res.* 1998, 103, 16159-16174.
11. A.M. Savel'ev, and A.M. Starik, *Fluid Dynamics*. 2001, 36, 95-103.
12. P. Schulte, H. Schlager, H. Ziereis, et al., *J. Geophys. Res.* 1997, 102, 21431-21442.
13. U. Schumann, H. Schlager, F. Arnold et al., *J. Geophys. Res.* 2000, 105, 3605-3631.
14. A.B. Lebedev, A.N. Secundov, A.M. Starik, S.A. Schepin, N.S. Titova In *Nonequilibrium processes: Combustion and Detonation*. Ed. G.D. Roy, S.M. Frolov, A.M. Starik. Moscow. Torus Press Ltd. 2005, 1, 158-167.
15. Prather M.J., Wesoky H.L., R.C. Miake-Lye and et al. *The Atmospheric Effects of Stratospheric Aircraft: A First Program Report*. NASA Reference Publication 1272. 1992.
16. G.P. Smith, D.M. Golden, M. Frenklach, N.W. Moriarty, B. Eiteneer, M. Goldenberg, C.T. Bowman, R.K. Hanson, S. Song, W.C. Gardiner, V.V. Lissianski, Z. Qin http://www.me.berkeley.edu/gri_mech/
17. A.A. Konnov Detailed reaction mechanism for small hydrocarbons combustion. 1998. Release 0.4 <http://homepages.vub.ac.be/~akonnov>.
18. N.G. Dautov and A.M. Starik, *Kinetics and Catalysis*. 1997, 38, 185-208.
19. A.B. Fialkov, *Prog. Energy Combust. Science*. 1997, 23, 339-528.
20. F. Yu, R.P. Turco, *J. Geophys. Res.* 1998, 103, 25.915-25.934.
21. A.M. Savel'ev and A.M. Starik, *Tech. Phys.* 2006, 51, 444-452.
22. P. Weilmuster, A. Keller, K.H. Homan, *Combust. Flame*. 1999, 116, 62-83.
23. A. Kiendler, St. Aberle, F. Arnold, *Atmos. Environ.* 2000, 34, 2623-2632.
24. J.M. Rodrigues, A. Agneray, X. Jaffrézic et al. *Plasma Sources Sci. Technol.* 2007, 16, 161-172.
25. H. Haverkamp, S. Wilhelm, A. Sorokin, and F. Arnold. *Atmos. Environ.*, 2004, 38, 2879-2884.
26. N. Peters. *Turbulent Combustion*, N.-Y.: Cambridge University Press. 2000.
27. A.M. Starik, A.M. Savel'ev and N.S. Titova *Proceedings of Second International Workshop on Cold Atmospheric Pressure Plasmas: Sources and Applications*. Bruges, Ghent University. 2005, 118-122.
28. *Soot Formation in Combustion: Mechanisms and Models*, Ed. by H. Bockhrom. Springer, Berlin. 1994.
29. D.D. Huang, J.H. Seinfeld, and K. Okuyama. *J. Colloid and Interface Science*. 1991, 141, 191-198.

30. A.M. Starik, O.B. Popovicheva, A.M. Savel'ev, N.S. Titova, O.E. Reyn Chemical Engineering Transaction. Proceedings of Advanced Atmospheric Aerosol Symposium. Ed. by E. Ranzi. 2006, 10, 541-546.
31. O.B. Popovicheva, N.M. Persiantseva, E.E. Loukhovitskaya et al. Geoph. Res. Lett. 2004, 31, L11104, doi: 10.1029/2003GL018888.
32. A.M. Starik, A.M. Savel'ev, N.S. Titova, O.E. Reyn. In Combustion and Atmospheric Pollution. Ed. by G.D. Roy, S.M. Frolov, A.M. Starik, Moscow Torus Press. 2003, 470-473.
33. S. Böckle, S. Einecke, F. Hildenbrand et al. Geophys. Res. Lett. 1999, 26, 1849-1852.
34. U. Schumann, H. Schlager, F. Arnold et al. J. Geophys. Res. 2000, 105, 3605-3631.
35. F. Arnold, K.H. Wohlfrom, M.W. Klemm et al. Geophys. Res. Lett. 1998, 25, 2137-2140.
36. A. Kiendler and F. Arnold, Atmosph. Environment. 2002, 36, 2979-2984.
37. U. Schumann, F. Arnold, R. Busen et al. J. Geophys. Res. 2002, 107, 10.1029/2001JD000813.
38. A.M. Starik, A.M. Savel'ev, N.S. Titova, E.E. Loukhovitskaya, and U. Schumann. Phys. Chem. Chem. Phys. 2004, 6, 3426-3436.
39. A. Petzold, A. Dopelheuer, C. Brock, F. Schroder. J. Geophys. Res. 1999, 104, 22171-22181.
40. R.C. Brown, R.C. Miake-Lye, M.R. Anderson, C.E. Kolb. Geoph. Res. Lett. 1996, 23, 3607-3610,
41. F.P. Schröder, B. Kärcher, A. Petzold et al. Geoph. Res. Lett. 1998, 25, 2789-2792.
42. F. Arnold, K.H. Wohlfrom, M.W. Klemm, J. Schneider, K. Gollinger, U. Schumann and R. Busen. Geophys. Res. Lett. 1998, 25, 2137.
43. N.K. Shonija, O.B. Popovicheva, N.M. Persiantseva, A.M. Savel'ev, and A.M. Starik. J. Geophys. Res. 2007, 112, D02208, doi:10.1029/2006JD007217.
44. D.K. Weisenstein, M.K.W. Ko, I.G. Dyominov et al. J. Geophys. Res. 1998, 103, 1527-1547.
45. S.L. Baughcum, S.C. Henderson Aircraft emission scenarios projected in year 2015 for the NASA technology concept aircraft (TCA) high speed civil transport. NASA/CR-1988-207635, National Aeronautics and Space Administration, Hampton, VA, 1998. 21 p.
46. S. Marquart, M. Ponater, F. Marger, and R. Sausen. "Future Development of Contrails: Impact of Increasing Air Traffic and Climate Change" in Air Pollution Report No.83 "Aviation, Atmosphere, and Climate" EC, 2003, 255-260.